Proceedings

of the

Seventh International Workshop

on

Dynamics and Aeroelastic Modeling of Rotorcraft

October 14-16, 1997

Holiday Inn Clayton Plaza

St. Louis, Missouri

	Report Documentation Page		*Form Approved* *OMB No. 0704-0188*

Public reporting burden for the collection of information is estimated to average 1 hour per response, including the time for reviewing instructions, searching existing data sources, gathering and maintaining the data needed, and completing and reviewing the collection of information. Send comments regarding this burden estimate or any other aspect of this collection of information, including suggestions for reducing this burden, to Washington Headquarters Services, Directorate for Information Operations and Reports, 1215 Jefferson Davis Highway, Suite 1204, Arlington VA 22202-4302. Respondents should be aware that notwithstanding any other provision of law, no person shall be subject to a penalty for failing to comply with a collection of information if it does not display a currently valid OMB control number.

1. REPORT DATE **OCT 1997**	2. REPORT TYPE	3. DATES COVERED **14-10-1997 to 16-10-1997**

4. TITLE AND SUBTITLE	5a. CONTRACT NUMBER
Proceedings of the Seventh International Workshop on Dynamics and Aeroelastic Modeling of Rotorcraft held in St. Louis, Missouri on 14-16 October,1997	5b. GRANT NUMBER
	5c. PROGRAM ELEMENT NUMBER
6. AUTHOR(S)	5d. PROJECT NUMBER
	5e. TASK NUMBER
	5f. WORK UNIT NUMBER
7. PERFORMING ORGANIZATION NAME(S) AND ADDRESS(ES) **U.S. Army Research Office,P.O. Box 12211,Research Triangle Park,NC,27709-2211**	8. PERFORMING ORGANIZATION REPORT NUMBER
9. SPONSORING/MONITORING AGENCY NAME(S) AND ADDRESS(ES)	10. SPONSOR/MONITOR'S ACRONYM(S)
	11. SPONSOR/MONITOR'S REPORT NUMBER(S)

12. DISTRIBUTION/AVAILABILITY STATEMENT
Approved for public release; distribution unlimited

13. SUPPLEMENTARY NOTES

14. ABSTRACT

15. SUBJECT TERMS

16. SECURITY CLASSIFICATION OF:			17. LIMITATION OF ABSTRACT	18. NUMBER OF PAGES	19a. NAME OF RESPONSIBLE PERSON
a. REPORT **unclassified**	b. ABSTRACT **unclassified**	c. THIS PAGE **unclassified**	**Same as Report (SAR)**	**624**	

Standard Form 298 (Rev. 8-98)
Prescribed by ANSI Std Z39-18

Invited Papers

An investigation of stall
on a 4.2m diameter experimental rotor

(D Petot / ONERA)

ABSTRACT

Stall on helicopter rotors has been investigated on a classical 4.2 m diameter model tested in the Modane S1 wind-tunnel on which large thrust coefficients could be obtained. The interest of this test lies in the fact that the model was very thoroughly instrumented with strain gauges and pressure transducers so that detailed investigations could be carried out.

Stall was taken into account in the calculations through two versions of the ONERA dynamic stall model. These models have been fitted to classical 2D wind tunnel tests independent from the rotor test prior to their use on the rotor. During this procedure, a hypothesis used in the linear model had to be refined and one of the objective of this paper is to describe this.

The ONERA dynamic stall models were tuned to 2D unsteady loops and then run on the experimental configurations. Results were compared to experiment.

On the average, calculations led to a well predicted general behavior of the stalled rotor, even if some flaws in the calculations were encountered and corrected. More important is the presence of a very strong unexpected negative moment at the mid-span of the retreating blade that was not reproduced by the models issued from 2D unsteady tests. This phenomenon needs further investigation to achieve reliable predictions of vibration.

1. INTRODUCTION

The confrontation of predictions with the Modane rotor test was presented at the European Rotorcraft Forum at Dresde in september 97 (ref 1). Results came from several research centers and manufacturers. This collaborative published work must be acknowledged for the help it brought to reach a number of important conclusions.

The objective of this paper is to show more in detail the ONERA results on the Modane rotor as well as to present a refinement that had to be introduced in the ONERA.Edlin model which is fairly widely used today.

ONERA results are not exactly the same here as in the European forum paper because wind tunnel corrections are added. These were not used in the collaboration to ensure that all the participants work with the same hypotheses. Moreover the blade finite element analysis used at the time produced such a strong a torsion / flapping coupling for this nearly straight blade, that it had to be replaced.

2. ONERA MODELS

2.1. The comprehensive rotor code

All the calculations were performed with ROTOR which is an ONERA code (ref 2). This comprehensive code can take into account many helicopter parameters including fuselage degrees of freedom. The Modane rotor were equipped with articulated blades fitted with parabolic tips. No particular computing problems were encountered for this application.

The code has several aerodynamic options, the more advanced being the ONERA dynamic stall models. These can be described as mathematical tools that reproduce the behavior of the non-stalled and stalled flow through differential equations. Two versions exist: The ONERA.Edlin model which uses linear differential equations and the more elaborate ONERA.BH model which uses a Van der Pol equation.

2.2. The ONERA.Edlin model (ref 3)

2.2.1. Non stalled flow

For the unstalled flow the dynamic model for lift can be summarized by:

$$C\dot{z} + \lambda Cz = \lambda Cz_S + b\dot{\theta} + s\ddot{\theta}$$

In fact more terms exist. These take into account heaving motion and the unsteady free stream. The equation is fitted to Theodorsen's equations at zero Mach number and to theoretical results for compressible flow. This model has always led to very good results when compared to experiment, even at very high reduced frequencies. As for Theodorsen, a differential equation was not needed for the moment which keeps an explicit form.

2.2.2. Stalled flow

The stalled flow is modelled as a correction to the non stalled regime. Small amplitude tests have shown that its behavior obeys a second order equation. The global set of equations thus has the following form:

$$Cz = Cz_1 + Cz_2$$

$$C\dot{z}_1 + \lambda Cz_1 = \lambda Cz_L + b\dot{\theta} + s\ddot{\theta}$$

$$\ddot{z}_2 + aC\dot{z}_2 + rCz_2 = -[r\Delta Cz + E\dot{\theta}]$$

where Cz_L stands for the general linear static curve (extended in the stalled domain) and ΔCz is the steady correction to be added to Cz_L in order to obtain the true steady curve Cz_S, see fig 1. ΔCz is a measure of stall and the equations' parameters may depend from it.

2.2.3. Transition

The static stall angle is the point were the non-stalled regime is no longer stable and skips to the stalled regime. This equilibrium point is of course sensitive to parameters, particularly to pitch velocity. Its position is modeled through the classical stall delay proposed by BEDDOES which is assumed constant when expressed in reduced time. In order to achieve this, the measure of stall, ΔCz, is simply kept at a zero value until the stall delay has passed, as shown in fig 2.
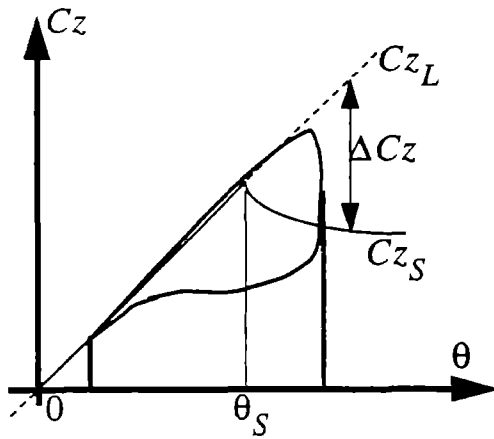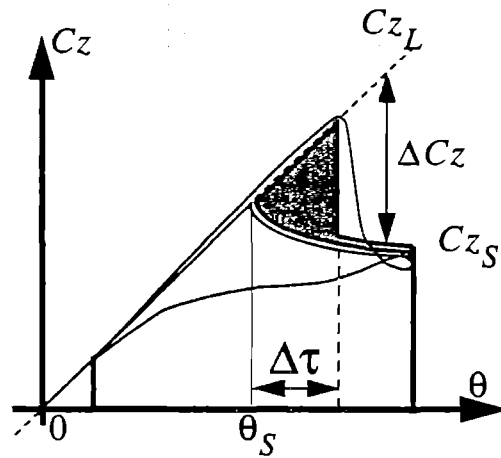
Fig 1: Definition of the steady terms

Fig 2: Taking stall delay into account

2.2.4. Refining the transition

To date, the model previously described has worked properly. The differential equation can be considered as the spring, mass and damper that describe the motion of Cz versus time, pulling it toward the quasi-steady position. Thus, neither lift nor moment can go too far from the quasi-steady curves (at least at the usual reduced frequencies).

The use of airfoils with more lift capabilities has brought severe negative Cm values at the onset of stall which are beyond the reach of classical differential equations (see moment on Fig 3 below). This is why the non linear differential equation model has been developed.
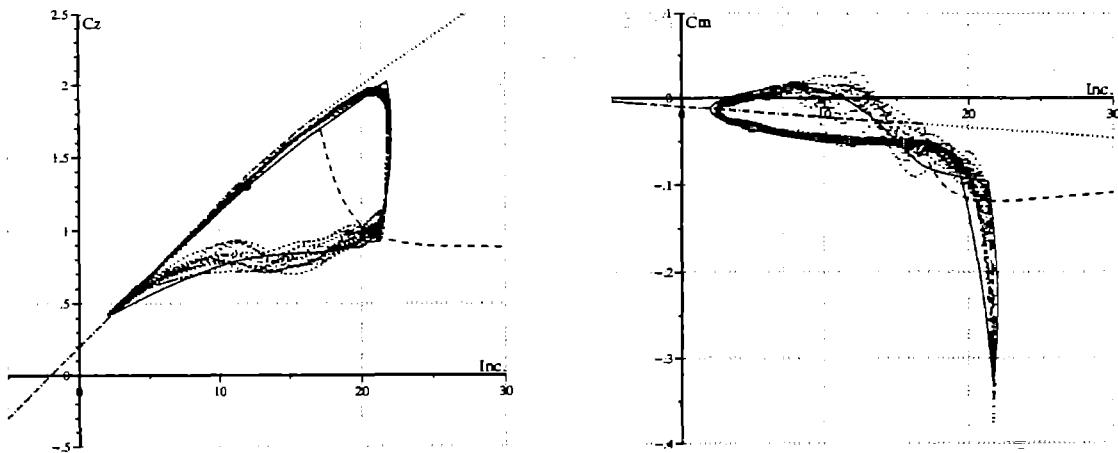
Fig 3: Dynamic stall on the OA213 airfoil

The lift correction used can be considered as an additional lift brought by unsteady stall. It was implicitly supposed in the earlier version of the model that this increase of lift capability created no moment and thus occurred right on the first quarter-chord of the airfoil. The very negative moment that is encountered on some airfoils shows that this is not always true.
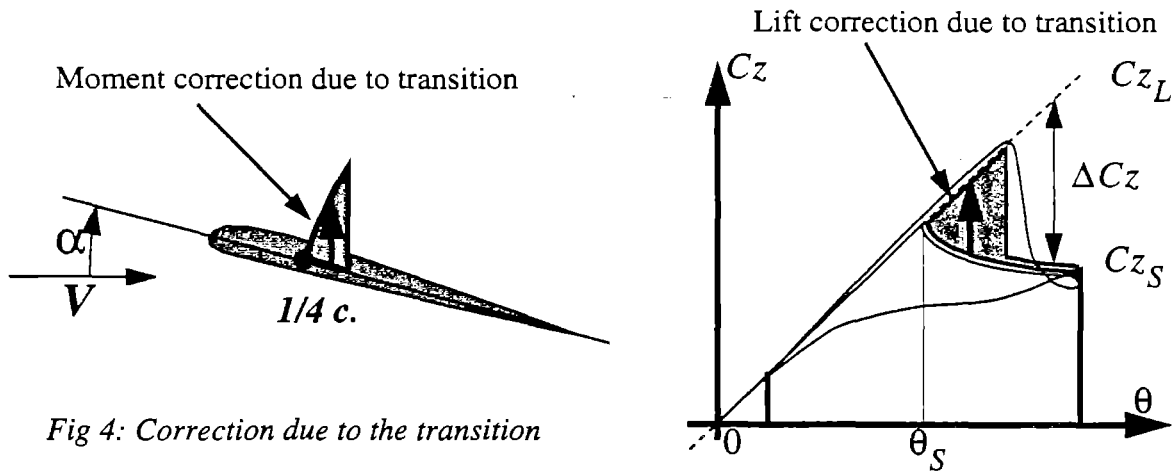
Fig 4: Correction due to the transition

The correction to the Edlin model consists simply in letting this additional lift be convected down the stream, at a small velocity which becomes a new parameter in the model. The use of a zero value of velocity reproduces the previous version of the model.

2.3. ONERA.BH model (ref 4)

The BH model is an advanced version of the ONERA.Edlin model. It uses the same principle by modelling the non-stalled regime, the stalled regime and the transition. Its main difference with the previous model lies in the global treatment of the different aerodynamic corrections (which are outside the Edlin model) and the use of a Van der Pol equation for stall conditions.

2.3.1. Non-stalled flow

The same equation is valid but the Cz_L term is replaced by a Cz_S term which takes into account the various aerodynamic corrections. Part of these corrections follow the description of the LEISHMAN-BEDDOES model. This allows to take into account the pre-stall behavior which is often simplified in the Edlin model.

$$C\dot{z} + \lambda Cz = \lambda Cz_S + b\dot{\theta} + s\ddot{\theta}$$

2.3.2. Stalled flow

The second order equation is replaced by a Van der Pol equation which characterizes the behavior of systems with transitions (the model name BH stands for "Hopf Bifurcation"). Lift (and moment) are given by expressions of the following type:

$$\begin{cases} Cz = Cz_1 + Cz_2 \\ C\dot{z}_1 + \lambda Cz_1 = \lambda Cz_S + b\dot{\theta} + s\ddot{\theta} \\ C\ddot{z}_2 - \omega\left(b - g \cdot Cz^2\right)C\dot{z}_2 + \omega^2 Cz_2 = -[E\dot{\theta} + D\ddot{\theta}] \end{cases}$$

When stall occurs, a non-linear $Cz_2^2 \cdot C\dot{z}_2$ term appears. The expression $\omega\left(b - g \cdot Cz^2\right)C\dot{z}_2$ induces the oscillations at the ω Strouhal frequency that can be seen on the calculated large amplitude loops. The parameter b then takes a negative value which is responsible for the swift response.

2.3.3. Transition

Transition is accounted for, as in the LEISHMAN-BEDDOES model, by a stall delay which includes both yaw and rotation effects.

3. AIRFOIL 2D TESTS

3.1. Experiment

Tests were carried out on a OA213 airfoil instrumented with 30 pressure transducers. The Mach number was left at the low value of 0.18. Lift and moment were measured on large amplitude oscillations, with no sweep as well as with a 22° sweep.

Measurements were performed with no averaging and several consecutive loops are shown in dotted lines in this paper.

3.2. Dynamic stall model tuning

- Cz loops (Fig 5a): The behavior of the 2 models can be clearly seen: The ONERA.Edlin is too simplified just ahead of the transition point and oscillations present in the experiment are seen with the ONERA.BH model in the stalled regime. Enough information is present in both models for the rotor analysis.
- Cm loops (Fig 6a): The negative peak of Cm is sharp in the Edlin model. It is smoother and comes along with the Strouhal oscillations in the BH model. Here also modelling seems complete enough to be used on a rotor.
- Loops with 22° sweep (Fig 5b and 6b): There is a problem here. The Edlin model uses the classical yaw correction in order to deal with sweep. It is obvious that this correction is not satisfactory here. On the other hand the BH model has its own build-in corrections for yaw and thus has the degrees of freedom to adapt to the measured loops and has the ability to adapt to experiment.

3.3. Conclusions

- No sweep:
  - The BH model with the larger number of parameters gives a better fit,
  - The BH model takes the vortex shedding effects into account,
  - Enough features seem present in all the results for a full rotor analysis.
- 22° sweep:
  - The airfoil does not behave as expected according to the classical sweep correction,
  - The BH model with its built-in yaw corrections is reasonably successful in reproducing the experimental results.

4. ROTOR TEST (4.2m diameter)

4.1. Experiment

The experiment was carried out collaboratively by Eurocopter and ONERA. The test took place in the ONERA S1 wind tunnel in Modane.

The rotor is 4 bladed and has a diameter of 4.2m. The blades are articulated and have parabolic swept tips. The chord inboard from the tip measures 0.14m. An OA213 section (13% thick) is used from the root to 75%R and a OA209 section (9% thick) from 90%R to the blade tip. Between these radii, the section is interpolated.

The blades are instrumented with pressure transducers (5 sections) and strain gauges (a total of 30 in flapwise and chordwise bending and in torsion). These strain gauges were used to measure the blade torsion through a strain pattern analysis.

High thrust coefficients were obtained (up to $C_T/\sigma = 0.125$) by using a slightly reduced rotational speed.

The calculated results will be shown in the Fig 7 to 11 along with the set of experimental measurements obtained at a thrust coefficient varying from 0.075 to 0.125 and an advance ratio of 0.40 . This shows the excellent experimental continuity obtained. Good duplication was also obtained during different test campaigns.

4.2. Calculation hypothesis

The calculations used the "official" Mach dependant quasi-steady curves of the two airfoil sections together with the unsteady parameters derived from the single OA213 2D test. They were performed with a classical prescribed wake (METAR from Eurocopter).

4.3. Calculations versus tests

• Cz (Fig 7): Cz is shown versus rotor thrust and blade radius. Starting from the blade tip, it is obvious that a secondary peak of Cz appears before the end of the stalled domain. It is prominent at 70%R and merges into a very large Cz peak at 50%R.

  Both dynamic stall models reproduce the blade unsteady behavior, the stall delay and the very large Cz values for R<50%. These large values come from unsteady linear terms proportional to the incidence derivative which is huge here because of the very large incidence angles (up to 50° at 270° azimuth and 50%R) and the very high reduced frequency (0.25) induced by the low Mach number.

  The results would thus be very satisfactory if the model had reproduced the large second Cz peak mentioned above. The resulting imbalance of the rotor is weak ($Cz.M^2$ is small), but it will be shown that this phenomenon has a more important effect on moment.

• $Cz.M^2$ (Fig 8): Excellent results are obtained. The rotor has a good equilibrium. The large peak of Cz ignored by the models is greatly reduced here and appears at 70%R and 82%R around azimuth 300°.

• Cm (Fig 9): The calculations stall a little late. The peak of Cm at the onset of stall is there with the dynamic stall models working well, but the same remark as for the Cz can be made: a large secondary peak of Cm appears below 82%R at azimuth 300°, which is not found in the calculations. The large values of Cm obtained at 50%R centered at azimuth 270° are due to the linear unsteady terms. They are negligible due to the low Mach number present here.

• $Cm.M^2$ (Fig 10): The $Cm.M^2$ curves are the most disappointing. All the problems merge here:

  -- As the onset of stall is far from azimuth 270°, it is associated with non negligible Mach numbers and a very strong pitching moment excitation exists inboard of 50%R which is totally absent from the calculations. The same remark is true for the secondary peak of Cm.

  -- A very negative value is measured at azimuth 120°. It might be due either to a wrong steady Cm, or to underestimated unsteady effects. Hover tests cannot solve this problems because they cannot be performed at a high enough Mach number,

  -- A positive value is measured at azimuth 180°. This might also be due to an incorrect steady curve or to a sweep effect. The unsteady effects should be weak here.

The two previous points add up to give a poor description of the aerodynamic moment. As the non-stalled unsteady linear model usually reproduce the experiment well (see Fig 6), some doubts arise on the true steady curves of the tested rotor.

• Blade torsional moment (Fig 11): it is satisfying to notice that the blade moments are in agreement with the Cm results. The blade moment at 75%R shows a positive tendency at 45° and 180° azimuths which the calculations cannot account for. On the other hand, the negative peak due to stall is predicted, although not sufficiently prominently.

As expected, a large moment peak appears inboard of 50%R due to the violent onset of stall which the model is unable to reproduce.

• Blade torsion (Fig 12): experimental blade torsion is not available for $C_T/\sigma=0.125$. Calculations suggest that the torsion here would simply be an amplification of the $C_T/\sigma=0.113$ measured torsion. The torsion obtained at $C_T/\sigma=0.113$ is consistent with the Cm at the blade tip: the calculated torsion is too negative at azimuth 45° and 180°, while a 1° torsion at the onset of stall is effectively predicted. The unexpected moment at 50%R is not important for torsion. Oscillation damping is consistent with the experiment.

• Flapping and lead-lag (Fig 13): flapping is predicted very well by the ONERA.Edlin model. As there is no reason why the ONERA.BH model should not give the same results, one may conclude that the correction due to yaw forced on the BH model by the 2D test has somehow unbalanced the rotor.

• Chord deflection and pitch-link loads (Fig 13): pitching moment predictions are useful for the calculation of the pitch link loads. Although a strong pitching moment exists at the onset of stall, it may be seen here that the pitch link loads are rather dominated by the chordwise deflection of the blade which reaches a value of one full chord at azimuth 120°, far more than the aerodynamic offset brought by stall.

5. CONCLUSIONS

The high quality of the measurements has led to a good understanding of the behavior of this rotor. Positive results were obtained with the prediction tools:

• The comprehensive code reproduced the overall equilibrium of the rotor quite well at very high loads,

• The dynamic stall models performed correctly at the reasonable amplitudes and low reduced frequencies for which they were tuned.

These good results allow a good identification of the difficulties that still subsist:

• The calculated blade moment lacks the very strong aerodynamic moment at mid-span of the retreating blade, a point that needs further investigation,

• The unstalled blade moment displays an unexpected behavior, as if the quasi-steady curves used by the calculation were distorted. This might in fact be true, but some unsteady wind velocity effects could play a role on the advancing blade as well as yaw effects on the fore position of the blade. Analysis of hover conditions could partly settle the problem.

• Blade torsion is sensitive to rotor thrust in the calculations with these parabolic tip blades. Careful blade modelling is necessary,

• The classical yaw correction was not satisfactory on the 2D tests. This point needs to be clarified in the future.

6. REFERENCES

Réf 1 -   D. PETOT, G. ARNAUD, R. HARRISON, J. STEVENS, D. TEVES, B.G. Van der WALL, C. YOUNG, E. SZECHENYI - *Stall Effects and Blade Torsion - An Evaluation of Predictive Tools* - 23rd European Rotorcraft Forum - Dresden, September 97.

Réf 2 -   D. PETOT, J. BESSONE - *Numerical Calculation of Helicopter Equations and Comparison with Experiment* - 18th European Rotorcraft Forum - Avignon - Septembre 92.

Réf 3 -   D. PETOT - *Differential Equation Modelling of Dynamic Stall*, La Recherche Aérospatiale n°5, September 89. (If interested, please ask the author for an errata page for this paper)..

Réf 4 -   VK TRUONG - *Prediction of Helicopter Airloads Based on Physical Modelling of 3D Unsteady Aerodynamics* - 22nd European Rotorcraft Forum - Brighton - September 96.

OA213 Airfoil lift / No sweep

OA213 Airfoil lift / Sweep = 22deg

ONERA.Edlin model · ONERA.BH model · ONERA.Edlin model · ONERA.BH model
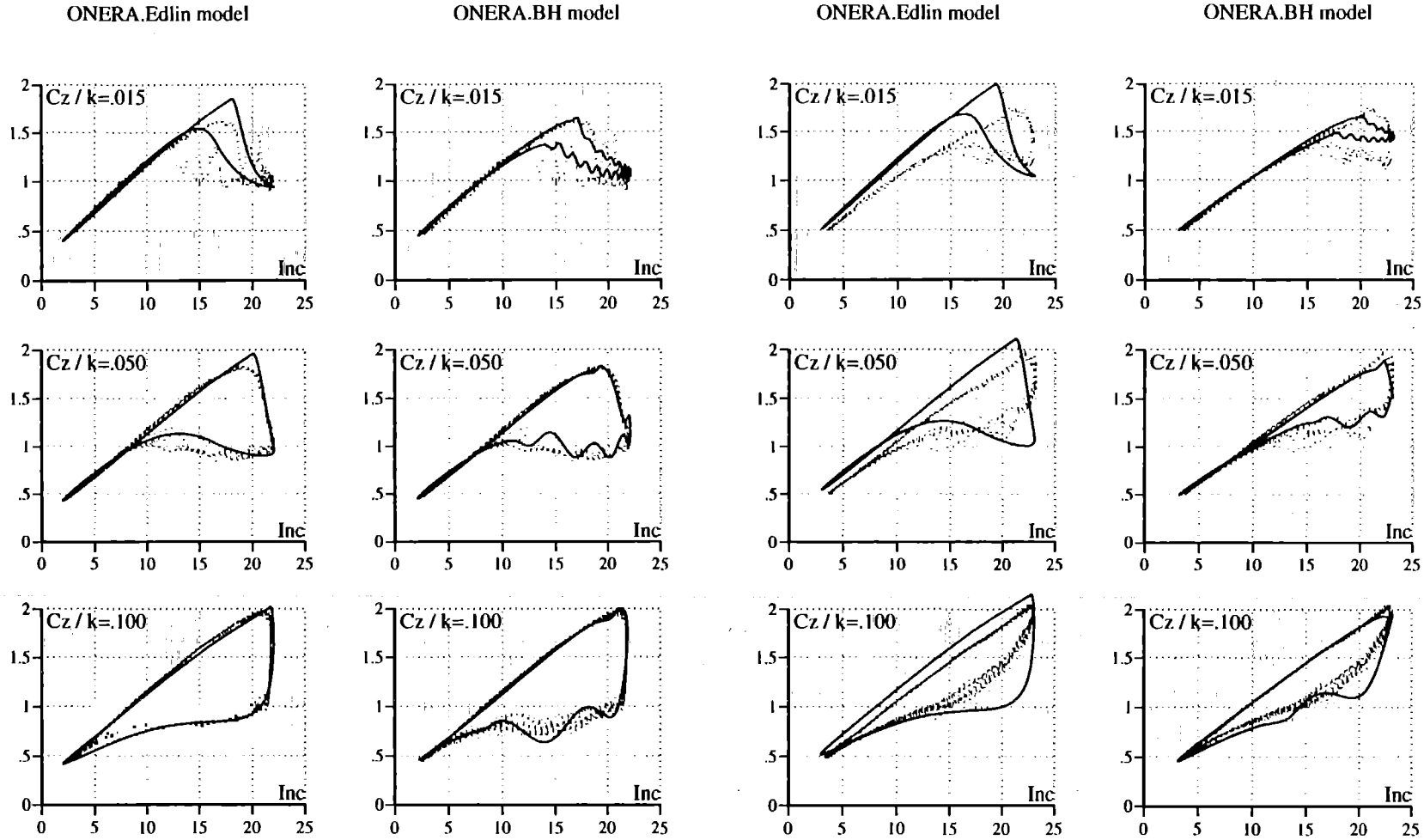
Fig 5: Lift coefficient for OA213 large amplitude loops, with and without sweep (dots = experiment)

OA213 Airfoil moment / No sweep

OA213 Airfoil moment / Sweep = 22deg

ONERA.Edlin model

ONERA.BH model

ONERA.Edlin model

ONERA.BH model
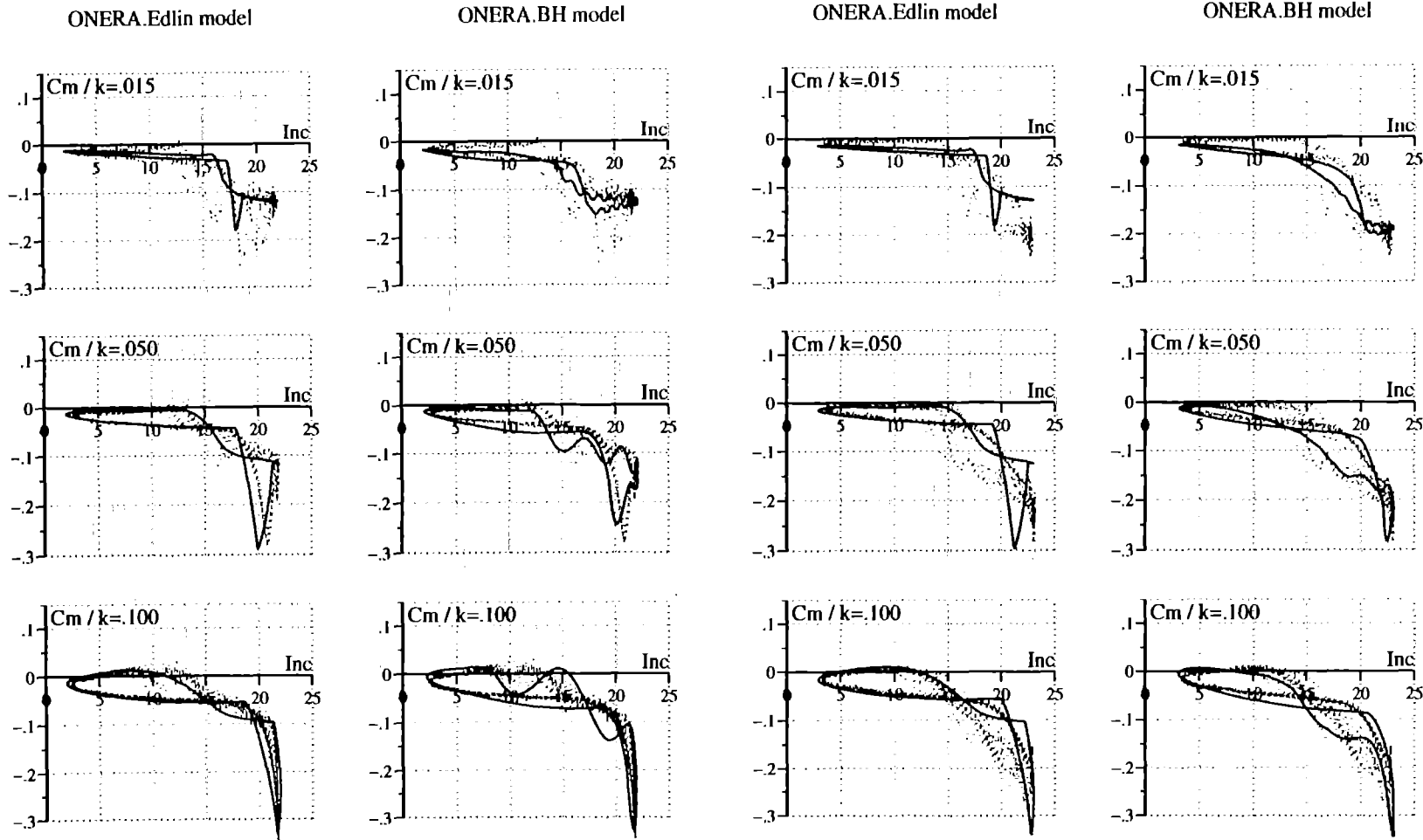
Fig 6: Moment coefficient for OA213 large amplitude loops with and without sweep (dots = experiment)
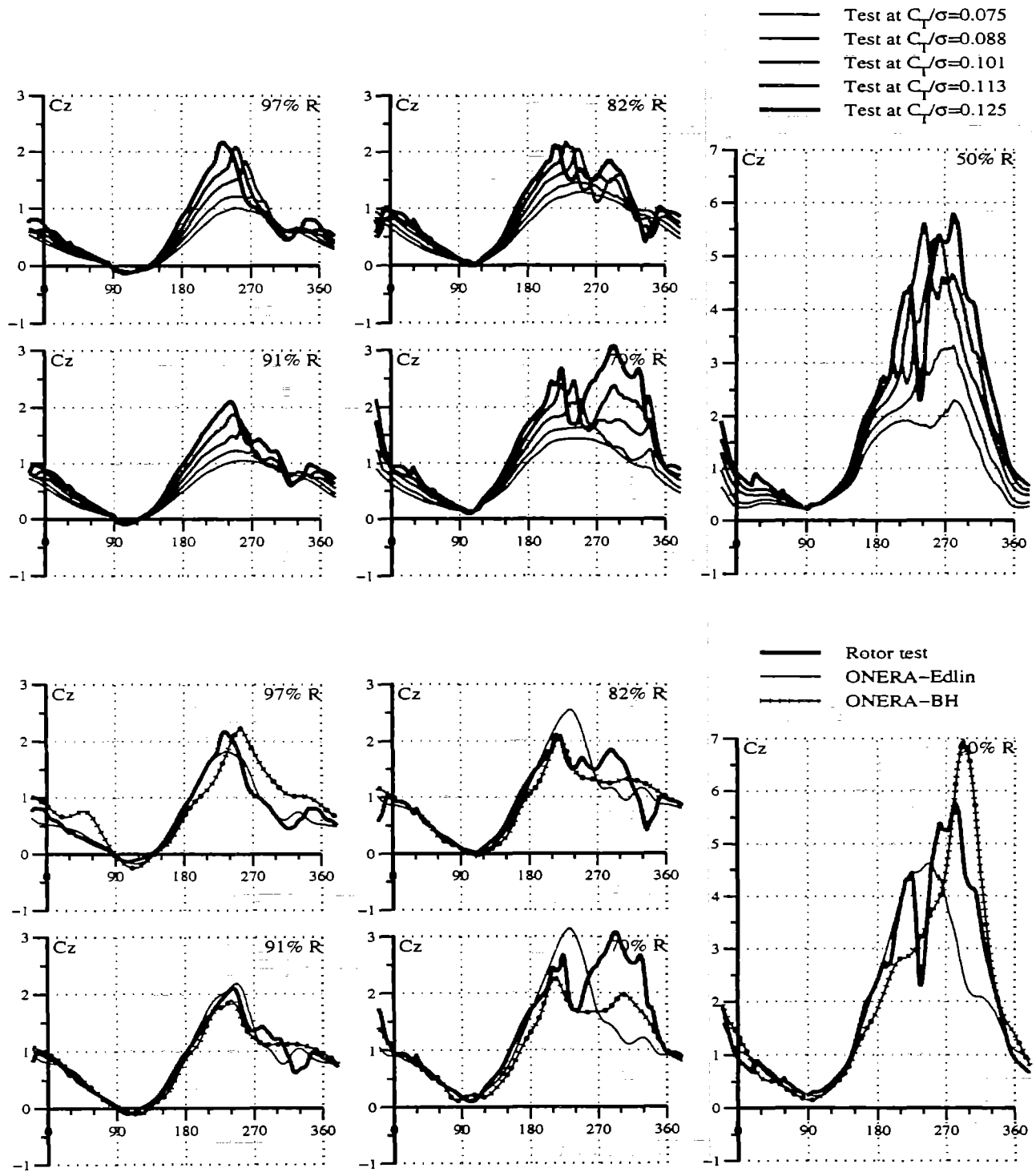
Fig 7: Measured and calculated lift coefficient
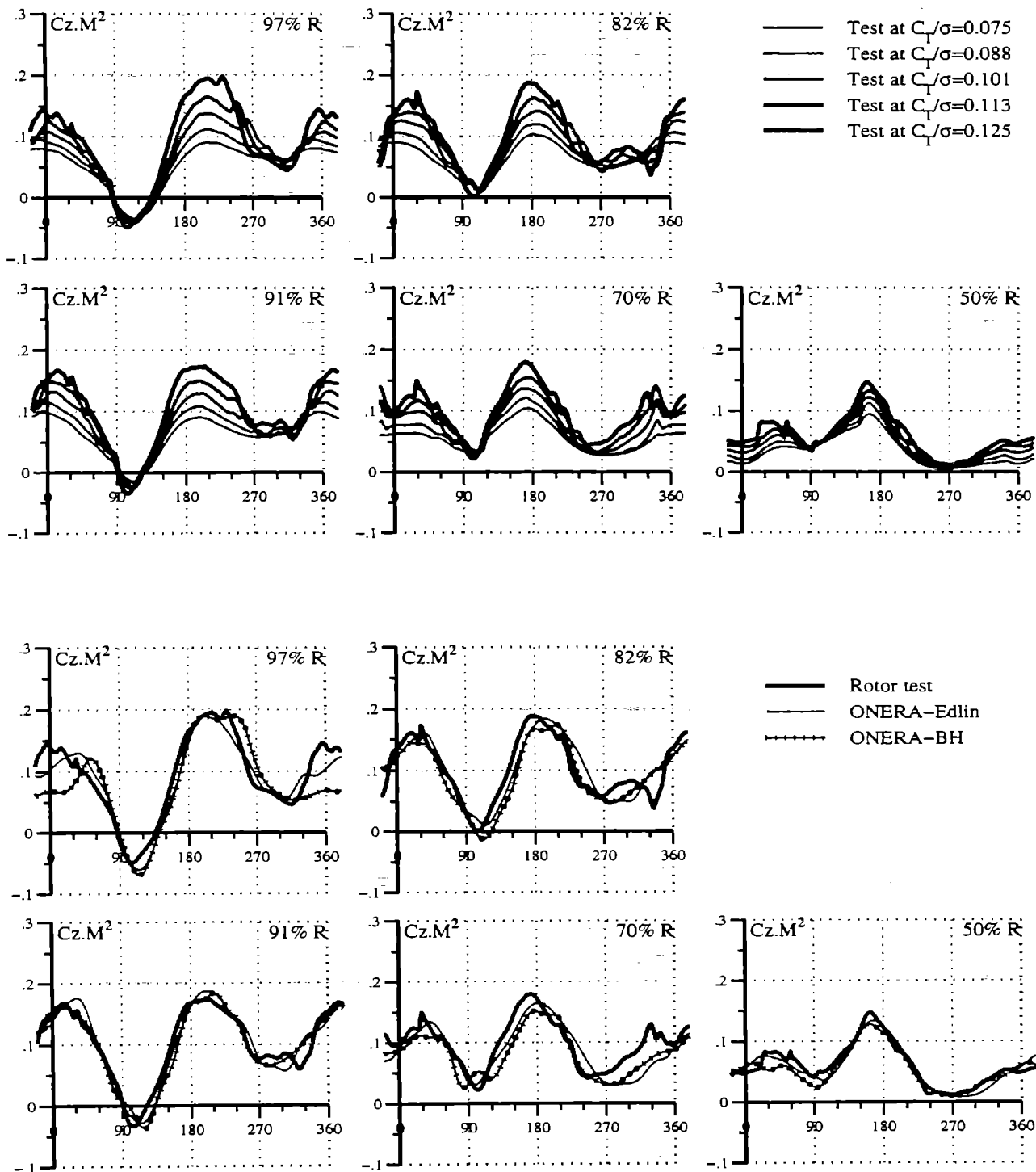
Fig 8: Measured and calculated lift coefficient*Mach²
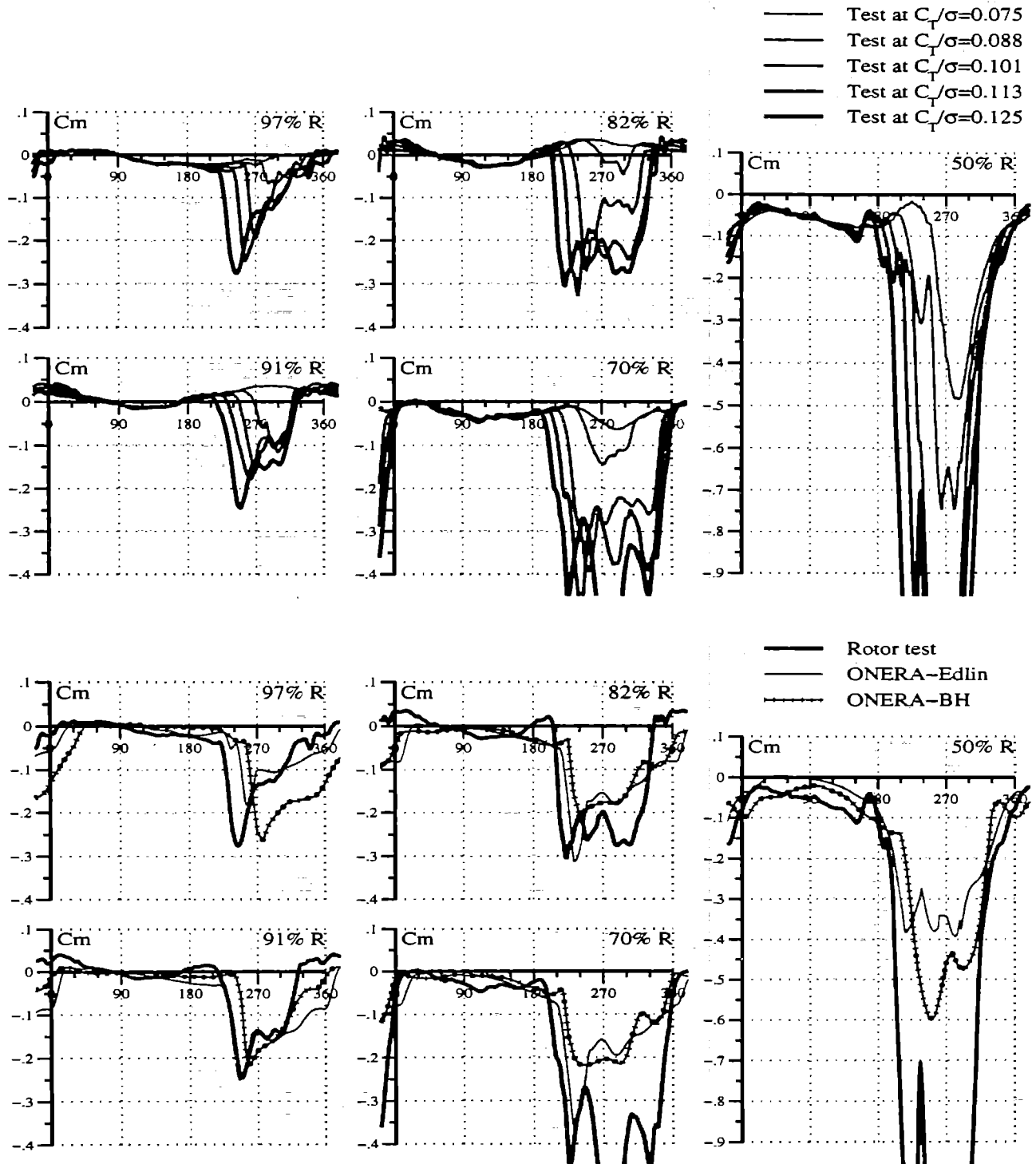
Fig 9: Measured and calculated moment coefficient
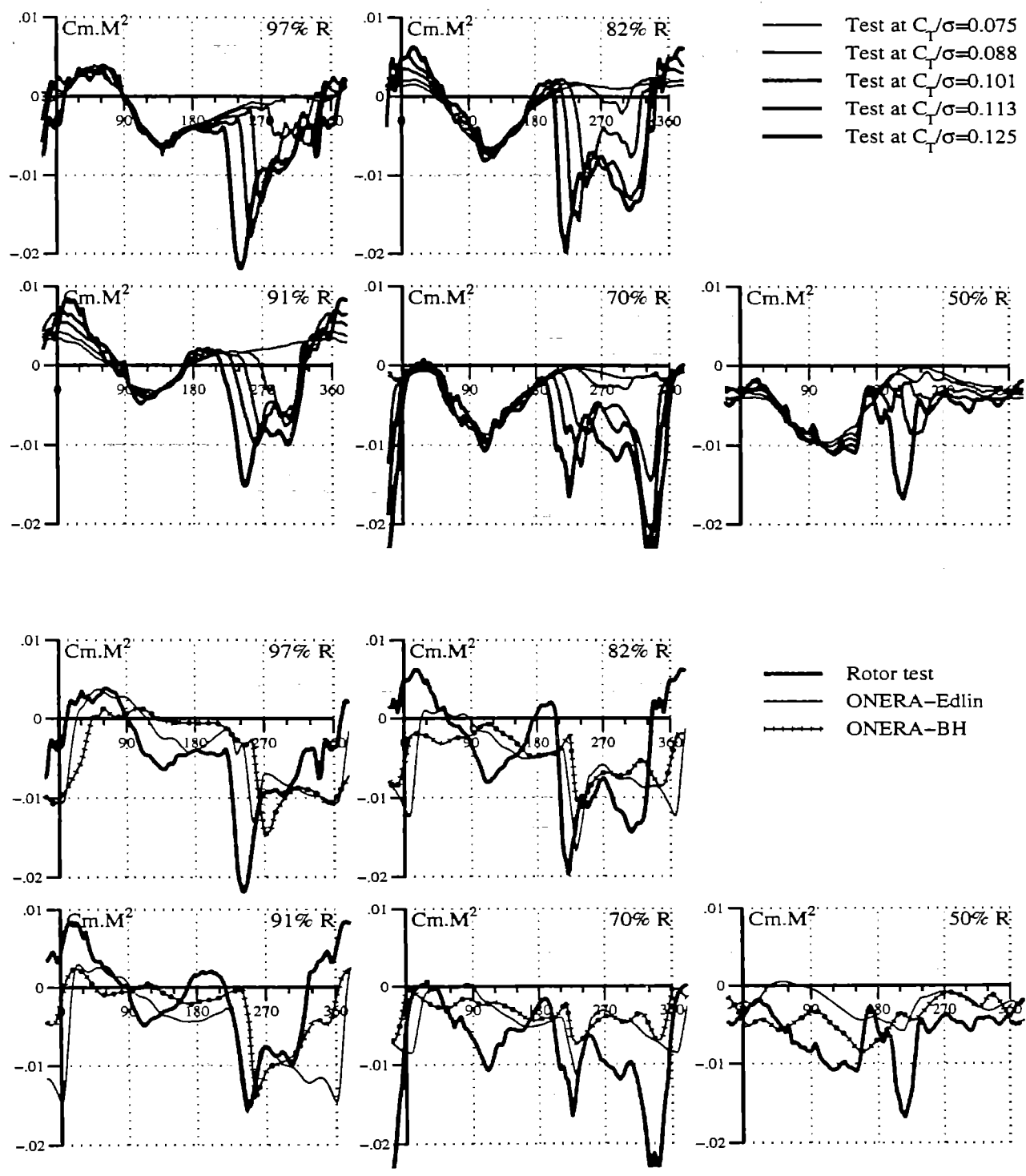
Fig 10: Measured and calculated moment coefficient*Mach²
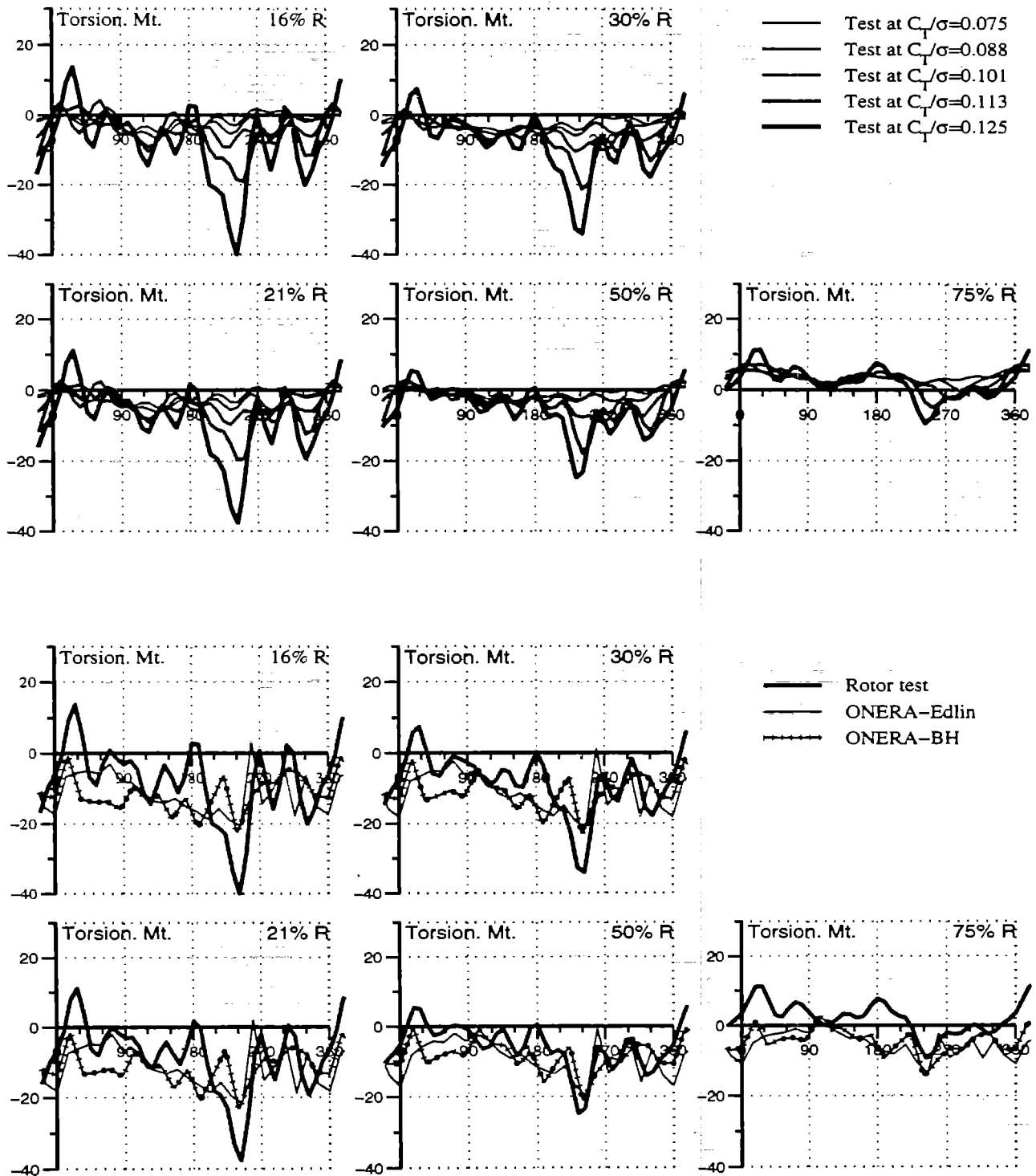
Fig 11: Measured and calculated blade torsional moment
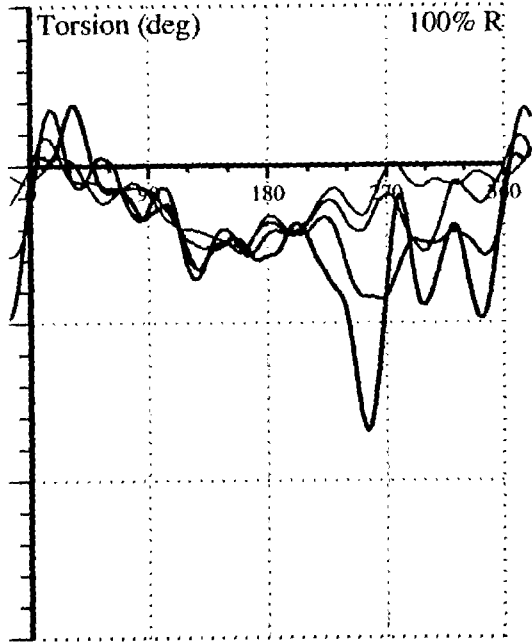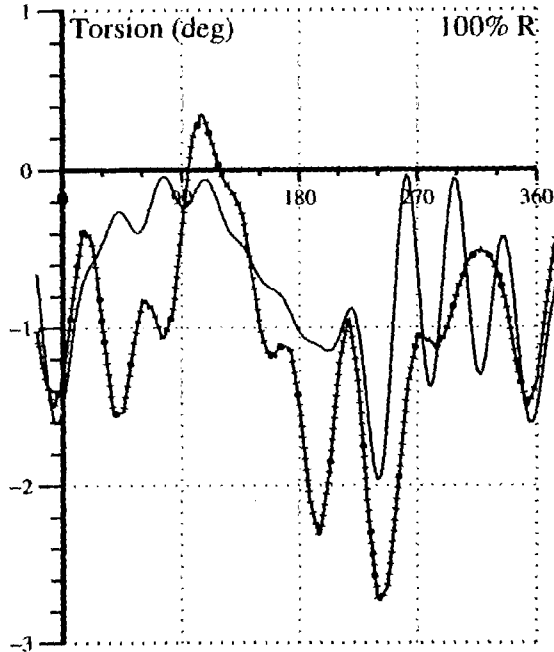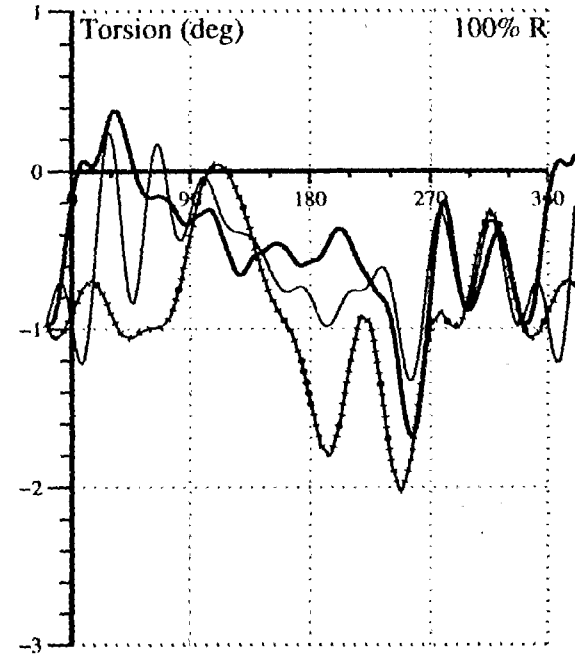
Fig 12: Measured and calculated Torsion
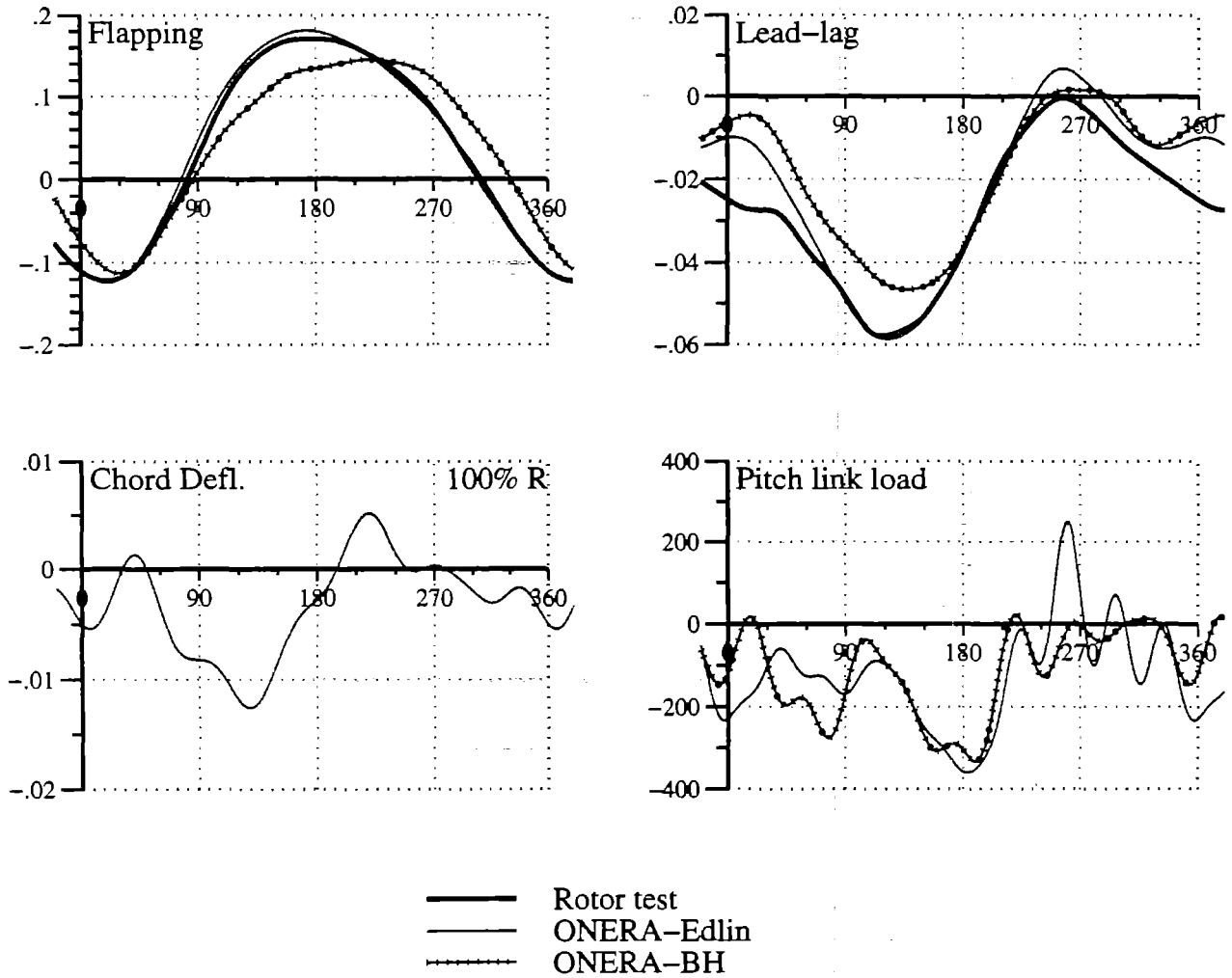
Fig 13: Rotor parameters for thrust condition Ct/s=0.125

Session I
Aeroelastic Stability

GROUND/AIR RESONANCE SIMULATION OF HELICOPTER ROTOR SYSTEMS BASED UPON FULL NON-LINEAR EQUATIONS OF MOTION

C. S. Robinson, E. R. Wood and R. L. King

Naval Postgraduate School
Monterey, California

I. INTRODUCTION

Current trends in helicopter technology and manufacturing have favored the use of bearingless rotor designs that make use of advanced composite materials. These designs offer many advantages over more conventional articulated rotors when reliability and maintainability are considered. Additionally, future helicopter development promises the inclusion of smart material technology and active rotor control as engineers strive to optimize dynamic, acoustic and performance characteristics of the helicopter.

A potential payoff from the successful use of the technologies mentioned above is the damperless rotor; a design that offers major returns in the form of decreased rotor system weight, reduced parts count, and reduced maintenance requirements. The designers of such complex rotors will require reliable simulations of the rotor mechanics in order to take advantage of these new innovations in rotor technology. The developed simulation should have sufficient fidelity so that the effects of introducing advanced technologies into rotor system designs could be accurately evaluated.

The goal of the study described in this paper is the development of a computational tool to analyze the dynamic behavior of advanced technology coupled rotor/fuselage systems. A series of programs have been developed utilizing the symbolic processing software, MAPLE®; the computational software, MATLAB®; and the dynamic simulation software, SIMULINK® [Ref. 1]. It is desired that the computational tool be simple to understand and lend itself to easy reprogramming.

II. THE COMPUTATIONAL TOOL

The computational tool is comprised of four basic parts:

1. Derivation of the rotor/fuselage system equations of motion by the symbolic manipulation software MAPLE®.
2. Automatic generation of computer code from the algebraic representation of the equations of motion.
3. Transportation of the generated computer code from the symbolic processing environment into the simulation environment.
4. Implementation of the nonlinear simulation in the SIMULINK® environment.

Initial work focused on modeling the phenomenon of ground resonance. A helicopter was modeled using spring restrained rigid rotor blades attached to a spring mounted rigid fuselage. Two cases were explored. The first case was a simple model, similar to that used by Coleman and Feingold [Ref. 2]. This case allowed for rotor blade lead-lag and fuselage translational degrees of freedom and was absent of aerodynamic effects. The second model was more complex, with fuselage rotational degrees of freedom, rotor blade flap, and aerodynamic effects.

The symbolic processing software MAPLE® was used to systematically apply Lagrange's equation,

$$\frac{d}{dt}\left(\frac{\partial T}{\partial \dot{q}_i}\right) - \frac{\partial T}{\partial q_i} + \frac{\partial U}{\partial q_i} + \frac{\partial D}{\partial \dot{q}_i} = Q_i \qquad (1)$$

to derive equations of motion from kinetic, potential and dissipative energy expressions in terms of system degrees of freedom.

The program applies the necessary coordinate transformations so that the velocity of an arbitrary point on a rotor blade elastic axis is expressed in inertial coordinates.

The expressions for fuselage kinetic, potential and dissipative energy as well as the expressions for rotor blade potential and

dissipative energy are entered into the symbolic worksheet directly by the user.

With the energy expressions defined for each component of the rotor/fuselage model, the contributions are added and processed following the Lagrangian approach by the symbolic processing program. The result is a system of second order nonlinear differential equations stored symbolically in a vector of the following form

$$\left[A\!\left(\dot{\vec{x}}, \vec{x}, t\right) \right] \ddot{\vec{x}} = \vec{f}\!\left(\dot{\vec{x}}, \vec{x}, t\right) \qquad (2)$$

where A is a matrix of coefficients of the second derivative terms, $\vec{f}$ is a vector containing the system elastic, dissipative, generalized force and nonlinear terms, and $\vec{x}$ is the vector of degrees of freedom.

The MAPLE® program then generates computer code for use in the nonlinear simulation. The algebraic expressions in the matrix, A, and vector, $\vec{f}$, are converted to optimized C code to minimize the number of floating point operations required in the simulation.

The third part of the process is completed when the generated code is incorporated into the MATLAB®-SIMULINK® environment via the S-function interface [Ref. 3]. An S-function is a generically formatted subroutine which communicates the dynamics of a system to a numerical integration routine so that those dynamics can be incorporated into more complex models in a straight forward manner. S-functions can be coded in either C, Fortran, or MATLAB® m-file format.

The equations of motion are numerically integrated in their complete nonlinear form using the following format,

$$\dot{\vec{x}} = \vec{w}$$
$$\dot{\vec{w}} = [A]^{-1}\vec{f} \qquad (3)$$

Eqn. (3) is used to evaluate the system state derivatives at each time step. These state derivatives are then used by a numerical integration algorithm included with the SIMULINK® software package (Runge-Kutta 4-5 primarily used for this study).

III. SIMULATION VALIDATION

Presented in this section are the results of several simulations that demonstrate the unique capabilities and flexibility of the nonlinear modeling method. Direct simulation allows analysis of any number of different configurations or scenarios, such as non-isotropic hub, one damper inoperative, and simulated rotor blade damage. Geometric and mass properties can be changed at any point in the time history, so configuration changes do not have to be artificially implemented as initial conditions. Though the time history plots in the following subsections do not indicate it, SIMULINK® offers the useful capability of being able to visualize the dynamics of a model as it progresses in development.

The baseline case implemented is an articulated 3-bladed rotor which is intentionally set up with zero damping and with a rotor speed set approximately at the center of the regressing lead-lag mode instability region. The first set of simulations demonstrates the system behavior when excited with an initial fuselage velocity. Figures 1.1 and 1.2 show the lead-lag time histories and the fuselage center of mass trajectory (displacements in feet) for this case.
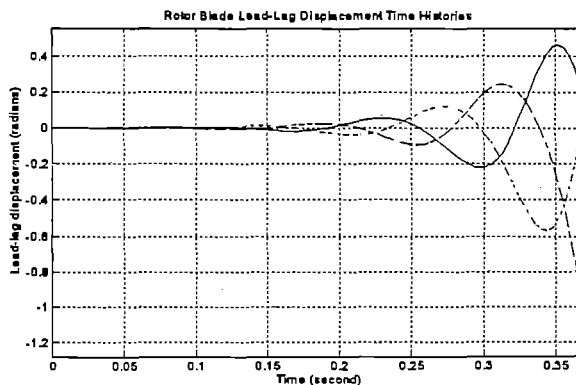

Figure 1.1 Rotor Lead-lag Displacements for Basic Parameter Case Settings, Center of Self Excited Region.

As expected, Figures 1.1 and 1.2 show the rapid divergence of the model as a result of being in the center of the self excited region. The diverging spiral path of the fuselage center of mass is a characteristic result of the regressing lead-lag mode instability.
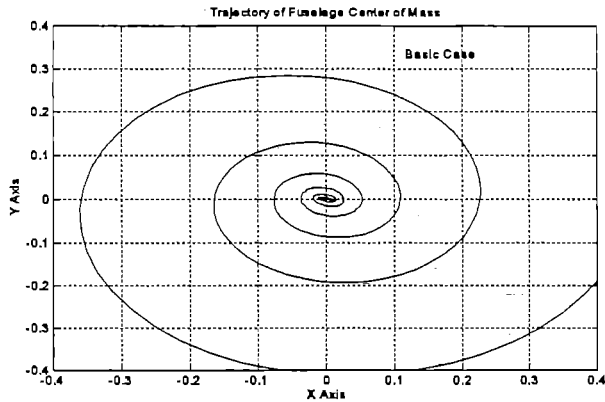
Figure 1.2 Fuselage Trajectory for Basic Parameter Settings, Center of Self Excited Region.

Figures 1.3 and 1.4 show corresponding results for operation just below the self excited region. Figure 1.3 shows a beat or modulation of the blade response but no divergence.
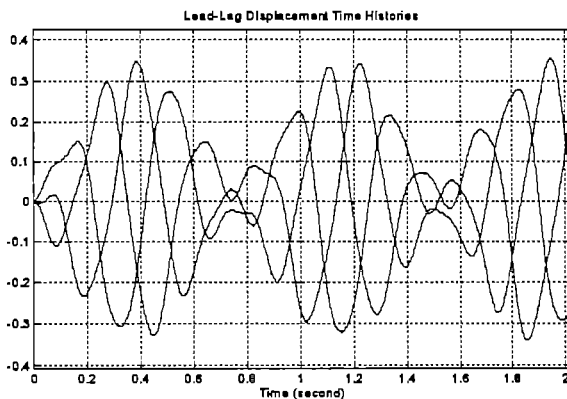

Figure 1.3 Rotor Lead-lag Time Histories, Rotor Speed Below Self Excited Region
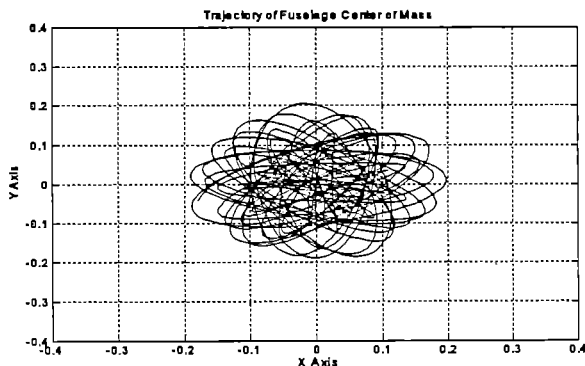

Figure 1.4 Fuselage Trajectory for Basic Parameter Settings, Rotor Speed Below Self Excited Region

The fuselage center of mass trajectory shown in Figure 1.4 shows an elliptical path with the major axis of the ellipse precessing about the zero displacement position.

Both the beat phenomenon and the precession type motion of the hub are characteristic behavior of a system operating outside the self excited region. The precessing ellipse is also characteristic of spherical pendulums and cannot be modeled in a linear analysis.

Figures 1.5 and 1.6 show the results of a simulation where rotor speed was set just above the self excited region. Again, the fuselage exhibits an elliptic whirling motion with the major axis of the ellipse rotating about the zero displacement position while the blade lead lag motion again follows a beat pattern. Note the increase in beat and lead/lag frequencies.
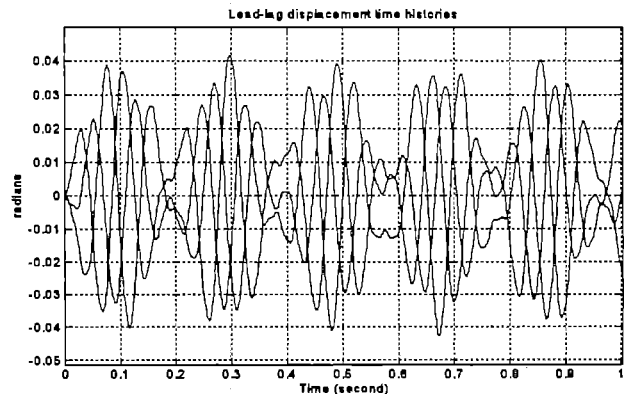

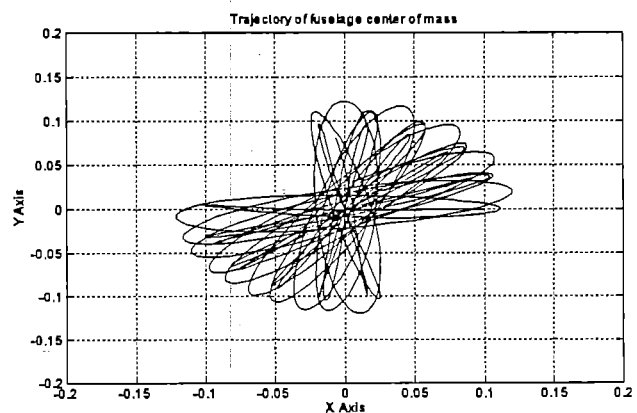**Figure 1.5 Rotor Lead-lag Time Histories, Rotor Speed Above Self Excited Region**

Figure 1.6 Fuselage Center of Mass Trajectory, Rotor Speed Above Self Excited Region

3

Figure 1.7 is the Coleman stability plot [Ref. 1] for the basic configuration. The solid lines indicate the boundaries of the self excited region and the dashed line marks the center of the self excited region. The X's indicate the operating points for the three cases shown in Figures 1.1 through 1.6.
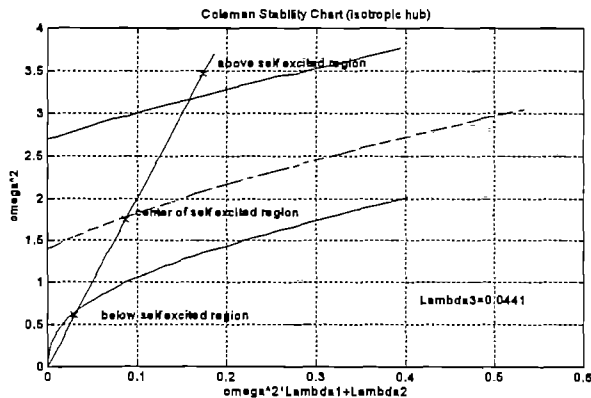
Coleman Stability Chart (isotropic hub)

Figure 1.7 Coleman Stability Plot for Basic Case

A comparison was also made between the simulation model and a time history solution of Coleman's and Feingold's equations. Bramwell [Ref. 4] derives Coleman's and Feingold's equation in a form equivalent to that of the simulation model with the blade displacements expressed in the rotating coordinate system and the fuselage displacements expressed in the fixed coordinate system. These equations were solved in the fixed coordinate system using an eigenvalue analysis and the solutions transformed back to the rotating coordinate system. A comparison was then made with the lead-lag displacement time history of the simulation model.

Figure 1.8 shows the result of the comparison using the parameters of the basic configuration with a moderate amount of damping added to rotor blades and fuselage. Figure 1.8 shows excellent agreement between the two solutions with a departure between the two occurring only when displacements are no longer small. Thus, for the case of an isotropic hub with linear spring stiffness and damping, the new comparison validates the accuracy of the simulation model.
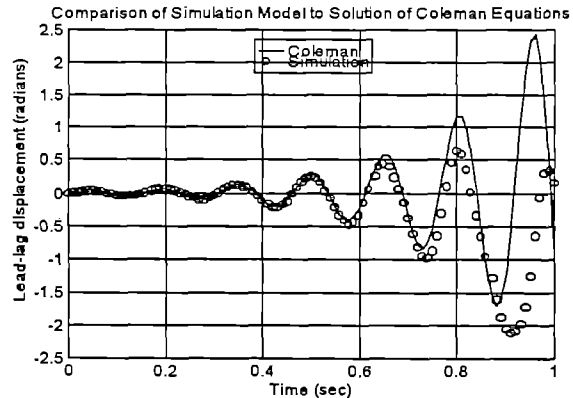
Comparison of Simulation Model to Solution of Coleman Equations

Figure 1.8 Comparison of Simulation Model to Coleman's Model

IV. EXAMPLE CASES

Moving on from baseline results and model verification, a comparison is run between a case where all blade lead-lag dampers are operating and a case where one damper is inoperative. The top plot of Figure 1.9 shows a rotor with all blade dampers operating. In the lower plot, the blade associated with the bubble-line time history has its damper disabled by reducing the damping coefficient by two-thirds. We note that the neutrally stable case with full damper operation becomes highly unstable by failing one damper.

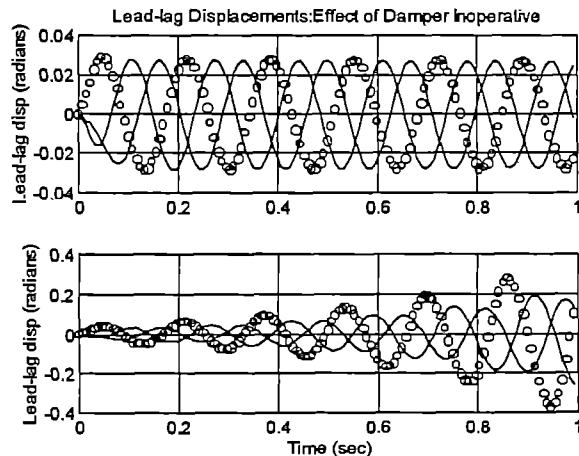**Lead-lag Displacements:Effect of Damper Inoperative**

Figure 1.9 One Lead-Lag Damper Inoperative

Figure 1.10 shows results of simulating damage to a rotor blade by reducing the mass of the blade by 20%. The undamaged blades are seen to oscillate around a non-zero displacement position to compensate for the damaged blade, but amplitudes of all blade oscillations remain constrained. This makes

4

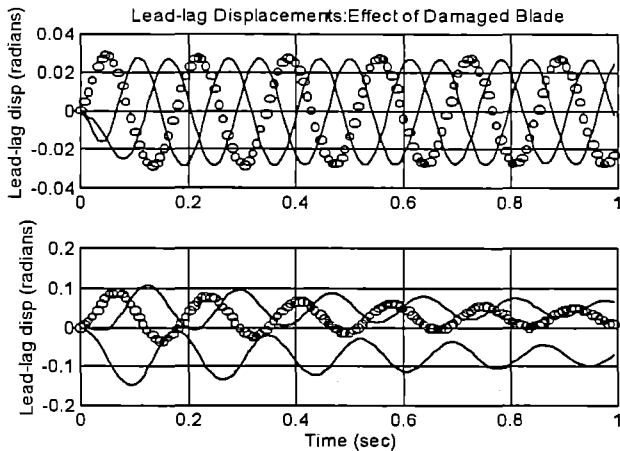sense since overall damping remains unchanged.

Figure 1.10 Simulated One Rotor Blade Damaged

Figure 1.11 shows the effect of introducing lead-lag stops in the model. The figure compares the time history of a blade with no stops with that of a blade with spring stops positioned at ± 15 degrees (0.262 radians).
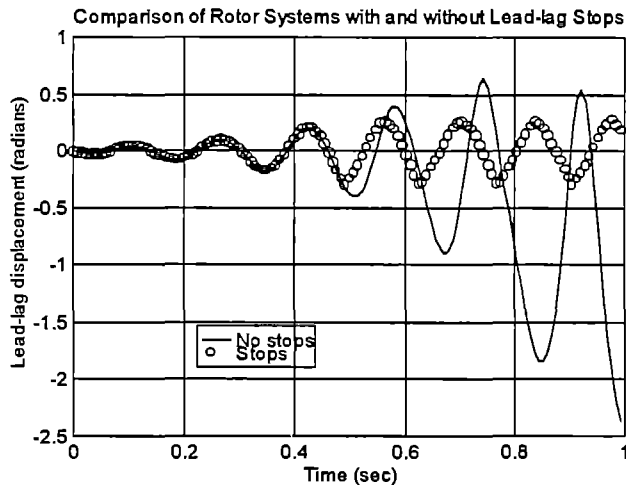

Figure 1.11 Effect of Lead-Lag Stops

V. NONLINEAR SPRING RESULTS

The objective of the next set of simulations was to examine the effect of a nonlinear flexbeam incorporated into a bearingless rotor design. The nonlinear behavior of the flexbeam was assumed to be that of a Duffing spring where the restoring moment is given by

$$\left(M_\zeta\right)_{Blade} = K_e\zeta + K_d\zeta^3 \qquad (4)$$

K_e is the linear stiffness and K_d the nonlinear stiffness. Simulations were conducted for several values of the nonlinear spring constant keeping the linear coefficient constant at 22,000 ft-lbs/radian. Results in Figure 1.13 show the primary effect of increasing the nonlinear spring constant is in limiting the amplitude of the lead-lag response. The case for $K_d = 0$ is very unstable and would result in the loss of the helicopter. By adding the hardening (cubic) term, the unbounded growth in amplitude can be checked, as is apparent from the response for the case of K_d=80,000 ft-lbs/radian^3. As the amplitude increases, the magnitude of the nonlinear term becomes more influential and effectively changes the frequency of oscillation, shifting it outside of the unstable region and allowing the oscillations to decay. While the limiting amplitudes for the nonlinear case of Figure 1.13 are still large for lead-lag displacements (on the order of 15 to 20 degrees), this limiting behavior may be enough to prevent destruction of an aircraft if ground resonance were excited. When lead-lag displacements are very small, the hardening effect of a nonlinear flexbeam would be negligible, and could be designed to act as soft-in-plane in order to minimize hub moments.
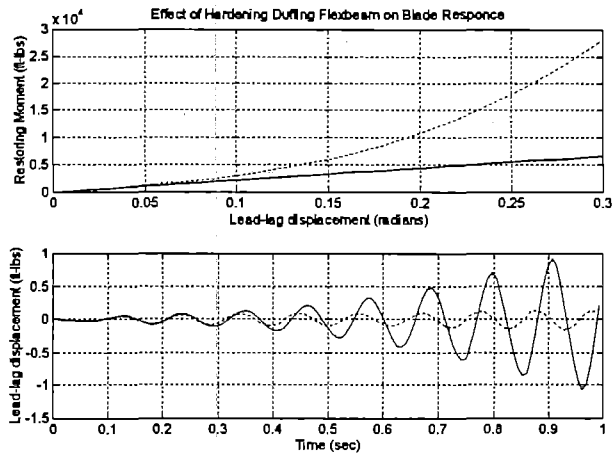

Figure 1.13 Effect of Hardening Duffing Flexbeam on Lead-lag Response

It is important to note that the elastic behaviors of the flexbeams modeled by the curves in the upper plot of Figure 1.13 are purely hypothetical and were selected to

5

illustrate the effect of nonlinear elastic behavior on rotor system response and stability. Further research in this area appears promising and will be continued.

VI. THE MOVING BLOCK TECHNIQUE

One of the drawbacks of performing direct numerical simulation of dynamic systems is that time histories of system degrees of freedom only offer qualitative information on the effect that certain system parameters have on system stability or performance. In order to quantify the effects of varying certain system parameters, such as rotor speed, flex-beam stiffness, and active control inputs on rotor-fuselage stability, a method was needed to determine system damping levels from the system time histories. Moving Block Analysis, a technique first applied at Lockheed in the 1970's, is a discrete method of analyzing a transient time history to obtain modal damping and frequency. The technique is described in some detail by Hammond and Dogget [Ref. 5] and Bousmann and Winkler [Ref. 6].

A MATLAB® based program was developed to apply the moving block technique to time history traces generated from coupled rotor fuselage simulations. For a sampled signal (in this case, the time trace resulting from a simulation) the Moving Block method is applied by first estimating the frequency of interest embedded in the signal using a Fast Fourier Transform (FFT). A block length is selected consisting of N_b data points. The magnitude of the Discrete Fourier Transform (DFT) of this block is then calculated. The block is then shifted one time step, and the DFT magnitude is calculated again. This process is repeated until the time block is at the end of the signal. The log of the magnitude of the DFT of each block is plotted against the start times of each block. The negative of the slope of the least squares fit of this plot divided by the damped frequency of the mode measured yields the damping ratio.

For this study, stability measurements were made based on time histories of the orthogonal components of the rotor center of gravity offset. These time histories contain both the regressing and progressing mode contributions. The damping levels of these modes for various gain and phase settings were determined using the Moving Block program.

Figure 1.14 shows the rotor center of gravity offset response to a lead-lag perturbation for a baseline case. The high frequency component

present in the initial part of the simulation is the progressing lead-lag mode which is seen to damp out very quickly. The dominant low frequency trace is the regressing mode, which is unstable for this case. Figure 1.15 shows results of analyzing the time trace in figure 1.14 with the Moving Block analysis.
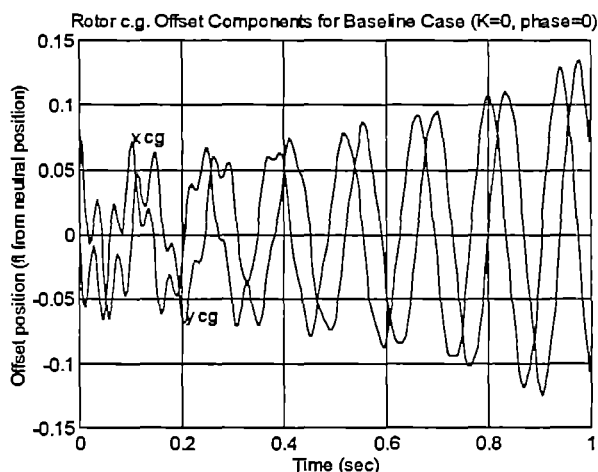

Figure 1.14 Rotor c.g. Offset Components for Baseline Case (K=0, φ=0)

The upper plot of Figure 1.15 is the initial spectral analysis of the time trace computed by using a Fast Fourier Transform. The second plot refines the resolution of the FFT about the frequencies of interest. The third part of Figure 1.15 shows the plot of the moving block functions [Ref. 7] for the regressing and progressing lead-lag modes with linear least square fits superimposed.
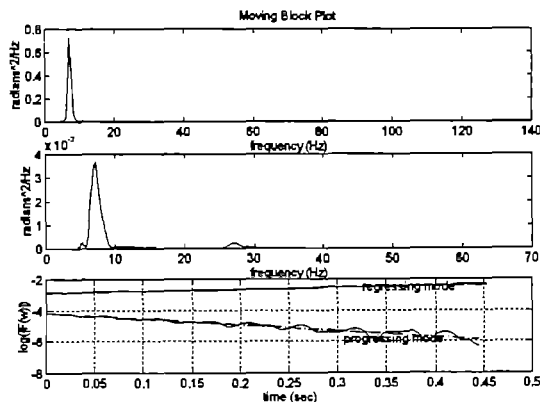

Figure 1.15 Results of Moving Block Analysis on Baseline Simulation (K=0, φ=0)

6

VII. CONCLUDING REMARKS

A method for formulating and automatically coding the equations of motion of a coupled rotor-fuselage system by use of symbolic processing software and dynamic simulation software has been developed. All terms are included in the equations of motion at each time step of the simulation. All restrictions with respect to small angles and small displacements have been eliminated and no ordering schemes were used.

The resulting mathematical models were used to perform simulations of coupled rotor-fuselage systems in ground resonance. Analysis of the dynamic and stability characteristics were quantified using the moving block technique. A simple rotor model was used to demonstrate essential characteristics of air/ground resonance and the effects that parameter variations such as rotor speed, flexbeam elastic behavior, damper failure, and rotor blade damage have on those characteristics. The modeling technique proved to be a very powerful tool in that it eliminated the time consuming process of manually deriving and coding the very complex equations of motion of a multi-degree of freedom rotor system. As the simulation component of the method, SIMULINK® provided a generic control/ simulation environment that offered a broad range of analysis capability for exploring air/ground resonance characteristics of both linear and non-linear rotor.

The technique has direct application to the design of future advanced technology rotor systems.

VIII. REFERENCES

1. Robinson, C. S., "Modeling and Analysis of Helicopter Ground Resonance Utilizing Symbolic Processing and Dynamic Simulation Software," Aeronautical Engineer's Thesis, Naval Postgraduate School, March 1997.

2. Coleman, R. P., and Feingold, A. M., "Theory of Self Excited Mechanical Oscillations of Helicopter Rotors with Hinged Blades," NACA Report 1351, 1958.

3. SIMULINK® Dynamic Simulation Software User's Guide, The MathWorks, Inc. ,1992.

4. Bramwell, A. R. S., Helicopter Dynamics, Edward Arnold Publishers Ltd., London, 1976.

5. Hammond, C. E., and Doggett, R. V. , "Determination of Subcritical Damping by Moving-Block/Randomdec Applications," NASA Symposium on Flutter Testing Techniques, NASA SP-415, Oct. 1975.

6. Bousman, W. G, and Winkler, D. J., "Application of the Moving Block Technique", Proceedings of the 22nd Annual AIAA Structural Dynamics and Materials Conference, 81-0653CP, April 1981.

7. Weller, W. H., "Fuselage State Feedback for Aeromechanical Stability Augmentation of a Bearingless Main Rotor," Journal of the American Helicopter Society, April 1996, pp. 85-93.

Lag-Damping Prediction of Hingeless Rotors in Trimmed Flight With Experimental Correlation

S. Subramanian
Research Associate

G. Ma
Research Assistant

G. H. Gaonkar
Professor

Department of Mechanical Engineering
Florida Atlantic University
Boca Raton, FL 33431

Summary

This paper investigates the trim and stability of isolated hingeless rotors in forward flight with experimental correlation. A modal approach with both the nonrotating and rotating modes, the ONERA dynamic stall models of lift, drag and pitching moment, and a three-dimensional state-space wake model are used. The experimental rotor has four blades that are soft in lead-lag and torsion, and it is tested at realistic tip speeds. The collective pitch and shaft angle are set prior to each test run, and the rotor is trimmed as follows: the longitudinal and lateral cyclic pitch controls are adjusted through a swashplate to minimize the 1/rev flapping moment at the 12% radial station. The database includes the lateral and longitudinal cyclic pitch controls, steady root-flap moment and lag regressive-mode damping levels for two coning angles with variations in advance ratio, shaft tilt and collective pitch control. The cyclic pitch controls and the corresponding periodic responses are computed by the periodic shooting method with damped Newton iteration; this method is based on the fast-Floquet theory and generates the equivalent Floquet transition matrix (EFTM) as a byproduct. The modal frequencies and damping levels are estimated from the eigenvalues and eigenvectors of the EFTM. All the structural and aerodynamic states are included, from the trim analysis to the eigenanalysis, and the flap-moment predictions are based on both the force-integration and mode-deflection methods. The convergence of the damping, control-input and flap-moment predictions with respect to the number and type of modes is included as well. A major finding is that dynamic wake dramatically improves the correlation of the lateral cyclic pitch control.

Lag-Damping Prediction of Hingeless Rotors in Trimmed Flight With Experimental Correlation

S. Subramanian
Research Associate
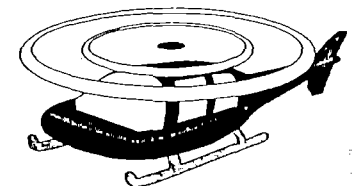
G. Ma
Research Assistant

G. H. Gaonkar
Professor

Department of Mechanical Engineering
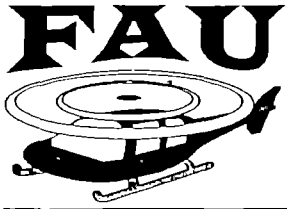**Florida Atlantic University**
Boca Raton, FL 33431

Presented at the Seventh International Workshop on Dynamics and Aeroelastic Stability Modeling of Rotorcraft Systems, Washington University, St. Louis, MO, October 14-16, 1997
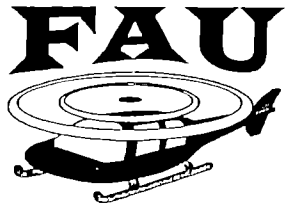
FAU

Outline

◆ **Introduction**

  ☆ Background and Motivation

  ☆ Contributions

◆ **Experimental Rotor**

◆ **Modeling and Analysis**

  ☆ Structural Dynamics

  ☆ Aerodynamics

  ☆ Trim and Stability Analyses

◆ **Results**

  ☆ Convergence

  ☆ Comparison with Experiment

◆ **Concluding Remarks**

Introduction

Provision for adequate lead-lag damping is an important element of rotorcraft design

- ☛ Requires an accurate prediction method

Lag damping prediction is sensitive to

- ☛ Approximations in modeling aerodynamic and structural components
- ☛ Trim results of control inputs and the corresponding periodic responses

Virtually imperative that the theoretical calculations are correlated with a comprehensive database
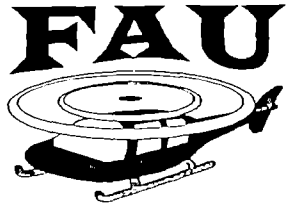
Background and Motivation

Experimental Investigations	Analytical Investigations
McNulty '89	Gaonkar, McNulty and Nagabhushanam '90
	Barwey, Gaonkar and Ormiston '91
	Torok and Chopra '91
	Barwey and Gaonkar '94
	Tang and Dowell '95
	Subramanian, Chunduru and Gaonkar '94, '97
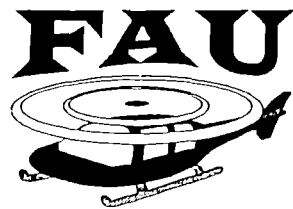
Background and Motivation

Experimental Investigations	Analytical Investigations
Sharpe '86	De Andrade, Da Silva Correa and Peters '96
---	Cho, Jeon, Woo and Lee '97
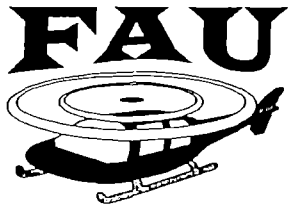
Background and Motivation

Experimental Investigations	Analytical Investigations
Maier, Sharpe and Lim '95	Subramanian and Gaonkar '96
	Tang and Dowell '96
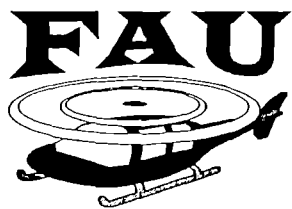
Background and Motivation

Experimental Investigations	Analytical Investigations
Maier '97 (corrected and updated)	Subramanian, Gaonkar and Maier '97
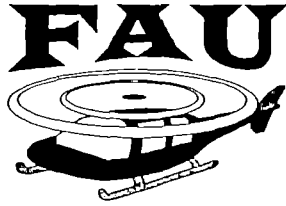
Contributions

◆ **Develops a flap-lag-torsion analysis**

  ✏ Based on the fast-Floquet theory

◆ **Correlates with the updated and corrected database on trim and stability**

  ✏ Includes convergence of trim and stability with respect to the number and type of modes

◆ **Identifies the effects of quasisteady stall, dynamic stall and dynamic wake and shows how these effects participate in the correlation**
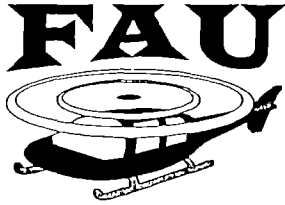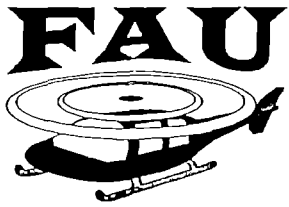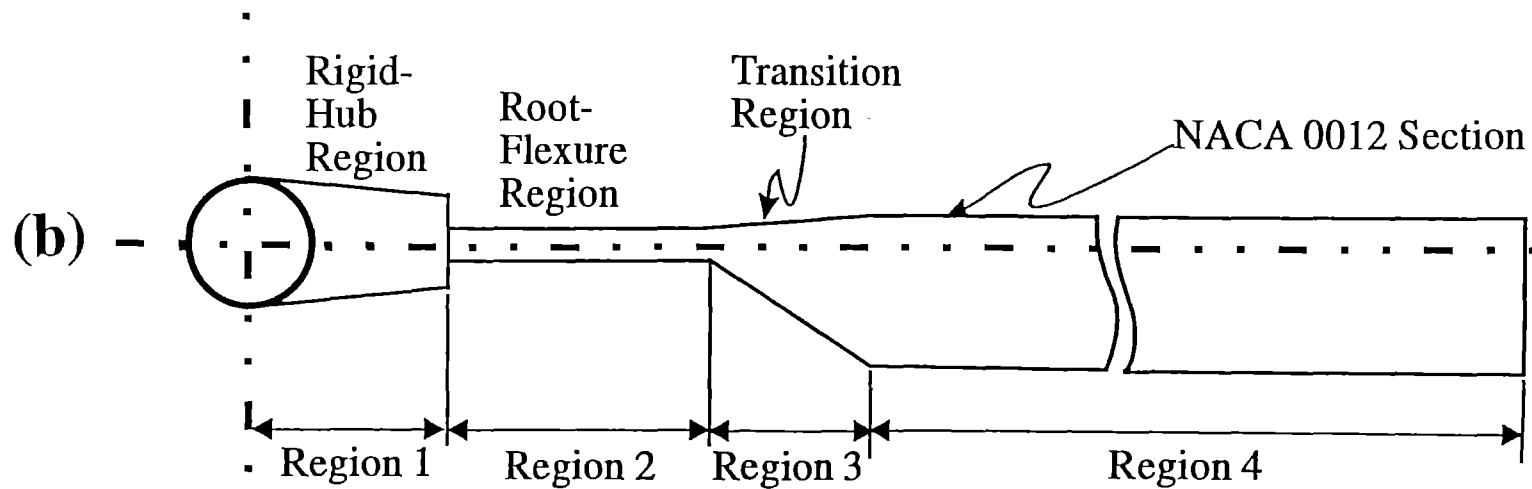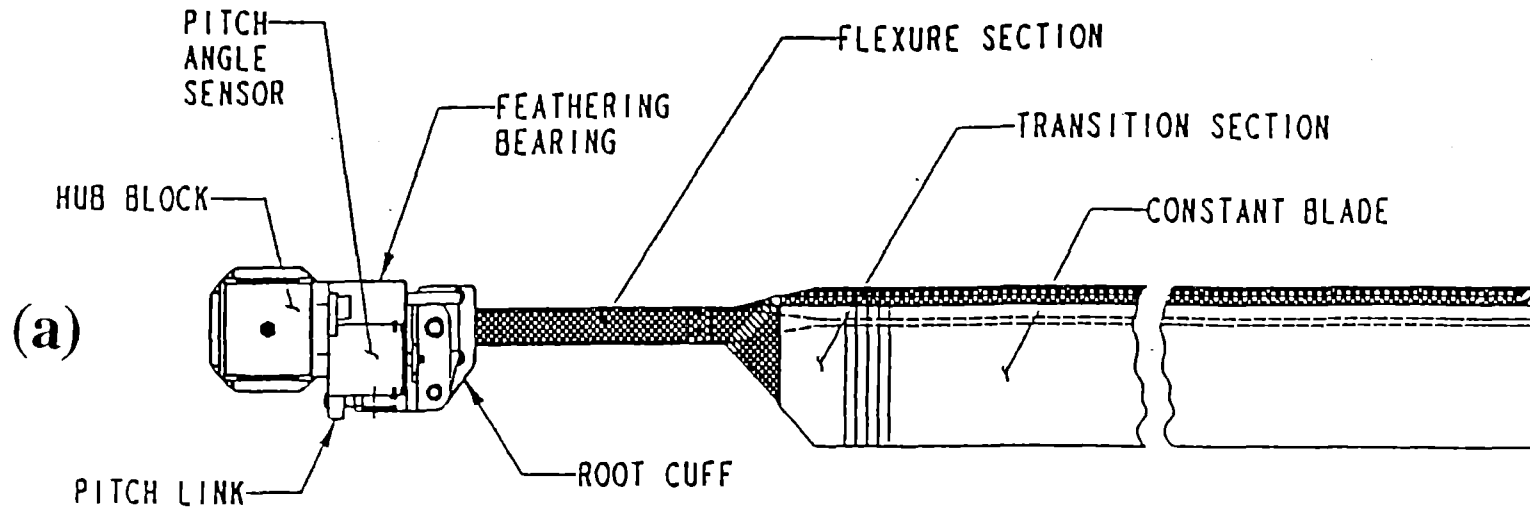
Experimental Rotor
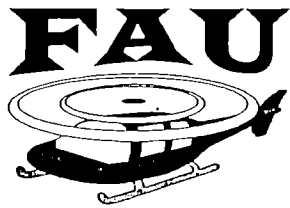
- Soft inplane, four-bladed torsionally soft rotor

- Blades have a rectangular planform with zero degree pretwist and droop
  - Also have a provision for varying precone

- Operated trimmed by minimizing the 1/rev flap moment at the 12% radial station

- Collective pitch and shaft angles are set prior to the test run; cyclic pitch controls are exercised through a swashplate to minimize the flap moment

- NACA 0012 airfoil section; $Re = 1.26 \times 10^6$ in hover; $M = 0.6$ at the blade tip in hover

(a)

PITCH ANGLE SENSOR

FEATHERING BEARING

FLEXURE SECTION

TRANSITION SECTION

HUB BLOCK

CONSTANT BLADE

PITCH LINK

ROOT CUFF

(b)

Rigid-Hub Region

Root-Flexure Region

Transition Region

NACA 0012 Section

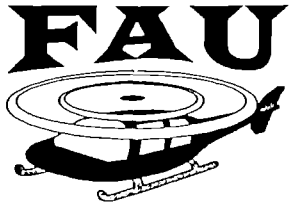Region 1   Region 2   Region 3   Region 4

Test Configurations for the Corrected and Updated Database in Trimmed Flight

Test Configuration	Collective Pitch, θ_0(deg)	Shaft Tilt, α_s (deg)	Blade Precone, β_{pc} (deg)	Advance Ratio, μ
I	3^0	0^0	2^0	0.0 - 0.31
II	3^0	-3^0	2^0	0.0 - 0.31
III	3^0	-6^0	2^0	0.0 - 0.31
IV	5.9^0	-6^0	2^0	0.0 - 0.36
V	3^0	0^0	0^0	0.0 - 0.187

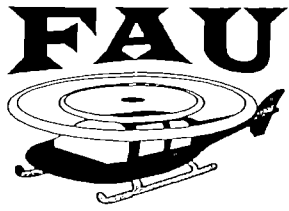## *Structural Dynamics*

➥**Elastic Flap-Lag-Torsion Model**

   ⇨Flap-lag bending and torsion degrees of freedom

   ⇨Quasisteady treatment for axial deformation

➥**Galerkin-type scheme**

➥**Nonrotating and rotating normal modes**

   ⇨Myklestad-type approach

Aerodynamics

❶ **Dynamic Stall Theory**

➭ONERA dynamic stall models of lift, drag and pitching moment

❷ **Quasisteady Stall Theory**

➭Dynamic stall characteristics suppressed

❸ **Dynamic Stall and Wake Theory**

➭Relatively complete aerodynamic representation

➭Dynamic stall effects based on the ONERA models

➭Wake effects based on a finite-state three-dimensional wake model (Peters, Boyd and He)
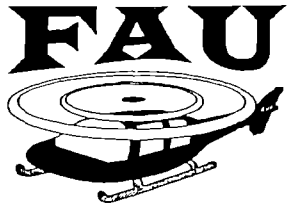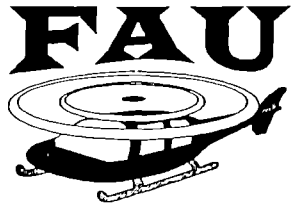
Trim and Stability Analyses

➡ **Compute the lateral and longitudinal cyclic control inputs**

  ⇨ Wind-tunnel trim

  ⇨ Minimize the 1/rev flap moment at the 12% radial station

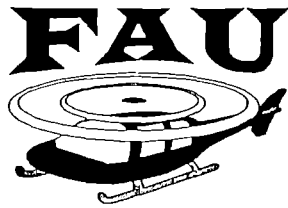➡ **Find the corresponding initial conditions for the periodic response**

Periodic Shooting Method

➥ **With damped Newton iteration**

➥ **Based on the fast-Floquet theory**

➥ **Generates the equivalent Floquet transition matrix (EFTM)**

Modal damping levels and frequencies from the eigenvalues and eigenvectors of the EFTM

Flap Moment - Force Integration Method

➡ **Integrate sectional forces and moments over the blade span to get total flap moment**

Trim equations:

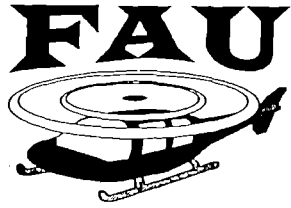$$\int_0^{2\pi} [\text{Total Flap Moment}]_{0.12R} \cos\psi\, d\psi = 0$$

$$\int_0^{2\pi} [\text{Total Flap Moment}]_{0.12R} \sin\psi\, d\psi = 0$$

Steady Flap Moment

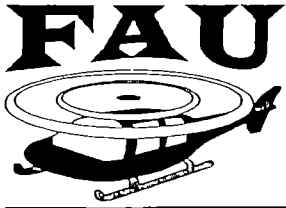$$\frac{1}{2\pi} \int_0^{2\pi} [\text{Total Flap Moment}]_{.12R}\, d\psi$$

Flap Moment - Mode Deflection Method

Total Flap Moment = [Flap Stiffness x Flap deflection'']$_{.12R}$

Steady Flap Moment

$$\frac{1}{2\pi} \int_{0}^{2\pi} [\text{Total Flap Moment}]_{.12R} \, d\psi$$

Lag Regressive-Mode Damping Level (1/sec)

Lag Regressive-Mode Damping Level (1/sec)

Shaft Tilt=-6⁰

Advance Ratio (μ)

FAU

Convergence of Steady Flap Moment
for 3^0 Collective and 2^0 Precone
(Nonrotating modes)

**Force Integration Method
Steady Flap Moment (in-lb)
Shaft Tilt=-6⁰**

Dynamic Stall and Wake

2-2-2
3-3-3
4-4-4
5-5-5

Advance Ratio (μ)

FAU Convergence of Lag-Regressive Mode Damping Level for 3^0
Collective and 2^0 Precone
(Rotating modes)

Lag Regressive-Mode Damping Level (1/sec)
Shaft Tilt=-6⁰

Dynamic Stall and Wake

Legend:
- 2-1-1
- 3-2-1
- 4-2-2
- 5-2-3
- 5-3-3

Advance Ratio (μ)

Lateral-Cyclic Pitch Angle (deg)
Shaft Tilt=-6⁰

Dynamic Stall and Wake

2-1-1
3-2-1
4-2-2
5-2-3
5-3-3

Advance Ratio (μ)
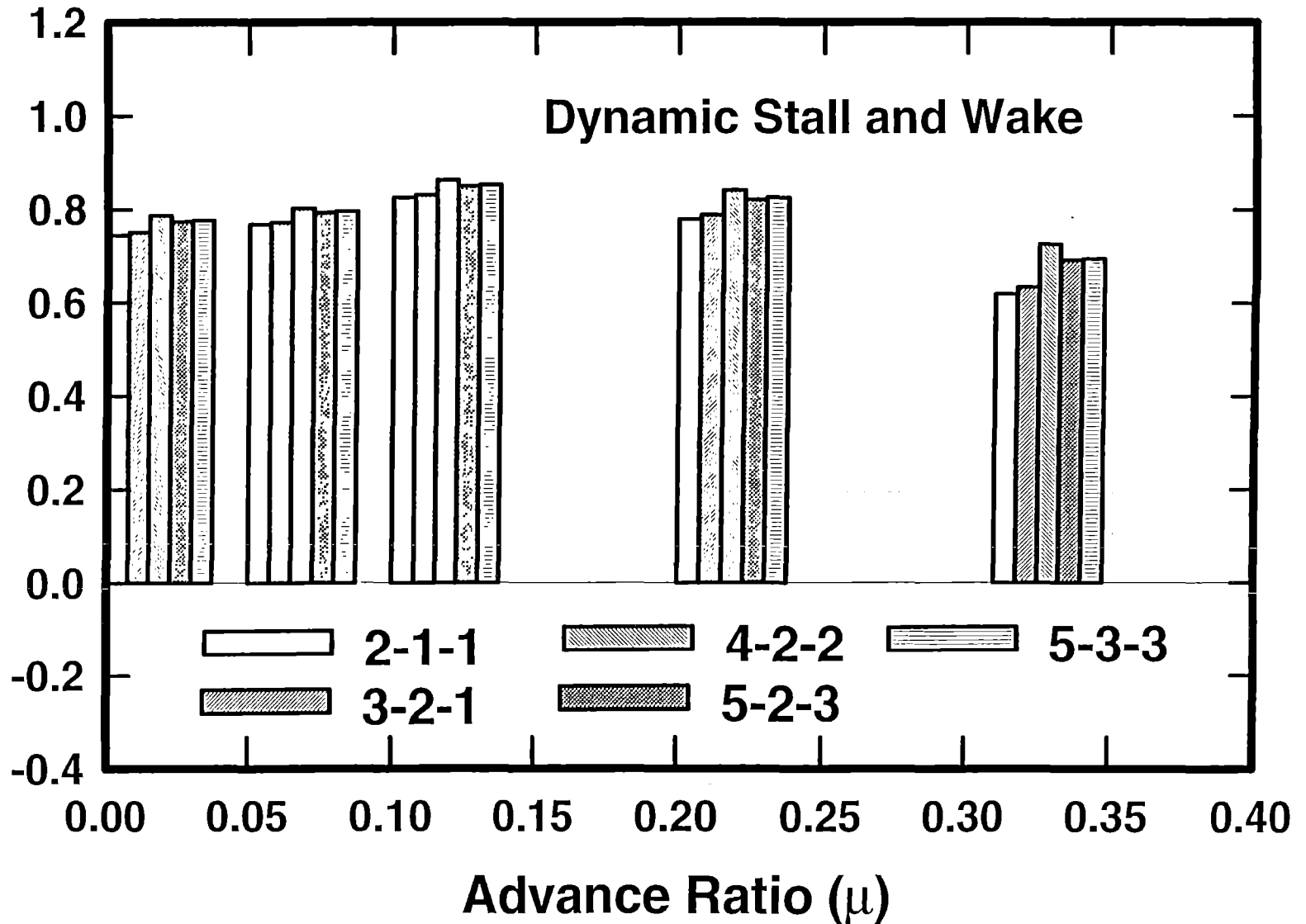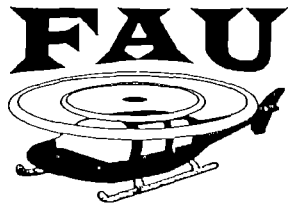
Convergence of Longitudinal-Cyclic Pitch Angle for 3^0 Collective and 2^0 Precone (Rotating modes)
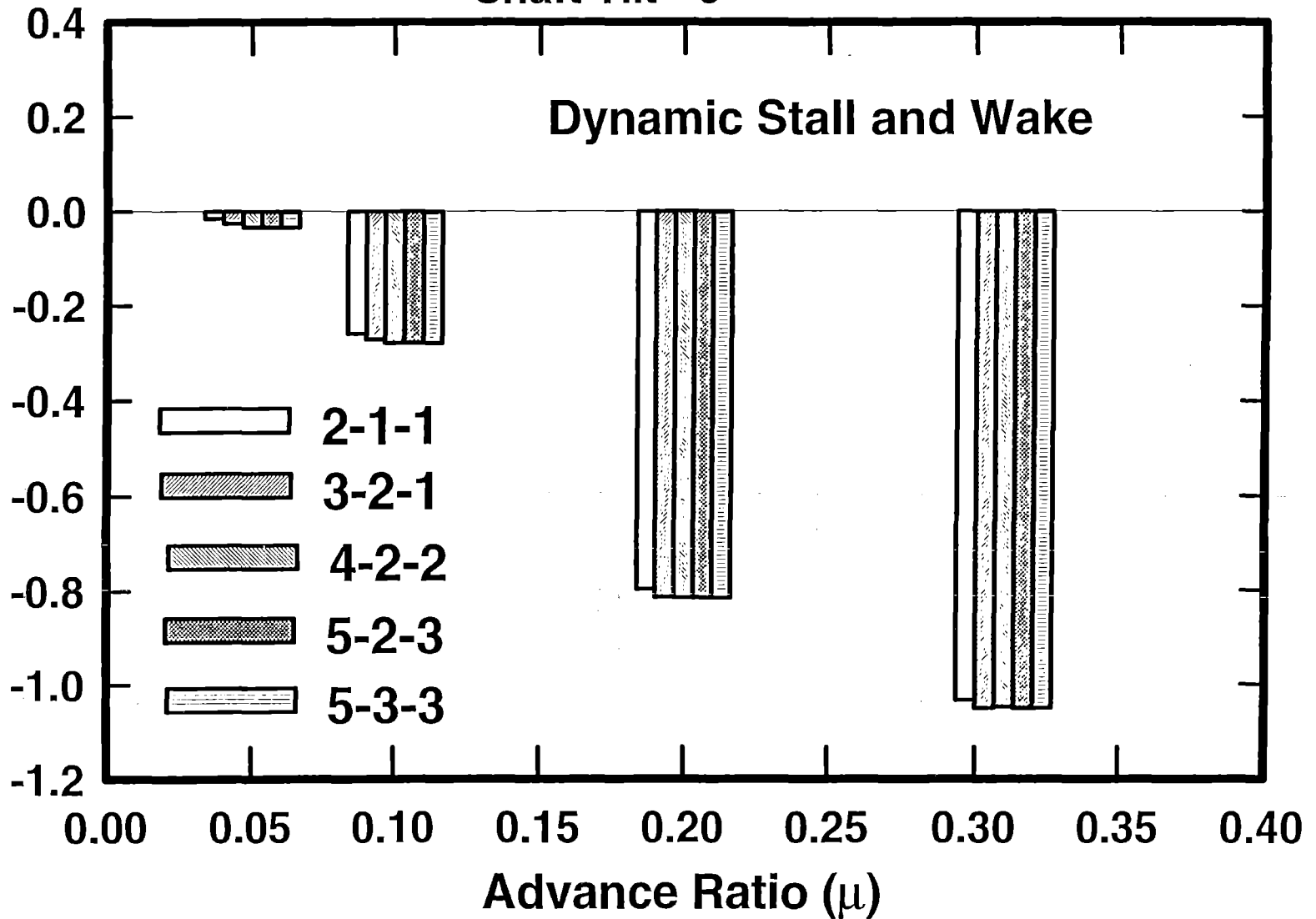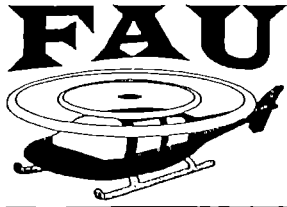
Convergence of Steady Flap Moment
for 3⁰ Collective and 2⁰ Precone
(Rotating modes)

Force Integration Method
Steady Flap Moment (in-lb)
Shaft Tilt=-6⁰

**Convergence of Steady Flap Moment
for 3⁰ Collective and 2⁰ Precone
(Rotating modes)**
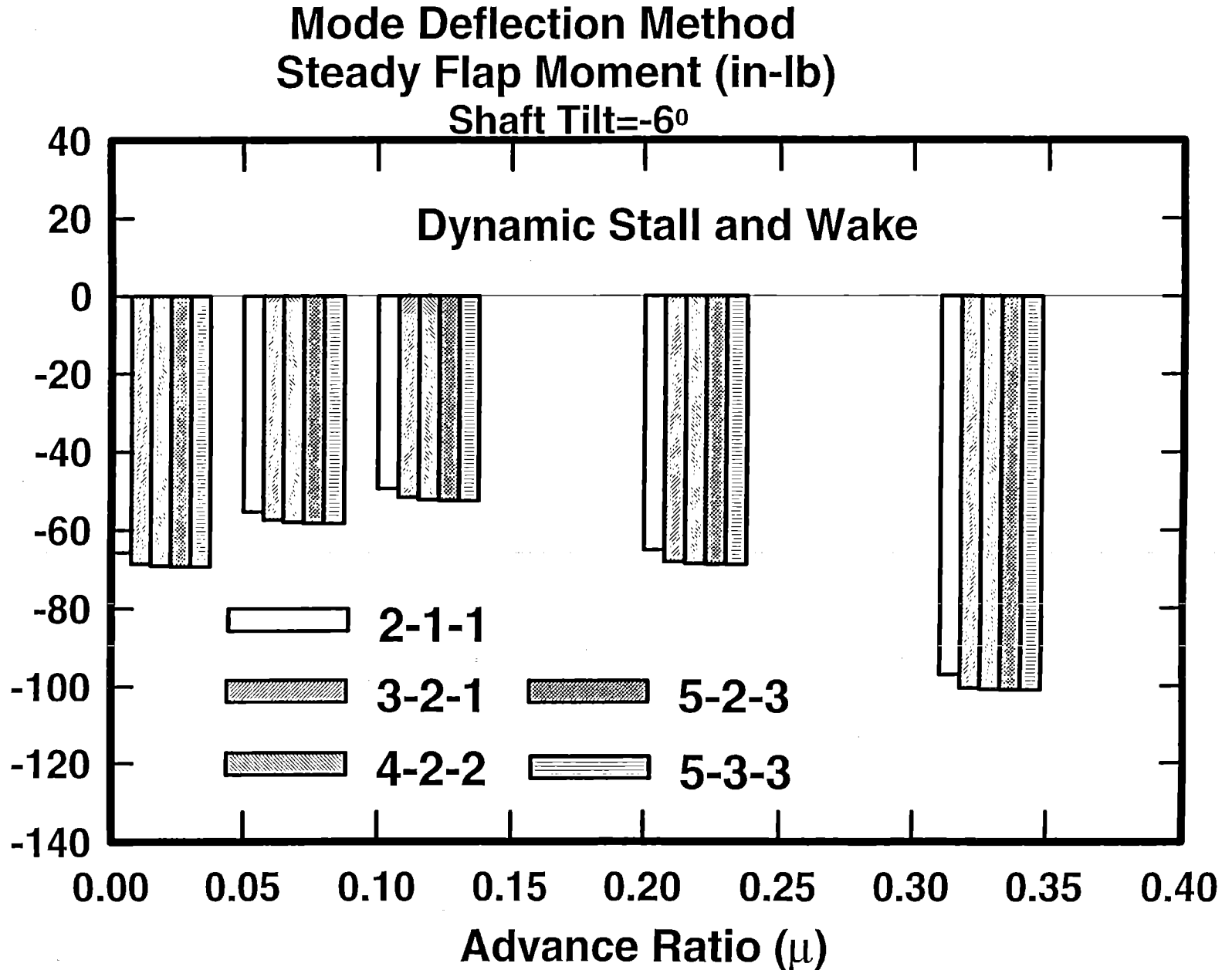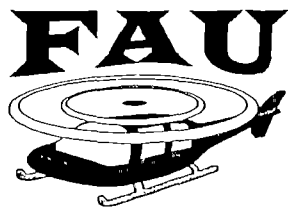
Mode Deflection Method
Steady Flap Moment (in-lb)
Shaft Tilt=-6⁰
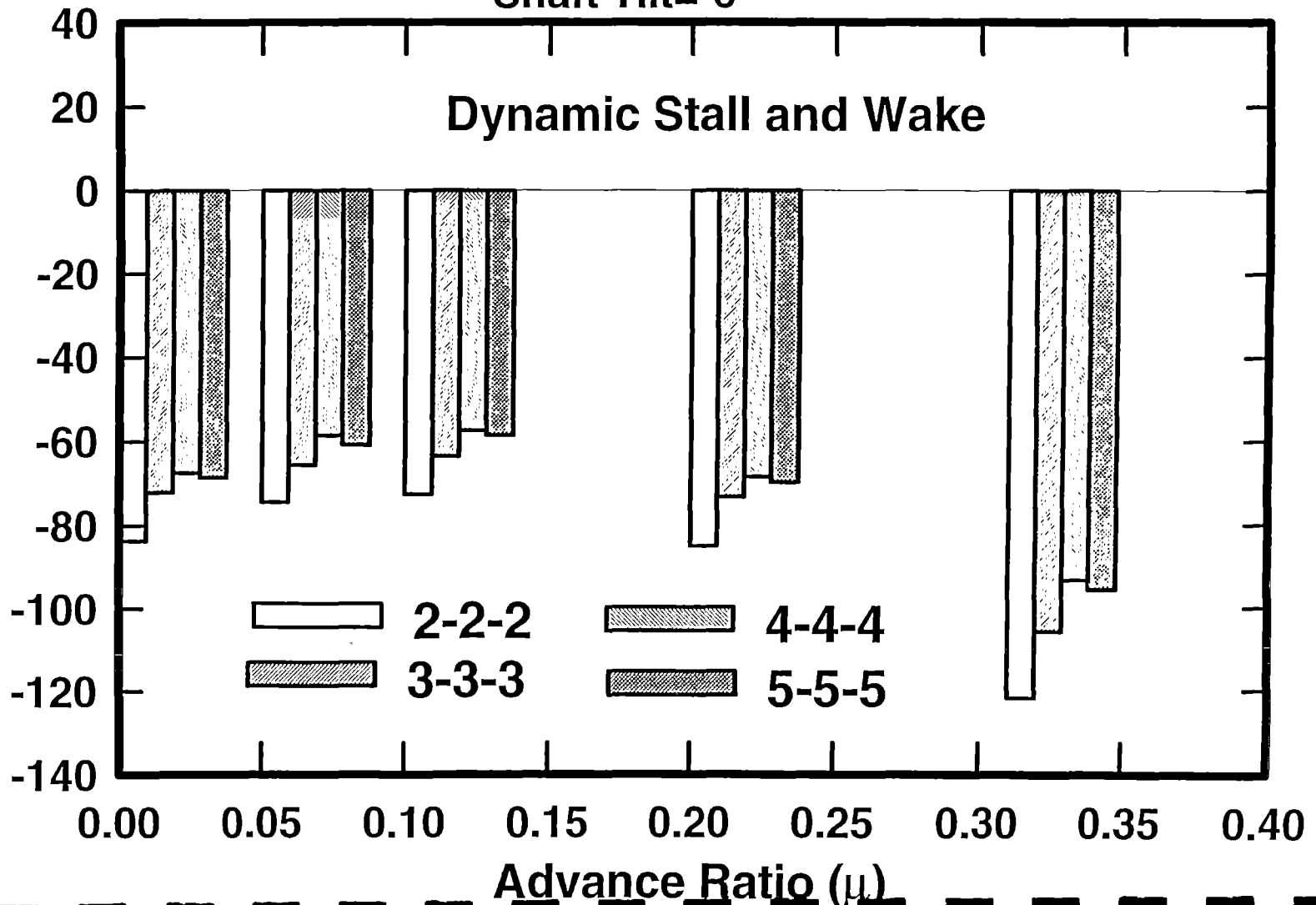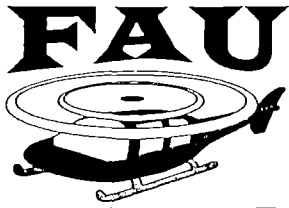
Dynamic Stall and Wake

Legend:
- 2-1-1
- 3-2-1
- 4-2-2
- 5-2-3
- 5-3-3

Advance Ratio (μ)

Lag Regressive-Mode Damping Correlation
for 3^0 Collective and 2^0 Precone

$$\theta_0 = 3^0 \text{ and } \beta_{pc} = 2^0$$

Lag Regressive-Mode Damping Level (1/sec)

● **Test Data**

Shaft Tilt = -3^0

Shaft Tilt = -6^0

Quasisteady Stall

Dynamic Stall

Dynamic Stall and Wake

Advance Ratio (μ)

Quasisteady Stall

Dynamic Stall

Dynamic Stall and Wake

Advance Ratio (μ)

Lag Regressive-Mode Damping Correlation for 5.9⁰ Collective and 2⁰ Precone

Lag Regressive-Mode Damping Level (1/sec)

Shaft Tilt = -6^0

Quasisteady Stall

Dynamic Stall

Test Data

Dynamic Stall and Wake

Advance Ratio (μ)

Lag Regressive-Mode Damping Correlation for 3^0 Collective and 0^0 Precone

Lag Regressive-Mode Damping Level (1/sec)

Lateral-Cyclic Pitch Correlation
for 3^0 Collective and 2^0 Precone

$$\theta_0 = 3^0 \text{ and } \beta_{pc} = 2^0$$

Lateral-Cyclic Pitch Angle (deg)

● **Test Data**

Shaft Tilt = -3^0

Dynamic Stall and Wake

Quasisteady Stall

Dynamic Stall

Advance Ratio (μ)

Shaft Tilt = -6^0

Dynamic Stall and Wake

Dynamic Stall

Quasisteady Stall

Advance Ratio (μ)

Lateral-Cyclic Pitch Correlation for 5.9⁰ Collective and 2⁰ Precone

Lateral-Cyclic Pitch Angle (deg)

Shaft Tilt = -6^0

Dynamic Stall and Wake

Test Data

Dynamic Stall

Quasisteady Stall

Advance Ratio (μ)

Lateral-Cyclic Pitch Correlation for 3^0 Collective and 0^0 Precone

Lateral-Cyclic Pitch Angle (deg)

Shaft Tilt = 0^0

Dynamic Stall and Wake

Test Data

Dynamic Stall

Quasisteady Stall

Advance Ratio (μ)

Longitudinal-Cyclic Pitch Correlation
for 3^0 Collective and 2^0 Precone

$$\theta_0 = 3^0 \text{ and } \beta_{pc} = 2^0$$
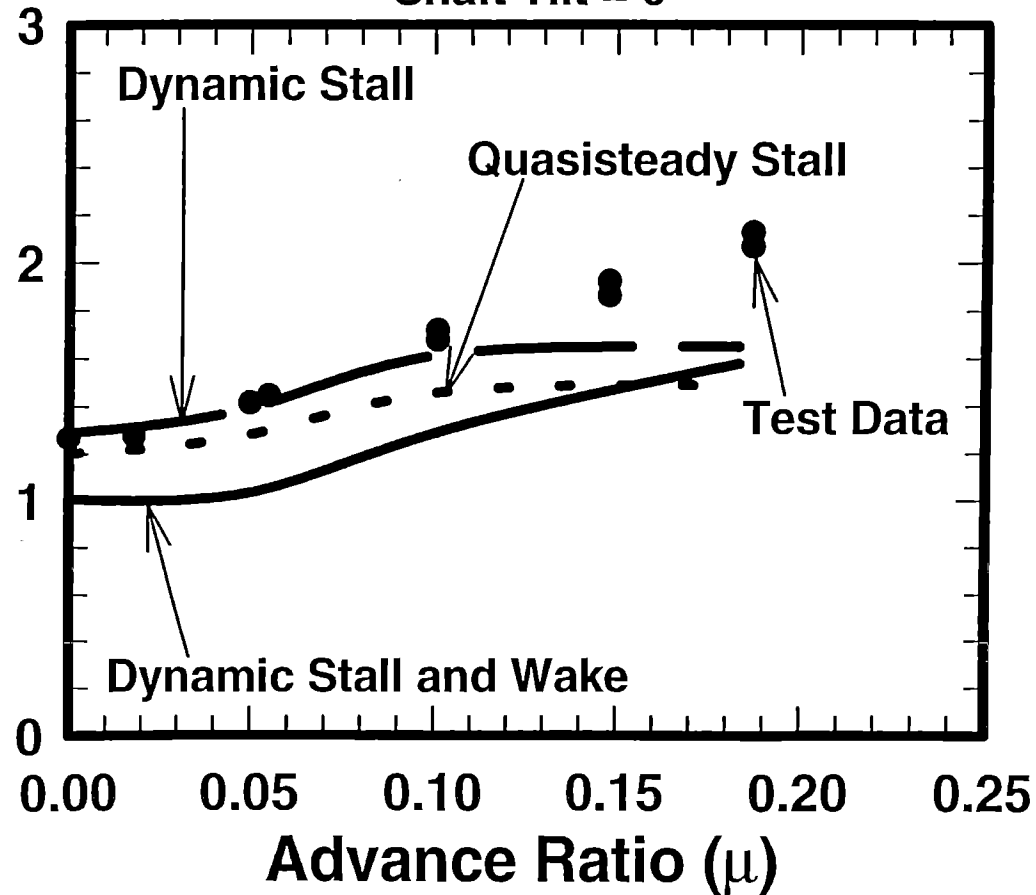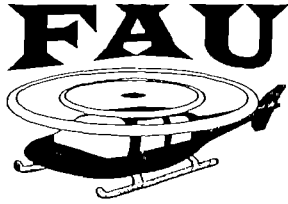
Longitudinal-Cyclic Pitch Angle (deg)

● Test Data

Longitudinal-Cyclic Pitch Correlation
for 5.9⁰ Collective and 2⁰ Precone
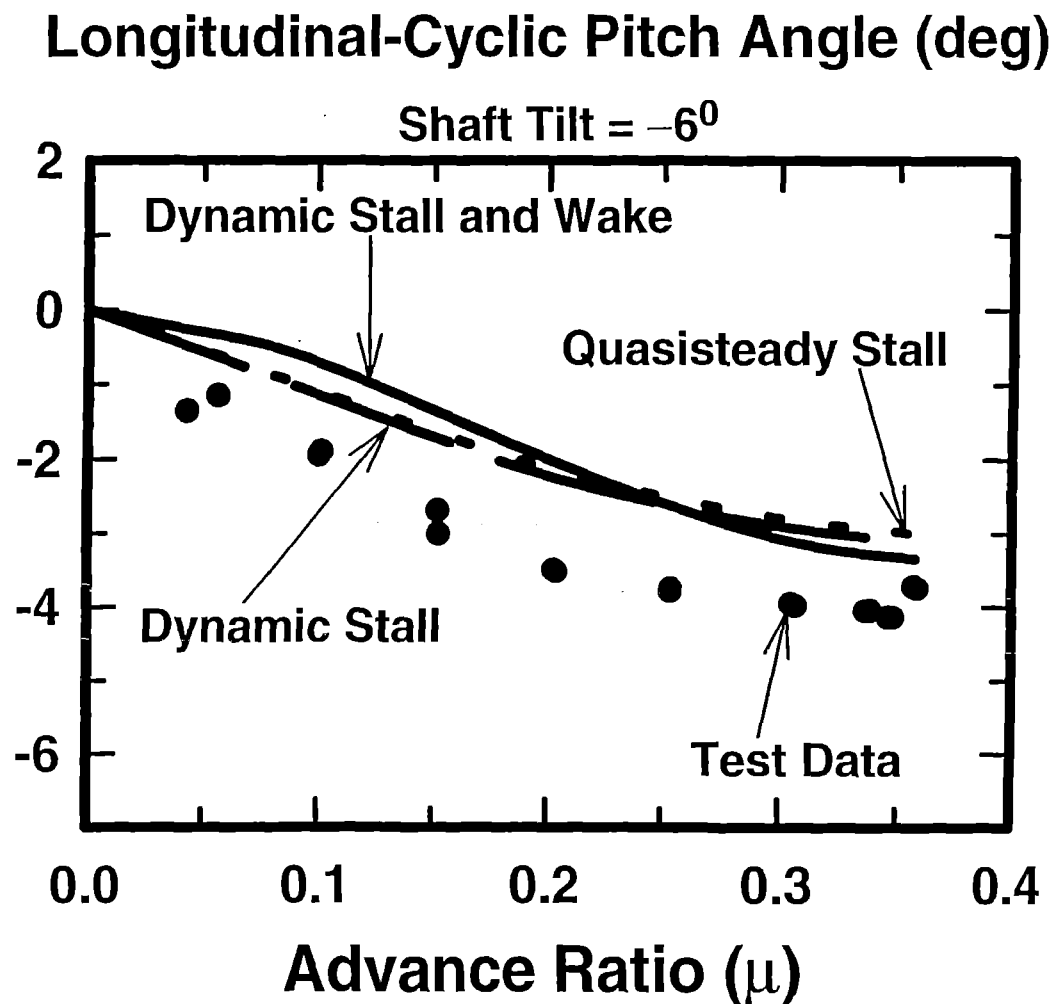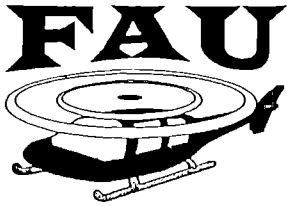
$$\text{for } 5.9^0 \text{ Collective and } 2^0 \text{ Precone}$$

Longitudinal-Cyclic Pitch Angle (deg)

Shaft Tilt = -6^0

Dynamic Stall and Wake

Quasisteady Stall

Dynamic Stall

Test Data

Advance Ratio (μ)

Longitudinal-Cyclic Pitch Correlation
for 3^0 Collective and 0^0 Precone

Longitudinal-Cyclic Pitch Angle (deg)

FAU
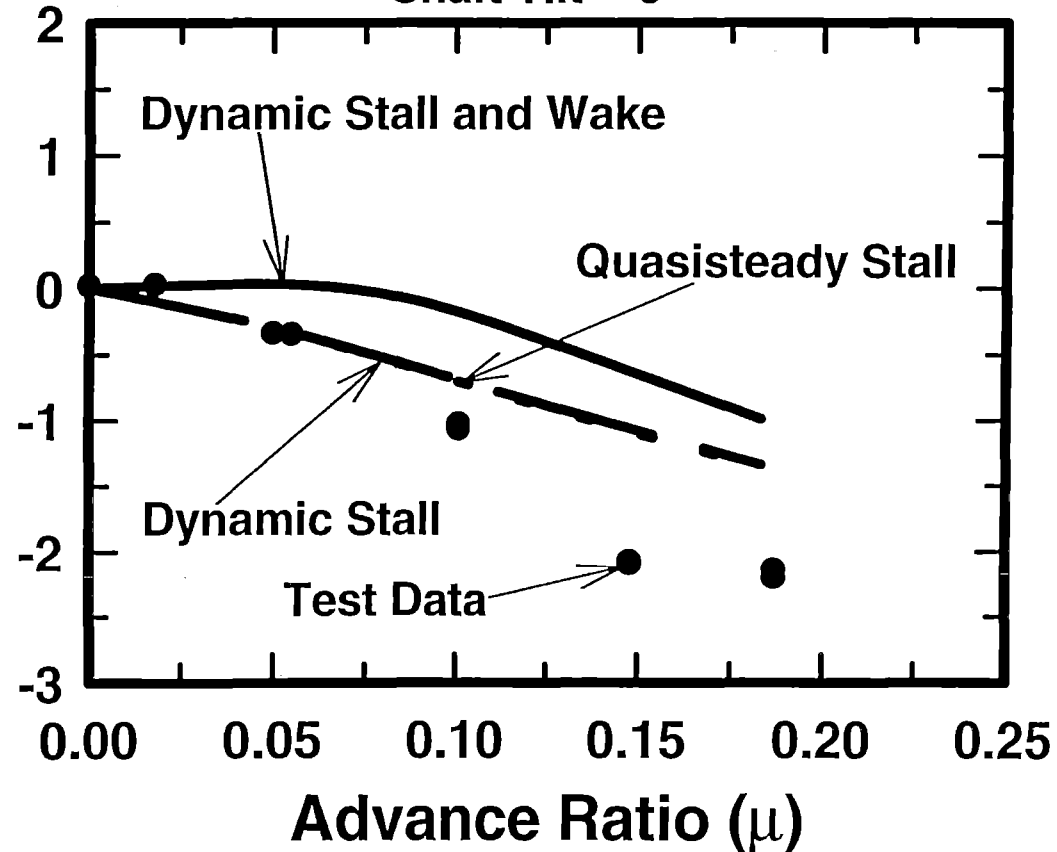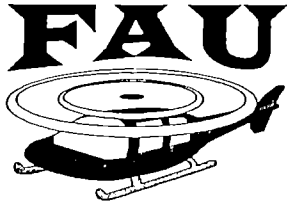
Flapping Moment Correlation
(Nonrotating Modes)

Collective = 3^0, Shaft Tilt = -6^0, Precone = 2^0

Steady Flap Moment (in-lb)

● **Test Data**

Force Integration

Dynamic Stall and Wake

Quasisteady Stall

Dynamic Stall

Advance Ratio (μ)

Mode Deflection

Dynamic Stall and Wake

Dynamic Stall

Quasisteady Stall

Advance Ratio (μ)
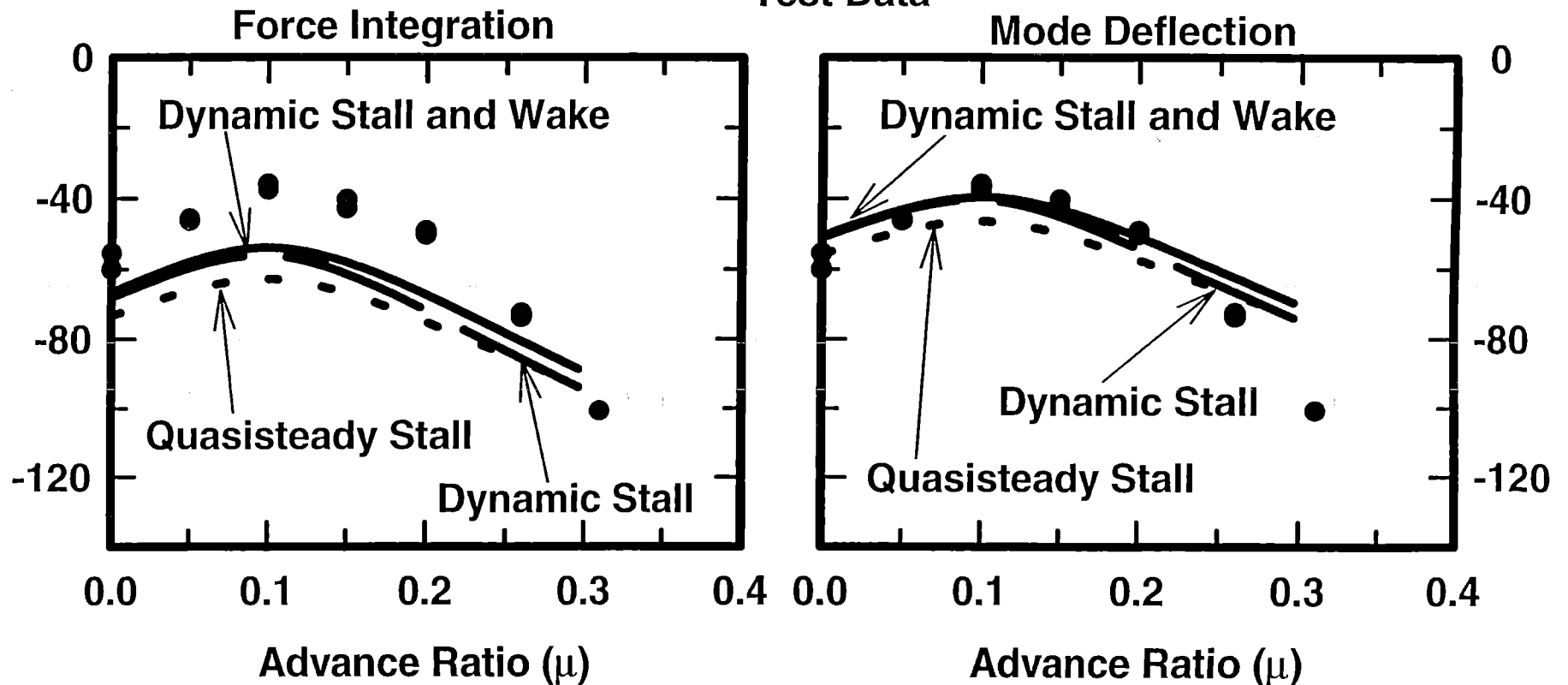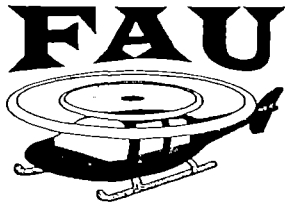
Flapping Moment Correlation
(Rotating Modes)

Collective=3^0, Shaft Tilt=-6^0, Precone=2^0

Steady Flap Moment (in-lb)

● Test Data

Force Integration

Mode Deflection

Dyanmic Stall and Wake

Dynamic Stall and Wake

Advance Ratio (μ)
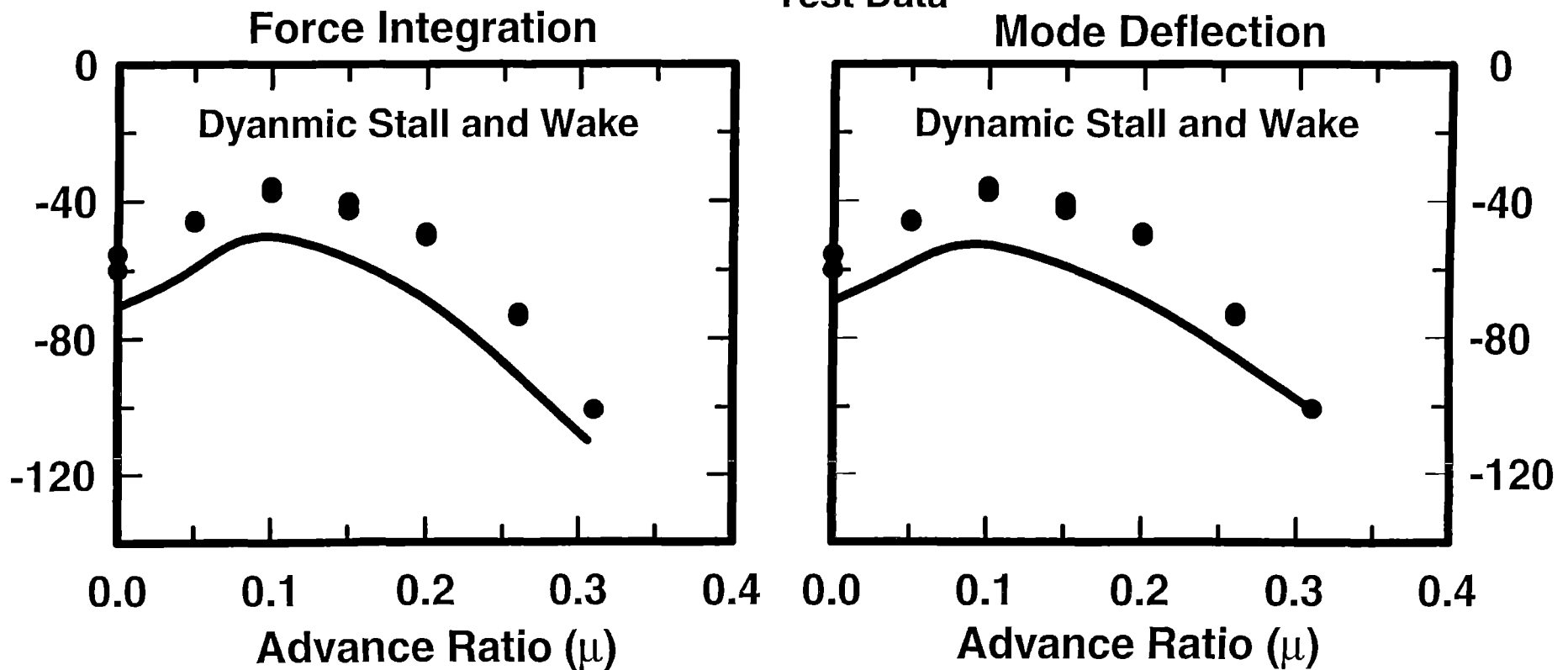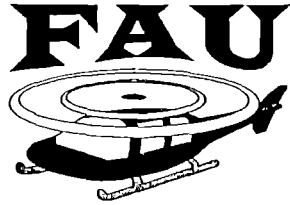
Advance Ratio (μ)

Concluding Remarks

The preceding study

- ☞ Quasisteady stall, dynamic stall, and dynamic stall and wake theories

- ☞ Lag regressive-mode damping level, cyclic controls and steady root flap moment

- ☞ Function of advance ratio

- ☞ Includes convergence with respect to the number and type of modes

☒ **The dynamic stall and wake theory provides the best correlation**

FAU
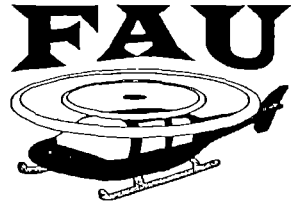
Concluding Remarks *Contd..*

Rotating Modes

⊠ A structural representation with five modes in flap, two in lag and three in torsion gives converged results for trim and stability

Nonrotating Modes

⊠ A structural representation with five modes each in flap, lag and torsion:

(a) Lag regressive-mode damping levels, cyclic pitch controls and steady flap moment based on the force-integration method converge

(b) Steady flap moment based on the mode-deflection method converges very slowly
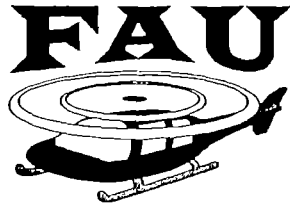
Concluding Remarks *Contd..*

☒ **Quasisteady stall and dynamic stall theories predict the damping levels fairly well**

☒ **Dynamic stall and wake theory shows better correlation**
  - ☛ Trend of the damping level is closer to the data

☒ **An exception occurs for the configuration with-three degree collective and six-degree shaft tilt at high advance ratios**
  - ☛ Data show that the damping level decreases rapidly and becomes nearly zero (neutrally stable)
  - ☛ None of the three theories predict this; they predict nearly identical damping showing a fairly stable lag regressive mode
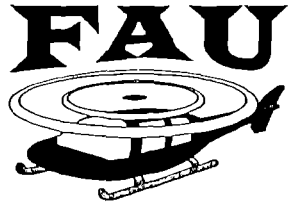
Concluding Remarks *Contd..*

- ✉ Concerning correlation of the lateral cyclic pitch angle, the quasisteady stall and dynamic stall theories do not provide a satisfactory correlation. By comparison, the dynamic stall and wake theory dramatically improves the correlation and provides satisfactory correlation

- ✉ The calculations of the steady root flap moment from all three theories are close

A Two-Bladed Rotor Helicopter Ground Resonance Simulation Including Eigenvector Analysis

Daniel José Arcos
Graduate Student

Donizeti de Andrade
Associate Professor

Technological Institute of Aeronautics (ITA)
Aerospace Technical Center (CTA)
12228-900 São José dos Campos, São Paulo, Brazil

A Two-Bladed Rotor Helicopter Ground Resonance Simulation Including Eigenvector Analysis

Daniel José Arcos
Graduate Student

Donizeti de Andrade
Associate Professor

Technological Institute of Aeronautics (ITA)
Aerospace Technical Center (CTA)
12228-900 São José dos Campos, São Paulo, Brazil

Abstract

This paper deals with the helicopter ground resonance phenomenon, more specifically, with a simplified two-bladed hingeless rotor model analysis, which takes into account the lead-lag degree-of-freedom of a rigid blade and the longitudinal and lateral degrees-of-freedom of the rotor support. The analysis neglects both the blade out-of-plane motion and aerodynamics effects. The stability analysis of the dynamics system takes the state-variable approach and utilizes the Floquet theory for solving the differential equations in the nonrotating reference system. Results show modal frequency and damping diagrams as function of rotor rotational speed for hingeless rotor configurations including no damping on both support and blades, including damping on both blades, and including an inoperative blade damper. Similar results are shown for an articulated rotor configuration including an anisotropic support. Modal damping diagrams for both rotating and nonrotating frame analyses are presented for hingeless rotor configurations including damping on both blades and including an inoperative blade damper. Results also include effects of inertial coupling variation in the rotating frame. Eigenvector analysis enlightens the inherent connection of divergence and resonance instabilities with in-phase components of displacements and corresponding time rates for all configurations studied.

Introduction

Helicopter ground resonance is a catastrophic dynamic instability, characterized by the coupling of the whirling movement of the combined center of mass of the blades around their respective shaft and the shaft (support) displacement itself. Rotational energy from the rotor is converted into oscillatory energy of the blades through the fuselage coupled oscillations. Inertia forces caused by the out-of-phase displacement of the blades around their hinges (real, as in articulated rotors, or virtual, as in hingeless rotors) react with the fuselage (body, support) movement. Once the rotor common mass center is offset from its support, a possible path for it consists of a divergent elliptical spiral, characterizing the resonance phenomenon. The movement of the rotor common center of mass is directly associated with the rotor rotational speed. As a consequence, ground resonance depends on the rotor rotational speed range, and the design engineer is

1

led to choose rotor elastomechanical characteristics and rotational speed domain in a way that this kind of instability is excluded from the helicopter operational envelope. Both experimental and theoretical research pointed out the need of placing damping on both rotor lead-lag hinges and support (in particular, placement of damping on the landing gear). Correctly choosing the damping placement is one of the key-points regarding ground resonance avoidance.

The classical approach for studying the phenomenon is due to Coleman and Feingold [1]. Their work became the most comprehensive theoretical investigation ever done on this subject, becoming a cornerstone for more recent investigation. Johnson [2] presents a detailed analysis of the ground resonance phenomenon, following basically Coleman and Feingold's work. It is treated considering the presence of fully articulated rotor system which does not show a significant coupling of inplane and out-of-plane blade degrees of freedom. Under this approach, the instability is governed mainly by both the lead-lag elastomechanical blade characteristics and rotor support stiffness characteristics, with no influence of the rotor aerodynamics in the analytical results. As all classical work, it considers only the degrees of freedom from the support and from the blade lead-lag motion, neglecting both blade out-of-plane dynamics and aerodynamics loads. Based on Newton's method, hingeless rotor equations of motion are derived, taking into account isotropic only characteristics. This yields a stability analysis involving a constant coefficient system of equations. Hammond [3] introduces a general analysis, treating the problem in the nonrotating coordinate system through Floquet theory, along with a rotor and support anisotropic model.

The advent of rotor hingeless and bearingless configurations, with their inherent strong structure-flow couplings, made mandatory the inclusion of rotor aerodynamics in the analysis, in order to improve correlation with experimental results. Trying to correlate Bousman's experimental results [4], Johnson [5] showed some aspects of the influence of unsteady aerodynamics on hingeless rotor ground resonance, opening doors for the upcoming (now current) aeromechanical type of investigation.

McNulty [6] calls attention to the importance of understanding the general characteristics of the response of periodic coefficient systems and how they differ from the constant coefficient results. In a constant coefficient system analysis, each natural mode is completely described by its natural frequency, damping and mode shape, the latter being a constant vector. For a periodic coefficient system, Floquet-Liapunov's theorem predict that the individual modes of the system will each contain responses at any number of frequencies which are separated from each other by integer multiples of the rotor speed. The complete response of each mode is then given by the product of a sinusoidal term with a "natural frequency," an exponential damping term, and this periodic mode shape vector. The usual practice is to add enough multiples of the rotor speed so one can obtain the so called "natural frequencies" of the system which indeed are frequencies associated with the natural frequencies of an appropriate constant coefficient system. This procedure seems to have led to a certain amount of confusion about this seemingly multivalued "natural frequency." This is probably due to the fact that most publications including Floquet results are focused on eigenvalues, paying little or no attention to the periodic eigenvector. An exception can be found in Ormiston's [7].

Equations of Motion and Solution Approach

The derivation of the equations of motion follows Johnson's [2] procedure and nomenclature. Figure 1 shows a drawing sketching the dynamic system model in analysis. The analysis consists basically in first obtaining the equations of motion for the rotor in the rotating frame in terms of the differential lead-lag

degree of freedom, and the support equations in terms of its longitudinal and lateral degrees of freedom in the nonrotating frame, through the reactions acting upon it due to the blade spanwise forces. Then, the equations of motion are obtained through the coupling of the just mentioned equations written for a unified reference system. Equations can be either expressed in the rotating frame, with shaft and support contributions being transformed into the rotating coordinates by means of a harmonic balance strategy, which leads to a constant coefficient matrix stability analysis, or expressed in the nonrotating frame by means of transforming the rotor equations using the multiblade coordinate transformation [8], which leads to a periodic coefficient matrix stability analysis, here solved utilizing the Floquet method [9, 10].

The equations of motions in the rotating frame for the ground resonance dynamics are given by

$$[M]\{y\}^{**} + [C]\{y\}^{*} + [K]\{y\} = 0,$$

where

$$[M] = \begin{bmatrix} I_\zeta^\# & 0 & \overline{S}_\zeta^\# & 0 \\ 0 & I_\zeta^\# & -\overline{S}_\zeta^\# & 0 \\ \frac{\overline{S}_\zeta^\#}{2} & -\frac{\overline{S}_\zeta^\#}{2} & \overline{M}_x^\# & 0 \\ 0 & 0 & 0 & \overline{M}_x^\# \end{bmatrix}, \qquad [C] = \begin{bmatrix} I_\zeta^\# \, \overline{c}_{\zeta 1} & 0 & 0 & 2\overline{S}_\zeta^\# \\ 0 & I_\zeta^\# \, \overline{c}_{\zeta 2} & 0 & -2\overline{S}_\zeta^\# \\ 0 & 0 & \overline{M}_x^\# \, \overline{c}_x & 2\overline{M}_x^\# \\ -\overline{S}_\zeta^\# & \overline{S}_\zeta^\# & -2\overline{M}_x^\# & \overline{M}_x^\# \, \overline{c}_x \end{bmatrix},$$

$$[K] = \begin{bmatrix} I_\zeta^\# \, \overline{v}_{\zeta 1}^2 & 0 & -\overline{S}_\zeta^\# & 0 \\ 0 & I_\zeta^\# \, \overline{v}_{\zeta 2}^2 & \overline{S}_\zeta^\# & 0 \\ -\frac{\overline{S}_\zeta^\#}{2} & \frac{\overline{S}_\zeta^\#}{2} & \overline{M}_x^\# \, (\omega_x^2 - 1) & \overline{M}_x^\# \, \overline{c}_x \\ 0 & 0 & -\overline{M}_x^\# \, \overline{c}_x & \overline{M}_x^\# \, (\omega_x^2 - 1) \end{bmatrix} \qquad \text{and} \qquad \{y\} = \left\{ \begin{array}{c} \zeta^{(1)} \\ \zeta^{(2)} \\ \overline{y}_r \\ \overline{x}_r \end{array} \right\}.$$

The state variable representation for this system of equations can be written as

$$[J]\{x\}^{*} + [A]\{x\} = \{0\} \quad \Rightarrow \quad \{x\}^{*} = [J]^{-1}[A]\{x\} \equiv [D]\{x\},$$

where

$$[J] = \begin{bmatrix} [I] & 0 \\ 0 & [M] \end{bmatrix}, \quad [A] = \begin{bmatrix} 0 & -[I] \\ [K] & [C] \end{bmatrix}, \quad \{x\} = \left\{ \begin{array}{c} \{y\} \\ \{y\}^{*} \end{array} \right\}$$

and $[D]$ is a constant coefficient matrix.

The stability of the dynamic system depends upon the solution of constant coefficient differential equations, yielding a solution of the type

$$\{x\} = \{\varphi_i\} \, e^{\eta_i \overline{t}},$$

where one observes that η_i and $\{\varphi_i\}$ are the eigenvalues and eigenvectors of the stability matrix $[D]$, respectively. In general, η_i is complex, and can be written as

$$\eta_i = \sigma \pm i\omega \quad \text{where} \quad \left\{ \begin{array}{l} \sigma = \text{Modal damping} \\ \omega = \text{Modal frequency} \end{array} \right. .$$

Now, the equations of motions in the nonrotating frame are given by

$$[M]\{y\}^{**} + [C]\{y\}^{*} + [K]\{y\} = 0,$$

3

where

$$[M] = \begin{bmatrix} I_\zeta^\# & -\overline{S}_\zeta^\# \cos\psi & \overline{S}_\zeta^\# \sin\psi \\ -\overline{S}_\zeta^\# \cos\psi & \overline{M}_y^\# & 0 \\ \overline{S}_\zeta^\# \sin\psi & 0 & \overline{M}_x^\# \end{bmatrix}, \qquad [C] = \begin{bmatrix} I_\zeta^\# \, \overline{c}_\zeta & 0 & 0 \\ 2\overline{S}_\zeta^\# \sin\psi & \overline{M}_y^\# \, \overline{c}_y & 0 \\ -2\overline{S}_\zeta^\# \cos\psi & 0 & \overline{M}_x^\# \, \overline{c}_x \end{bmatrix},$$

$$[K] = \begin{bmatrix} I_\zeta^\# \, \overline{v}_\zeta^2 & 0 & 0 \\ \overline{S}_\zeta^\# \cos\psi & \overline{M}_y^\# \, \omega_y^2 & 0 \\ -\overline{S}_\zeta^\# \sin\psi & 0 & \overline{M}_x^\# \, \omega_x^2 \end{bmatrix} \qquad \text{and} \qquad \{y\} = \left\{ \begin{array}{c} \zeta_1 \\ \overline{y}_h \\ \overline{x}_h \end{array} \right\}.$$

Also, within the $[K]$ matrix, $\overline{v}_\zeta^2 = K_1 + K_2\overline{\Omega}^2$, where K_1 and K_2 are Southwell coefficients [2]. The state-variable representation for this system of equations can be written as

$$\{x\}^* = [J]^{-1}[A]\{x\} \equiv [D]\{x\}, \text{ where } [D(\psi)] = [D(\psi + 2\pi)].$$

The stability of the dynamic system depends upon the solution of a periodic coefficient differential equations, for which the Floquet method is employed, yielding a solution of the type

$$\{x(\overline{t})\} = [\Phi(\overline{t}, \overline{t}_0)]\{x(\overline{t}_0)\},$$

where $[\Phi(\overline{t}, \overline{t}_0)]$ is a $n \times n$ nonsingular matrix, named state transition matrix, which satisfies the equation

$$[\Phi(\overline{t}, \overline{t}_0)]^* = [D(\overline{t})][\Phi(\overline{t}, \overline{t}_0)], \quad [\Phi(\overline{t}_0, \overline{t}_0)] \equiv [I].$$

From the theory, if $[D(\overline{t})]$ is periodic, one can analyze the system stability by observing the perturbation solution at the end of one period. Therefore,

$$\left\{x(\overline{T})\right\} = \left[\Phi(\overline{T}, 0)\right]\{x(0)\}.$$

By defining the Floquet transition matrix, $\left[Q(\overline{T})\right]$ as the state transition matrix at the end of one period, considering the Floquet-Liapunov theorem, and defining $\Lambda_k = e^{\eta_k \overline{T}}$, the system stability equation is given by

$$\left(\left[Q(\overline{T})\right] - \Lambda_k[I]\right)\{e_0\}_i = 0, \quad i = 1, 2, \cdots, n,$$

where one observes that Λ_k and $\{e_0\}_i$ are the eigenvalues and eigenvectors of the matrix $\left[Q(\overline{T})\right]$, respectively. In general, η_k is complex, and can be written as

$$\Lambda_k = e^{\eta_k \overline{T}} = e^{(\sigma_k + i\omega_k)\overline{T}} = e^{\sigma_k \overline{T}}\left(\cos\omega_k\overline{T} + i\sin\omega_k\overline{T}\right).$$

The stability of the system is directly related with σ_k, the real part of the eigenvalue exponent. Real and imaginary parts of the exponents are related to the eigenvalue itself as follows

$$\sigma_k = Re\left(\frac{1}{\overline{T}}\ln\Lambda_k\right), \quad \text{and}$$

$$\omega_k = Im\left(\frac{1}{\overline{T}}\ln\Lambda_k\right) = Abs\left(\frac{1}{\overline{T}} \pm \left(ArcTan\left(\frac{Im\Lambda_k}{Re\Lambda_k}\right) \pm 2n\pi\right)\right).$$

One observes that due to the fact that *ArcTan* be a multiple-valued function, the modal frequency is undetermined through a multiple of $\frac{2\pi}{T}$. The stability analysis involves only the real part of the eigenvalue exponent η_k, i.e., the modal damping σ_k. The modal frequency indeterminacy does not affect the stability characteristics of the system as predicted by the Floquet analysis. The key-point in the Floquet method is the evaluation of the state transition matrix at the end of one period, what sets it as a suitable computational tool to handle periodic coefficient differential equations.

Results and Discussion

A symbolic algebra software [12] is chosen for the establishment of a very concise building-block code [13, 14], taking advantage of the software efficient way of handling problems by means of its powerful symbolic, numerical and plotting features.

In the absence of experimental data to correlate with, an extensive comparison with Coleman and Feingold's results is performed. Some of the stability results obtained are shown herein. Figures from 2 to 7 show results for configuration sets involving soft inplane hingeless rotor analyzed in the rotating frame. Figures 8 and 9 show results for an articulated rotor configuration analyzed in the nonrotating frame. Figures 2 and 3 show results from an isotropic case application including a soft inplane hingeless rotor in the presence of no dampers on both support and blades. Configuration data are shown on Table 1. Diagrams in Figure 2(a) correlates modal frequency in terms of rotor rotational speed for both Coleman and Feingold [1], displayed in dashed lines, and the present works, displayed in full lines. The uncoupled system solution is presented along by means of curves carrying short-long dashed lines. One observes both the auto-excited divergence associated with the shaft critical speed and rotor auto-excited dynamics vibration, typical of helicopter ground resonance. One observes a very good agreement for both the location and magnitude of the instability regions. These regions can be observed in Figure 2(b), where positive modal damping shows up. Phase diagrams (eigenvectors) for each of the rotor and support displacements and their respective time rates are presented in Figure 3, enlightening mode shapes couplings. As happened in all of the configuration sets investigated, in the instability ranges one finds displacements and their time rates containing in-phase components, for both rotor and support modes; this points toward unstable mode couplings, being probably responsible for the catastrophic exchange of energy. Elsewhere, out of the instability regions, corresponding displacements and respective time rates phasors are 90 degrees out-of-phase, representing stable conditions. An isotropic case application of soft inplane hingeless rotor with damping on both blades has results shown in Figures 4 and 5. Configuration data are shown on Table 2(a). Figure 4(a) presents diagrams for modal frequency in terms of rotor rotational speed and Figure 4(b) presents modal damping for the same range of rotor rotational speed. It can be observed in the diagram of the modal damping that the introduction of external damping in the support and in the rotor produces the separation of the different modes, leading to a decrease in the damping amplitude as compared to what is observed in Figure 2(b), along with the displacement of the curves to the fourth quadrant of the diagram. This effect of the external damping is analyzed by Gandhi and Chopra [11] for the case of a multibladed rotor. Such effects on the modal damping, along with the disappearance of the coalescence of frequencies in the diagram of the modal frequency, show the importance of the external damping in avoiding the presence of rotor auto-excited dynamics vibration which characterizes the ground resonance. It can also be noticed that the introduction of the external damping reduces the rotor auto-

5

excited divergence to a narrow strip of frequencies around $\Omega = 0.9$/rev. Corresponding phase diagrams can be observed in Figure 5. One observes that displacements and respective time rates phasors are 90 degrees out-of-phase, representing stable conditions, for almost the whole range of rotor speed, except for the neighborhood of the shaft critical speed. Results from an application including a soft inplane hingeless rotor with an inoperative blade damper are presented in Figures 6 and 7. Configuration data are shown on Table 3(a). Figure 6(a) presents diagrams for modal frequency and Figure 6(b) presents diagrams modal damping in terms of rotor rotational speed. The frequency coalescence here carries ground resonance instability, as evidenced by a strip with positive values of modal damping. Corresponding phase diagrams can be observed in Figure 7.

Results from an application of nonrotating frame analysis are shown in Figures 8 and 9, for an extreme case involving anisotropy of an articulated rotor support in the presence of no dampers on both support and blades. Configuration data are shown in Table 4. Figure 8(a) correlates modal frequency in terms of rotor rotational speed diagrams for both Coleman and Feingold [1], shown in dashed lines, and present work, shown in full lines. Figure 8(b) presents modal damping in terms of rotor rotational speed diagrams. Corresponding phase diagrams can be observed in Figure 9. A similar analysis like the one conducted above for the rotating frame eigenvectors is valid here.

In order to check upon accuracy of rotating and nonrotating analyses as far as this investigation is concerned, two comparisons of modal damping results in terms of rotor rotational speed are shown in Figures 10 and 11. First, Figure 10 displays results from an application including soft inplane hingeless rotor with same damping on both blades are shown (configuration data are in Table 2), for both rotating and nonrotating frame analyses. Rotating frame results are displayed in full lines and the nonrotating counterparts in dashed lines. Here, one observes an overall results agreement, confirming the equivalence of Floquet and standard constant coefficient matrix eigenvalue analysis. Second, Figure 11 shows results from an application involving a soft inplane hingeless rotor with an inoperative blade damper (configuration data are in Table 3). It has been decided to adopt the same procedure as in Hammond's [3], when investigating this phenomenon for a 4-bladed rotor. This procedure leads to the presence of an extra, degenerating mode, which is credited in his paper to the evolution of one of the two collective modes present in the isotropic configuration analysis. Here one can also identify the presence of an extra, stable mode, as well.

Finally, results from a rotating frame analysis on the influence of inertial coupling variation for a soft inplane hingeless rotor configuration are shown in Figure 12 (configuration data are shown in Table 5). Present results are plotted along Coleman and Feingold's counterparts (their parametric charts are taken and transformed into a 3-D plot for this operation). One can observe clearly that the region of instability increases with the increasing of inertial coupling. Here also it is confirmed the good correlation of present and Coleman and Feingold's results.

Conclusions

A two-bladed rotor helicopter ground resonance simulation is performed, based on a simplified hingeless rotor model. The model involves only the rigid blades lead-lag degrees-of-freedom and rotor support longitudinal and lateral degrees-of-freedom. An extensive comparison is performed with classical Coleman and Feingold's results showing an overall good agreement for all the configuration analyzed. Results shown here involve soft hingeless rotor including isotropic configurations (1) with no dampers on both blades and support and (2) with same damping on both blades, as well as an anisotropic application including

6

an inoperative blade damper. An anisotropic application involving an articulated rotor configuration in the presence of no dampers on both blades and support is also presented. Comparisons of rotating and nonrotating frame results confirm the equivalence of Floquet and standard constant coefficient matrix eigenvalue analyses. Inertial coupling influence is also investigated, and 3-D diagrams are shown correlating present and Coleman and Feingold's results under a rotating frame analysis. Eigenvector analysis is extensively applied in this investigation and phase diagrams enlighten mode shapes couplings pointing towards a clear pattern involving displacements and corresponding time rates for both unstable and stable rotor rotational speed ranges.

Acknowledgments

References

[1] Coleman, R.P. and Feingold, A.M., "Theory of Self-Excited Mechanical Oscillations of Helicopter Rotors with Hinged Blades." NACA Report 1351, 1958.

[2] Johnson, W., **Helicopter Theory**. Princeton University Press, Princeton, 1980.

[3] Hammond, C.E., "An Application of Floquet Theory to Prediction of Mechanical Instability." *Journal of the American Helicopter Society*, Vol. 19, No. 4, October 1974.

[4] Bousman, W.G., "An Experimental Investigation of the Effects of Aeroelastic Couplings on Aerome- chanical Stability of a Hingeless Rotor Helicopter." *Journal of the American Helicopter Society*, Vol. 26, No. 1, January 1981, pp. 46-54.

[5] Johnson, W., "Influence of Unsteady Aerodynamics on Hingeless Rotor Ground Resonance." *Journal of the Aircraft*, Vol. 19, No. 8, August 1982, pp. 668-673.

[6] McNulty, M.J., "Effects of Blade-to-Blade Dissimilarities on Rotor-Body Lead-Lag Dynamics." *Journal of the American Helicopter Society*, Vol. 33, No. 1, January 1988.

[7] Ormiston, R.A., "Rotor-Fuselage Dynamics of Helicopter Air and Ground Resonance." *Journal of the American Helicopter Society*, Vol. 36, No. 2, April 1991.

[8] Hohenemser, K.H. and Yin, S.K., "Some Applications of the Method of Multiblade Coordinates." *Journal of the American Helicopter Society*, Vol. 17, No. 3, July 1972.

[9] Peters, D.A. and Hohenemser, K.H., "Application of the Floquet Transition Matrix to Problems of Lifting Rotor Stability." *Journal of the American Helicopter Society*, Vol. 16, No. 2, July 1971.

[10] Friedmann, P., Hammond C.E., and Tze-Hsin Woo, "Efficient Numerical Treatment of Periodic Systems with Application to Stability Problems." *International Journal for Numerical Methods in Engineering.* Vol. 11, No. 7, 1977, pp. 1117-1136.

[11] Gandhi, F. and Chopra, I., "An Analytical Model for a Nonlinear Elastomeric Lag Damper and Its Effect on Aeromechanical Stability in Hover." *Journal of the American Helicopter Society*, Vol. 38, No. 4, April 1994.

[12] Wolfram, S., **Mathematica—a System for Doing Mathematics by Computer.** Addison-Wesley Publishing Co., Second Edition, 1991.

[13] de Andrade, D., "On a Symbolic and Numerical Simulation of a Simplified Helicopter Ground Resonance Analytical Model." *Proceedings of The Fourth Pan-American Congress of Applied Mechanics*, Vol. II, pp. 48-53, Buenos Aires, Argentina, 1995.

[14] Arcos, D.J. and de Andrade, D., "On a Floquet Theory Application to a Simplified Two-Bladed Hingeless Rotor Ground Resonance Analysis." *Proceedings of The Fifth Pan American Congress of Applied Mechanics,* Vibrations and Dynamics Section, pp.443-448, San Juan, Puerto Rico, January 2-4, 1997.

Arcos, D.J. and de Andrade, D.
"A Two-Bladed Rotor Helicopter Ground Resonance Simulation Including Eigenvector Analysis"
Seventh International Workshop on Dynamics and Aeroelastic Stability Modeling of Rotorcraft Systems

Table 1 - Parameters for the analysis of the model including no dampers.

$K_1 = 0.2$	$K_2 = 0.05$	$M_y^* = 3.0$	$\overline{\omega}_x = \overline{\omega}_y = 1.0$
$I_\zeta^* = 0.6$	$\overline{S}_\zeta^* = 0.6$	$\overline{c}_y^* = 0.$	$\overline{c}_{\zeta 1}^* = \overline{c}_{\zeta 2}^* = 0.$

Table 2 - Parameters for the analysis of the model including dampers.

a) Rotating system.

$K_1 = 0.2$	$K_2 = 0.05$	$M_y^* = 3.0$	$\overline{\omega}_x = \overline{\omega}_y = 1.0$
$I_\zeta^* = 0.6$	$\overline{S}_\zeta^* = 0.6$	$\overline{c}_{\zeta 1}^* = 0.2449$	$\overline{c}_{\zeta 2}^* = \overline{c}_y^* = 0.2449$

b) Nonrotating system.

$K_1 = 0.2$	$K_2 = 0.05$	$M_y^* = 3.0$	$\overline{\omega}_x = \overline{\omega}_y = 1.0$
$I_\zeta^* = 0.6$	$\overline{S}_\zeta^* = 0.6$	$\overline{c}_\zeta^* = 0.2449$	$\overline{c}_x^* = \overline{c}_y^* = 0.2449$

Table 3 - Parameters for the analysis of the model including an inoperative blade damper.

a) Rotating system.

$K_1 = 0.2$	$K_2 = 0.05$	$M_y^* = 3.0$	$\overline{\omega}_x = \overline{\omega}_y = 1.0$
$I_\zeta^* = 0.6$	$\overline{S}_\zeta^* = 0.6$	$\overline{c}_{\zeta 1}^* = 0.$	$\overline{c}_{\zeta 2}^* = \overline{c}_y^* = 0.2449$

b) Nonrotating system.

$K_1 = 0.2$	$K_2 = 0.05$	$M_y^* = 3.0$	$\overline{\omega}_x = \overline{\omega}_y = 1.0$
$I_\zeta^* = 0.6$	$\overline{S}_\zeta^* = 0.6$	$\overline{c}_\zeta^* = 0.1225$	$\overline{c}_x^* = \overline{c}_y^* = 0.2449$

Table 4 - Parameters for the analysis of the model including anisotropic support.

$K_1 = 0.$	$K_2 = 0.1$	$M_x^* = M_y^* = 3.0$	$\overline{\omega}_x = 1.0, \overline{\omega}_y = 0.$
$I_\zeta^* = 0.6$	$\overline{S}_\zeta^* = 0.6$	$\overline{c}_\zeta^* = 0.$	$\overline{c}_x^* = \overline{c}_y^* = 0.$

Arcos, D.J. and de Andrade, D.
"A Two-Bladed Rotor Helicopter Ground Resonance Simulation Including Eigenvector Analysis"
Seventh International Workshop on Dynamics and Aeroelastic Stability Modeling of Rotorcraft Systems

Table 5 - Parameters for the analysis of the inertial coupling variation.

$K_1 = 0.2$	$K_2 = 0.05$	$M_y^* = 3.0$	$\overline{\omega}_x = \overline{\omega}_y = 1.0$
$I_\zeta^* = 0.6$	$\overline{S}_\zeta^* = 0. \rightarrow 0.7348$	$\overline{c}_y^* = 0.$	$\overline{c}_{\zeta 1}^* = \overline{c}_{\zeta 2}^* = 0.$

Figure 1 - Dynamical system model.

Arcos, D.J. and de Andrade, D.
"A Two-Bladed Rotor Helicopter Ground Resonance Simulation Including Eigenvector Analysis"
Seventh International Workshop on Dynamics and Aeroelastic Stability Modeling of Rotorcraft Systems
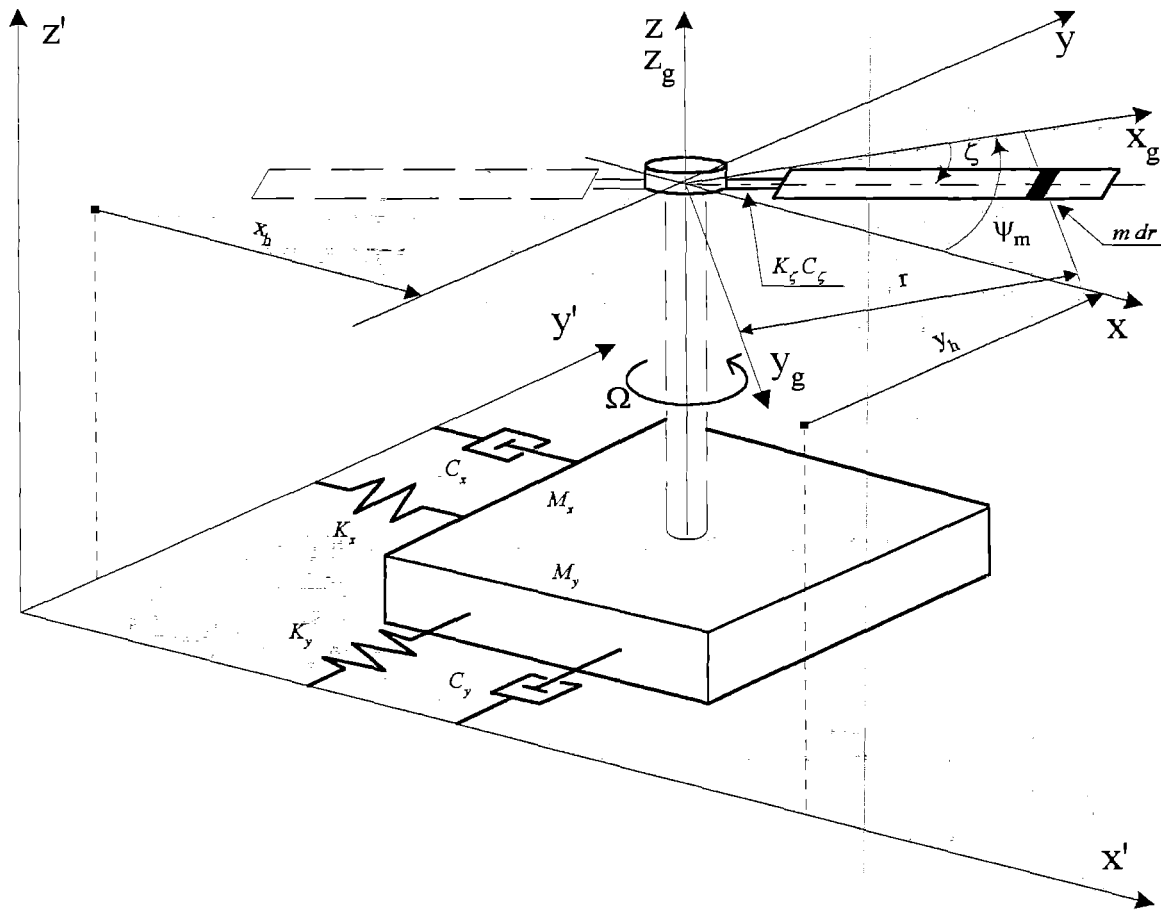
(a) modal frequency.

(b) modal damping.

Figure 2 - Soft inplane hingeless rotor with no dampers
(rotating frame analysis).

Figure 3 - Soft inplane hingeless rotor with no dampers, phasor diagrams
(rotating frame analysis).

Arcos, D.J. and de Andrade, D.
"A Two-Bladed Rotor Helicopter Ground Resonance Simulation Including Eigenvector Analysis"
Seventh International Workshop on Dynamics and Aeroelastic Stability Modeling of Rotorcraft Systems

(a) modal frequency

(b) modal damping

Figure 4 – Soft inplane hingeless rotor with damping on both blades
(rotating frame analysis).

Figure 5 - Soft inplane hingeless rotor with damping on both blades, phasor diagrams
(rotating frame analysis).

12

Arcos, D.J. and de Andrade, D.
"A Two-Bladed Rotor Helicopter Ground Resonance Simulation Including Eigenvector Analysis"
Seventh International Workshop on Dynamics and Aeroelastic Stability Modeling of Rotorcraft Systems
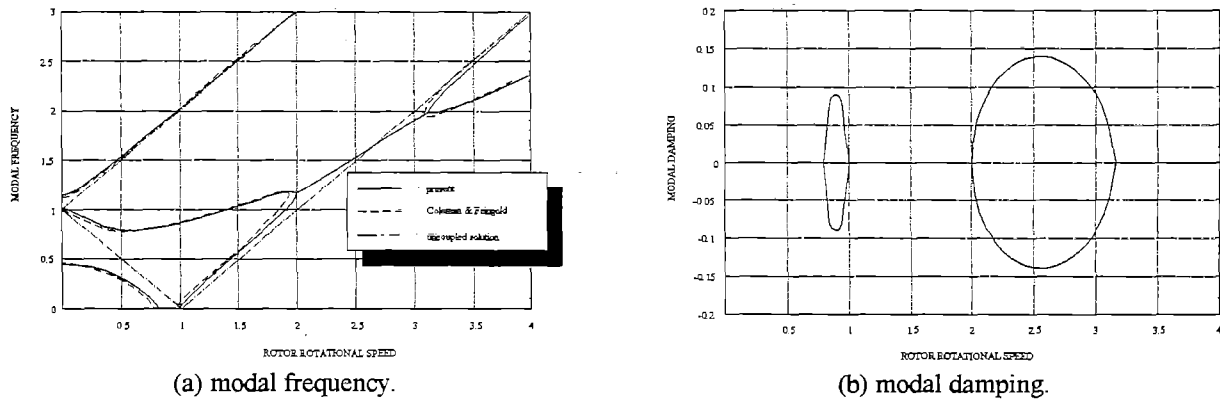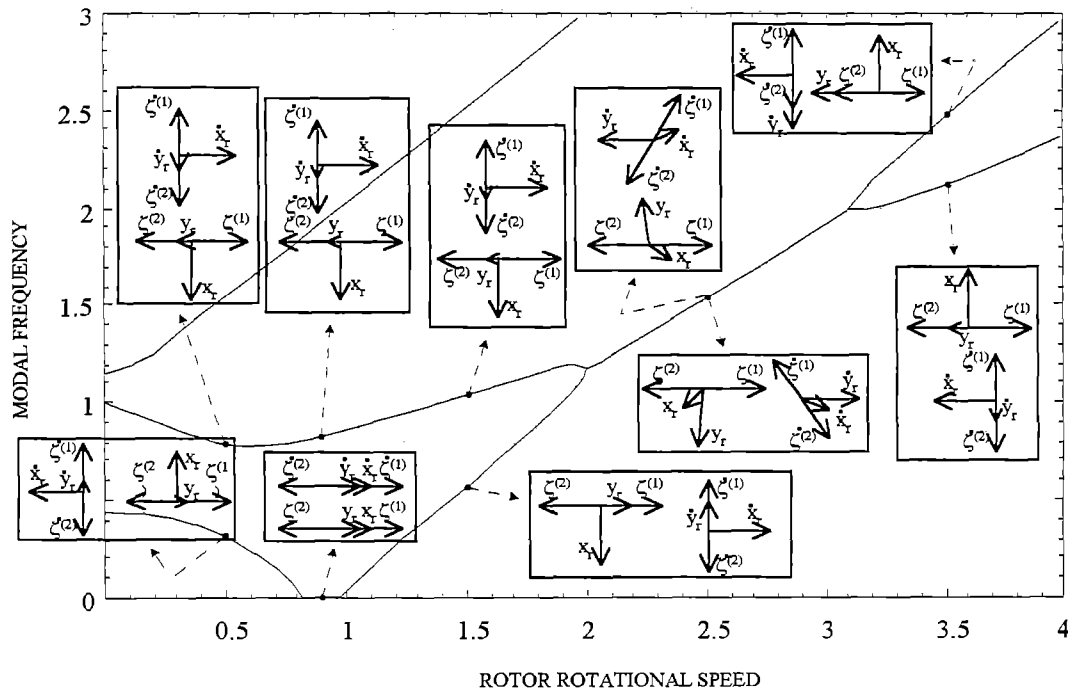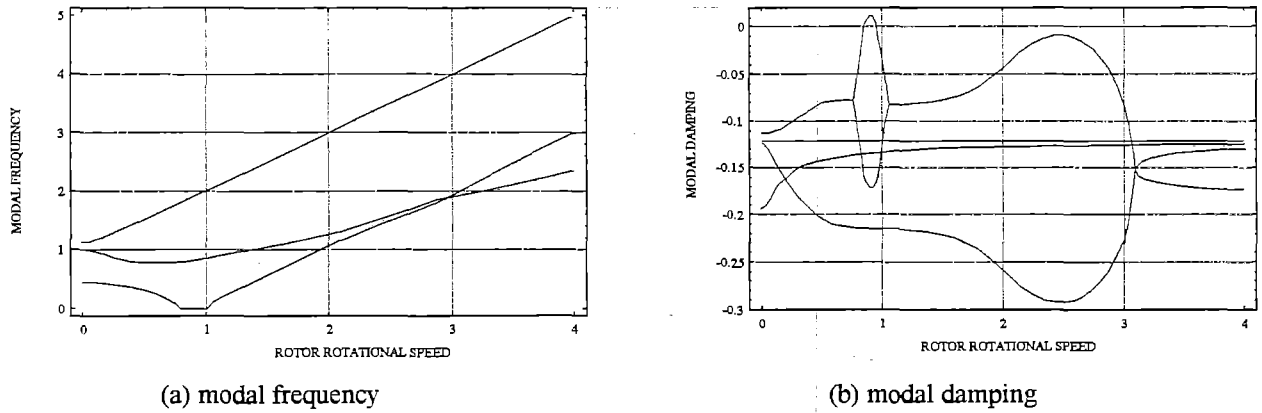
(a) modal frequency

(b) modal damping
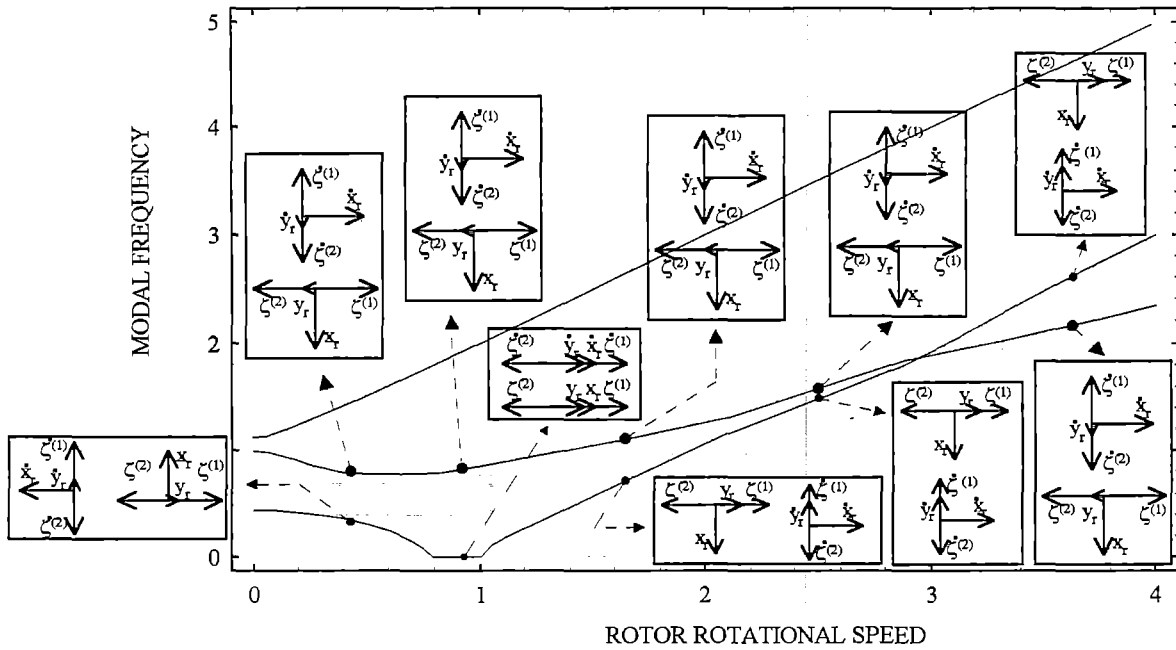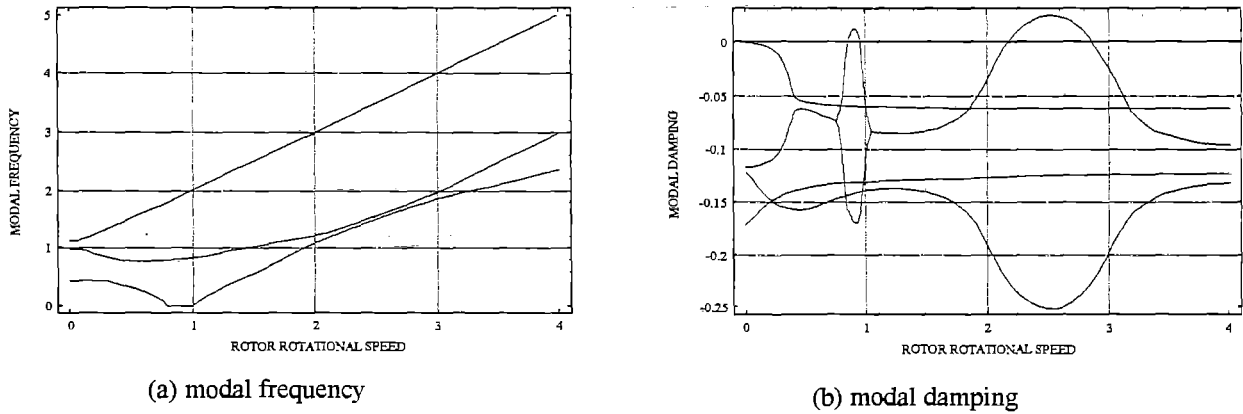
Figure 6 - Soft inplane hingeless rotor with an inoperative blade damper
(rotating frame analysis).
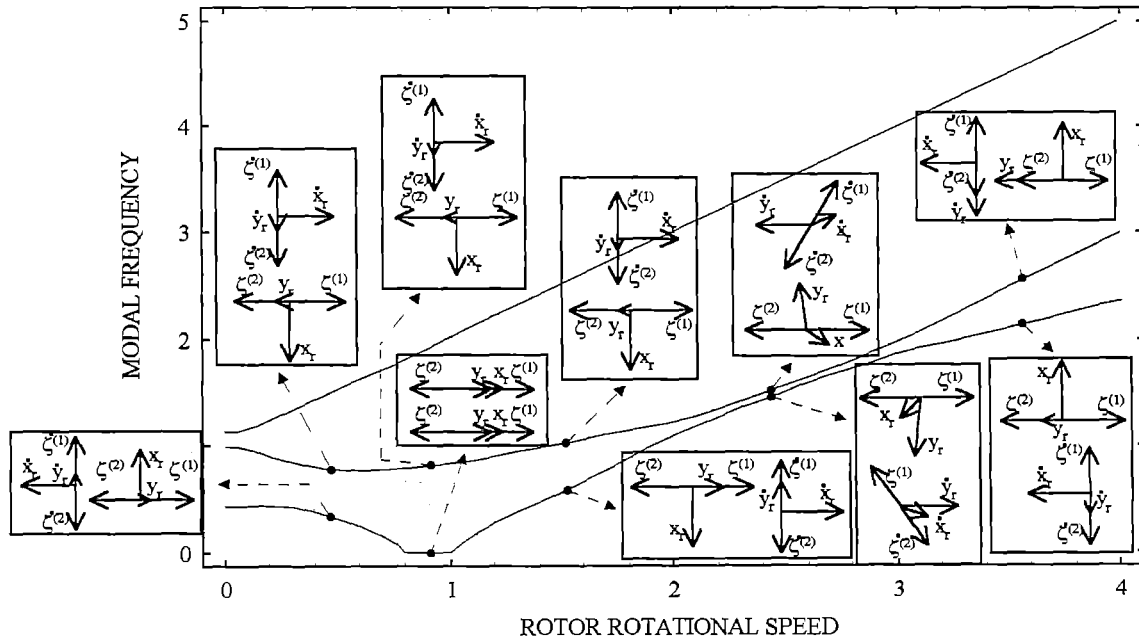
Figure 7 - Soft inplane hingeless rotor with an inoperative blade damper, phasor diagrams
(rotating frame analysis).

13

Arcos, D.J. and de Andrade, D.
"A Two-Bladed Rotor Helicopter Ground Resonance Simulation Including Eigenvector Analysis"
Seventh International Workshop on Dynamics and Aeroelastic Stability Modeling of Rotorcraft Systems

(a) modal frequency

(b) modal damping
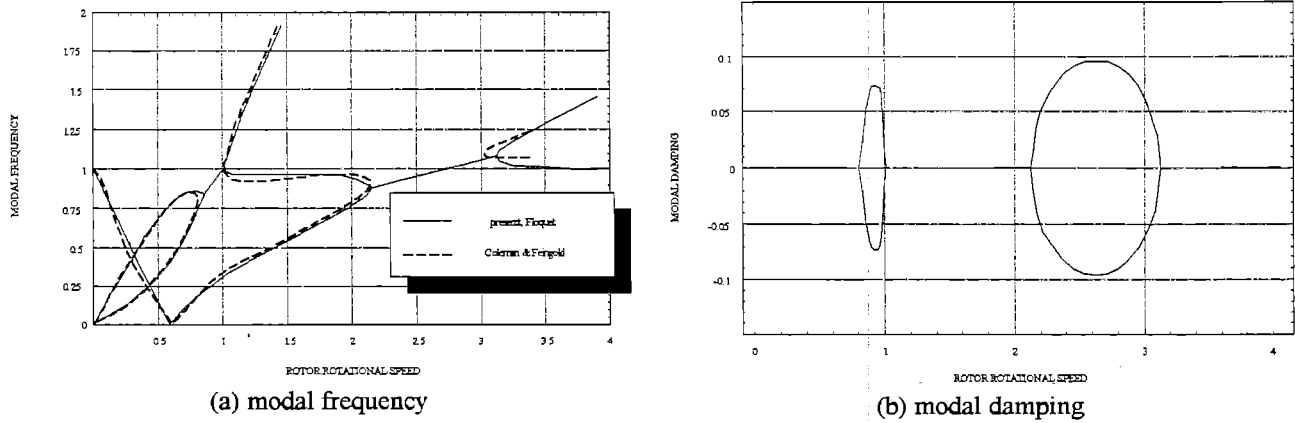
Figure 8 - Articulated rotor with anisotropic support
(nonrotating frame analysis).
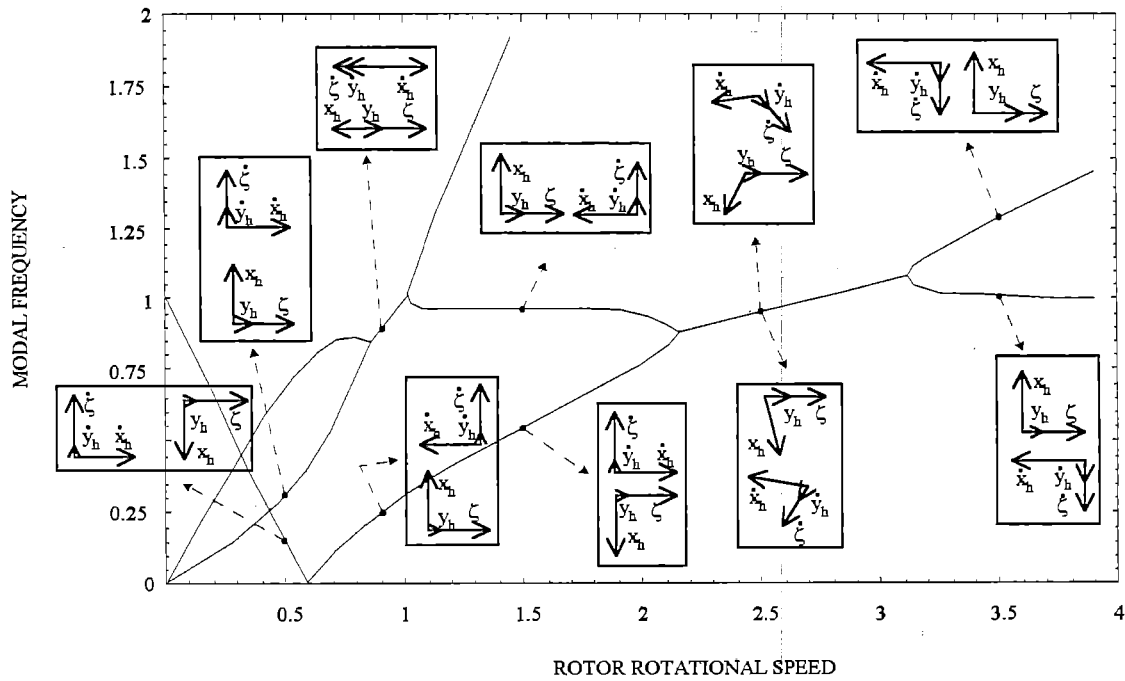
Figure 9 - Articulated rotor with anisotropic support, phasor diagrams
(nonrotating frame analysis).

14

Arcos, D.J. and de Andrade, D.
"A Two-Bladed Rotor Helicopter Ground Resonance Simulation Including Eigenvector Analysis"
Seventh International Workshop on Dynamics and Aeroelastic Stability Modeling of Rotorcraft Systems
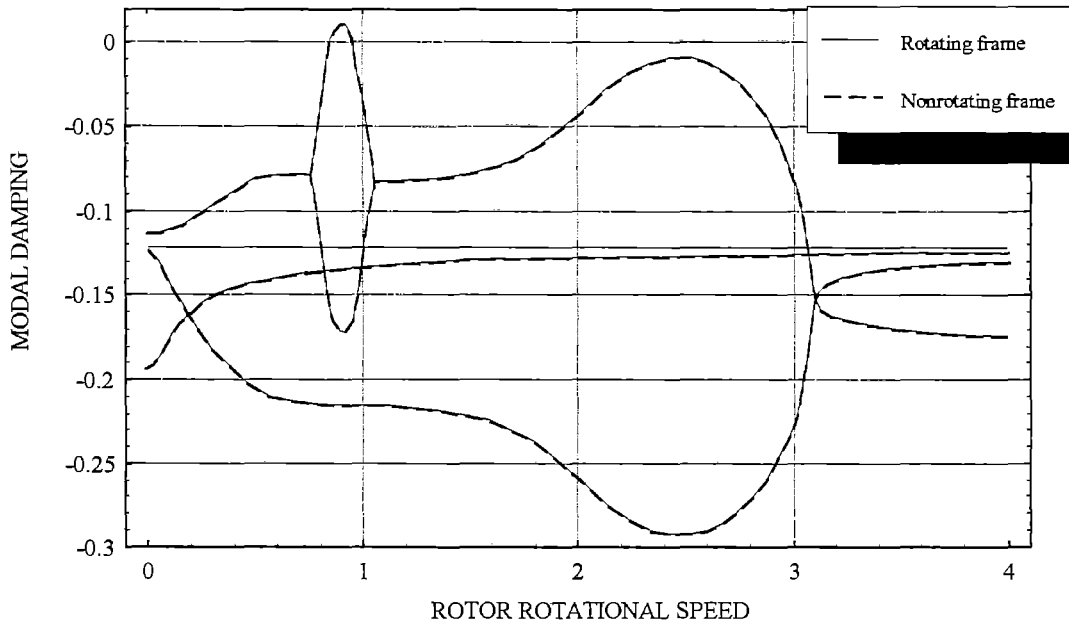
Figure 10 - Soft inplane hingeless rotor with damping on both blades.
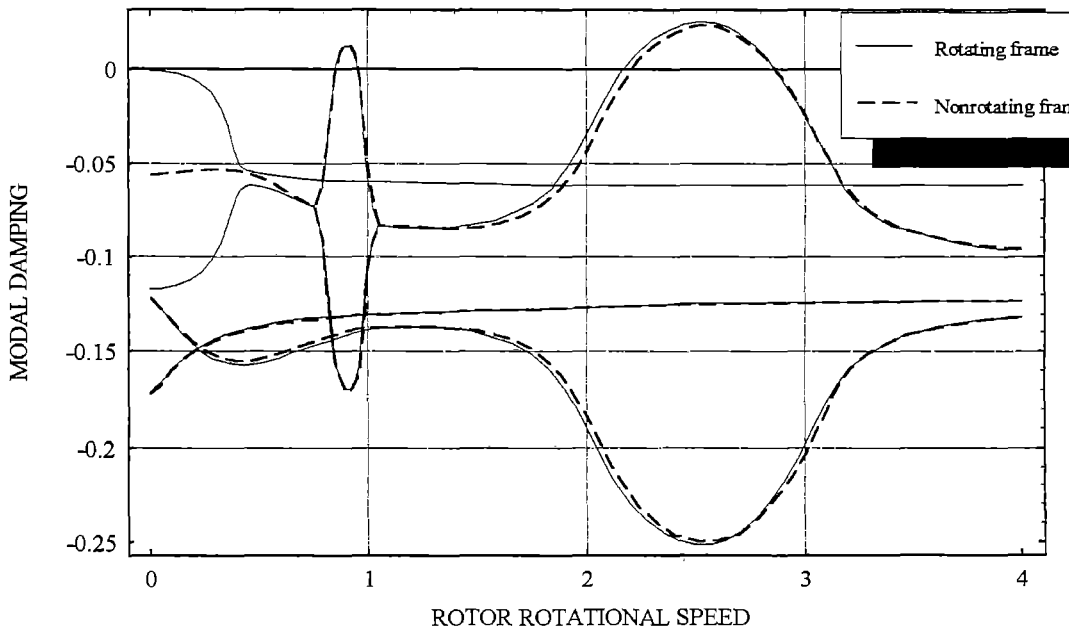
Figure 11 - Soft inplane hingeless rotor with an inoperative blade damper.

15

Arcos, D.J. and de Andrade, D.
"A Two-Bladed Rotor Helicopter Ground Resonance Simulation Including Eigenvector Analysis"
Seventh International Workshop on Dynamics and Aeroelastic Stability Modeling of Rotorcraft Systems
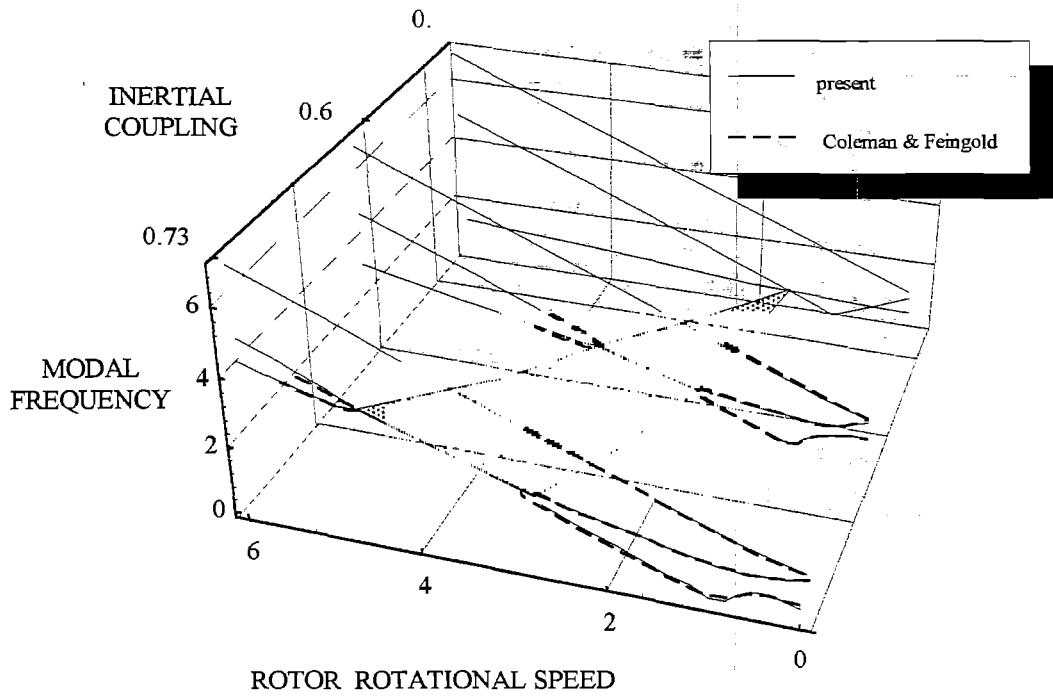
Figure 12 - Effects of inertial coupling variation in the rotating frame
(rotating frame analysis).

Floquet Analysis in the Absence of Complete Information on States and Perturbations

Research Assistant Xin Wang
Professor David A. Peters
Washington University in St.Louis

Floquet Theory

- Floquet theory is a powerful method that is still widely used.
- Fast Floquet theory and Floquet Theory can not be effectively used to analyze experiment data since they require excitations and measurements of all states. But it is too hard and even impossible to excite and measure all states in real experiments.
- We need a method that can be used to analyze data with the absence of states or perturbations.

Embedding theory

A [shape: sector with vertices A, B, C, D] B ⇒ A [square with vertices A, B, C, D] B
D   C   D   C
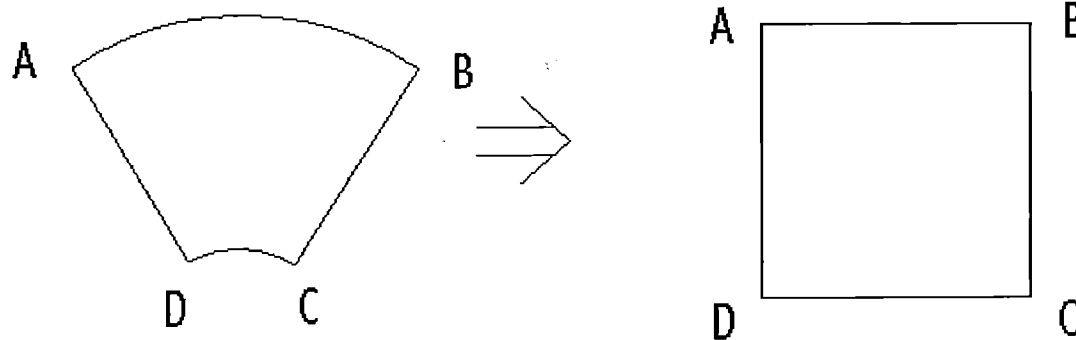
Embedding theory: Construct another space and project old
   working space to new space by mapping.

Advantage: New space can be constructed with known states,
   unknown states in the old space can be omitted

Disadvantage: May cause error.

Pseudo states: States used in the new space but not significantly
   used in the old space(or states used in the new space)

Pseduo-States

Floquet Theory solutions for nonlinear differential equations with periodic coefficients

$$\{\dot{x}\} + [D(t)]\{x\} = \{G(t)\}$$

is

$$\{x(T)\} = [Q]\{x(0)\}$$

Old states: $X_{old} = [x_1, x_2, x_3, \dots x_n]$

New pseudo-states:

$$X_{new} = [x_1(t), x_1(t + \Delta t), x_1(t + 2\Delta t), \dots x_1(t + (n-1)\Delta t)]$$

Two-state case in old space

$$
\begin{bmatrix} x_1(t) \\ x_2(t) \end{bmatrix} = \begin{bmatrix} A_{11}(t) & A_{12}(t) \\ A_{21}(t) & A_{22}(t) \end{bmatrix} \begin{bmatrix} e^{\eta_1 t} & 0 \\ 0 & e^{\eta_2 t} \end{bmatrix} \begin{bmatrix} c_1 \\ c_2 \end{bmatrix}
$$

$$
= \begin{bmatrix} A_{11}(t) & A_{12}(t) \\ A_{21}(t) & A_{22}(t) \end{bmatrix} \begin{bmatrix} e^{\eta_1 t} & 0 \\ 0 & e^{\eta_2 t} \end{bmatrix} \begin{bmatrix} A_{11}(0) & A_{12}(0) \\ A_{21}(0) & A_{22}(0) \end{bmatrix}^{-1} \begin{bmatrix} x_1(0) \\ x_2(0) \end{bmatrix}
$$

Transfer matrix

$$
Q_{old} = \begin{bmatrix} A_{11}(t) & A_{12}(t) \\ A_{21}(t) & A_{22}(t) \end{bmatrix} \begin{bmatrix} e^{\eta_1 t} & 0 \\ 0 & e^{\eta_2 t} \end{bmatrix} \begin{bmatrix} A_{11}(0) & A_{12}(0) \\ A_{21}(0) & A_{22}(0) \end{bmatrix}^{-1}
$$

Two-state case in new space

$$\begin{bmatrix} x_1(t) \\ x_1(t+\Delta t) \end{bmatrix} = \begin{bmatrix} A_{11}(t) & A_{12}(t) \\ A_{11}(t+\Delta t)e^{\eta_1 \Delta t} & A_{12}(t+\Delta t)e^{\eta_2 \Delta t} \end{bmatrix} \begin{bmatrix} e^{\eta_1 t} & 0 \\ 0 & e^{\eta_2 t} \end{bmatrix} \begin{bmatrix} c_1 \\ c_2 \end{bmatrix}$$

$$\begin{bmatrix} x_1(0) \\ x_1(0+\Delta t) \end{bmatrix} = \begin{bmatrix} A_{11}(0) & A_{12}(0) \\ A_{11}(\Delta t)e^{\eta_1 \Delta t} & A_{12}(\Delta t)e^{\eta_2 \Delta t} \end{bmatrix} \begin{bmatrix} c_1 \\ c_2 \end{bmatrix}$$

New transfer matrix

$Q_{new} =$

$$\begin{bmatrix} A_{11}(t) & A_{12}(t) \\ A_{11}(t+\Delta t)e^{\eta_1 \Delta t} & A_{12}(t+\Delta t)e^{\eta_2 \Delta t} \end{bmatrix} \begin{bmatrix} e^{\eta_1 t} & 0 \\ 0 & e^{\eta_2 t} \end{bmatrix} \begin{bmatrix} A_{11}(0) & A_{12}(0) \\ A_{11}(\Delta t)e^{\eta_1 \Delta t} & A_{12}(\Delta t)e^{\eta_2 \Delta t} \end{bmatrix}^{-1}$$

Conclusions

1.New Floquet transfer matrix and old Floquet transfer matrix have the same eigenvalues but different eigenvectors.

2.Relation between old and new states

$$
\begin{bmatrix} x_1(t) \\ x_1(t + \Delta t) \end{bmatrix} =
$$

$$
\begin{bmatrix} A_{11}(t) & A_{12}(t) \\ A_{11}(t + \Delta t)e^{\eta_1 \Delta t} & A_{12}(t + \Delta t)e^{\eta_2 \Delta t} \end{bmatrix}
\begin{bmatrix} A_{11}(t) & A_{12}(t) \\ A_{21}(t) & A_{22}(t) \end{bmatrix}^{-1}
\begin{bmatrix} x_1(t) \\ x_2(t) \end{bmatrix}
$$

3. Relation matrix

$$\begin{bmatrix} A_{11}(t) & A_{12}(t) \\ A_{11}(t+\Delta t)e^{\eta_1 \Delta t} & A_{12}(t+\Delta t)e^{\eta_2 \Delta t} \end{bmatrix} \begin{bmatrix} A_{11}(t) & A_{12}(t) \\ A_{21}(t) & A_{22}(t) \end{bmatrix}^{-1}$$

will decide the error of mapping.

Pseudo-state vectors

A typical state vector for a one-blade, no-inflow system is

$$\{X\}=[\ \beta,\dot\beta,\zeta,\dot\zeta\ ]$$

new pseudo-state vector can be

$$\{X\}=[\beta(t),\beta(t+\Delta t),\beta(t+2\Delta t),\beta(t+3\Delta t)]$$

$$\{X\}=[\dot\zeta(t),\dot\zeta(t+\Delta t),\dot\zeta(t+2\Delta t),\dot\zeta(t+3\Delta t)]$$

or even

$$\{X\}=[\dot\zeta(t),\beta(t+5\Delta t),\beta(t+2\Delta t),\zeta(t+3\Delta t)]$$

A more general new state vector form

$$X^{(t+n\delta t)} =$$
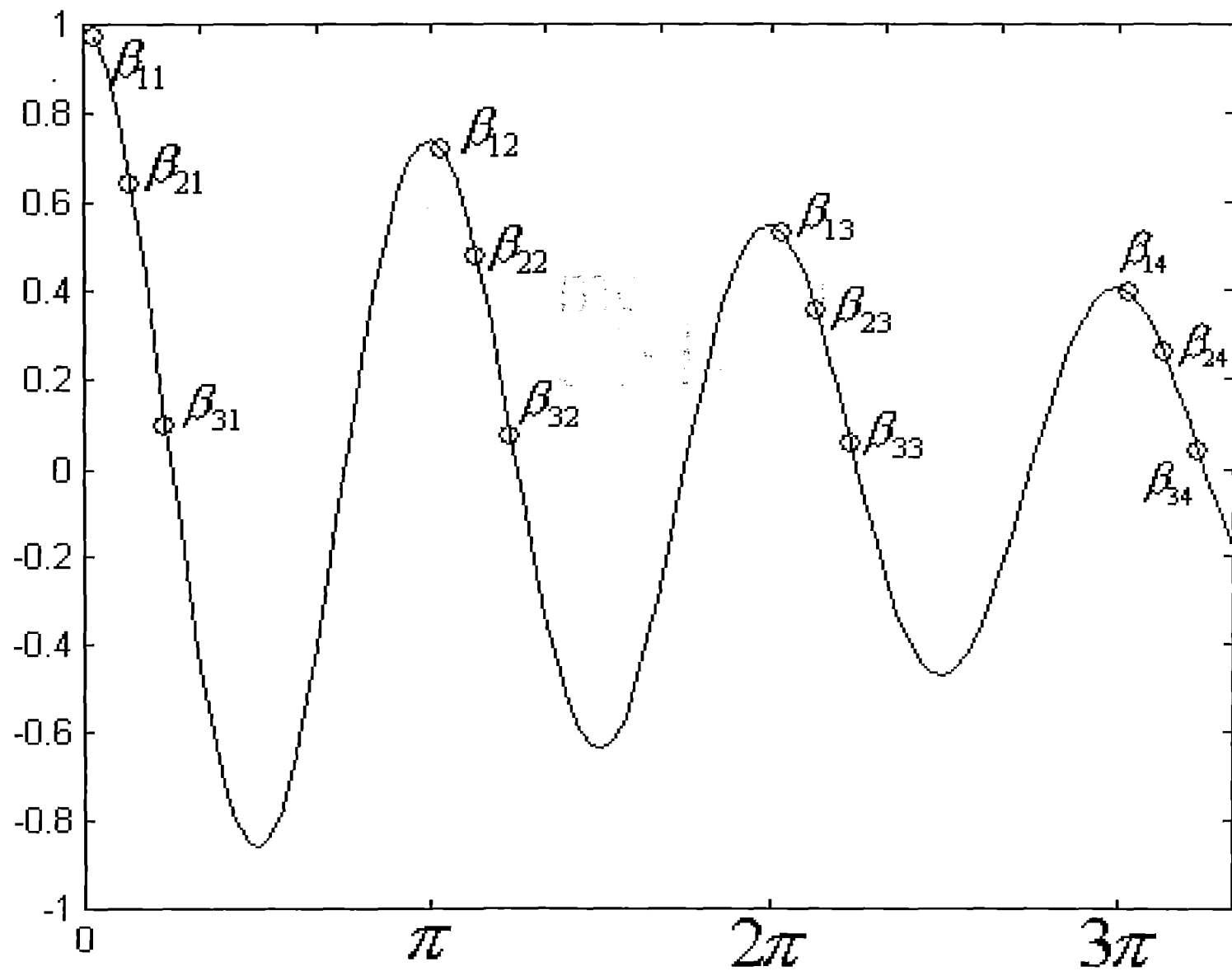$$[x(t), x(t+n\delta t), x(t+2n\delta t)\ldots x(t+mn\delta t)]$$
$$(x \text{ can be } \beta, \dot{\beta} \ldots;)$$

There are three variables: x, δt, n

Note: δt is one time marching step, the smallest time unit used in the calculation.

$$\left\{ \begin{matrix} \beta_{12} & \beta_{13} & \beta_{14} \\ \beta_{22} & \beta_{23} & \beta_{24} \\ \beta_{32} & \beta_{33} & \beta_{34} \end{matrix} \right\} = [Q] \left\{ \begin{matrix} \beta_{11} & \beta_{12} & \beta_{13} \\ \beta_{21} & \beta_{22} & \beta_{23} \\ \beta_{31} & \beta_{32} & \beta_{33} \end{matrix} \right\}$$

Conclusions

1. The smaller δt is, the better the result is.

For example, if only β is used as pseudo state, $\dot{\beta}$ can be expressed by β :

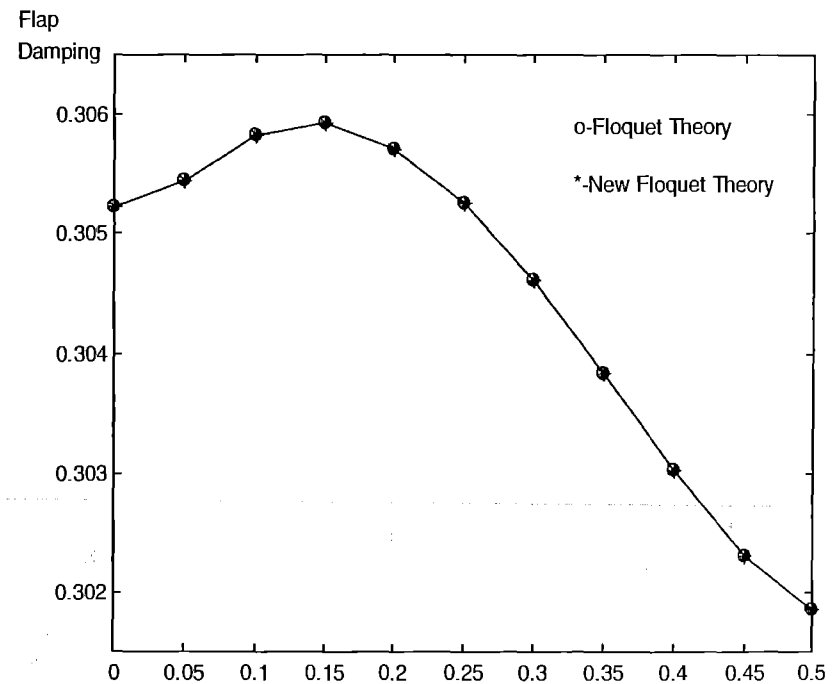$$\dot{\beta} = \frac{\beta(t + \delta t) - \beta(t)}{\delta t}$$

2. Select $X = \beta, \dot{\beta}$ give more accurate flap damping, select $X = \zeta, \dot{\zeta}$ give more accurate lag damping.

3.When selecting $X=\beta$ or ζ, or ..., solutions achieve good accuracy if n is corresponding to a better relation matrix.

Calculation:
1.How good the new method can be.
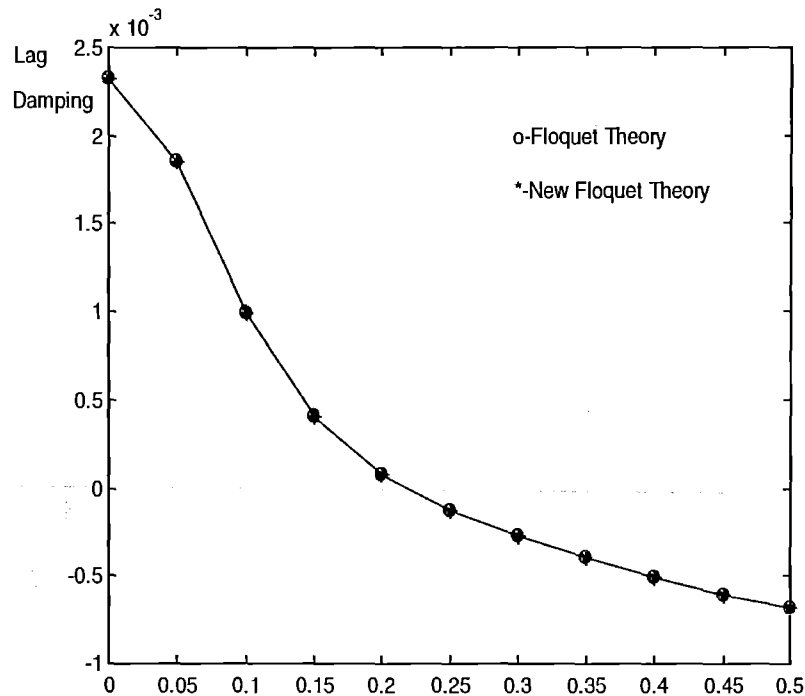
Comparision of Floquet theory solution and pseudo-states solution(excite and measure β only).

Max relative lag damping error of the new method : 0.13%,
Max relative flap damping error :
8.6×10^{-5} %

2. How to choose a good time-delay factor n?

Use something that can show the quality of relation matrix, such as

a. Condition number of relation matrix- the ratio of the largest eigenvalue to the smallest.

b. Singular Values of relation matrix found by SVD(Singular Value decomposition).

Singular Value decomposition

SVD of A produces a diagonal matrix S, of the same dimension as X and with nonnegative diagonal elements in decreasing order, and unitary matrices U and V so that $X = U*S*V'$. If A is a diagonal matrix, S is the eigenvalue matrix. U is the eigenvector matrix, and V=U.

Condition number

Max relative error of Flap damping for advance ratio 0~0.5
Time delay factor n

Maxim condition number for advance ratio 0~0.5 vs time delay factor
Time delay factor n
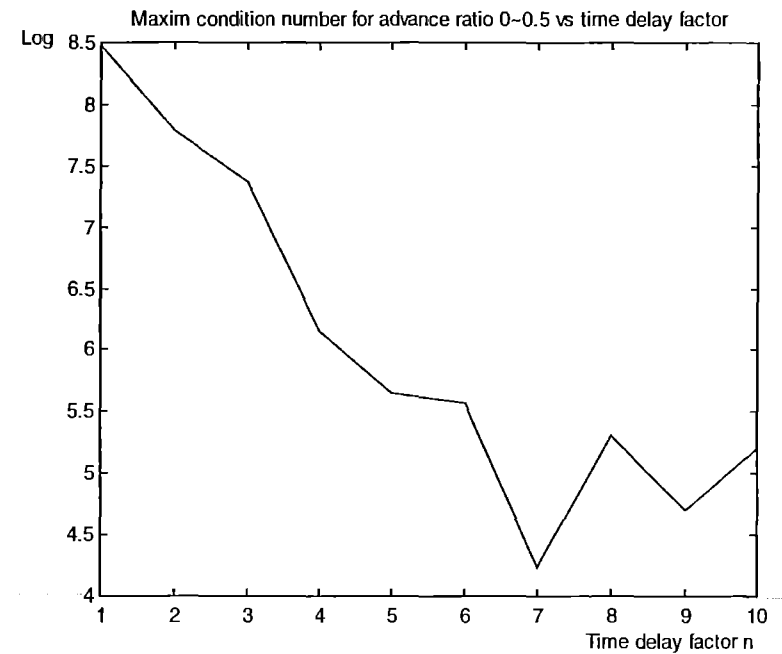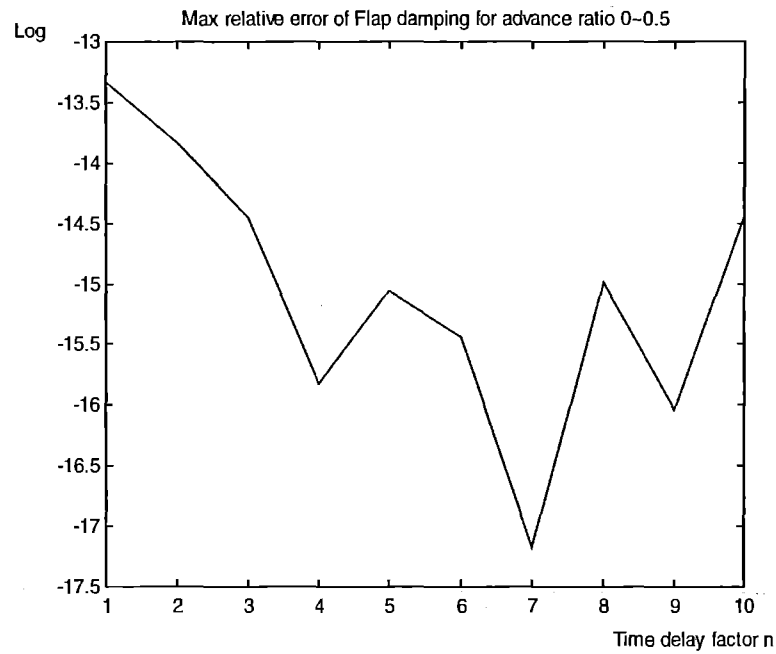
Calculations of a four-blade system

Exact Fast Floquet Theory Solution

Fast Floquet Theory only		Lag damping+ frequency	Flap damping+ frequency
	R	-8.943e-3+0.4196i	-1.699e-1+0.1022i
	D	-1.093e-2+0.5881i	-2.716e-1+0.8323i
	P	-7.094e-3+1.5880i	-2.915e-1+1.8667i
	C	-6.707e-3+1.4156i	-2.699e-1+1.0887i

Average Relative Errors of Lag Damping and Frequency

Lag	E β -8/31	E ζ -8/31	E $\dot{\beta}$ -8/31	E $\dot{\zeta}$ -8/31
M β -8/31	*266.83	55.93	**434.96	71.05
M ζ -8/31	17.91	3.99	41.99	3.93
M $\dot{\beta}$ -8/31	*367.68	41.61	*446.88	53.43
M $\dot{\zeta}$ -8/31	19.73	58.82	15.03	21.69

Average Relative Errors of Flap Damping and Frequency

Flap	E β -8/31	E ζ -8/31	E $\dot{\beta}$ -8/31	E $\dot{\zeta}$ -8/31
M β -8/31	3.1075	18.92	11.88	*46.74
M ζ -8/31	6.09	*14.71	5.12	10.16
M $\dot{\beta}$ -8/31	3.69	*12.90	6.61	*20.47
M $\dot{\zeta}$ -8/31	3.89	*16.71	6.2	7.48

Conclusions:

1. Some lag(flap) damping and frequencies are missing when we only excite and measure flap(lag) vibration states.

2. Exciting and measuring lag(flap) states give good lag(flap) damping and frequencies but give bad flap(lag) damping and frequencies.

3. The system seems more sensitive to displacement perturbation and less sensitive to vibration perturbation. So it is good to excite displacement states.

4. Measuring lag vibration states give better results than measuring flap vibration states.

Least Square Method

Add More Measurements

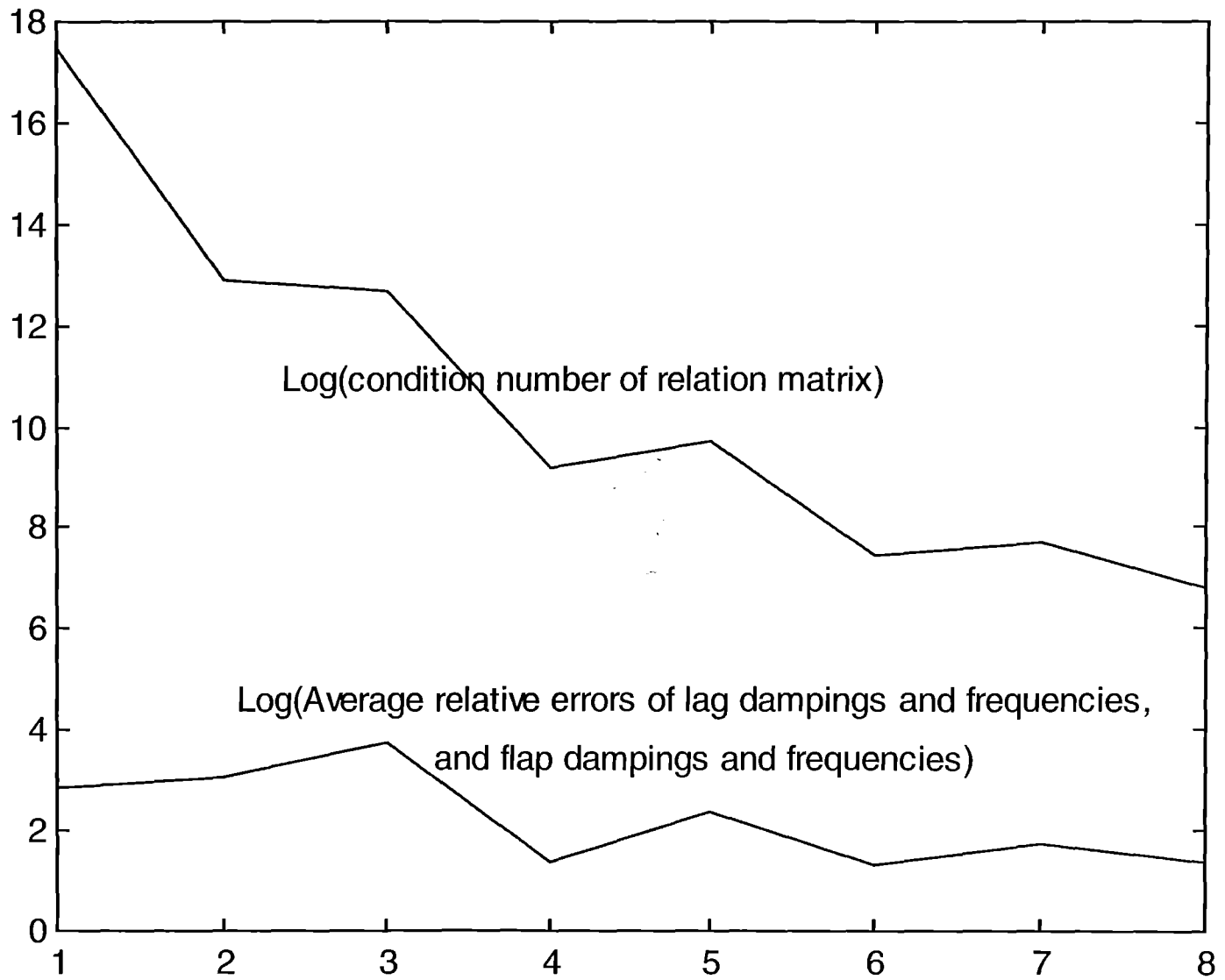| Measurement	Average error of lag damping and frequency	Average error of flap damping and frequency
$M\beta$-8	***32.25%	11.99%
$M\beta$-16	**361.32%	4.59%
$M\beta$-24	*188.66%	5.92%
$M\beta$-32	216.40%	5.50%
$M\beta$-40	75.43%	2.68%

Add More Excitations

Excitation and Measurement	Average error of lag damping and frequency	Average error of flap damping and frequency
Eβ -4, Eζ -4, Mβ -4, Mζ -4	3.41%	16.93%
Eβ -6, Eζ -6, Mβ -4, Mζ -4	2.38%	13.21%
Eβ -8, Eζ -8, Mβ -4, Mζ -4	2.68%	11.96%

Time Delay Factor n

Time delay, EB-2, Mζ -8/(cut to 31*31 matrix)

Time delay factor	Average error of lag damping and frequency	Average error of flap damping and frequency	Average error of lag and flap damping and frequency
n =1	13.76	20.47	17.12
n =2	9.55	32.69	21.12
n =3	59.66	24.46	42.06
n =4	4.77	3.11	3.94
n =5	3.19	18.16	10.68
n =6	1.88	5.50	3.69
n =7	4.48	6.71	5.60
n =8	2.43	5.28	3.86

Log(condition number of relation matrix)

Log(Average relative errors of lag dampings and frequencies, and flap dampings and frequencies)

Conclusions drew from condition number

Log(condition number) for different measurements and time delay factors

Time delay factor	Measure β	measure ζ	Measure $\dot{\beta}$	Measure $\dot{\zeta}$
n =1	18.53	17.46	18.01	16.19
n =2	15.85	12.89	14.81	11.22
n =3	11.59	12.68	12.17	9.64
n =4	10.98	9.17	9.75	8.65
n =5	10.13	9.74	8.33	8.49
n =6	9.95	7.47	7.78	7.71
n =7	8.29	7.70	7.14	6.78
n =8	9.16	6.79	6.41	5.20

1. Measuring lag vibration states give better results than measuring flap vibration states.

2. It is good to measure velocity states.

3. Measuring β gives the worse results, that is why me missing 3 lag damping in one previous case.

Future work

1. Find the best construction of pseudo state vectors to minimize error.

2. Find further relationship between relation matrix and errors.

3. Inflow damping

A Comparison of Various Methods
for Stability Analysis
of Large Scale Rotorcraft Systems

O.A. Bauchau and Y. Nikishov
Georgia Institute of Technology.
David A. Peters
Washington University

an abstract submitted for presentation at the

Seventh International Workshop on Dynamics and
Aeroelastic Stability Modeling of Rotorcraft Systems.

Due to increased available computer power, rotorcraft comprehesive analysis codes are relying on increasingly complex, large scale models. Full finite element analysis codes and computational dynamics codes are now routinely used as structural dynamics, and aerodynamic tools, respectively. Theses codes should provide increasingly reliable predictions of the aeroelastic response of rotorcraft systems.

An important aspect of the aeroelastic response is the prediction of potential instabilities which can occur both on the ground and in the air. Typically, Floquet theory has been used for this purpose. Floquet theory requires the computation of a transition matrix which size is equal to the total number of degrees of freedom in the system, and extracts system stability information from the eigenvalues of this matrix. The transistion matrix stores the response of the system to excitations in each of its degrees of freedom. As the complexity and number of degrees of freedom of the simulation increases, application of this theory rapidly becomes unmanagable.

Similarly, when performing experimental investigations, the use Floquet theory is very difficult because the experimental system theoretically involves an infinite number of degrees of freedom, and because it is difficult to individually excite these degrees of freedom in an experimental setting. As

a result, frequency domain methods, such as Moving Block method or time domain methods, such as Ibrahim method or Complex Exponential method are preferred when performing experimental studies.

In the partial Floquet method, a limited number of degrees of freedom will be excited, and the response of a limited number of degrees of freedom is monitored. Stability information is then assessed from the partial transition matrix based on the available information.

In this paper, the predictions of several methods will be compared; they include Floquet theory, partial Floquet theory, the Moving Block method, the Ibrahim time domain method, and the Complex Exponential method. The limitations and advantages of these various methods will be discussed. The ground resonance problem will be taken as an example to compare the various methods. A full finite element simulation will be used to model the problem. Estimations of the damping ratio based on the various methods will be presented. Predictions based on energy arguments will also be presented.

A Comparison of Various Methods

for Stability Analysis

Olivier A. Bauchau

Yuri G. Nikishkov

School of Aerospace Engineering,
Georgia Institute of Technology.

Outline of the Presentation

- Statement of the problem

- Theoretical background

- Comparison of the various methods

- Conclusions and future work

Statement of the Problem

- **Model:**
  Linear system with many degrees of freedom
  with periodic coefficients

- **Objectives:**
  1. Assess the stability of the system
  2. Determine the damping in the system

Theoretical Background

Methods presented:

- Partial Floquet Theory

- Ibrahim Time Domain Method

- Complex Exponential (Prony) Method

- Moving Block Method

Partial Floquet Theory

- **Full Floquet Theory**

  requires the excitation and measurement of *all degrees of freedom* of the system *after one period* to form Floquet Transition Matrix

- **Partial Floquet Theory**

  requires the excitation and measurement of a *limited number of degrees of freedom after one period* to approximate Floquet Transition Matrix

- Can use measurements *for several periods* to get additional information from the data

- Based on sound theoretical basis

- **Principal Problem:**

  select proper degrees of freedom or modes to excite and measure

Full Floquet Theory: Basic Equations

Floquet Transition Matrix A is defined as:

$$\vec{y}(T) = A(T,0)\vec{y}(0)$$

If $Y(T)$ is the matrix of responses of independent excitations $Y(T) = [\vec{y}_1, \vec{y}_2, ..., \vec{y}_n]$ then the Transition Matrix can be found as:

$$A(T,0) = Y(T)Y^{-1}(0)$$

The system damping then is defined as:

$$d = \frac{1}{T} \log \rho(A)$$

Partial Floquet Theory: Basic Equations

Excite and measure a limited number of degrees of freedom:
B is excitation matrix, C is measurement matrix

$$U(T) = CY(T)B, \quad U(0) = CB$$

Approximate Transition Matrix using Pseudo-Inverse

$$A = C^T[CC^T]^{-1}U(T)[B^TB]^{-1}B^T$$

Ibrahim Time Domain Method

- Requires *one excitation* of all modes

- Requires measurement of *selected degrees of freedom for several periods*

- Used mostly in the experimental work

- **Principal Problem:**

  o select proper degrees of freedom or modes to measure

  o needs longer time history

Ibrahim Time Domain Method: Basic Equations

Build Transition Matrix reusing measurements at periods:

$$A\vec{y}(t_n) = \vec{y}(t_{n+1}) \quad or \quad AZ = \tilde{Z}$$

Approximate Transition Matrix using Pseudo-Inverse

$$A = \tilde{Z}Z^T[ZZ^T]^{-1}$$

Last inverse is usually ill-determined so that
Singular Value Decomposition method seems to be more efficient.
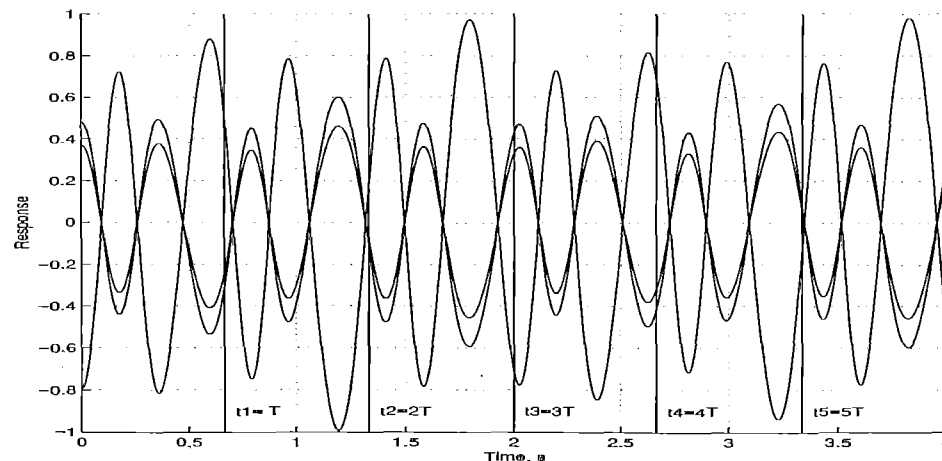
Complex Exponential (Prony) Method

- Fits the response of *one excitation* to the set of damped exponential responses

- Requires measurement of *one degree of freedom* or mode *for several periods*

- Curve fitting method, used mostly in the experimental work

- **Principal Problem:**

  - select proper degree of freedom or mode to measure

  - needs even longer time history than Ibrahim Method

Complex Exponential Method: Basic Equations I

Form the set of data measured at $t = t_n$ and try to fit them
to the set of exponential responses

$$y(t_n) = \sum_{k=1}^{q} a_k e^{s_k t_n}$$

A linear combination of the $y(t_n)$

$$\sum_{n=0}^{q} \beta_n y(t_n) = \sum_{k=1}^{q} A_k \sum_{n=0}^{q} \beta_n e^{n(s_k T)}$$

β_n are the coefficients of polynomial equation for exponents

$$\sum_{n=0}^{q} \beta_n e^{n(sT)} = 0$$

such that s_k are the roots.

Complex Exponential Method: Basic Equations II

To find these coefficients rearrange the equation above

$$\sum_{n=0}^{q-1} \beta_n y(t_n) = -y(t_q)$$

Successive applications of this procedure lead to a full set of equations:

$$\begin{bmatrix} y(t_0) & y(t_1) & \ldots & y(t_{q-1}) \\ y(t_1) & y(t_2) & \ldots & y(t_q) \\ \ldots & \ldots & \ldots & \ldots \\ y(t_{q-1}) & y(t_q) & \ldots & y(t_{2q-2}) \end{bmatrix} \left\{ \begin{array}{c} \beta_0 \\ \beta_1 \\ \ldots \\ \beta_{q-1} \end{array} \right\} = - \left\{ \begin{array}{c} y(t_q) \\ y(t_{q+1}) \\ \ldots \\ y(t_{2q-1}) \end{array} \right\}$$

Use Pseudo-Inverse or Singular Value Decomposition to determine coefficients β_n, find roots and determine damping as $Re(s_k)$.

Moving Block Method

- Fits the response to a *single excitation* to
  the dominant mode determined using FFT

- Requires measurement of *one degree of freedom*
  or mode *for some time history*

- Widely used in experimental work

- **Principal Problem:**

  - select proper degree of freedom or mode to excite and measure

  - needs very detailed time history to determine
    dominant frequency accurately

  - must be almost single mode response

Moving Block Method: Basic Equations

Compute Fourier Transform of a single response from some varying time τ to $\tau + T$.

$$F(\omega) = \int_{\tau}^{\tau+T} ae^{-\zeta\omega_n t}\sin(\omega t + \phi)e^{-i\omega t}dt$$

Analytical integration gives

$$\ln|F(\omega)| = -\zeta\omega\tau + \frac{1}{2}\zeta\sin 2(\omega\tau + \phi) + \ln\left(\frac{A}{2\omega}\right) + \ln(\omega T) - \frac{1}{2}\zeta\omega T$$

Procedure:

- Compute the dominant damped frequency ω from FFT

- Determine ζ from least-squares fit for different τ

Problem 1: Multiple pendulum with moving support
6 degrees of freedom model in state form
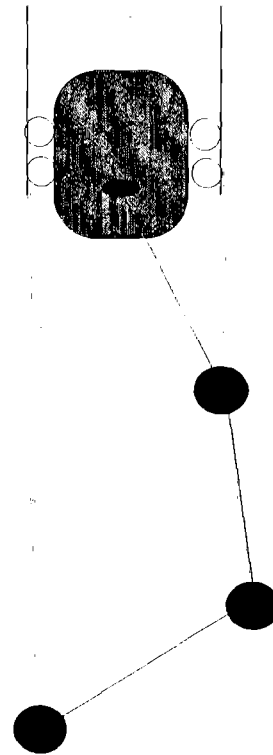
Specific feature of the problem:
structural modes does not change with time

Partial Floquet Theory results

Modes decoupling: for each of 3 modes
2 experiments and 2 measurements
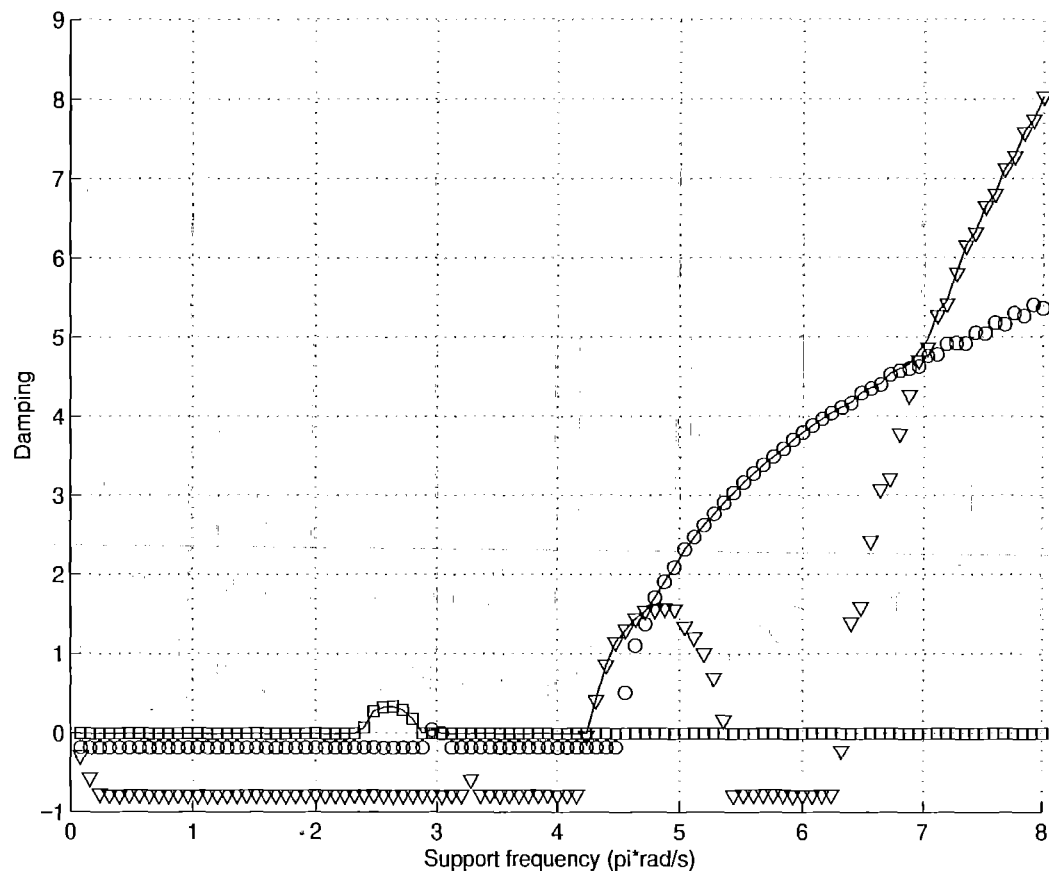
Full Floquet results are shown as a solid curve

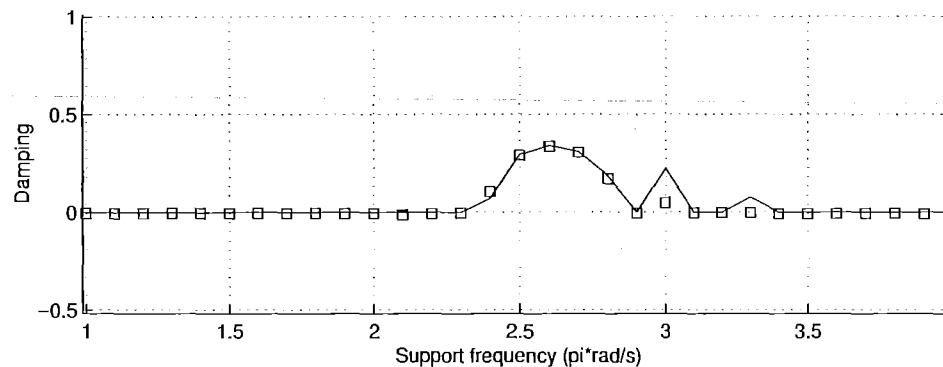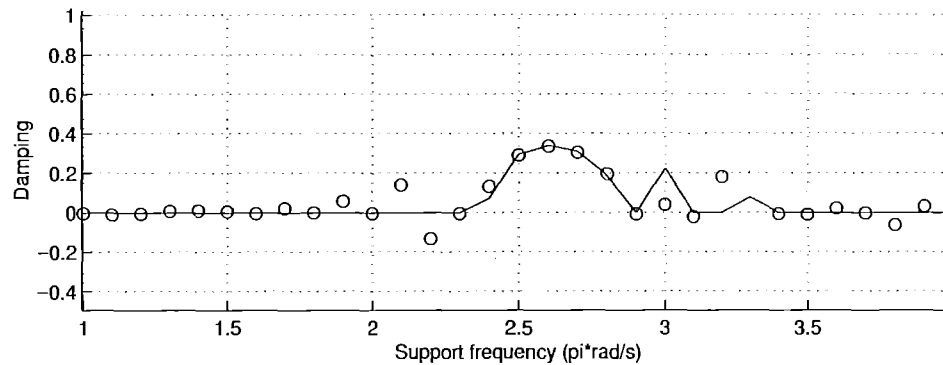# Ibrahim Time Domain Method results I

One experiment, all degrees of freedom measured
6 and 12 period integration
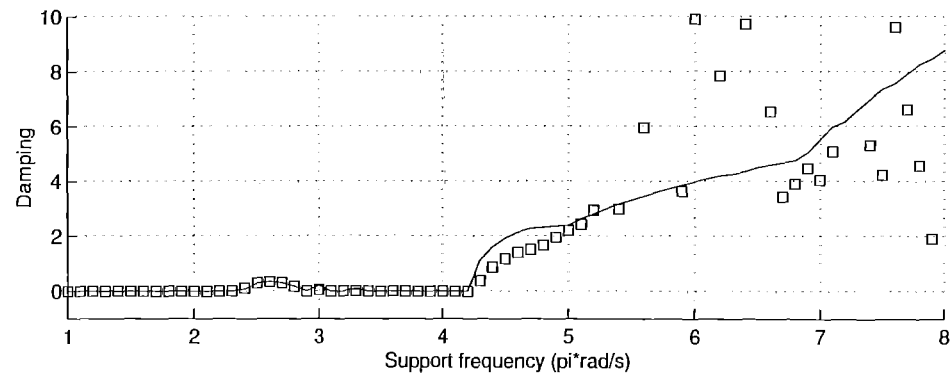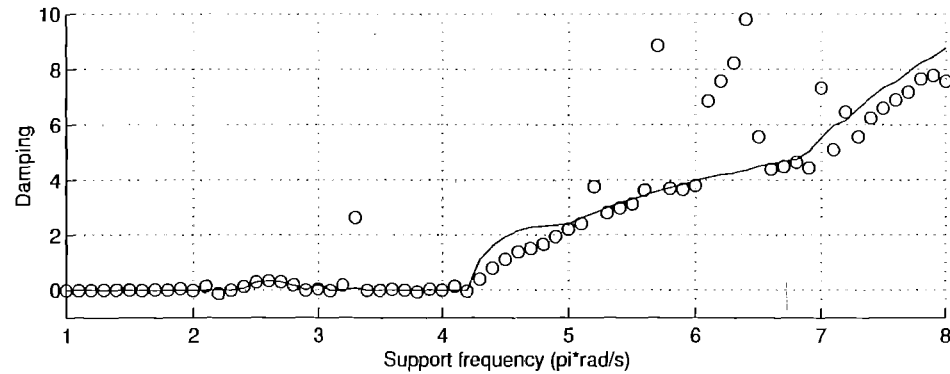
Full Floquet results are shown as a solid curve

Ibrahim Time Domain Method results II

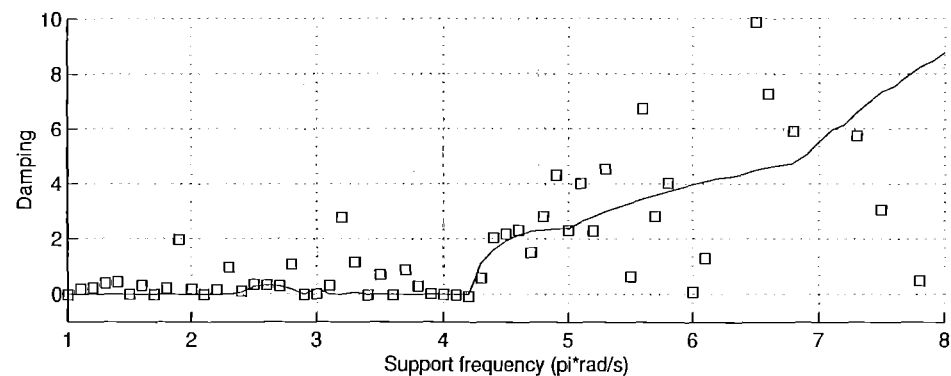One experiment, all degrees of freedom measured
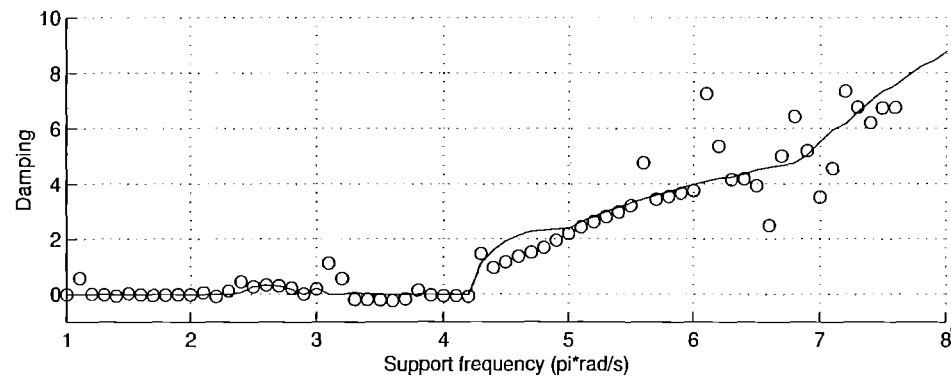6 and 12 period integration (zoom)

Full Floquet results are shown as a solid curve
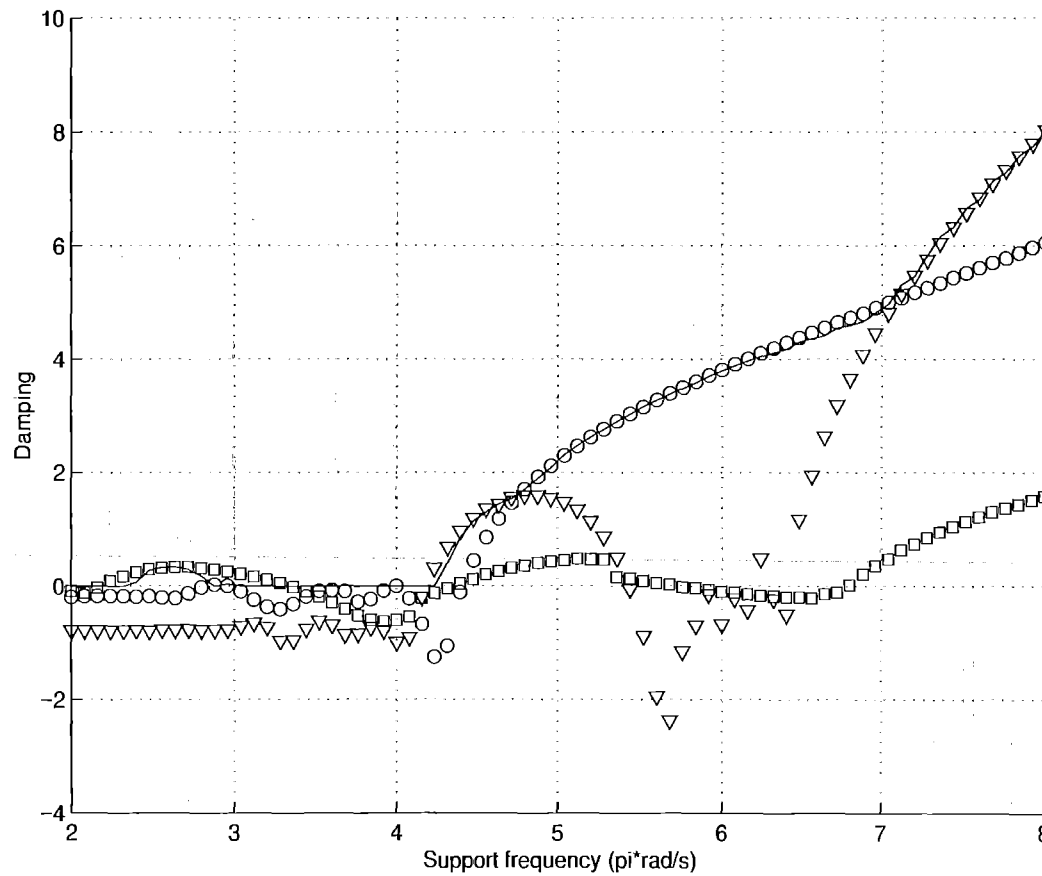
Complex Exponential Method results

One experiment, one degree of freedom measured
7 and 13 period integration

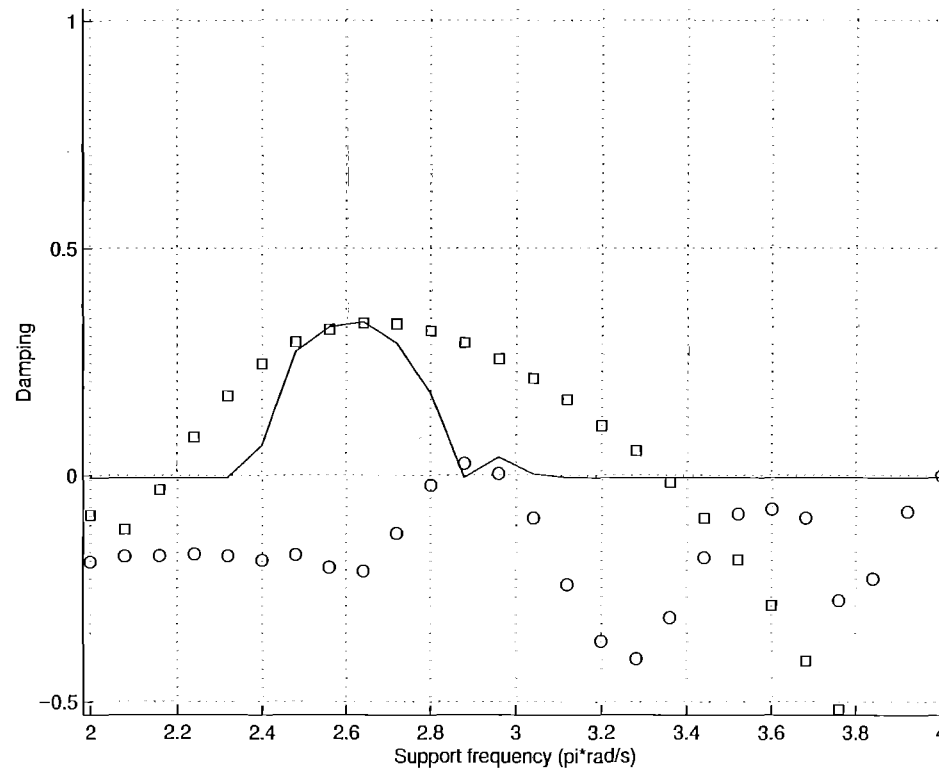Full Floquet results are shown as a solid curve

Moving Block Method results I

Each structural mode excited and measured
4 period integration

Full Floquet results are shown as a solid curve

Moving Block Method results II

Each structural mode excited and measured
4 period integration (zoom)

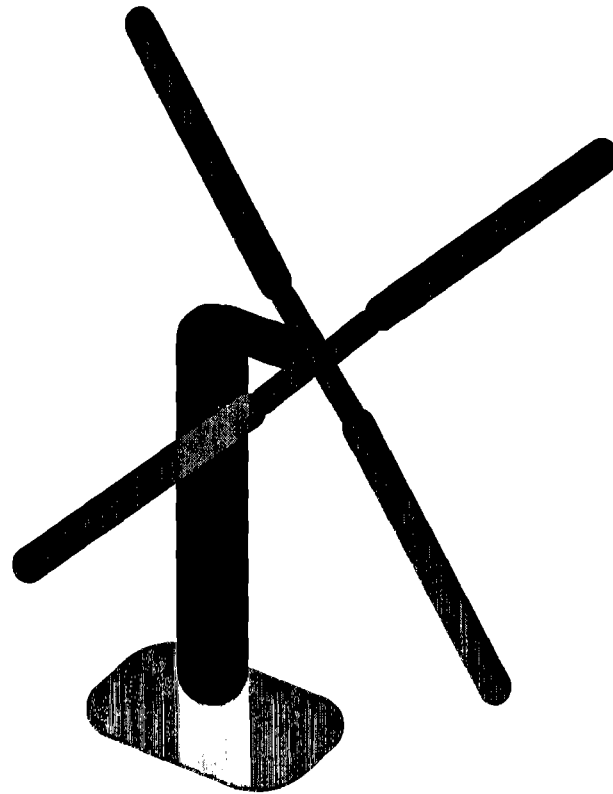Full Floquet results are shown as a solid curve

Discussion

- Partial Floquet Theory showed the ability to predict exact values of damping in different modes

- Ibrahim Time Domain Method showed good performance for long integration time and at the same time loss of accuracy in the unstable region

- Complex Exponential method was unable to consistently yield qualitatively good results and also demonstrated loss of accuracy for longer integration time

- Moving Block Method showed reasonable results for damping values in different modes but only due to specific features of this problem

Comparison of the methods II

Problem 2: Ground Resonance Problem
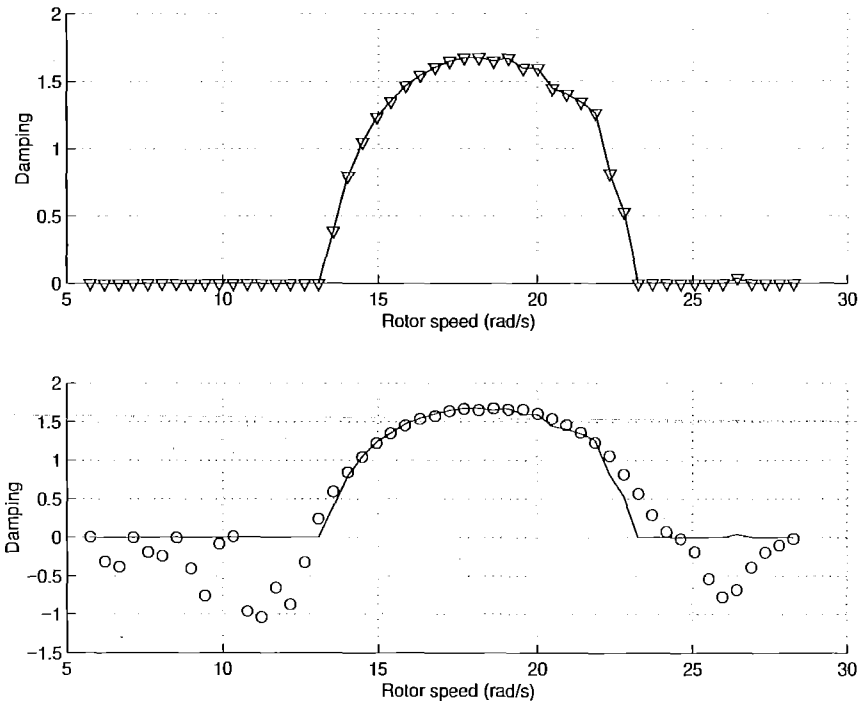10 degrees of freedom model in state form

Comparison of the results

Partial Floquet Theory:

6 experiments, 6 measurements in multi-blade modes
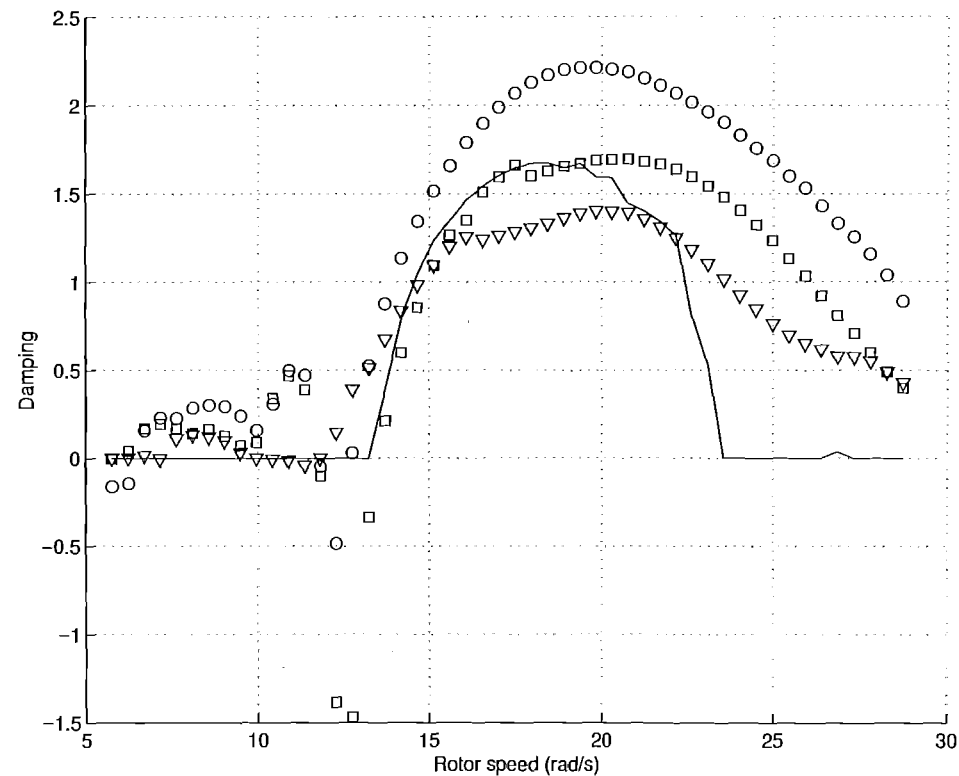
Ibrahim Time Domain Method:

One experiment, 6 periods, 3 degrees of freedom measured

Full Floquet results are shown as a solid curve

Comparison of the results

Moving Block Method:
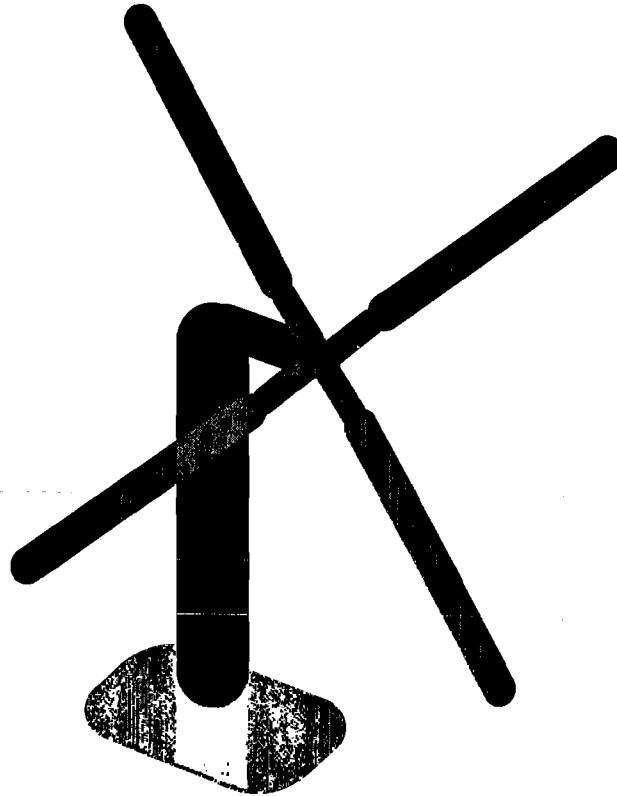### 3 multi-blade modes excited and measured
4 period integration

Full Floquet results are shown as a solid curve

Comparison of the methods II

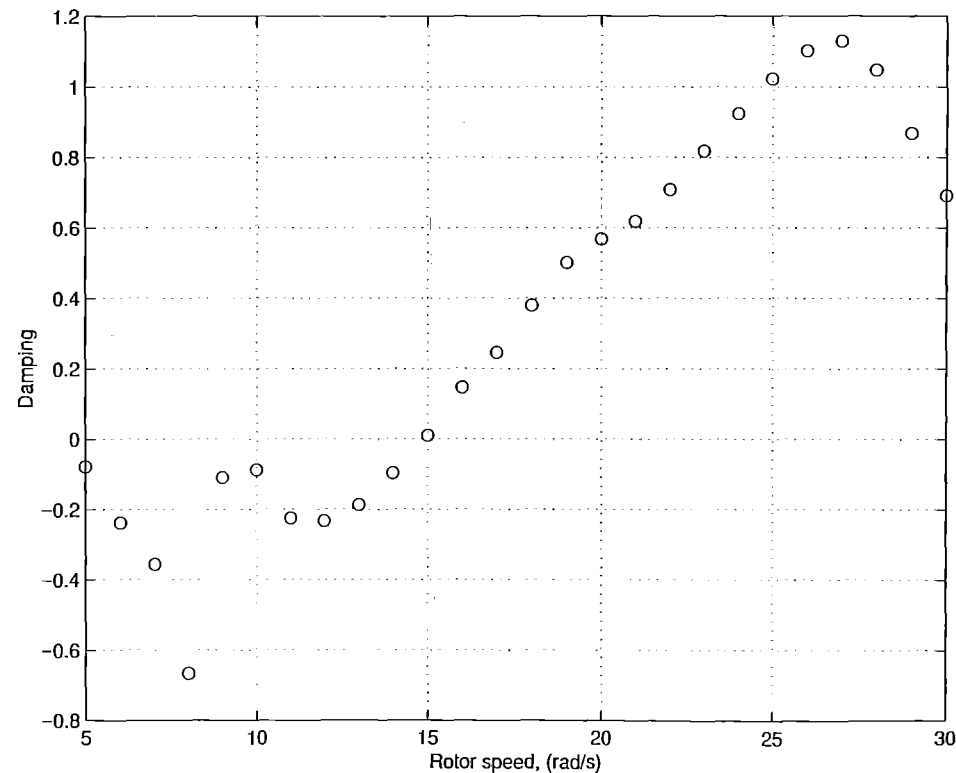**Problem 2:** Ground Resonance Problem
FEM model, 257 degrees of freedom

Comparison of the results

Ibrahim Time Domain Method:
One experiment, 3 periods, 3 degrees of freedom measured
(Fast Floquet used, 4 measurements per period)

Longer integration showed that 15 rad/s is stability boundary

Conclusions I

- **Partial Floquet Theory** is shown to be an efficient tool
  to assess the stability and damping of various systems

- It can be used as a post-processing tool for any Rotorcraft analysis

- For some problems it provides a good method to decouple
  the stability curve to several modal curves

- It is based on a sounder mathematical basis that the other methods

- Partial Floquet Theory is shown to be more efficient and
  accurate than other methods when dealing with complex
  computational models

Conclusions II

- **Ibrahim Time Domain Method** is a particular case of Partial Floquet Theory

- It seems to be less accurate than Partial Floquet Theory

- **Moving Block Method** and **Complex Exponential Method** are curve fitting methods. Their approaches do not seem to be suitable in numerical work

Future Work

- Application of presented Theory to aeroelastic and contact problems

- Extension to nonlinear systems

- Development of post-processing routines to implement the proposed methods

- Relationship to energy flows

Fast-Floquet Analysis of Helicopter Trim and Stability With Distributed and Massively Parallel Computing

S. Venkataratnam
Research Assistant

S. Subramanian
Research Associate

G. H. Gaonkar
Professor

Department of Mechanical Engineering
Florida Atlantic University
Boca Raton, FL 33431

Summary

Prediction of helicopter stability in trimmed flight is often based on Floquet theory. It involves a nonlinear trim analysis for the control inputs and corresponding periodic responses, and then a linearized stability analysis for the Floquet transition matrix (FTM), and the eigenvalues and eigenvectors of this matrix. The shooting method with damped Newton iteration is used for the trim analysis and generates the FTM as a byproduct. The QR method is used for the eigenanalysis. The Floquet analysis comprises the shooting and QR methods. A rotor with Q identical and equally spaced blades has Q planes of symmetry. The fast-Floquet analysis exploits this symmetry, and thereby provides nearly a Q-fold reduction in run time and frequency indeterminacy of the Floquet analysis. Still, the run time for the fast-Floquet analysis on serial computers becomes prohibitive for large models (order or number of states > 100); in fact, it grows between quadratically and cubically with the order, and the bulk of it is for the trim analysis. Accordingly, a parallel fast-Floquet analysis is developed for two types of mainstream parallel computing hardware: distributed computing systems of networked workstations and massively parallel computers; algorithmically, both types belong to the MIMD (Multiple-Instruction, Multiple-Data) architecture. Large models with hundreds of states are treated, and a comprehensive database on parallel performance and computational reliability is generated. Computational reliability is quantified by parameters such as the eigenvalue condition number. Similarly, parallel performance is measured by parameters such as speedup and efficiency, which collectively provide a measure of how fast a job can be completed with a set of processors and how well the processors are utilized. Compared to the serial fast-Floquet analysis, the parallel analysis reduces the run time dramatically and provides a practical means of controlling the growth of run time with the order by a judicious combination of speedup and efficiency.

Fast-Floquet Analysis of Helicopter Trim and Stability With Distributed and Massively Parallel Computing

S. Venkataratnam
Research Assistant

S. Subramanian
Research Associate

G. H. Gaonkar
Professor

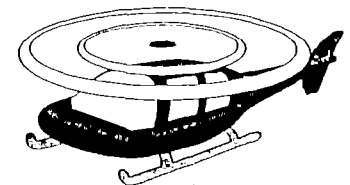Department of Mechanical Engineering
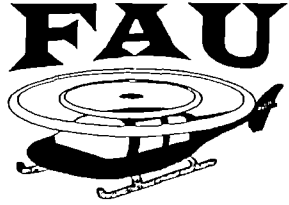Florida Atlantic University
Boca Raton, FL 33431, U. S. A.

FAU
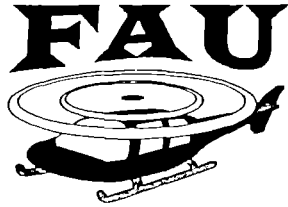
Outline

◆ **Introduction**

    ☆ Floquet Analysis

    ☆ Motivation, Background and Objectives

◆ **Distributed Computing**

◆ **Conventional and Fast-Floquet Analyses**

◆ **Parallel Fast-Floquet Analysis**

    ☆ Sequential and Parallel Fast Shooting

    ☆ Computational Reliability

    ☆ Performance Metrics

◆ **Modeling and Results**

◆ **Conclusions**

Floquet Theory

    ✳ Primary mathematical tool for helicopter stability in trimmed flight

    ✳ Routinely applied to small models (order or number of states < 100)

Investigation consists of:

    ❶ Trim analysis of computing control inputs for the required flight conditions and the corresponding periodic forced response

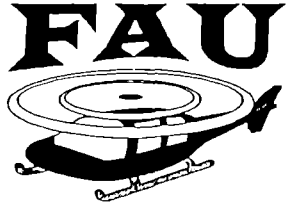   ❷ Stability analysis of generating the Floquet Transition Matrix (FTM), and its eigenvalues and eigenvectors

Periodic Shooting for Trim Analysis

    ⇨ Generates the FTM as a byproduct

QR Method for Eigenanalysis of the FTM

Collectively referred to as Floquet Analysis

Motivation

Run Time for Trim Analysis

- ✪ Becomes prohibitive on serial computers
- ✪ Increases rapidly with the system order --- between quadratically and cubically
- ✪ Consumes nearly 99% of the total run time

Full Potential of Structural and Aerodynamic Sophistication is not Completely Exploited

- → Even research models lead to large systems
- → Example: Flap-Lag-Torsion Analysis with 2 modes each in flap bending, lag bending and torsion with stall and 3-D finite state wake dynamics

    12 states/blade x 4 blades + 6 states/element x

    7 elements/blade x 4 blades + 55 wake states (9 harmonics)

    ≈ 271 States
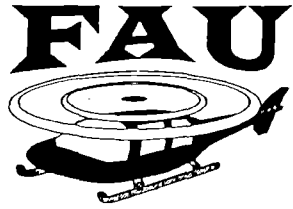
Motivation *Contd..*

Utility of the Floquet Analysis is limited to small
models

Not Practical for comprehensive- and design-analysis
applications (Order >> 100)

Motivation *Contd..*

Why Parallel Fast-Floquet Analysis?

Trim analysis

✪ Requires simultaneous solution of equations of motion and trim

✪ Control inputs appear in system and forcing function matrices

✪ Iterative strategy --- solving a sequence of linearized problems

✪ Involves perturbing initial values one at a time, integrating through T, generating the Jacobian and improving by damped Newton iteration

✪ The bulk of the run time is for repeated integrations

M - Model order or number of states including control settings

k - Number of iteration cycles for convergence

Number of independent integrations = $k(M+1)$, $M > 100$
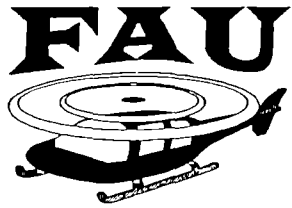
Motivation *Contd..*

Why Parallel Fast-Floquet Analysis?

```
Interval of          ──→  ┌──────────────┐
Integrations              │ T (Floquet ) │
                          └──────────────┘

                          ┌───────────────────┐
                     ──→  │ T/Q (Fast-Floquet; │
                          │ for a rotor with Q │ ──┐
                          │ identical and      │   │    ┌──────────┐
                          │ equally            │   ├──→ │ Parallel │
                          │ spaced blades)     │   │    │ fast     │
                          └───────────────────┘   │    │ Floquet  │
                                                   │    └──────────┘
Independent          ──→  ┌──────────────────┐   │
Integrations              │ Ideal for parallel│──┘
                          │ computing         │
                          └──────────────────┘

                          ┌───────────────┐
                     ──→  │ Sequentially  │
                          └───────────────┘
```
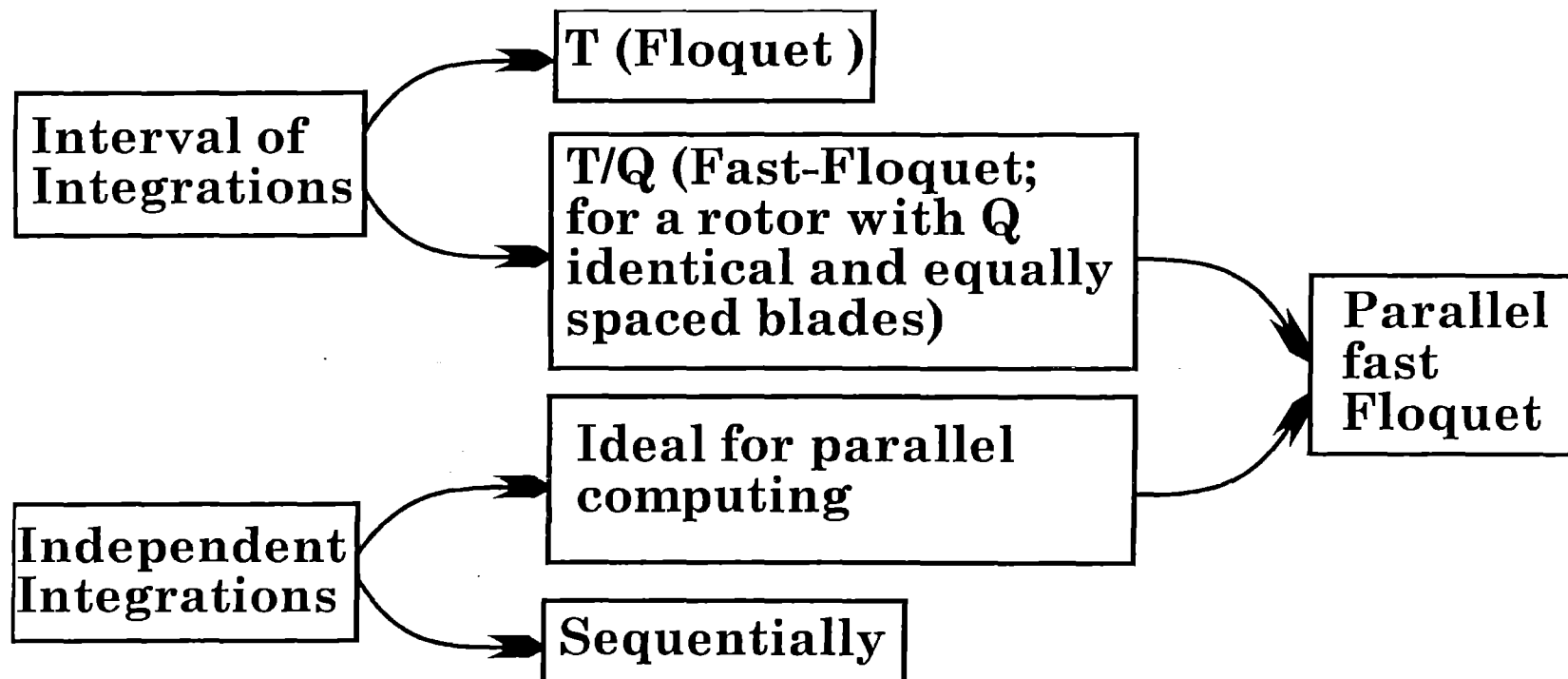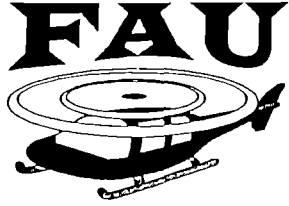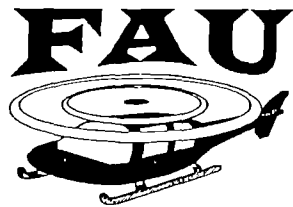
Motivation *Contd..*

Why Parallel Fast-Floquet Analysis?

Benefits

☛ Exploits the Q planes of symmetry and performs operations concurrently

☛ Results in nearly a Q-fold reduction in run time

☛ Provides simpler means of identifying modal frequencies (reduces frequency indeterminacy by a factor of Q)

Background

Serial Analysis (Fast Floquet)
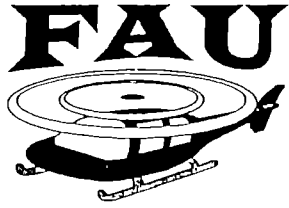
McVicar and Bradley (1995)

Peters (1995)

Chunduru (1995)

Parallel Analysis

Subramanian, Gaonkar, Nakadi and Nagabhushanam
  (Conventional Floquet; 1996)

Subramanian and Gaonkar (Fast Floquet; 1996)

Objectives and Scope

☞ **Develop a Parallel Fast-Floquet Analysis**

> ▶ Suitable for distributed computing of networked workstations and for massively parallel MIMD computers

> ▶ Exploits the fast-Floquet theory and the MIMD computational strategy

☞ **Demonstrate the practical utility of the parallel fast-Floquet analysis in comprehensive and design analysis applications by treating models with hundreds of states**
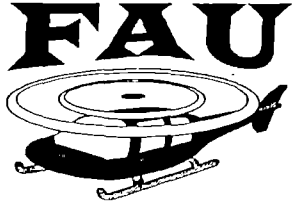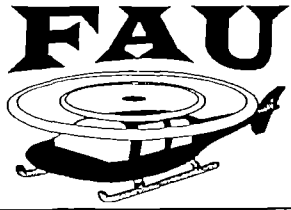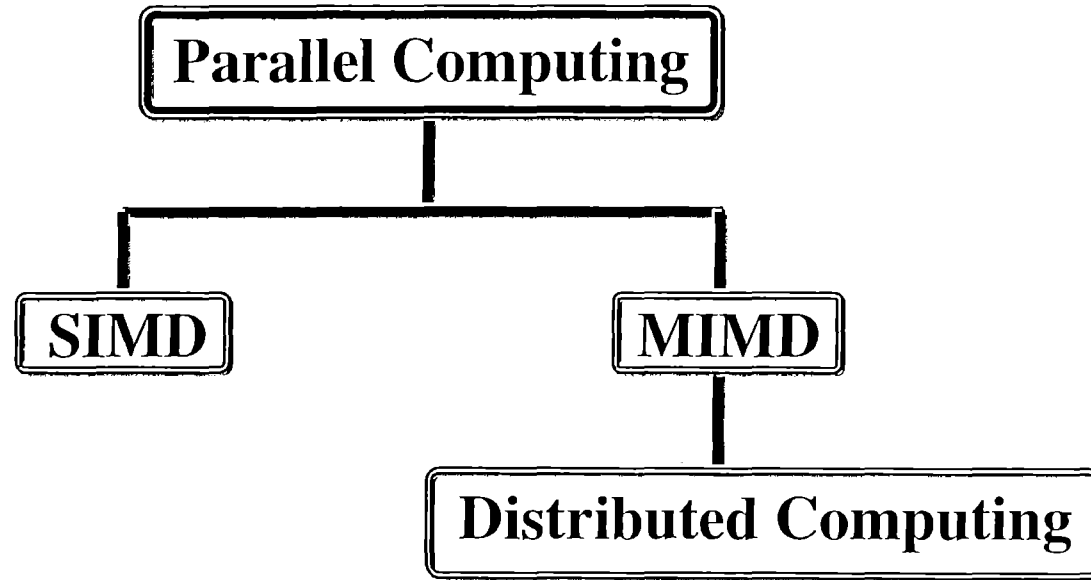
Objectives and Scope *Contd..*

☞ **Present a comprehensive database on parallel performance metrics and computational reliability**

- ▶ Compares distributed computing with serial computing on a conventional main-frame computer

- ▶ Compares distributed computing with massively parallel computing with respect to performance and computational reliability

Distributed Computing

```
          ┌─────────────────────┐
          │  Parallel Computing │
          └─────────────────────┘
                     │
          ┌──────────┴──────────┐
      ┌────────┐            ┌────────┐
      │  SIMD  │            │  MIMD  │
      └────────┘            └────────┘
                                │
                    ┌───────────────────────┐
                    │ Distributed Computing │
                    └───────────────────────┘
```
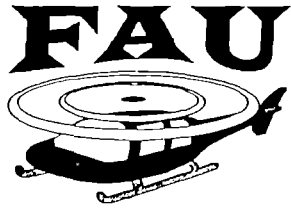
Distributed Computing

- Involves a set of networked computers (in practice, workstations)

- Minimum turnaround time and cost --- "lowly parallel computing"

- Portability --- The same algorithm/code can be run on both distributed and massively parallel computing systems

Conventional Floquet Analysis

With unknown control input vector c explicitly stated
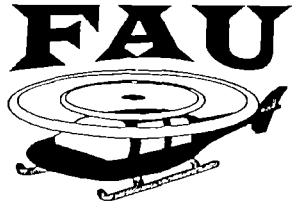
$$\dot{x} = G(x, c, t)$$

Condition for response periodicity

$$x(2\pi, x(0)) - x(0) = 0$$

Control inputs satisfying the trim equations are represented by

$$f(x, c) = 0$$

Response-periodicity condition and trim equations are jointly represented as

$$f(s) = 0 \text{ where } s = \lfloor x, c \rfloor^{T}$$

These equations are solved by combining shooting technique and damped Newton iteration

$$\left\{ \begin{matrix} x_E(0) \\ c \end{matrix} \right\}_{k+1} = \left\{ \begin{matrix} x_E(0) \\ c \end{matrix} \right\}_k - \chi \begin{bmatrix} \Phi_{11} - I & \Phi_{12} \\ \Phi_{21} & \Phi_{22} \end{bmatrix}^{-1} \left\{ \begin{matrix} x_E(2\pi) - x_E(0) \\ \delta \end{matrix} \right\}$$

$x_E(0)$ arbitrary initial state

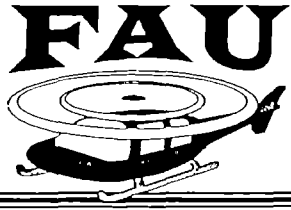$x_E(2\pi)$ non periodic solution at 2π

δ error in satisfying trim equations

$\Phi_{11} \Rightarrow$ converges to FTM

$$\sigma_k = \frac{1}{2\pi} \ln |z_k|$$

$$\xi_k = \frac{1}{2\pi} \tan^{-1} \left(\frac{\mathrm{Im}(z_k)}{\mathrm{Re}(z_k)} \right)$$

Fast Floquet Analysis

Periodic variations in blade sectional angle of attack

⇨ air velocity components, rotor forces and moments

⇨ period depends on the number of blades (Q)

$$[\text{Forces and Moments}]_{\psi=0} = [\text{Forces and Moments}]_{\psi=T/Q}$$

$$[\text{Wake States}]_{\psi=0} = [\text{Wake States}]_{\psi=T/Q}$$

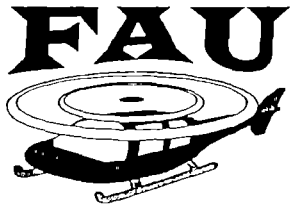$$[\text{Blade States}]_{\psi=T/Q} = [\text{Permutation matrix}][\text{Blade States}]_{\psi=0}$$

$$\{x\}_{\psi=T/Q} = P\{x\}_{\psi=0}, \quad \text{e.g. } P = \begin{bmatrix} 0 & I_b & 0 & 0 \\ 0 & 0 & I_b & 0 \\ I_b & 0 & 0 & 0 \\ 0 & 0 & 0 & I_w \end{bmatrix} \text{for } Q = 3$$

I_b and I_w are unit matrices of order $N_b \times N_b$ and $N_w \times N_w$

N_b = number of blade fixed states

N_w = number of body fixed states

$$\left\{\begin{matrix} x_E(0) \\ c \end{matrix}\right\}_{k+1} = \left\{\begin{matrix} x_E(0) \\ c \end{matrix}\right\}_k - \chi \begin{bmatrix} \Phi_{11}-P & \Phi_{12} \\ \Phi_{21} & \Phi_{22} \end{bmatrix}^{-1} \left\{\begin{matrix} x_E(\Delta T)-Px_E(0) \\ \delta \end{matrix}\right\}, \; \Delta T = T/Q$$

$P^T \Phi_{11} \Rightarrow$ converges to $P\phi(\Delta T)$

The general relation

$P^n \, x[(n+1)\,\Delta T] = \phi(\Delta T)\,P^n\,x[n\Delta T], \, n=0,1,\ldots,Q-1$

Thus,

$Px(\Delta T) = P\phi(\Delta T)\,x(0)$

$P^2 x(2\Delta T) = [P\phi(\Delta T)]^2\,x(0)$

$P^Q x(Q\Delta T) = [P\phi(\Delta T)]^Q\,x(0)$
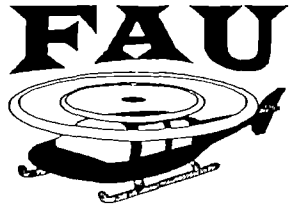
Leads to

$$\phi(2\pi) = [P\phi(\Delta T)]^Q$$

where $[P\phi(\Delta T)]$ is the equivalent Floquet transition matrix (EFTM)

From the eigenvalues $\bar{z}_k$ **of** $[P\phi(\Delta T)]$

$$\bar{\sigma}_k = \frac{Q}{2\pi} \ln|\bar{z}_k|$$

$$\bar{\xi}_k = \frac{Q}{2\pi} \arg(\bar{z}_k) = \frac{Q}{2\pi} \tan^{-1}\left(\frac{\text{Im}(\bar{z}_k)}{\text{Re}(\bar{z}_k)}\right)$$

Reduces frequency indeterminacy by a factor of Q

There are seven instructions:

Instruction 1: Assume N+c=M initial values of initial state x(0) and control vector c; s = x + c

Instruction 2: Form the permutation matrix P

Instruction 3: Perturb each element of s by a small amount ε_j, j=1,2,...M and generate (M+1) vectors

$$s + \begin{Bmatrix} \varepsilon_1 \\ 0 \\ \vdots \\ 0 \end{Bmatrix}, s + \begin{Bmatrix} 0 \\ \varepsilon_2 \\ \vdots \\ 0 \end{Bmatrix}, \cdots\cdots, s + \begin{Bmatrix} 0 \\ 0 \\ \vdots \\ \varepsilon_M \end{Bmatrix}, s$$
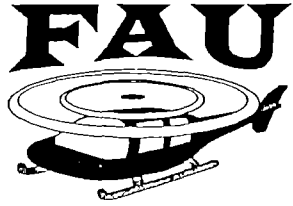
Instruction 4: Generate the corresponding (M+1) vectors after integration through $2\pi / Q$

$$Y = \left\{ \begin{array}{c} x(2\pi/Q) \\ \\ \delta \end{array} \right\}_{s} \qquad Y_i = \left\{ \begin{array}{c} x(2\pi/Q) \\ \\ \delta \end{array} \right\}_{s+\varepsilon_i} \qquad i=1,2,\ldots M$$

Instruction 5: Form the columns of the Jacobian or Partial Derivative Matrix Φ

$$\left\{ \frac{Y_1 - Y}{\varepsilon_1} \right\}, \left\{ \frac{Y_2 - Y}{\varepsilon_2} \right\}, \ldots, \left\{ \frac{Y_i - Y}{\varepsilon_i} \right\}, \ldots, \left\{ \frac{Y_M - Y}{\varepsilon_M} \right\}$$
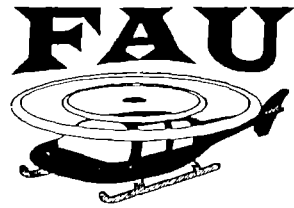
Instruction 5 (Contd.):

Or, equivalently

Jacobian or partial derivative matrix

$$\Phi = \begin{bmatrix} \Phi_{11} - P & \Phi_{12} \\ \\ \Phi_{21} & \Phi_{22} \end{bmatrix}, \text{ P - permutation matrix}$$

$P^T \Phi_{11}$ **leads to**

equivalent Floquet transition matrix (EFTM)

after convergence
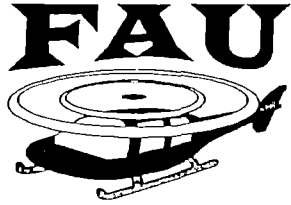
Instruction 6: Generate the error vector E_i at the i-th iteration

$$E_i = \left\{ \frac{x(2\pi/Q) - Px(0)}{\delta} \right\}_i$$

Instruction 7: Improve the solution according to Newton iteration

$$s_{i+1} = s_i - \chi[\Phi]^{-1}E_i$$

Assume a vector of initial conditions **s**

Form permutation matrix **P**

Form (**M+1**) sets of initial-condition vectors

Parallel step

Send one vector to each slave processor

Receive solutions from slaves

All (**M+1**) sets are exhausted? — No / Yes

Send end signal to slaves

Form Jacobian matrix Φ

Generate error vector E_k

Improve solution

Check for convergence — No / Yes

Output converged solution
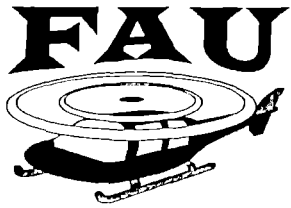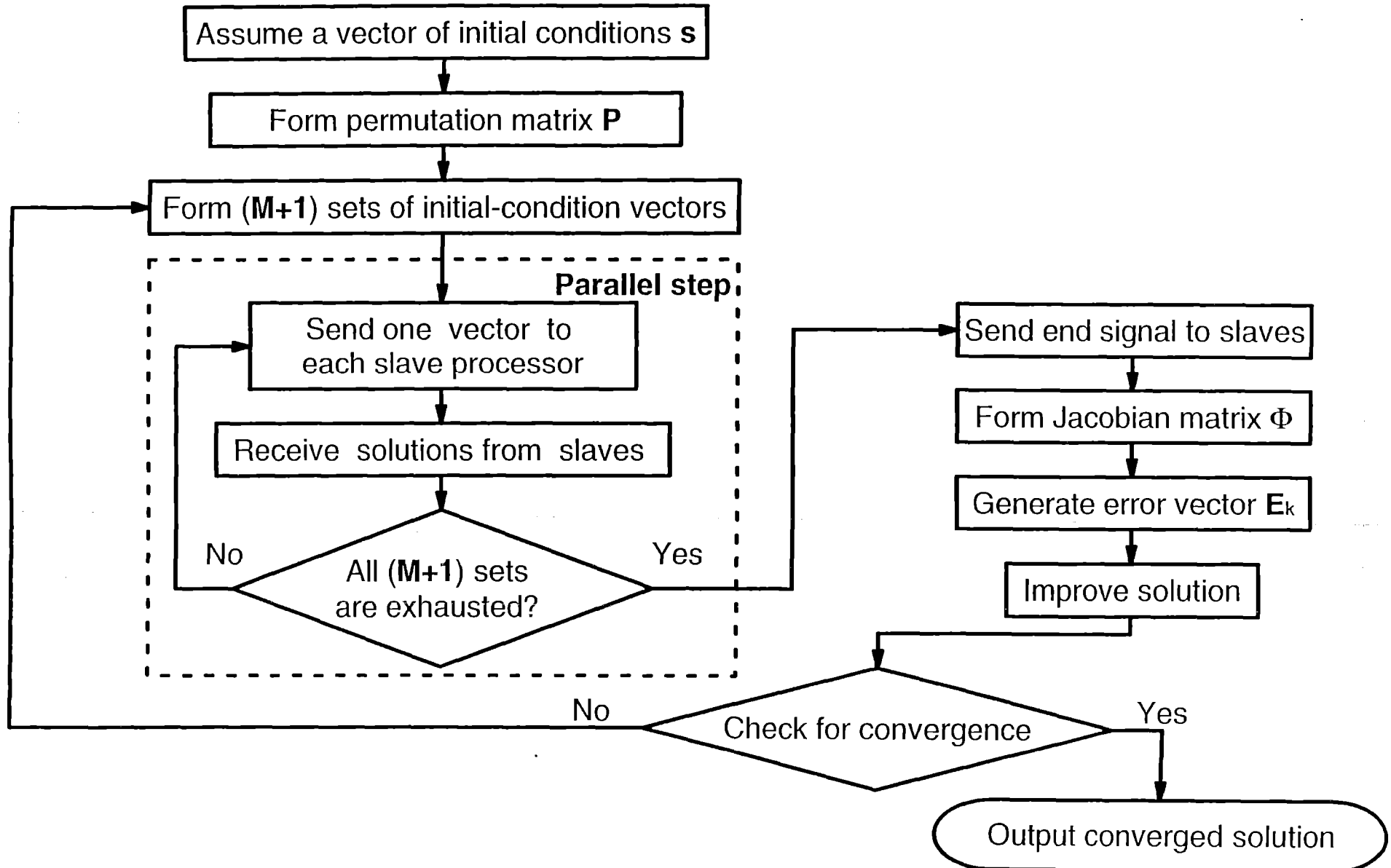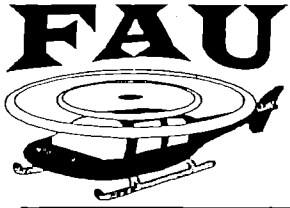
Parallel Fast Shooting
Slave Part

Receive a vector from master

End signal received?

No — Generate a column of Jacobian

Send solution to master

Yes — Return control to master
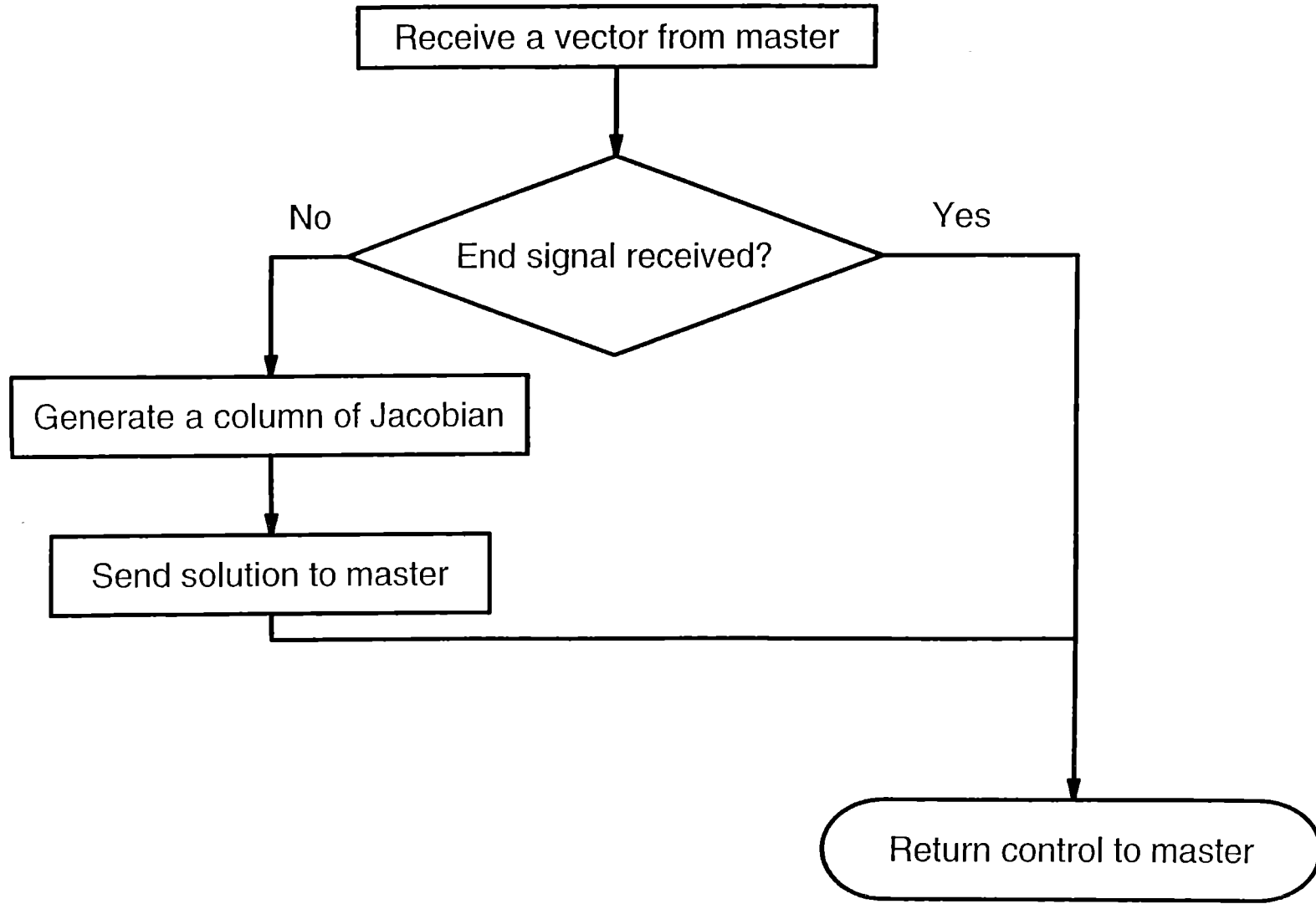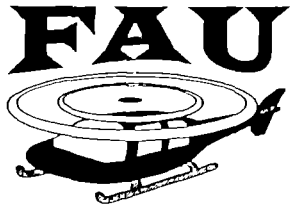
Computational Reliability

Concerns both trim analysis and eigenanalysis

Reliability Parameters

❶ condition number of the converged Jacobian matrix in the Newton iteration

❷ condition numbers of the eigenvalues of the EFTM that correspond to the damping levels of interest

❸ corresponding residual errors of the eigenpairs
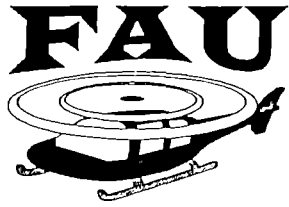
Performance Metrics

⇨ **Speedup S_p**

- ⊷ Defined as a measure of how a parallel algorithm, say running on p processors, compares itself running sequentially on one processor

$$S_p = t_1/t_p$$

$$t_1 = t_{1s} + t_{1p} = \text{predicted uniprocessor run time}$$

$$t_{1s} - \text{serial portion}$$

$$t_{1p} - \text{parallel portion}$$

$$t_p = t_{1s} + t_{1p}/p = \text{measured parallel run time}$$

$$\text{Ideal speedup} = \frac{t_1 \approx t_{1_p}}{t_p \approx t_{1_p}/p} = p$$
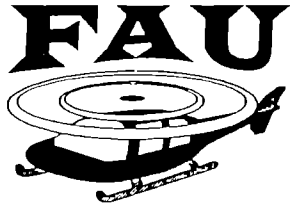
Performance Metrics *Contd..*

$$t_1 = t_{1s} + t_{1p}$$

t_{1s} - serial portion

t_{1p} - parallel portion

$t_{1s}/t_1 = f$ = serial fraction

$t_{1p}/t_1 = 1 - f$ = parallel fraction
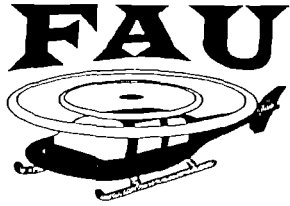
Efficiency E_p

$$E_p = S_p/p < 1$$

E_p is a measure of how effectively the processors
are used

$$E_p = 1$$

$\Rightarrow$ we are getting to the best the processors
can do

S_p and E_p provide a means of compromising between
how fast the job needs to be completed and how the
processors are kept busy
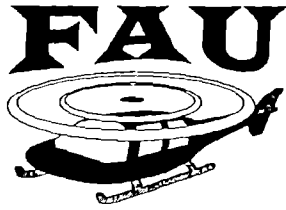
☞ **dominant influence of the parallel fraction**

$$\frac{d}{dp}\left(\frac{1}{E_p}\right) = f$$

☞ **f is an indirect measure of efficiency**

☞ **Portability is the ease with which the same parallel algorithm can be implemented on different machines/architectures**

Message Passing Interface (MPI) is used

Facilitates development of portable algorithms
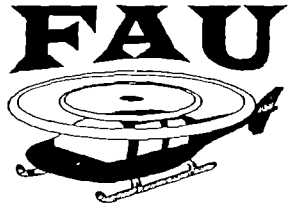
Modeling and Results

- Isolated-rotor stability in trimmed flight

- Rigid flap-lag models
  - number of blades: 5

- Airfoil aerodynamics based on the ONERA dynamic stall models of lift and drag
  - number of aerodynamic elements: 10

- Downwash dynamics based on a three-dimensional finite - state wake model
  - number of harmonics: 1 to 15

Total model order or number of states: 79 to 395
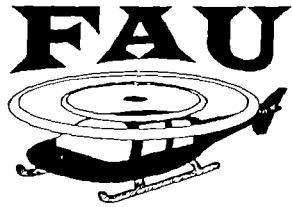
Computational Reliability Results

Condition number of the eigenvalue $\quad \text{Cond.}(\lambda) = \left| \mathbf{y}^{\mathrm{T}}\mathbf{x} \right|^{-1}$

Residual error of the eigenpair $\quad \varepsilon = \dfrac{\left\| \, [\mathbf{P}\phi(\Delta\mathbf{T})]\,\mathbf{x} - \lambda\mathbf{x} \, \right\|}{\left\| \, \lambda\mathbf{x} \, \right\|}$

For M = 395

Cond.(λ) = 2.6393 (Massively Parallel)

Cond.(λ) = 2.6412 (Distributed Computing)

ε = 0.2812E-13 (Massively Parallel)

ε = 0.2223E-13 (Distributed Computing)

Run-Time Variations with the Order and Number of Processors

IBM SP-2

Run Time (seconds)

M = 395

M = 329

M = 227

Number of Processors, p

Distributed Computing

Run Time (hrs)

M = 395

M = 329

M = 227

Number of Processors, p

IBM SP-2

Speedup and Efficiency plots vs. Number of Processors, p, for M = 395, M = 329, and M = 227.

Distributed Computing
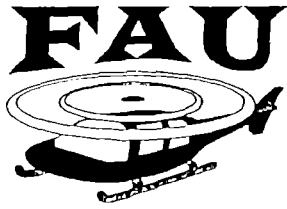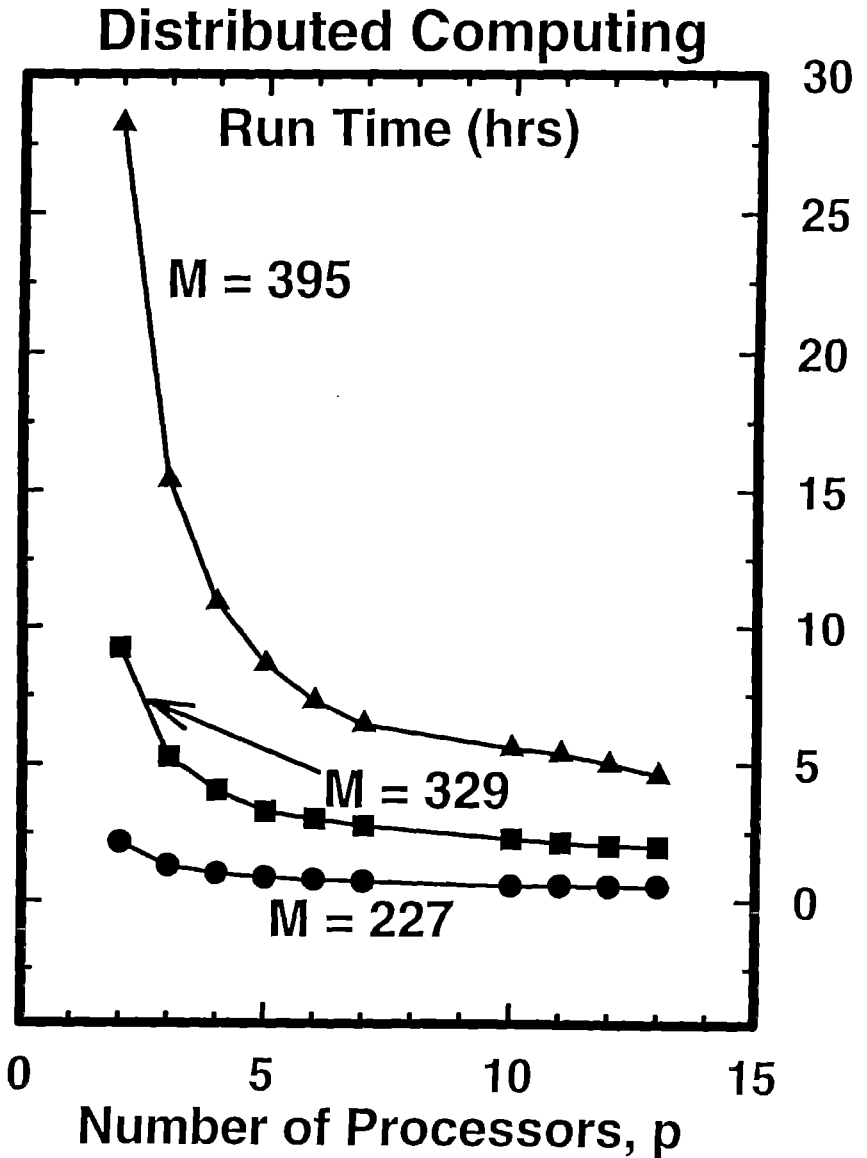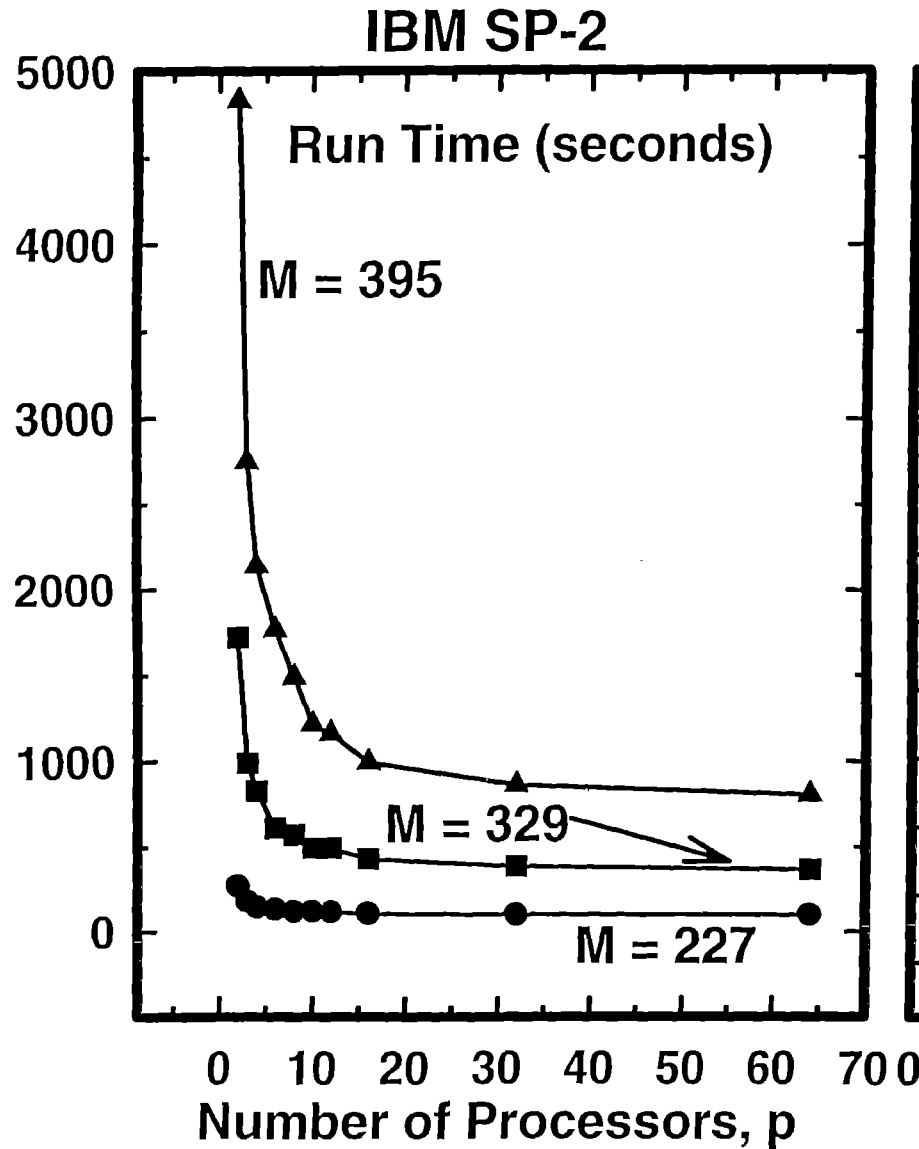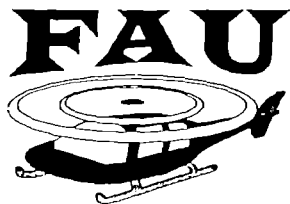
Speedup and Efficiency Variations with the Order and Number of Processors
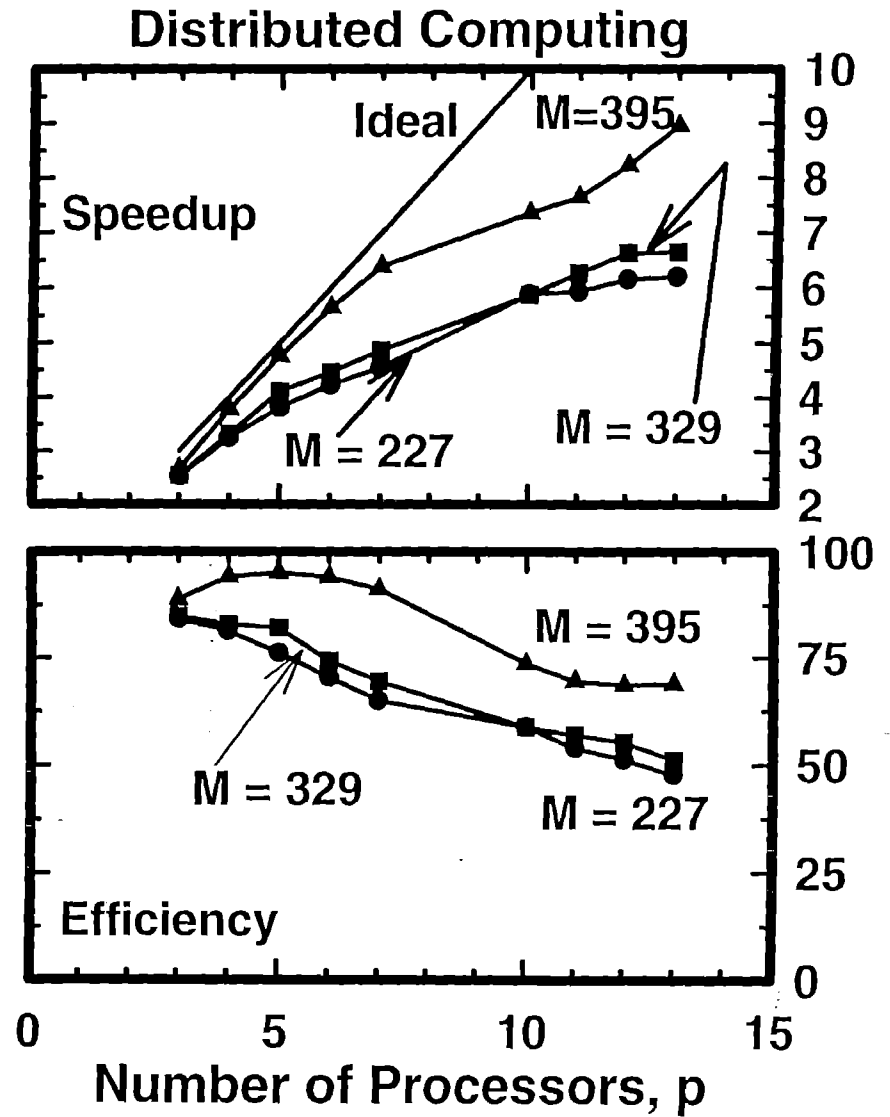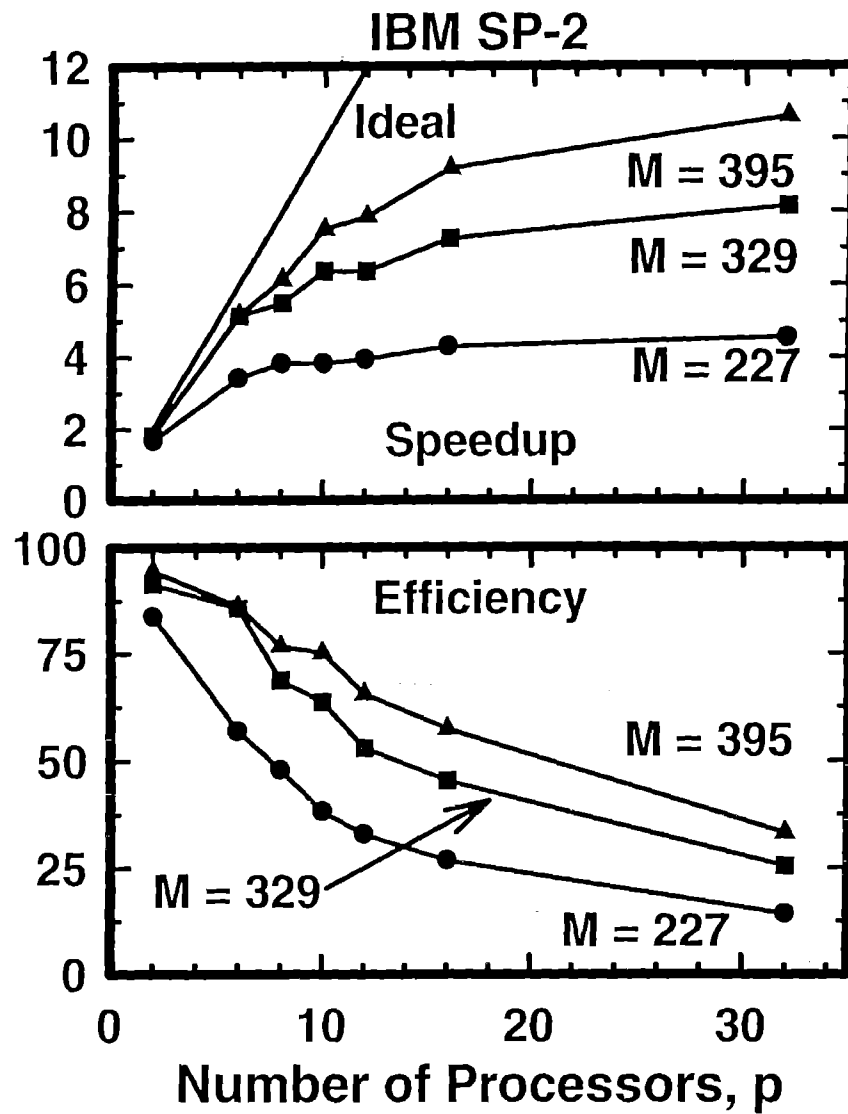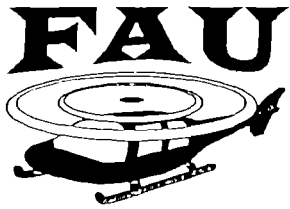
$1/E_p$-versus-p Curve
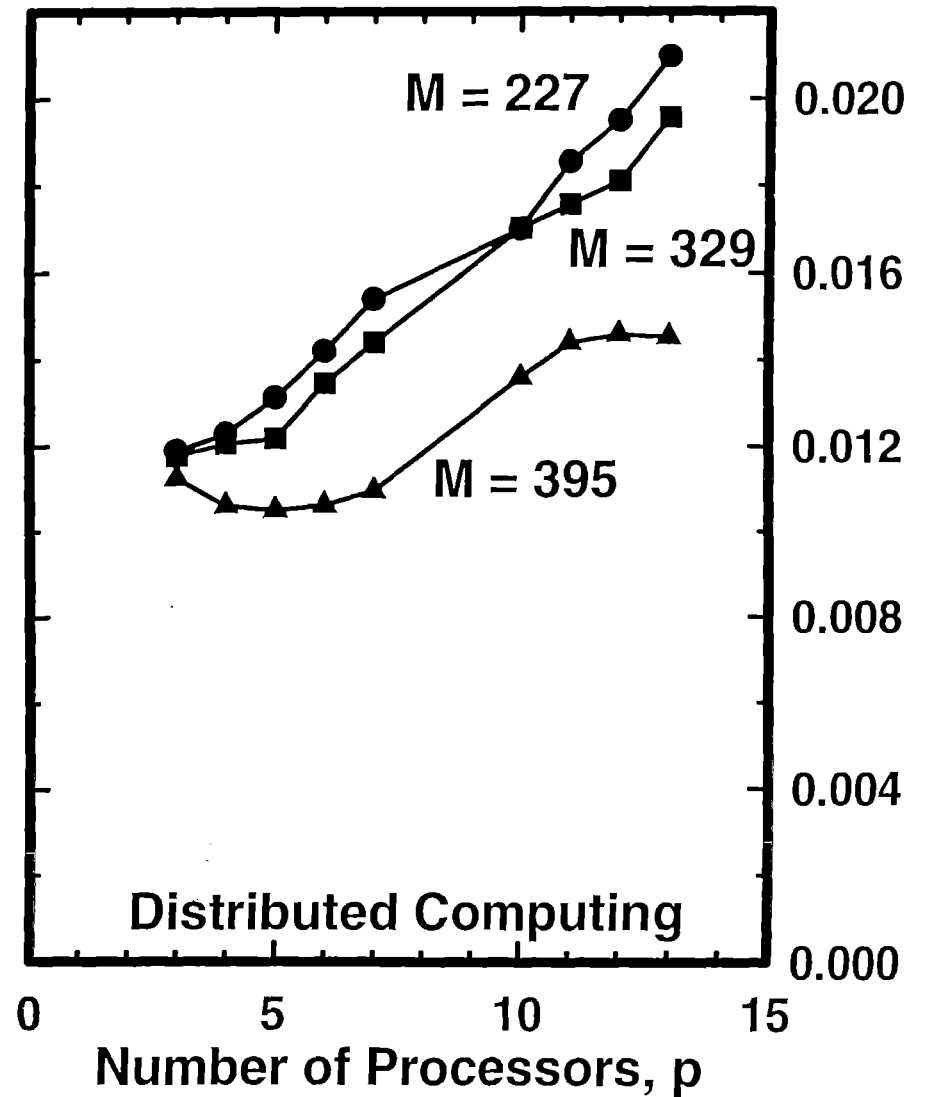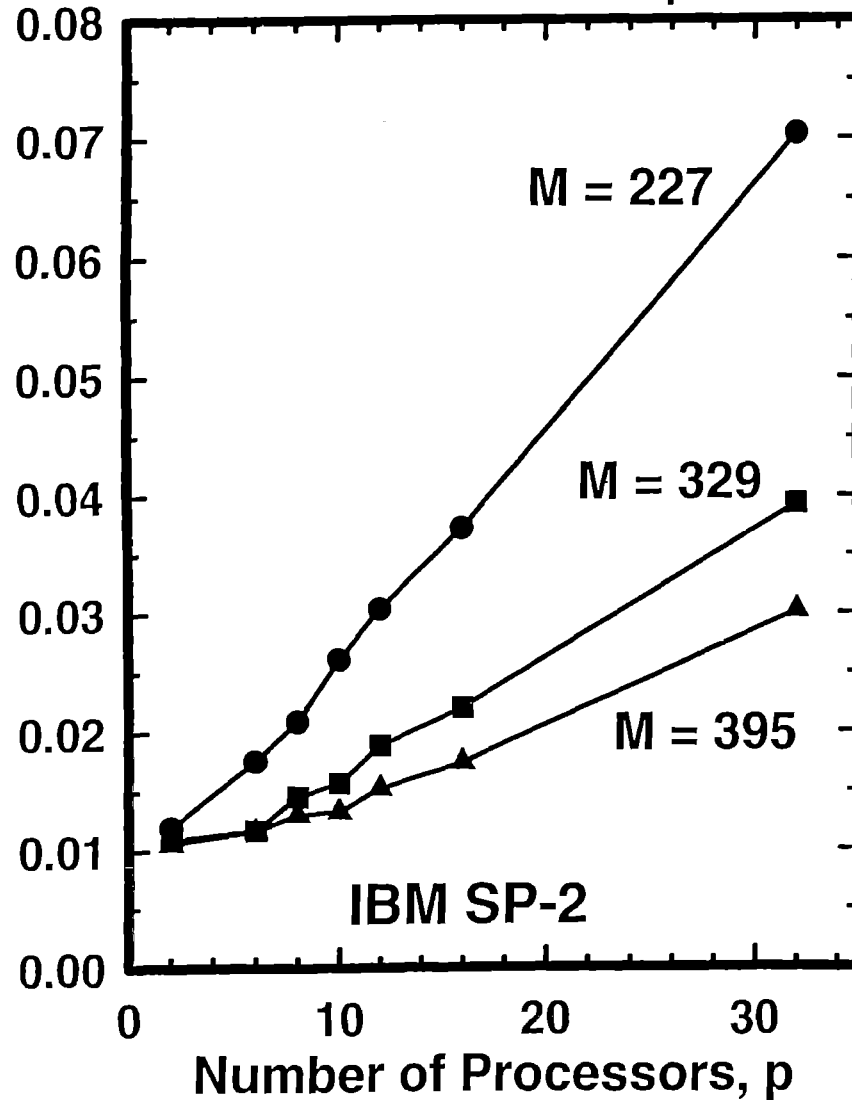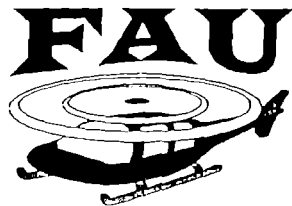
Variations of Serial and Parallel Fractions with the Order

IBM SP-2

Distributed Computing

Serial Fraction

Serial Fraction

Parallel Fraction

Parallel Fraction

Model Order, M

Model Order, M
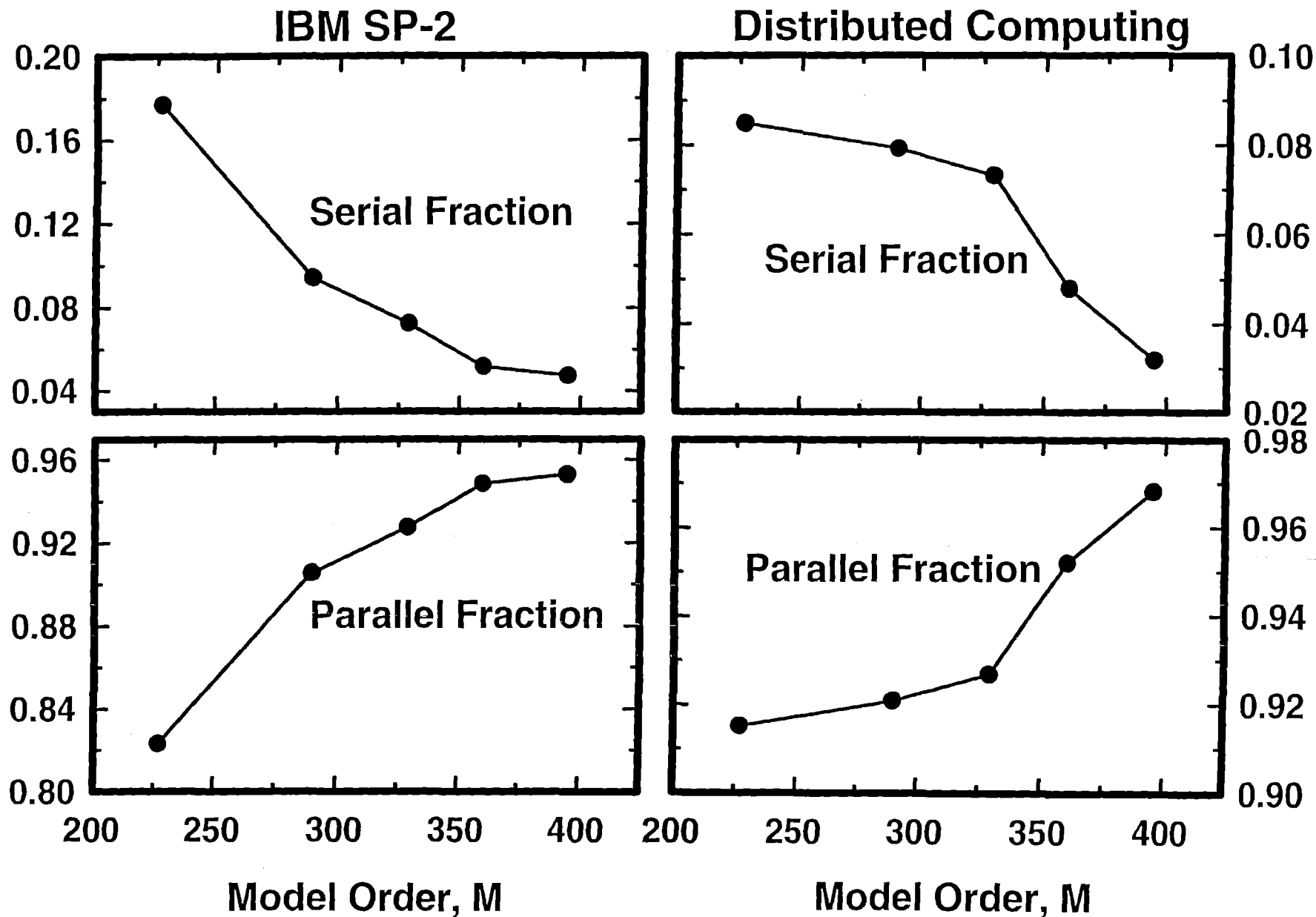
Run-Time Variations on Serial, Parallel and Distributed Computing Systems

Run Time (hours)

Model Order or Number of States
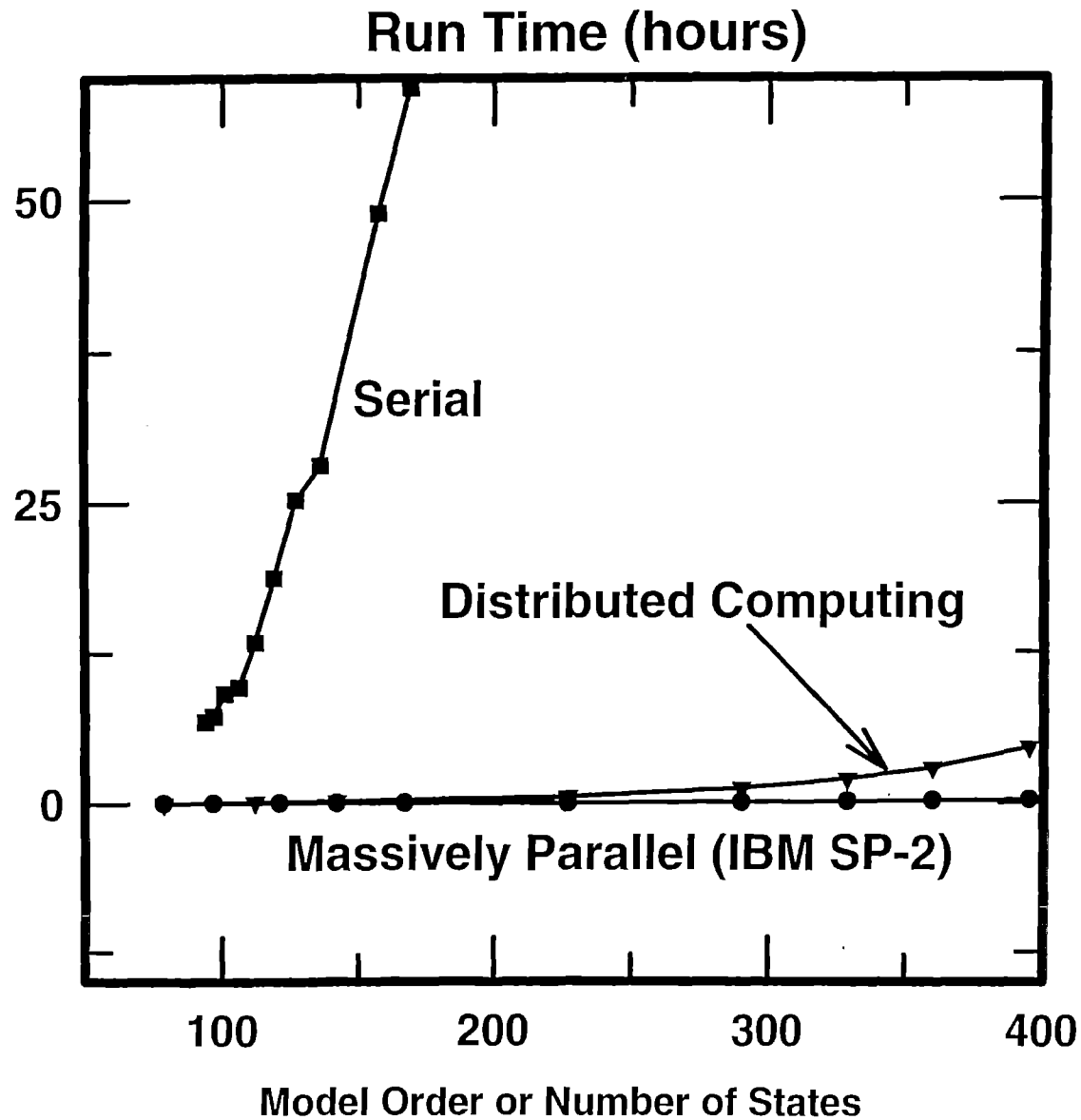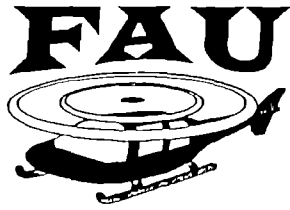
Conclusions

A parallel Fast-Floquet analysis is developed. It is designed for MIMD computing architecture, which is almost exclusively used in mainstream parallel computing systems of networked workstations (distributed computing) and massively parallel computers

☞ It is portable in that it can be directly implemented on both the systems
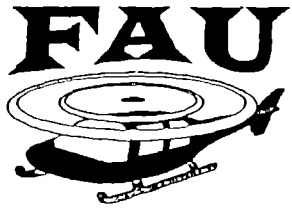
➡ The serial run time grows between quadratically and cubically with the order. By comparison, both the parallel systems reduce the run time dramatically; in fact, the corresponding ratios of serial versus parallel run times rapidly increase with increasing order.

➡ More importantly, both the parallel implementations provide a means of controlling the growth of run time with the order by a judicious combination of speedup and efficiency; that is, increasing the number of processors with the order.
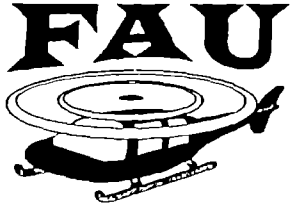
▱ The parallel-performance data of speedup, efficiency and parallel
fractions from the two parallel implementations are comparable;
so are the computational reliability figures from the serial and two
parallel implementations. In particular, the speedup and efficiency
figures are close to the ideal values for some combinations of
model order and number of processors.

Conclusions

⊜ With respect to developing a parallel algorithm and turnaround time, treating a large model with hundreds of states on networked workstations is as routine as treating a small model (N < 100) on a workstation. This is a measure of the practical utility of distributed computing in treating large models and offers considerable promise for comprehensive- and design-analysis applications.

Session II
Individual Blade Control

STABILIZATION OF PERIODIC-COEFFICIENT FLAP-LAG DYNAMICS THROUGH APPLICATION OF DISCRETE CONTROL

P.V. Bayly, J.M. Schmitt and D.A. Peters
Washington University
St. Louis, MO 63130

Abstract

Periodic flapping and lead-lag oscillations occur in rotor blades during forward flight; the governing equations are nonlinear with periodic coefficients. Oscillations become unstable as the advance ratio of the helicopter increases. Stabilization may be achieved by control of the mean pitch angle of the blade once per period according to a discrete control law. The control law is applied to the Poincaré map which governs samples of the system obtained once per period. The controller stabilizes but does not attempt to change underlying periodic orbits. This approach is particularly well-suited to systems with periodic coefficients (such as rotorcraft) since the discrete version of the system is time-invariant.

1 Introduction

Rotorcraft dynamics are dominated by periodic orbits of varying stability. For example, the flap-lag dynamics of helicopter rotor blades can become unstable as forward flight speed is increased at a given rotor speed [1]. The equations governing flap-lag dynamics in forward flight are nonlinear and contain strongly time-varying coefficients [1].

Presently helicopter designs incorporate extra components such as mechanical lag dampers to improve stability. "Smart" blade materials, as well as active servoflaps, are currently being considered for use in rotorcraft [2]. Control of rotor blade instability is complicated by three factors, however: (1) the steady state is intrinsically periodic; (2) coefficients are also periodic; and (3) behavior is nonlinear. These complications are addressed by the use of the Poincaré map which describes the behavior of samples of the system taken once per blade-passing period. The behavior of a periodic-coefficient, continuous system near a periodic orbit is thus reduced to the dynamics of an equivalent discrete, time-invariant system near a fixed point.

The use of a linearized Poincaré map to stabilize periodic orbits was first proposed by Ott, Grebogi, and Yorke [3] (OGY) for the purpose of controlling chaos. Since the original algorithm was described it has been modified by several investigators [4, 5, 6]. and validated in experiments [6, 7, 8]. However,
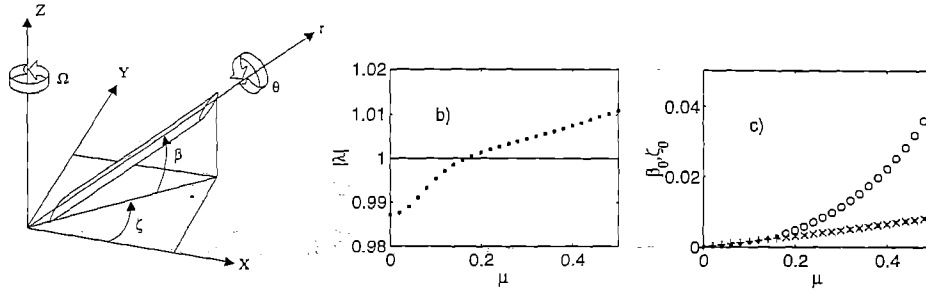
Figure 1: a) The rotor blade coordinate system and generalized coordinates β (flap angle) and ζ (lag angle). The pitch angle of the blade is θ. The $X - Y$ axes rotate about the Z-axis with angular velocity Ω. b) The magnitude of the largest eigenvalue of the Floquet transition matrix plotted vs advance ratio μ. c) Amplitudes of flap ($\cdot$ stable, o unstable) and lag (+ stable, × unstable) displacement as a function of μ.

for a number of possible reasons [9] benefits of these methods have not been demonstrated in practical mechanical or aerospace systems.

In this paper, stabilization of periodic orbits is investigated in an aeroelastic system that does not exhibit chaos: a helicopter rotor blade in forward flight. We extend the basic procedure presented by Ott, Grebogi, and Yorke [3] in the following ways: (1) The control law is optimized, taking into account the control effort; (2) Unstable orbits possessing two complex unstable eigenvalues are controlled; (3) Control is implemented without knowledge of fixed point location; (4) Constraints on the performance in steady state ("trim" constraints) are satisfied; (5) Control strategies to cope with (i) lack of knowledge of state variables and (ii) delay in implementation of control are used.

2   Rotor blade flap-lag dynamics

The rotor blade model was developed by Peters [1]. In this model, a thin rigid blade rotates at a specified speed about a fixed hub. The blade is connected to the hub by root hinges with linear torsional springs. The governing equations of the flap-lag system are derived in a rotating coordinate system (Figure 1a). The coordinate system is defined with the Z axis oriented along the rotor shaft. The $X - Y$ axes are rotated about the Z axis with an angular displacement $\psi = \Omega t$.

The position of a single blade with no hinge offsets is uniquely determined by three angles: the flap angle (β), the lag angle (ζ), and the pitch angle (θ). Dimensionless airloads on the blade in the flap and lag directions, F_β and F_ζ, are determined through quasi-steady airfoil theory (see the Appendix). The

2

resulting nondimensional nonlinear equations for coupled flap-lag motion may be written as [1]

$$\ddot{\beta} + \sin\beta\cos\beta(1+\dot{\zeta})^2 + \omega_\beta^2\beta = \int_0^1 F_\beta r \, dr \qquad (1)$$

$$\cos^2\beta\ddot{\zeta} - 2\sin\beta\cos\beta(1+\dot{\zeta})\dot{\beta} + \omega_\zeta^2\zeta = \cos\beta\int_0^1 F_\zeta r \, dr. \qquad (2)$$

Dots ( ) indicate differentiation with respect to $\psi = \Omega t$. The parameters ω_β and ω_ζ are the dimensionless natural frequencies in the flap and lag directions of the non-rotating system [1]. The pitch angle is prescribed to be $\theta = \theta_0 + \theta_s\sin\psi + \theta_c\cos\psi$, where θ_0, θ_s, and θ_c are input parameters. The pitch angle and the advance ratio μ (the ratio of forward flight speed to rotor tip speed) affect motion through the aerodynamic forces on the blade, which also depend on β and ζ (see the Appendix). All other parameters are fixed at values given in the Appendix.

Trimmed solutions of these equations are found from a Newton-Raphson technique applied to Runge-Kutta simulations [10]. Initial conditions and values for θ_0, θ_s, and θ_c are found that (1) provide periodic motion, (2) suppress the first harmonic component of β, and (3) achieve a specified coefficient of thrust; this combination is known as moment trim [1].

As the advance ratio μ is increased, stability of the trimmed solution is lost. The magnitude of the largest eigenvalue of the Floquet matrix exceeds unity for $\mu > 0.17$ (Figure 1b). The amplitude of oscillations also increases (Figure 1c), but remains reasonably small even at large values of μ. If these unstable orbits could be stabilized, the range of useful performance of the system could be significantly increased.

3   Discrete control methods

The general approach used here is motivated by the OGY approach to stabilizing unstable periodic orbits in chaotic nonlinear systems [3, 6]. Several concepts have been modified or generalized to apply control to the flap-lag system. The control technique is applicable to continuous dynamical systems of the form $\dot{\mathbf{x}} = \mathbf{f}(\mathbf{x}, t; \eta)$. In the flap-lag system the state-vector $\mathbf{x}$ is the vector $[\beta, \dot{\beta}, \zeta, \dot{\zeta}]^T$; η is a control parameter, which is taken to be the mean blade pitch angle θ_0. A discrete Poincaré map is obtained that describes the dynamics of the system sampled once every period, T: $\mathbf{x}_{n+1} = \mathbf{g}(\mathbf{x}_n; \eta)$. A periodic orbit in the continuous system ($\mathbf{x}(t + T) = \mathbf{x}(t)$) becomes a fixed point of the associated Poincaré map ($\mathbf{x}_{n+1} = \mathbf{x}_n$). Also, periodic coefficients in the original system are eliminated.

3

3.1 Background: OGY control

The original OGY approach [3] follows the following argument. Near a fixed point, the Poincaré map may be linearized and represented by a matrix equation:

$$\xi_{n+1} = A\,\xi_n + \mathbf{h}\,\delta\eta, \tag{3}$$

where ξ_n is the location in state space relative to the fixed point: $\xi_n = \mathbf{x}_n - \mathbf{x}_f$. The characteristic matrix A in this approximation is the Floquet transition matrix. The vector $\mathbf{h}$ represents the effect of a small change in the parameter η on the location of ξ_{n+1}.

Suppose (as in reference [3]) that the matrix A has one unstable eigenvalue λ_u. Let ξ_n^u be the component of ξ_n in the direction of the unstable contravariant eigenvector: $\xi_n^u = \mathbf{f}_u^T \xi_n$. Then, at each iteration the control parameter is perturbed in proportion to the unstable component: $\delta\eta_n = \alpha \mathbf{f}_u^T \xi_n$. Stabilization is achieved by directing ξ_{n+1} onto the stable manifold, which occurs if $\alpha = -\lambda_u/(\mathbf{h}^T \mathbf{f}_u)$.

3.2 Generalized discrete control methods

Several shortcomings exist in the basic OGY procedure, if we wish to apply it to a general non-chaotic system. First, the algorithm requires knowledge of the location of the fixed point. Second, performance criteria other than stability must often be achieved. Third, instability due to pairs of complex conjugate eigenvalues penetrating the unit circle is not considered. Fourth, the cost of the prescribed control effort may be excessive. Finally, changes in the control parameter may not be instantaneous, and must often be based on incomplete or imprecise knowledge of the system.

3.2.1 Control of the difference map

To overcome lack of knowledge of the fixed point, we use an idea presented in reference [6] and implement control based on the difference between consecutive iterates of the Poincaré map. Subtraction from Equation 3 the equation for the previous iteration of the map, it can be seen that

$$\mathbf{d}_{n+1} = A\,\mathbf{d}_n + \mathbf{h}\,e_n, \tag{4}$$

where $\mathbf{d}_n = \mathbf{x}_n - \mathbf{x}_{n-1}$ and $e_n = \delta\eta_n - \delta\eta_{n-1}$. The fixed point is no longer explicitly included in the linearized map. The stability of the map in Equation 4 is still governed by the eigenvalues of the Floquet matrix A.

3.2.2 Pole placement and optimal control

By the application of state feedback, the difference in the control parameter from cycle to cycle (e_n) can be made a function of the difference between successive

4

iterates of the Poincaré map. Specifically, a linear control law can be expressed as $e_n = \mathbf{k}^T \mathbf{d}_n$, where $\mathbf{k}$ is a gain vector. The control problem is then reduced to finding the gain vector $\mathbf{k}$ so the eigenvalues of $(A - \mathbf{h}\mathbf{k}^T)$ are inside the unit circle.

The choice of gain proposed by Ott, Grebogi, and Yorke [3] is only one of an infinity of possible values. It is the gain which leads to the *most stable* controlled system. However, if control effort is not free, it is probably not the best choice of gain. By introducing a cost function $J = \sum_{n=1}^{\infty} \mathbf{d}_n^T Q \mathbf{d}_n + Re_n^2$, one can find a set of gains which minimizes a logical combination of transient dynamics and control effort [11]. In this paper $Q = nI$ and $R = 1$ are chosen for several values of n. The gain vector $\mathbf{k}$ which minimizes J is found from the matrix Riccati equation [11].

3.2.3 Trim

In rotorcraft applications certain performance or trim criteria (other than stability) must be met. For example, a rotorcraft should maintain a specified thrust. The trim problem is posed as follows: select values for K parameters which will drive an N-dimensional system to a steady state satisfying K constraints. The chosen performance measure (average thrust, for example) depends on the state variables of the system and on the control parameters. Close to the trimmed condition we can write the linear approximation

$$\mathbf{p}_{n+1} = J_{px}\,\mathbf{x}_n + J_{p\eta}\,\eta_n + \mathbf{b} \tag{5}$$

where the vector $\mathbf{p}_n$ contains all the trim errors for the nth period. Subtracting the equation governing the previous iteration to eliminate the unknown constant vector $\mathbf{b}$, and combining with Equation 4, we obtain

$$\begin{bmatrix} \mathbf{d}_{n+1} \\ \mathbf{p}_{n+1} \end{bmatrix} = \begin{bmatrix} A & 0 \\ J_{px} & I \end{bmatrix} \begin{bmatrix} \mathbf{d}_n \\ \mathbf{p}_n \end{bmatrix} + \begin{bmatrix} \mathbf{h} \\ J_{p\eta} \end{bmatrix} e_n \tag{6}$$

where $\mathbf{d}_n = \mathbf{x}_n - \mathbf{x}_{n-1}$ and $e_n = \eta_n - \eta_{n-1}$. The system is now represented compactly in the same form as Equation 4.

3.3 Practical concerns and necessary enhancements

Limited measurements and state estimation   In many situations, not all state variables are accessible for measurement. A discrete observer is used to control the system when only the lead-lag state variables are measured. The output (measured) variables are expressed as $\mathbf{y}_n = C\mathbf{d}_n$. A dynamic estimate of the entire state can be formed from the input and output of the true system [11]:

$$\hat{\mathbf{d}}_{n+1} = A_c \hat{\mathbf{d}}_n + \mathbf{L}y_n + \mathbf{h}_c e_n, \tag{7}$$

5

where $A_c = A - \mathbf{L}CA$ and $\mathbf{h}_c = \mathbf{h} - \mathbf{L}C\mathbf{h}$. If $\mathbf{L}$ is chosen so that the eigenvalues of A_c are all small magnitude, then the estimate will converge rapidly to the true state.

Actuator dynamics Physical actuators do not change state instantly. To investigate the effects of a finite actuation delay, we model the actuator as a first-order system with a specified time constant: $\dot{\theta}_0 = (\tilde{\theta}_0 - \theta_0)/\tau_\theta$. The commanded pitch position, $\tilde{\theta}_0$ could change instantly, however. The order of the system is increased by one state variable, and the commanded pitch angle becomes the control input.

Model and parameter identification No mathematical model acn exactly describe a physical system. Accordingly, we attempt to stabilize the flap-lag system (a) with gains computed for erroneous parameters, and (b) with control laws developed from models fitted to simulated noisy data, without use of the equations of motion. All methods are tested in the presence of white noise measurement errors and random disturbances of the simulated system.

4 Results

4.1 Control of the ideal system including trim

To stabilize unstable periodic orbits, the eigenvalues of the Floquet matrix must be moved within the unit circle. The eigenvalues of the Floquet matrix A, for the unstable orbit at $\mu = 0.4$, are slightly outside of the unit circle, as illustrated in Figure 2. An optimal gain vector $\mathbf{k}$ is calculated to minimize the cost function J defined above. The eigenvalues of the Floquet matrix of the stabilized system, $(A - \mathbf{h}\mathbf{k}^T)$ are moved significantly inside the unit circle by this algorithm, as shown in Figure 2.

The ability to control unstable orbits in the flap-lag system is demonstrated in simulations of the full nonlinear system (Figure 3). Simulations are started near an unstable periodic orbit and control is then applied. The oscillations gradually approach the stabilized periodic orbit. The required deviation in mean pitch angle has a maximum value near 0.01 and decays with time.

4.2 Control of imperfect systems

Noise and measurement error In the next results, random disturbances of amplitude 5% of the RMS amplitude of each state variable are added to the corresponding variable every period. The results of a controlled simulation are illustrated in Figure 4; control is turned off after 20 periods to show the underlying instability. While the deviation in the pitch angle decreases significantly after the initial perturbation, the control effort will fail to decay to zero.

6
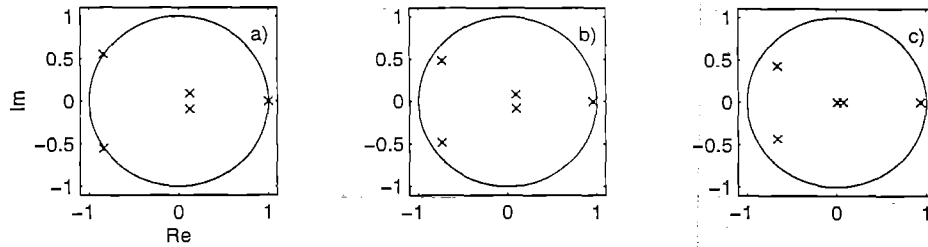
Figure 2: Eigenvalues of the Floquet matrix at an advance ratio of $\mu = 0.4$ for (a) the uncontrolled system, (b) the optimally controlled system with weighting matrices $Q = I$ and $R = 1$, and (c) the optimally controlled system with $Q = 100I$ and $R = 1$.
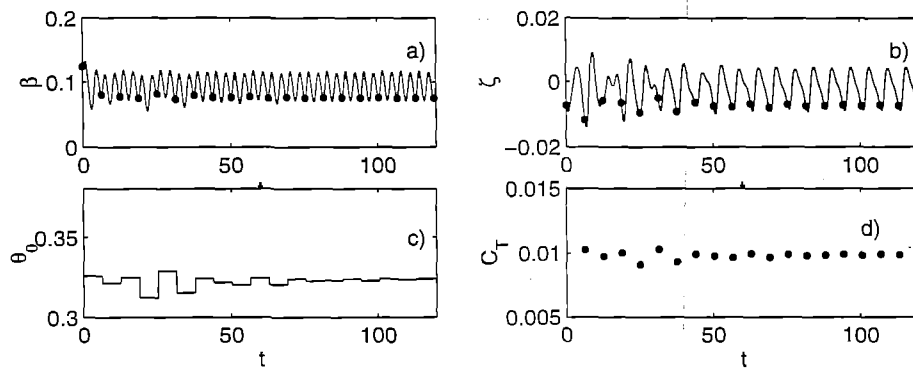
Figure 3: Response of the controlled flap-lag system to an initial perturbation (0.05 radians in β) from the periodic orbit. Time series of the flap (β) and lag (ζ) displacements, the control parameter (mean pitch angle, θ_0), and the coefficient of thrust, C_T are shown.

7
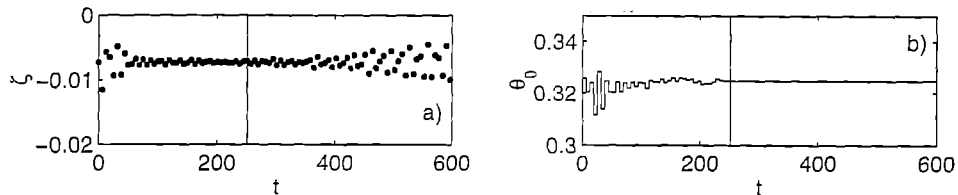
Figure 4: Response of the controlled flap-lag system to an initial perturbation from the periodic orbit and additive random noise (5% of RMS amplitude of each state variable). Discrete points from the lag (ζ) response, and the mean pitch angle (θ_0) are shown. Control is turned off after 40 periods (to the right of the vertical line).

Observer-based control Control is implemented with only knowledge of the flap angle and flapping velocity (β and $\dot{\beta}$). The poles of the observer are chosen to be ten times faster than the poles of the controller. The resulting performance of the controller is shown in Figures 5a-c. The success of this control strategy depends on the observability of the system [11].

Control including actuator dynamics In the results so far, we have assumed that any desired change in θ_0 can be made instantly. However, any change in mean pitch angle must take a finite time to complete. A controlled simulation in which the mean pitch angle exhibits first order dynamics with a time constant $\tau_\theta = 1.0$ is shown in Figures 5d-f. The deviations in mean pitch angle are smaller than the cases above, and the system takes slightly longer to converge, but remains stable.

Control with imprecise models The control strategy is generally robust to errors in model and parameter estimates. Control is applied at an advance ratio of $\mu = 0.4$ using a control gain vector estimated for $\mu = 0.3$. The results are shown in Figures 5g-i, they exhibit rapid convergence. Models can be also derived based on data from experiment or simulation, without the benefit of equations of motion. We deliberately misidentify the system as two-dimensional (2-D) and use a least-squares fit to derive an empirical model of the form $x_{n+1} = Ax_n + h\eta_n$. The results of successful a control based on this model are shown in Figures 5j-l. Here the transient is long, indicating less effective control.

5   Summary

Unstable periodic orbits in simulations of flap-lag dynamics are stabilized by the periodic application of very small perturbations of the blade pitch angle.

8
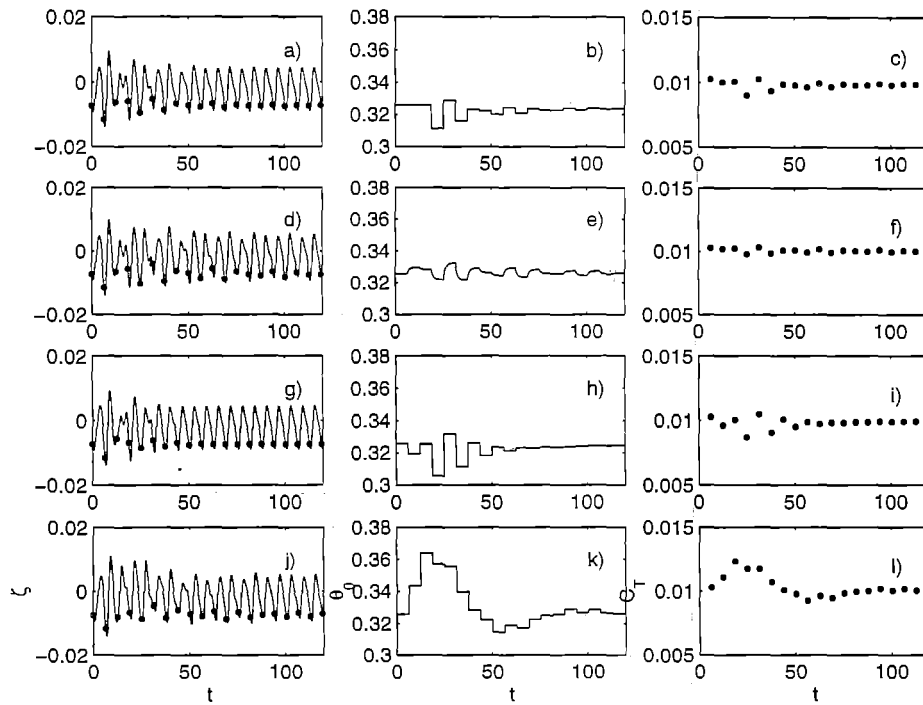
Figure 5: Lag displacement, mean pitch angle, and thrust coefficient for different control cases with advance ratio $\mu = 0.4$. a-c) Observer-based control. d-f) Control of a system including actuator dynamics. g-i) Control using gains estimated for $\mu = 0.3$. j-l) Control based on a 2-D model fitted to noisy data from simulation.

Transient effects in weakly stable periodic orbits can also be reduced by this method. Detailed knowledge of the equations of motion is not required to implement control, so long as the stability properties of the underlying motion can be estimated. The control law used to stabilize these orbits may also be optimized with respect to different performance or cost functions. The control strategy is applicable even if some states are not measurable, even if control can not be applied instantly, or even if the model is only approximate. The general approach is particularly useful for nonlinear systems with periodic coefficients. As active blade control becomes feasible, this general approach may be practical for improving the performance and simplifying the design of rotorcraft.

References

[1] D.A. Peters. Flap-lag stability of helicopter rotor blades in forward flight. *Journal of the American Helicopter Society*, 20(4):2–13, 1974.

[2] F.K. Straub and D.J. Merkley. Design of a servo-flap rotor for reduced control loads. In *Proc. American Helicopter Society 50th Annual Forum*, pages 305–314, 1994.

[3] E. Ott, C. Grebogi, and J.A. Yorke. Controlling chaos. *Phys. Rev. Lett.*, 64(11):1196–1199, 1990.

[4] E.R. Hunt. Stabilizing high-period periodic orbits in a chaotic system: the diode resonator. *Phys. Rev. Lett.*, 67(15):1953–1955, 1991.

[5] V. Petrov, B. Peng, and K. Showalter. A map-based algorithm for controlling low-dimensional chaos. *J. Chemical Physics*, 96:7506–7513, 1992.

[6] S. Bielawski, D. Derozier, and P. Glorieux. Experimental characterization of unstable periodic orbits by controlling chaos. *Phys. Rev. A*, 47:R2492–R2495, 1993.

[7] W.L. Ditto, S.N. Rauseo, and M.L. Spano. Experimental control of chaos. *Phys. Rev. Lett.*, 65(25):3211–3214, 1991.

[8] P. Parmananda, P. Sherard, R.W. Rollins, and H.D. Dewald. Control of chaos in an electrochemical cell. *Phys. Rev. E*, 47(5):3003–3006, 1993.

[9] P.V. Bayly and L.N. Virgin. Practical considerations in the control of chaos. *Phys. Rev. E*, 50(1):604–607, 1994.

[10] D.A. Peters and A. Izadpanah. Helicopter trim by periodic shooting with Newton-Raphson iteration. In *Proceedings of the 37th Annual National Forum of the American Helicopter Society*, pages 81–93, May 1981.

[11] W.L. Brogan. *Modern Control Systems*. Prentice-Hall, Englewood Cliffs, NJ, 1991.

A   Aerodynamic forces

The dimensionless aerodynamic forces in Equations 1 and 2 are [1]

$$F_\beta = \pm \frac{\gamma}{2}[U_t^2 \sin\theta - U_t U_p(\cos\theta + \frac{c_{d_0}}{a})] \qquad (8)$$

$$F_\zeta = \pm \frac{\gamma}{2}[U_p^2(\cos\theta - \frac{c_{d_0}}{2a}) - U_p U_t \sin\theta - U_t^2 \frac{c_{d_0}}{a}] \qquad (9)$$

where U_t and U_p are the dimensionless velocities tangent and perpendicular to the plane of rotation of the rotor blades. The force expressions are negative if reversed flow is present, i.e. if $U_t \cos\theta + U_p \sin\theta < 0$. The dimensionless velocities are

$$U_t = (1 + \dot{\zeta})r\cos\beta + \mu\sin(\psi + \zeta) \qquad (10)$$

$$U_p = r\dot{\beta} + \lambda\cos\beta + \mu\sin\beta\cos(\psi + \zeta). \qquad (11)$$

The inflow λ is related to the coefficient of thrust by simple momentum theory: $c_T = 2\lambda\sqrt{\mu^2 + \lambda^2}$ (for zero climb rate). The coefficient of thrust is also equal to the integrated vertical force:

$$c_T = \frac{\sigma a}{2\pi\gamma}\int_0^{2\pi}\cos\beta\int_0^1 F_\beta \, dr \, d\psi \qquad (12)$$

where the slope of the lift curve $a = 2\pi$, the rotor solidity $\sigma = 0.05$, the Lock number $\gamma = 5$, and the coefficient of drag $c_{d_0} = 0.01$. Frequencies are taken as $\omega_\beta = 0.15$ and $\omega_\zeta = 1.4$. The advance ratio μ is varied.

VIBRATION REDUCTION IN HELICOPTER ROTORS USING AN ACTIVELY CONTROLLED FLAP AND IMPROVED UNSTEADY AERODYNAMICS*

T.F. Myrtle and P.P. Friedmann
Mechanical and Aerospace Engineering Department
University of California, Los Angeles

Seventh International Workshop on Dynamics and
Aeroelastic Stability Modeling of Rotorcraft Systems
Sponsored by the U.S. Army Research Office and
Washington University in St. Louis
October 14-16, 1997

INTRODUCTION AND BACKGROUND

- Achieving acceptable vibration levels is an important part of the helicopter design process

- Vibration Reduction Approaches:

<u>Passive Methods</u>

- – Dampers

- – Structural Optimization

<u>Active Methods</u> (See Friedmann and Millott (1995))

- – Higher Harmonic Control (HHC)

- – Individual Blade Control (IBC)

- – Active Control of Structural Response (ACSR)

- – Actively Controlled Flap (ACF)

INTRODUCTION AND BACKGROUND (CONT.)

- Actively Controlled Flap (ACF):

  - An actively controlled, partial span trailing edge flap located on the outboard section of the blade is used to modify the aerodynamic loading on the blade in such a way that the vibratory loads are minimized.

  - Approach is similar to IBC approach, but retains conventional swashplate. Actively controlled flap has no effect on airworthiness of helicopter.

INTRODUCTION AND BACKGROUND (CONT.)

- Actively Controlled Flap (Cont.):

  - Investigated by Millott and Friedmann (1994) using elastic blade model and quasisteady Theodorsen aerodynamics.

  - Also investigated by Milgram and Chopra (1995) using rotor analysis code UMARC. Aerodynamics based on a compressible, unsteady model developed by Leishman combined with a free wake model.

  - Studied experimentally by Straub (1995).

OBJECTIVES OF THE PRESENT STUDY

- To develop a new compressible unsteady aerodynamic model for an airfoil/flap combination that is suitable for rotary wing applications.

- To implement the aerodynamic model in an aeroelastic response analysis of a flexible hingeless blade incorporating an actively controlled flap.

- To conduct control studies of vibration reduction using the actively controlled trailing edge flap.

UNSTEADY AERODYNAMIC MODELING

- Rotor aerodynamics modeled using a 2-D blade element formulation, with far wake effects taken into account through an additional induced angle of attack.

- Desired Capabilities for the 2-D Linear Aerodynamic Model:

  - Unsteady aerodynamic forces due to arbitrary motion of an airfoil/flap combination.

  - Unsteady flap hinge moment.

  - Compressibility effects.

  - Unsteady freestream velocity effects.

UNSTEADY AERODYNAMIC MODELING (CONT.)

- Aerodynamic Theories Developed for Rotary Wing Applications that Include a Flap Modeling Capability:

Incompressible

- Modified quasisteady Theodorsen aerodynamics (see Millott and Friedmann (1994))

- Finite state airload model developed by Peters and his associates (1994)

Compressible

- Leishman and his associates (1990,1994,1995)

UNSTEADY AERODYNAMIC MODELING (CONT.)

- Rational Function Approximation (RFA) Approach:

  - Approach commonly employed in fixed wing aeroelastic analyses.

  - Oscillatory aerodynamic response data is used to generate approximate transfer functions that relate generalized motion to aerodynamic loads.

  - Transformation to the time domain to produces a state space aerodynamic model.

- Advantages:

  - Compressible oscillatory response data easily obtained using a doublet lattice method.

  - Method easily applicable to any airfoil/flap geometry.

UNSTEADY AERODYNAMIC MODELING (CONT.)

- Define the generalized motion and force vectors $\mathbf{h}(t)$ and $\mathbf{f}(t)$ respectively as

$$\mathbf{h}(t) = \begin{bmatrix} W_0(t) \\ W_1(t) \\ D_0(t) \\ D_1(t) \end{bmatrix}, \quad \mathbf{f}(t) = \begin{bmatrix} C_l(t) \\ C_m(t) \\ C_h(t) \end{bmatrix}.$$

- Derivation of the aerodynamic model is carried out in terms of nondimensionalized time $\bar{t}$, given by

$$\bar{t} = \frac{1}{b} \int_0^t U(\tau) d\tau.$$

This transformation is necessary to properly account for the effects of pulsating flow.

UNSTEADY AERODYNAMIC MODELING (CONT.)

- Aerodynamic system is represented in the frequency domain as:

$$\mathbf{G}(\bar{s}) = \mathbf{Q}(\bar{s})\mathbf{H}(\bar{s}),$$

  - $\mathbf{Q}(s)$ is a matrix of aerodynamic transfer functions.

  - $\mathbf{G}(\bar{s}) = \mathcal{L}[\mathbf{f}(\bar{t})U(\bar{t})]$ and $\mathbf{H}(\bar{s}) = \mathcal{L}[\mathbf{h}(\bar{t})]$.

  - $\bar{s}$ is the nondim. Laplace variable, $\bar{s} = \frac{sb}{U}$

UNSTEADY AERODYNAMIC MODELING (CONT.)

- Rational Function Aproximation (RFA) using the Least Squares Approach (Roger, 1977):

$$\tilde{\mathbf{Q}}(s) = \mathbf{C}_0 + \mathbf{C}_1 s + \sum_{j=1}^{n_L} \frac{s}{s + \gamma_j} \mathbf{C}_{j+1}.$$

- The n_L lag terms produce additional states in the time domain, forming an 'aerodynamic dimension.'

- Poles γ are assumed positive to produce stable open loop roots.

- The matrix coefficients $\mathbf{C}_i$, $i = 0, n_L + 1$ are identified using a fitting process.

- The approximation can be constrained at the two ends of the reduced frequency spectrum, $k = 0$ and $k = \infty$.

UNSTEADY AERODYNAMIC MODELING (CONT.)

Least Squares Fit
of Oscillatory Response Data

Tabulated Oscillatory
Response Data

k_n	$Q(k_n)$	
	Real	Imag
0.00	--	--
0.02	--	--
0.04	--	
0.06		
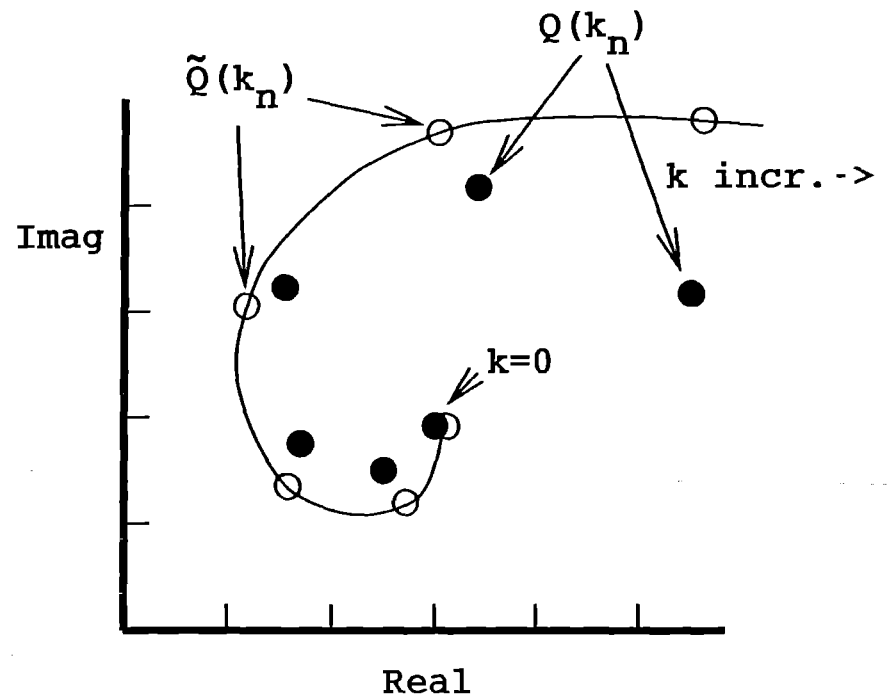
UNSTEADY AERODYNAMIC MODELING (CONT.)

- To further increase the efficiency of the model, pole locations are optimized such that the approximation error is minimized:
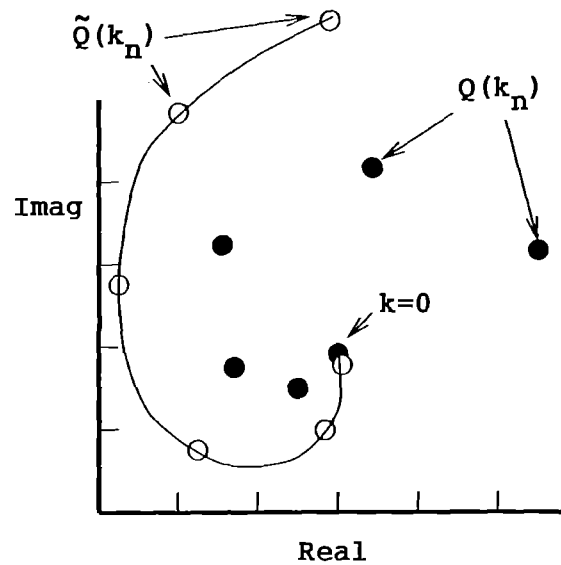
Before Pole Optimization   After Pole Optimization
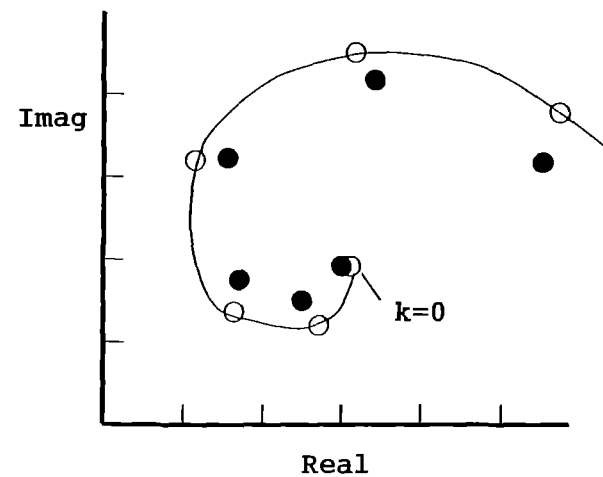
UNSTEADY AERODYNAMIC MODELING (CONT.)

- Generalized Airfoil Motions:

U

W_0 W_1
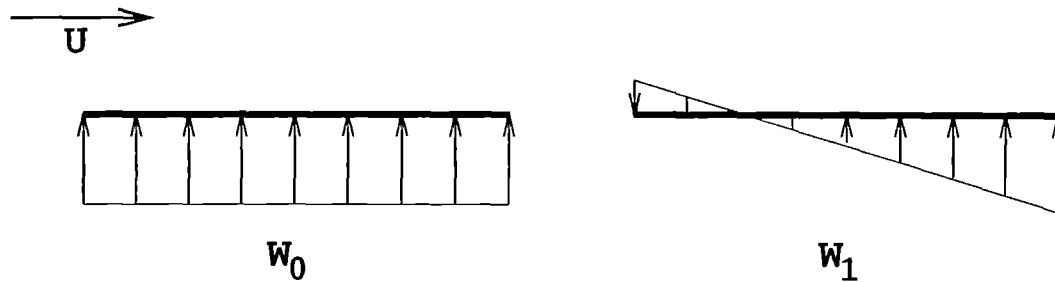
- Generalized Flap Motions:

U

D_0 D_1
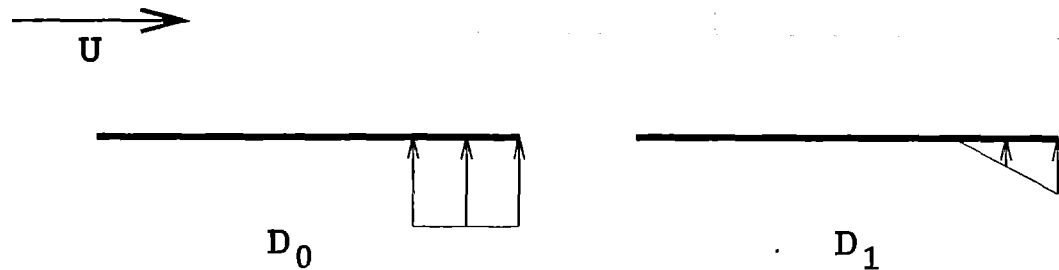
UNSTEADY AERODYNAMIC MODELING (CONT.)

- State Space Model:

  - The Rational Approximant is rewritten as

$$\tilde{\mathbf{Q}}(\bar{s}) = \mathbf{C}_0 + \mathbf{C}_1 \bar{s} + \mathbf{D} \left(\mathbf{I}\bar{s} - \mathbf{R} \right)^{-1} \mathbf{E}\bar{s},$$

where $\bar{s}$ is the nondim. Laplace variable, $\bar{s} = \frac{sb}{U}$,

$$\mathbf{D} = \begin{bmatrix} \mathbf{I} & \mathbf{I} & \ldots & \mathbf{I} \end{bmatrix},$$

$$\mathbf{R} = - \begin{bmatrix} \gamma_1 \mathbf{I} & & & \\ & \gamma_2 \mathbf{I} & & \\ & & \ldots & \\ & & & \gamma_{n_L} \mathbf{I} \end{bmatrix}, \quad \mathbf{E} = \begin{bmatrix} \mathbf{C}_2 \\ \mathbf{C}_3 \\ \vdots \\ \mathbf{C}_{n_L+1} \end{bmatrix}.$$

UNSTEADY AERODYNAMIC MODELING (CONT.)

- State Space Model:

  - Using the inverse Laplace transform produces a state space aerodynamic model:

$$\mathbf{f}(t) = \frac{1}{U(t)} \left(\mathbf{C}_0 \mathbf{h}(t) + \mathbf{C}_1 \frac{b}{U(t)} \dot{\mathbf{h}}(t) + \mathbf{D}\mathbf{x}(t) \right).$$

$$\dot{\mathbf{x}}(t) = \frac{U(t)}{b} \mathbf{R}\mathbf{x}(t) + \mathbf{E}\dot{\mathbf{h}}(t),$$

  - $\mathbf{x}(t)$ is the vector of aerodynamic states

Rational Function Approximation of the Lift Response to W_0/U, $M = 0.5$
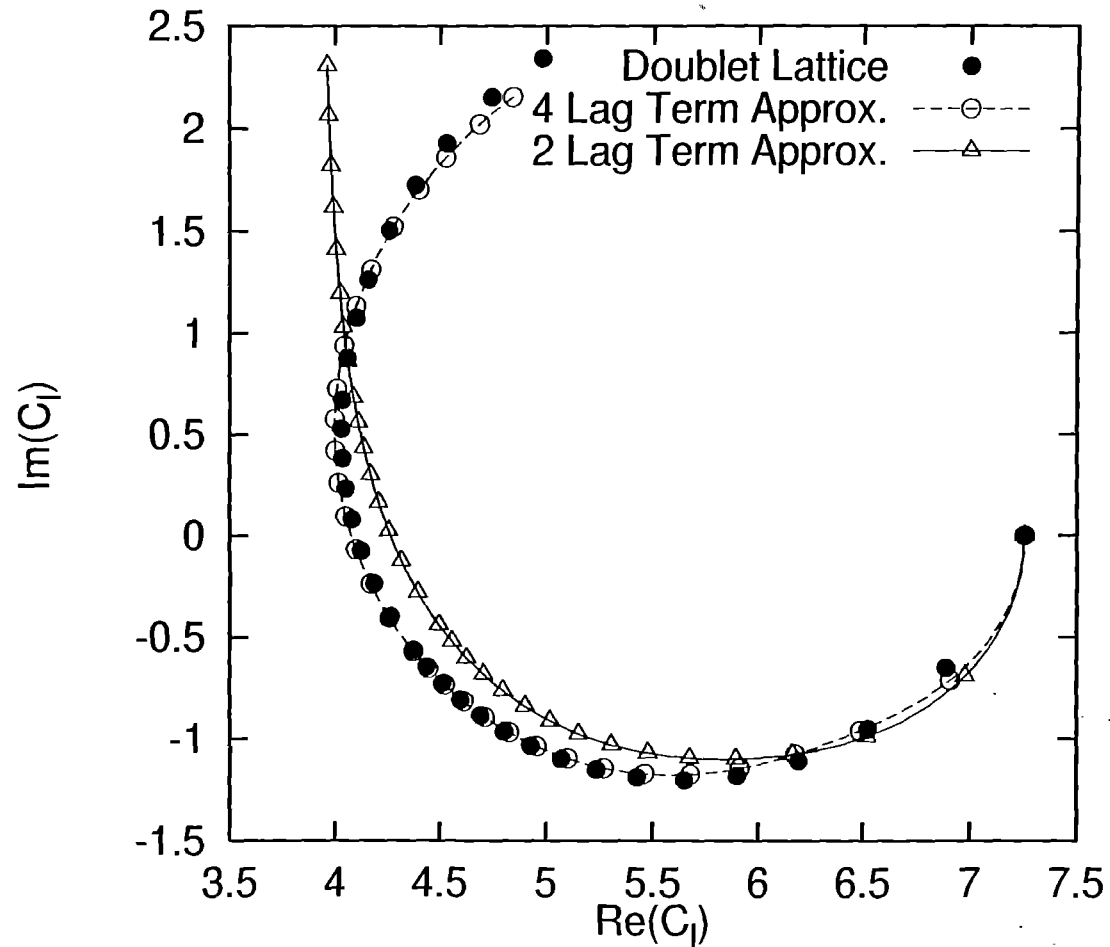
MODEL VALIDATION

- Comparison performed with an exact, incompressible solution to the time varying freestream problem developed by Isaacs.

- Numerical experiments were performed for unsteady freestream conditions represented by

$$U(\psi) = U_o(1 + \lambda \sin \psi),$$

- Pitch motion:

$$\alpha = \alpha_o \sin \psi$$

RFA, 1 Lag
RFA, 2 Lag
Isaacs

$C_{lo} = 2 \pi \alpha_o$
$U = U_o (1 + \lambda \sin(\psi))$
$\alpha = \alpha_o \sin(\psi)$
$k = 0.20$
$\lambda = 0.80$

C_l/C_{lo}

ψ (deg)
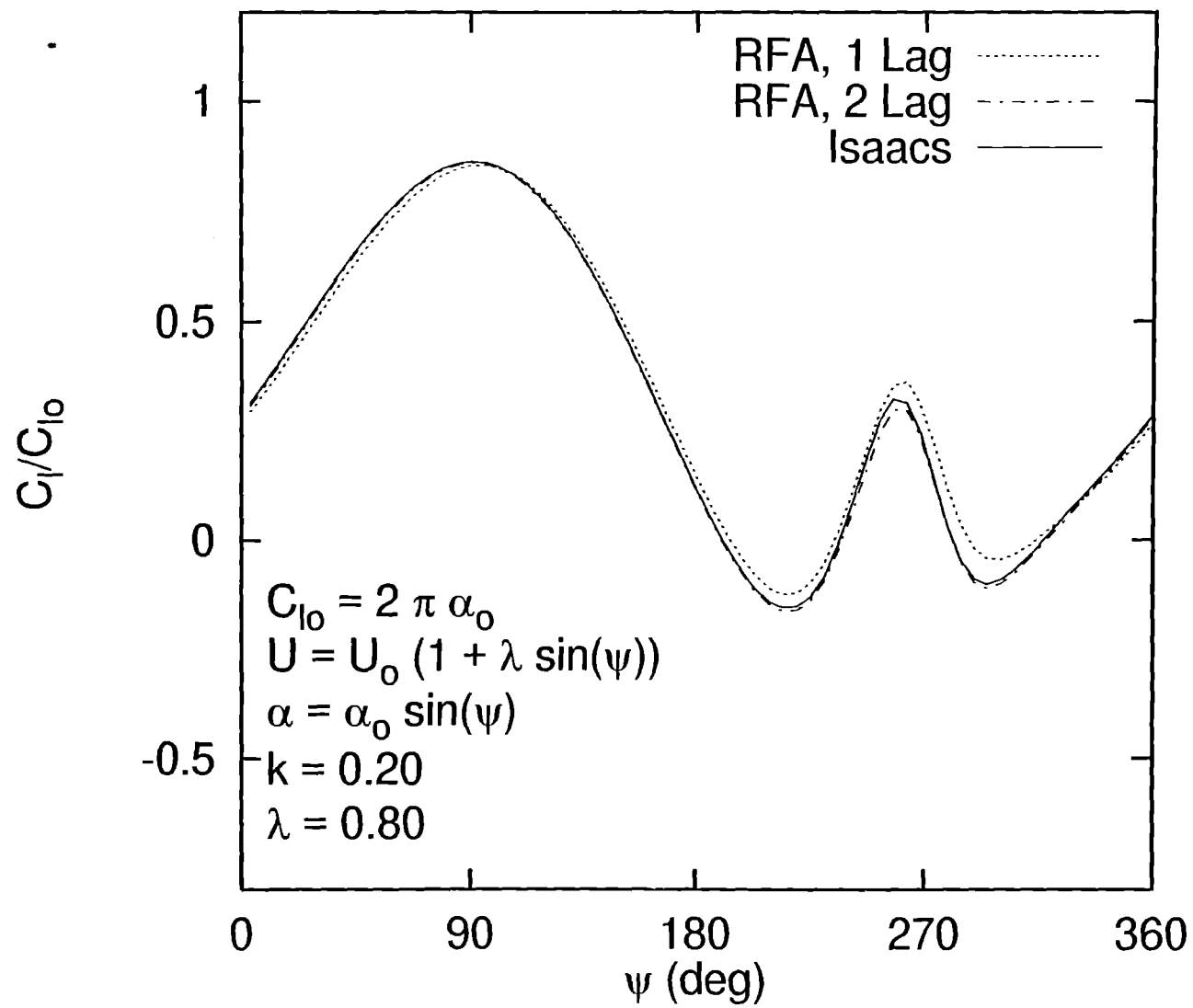
STRUCTURAL MODEL

- Structural model for a blade/flap combination is similar to that used by Millott and Friedmann (1994)

- An elastic blade model with fully coupled flap-lag-torsional dynamics is used which includes geometric nonlinearities due to moderate deflections.

- The control surface is assumed to be an integral part of the blade, but does not provide a structural contribution.

- Flap deflection is assumed to be a controlled quantity.

- Four identical blades are combined to represent a four-bladed, fixed hub hingeless rotor.

PROBLEM FORMULATION AND SOLUTION

Fixed Radial Station

U ↓

ψ

y

x ↓

Mach Number

ψ
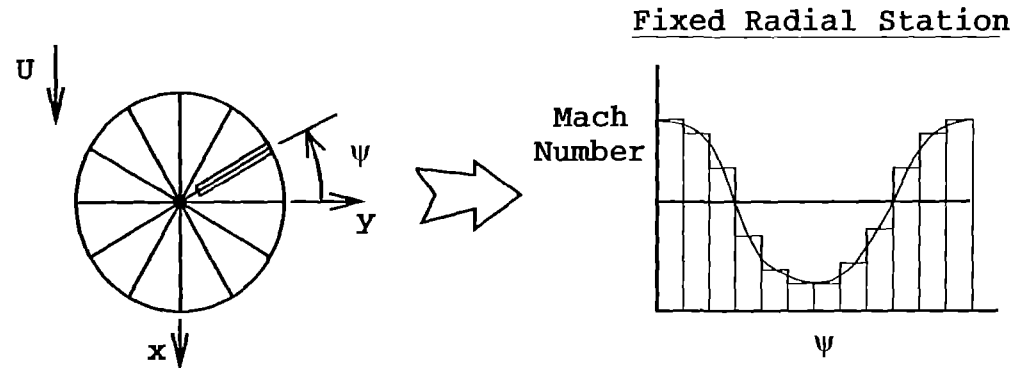
- Coefficients indexed by azimuthal segment:

$$\mathbf{f} = 1/U \left(\mathbf{C}_{0i}\mathbf{h} + \mathbf{C}_{1i}(b/U)\dot{\mathbf{h}} + \mathbf{Dx} \right)$$

$$\dot{\mathbf{x}} = U/b\mathbf{Rx} + \mathbf{E}_i\dot{\mathbf{h}}$$

- As number of segments is increased the coefficients will approach a continuous change:

$$\mathbf{f} = 1/U \left(\mathbf{C}_0(M)\mathbf{h} + \mathbf{C}_1(M)(b/U)\dot{\mathbf{h}} + \mathbf{Dx} \right)$$

$$\dot{\mathbf{x}} = (U/b)\mathbf{Rx} + \mathbf{E}(M)\dot{\mathbf{h}}$$

PROBLEM FORMULATION AND SOLUTION

- Constant inflow is assumed.

- Each station on the blade span where aerodynamic loads are evaluated contributes a number of aerodynamic state equations.

- The combined structural and aerodynamic equations form a coupled system of nonlinear ordinary differential equations.

- Time domain response solution is obtained using direct numerical integration using the ODE solver DE/STEP.

- The coupled trim/response solution is obtained using a simple autopilot type controller using a performance index which is a quadratic function of the trim equation residuals.

VIBRATION REDUCTION USING ACTIVE CONTROL

- Control strategy is based on the minimization of a performance index that is a quadratic function of the 4/rev vibration magnitudes $\mathbf{z}$ at the $i - th$ time step:

$$J = \mathbf{z}_i^T \mathbf{W}_\mathbf{z} \mathbf{z}_i$$

- Flap deflection consists of a sum of 2, 3, 4, and 5/rev harmonics

- An optimal discrete time controller is used based on a linear, quasistatic, frequency domain representation of the vibratory response to control.

- $\mathbf{W}_\mathbf{z}$ is assumed to be an identity matrix.

RFA Aerodynamic Model Parameters

Number of lag terms:	5 Lag Terms
Reduced Freq. Range:	0.0-1.5,2.0,3.5
# of Blade Stations:	9 (2 Flap)
Total Aerodynamic States:	100

Soft-In-Plane Elastic Blade Configuration

Rotor Data

$N_b = 4$	$L_b = 1.0$
$c_b = 0.05498$	$\theta_{pt} = 0$
$\omega_F = 1.123, 3.41, 7.62$	$C_{do} = 0.01$
$\omega_L = 0.732, 4.46$	
$\omega_{T1} = 3.17$	
$\gamma = 5.5$	$\sigma = 0.07$

Helicopter Data

$C_W = 0.00515$	$fC_{df} = 0.01 A_R$
$X_{FA} = 0.0$	$Z_{FA} = 0.3$
$X_{FC} = 0.0$	$Z_{FC} = 0.3$

Change in 4/Rev Hub Loads with Number of Lag Terms
1 deg, 5/rev Flap Deflection
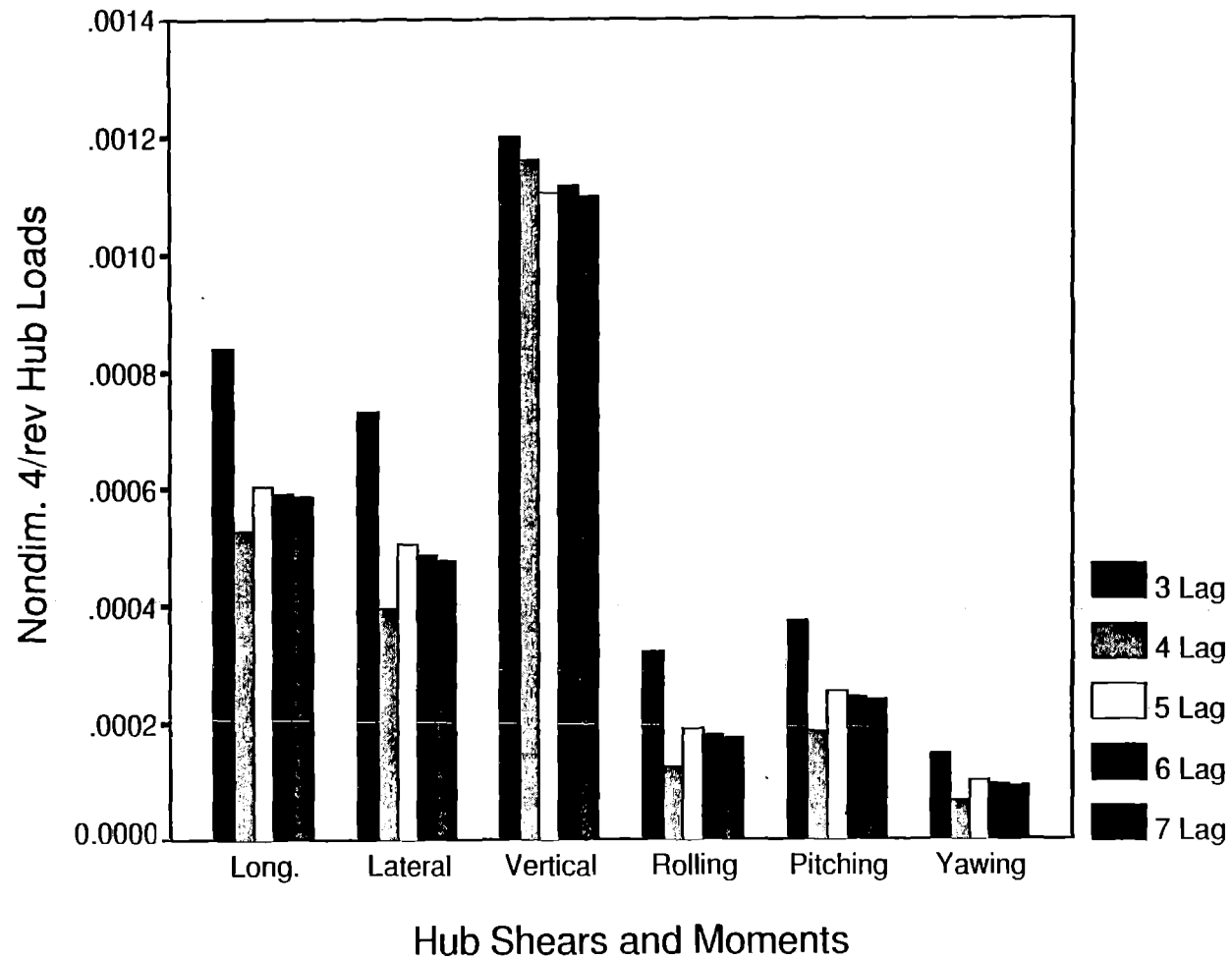
Simultaneous Reduction of 4/Rev Hub Loads Using the ACF, $\mu = 0.3$, $\omega_{T1} = 3.14/rev$
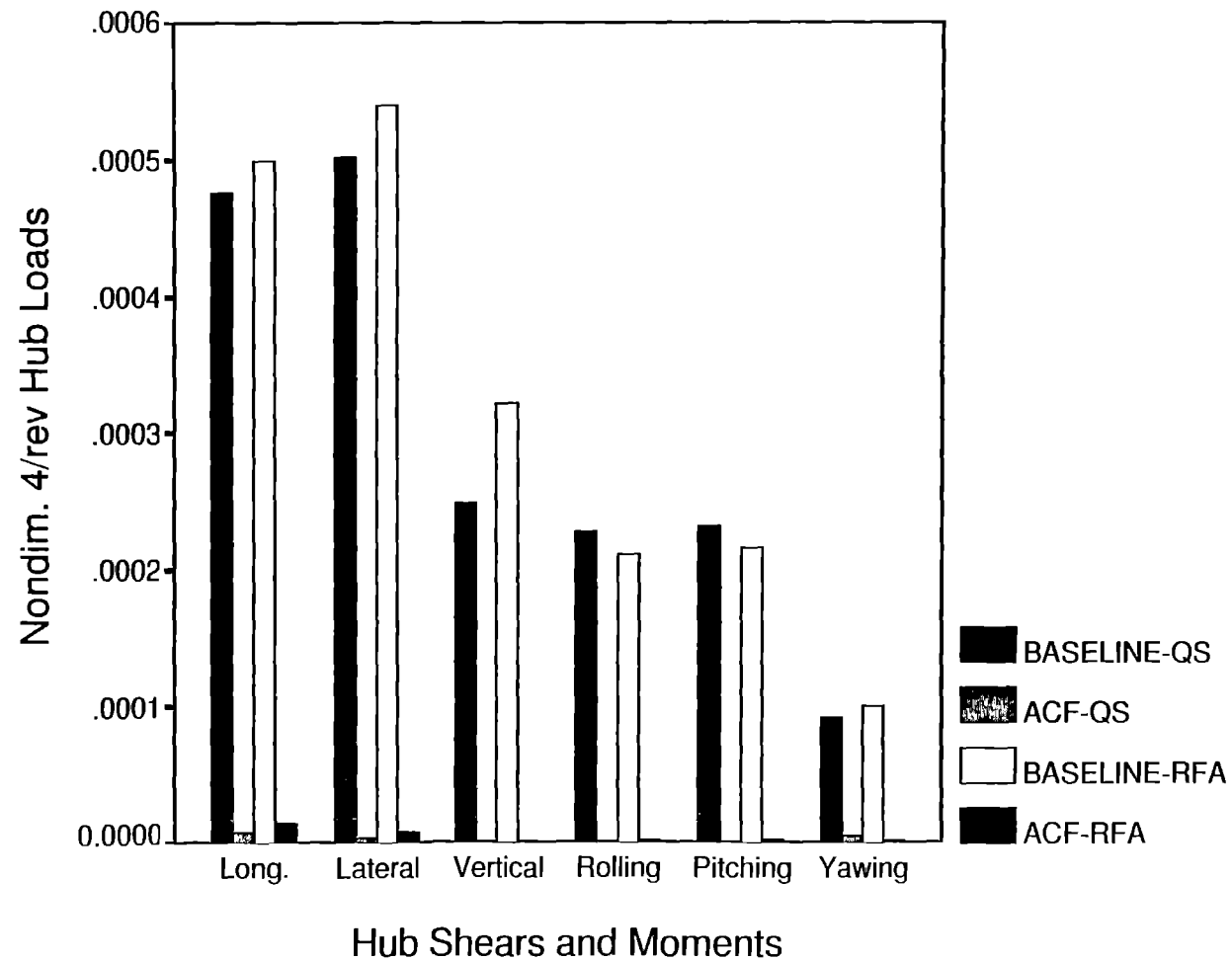
Flap Deflection over One Revolution, $\mu = 0.3$, $\omega_{T1} = 3.14/rev$
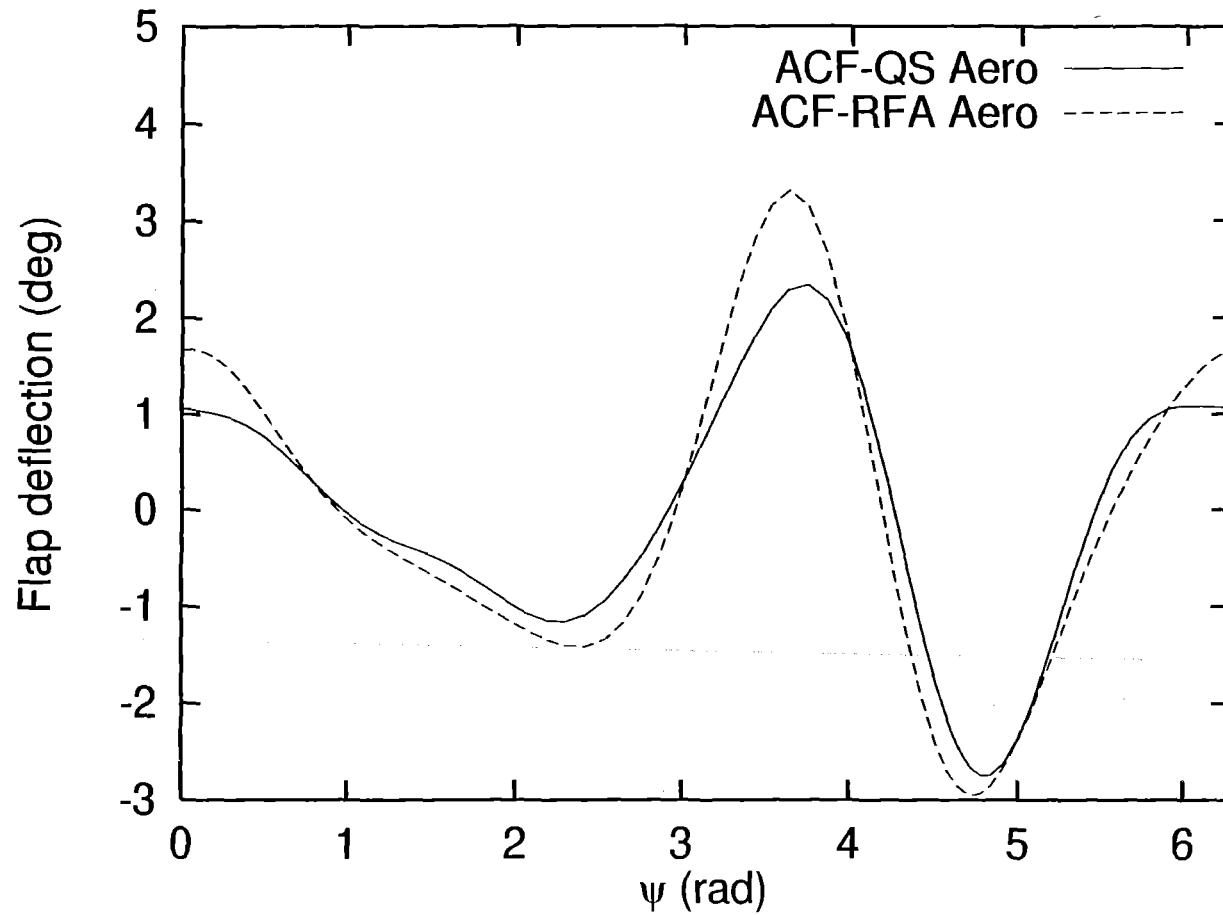
Maximum Flap Deflection, $\mu = 0.3$
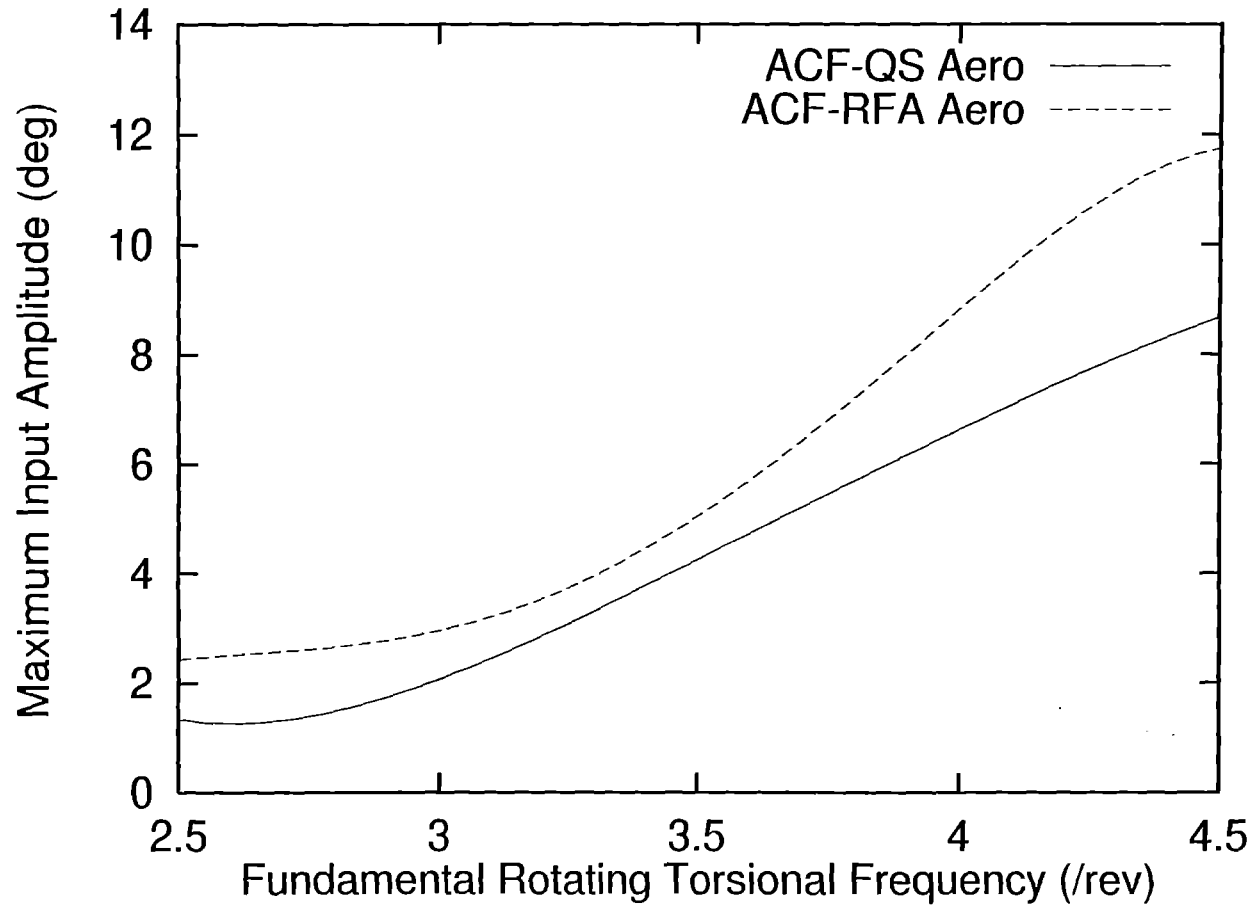
Average Control Power, $\mu = 0.3$
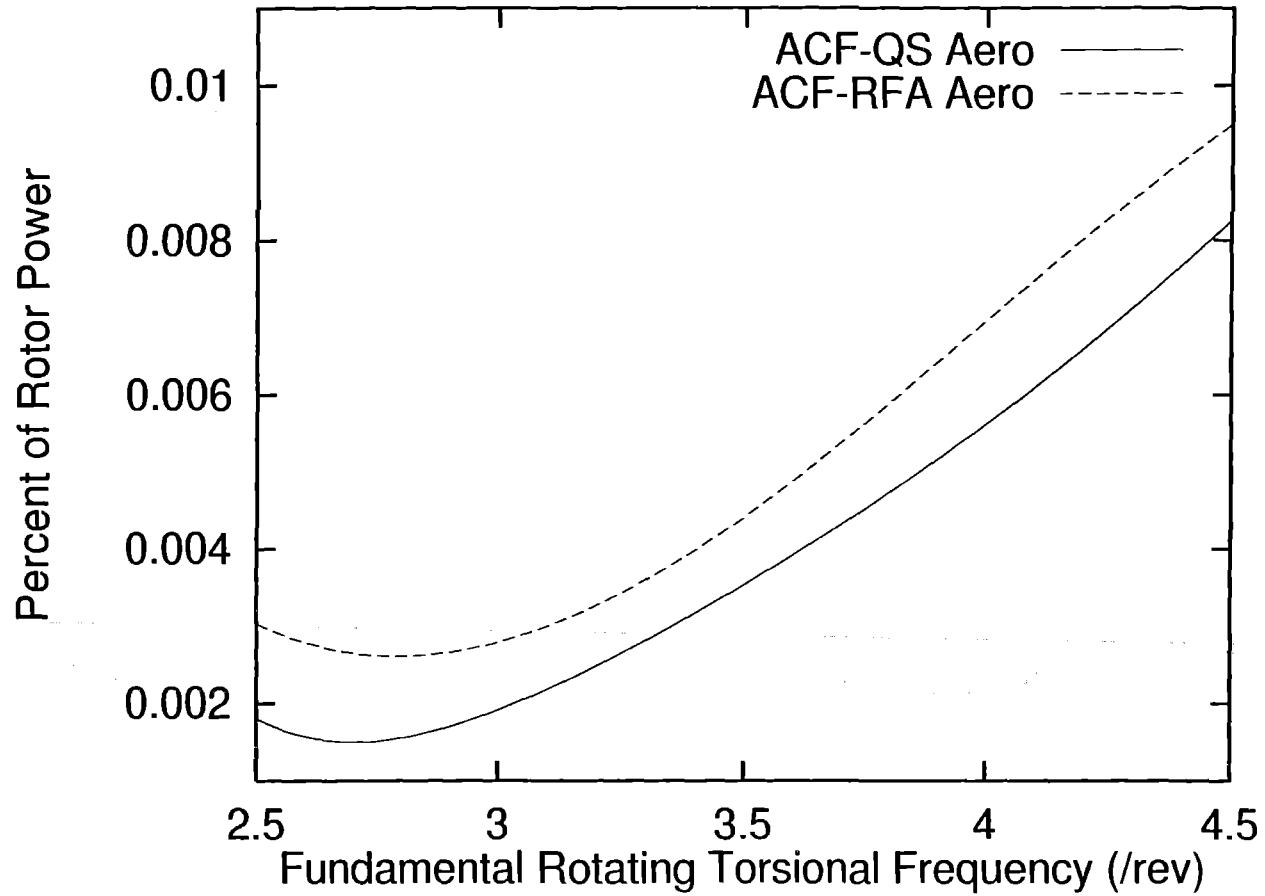
Control Power Requirements Over One Revolution for a Single Flap, $\mu = 0.3$, $\omega_{T1} = 3.14/rev$
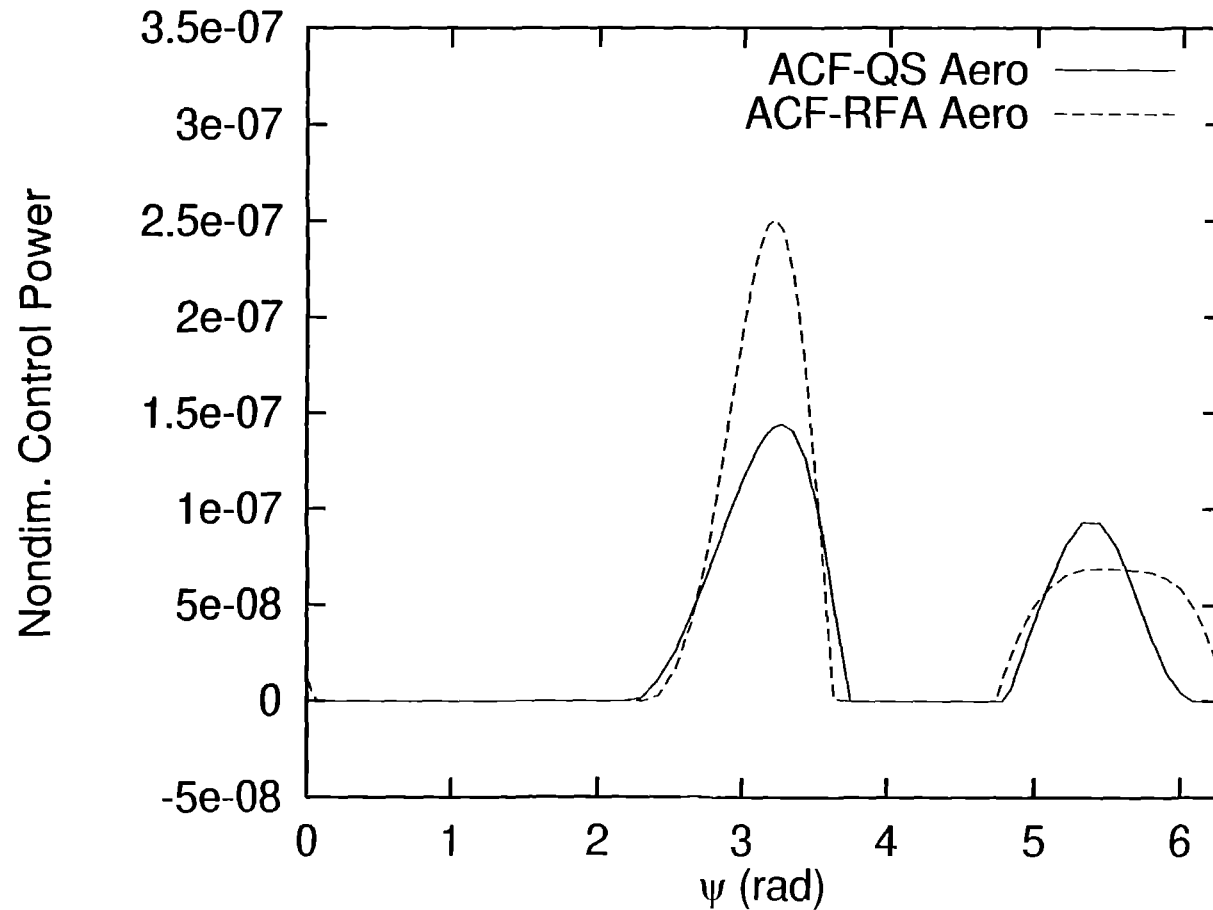
Change in Rotor Power With Actively Controlled Flap, $\mu = 0.3$
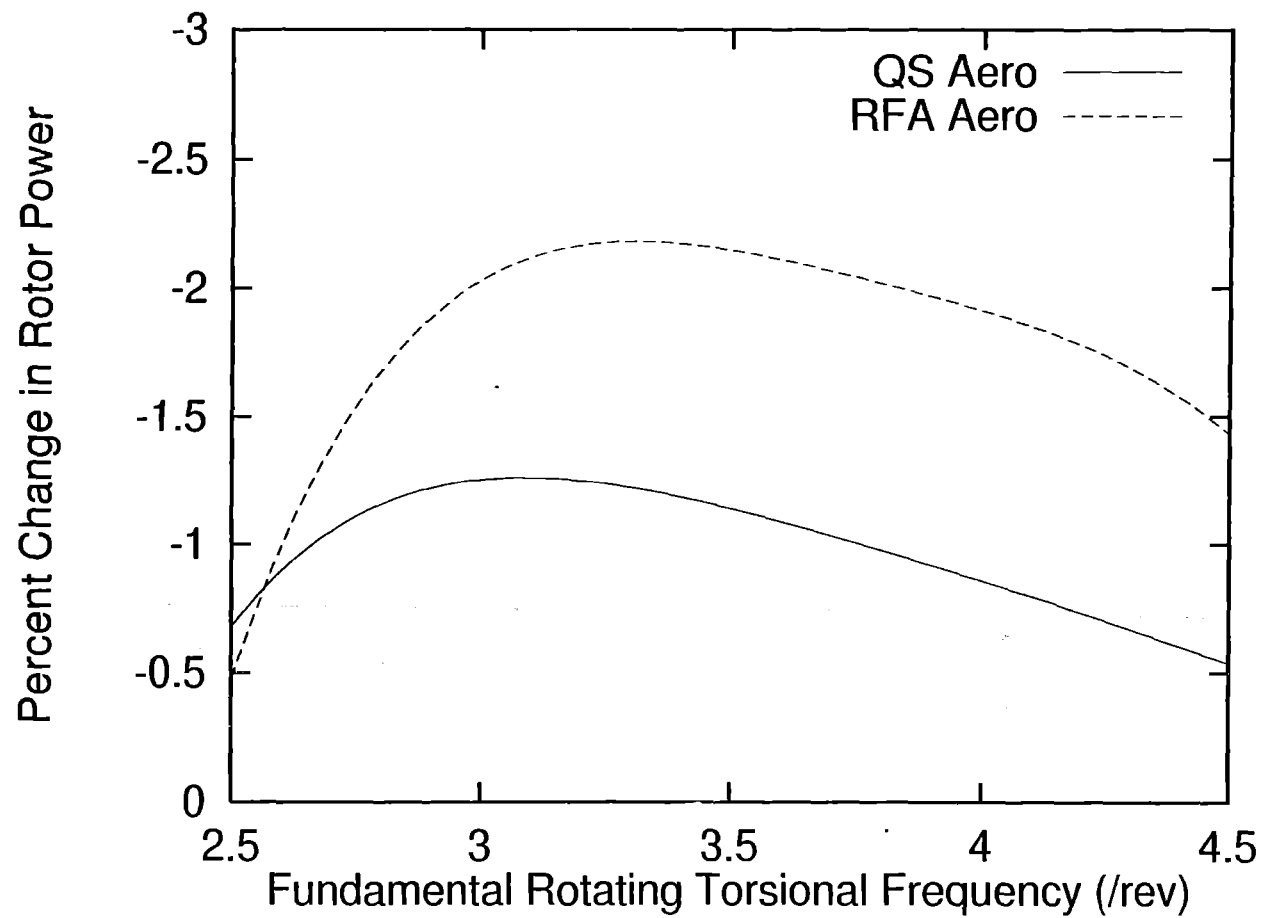
CONCLUDING REMARKS

- With a suitable source of oscillatory response data, the RFA approach can be used to develop a compressible unsteady aerodynamic model for an airfoil/flap combination that is suitable for rotary wing applications.

- Control studies confirm the effectiveness of the actively controlled trailing edge flap at reducing 4/rev vibratory loads.

- The addition of unsteady aerodynamics and compressibility effects is necessary to properly characterize the operational requirements of the actively controlled trailing edge flap.

HHC AND IBC FOR A SERVO-FLAP CONTROLLED MAIN ROTOR

Fu-Shang Wei
Chris A. Tomashofski
Kaman Aerospace Corporation
Bloomfield Connecticut 06002

ABSTRACT

A servo-flap rotor control system using Higher Harmonic Control (HHC) and Individual Blade Control (IBC) to significantly reduce helicopter vibration and improve blade performance has been investigated. This is achieved by maintaining the control modules in the fixed system and transferring the control actuators to the rotating system. The Kaman SH-2G helicopter and the second generation composite main rotor blade (CMRBII) are used as the baseline in the design. The servo-flap rotor system has the inherent advantages of low control loads, low blade induced vibration, low control system weight, and high control sensitivity. Three different design approaches have been considered. In order to further lower main rotor control power and heat rejection requirements and to enhance flight safety by providing a fail-safe installation, the collective and 1/rev cyclic inputs needed for normal servo-flap flight remain unaltered from their conventional mechanical paths. The HHC system needs only to introduce the HHC or IBC signal into the main rotor blade control which is introduced in parallel with the basic control system. From the design study, the servo-flap method of control is ideally suited to both HHC and IBC for an advanced helicopter main rotor control system in the future.

INTRODUCTION

It has been a long-standing goal of the rotorcraft community to develop a practical system for main rotor Higher Harmonic Control (HHC) and Individual Blade Control (IBC) in order to benefit from its potential for significant vibration reduction and performance improvement[1-14]. Numerous research efforts have been conducted over the years with mixed results, partly due to the large control force and power requirements inherent in conventional pitch horn control systems[7-14]. This realization has recently led to increased attention to the servo-flap method of main rotor control[15-19]. As the only manufacturer with 50 years experience in fielding successful production servo-flap controlled helicopters [20-25], Kaman is uniquely positioned to make a significant

contribution to the HHC/IBC effort.

a) Review Of Existing HHC Systems:

During the early 1980's, McDonnell Douglas Helicopter Company (MDHC) investigated HHC through wind tunnel and flight tests[7-8]. The flight tests were conducted on an OH-6A helicopter and evaluated for both open loop and closed loop higher harmonic controllers. Vibration reductions were demonstrated for airspeeds up to 100 knots and for limited maneuvers. The algorithms implemented for the OH-6A HHC flight test were designed specifically to minimize vibrations under steady flight or for slowly varying flight conditions.

During the mid 1980's at Sikorsky, the analysis for the S-76 helicopter indicated that HHC inputs of $\pm 2°$ would be sufficient to reduce vibration at 145 knots. The open loop HHC system tested gave maximum higher harmonic blade pitch amplitudes approximately $\pm 1°$. Due to hydraulic flow capability, the ratio of design value to flight test value was 2:1, representing only 50% effectiveness. More hydraulic power with its attendant weight penalty would be required to achieve the analytically desired pitch excursions. Also, flight test showed that the vibratory control loads were increased with HHC inputs[9-10].

During the early 1980's, closed loop HHC was demonstrated on a three-bladed CH-47D model rotor in the Boeing Helicopter V/STOL wind tunnel[12-13]. Vertical and inplane 3/rev hub forces were reduced simultaneously for airspeeds up to 188 knots. The reduction was accomplished with a fixed-gain feedback control law which was simpler and faster than the adaptive control laws previously investigated. The controller applied oscillatory swashplate motion which produced blade pitch up to $\pm 3.0°$ at high speed.

In 1986, a research program was conducted by Aerospatiale Helicopter division to flight test an SA 349 Gazelle helicopter · using active control to reduce vibration via HHC[11]. Three control algorithms were developed and tested. Vibration reduction using a closed-loop self-adaptive HHC system demonstrated 80% reduction in the cabin at an airspeed of 134 knots.

1

At Kaman, full scale wind tunnel testing was conducted on the Multi-cyclic Controllable Twist Rotor (MCTR)[1-4]. The MCTR is a hybrid system which consists of a torsionally flexible blade that is controlled directly by a conventional pitch horn at the blade root and a servo-flap located at approximately 75% radius. The pitch horn is the primary control introducing collective and 1/rev cyclic for trim. The servo-flap introduces torsional moments with collective, 1/rev, and multi-cyclic inputs that elastically twist the blade about the trim position for vibration reduction, blade tracking, blade stall alleviation, and optimum aerodynamic performance. Wind tunnel test results showed flatwise bending moment reduction of 22% to 30% with concurrent 83% reductions in control loads of the MCTR at several forward flight conditions and at advance ratios of 0.22 and 0.33. Also, flatwise bending reductions of about 50% with lesser control load reductions of 30% to 60% were achieved with different control schedules. However, no flight tests of the MCTR or servo-flap type of main rotors were ever conducted on a production helicopter using HHC.

b) Deficiencies Of Existing HHC Systems:

Previous flight testing of HHC concepts has shown some success in reducing blade vibration. However, several problems come to light which will not be easily resolved based on the results of past flight testing. Significant research is needed in these areas to produce better HHC and IBC systems.

1. **HHC Sensitivity:** HHC control input requirements have tended to be much greater than analytically predicted, because the effectiveness of the designed value used for pitch horn rotor HHC flight testing can only generate approximately 50% of the required HHC control input.
2. **Power Required:** Power required to achieve the HHC inputs tend to be much greater than anticipated, because the majority of the power required to achieve the HHC inputs are consumed in the shaking the swashplate in the fixed system.
3. **Algorithm Requirements:** The control algorithms were only successful in steady state and slow transient flight conditions. Most of the HHC flight testing was concentrated in reducing rotor induced vibration in steady state flight conditions. Very little consideration was given to or very little success was achieved in most transient and maneuver flight conditions.

For example, the OH-6A HHC flight test program has shown insufficient vibration reduction in acceleration/deceleration between 0 and 40 knots, very high speed maneuvers, and turbulent wind conditions. The lack of success in these conditions can be attributed primarily to two factors: i) The quasi-steady algorithm cannot keep up with the varying vibration level; ii) The underlying vibration phenomena is a dynamic process not amenable to quasi-steady solution.

For the S-76 helicopter flight test, the aircraft vibration reduction would likely have been achieved if the HHC system had provided the required control inputs. The open loop HHC system gave maximum higher harmonic blade pitch amplitudes only ± 1°. A more powerful and larger HHC system would be needed to achieve the vibration reduction goal at most critical flight conditions. The added weight penalty to increase the hydraulic effectiveness was estimated to be at least double the originally designed value which may become impractical for the design.

For the SA 349 Gazelle helicopter HHC flight tests, significant vibration reduction was successful for steady state flight conditions even including high load factor bank turns where the basic vibration level is typically high for this type of helicopter. However, test results indicated that the HHC system has very poor vibration reduction through transition flight. These poor test results may be due to the interaction of the rotor wake on the airframe encountered at low forward airspeed. The mechanism of the generation of vibrations in these flight cases is very different from the other flight conditions. More research efforts are needed in these areas.

c) Why HHC On An Advanced Servo-Flap Rotor?

There are many reasons for choosing a servo-flap controlled rotor over a pitch horn controlled rotor for HHC and IBC applications. These reasons are the inherent advantages of low control loads, low blade induced vibration, light control system weight, and high blade control sensitivity.

Control power requirements for a servo-flap controlled main rotor system are much lower than those of swashplate shaking. There is a significant weight difference between servo-flap and main rotor blades. A typical servo-flap weighs about 6 lbs, while a typical main rotor blade weighs about 200 lbs, therefore, a significant control power difference exists in moving a servo-flap versus moving a pitch horn main rotor under steady, 1/rev cyclic and higher harmonic motion. For a typical pitch horn controlled rotor, shaking a rigid control system requires approximately 120 HP per inch of motion[10]. This implies that much of the horsepower

required is due to shaking the fixed control system. For a servo-flap controlled rotor, even including collective and 1/rev cyclic control power, less than 2.5 HP per blade are required to achieve the same amount of HHC motion[15]. Therefore, for a servo-flap rotor control system, less control force and heat-rejection management are required within the electrical and hydraulic control systems.

Normally, a servo-flap main rotor control system uses very light weight mechanical collective and 1/rev servo-flap control to fly the helicopter which does not rely on hydraulic boost for flight safety. The aircraft can continue to fly and maneuver manually with relatively low pilot workload even in the event of total hydraulic boost failure and Automatic Stabilization Equipment (ASE) failure. This is an extremely robust, reliable, and naturally stable system proven by 50 years service in military and commercial helicopters. This type of control has very light control system weight and actuation loads.

Also, for a servo-flap controlled main rotor, control inputs are not limited to mutually correlated harmonic functions but can include any type of waveform and true IBC. For a pitch horn controlled rotor, all HHC introduced in the fixed system must be achieved by shaking the swashplate collectively and cyclically at the appropriate (n-1), n, and (n+1)/rev frequency, limiting such inputs to mutually correlated harmonic functions.

The servo-flap main rotor design has the servo-flap located at 75% radius of the main rotor blade. From the blade aerodynamic point of view, due to the high rotational speed about the rotor shaft, the local airspeed and dynamic pressure at the servo-flap surface are very high. The sensitivity of a servo-flap rotor per degree of HHC input is much greater than that of a pitch horn rotor. Therefore, it is much easier to design a low vibration blade by tailoring main rotor aerodynamic airload distribution and reducing servo-flap-introduced aerodynamic excitation. Also, the required change in blade pitch amplitude can be achieved with less actuator deflection.

From the rotor control system design point of view, it is relatively easy to place actuators in the rotating system such that blade camber can be modified with 2/rev or other servo-flap inputs. This achieves performance improvements by producing variation in blade angle of attack and airload distribution resulting in stall alleviation and thrust improvement. The servo-flap method of control is ideally suited to both HHC and IBC for advanced helicopter main rotor control systems.

BASELINE ROTOR

The Kaman SH-2G helicopter (Fig. 1) and CMRBII (Figs. 2-4) servo-flap controlled main rotor system are selected as the baseline design aircraft. The CMRBII rotor system, in addition to the inherent advantages mentioned above, has better blade aerodynamic performance and fatigue life than the original production metal blades. It is also representative of current composite blade manufacturing technology used throughout the helicopter industry. Especially important is that this type of control system has been proven in 50 years of production experience and well over 2 million customer flight hours and it does not rely on hydraulic boost or automatic stabilization for flight safety.

The SH-2G helicopter has a 4-bladed main rotor system. The main rotor nominal speed is 298 rpm and the maximum take-off gross weight is 13,500 lbs. The flat plate drag area of the SH-2G configured for the anti-submarine warfare (ASW) mission, including all sensor and weapon systems, is 32 square feet. The rotor shaft has built-in 6° forward tilt and 4° lateral tilt. The maximum forward speed is 141 knots. The blade has a 266 inch radius and a 23 inch chord. The blade planform is rectangular and consists of a modified 230-series airfoil transitioning linearly in thickness along the blade span.

Both blade flapping and lead-lag hinge offsets are coincident at station 8.25 inch. The inboard and outboard stations of the pitch barrel are located at stations 17.5 and 42, respectively. The blade lead-lag hinge gives a soft inplane frequency of 0.2/rev which uses a lead-lag damper to increase blade inplane stability. The CMRBII blade produces a pitch-flap coupling ($\delta_3 = 23°$) that is introduced by the combined effects of servo-flap/feathering and servo-flap/flapping coupling during operation. The inboard servo-flap station is 180.8 and the outboard flap station is 217.2. The servo-flap is an NACA 63_3018 airfoil with an 8 inch chord and 36 inch length. It is made from graphite/epoxy fabric and is designed as a three-cell box beam.

The total pilot collective stick travel is 11.5 inches which is equivalent to 16° servo-flap angular motion. The total cyclic stick travels for 1/rev longitudinal and lateral are 14 inches and 11.2 inches, respectively, which are equivalent to 24° and 10.6° servo-flap angular motion.

TECHNICAL APPROACH

The technical approach for the HHC system is that the HHC system does not completely replace this highly

effective production design which already provides one of the lowest vibration rotors in the industry today. Rather, the HHC/IBC signal is introduced in parallel with the basic control system. The HHC hardware is designed to fit in conjunction with the present control system. There is only a minimum of modification required to accommodate the HHC system.

The actuators are mounted in the rotating system, closer to the actuated mass than is possible with swashplate shaking. This approach greatly reduces the adverse effects of lost motion due to control system spring rates. The HHC system design has features built in to handle electrical, hydraulic, or mechanical failure separately. The actuators have a centering and locking mechanism which can bring the HHC actuators to the rig neutral position and locks in case of electrical or hydraulic failure. The mechanism also operates simultaneously for all four actuators in the case of single or multiple failures. The servo-flap HHC system is fail-safe for any single electrical or hydraulic failure and has no degradation of the present flight safety of the helicopter.

In order to avoid the adverse effects within the entire flight test envelope, the maximum servo-flap deflection used in the HHC/IBC design are limited as follows: i) $\pm$ 1° collective control input for IBC, ii) $\pm$ 2° 2/rev cyclic control input for IBC, and iii) $\pm$ 2° 3/rev, 4/rev and 5/rev cyclic control inputs for both IBC and HHC.

Servo-flap blade index angle is an important design factor which affects blade performance, helicopter vibration (Fig. 5), and blade bending moment (Fig. 6). Kaman's flight test experience has shown that increasing index angle produces increased rotor vibration. Therefore, servo-flap blade index angle will be used to simulate the blade vibration level during the HHC flight test without any degradation of safety.

The HHC system is installed completely independent of the ASE. With the HHC system either engaged or disengaged, there is no feedback to the ASE and, therefore, will not degrade the aircraft handling qualities with or without the ASE.

The control algorithm is an adaptive system which works like a higher harmonic analogy to the existing Kaman blade tracking system (Fig. 7). The blade tracking system, which has been in production on all Kaman helicopters since the 1950's, is a true quasi-steady IBC. This proven system works by sensing 1/rev vibrations in the fixed system and coupling that measurement with phasing information from the main gearbox resolver to determine which blade is flying out-of-track. A small tracking motor in the rotating system is then commanded to provide an automatic null offset to the servo-flap of the errant blade to bring the 1/rev vibration back to zero. The offset is applied to the control rods actively, in-flight, in parallel to the normal trim and maneuver control system.

In a similar fashion, the proposed HHC/IBC system can sense high frequency tube load magnitude and phasing in the main gearbox mounting tubes and can also share the resolver phasing signal with the blade tracker. Using a system similar to HALMARS, a holometric load monitoring system developed by Kaman[26], this fixed system information can be used to determine vibratory bending moments in the rotating system and select the appropriate IBC waveform to send to each blade. The calculation/refresh rate required is estimated to be about 20 milliseconds.

Existing test data of the SH-2G helicopter including blade bending moments and transmission tube loads were analyzed to determine vibration as a function of such independent variables as speed, control position, and attitude. Rate changes in control position, speed and fuselage attitude were utilized to determine vibration in maneuvers. Excellent comparison between the HALMARS synthesized data and directly slip-ring transduced transient flatwise bending moment has been achieved using maneuver flight[26] conditions. This correlation confirms that HALMARS can be used for HHC in maneuver flight test.

The arrangement of placing actuators in the rotating system can modify blade airloads to achieve performance improvements by varying blade 2/rev angle of attack with IBC control inputs. The 2/rev blade angle of attack change generates more rotor thrust in the fore and aft direction of the aircraft to result in stall alleviation and performance improvement.

HHC DESCRIPTION

Some of the major areas Kaman has been investigating in the HHC design are the hydraulic power requirements at high speed to implement HHC inputs, the sensitivity required to minimize vibration with proper HHC inputs, the algorithms required to achieve active control at all flight conditions, and the impact on helicopter performance. Kaman has been considering several different design approaches. These include:

1. Electromechanical actuators placed in the rotating system;

4

2. Hydraulic actuators placed in the rotating system with hydraulic power supply in the fixed system and utilizing a liquid slip ring;
3. Hydraulic actuators placed in the rotating system with hydraulic power supply in the rotating system, requiring no liquid slip ring or power slip rings (only signal slip rings are required).

Common to each of these designs is the method of introducing the HHC/IBC signal into the blade control linkage. Kaman helicopters already incorporate the necessary mechanical pathway for introducing Individual Blade Control (IBC) signals into the linkage in parallel with the normal trim and maneuver control system without jeopardizing the safety or robustness of the basic flight critical controls.

The HHC/IBC input path works similarly to the Kaman automatic, in-flight blade tracking system but is at a different location on the blade to take advantage of the shortest possible path to the servo-flap. This minimizes lost motion due to linkage spring rate and maximizes isolation of the fixed system controls from the vibratory input.

The inboard end of the long, spanwise rod terminates at the midpoint of a chordwise idler crank which is rigged as a class 2 lever. The trailing edge end of the idler is fixed to an A-frame brace on the blade root structure (Fig. 8), while the leading edge end serves as the input point for the collective, 1/rev cyclic, and quasi-steady blade tracking IBC motions. In the proposed HHC/IBC design, the A-frame brace is modified so that it supports the fixed end of an actuator (either electromechanical or hydraulic) rather than the fixed fulcrum of the idler. The idler fulcrum is instead driven by the actuator according to any command signal received from the fixed system flight computer (Fig. 9).

No modification is required to the blade root, to other control rod linkages, or to the existing primary flight controls. Thus the system is fail-safe (i.e., if the HHC actuator fails, the idler simply reverts to fixed fulcrum behavior), and it is robust (i.e., it retains the fleet-proven design for primary controls--no new unproven hardware is introduced into the flight critical path).

The benefits of using this entry point are several, but all focus upon one overriding goal which impacts all HHC systems: reduction of control power requirements. The benefits can be summarized as follows:

1. The fulcrum of the idler crank is in a location which is very sensitive to small displacements. For electromechanical actuators this reduces power draw by reducing the acceleration required to meet peak-to-peak displacements. For hydraulic actuators, fluid flow rate is the more critical parameter and is also commensurately reduced.
2. This position is kinematically closer to the driven mass (servo-flap), thus less motion is absorbed in linkage flexibility.
3. Use of this point relieves the HHC actuator from the need to supply all the control power. Collective and 1/rev cyclic primary control is still supplied by the mechanical system. It is estimated that the HHC portion of the control will consume only about 0.23 HP per blade , which is about 9% of the total control power required (the majority goes to 1/rev cyclic with the remainder going to collective).

Referring again to Figure 9, the kinematics of the idler are such that the radial component of the force supplied by the HHC actuator, R_{2x}, is

$$R_{2x} = \frac{R_1(b + a\tan\alpha)}{(b + y + a\tan\alpha)}$$

where R_1 is the force in the spanwise servo-flap rod and a, b, and α are geometric parameters defined in the figure. The HHC actuator must react, at zero deflection, the maximum stacked collective and 1/rev cyclic loads introduced by the mechanical primary controls. To supply HHC motion, it must support an additional HHC load due to increased pitching moment on the flap at the high end of the cycle and acceleration of the flap mass:

$$\ddot{\theta}(t) = -\theta_P\omega^2\sin\omega t$$

where θ_P is the peak HHC pitch angle of the servo-flap, limited here to ± 2°, and ω is the frequency of the higher harmonic cycle, limited here to 5/rev (156 radians/sec). The stacked primary plus HHC peak load equates to an actuator load of:

$$R_{2x,PEAK} = \frac{1.5\left[\begin{matrix}Stacked \\ Primary\end{matrix} + \begin{matrix}Peak \\ HHC\end{matrix}\right](b + a\tan\alpha)}{(b + y + a\tan\alpha)}$$

where a contingency factor of 1.5 is included to assure adequate capability. For the case of hydraulic actuators, the required piston area is :

5

$$A = \frac{R_{2x,PEAK}}{P}$$

where P is the system pressure. Figure 10 shows the required piston area for various system pressures as a function of y. The most reasonable values for y (minimum impact on design modifications) are shown boxed in between 3.5 and 6 inches. For a 2000 psi hydraulic system and y in the boxed region, required piston area is seen to be only slightly greater than one-quarter square inch. Clearly, piston area and thus actuator diameter would not be a limiting factor in creating a feasible design. Similarly, the flow rate requirements are:

$$Q = \frac{Volume\ Displaced}{\left(\tfrac{1}{2}\ 5P\ Cycle\right)}$$

$$Q = \frac{A\delta_{R2x}}{0.02013\ sec} \times \frac{60\ gallons \cdot seconds}{231\ inches^3 \cdot minute}$$

where Q is in gallons per minute and δ_{R2x} is the deflection of force R_{2x}. Figure 11 shows the required flow rate for various system pressures as a function of y. For a 2000 psi system and y in the boxed region, flow rate is approximately 0.8 gallons/minute per blade or 3.2 gallons/minute total. Flow rate, therefore, will not be a limiting factor for this design.

For the electromechanical design, shown in Fig. 12, a miniature electric motor and ball screw assembly is mounted directly on the A-frame and receives the command signal from the fuselage based flight computer via signal slip rings in the rotorhead. Motive power must be supplied through power slip rings, also in the rotorhead.

For both of the hydraulic designs, a miniature hydraulic cylinder and servo-valve assembly are mounted on the A-frame in place of the electric motor. The command signal, in each case, is received by the servo-valve from the flight computer in the same way as for the electromechanical design. The difference lies in the source of motive power.

For the split hydraulic design, shown in Fig. 13, the hydraulic power supply resides in the fuselage in a conventional manner. The high pressure working fluid is pumped up to the rotating system through a rotary union (hydraulic slip ring) assembly located in the rotorhead. From there it is distributed to the individual cylinders. Placing the servo-valves directly on the actuators and pumping a single channel of pressurized fluid through the rotary union is preferrable to servo-valving the flow in the fixed system and pumping four individual channels of metered, reversing fluid across the union because head loss effects in the complex fluid column will tend to wash out the command signal and because a single channel, uniform pressure rotary union will be much less costly and less maintenance intensive.

For the self-contained hydraulic design, the hydraulic power supply is mounted directly on top of the control can at the center of the main rotor hub. Mechanical rotary power is obtained by keying the hydraulic pump to a long drive rod which reaches down the hollow hub centerline to anchor in the fixed system. Appropriate pump speed can be attained either by integral gearing or by spinning the fixed system end of the drive rod in the opposite direction by a roof-mounted electric motor. The internal gearing approach permits all HHC power to be drawn directly from the main gas turbines via mechanical shafting without impact on the aircraft electrical system. The counter-spinning motor option reduces the cost, weight, and drag area of the topside pump, but adds electrical load to the aircraft and some additional weight penalty. High pressure working fluid is then pumped directly to the individual actuator servo-valves without the need to cross a rotary union. The basic benefits and penalties of each design are also investigated.

The estimated total weight of the HHC system, including actuators, sensors, and electronics is approximately 35 lbs. Most of the weight increase represents new equipment as there is relatively little modification to the existing servo-flap control system. The weight penalty is less than 0.3% of the aircraft maximum gross weight. Also, the HHC system components are designed for convenience of access during servicing and the effects of the additional vibratory load on the fatigue life of all associated components are minimized by the design.

CONCLUSIONS

1. A conceptual design of servo-flap rotor control system using HHC and IBC directly in the rotating system to reduce aircraft vibration and improve blade performance has been presented. This is achieved by maintaining the control modules in the fixed system and transferring the control actuators to the rotating system.
2. The original mechanical collective and 1/rev cyclic control for the servo-flap remain unchanged. The

HHC system needs only to introduce the HHC or IBC signal into the main rotor blade control in parallel with the basic control system.

3. Servo-flap blade index angle can be used to simulate the blade vibration level during the test.

4. Control power requirements for a servo-flap control system are much lower than those of swashplate shaking. Less heat-rejection management is required within the electrical and hydraulic control systems.

5. Control inputs for servo-flap rotors are not limited to mutually correlated harmonic functions but can include any type of waveform and true IBC.

6. The sensitivity of a servo-flap rotor per degree of HHC input is much greater than that of a pitch horn rotor. The required change in blade pitch amplitude can be achieved with less actuator deflection.

7. It is relatively easy to place servo-flap actuators in the rotating system such that blade camber can be modified with 2/rev or higher servo-flap inputs to achieve performance improvements by producing variation in blade angle of attack and airload distribution resulting in stall alleviation and thrust improvement.

8. The HHC portion of the signal consumes only about 9% of the total control power required.

9. The weight of the HHC system, including actuators, sensors, and electronics is estimated to be approximately 35 lbs. The weight penalty is less than 0.3% of the aircraft maximum gross weight.

10. HALMARS can use fixed system vibratory tube loads information to determine vibratory bending moments in the rotating system and select the appropriate HHC or IBC waveform to send to each blade. The calculation/refresh rate required is estimated to be about 20 milliseconds.

11. The servo-flap method of control is ideally suited to both HHC and IBC for advanced helicopter main rotor control systems.

REFERENCES

1. Wei, F.S., and Weisbrich, A.L., "Multicyclic Controllable Twist Rotor Data Analysis," NASA CR-152251, January 1979.

2. McCloud, J.L., III, "An Analytical Study of a Multicyclic Controllable Twist Rotor," Proceedings of the 31st AHS Annual Forum, Washington, D.C., May 1975.

3. Lemnios, A.Z., and Howes, H.E., "Wind Tunnel Investigation of the Controllable Twist Rotor Performance and Dynamic Behavior," USAAMRDL TR-77-20, June 1977.

4. Wei, F.S., Basile, J.P., and Jones, R., "Vibration Reduction on Servo Flap Controlled Rotor Using

HHC," AHS National Specialists Meeting on Rotorcraft Dynamics, Arlington, Texas, November 1989.

5. Lemnios, A.Z., and Smith, A.F., "An Analytical Evaluation of the Controllable Twist Rotor Performance and Dynamic Behavior," USAAMRDL TR-72-16, May 1972.

6. Lemnios, A.Z., and Jones, R., "The Servo Flap - An Advanced Rotor Control System," American Helicopter Society Design Specialists' Meeting on Vertical Lift Aircraft Design, January 1990.

7. Gupta, B.P., Wood, E.R., Logan, A.H., and Cline, J.H., "Recent Higher Harmonic Control Development and OH-6A Flight Testing," Proceedings of the 41st AHS Annual Forum, Fort Worth, Texas, May 1985.

8. Wood, E.R., Powers, R.W., Cline, J.H., and Hammond, C.E., "On Developing and Flight Testing A Higher Harmonic Control Development System," Proceedings of the 39 th AHS Annual Forum, St. Louis, Missouri, May 1983.

9. Walsh, D.M., "Flight Tests of an Open Loop Higher Harmonic Control System on an S-76A Helicopter," Proceedings of the 42nd AHS Annual Forum, Washington, D.C., June 1986.

10. Miao, W., Kottapalli, S.B.R., and Frye, H.M., "Flight Demonstration of Higher Harmonic Control on S-76," Proceedings of the 42nd AHS Annual Forum, Washington, D.C., June 1986.

11. Polychroniadis, M., and Achache, M., "Higher Harmonic Control : Flight Tests of an Experimental System on SA 349 Research Gazelle," Proceedings of the 42nd AHS Annual Forum, Washington, D.C., June 1986.

12. Shaw, J., and Albion, N., "Active Control of the Helicopter Rotor for Vibration Reduction," Proceedings of the 36th AHS Annual Forum, Washington, D.C., May 1980.

13. Shaw, J., Albion, N., Hanker, E.J., and Teal, R.S., "Higher Harmonic Control: Wind Tunnel Demonstration of Fully Effective Vibratory Hub Force Suppression," Proceedings of the 41st AHS Annual Forum, Fort Worth, Texas, May 1985.

14. Hammond, C.E., "Wind Tunnel Results Showing Rotor Vibratory Loads Reduction Using Higher Harmonic Blade Pitch," AHS Journal Vol. 28, No. 1, January 1983.

15. Giansante, N., "Advanced Rotor Actuation Methods(ARAM)," USAATCOM TR 95-D-10, June 1996.

16. Staub, F.K., and Charles, R.D., "Preliminary Assessment of Advanced Rotor/Control System Concepts (ARCS)," USAAVSCOM-TR-90-D-3, August 1990.

17. Phillips, N.B., and Merkley, D.J., "BHTI's Technical Assessment of Advanced Rotor and Control Concepts," AHS Design Specialists' Meeting on Vertical Lift Aircraft Design, San Francisco, California, January 1990.

18. Giurgiutiu, V., Chaudhry, Z., and Rogers, C.A., "Engineering Feasibility of Induced Strain Actuators for Rotor Blade Active Vibration Control," Journal of Intelligent Material Systems and Structurals, Vol. 6, September 1995.

19. Millott, T.A., and Friedmann, P.P., "The Practical Implementation of an Actively Controlled Flap to Reduce Vibrations in Helicopters Rotors," AHS 49th Annual Forum, St. Louis, Missouri, May 1993.

20. Wei, F.S., "Developmental Flight Testing of the Second Generation Composite Blades (CMRBII)," American Helicopter Society 53rd Annual Forum, Virginia Beach, Virginia, May 1997.

21. Wei, F.S. and Jones, R., "Dynamic Tuning of the SH-2F Composite Main Rotor Blade," American Helicopter Society 43rd Annual Forum, St. Louis, Missouri, May 1987.

22. Wei, F.S., and Jones, R., "Optimal Design Application on the Advanced Aeroelastic Rotor Blade," 2nd Decennial Specialists Meeting on Rotorcraft Dynamics, Moffett Field, California, November 1984.

23. Wei, F.S., "Final Report for Rotorcraft Reconfigurable Flight Controls," Kaman Aerospace Report R-2112, October 1994.

24. Wei, F.S., "Active Trailing Edge Tab Control for Helicopter Rotor Vibration Reduction," AIAA Dynamics Specialists Conference, April 1996.

25. Wei, F.S. and Jones, R., "Correlation and Analysis for SH-2F 101 Rotor," AIAA Dynamics Specialists Conference, Monterey, California, April 1987.

26. Gustavson, B., "Final Report for Holometric Flight Load Determination," Kaman Aerospace Report No. R-1973, February 1991.
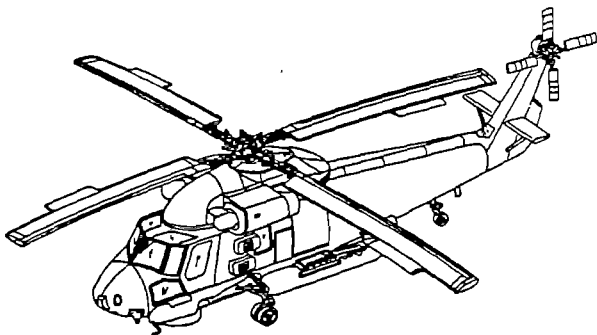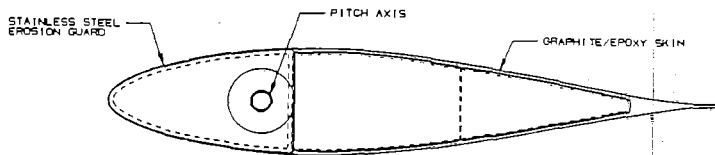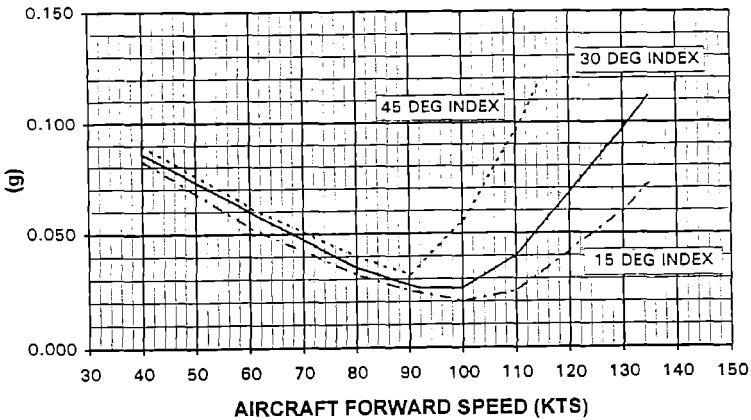
Fig. 1. SH-2G Helicopter Overview
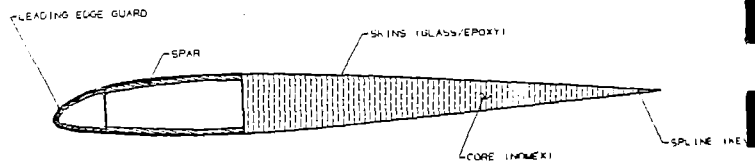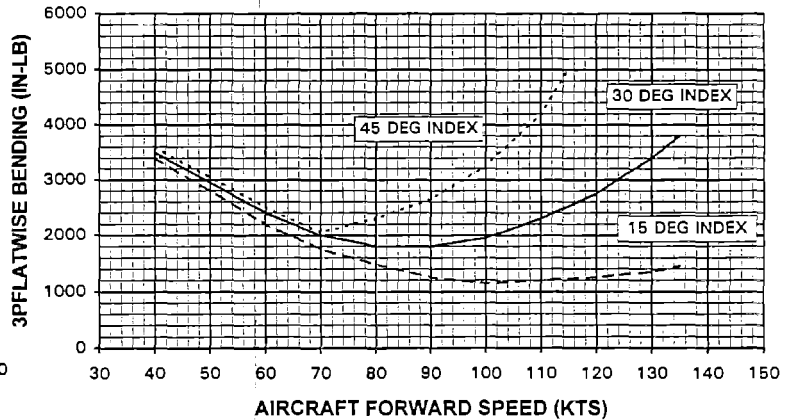

Fig. 3. CMRBII Blade Cross Section

Fig. 2. CMRBII Blade

8
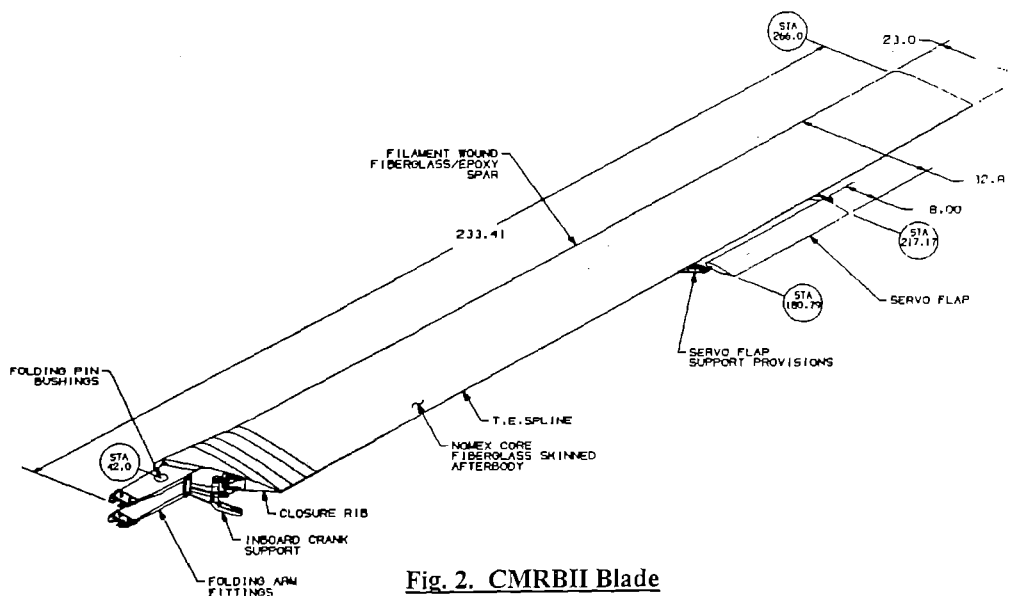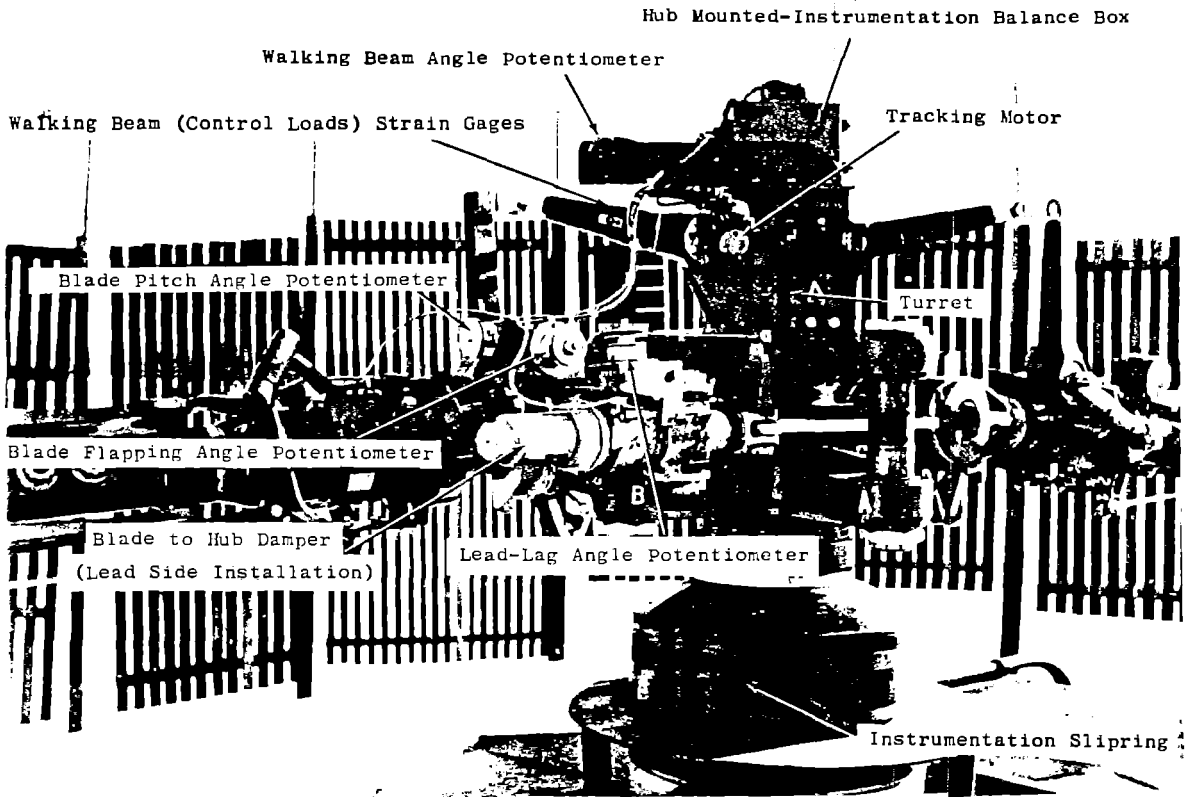
Fig. 4. CMRBII Composite Servo-Flap Cross Section
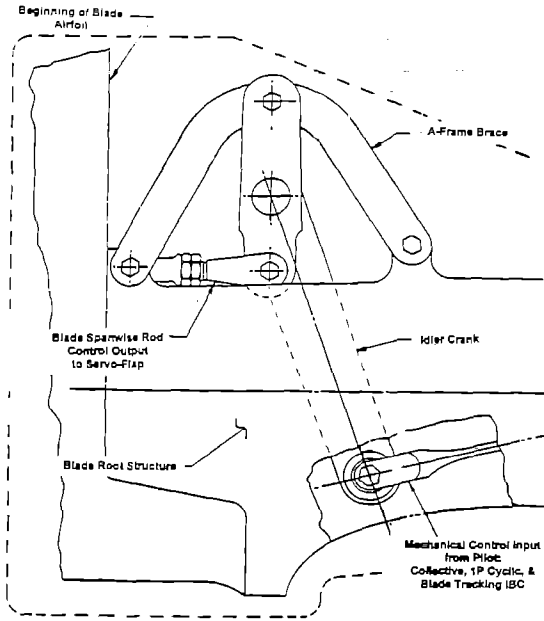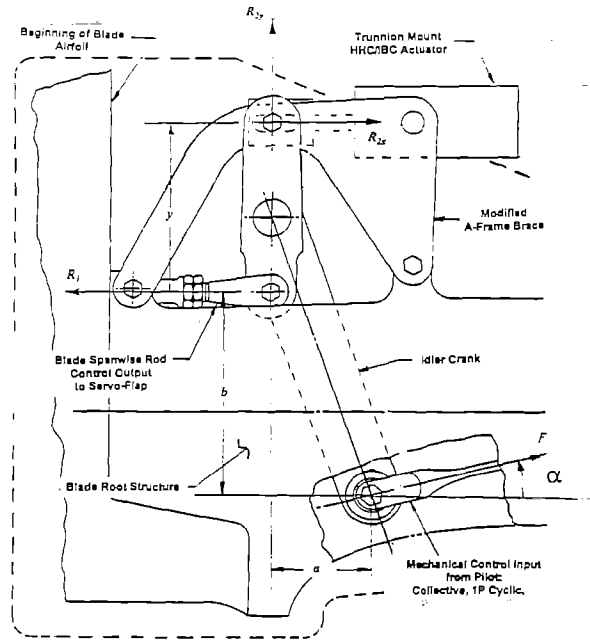

Fig. 5. SH-2G 4/rev Pilot Seat Vertical Vibration

Fig. 6. SH-2G 3/rev Blade Flatwise Bending Moments @sta. 44.5

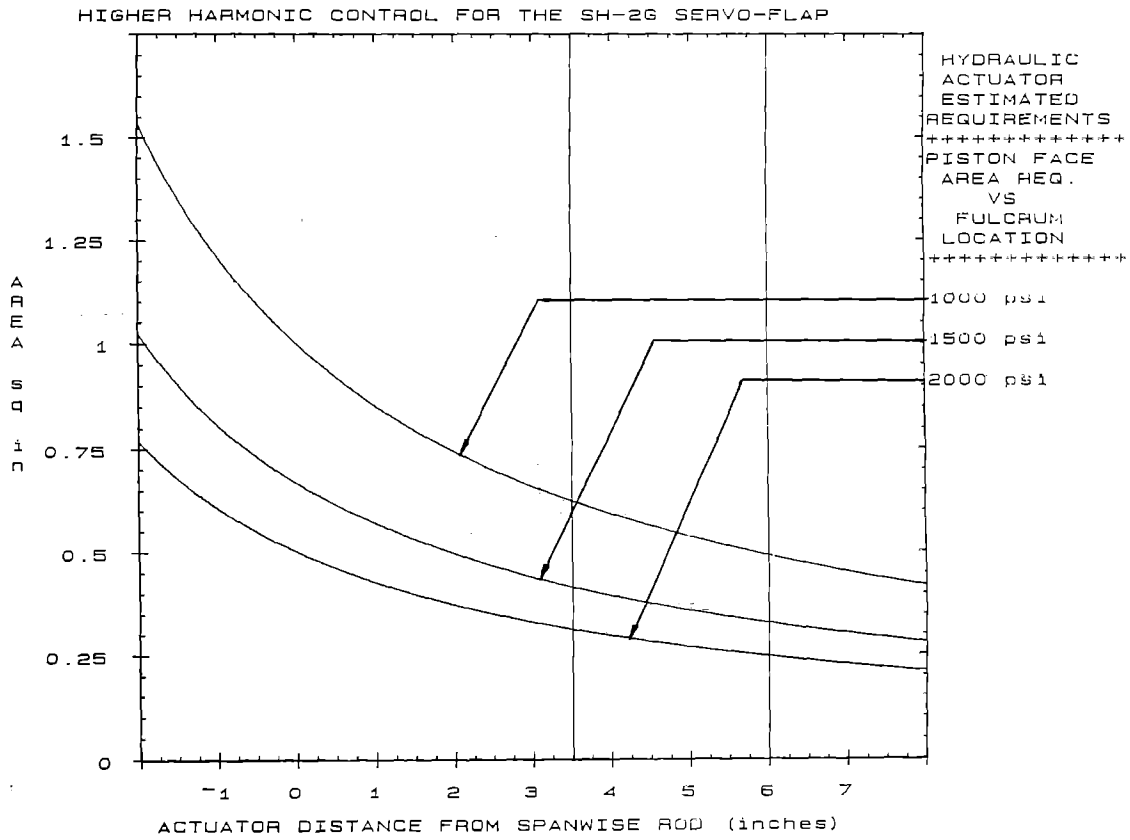Fig. 7. Kaman Blade Tracking System

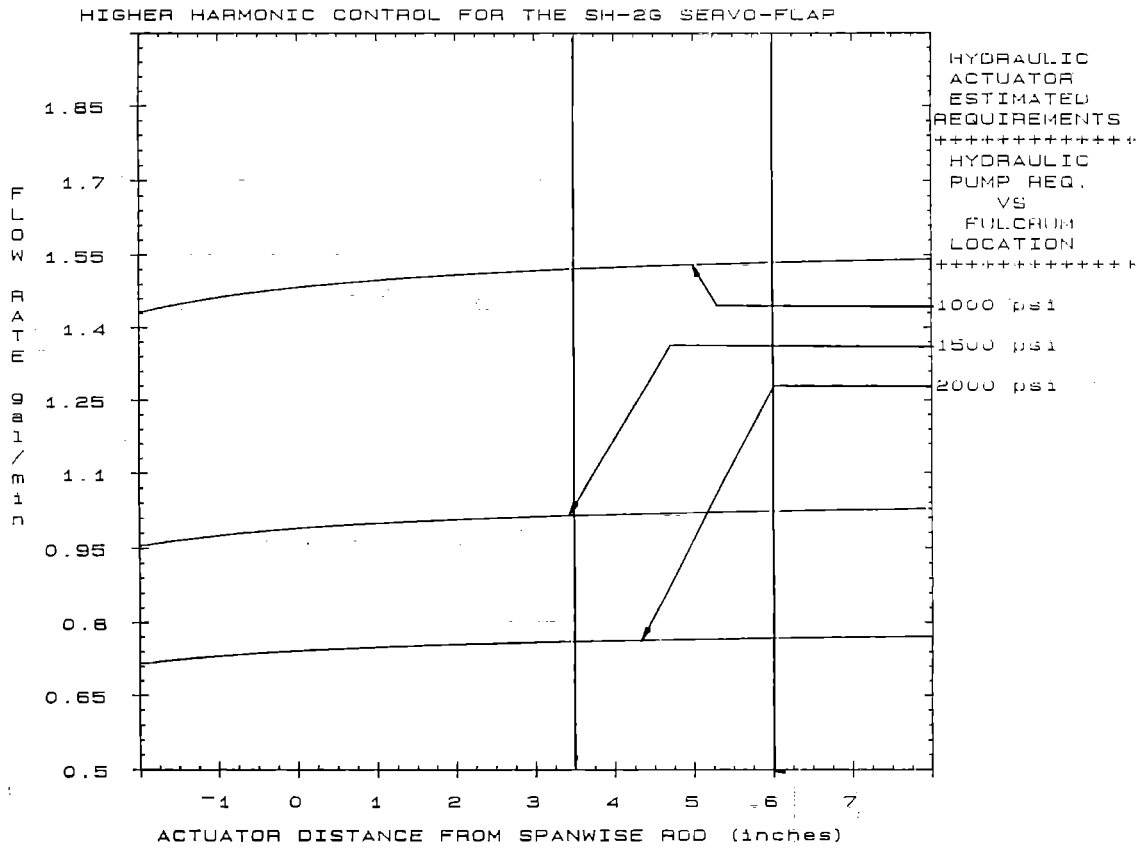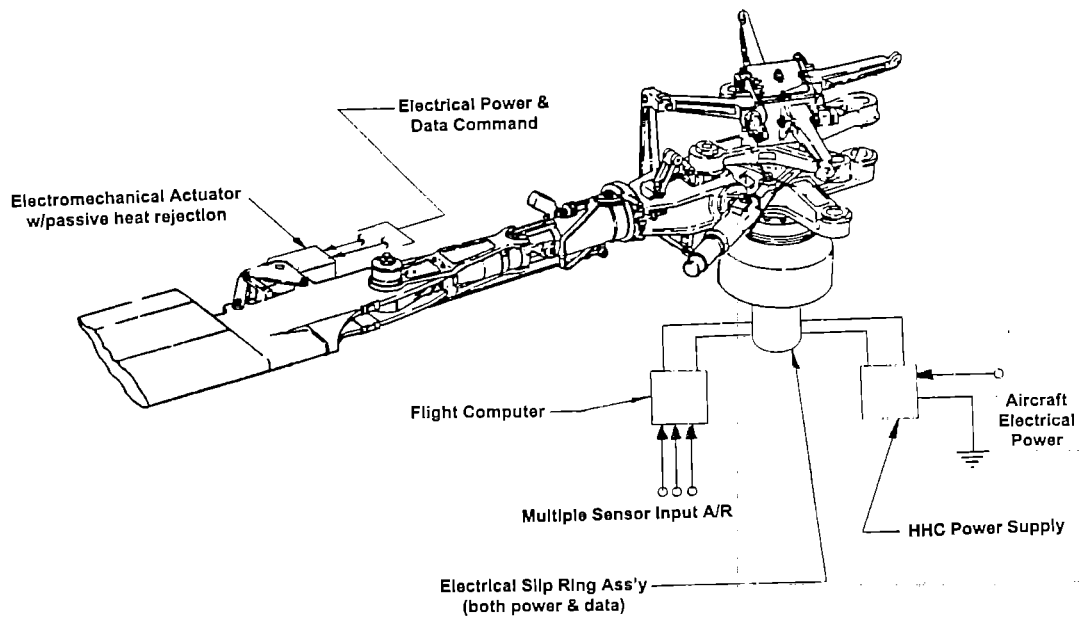Fig. 8. SH-2G Existing Inboard Control Rod
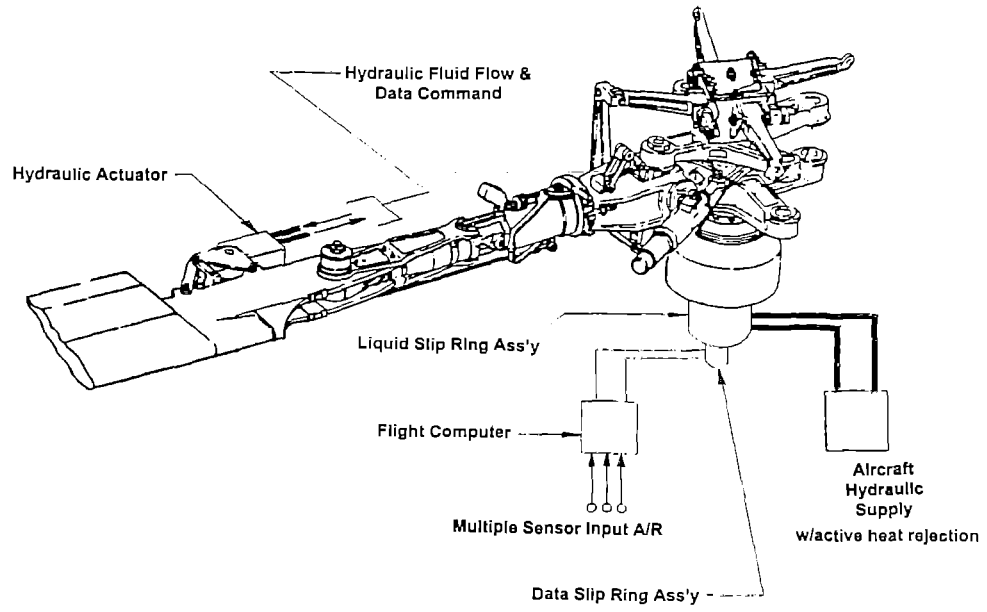

Fig. 9. Modification for HHC/IBC Actuator

Fig. 10. Hydraulic Design, Required Piston Area vs. System Pressure

Fig. 11. Hydraulic Design, Required Flow Rate vs. System Pressure

Fig. 12. Electromechanical Design, System Layout

11

Fig. 13. Split Hydraulic Design, System Layout

Individual Blade Control for Alleviation of Helicopter Ground Resonance

Eric Hathaway
Graduate Research Assistant

Dr. Farhan Gandhi
Assistant Professor, Aerospace Engineering

Rotorcraft Center of Excellence, Penn State University

Presented at the ARO Workshop on Dynamics and Aeroelastic Stability
Modeling of Rotorcraft Systems, St. Louis, Missouri, October 14-16, 1997

Problem Statement

Poor damping in the lag mode can result in
aeromechanical instabilities such as ground-
and air-resonance

Traditionally, lead-lag dampers used to alleviate
these instabilities

Associated with the use of lag dampers -

• Hub complexity, weight, drag, maintenance requirements

• Elastomeric dampers - amplitude/frequency/temperature
  dependent, limit cycles, susceptible to fatigue,

Can dampers be eliminated while maintaining
adequate aeromechanical stability?

Damperless Rotors

PENNSTATE

- **Aeroelastic Couplings**
  Pitch-Lag, Pitch-Flap, & Flap-Lag couplings used
  Ormiston, Bousman, Gaonkar, Lowey, Gandhi,....

- **Active Control through Swashplate**
  Generally based on fuselage state-feedback
  Straub, Warmbrodt, Friedman, Weller, Gandhi,....

- **Individual Blade Contol (IBC)**
  Relatively unexplored

- **Other Concepts** - High damping flexures
  - Blade-to-blade dissimilarities

Objective of Present Study

PENNSTATE

Examine the effectiveness of IBC for aeromechanical stability augmentation
(different rotational speeds, thrust, body inertia, ground/hover condition)

Comparison on two different model rotors
- AFDD (Bousman/Ormiston)
- UTRC (Weller)

Comparison of IBC versus
- Aeroelastic Couplings
- Swashplate Control using Fuselage State Feedback

2

Individual Blade Control

Active Control via root pitch actuators, in the rotating system

Active pitch inputs proportional to blade flap and lag states

$$\Delta\theta = -G_{P\beta}\beta - G_{P\zeta}\zeta - G_{V\beta}\left(\frac{\Omega}{\Omega_o}\right)\overset{*}{\beta} - G_{V\zeta}\left(\frac{\Omega}{\Omega_o}\right)\overset{*}{\zeta}$$

Fixed-Gain Controller (Fixed $G_{P\beta}$, $G_{P\zeta}$, $G_{V\beta}$, $G_{V\zeta}$)

- parametric study to examine influence of individual gains
- Constrained optimization study to evaluate optimial combination of controller gains

AFDD Rotor

Extensive studies examining the influence of Aeroelastic Couplings on this model rotor

Aeroelastic Couplings: $\Delta\theta = -K_{P\beta}\beta - K_{P\zeta}\zeta$

Individual Blade Control:

$$\Delta\theta = -G_{P\beta}\beta - G_{P\zeta}\zeta - G_{V\beta}\left(\frac{\Omega}{\Omega_o}\right)\overset{*}{\beta} - G_{V\zeta}\left(\frac{\Omega}{\Omega_o}\right)\overset{*}{\zeta}$$
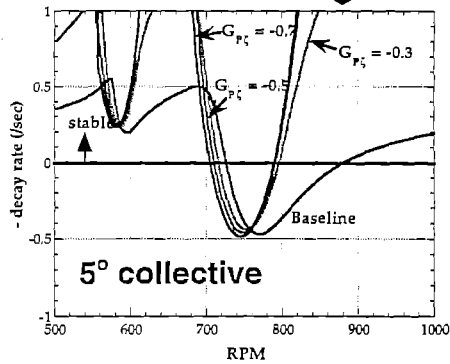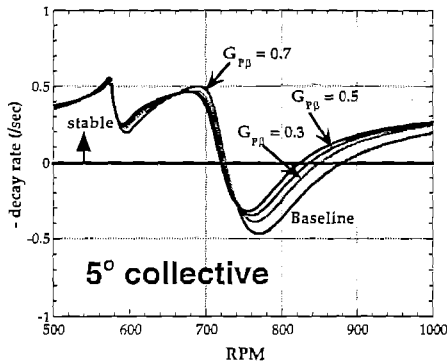
Position Feedback

Velocity Feedback

FOR THIS ROTOR - Aeroelastic couplings unable to stabilize resonance simultaneously at low and high thrust conditions
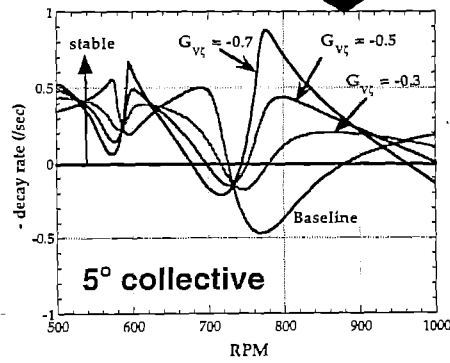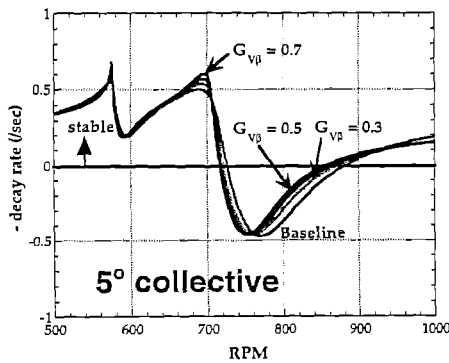
3

IBC - AFDD Rotor — PENNSTATE

Influence of Position Feedback
- Positive $G_{P\beta}$ beneficial at resonance
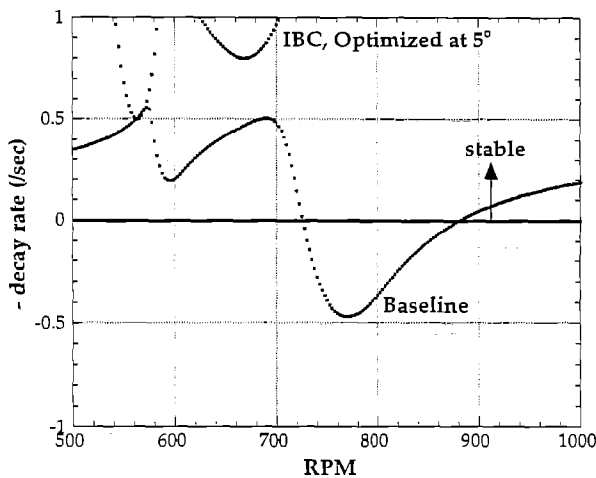- Negative $G_{P\zeta}$ beneficial off resonance

IBC - AFDD Rotor — PENNSTATE

Influence of Velocity Feedback
- $G_{V\beta}$ no significant influence
- Negative $G_{V\zeta}$ beneficial at resonance,
  but shaft-fixed stability may be reduced

IBC - AFDD Rotor

PENNSTATE
1855

5° collective
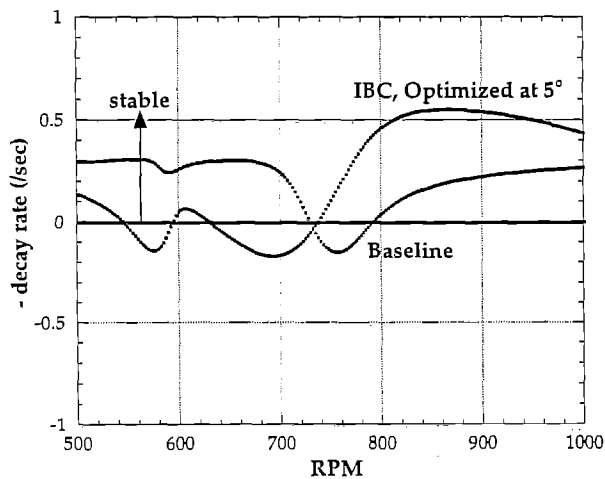
$G_{P\beta} = 0.5837$

$G_{P\zeta} = -1.0$

$G_{V\beta} = -0.5564$

$G_{V\zeta} = -0.7414$

Optimization at 5° collective - Resonance Stabilized
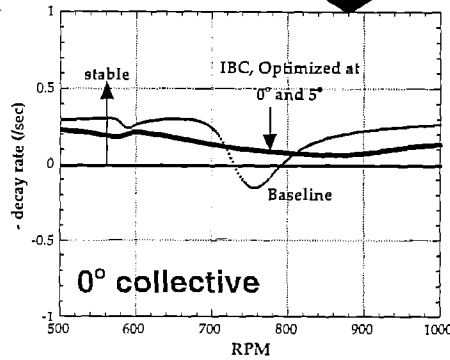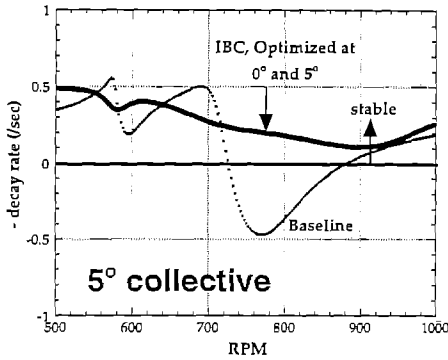
IBC - AFDD Rotor

PENNSTATE
1855

Resonance NOT stabilized at 0° collective

Influence of Optimal Design at 0° collective

IBC - AFDD Rotor

PENN**S**TATE
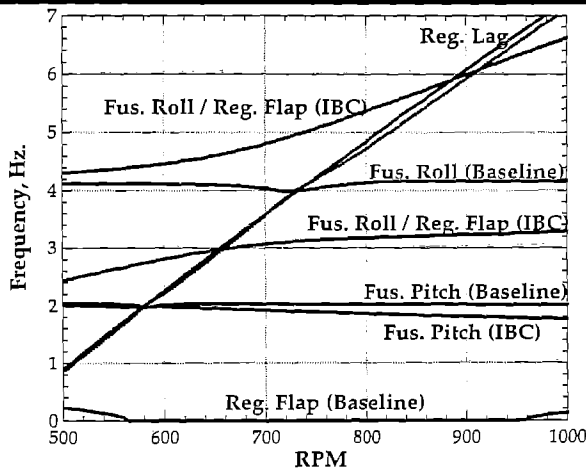
$G_{P\beta} = 0.5212 \quad G_{P\zeta} = -0.1022 \quad G_{V\beta} = -0.6252 \quad G_{V\zeta} = -0.2787$

Multi-Point Optimization at 0° and 5° collective
- Resonance Stabilized at both pitch values

IBC - AFDD Rotor
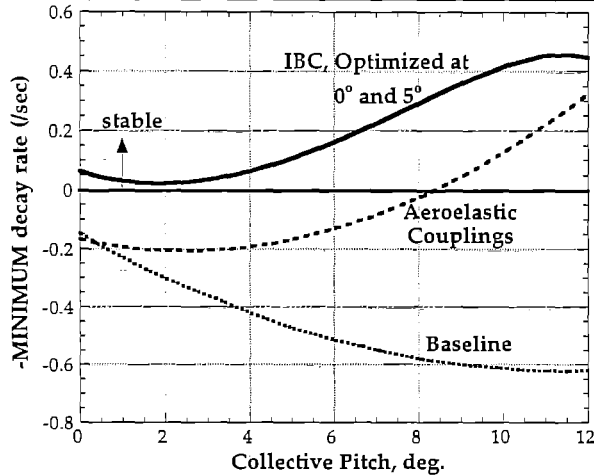
PENN**S**TATE

5° collective

MODAL
FREQUENCIES

IBC results in coupled Fus. Roll/Reg. Flap mode,
and nature of interaction with Reg. Lag changes
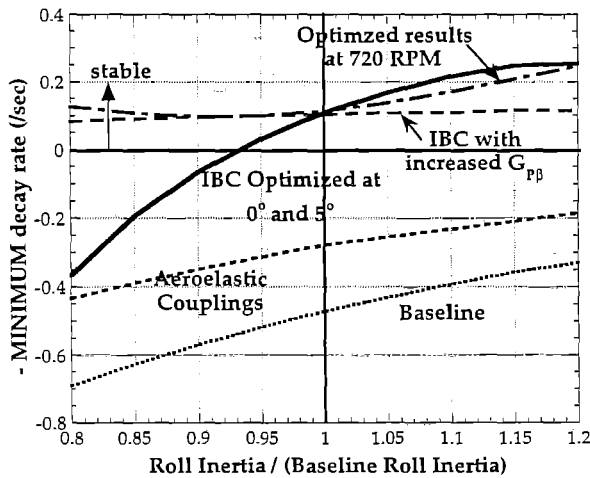
IBC - AFDD Rotor

PENNSTATE

- Destabilizing trend with increasing collective alleviated
- IBC able to stabilize resonance over entire collective range
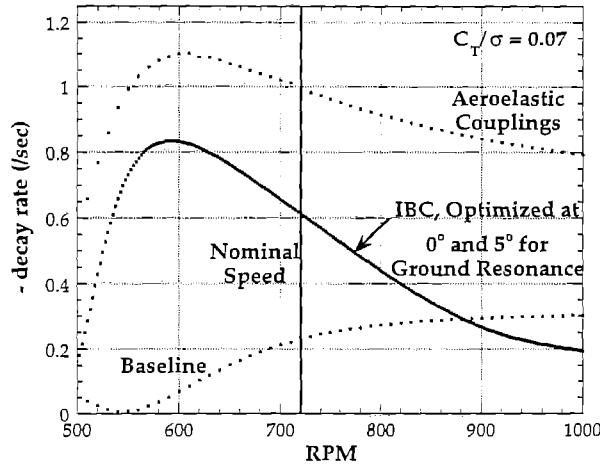
IBC - AFDD Rotor

PENNSTATE

Damping variation versus Body Roll Inertia

7

IBC - AFDD Rotor

$C_T/\sigma = 0.07$

Aeroelastic Couplings

IBC, Optimized at 0° and 5° for Ground Resonance

Nominal Speed

Baseline

(y-axis: - decay rate (/sec); x-axis: RPM)

Around nominal RPM, IBC stabilizes air-resonance

Air Resonance in Hover

UTRC Rotor

Influence of active swashplate control using fuselage state feedback examined on this rotor

Vector of Loads due to active control →

$$\begin{Bmatrix} F_{\beta c} \\ F_{\beta s} \\ F_{\zeta c} \\ F_{\zeta s} \\ F_{\alpha x} \\ F_{\alpha y} \end{Bmatrix} = \begin{bmatrix} \text{Adds to open-} \\ \text{loop stiffness or} \\ \text{damping matrix} \end{bmatrix} \begin{Bmatrix} \beta_c \\ \beta_s \\ \zeta_c \\ \zeta_s \\ \alpha_x \\ \alpha_y \end{Bmatrix}$$

Position (or velocity) vector for position (or rate) feedback

corresponds to IBC (or rotor state feedback)

corresponds to fuselage state feedback

Mathematically, IBC directly controls lag mode characteristics, through diagonal terms

8

IBC - UTRC Rotor

PENNSTATE

5° collective

$G_{P\beta} = 0.4514$

$G_{P\zeta} = -0.2752$

$G_{V\beta} = -0.4802$

$G_{V\zeta} = -0.3298$

Optimization at 5° collective

IBC - UTRC Rotor

PENNSTATE

0° collective

Influence of Optimal Design at 0° collective

9

IBC - UTRC Rotor

PENNSTATE

- Destabilizing trend with increasing collective weakened
- IBC able to stabilize resonance over entire collective range

IBC - UTRC Rotor

PENNSTATE
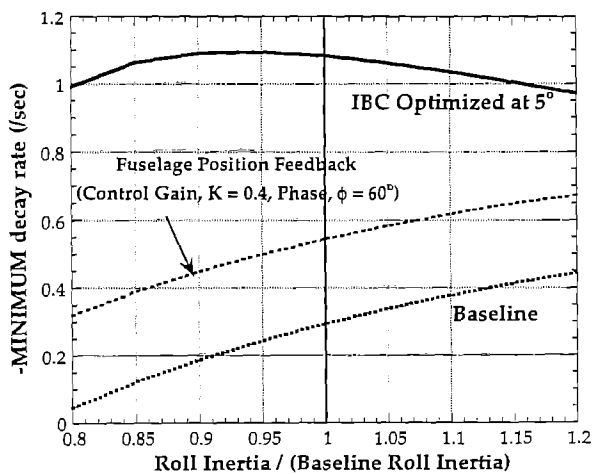
5° collective

Damping variation versus Body Roll Inertia

IBC - UTRC Rotor
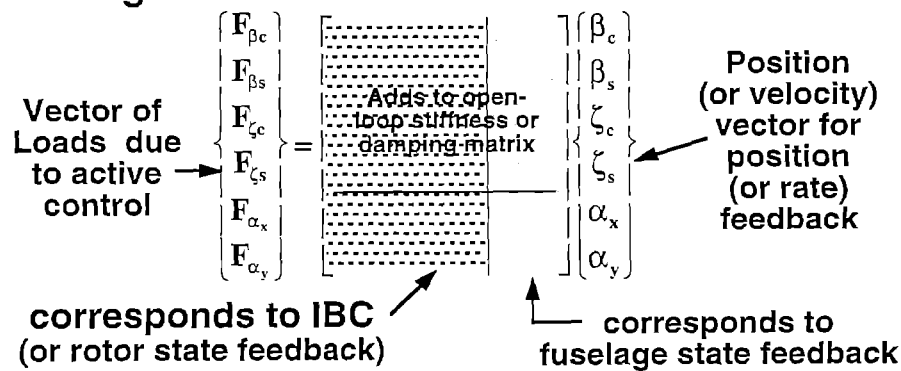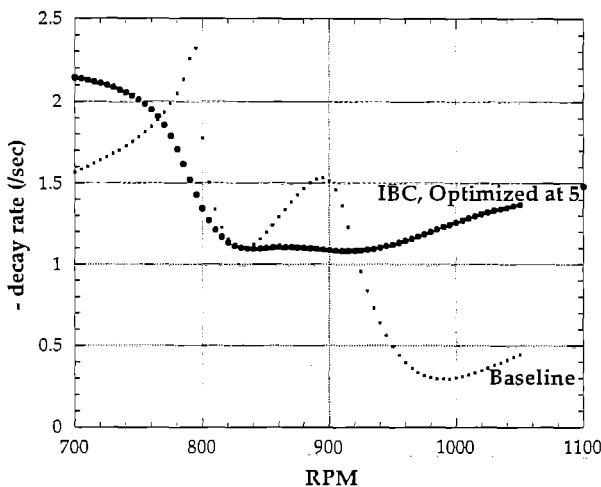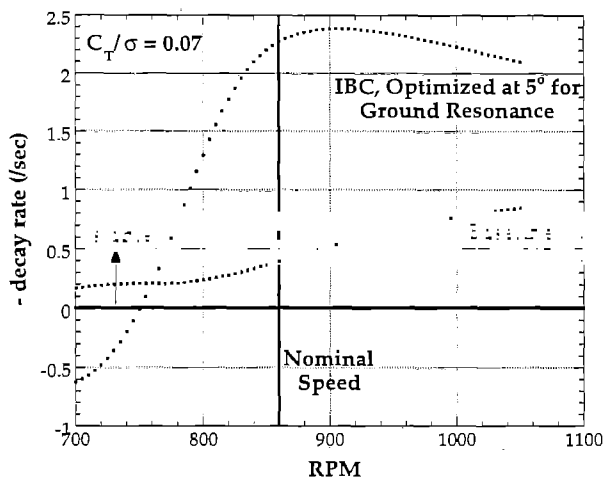
Around nominal
RPM, IBC
stabilizes
air-resonance

Air Resonance in Hover

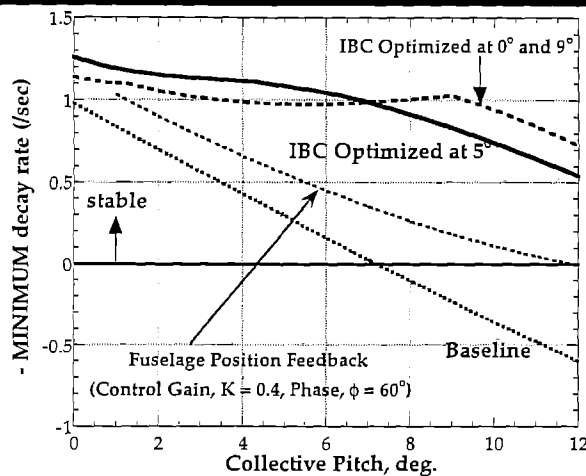## Concluding Remarks

For AFDD Rotor -

Conflicting control gain requirements at 0° and 5° collective

IBC with Multi-point Optimization at 0° and 5° can stabilize ground resonance over range of collective pitch values (Aeroelastic couplings unable to accomplish complete stabilization)

Destabilizing trend with decreasing roll inertia may be alleviated (with larger gains)

Hover air resonance stability margin around nominal RPM can be improved

11

Concluding Remarks

For UTRC Rotor -

IBC optimized at 5° can stabilize ground resonance over range of collective pitch values (Greater stability margins achieved at higher collective as compared to fuselage state feedback)

Destabilizing trend with decreasing roll inertia alleviated

Hover air resonance stability margin around nominal RPM significantly improved

Concluding Remarks

IBC succesful on two different model rotors -

Some differences between the control design process required as well as the Individual Blade Control gains for the two rotors suggest that generalizations may not be possible

Although it may be more challenging to implement Individual Blade Control, it appears to have greater effectiveness in alleviating aeromechanical instabilities

12

Analytic Modeling and Design Studies of Trailing Edge Flap Systems for Helicopters

Judah Milgram

Research Associate

Inderjit Chopra

Professor and Director

Alfred Gessow Rotorcraft Center
Department of Aerospace Engineering
University of Maryland
College Park, Maryland 20742

June 20, 1997

In the course of early rotorcraft development, the combination of feathering blade and swashplate emerged as the favored form of rotor control. Nevertheless, it may be noted that the earliest successful implementation of 1/rev cyclic control utilized a trailing edge flap [13]. Recently, trailing edge flaps for helicopter main rotors have again received considerable attention as a means for vibration control. An early analytic and experimental study of servo flaps conducted by Lemnios and others [3,4] predicted considerable reductions in vibration with single frequency 2/rev control ($N_b = 4$). Subsequent analytic studies by Millott and Friedmann [9,10,12] have suggested that servo flap systems offer considerable potential for vibration reduction when combined with multicyclic control algorithms.

Despite their apparent promise and successful service history in 1/rev cyclic control applications, servo flaps incur aerodynamic and maintainabil-

ity penalties related to their external location aft of the rotor blade. An alternative configuration, the plain trailing flap, is the subject of the present investigation. Plain trailing edge flap systems are the focus of an ongoing study by the authors [5–8]. Here the flap is integrated into the rotor blade in the manner of an aileron (they were in fact termed "ailerons" by Sikorsky [14], who considered them as a means for 1/rev cyclic control). The proposed workshop presentation will outline this investigation and present some results obatained to date.

The blade is modeled using spatial finite elements, one or more of which may have trailing edge flaps with deflections prescribed as a function of azimuth. The Leishman aerodynamic model [1] with unsteady circulatory and impulsive loads due to flap motion is used. A free-wake analysis is included as well. The equations of motion are solved using the finite element in time method integrated into a coupled trim formulation. The analysis includes calculation of blade loads and trailing edge flap power requirements. Flap inputs may be prescribed or determined automatically through a multicyclic control algorithm [2]. The weighting parameters in the multicyclic algorithm are varied to examine the influence of weighting assumptions. The analysis is described in more detail in References 6 and 5.

An extensive correlation study has been conducted using wind tunnel data from the McDonnell-Douglas Helicopter Systems Active Flap Rotor (AFR) model. Correlation between predicted and measured blade natural frequencies was fair. Results for hover thrust and power agreed well with the experimental data. In forward flight, fair correlation was observed for the power required and trim controls. For the rotor with no trailing edge flap motion, overall correlation of blade loads was fair to good, although significant discrepancies were observed in individual cases. Typical results with flap input are presented in Figure 1, which shows blade flatwise bending at $0.33R$ with a flap input of $\delta = -4° \cos 5\psi$. The experimental data show a pronounced 4/rev flatwise bending load resulting from the 5/rev flap motion. This is captured fairly well in the UMARC results, with the unsteady aerodynamic model offering some improvement. However, at $\mu = 0.30$ the 4/rev bending is significantly underpredicted. CAMRAD/JA results (shown for comparison) do not correlate as well. Both analyses overpredict the 3/rev component, although the advance ratio trend is properly represented. For the 5/rev bending moment, the UMARC predictions agree fairly well and the CAMRAD/JA correlation is very good. More detailed information concerning the correlation study may be found in References 8 and 5.

Representative results from a related parametric study using the Sikorsky S-76 as a baseline rotor are in Figures 2-3.

Figure 2 shows the effects of varying the flap length. The figure shows the controlled objective function J, the trailing edge flap power required, and the peak trailing edge flap deflection $\|\delta\|$ as a function of flap length, l_f. Results are shown for three spanwise locations: $r_{\text{mid}} = 0.60, 0.70$ and 0.80. Figure 2(a) shows that at every spanwise location, the peak flap deflections increase as the flap size is decreased, until a prescribed limit of $\pm 10°$ is encountered. In Figure 2(c), the controlled vibration objective function is relatively insensitive to flap length l_f, provided the peak flap deflections are within the prescribed limit. This shows that the controller is able to compensate for changes in flap length by increasing the flap deflections. If the flap length is decreased past the point where the flap deflection limit is encountered, the vibration levels increase rapidly (Fig. 2(c)). As may be expected, the flap deflections are directly related to the spanwise location of the flap. The deflections are greatest at $l_f = 0.60$, where the dynamic pressure is lowest. However, the trailing edge flap power required (Fig. 2(b)) was greatest with the flap located at $l_f = 0.60$. Apparently, the large flap deflections required at that location (Fig. 2(a)) more than offset the effects of reduced dynamic pressure at that spanwise location. At $l_f = 0.70$, the deflections are greater than at $l_f = 0.80$; however, the power required is actually lower. In this case the differences in the required flap deflection are not as great, and the increased dynamic pressure at $0.80R$ suffices to increase the trailing edge flap power requirements. The fluctuation in performance near $l_f = 0.08$ is attributed to a variation in the performance of the multicylic algorithm.

Figure 3 presents the controlled vibration objective function, the trailing edge flap power required, and the peak flap deflections as a function of flap-chord ratio, $\bar{c}_f$. The objective function results (Fig. 3(c)) show almost no change as the $\bar{c}_f$ is varied (a similar finding is stated briefly as a conclusion in Reference 11). This result is a reflection of the HHC algorithm's ability to compensate for reductions in flap-chord ratio by increasing the flap inputs. This increase in peak flap input as $\bar{c}_f$ is decreased is evident in Fig. 3(a). The Figure shows that the flap deflections increase to the prescribed limit of $10°$ for small values of $\bar{c}_f$. As may be expected, the flap deflections are larger and the limit is reached earlier for the smaller flap ($l_f = 0.10$). In each case, limiting the flap amplitudes has the effect of reducing the ability of the flap to reduce vibrations. The results show that the larger ($l_f = 0.14$) flap has

the advantage of allowing smaller flap-chord ratios without encountering the flap deflection limit.

The trailing edge flap power required diminishes rapidly as the flap-chord ratio is decreased. Reference 5 shows this to be the expected result based on linear, incompressible, quasisteady flap-airfoil theory. Clearly it is advantageous to keep the flap chord as small as possible without incurring excessive flap deflections. From approximately $\bar{c}_f = 0.06$ to $\bar{c}_f = 0.10$, both the $l_f = 0.10$ and $l_f = 0.14$ flaps produced nearly the same vibration reduction and required virtually the same power. These factors being equal, the $l_f = 0.14$ flap is probability the preferred configuration as it requires lower flap deflections and is less likely to encounter difficulties caused by nonlinear aerodynamic effects.

References

[1] N. Hariharan and J. G. Leishman. Unsteady aerodynamics of a flapped airfoil in subsonic flow by indicial concepts. In *Proceedings of the 36th AIAA/ASME/ASCE/AHS/ASC Structures, Structural Dynamics, and Materials Conference*, New Orleans, LA, April 1995.

[2] W. Johnson. Self-tuning regulators for multicyclic control of helicopter vibration. NASA Technical Paper 1996, March 1982.

[3] A. Z. Lemnios and F. K. Dunn. Theoretical study of multicyclic control of a controllable twist rotor. NASA CR-151959, Moffett Field, California.

[4] J. L. McCloud III. An analytical study of a multicyclic controllable twist rotor. In *Proceedings of the 31st Annual National Forum of the American Helicopter Society*, Washington, D.C., May 1975.

[5] J. H. Milgram. *A Comprehensive Aeroelastic Analysis of Helicopter Main Rotors with Trailing Edge Flaps for Vibration Reduction*. PhD thesis, University of Maryland, College Park, Maryland, January 1997.

[6] J. H. Milgram and I. Chopra. Helicopter vibration reduction with trailing edge flaps. In *Proceedings of the 36th AIAA/ASME/ASCE/AHS/ASC Structures, Structural Dynamics, and Materials Conference*, New Orleans, LA, April 1995.

[7] J. H. Milgram and I. Chopra. Helicopter vibration reduction with trailing edge flaps. In *Proceedings of the American Helicopter Society Northeast Region Aeromechanics Specialists Meeting*, Stratford, CT, October 1995.

[8] J. H. Milgram, I. Chopra, and F. Straub. A comprehensive rotorcraft aeroelastic analysis with trailing edge flap model: Validation with experimental data. In *Proceedings of the 52nd Annual Forum of the American Helicopter Society*, June 1996.

[9] T. A. Millott and P. P. Friedmann. Vibration reduction in helicopter rotors using an active control surface located on the blade. In *Proceedings of the 33rd AIAA/ASME/ASCE/AHS Structures, Structural Dynamics and Materials Conference*, Dallas, Texas, April 1992. AIAA paper 92-2451.

[10] T. A. Millott and P. P. Friedmann. The practical implementation of an actively controlled flap to reduce vibrations in helicopter rotors. In *Proceedings of the 49th Annual Forum of the American Helicopter Society*, pages 1079–1092, St. Louis, May 1993.

[11] T. A. Millott and P. P. Friedmann. Vibration reduction in helicopter rotors using an actively controlled partial span trailing edge flap located on the blade. Contractor Report 4611, NASA, June 1994.

[12] T. A. Millott and P. P. Friedmann. Vibration reduction in hingeless rotors using an actively controlled trailing edge flap: Implementation and time domain simulation. In *Proceedings of the 35th Structures, Structural Dynamics and Materials Conference, Adaptive Structures Forum*, April 1994. AIAA-94-1306-CP.

[13] R. P. Pescara. Screw propeller of helicopter flying machines. U.S. Patent 1,449,129, filed July 17, 1920, issued March 20, 1923.

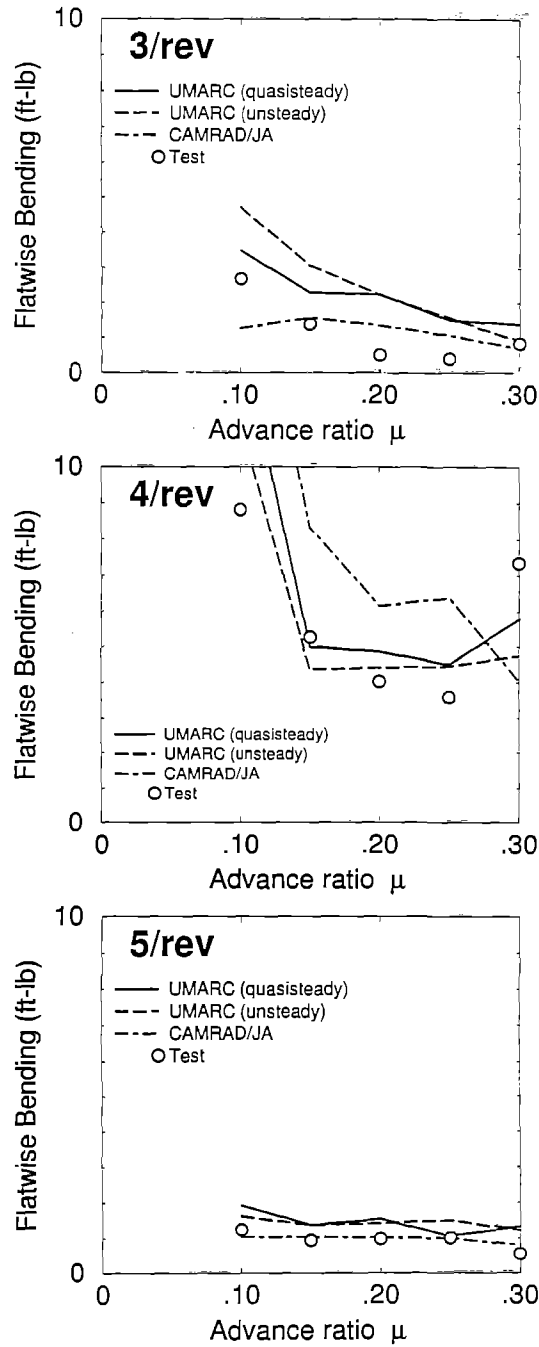[14] I. I. Sikorsky. Direct lift aircraft. U. S. Patent 1,994,488, filed June 27, 1931, issued March 19, 1935.

Figure 1: Harmonics of AFR blade flatwise (out of plane) bending at $0.33R$ with $\delta = -4° \cos 5\psi$. Wind tunnel trim at $0.10 \leq \mu \leq 0.30$ and $C_T/\sigma \approx 0.65$
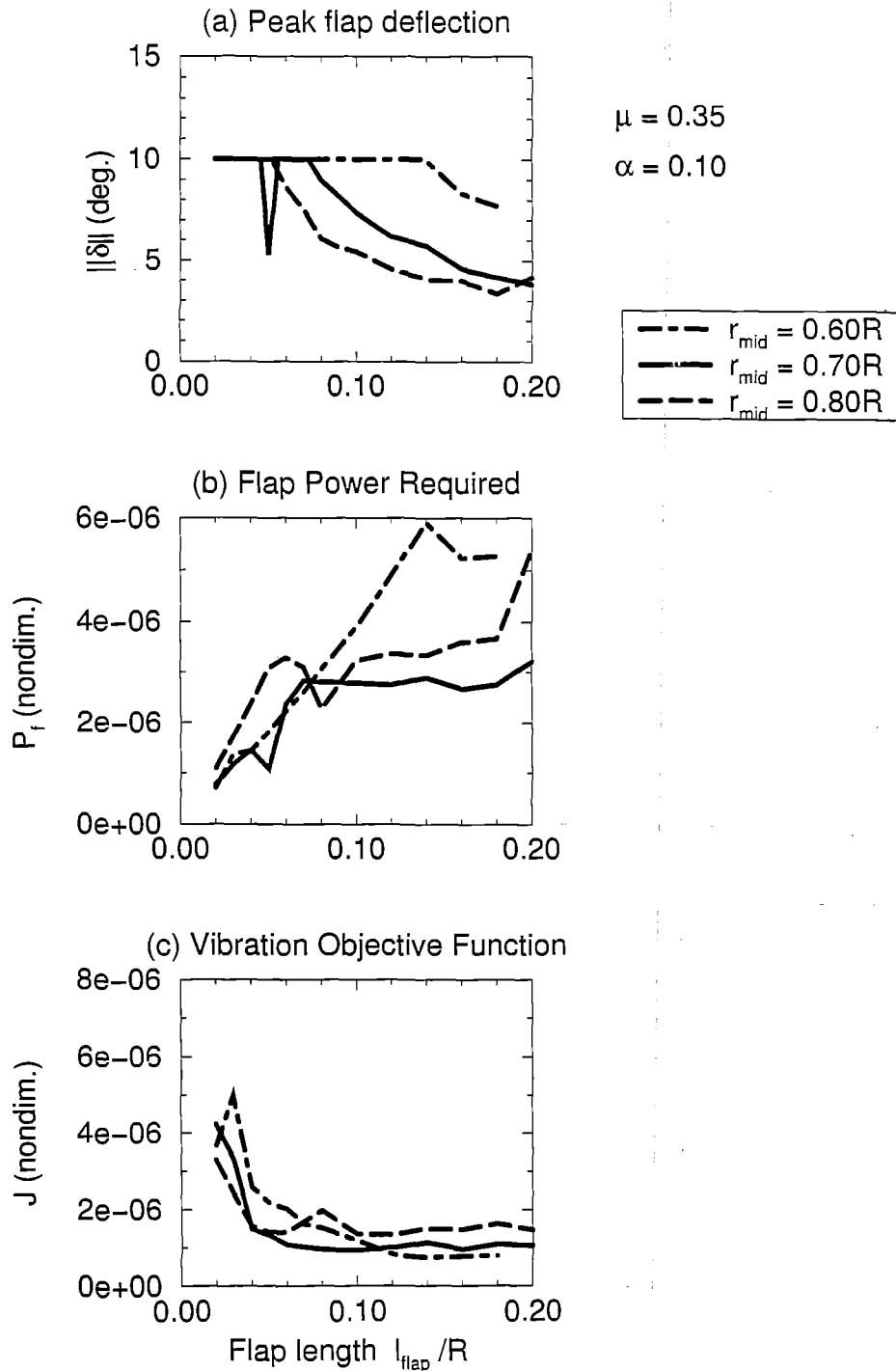
Figure 2: Effect of trailing edge flap length (l_f) on performance for three flap locations with $\bar{c}_f = 0.20$, global model multicyclic controller with $\alpha = 0.10$, and wind tunnel trim at $\mu = 0.35$, $\alpha = 5°$ nose down, $C_T/\sigma = 0.080$.
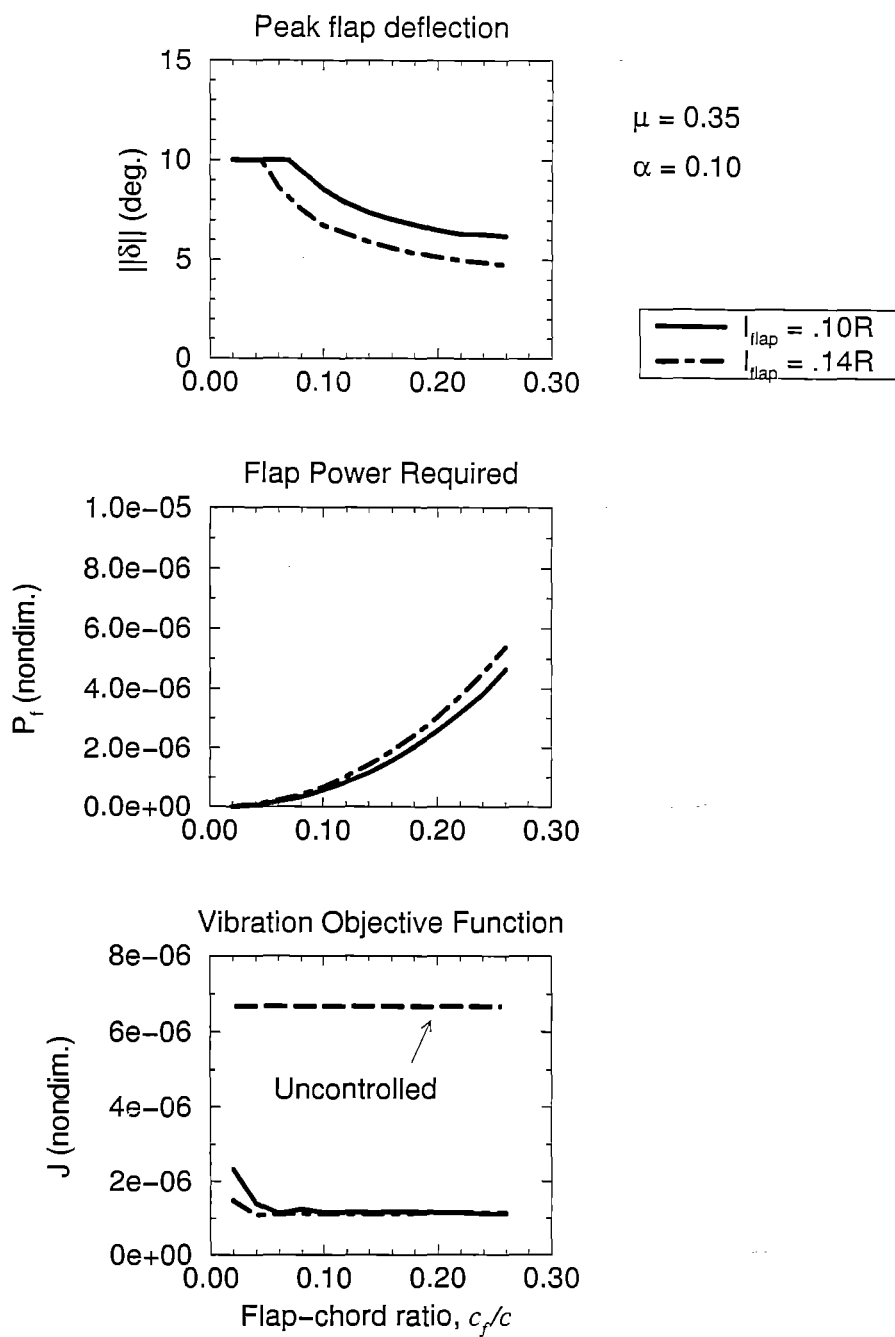
Figure 3: Effect of trailing edge flap-chord ratio (hinge location) on trailing edge flap system performance for two flap lengths, with $r_{\mathrm{mid}} = 0.74$, global model multicyclic controller with $\alpha = 0.10$, and wind tunnel trim at $\mu = 0.35$, $\alpha = 5°$ nose down, $C_T/\sigma = 0.080$.

Rotary-Wing Aeroelastic Scaling and Its Application to Adaptive Materials Based Actuation

Peretz P. Friedmann, Professor
Mechanical and Aerospace Engineering Department
University of California, Los Angeles, CA 90095-1597
Phone 310-825-6041
FAX 310-206-4830
E-mail friedman@seas.ucla.edu

ABSTRACT

Active materials have been considered as the basis for designing a variety of actuators employed in aeroservoelastic applications. The area of smart structures or adaptive structures, combining active materials, controls and microprocessors has been burgeoning in the last fifteen years. Active materials based actuation has been applied to a variety of aeroelastic and aeroservoelastic problems such as: static aeroelasticity and divergence control, supersonic panel flutter suppression, flutter and dynamic load alleviation in wings, wing/store flutter suppression and vibration reduction in helicopter rotors. Among these applications the rotary-wing applications seem to have the highest potential pay-offs and therefore a substantial body of research has been devoted to the vibration reduction problem. Other problems that can benefit from adaptive materials based actuation are the blade tracking problem and alleviation of the blade vortex interaction (BVI) problem.

Actuators built of adaptive materials for aeroservoelastic applications frequently require the construction of small scaled models that are used in wind tunnel tests to demonstrate the feasibility of a proposed approach. It is therefore important to relate the behavior of the scale model to the full scale configuration. In aeroelasticity such relations between the scale model and the full scale configuration are usually governed by aeroelastic scaling laws. The primary objective of the proposed paper is to develop aeroelastic scaling laws for rotary-wing aeroelastic and aeroservoelastic applications, and apply them to a number of typical examples in which adaptive materials based actuators have been used.

Classical scaling laws for fixed wing applications have been based on the concept of a typical cross, and Theodorsen type frequency domain aerodynamics.

1

These scaling laws have been extended recently by the author and his associates to situations involving actively controlled trailing edge flaps used for aeroservoelastic applications, where flutter suppression was the objective. Furthermore it was shown that computer simulations of the system can be combined with the scaling laws to provide scaling requirements for actuator power, stroke and force or hinge moment requirements. It is shown, in the proposed paper, that rotary-wing aeroelastic scaling laws can obtained by recognizing that the rotary-wing equivalent of a typical cross section model used for fixed wings is the offset hinged spring restrained blade model. Using appropriate springs the model can be used to represent either hingeless or articulated blade configurations. Aeroelastic scaling laws are obtained by combining dimensional analysis with the dynamic equations of motion of an offset hinged spring restrained blade undergoing coupled flap-lag-torsional dynamics in forward flight, including the geometrically nonlinear terms due to moderate blade deflections. Rewriting the rotordynamic problem in terms of three basic dimensions M, L and T (mass, length and time) it is shown that the aeroelastic response problem (or vibration problem) is governed by a number of nondimensional parameters, such as the Mach number, the Reynolds number, the advance ratio, the Lock number, the Froude number, several frequency ratios, the inflow ratio, non dimensional offsets, damping ratios and the reduced frequency. For complete similarity between the dynamic model and the full scale configuration these scaling requirements can be only satisfied by using the full scale configuration. It is shown the when one relaxes these requirements two alternatives exist. One satisfying Froude scaling requirements, which would be suitable for aeromechanical stability testing involving coupled rotor-fuselage problems where the role of gravity loads can be significant. The second alternative is to maintain Mach number similarity, which would correspond to situations where vibration reduction in forward flight is the objective. Furthermore, it is shown that the aeroelastic scaling laws described here, have to be combined with aeroelastic simulations to generate refined scaling laws involving actuator power, and force and moment requirements, such as needed when using adaptive materials based actuation combined with active control for vibration reduction.

Based on the examples considered it is shown that in a number of small scale tests due to the difficulties associated with aeroelastic scaling, scaling

2

considerations have not been carefully addressed, and the models used have been very soft (or flexible) so as to accommodate the limited strain and force producing capability of the current generation of adaptive materials. In such cases it is quite difficult to extrapolate from the scale tests to a full scale configuration. Finally, it is shown that the scaling relations developed are quite valuable for designing improved models for tests intended to demonstrate the feasibility of adaptive materials based actuation.

Acknowledgment

Session III
Structures, Structural Dynamics

Helicopter Rotor Blade Structural Modeling with Integral Actuation

Carlos E. S. Cesnik* and SangJoon Shin[†]
Department of Aeronautics and Astronautics
Massachusetts Institute of Technology, Cambridge, Massachusetts

Abstract

The technology of smart structures provides a new degree of design flexibility for advanced composite helicopter rotor blades. The key to the technology is the ability to allow the structure to sense and react in a desired fashion, improving rotor blade performance in the areas of structural vibration, acoustic signature, and aeroelastic stability.

There have been several approaches in the literature to take advantage of active materials for individual blade control. The one of interest in the present work is the integral actuation through the use of interdigitated electrode piezoelectric fiber composites (IDEPFC). This actuator concept provides a feasible way of integrally actuating a rotor blade instead of the direct use of piezoceramic crystals. Another concepts which have been currently studied include embedding banks of piezoceramic crystal elements in the upper and lower surface of the blade at$\pm45°$ orientation, however the maximum twist actuation obtained experimentally shows insufficient level for possible suppression of vibratory hub loads. On the other hand, preliminary results from the IDEPFC concept obtains the level of authority needed from the actuator. Basic material characterization and proof of concept of an integral twisted-actuated rotor blade have been under investigation at MIT's Active Materials and Structures Laboratory. However, in order to explore the IDEPFC technology through different actuation mechanisms and their interaction with the possible elastic tailoring of the blade, a full simulation environment for an active rotor in both hover and forward flight has to be developed.

The objective of this paper is to present a general methodology for analyzing advanced composite rotor blades with integral anisotropic active plies for improving vibration characteristics of helicopter rotor blades. Its analysis extends previous work done for modeling generically passive blades. The approach is based on the two-step solution of the original three-dimensional blade representation by means of an asymptotical approximation: a linear two-dimensional cross-sectional analysis and a nonlinear one-dimensional global analysis. The resulting model will be able to correctly predict the behavior of helicopter blades, accounting for the presence of different materials (passive and active) and actual blade shape. Different ways of actively deforming the blade will be numerically investigated.

The cross-sectional analysis revises and extends the closed form solution of a thin-walled, multi-cell asymptotic formulation originally presented by Badir [1995]. The variational-asymptotical method is used to formulate the stiffness constants of a two-cell cross section with the active plies consisting of piezoelectric fibers. It provides the expressions for the asymptotically-correct cross-sectional stiffness constants in closed form, facilitating design-trend studies. These stiffness constants will then be used in a beam finite element discretization of the blade reference line. The exact intrinsic equations for the one-dimensional analysis of rotating beams considering small strains and finite rotations of Hodges [1990] is extended to take into account the changes in the constitutive relation. Subject to external loads, active ply induced strains, and specific boundary conditions, the one-dimensional (beam) problem can be solved for displacements, rotations, and strains of the reference line. Eventually, these results will be combined with information from the cross-sectional analysis in a set of recovering relations for stress/strain distribution at each ply of the blade. Also later on, the finite-state inflow theory is expected to be coupled with the active structural model, and aeroelastic simulations can then be performed.

---

*Boeing Assistant Professor.
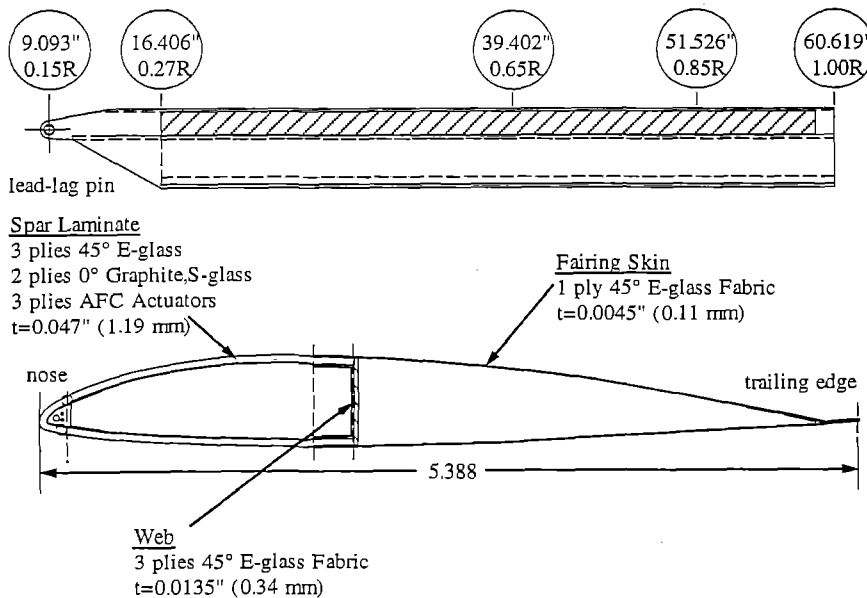[†] Graduate Research Assistant.

Introduction

- Individual Blade Control (IBC): improvement in the vibration and noise reduction
- Various actuation concepts under investigation

| Type of Control	Actuation	Actuator
Shape Control (Twist)	Integral Actuation	IDEPFC, Piezoceramic Banks
Camber Control	Trailing-Edge Flap	Bimorph, X Frame
Boundary Condition Control	Blade Root B.C.	-

Introduction

Active Twist Blade with IDEPFC

9.093" 0.15R   16.406" 0.27R   39.402" 0.65R   51.526" 0.85R   60.619" 1.00R

lead-lag pin

Spar Laminate
3 plies 45° E-glass
2 plies 0° Graphite,S-glass
3 plies AFC Actuators
t=0.047" (1.19 mm)

Fairing Skin
1 ply 45° E-glass Fabric
t=0.0045" (0.11 mm)

nose   trailing edge

5.388

Web
3 plies 45° E-glass Fabric
t=0.0135" (0.34 mm)

Objectives

- Capture the effects due to the presence of active materials in combination with a elastic tailored structure of realistic rotor blades.

- Create a framework for designing active twist rotors (ATR) to support a joint effort between the U.S. Army Vehicle Technology Center, at Langley, and MIT.

Framework for Active Blade Modeling

- Asymptotical Approximation: original 3-D blade represetation replaced by linear 2-D cross-sectional analysis + non-linear 1-D global analysis

- 2-D Cross-Sectional Analysis: stiffness matrix (based on Badir [1995]) and actuation forcing vector for two-cell thin-walled cross section

- 1-D Global Analysis
    - → Exact intrinsic equations of moving beams (small strains and finite rotations) of Hodges [1990]
    - → Combined with finite-state inflow theory for aeroelastic simulations (future extention)

Two-Cell Thin-Walled Cross-Sectional Analysis

Basic Configuration and Assumptions
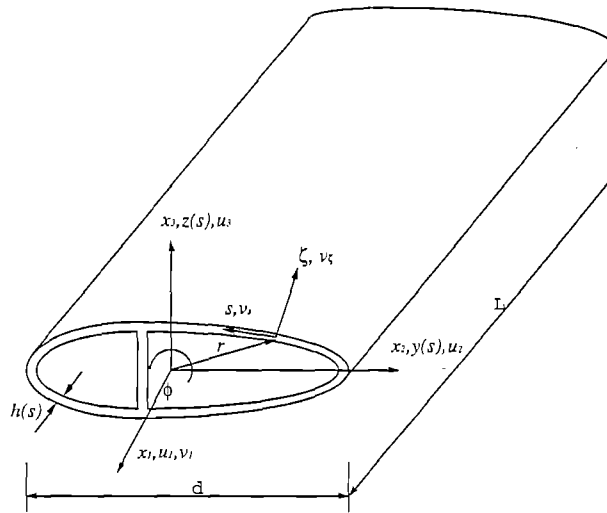
$$\frac{d}{L} \ll 1, \ \frac{h}{d} \ll 1, \ \text{and} \ \frac{h}{R} \ll 1$$

Two-Cell Thin-Walled Cross-Sectional Analysis

Starting Point:

Linear piezoelectric constitutive relation:

$$\varepsilon_{ij} = s^E_{ijkl}\sigma_{kl} + d_{kij}E_k$$

Shell functional:

$$2\Phi = \{< D^{\alpha\beta\gamma\delta} > \ \overline{\gamma}_{\alpha\beta} - 2 < D^{\alpha\beta\gamma\delta}d_{3\gamma\delta}E_3 >\}\overline{\gamma}_{\gamma\delta}$$
$$+ 2\{< D^{\alpha\beta\gamma\delta}\xi > \overline{\gamma}_{\alpha\beta} - < D^{\alpha\beta\gamma\delta}d_{3\gamma\delta}E_3\xi >\}\rho_{\gamma\delta}$$
$$+ < D^{\alpha\beta\gamma\delta}\xi^2 > \rho_{\alpha\beta}\rho_{\gamma\delta} + \Psi(E_3)$$

Two-Cell Thin-Walled Cross-Sectional Analysis

Forcing and Stiffness Constants

$$
\left\{ \begin{array}{c} F_1 \\ M_1 \\ M_2 \\ M_3 \end{array} \right\} = \left[\begin{array}{cccc} K_{11} & K_{12} & K_{13} & K_{14} \\ K_{12} & K_{22} & K_{23} & K_{24} \\ K_{13} & K_{23} & K_{33} & K_{34} \\ K_{14} & K_{24} & K_{34} & K_{44} \end{array} \right] \left\{ \begin{array}{c} \gamma_{11} \\ \kappa_1 \\ \kappa_2 \\ \kappa_3 \end{array} \right\} - \left\{ \begin{array}{c} F_1^{(a)} \\ M_1^{(a)} \\ M_2^{(a)} \\ M_3^{(a)} \end{array} \right\}
$$

where all the constants are function of the geometry and material distributions of the cross section, and the forcing constants are also function of the electric field.

1-D Beam Analysis

Extension of the exact nonlinear global analysis for small strain and finite rotations of Hodges [1990]—mixed variational intrinsic formulation of moving beams
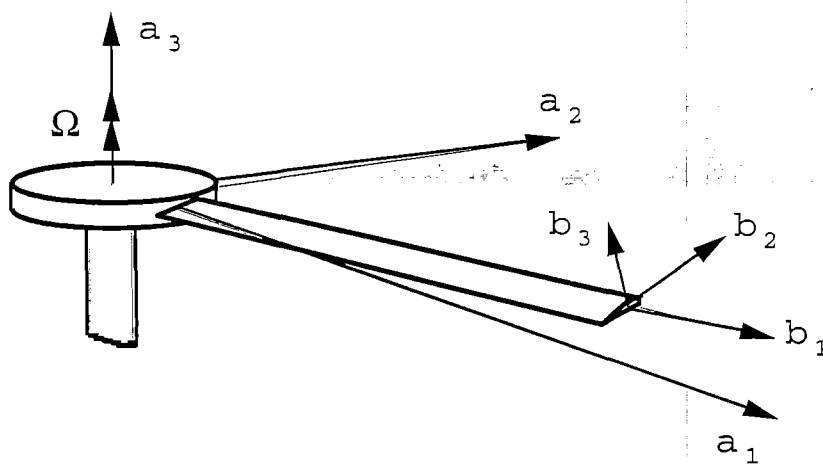
1-D Beam Analysis (Statics)

- Equilibrium equations

$$F' + \widetilde{K}F + f = 0$$

$$M' + \widetilde{K}M + (1 + \gamma_{11})\,\widetilde{e}_1\,F + m = 0$$

- Constitutive equations

$$\left\{ \begin{array}{c} F_1 \\ M_1 \\ M_2 \\ M_3 \end{array} \right\} = [\mathcal{K}] \left\{ \begin{array}{c} \gamma_{11} \\ \kappa_1 \\ \kappa_2 \\ \kappa_3 \end{array} \right\} - \left\{ \begin{array}{c} F_1^{(a)} \\ M_1^{(a)} \\ M_2^{(a)} \\ M_3^{(a)} \end{array} \right\}$$

- Kinematical equations

$$\gamma_{11} = e_1^T C(e_1 + u' + \widetilde{k}u) - 1 \qquad e_\alpha^T C(e_1 + u' + \widetilde{k}u) = 0$$

$$K = \kappa + k \qquad \widetilde{\kappa} = -C'C^T + C\widetilde{k}C^T - \widetilde{k}$$

Two-Cell Thin-Walled Box Beam Test Case
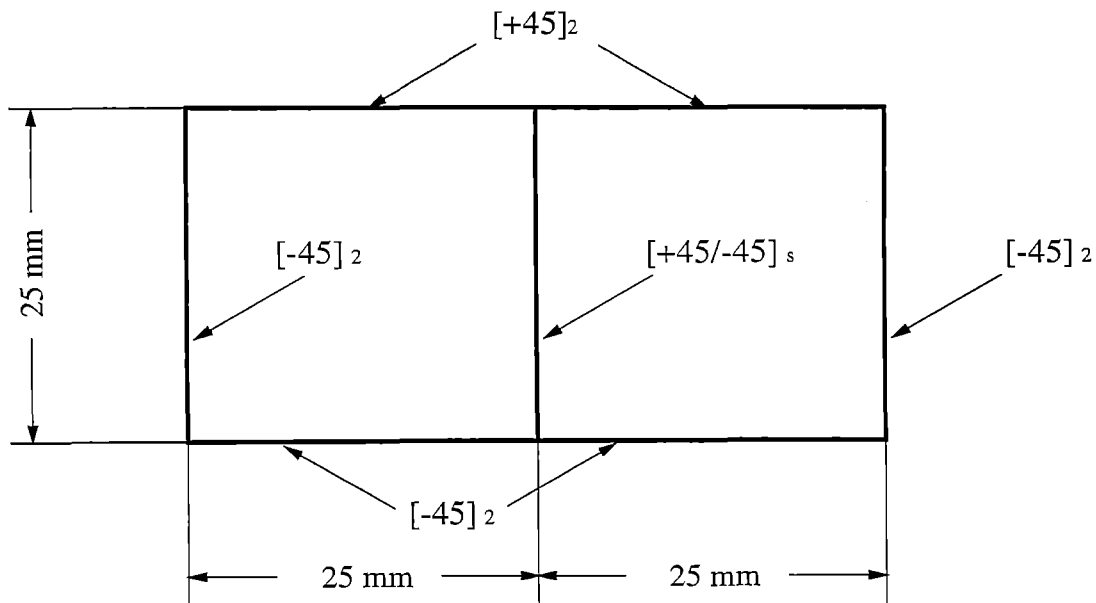
Two-Cell Thin-Walled Box Beam Test Case

Non-Zero Stiffness Results (N, N m, N m^2) for Two-Cell Box Beam (1 extension; 2 torsion; 3, 4 bending)

K_{ij}	Present	VABS	% Difference
K_{11}	$8.560\ 10^5$	$8.477\ 10^5$	-1.0
K_{12}	$-1.827\ 10^3$	$-1.794\ 10^3$	$+1.8$
K_{13}	$6.434\ 10^2$	$6.337\ 10^2$	-1.5
K_{22}	$1.298\ 10^2$	$1.278\ 10^2$	$+1.6$
K_{23}	$4.569\ 10^1$	$4.461\ 10^1$	$+2.4$
K_{33}	$9.855\ 10^1$	$9.567\ 10^1$	$+3.0$
K_{44}	$2.106\ 10^2$	$2.070\ 10^2$	$+1.7$

Single-Cell Active Blade Test Case
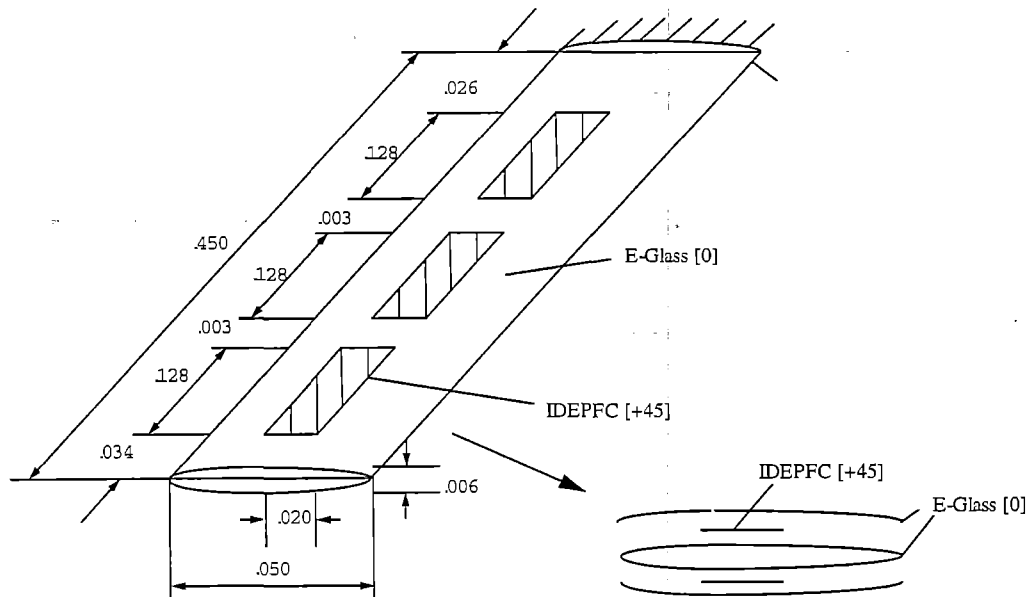
Single-Cell Active Blade Test Case
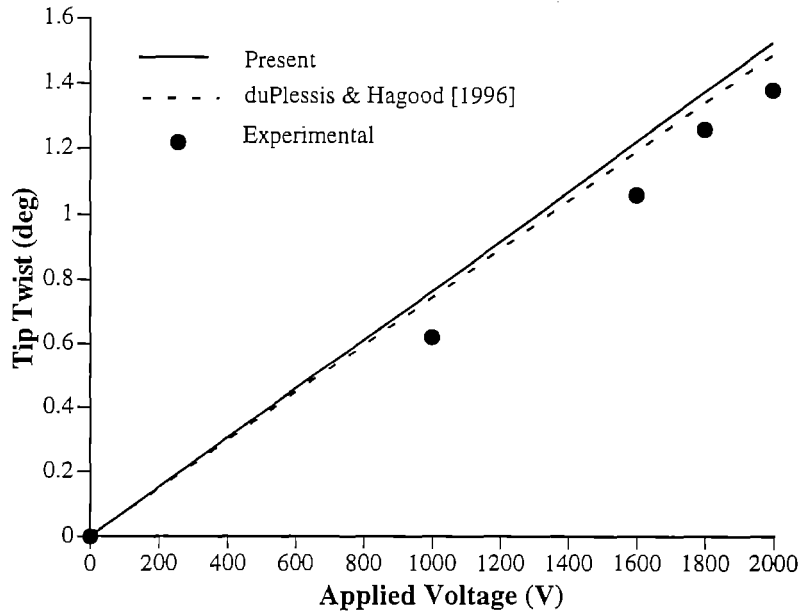
Conclusions

- A framework for designing active twist rotor blades was presented:

    → thin-walled two-cell cross-sectional analysis with active material layers

    → 1-D nonlinear beam equations (extension of Hodges [1990])

- Test and validation of each component of the analyses show good correlation with available data.

- More correlation is expected against the experimental data to be collected from the Boeing/MIT CH47-D blade test.

Nonlinear Bending of Anisotropic Tubes – Analytical Solution Using the Variational-Asymptotic Method

Dineshkumar Harursampath[*]and Dewey H. Hodges[†]
School of Aerospace Engineering
Georgia Institute of Technology, Atlanta, Georgia

1   Introduction

Beams of a circular cross section present a very striking nonlinearity in bending due to the reduction in bending stiffness with increasing deflection. This has motivated a rigorous study of tubular beams. An infinitely long thin tube, made of a generally anisotropic material, has been modeled as a beam, including those nonlinear effects that need to be considered, by virtue of its special geometry, to obtain asymptotical correctness. This was achieved by deriving its strain energy function in terms of 1-D quantities only.

   The Brazier effect, exhibited in tubular beams undergoing bending, is a well-known example of certain important phenomena that are not captured by a linear cross-sectional analysis. Brazier[1] was the first to take into account the nonlinear growth in curvature of thin-walled isotropic cylindrical tubes under pure bending due to the ovalization of the cross-section, resulting eventually in collapse at the maximum possible moment. Later Reissner published a series of improved results in Refs. 2 – 4. Thurston[5] has contributed substantially to this field, refining these results as well as extending them to include normal pressure, elliptic cross-sections and curved beams. Recently Li[6] investigated the dynamic instability of long isotropic circular cylindrical shells. Finally, there are a few treatments of orthotropic tubes by Spence and Toh,[7] Kedward[8] and Bert and Libai[9] The most recent work is that of Tatting, Gürdal and Vasiliev,[10] where the analysis is based on Vlasov's semi-membrane theory and the solution obtained using finite difference techniques. However, an asymptotically correct treatment of generally anisotropic circular tubes, with either analytical or numerical results, is not found in the literature.

   The Variational-Asymptotic Method (VAM) has been successfully used as a tool for dimensional reduction to obtain asymptotically correct closed form solutions to beam problems in earlier papers by the authors [Refs. 11 – 12]. Starting from Classical Laminated Shell Theory, VAM was used in this work as a tool to carry out the dimensional reduction from 2-D to 1-D. As a result the Brazier effect has been captured analytically. Previous results are
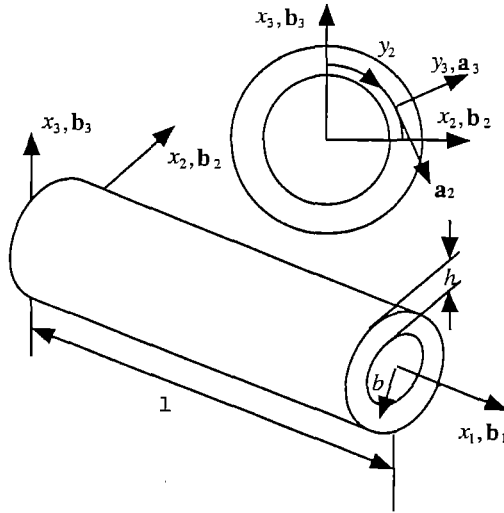
1

Figure 1: Circular Tube Configuration and Coordinate System

compared and shown to differ due to the asymptotically correct nature of the present result. The final paper would also include a numerical solution validating the analytical solution provided in this extended abstract.

2 Analysis

Asymptotic methods require small parameters. From the geometry of the tube, shown in Fig. 1, the natural small parameters in this problem are the thickness-to-radius ratio $(\delta_h = h/R)$ and the radius-to-length ratio $(\delta_R = R/\ell)$. The Cartesian coordinate measures x_i and the corresponding unit vectors $\mathbf{b}_i$ are directed as indicated. In order to take advantage of the thinness of the wall, a transformation of coordinates is best effected at this stage by introducing the cross-sectional arc-length y_2 and thickness coordinate y_3, along with corresponding unit vectors $\mathbf{a}_2(y_2)$ and $\mathbf{a}_3(y_2)$.

2.1 Kinematics

The position vector from a point fixed in an inertial reference frame a to an arbitrary material point in the undeformed tube is then

$$\check{\mathbf{r}}(y_1, y_2, y_3) = y_i \mathbf{a}_i. \tag{1}$$

If $u_i(y_1, y_2, y_3)$ are the 3-D displacement measures of an arbitrary material point, the position vector in the deformed configuration is given by

$$\check{\mathbf{R}}(y_1, y_2, y_3) = \check{\mathbf{r}} + u_i \mathbf{a}_i. \tag{2}$$

2

The contravariant base vectors $\mathbf{g}^i$ for the undeformed geometry and the covariant base vectors $\mathbf{G}_i$ for the deformed geometry are determined by standard means. We can now evaluate the deformation gradient tensor

$$\mathbf{A} = \mathbf{G}_i \mathbf{g}^i \tag{3}$$

and arrange its components in mixed bases into a matrix A. This enables determination of the zeroth order approximation to the 3-D Green strains

$$\Gamma = \frac{A^T A - I_3}{2} \tag{4}$$

where I_3 is the identity matrix. Using 3-D elasticity model, the strain energy per unit volume

$$U_{3D} = \frac{1}{2} E^{ijkl} \Gamma_{ij} \Gamma_{kl} \tag{5}$$

is obtained. A preliminary order of magnitude analysis is performed, retaining only the leading order terms in the energy. The mimimization of the energy gives rise to the following zeroth order approximations to the 3-D displacements:

$$\begin{aligned}
u_1^0(y_1, y_2, y_3) &= q_1(y_1) \\
u_2^0(y_1, y_2, y_3) &= q_2(y_1) + q_3(y_1) \cos\left(\tfrac{y_2}{R}\right) - q_4(y_1) \sin\left(\tfrac{y_2}{R}\right) \\
u_3^0(y_1, y_2, y_3) &= -\tfrac{q_2^2(y_1)}{2R} + q_4(y_1) \cos\left(\tfrac{y_2}{R}\right) + q_3(y_1) \sin\left(\tfrac{y_2}{R}\right)
\end{aligned} \tag{6}$$

The classical degrees of freedom extracted above are extension(q_1), torsion(q_2) and bending(q_3 and q_4).

The 3-D displacement field is then given by

$$u_i = u_i^0 + \overline{w}_i(y_1, y_2, y_3) \tag{7}$$

where $\overline{w}_i$ is the warping field. Motivated by the smallness of δ_h and the linearity of the Classical Laminated Shell Theory, we assume a linear expansion of the warping displacements about the thickness coordinate:

$$\overline{w}_i = w_i(y_1, y_2) + y_3 \phi_i(y_1, y_2). \tag{8}$$

Note that w_i are the warping measures of the middle surface material elements; ϕ_α are local rotation variables; and ϕ_3 is a measure of change in shell thickness. Due to the extraction of the rigid body displacements of the cross section at the zeroth order approximation, it can be shown that the warping variables are governed by the following constraints:

$$\begin{aligned}
\langle w_1 \rangle &= 0 \\
\left\langle \phi_2 \cos\left(\tfrac{y_2}{R}\right) + \phi_3 \sin\left(\tfrac{y_2}{R}\right) \right\rangle &= 0 \\
\left\langle w_2 \cos\left(\tfrac{y_2}{R}\right) + w_3 \sin\left(\tfrac{y_2}{R}\right) \right\rangle &= 0 \\
\left\langle w_3 \cos\left(\tfrac{y_2}{R}\right) - w_2 \sin\left(\tfrac{y_2}{R}\right) \right\rangle &= 0
\end{aligned} \tag{9}$$

where the angle brackets denote averaging around the mid-circumference.

3

2.2 Strain Energy in Bending

The stiffness coefficients for Classical Laminated Shell Theory are given by

$$C^{\sigma\nu\omega\theta} = E_{||}^{\alpha\beta\gamma\delta}\, \bar{\mu}_{\alpha}^{\sigma}\bar{\mu}_{\beta}^{\nu}\bar{\mu}_{\gamma}^{\omega}\bar{\mu}_{\delta}^{\theta} \tag{10}$$

where $\bar{\mu}_1^1 = 1$, $\bar{\mu}_1^2 = 0$, $\bar{\mu}_2^1 = 0$ and $\bar{\mu}_2^2 = 1 + \frac{y_3}{R}$.

Due to circular symmetry of the tube, bending in any one direction is similar to that in any other and there is no bending-torsion or bending-extension coupling. Hence extension-torsion and bending can be treated as two independent problems for any arbitrary material layup. Thus, in the analysis of the bending problem, three of the four classical degrees of freedom can be dropped for simplicity, without affecting any desired information. The only degree of freedom to be retained is q_3.

There are certain terms in the strain components which individually have an order of magnitude larger than that of the largest strain measure. However each of these is killed by other such terms in the same strain component. One such relation is between w_1 and ϕ_2:

$$w_{1,2} = q_3{}' \left[\phi_2 \sin\left(\frac{y_2}{R}\right) - \cos\left(\frac{y_2}{R}\right) \right] \tag{11}$$

Upon completion of an order of magnitude analysis for the energy terms, the shell bending strain energy density is given by

$$U_{2D} = \frac{1}{2} \left\{ \begin{array}{c} w_1{}' \\ \phi_{2,2} \end{array} \right\}^T \left[\begin{array}{cc} A_{11} & B_{12} \\ B_{12} & D_{22} \end{array} \right] \left\{ \begin{array}{c} w_1{}' \\ \phi_{2,2} \end{array} \right\} \tag{12}$$

where A_{11}, D_{22} and B_{12} are membrane, bending and coupling stiffnesses defined similar to those in Classical Laminated Plate Theory, but with $E_{||}^{\alpha\beta\gamma\delta}$ replaced by $C^{\alpha\beta\gamma\delta}$, defined in Eq. (10).

The beam strain energy density (the integral of U_{2D} over the shell mid circumference) is then minimized with respect to the warping field subject to Eq. (9) and Eq. (11).

This requires solving the following differential equations:

$$R^3\, \rho \sin^2\theta\, A_{11}\, \psi - R\, \cos\theta\, B_{12}\, \psi_{,\theta} + R^2\, \rho \sin^2\theta\, B_{12}\, \phi_{2,\theta} +$$
$$R\, \sin\theta\, B_{12}\, \psi_{,\theta\theta} - \cos\theta\, D_{22}\, \phi_{2,\theta\theta} + \sin\theta\, D_{22}\, \phi_{2,\theta\theta\theta} \ = 0 \tag{13}$$
$$R\, \rho \cos\theta + R\, \rho \sin\theta\, \phi_2 - \psi_{,\theta} \ = 0 \tag{14}$$

where $\theta = \frac{y_2}{R}$, $\rho = q_3{}''$ and $\psi = w_1{}'$. These differential equations are solved by a Fourier series approximation for an infinitely long tube. This boundary value problem has also been solved numerically using the shooting method for comparison. The numerical results would be presented at the workshop.

4
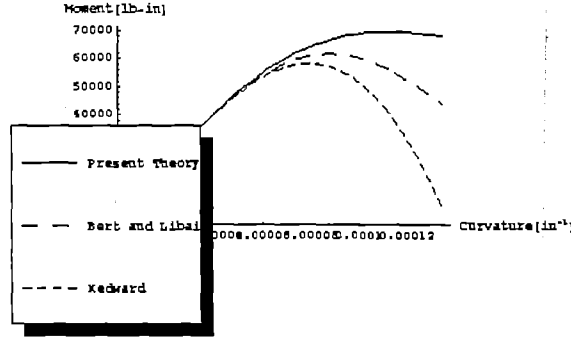
Figure 2: Nonlinear Bending of $[0°_8]$ Laminates

3   Results

Defining $\mu = \frac{D_{22}}{R^2 A_{11}}$, the first order approximation to the mid-surface warping field is given (upto 4th harmonics) by:

$$
\begin{aligned}
w_1 =&\ -q'\frac{(R\rho)^2}{3(16\mu+(R\rho)^2)}\sin(3\theta)\\
w_2 =&\ -\frac{32\mu(R\rho)^2+32\mu q'^2(R\rho)^2+2(R\rho)^4+q'^2(R\rho)^4}{3(16\mu+(R\rho)^2)^2}\sin(2\theta)+\frac{4(R\rho)^4}{15(16\mu+(R\rho)^2)^2}\sin(4\theta)\\
w_3 =&\ -\frac{32\mu q'^2(R\rho)^2+4(R\rho)^4+q'^2(R\rho)^4}{4(16\mu+(R\rho)^2)^2}+\frac{256\mu(R\rho)^2+160\mu q'^2(R\rho)^2+16(R\rho)^4+5q'^2(R\rho)^4}{12(16\mu+(R\rho)^2)^2}\cos(2\theta)\\
&\ -\frac{(R\rho)^4}{15(16\mu+(R\rho)^2)^2}\cos(4\theta)
\end{aligned}
\tag{15}
$$

Substituting for the warping field, one obtains the final expression for the beam strain energy density in bending. By differentiating it with respect to the elastic curvature, an expression for the bending moment in terms of the elastic curvature is determined:

$$
\begin{aligned}
M =&\ \pi R^3 \rho A_{11} - \frac{2\pi R^{15}\rho^7 A_{11}{}^4}{(R^4\rho^2 A_{11}+16 D_{22})^3} - \frac{32\pi R^{11}\rho^5 A_{11}{}^3 D_{22}}{(R^4\rho^2 A_{11}+16 D_{22})^3} + \frac{5\pi R^{11}\rho^5 A_{11}{}^3}{(R^4\rho^2 A_{11}+16 D_{22})^2}\\
&\ + \frac{32\pi R^7\rho^3 A_{11}{}^2 D_{22}}{(R^4\rho^2 A_{11}+16 D_{22})^2} - \frac{4\pi R^7\rho^3 A_{11}{}^2}{R^4\rho^2 A_{11}+16 D_{22}}
\end{aligned}
\tag{16}
$$

For small bending moments, this result is close to that of Kedward[8] However it significantly differs for large moments as shown in Figs. 2 – 4 for three different layups, the properties of which can be found in Kedward's paper.

Kedward's simple but excellent result has terms only upto $O[\rho^3]$. These terms match with the series expansion of our results. The improved result of Bert and Libai[9]

$$
M = \pi R^3 \rho A_{11} - \frac{\pi R^7 \rho^3 A_{11}{}^2}{8 D_{22}} + \frac{5\pi R^{11}\rho^5 A_{11}{}^3}{1152 D_{22}{}^2} + O[\rho^9]
\tag{17}
$$

differs from the current result for terms of $O[\rho^5]$ and higher.

5

Table 4.1: Rotor properties

Number of blades	3	
Radius of rotor disc	3.81	m
Blade cord	35.6	cm
Blade mass	47.48	kg
Precone angle	2.5	deg
Autorotation inertia	109.89	kgm^2
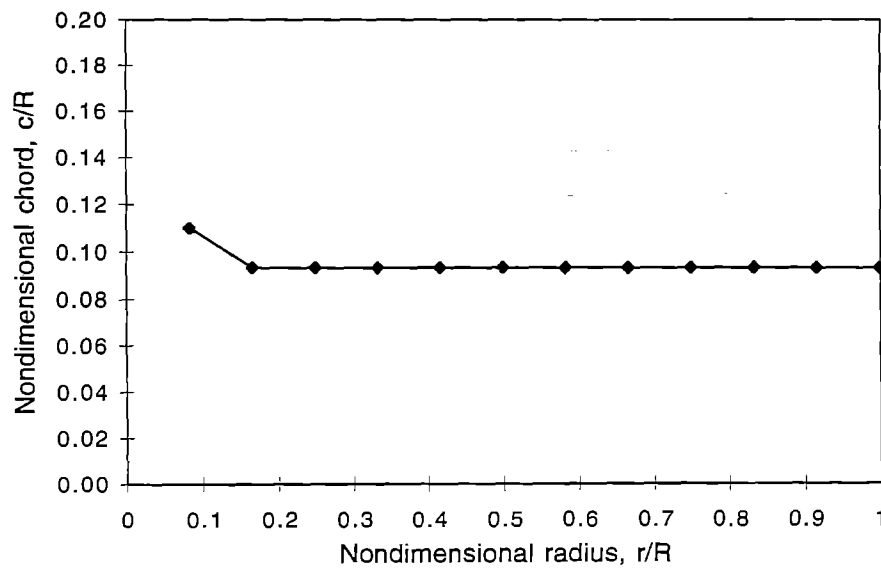
Figure 4.1: Blade chord distribution
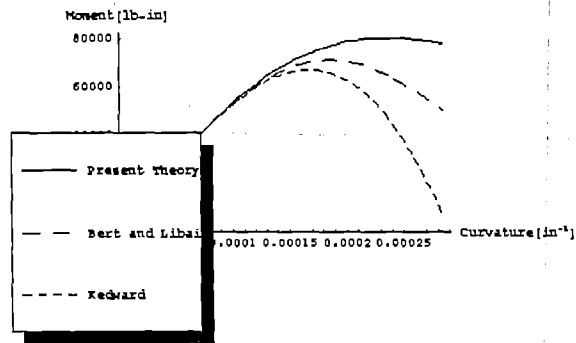
Figure 3: Nonlinear Bending of $[0°_2, \pm45°]_s$ Laminates
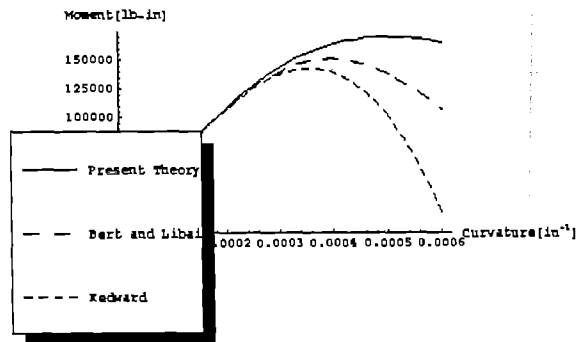
Figure 4: Nonlinear Bending of $[\pm45°, 0°_2]_s$ Laminates

The nondimensional nonlinear bending stiffness is given by

$$\overline{EI} \doteq \frac{\frac{\partial M}{\partial \rho}}{\pi R^3 A_{11}} = 1 - \frac{3(\rho R)^2}{8\mu} + \frac{15(\rho R)^4}{256\mu^2} + O[\rho^6] \quad (18)$$

Maximizing the moment with respect to the elastic curvature, the limit moment is obtained. Further bending occurs at a dropping moment which characterizes a limit load instability.

$$M_{cr} = \frac{3\sqrt{3}\,\pi\,R\,\sqrt{A_{11}}\,\sqrt{D_{22}}}{4} \quad (19)$$

The coefficient obtained by Kedward is $\frac{4\sqrt{2}}{3\sqrt{3}}$ instead of $\frac{3\sqrt{3}}{4}$, resulting in an estimate 16.2% lower than the current prediction. It should be noted that the recent numerical results obtained by Tatting et al[10] are very close to the approximate closed-form solution of Kedward.

4   Conclusions

An analytical result is obtained in this paper for the bending moment and stiffness of a long thin-walled circular tube. The presentation at the workshop would include numerical results validating the Fourier series solution. The warping of the cross section is obtained in closed form. The bending moment as a nonlinear function of the curvature is compared with those of Kedward[8] and Bert et al[9] The limit moment instability is evaluated and is shown to be higher than that in earlier works. Material failure and bifurcation buckling which are known to usually occur before limit moment instability[13] are not dealt with here. Whatever the mode of failure, it is strongly influenced by the nonlinear response. Moreover the response, by itself, is significant for tube design and analysis. And this paper provides a closed form solution which is quite different from all existing results, including numerical ones, due to its asymptotical correctness.

5   Acknowledgments

References

[1] Brazier, L. G., "On the Flexure of Thin Cylindrical Shells and Other Thin Sections," In *Proceedings of Royal Society of London Series A 116*, 1927, pp. 104 – 114.

[2] Reissner, E., "On Finite Bending of Pressurized Tubes," *Journal of Applied Mechanics*, Vol. 26, 1959, pp. 386 – 392.

[3] Reissner, E., "On Finite Pure Bending of Cylindrical Tubes," *Ingenieur-Archiv*, Vol. 15, 1961, pp. 165 – 172.

[4] Reissner, E. and Weinitschke, H. J., "Finite Pure Bending of Circular Cylindrical Tubes," *Quarterly of Applied Mathematics*, Vol. 20, No. 4, January 1963, pp. 305 – 319.

[5] Thurston, G.A., "Critical Bending Moment of Circular Cylindrical Tubes," *Journal of Applied Mechanics*, Vol. 44, 1977, pp. 173 – 175.

[6] Li, L. Y., "Approximate Estimates of Dynamic Instability of Long Circular Cylindrical Shells under Pure Bending," *International Journal of Pressure Vessels and Piping*, Vol. 67, 1996, pp. 37 – 40.

[7] Spence, J. and Toh, S. L., "Collapse of Thin Orthotropic Elliptical Cylindrical Shells under Combined Bending and Pressure Loads," *Journal of Applied Mechanics*, Vol. 46, 1979, pp. 363 – 371.

[8] Kedward, K. T., "Nonlinear Collapse of Thin-Walled Composite Cylinders under Flexural Loading," In *Proceedings 2nd International Conference on Composite Materials*, Toronto, Canada, 1978, pp. 353 – 365.

[9] Bert, C.W. and Libai, A., "The Generalized Brazier Problem for Orthotropic Straight Tubes of Finite Length," In *Proceedings of the 9th ASCE Conference on Engineering Mechanics*, College Station, Texas, May 1992, pp. 872 – 875.

[10] Tatting, B. F., Gürdal, Z., and Vasiliev, V. V., "Nonlinear Response of Long Orthotropic Tubes under Bending Including the Brazier Effect," *AIAA Journal*, Vol. 34, No. 9, September 1996, pp. 1934 – 1940.

[11] Cesnik, C. E. S., Hodges, D. H., Popescu, B., and Harursampath, D., "Composite Beams Cross-Sectional Modeling Including Obliqueness and Trapeze Effects," In *Proceedings of the 37th Structures, Structural Dynamics and Materials Conference*, Salt Lake City, Utah, April 15 – 17, 1996, pp. 1384 – 1397, AIAA Paper 96-1469.

[12] Hodges, D. H., Harursampath, D., and Cesnik, C. E. S., "Nonlinear Strain Field Effects in Anisotropic Strips," In *Proceedings of Recent Developments in Solid Mechanics*, Rio de Janeiro, Brazil, July 31 – August 2, 1996, pp. 71 – 78.

[13] Corona, E. and Rodrigues, A., "Bending of Long Cross-Ply Composite Circular Cylinders," *Composites Engineering*, Vol. 5, No. 2, 1995, pp. 163 – 182.

Refined Structural Modeling of Thick-Walled Composite Rotor Blades

Louis R. Centolanza, Department of Defense Fellow
Edward C. Smith, Assistant Professor

The Pennsylvania State University
Aerospace Engineering Department
University Park, PA 16801

Seventh International Workshop on Dynamics and Aeroelastic
Stability Modeling of Rotorcraft Systems

Abstract

In this presentation, a refined theory is developed that accurately models the cross-section elastic properties of thick-walled composite beams. The Vlasov-based model is refined to include a correction to the torsion component of the shear strain equation. In addition, a higher order plate theory is incorporated into the plate segment constitutive equations. The shear strain correction influences the torsion behavior while the higher order plate theory influences the transverse shear behavior. The theory is validated against 3-D finite element results. Baseline Vlasov theory does not accurately capture the thick-walled effects while the results generated by refined theory closely match the finite element results. The refined theory is used in parametric studies to determine the limits of Vlasov theory in predicting the cross-sectional properties of thick-walled beams. Because of the shear strain related effects, differences in results generated by Vlasov and the refined theory start to become significant at a thickness to depth ratios of approximately 15%. Results show that neglecting transverse shear has a noticeable effect on the coupling and stiffness calculations and lateral deflection under bending load calculations.

PENNSTATE

Refined Structural Modeling of Thick-Walled Composite Rotor Blades

Louis R. Centolanza, Department of Defense Fellow
Edward C. Smith, Assistant Professor

7th International Workshop on Dynamics and Aeroelastic
Stability Modeling of Rotorcraft Systems

October 15, 1997

PENNSTATE

Presentation Outline

➤ • **Introduction**
 - **Background**
 - **Related Research**
 - **Objectives**

• **Derivation of Refined Theory**

• **Finite Element Models for Validation**

• **Validation and Parametric Studies**

• **Conclusions**

PENN STATE

Benefits of composite rotor blades
• Improved fatigue life
• Hingeless and bearingless rotor designs
• Beneficial elastic couplings for enhanced
     stability, reduced vibration, improved performance

Vlasov Theory can be a valuable tool for blade design
• Models multi-cell cross-sections of arbitrary shape
• Does not require detailed finite element computations
• Produces accurate results for thin-walled beams

Background

PENN STATE

Some rotor blades have thick-walled cross sections

Lynx
30% t/d

t

CH-46
25%-30% t/d
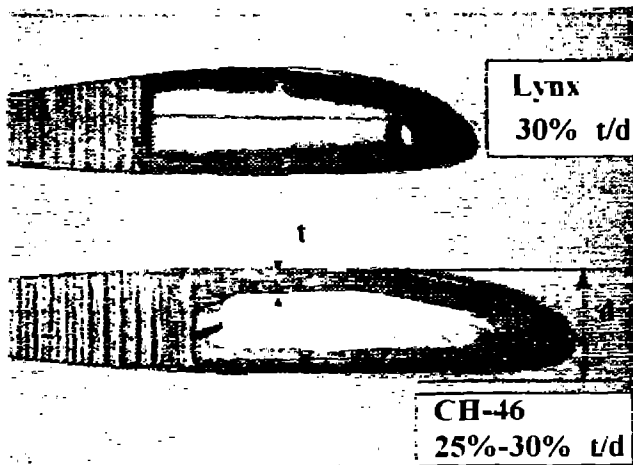
Kim and White (University of Illinois 1995-97)

- Thick-walled model that is extension of Smith and Chopra
- Validated with 3-D finite element
- Model includes both contour and thickness warping
- Developing warping function for representative blade cross-sections can be complex

Song and Librescu (Virginia Tech 1993)

- Free vibration of thick-walled composite box beams
- Incorporated first order transverse shear into theory

McCarthy, Chattopadhyay, Zhang, Jha (ASU 1996-97)

- Composite plate FE used to model thick-walled box beams
- Validated only against thin-walled data and models
- Model used in fixed wing flutter studies
- Higher order transverse shear distribution in plate segments

Hodges, Cesnik, et al (Georgia Tech 1993-95)

- Composite beam and plate models based on variational-asymptotic methods
- Predict cross sectional properties using 6 noded isoparametric elements

PENN STATE

Kollbrunner and Basler (1969)

- Studied the influence of thick walled effects on shear flow behavior of isotropic beams
- Derived equations for additional shear strain and torsional moment

ε_{zs}
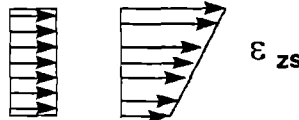
Reddy (1984)

- Developed higher order plate

  theory for laminated composite plates
- Stress-free boundary conditions satisfied

ε_{nz}
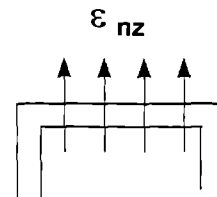
PENN STATE

Chandra and Chopra (University of Maryland 1992)

- Refined Vlasov theory to include transverse shear deformation of the cross-section
- Validated theory with experimental results

Centolanza, Smith, Kumar (Penn State 1995-1997)

- Refined Vlasov theory to include shear center calculation
- Performed preliminary structural dynamic analysis
- Non-uniform spanwise ply lay-up affects the twist component of the flap-torsion mode shape

Objectives

- Refine Vlasov Theory to improve accuracy of cross-section property calculations of thick-walled composite beams

  - Correction factor in shear strain eqn to account for non-uniform distribution of shear strain
  - Higher order transverse shear distribution in plate segment constitutive eqns

- Validate refined theory with 3-D solid element results

- Conduct parametric studies to determine limitations of Vlasov in modeling thick-walled cross-sections

Presentation Outline

- Introduction

→ - Derivation of Refined Theory

- Finite Element Models for Validation

- Validation and Parametric Studies

- Conclusions

Baseline Vlasov Derivation

- Plate segment displacements are expressed in terms of blade displacements (ε_z, $\boxed{\varepsilon_{zs}}$, κ_z, κ_{zs}, $\boxed{\varepsilon_{nz} = 0}$)

- Plate forces expressed in terms of plate displacements through $\boxed{ABD}$ matrices (N_z, N_{zs}, M_z, M_{zs})

Baseline Vlasov Derivation
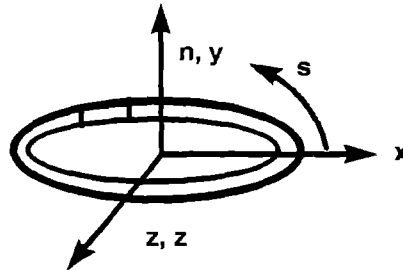
- Blade forces are related to plate forces through the principal of virtual work (N, M_x, M_y, T, M_w, $\boxed{F_x, F_y, G_x, G_y}$)

- Blade forces are finally related to blade displacements through a 9x9 stiffness matrix
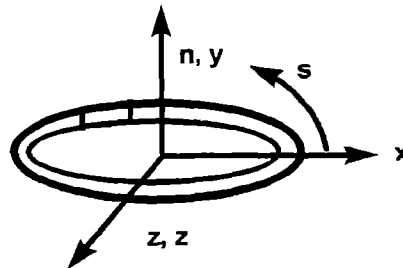
Shear Strain Correction

Shear Flow models assume uniform shear stress distribution

- Torsion component of shear strain eqn in Vlasov theory is based on this approach

$$\varepsilon_{zs} = \frac{\boxed{G_s(s)}\, \phi'_z(z)}{G_{eff}\, t}$$

Shear flow related G_s needs to be adjusted with a correction factor

---

Shear Strain Correction

Width

Wall Thickness

Depth

ε_{avg}

$\Delta\varepsilon$
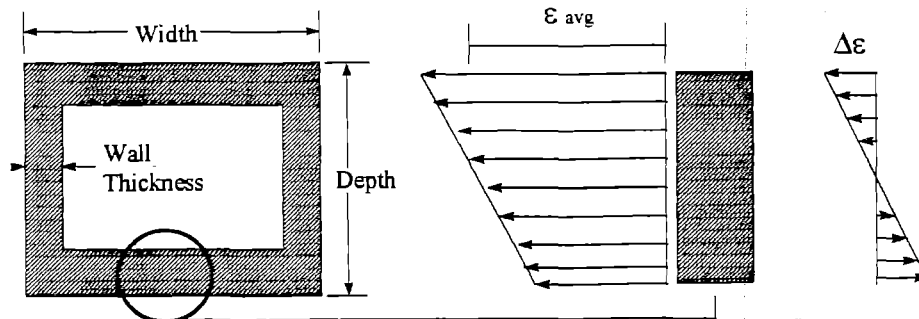
Shear strain no longer uniform through thickness

Shear Flow Correction

Additional shear strain results in an additional torsional moment:

$$\Delta\ T/T\ =\ \int t^3\ /\ 3J\ ds$$

Shear flow eqns:

$$G_{s\ thin}\ =\ T\ /\ 2A$$

$$G_{s\ thick}\ =\ (T\ +\ \Delta\ T)\ /\ 2A$$

Rearranging:

$$G_{s\ thick}\ =\ c\ G_{s\ thin}$$
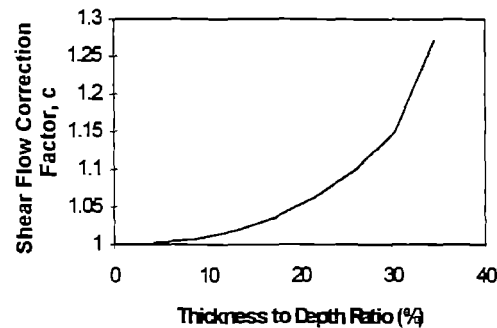
Correction factor: $c\ =\ 1\ +\ \Delta\ T\ /\ T$

Shear Strain Correction

The correction factor is incorporated into the shear strain eqn

• Correction influences the stiffnesses associated with torsion

For example:

The bending-torsion coupling stiffness:

$$K_{25} = \int [\ -2\ B_{16}\ y\ +\ \boxed{c\ A_{16}\ y\ G_s\ /\ Gt}\ -\ 2\ D_{16}\ \cos\ \theta$$

$$+\ \boxed{c\ B_{16}\ G_s\ \cos\ \theta\ /\ G\ t}\ ]\ ds$$

The refined theory assumes that any general plate segment is now governed by the higher order plate theory (Reddy)

• Formulation includes higher order stiffness matrices, force resultants, and curvatures not in CLPT

$$\begin{Bmatrix} N \\ M \\ P \end{Bmatrix} = \begin{bmatrix} A & B & E \\ B & D & F \\ E & F & H \end{bmatrix} \begin{Bmatrix} \varepsilon \\ \kappa \\ \kappa^2 \end{Bmatrix}$$

$(E_{ij}, F_{ij}, H_{ij}) = \int Q_{ij} (z^3, z^4, z^6) \, dz$

Q_{44} and Q_{55} also included

The transverse shear in a plate segment is no longer zero

• Plate segment transverse shear strain is related to cross section transverses shear deformations through geometric considerations

$\varepsilon^{\circ}_{nz} = \varepsilon_{xz} \sin \theta - \varepsilon_{yz} \cos \theta$
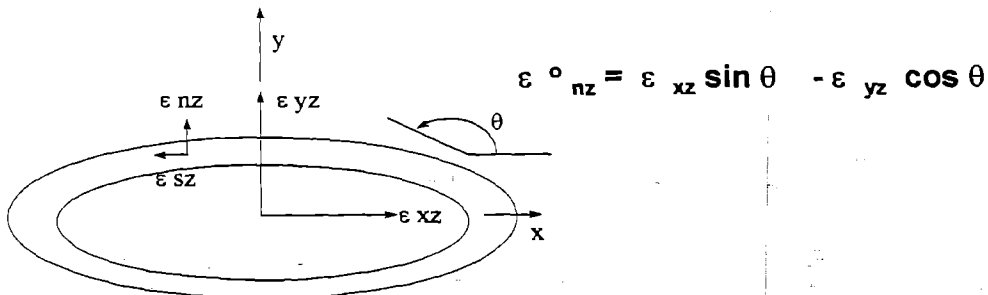
Higher Order Transverse Shear Theory

PENNSTATE

Higher order terms now appear in the derivation of the 9x9 stiffness matrix.

For example:

Energy Eqn:

$$\Pi = 1/2 \int (N_z \varepsilon_z + N_{zs} \varepsilon_{zs} + M_z \kappa_z + M_{zs} \kappa_{zs} + \boxed{P_z \kappa_z^2 + P_{zs} \kappa_{zs}^2 +}$$

$$\boxed{Q_z \varepsilon_{nz} + R_z \kappa_{nz}^2}) \ ds$$

Transverse Shear Blade Force Eqn:

$$G_x = \int (N_{zs} \cos \theta + \boxed{Q_z \sin \theta - 4/h^2 \ R_z \sin \theta}) \ ds$$

Higher Order Transverse Shear Theory

PENNSTATE

Incorporating the higher order theory leads to a refinement of the stiffnesses associated with transverse shear

For example:

Transverse shear stiffness:

$$K_{66} = \int [A_{66} \cos^2\theta - \boxed{A_{55} \sin^2\theta - 8/h^2 \ D_{55} \sin^2\theta}$$

$$+ \boxed{16/h^4 \ F_{55} \sin^2\theta}] \ ds$$

10

Presentation Outline

- Introduction

- Derivation of Refined Theory

→ • Finite Element Models for Validation

- Validation and Parametric Studies

- Conclusions

Finite Element Models Used for Validation

Solid parametric brick elements are used in the detailed
finite element modeling of the composite blades

- Advantage of refined theory is that it gives results of
  comparable accuracy to that of FEM in a fraction of the time

- Run Time: FEM - 15 minutes   Refined Vlasov - 2 seconds

- Finite element results were generated using IDEAS Master
  Series 3 and NASTRAN Version 69.1

Finite Element Models Used for Validation

PENNSTATE

Element convergence study conducted
- 1156 total elements
- 68 cross-section elements

Solid parabolic element has
20 nodes with 3 dof/node
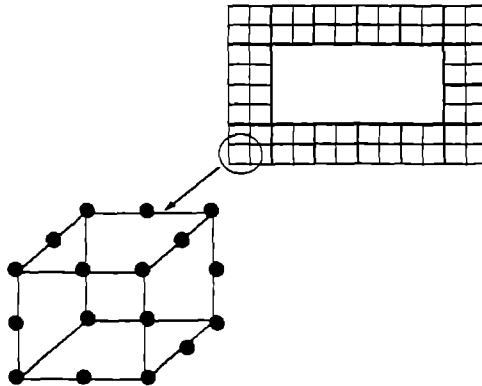
Presentation Outline

PENNSTATE

- Introduction

- Derivation of Refined Theory

- Finite Element Models for Validation

→ • Validation and Parametric Studies

- Conclusions

Validation: Tip Twist Due to Tip Torque
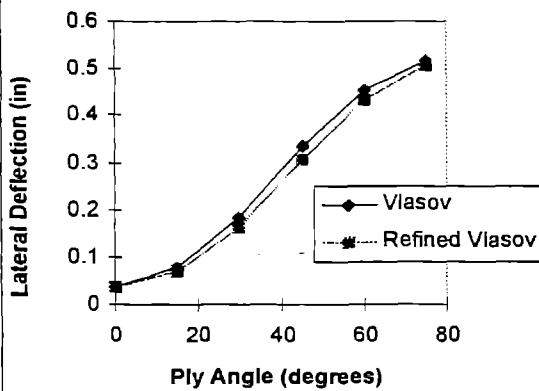
PENNSTATE
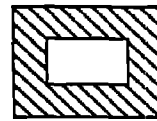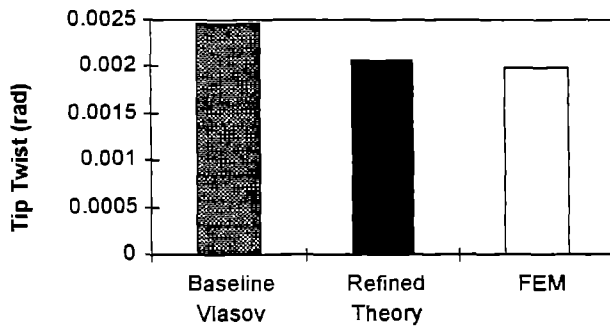
15° Bending-Torsion Coupled Graphite/Epoxy Box Beam
(L/D = 20)

Validation: Lateral Deflection Due to Tip Torque

PENNSTATE
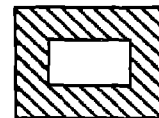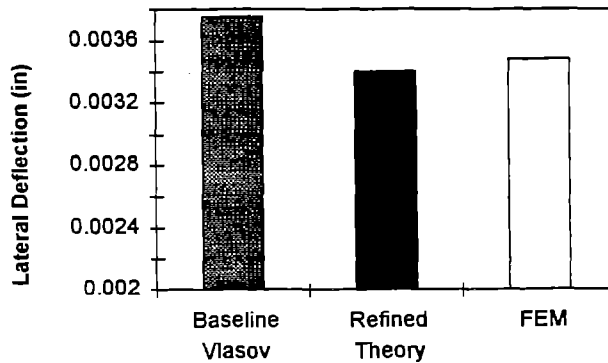
15° Bending-Torsion Coupled Graphite/Epoxy Box Beam
(L/D = 20)

Validation: Tip Deflection Due to Tip Bending Load
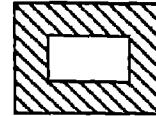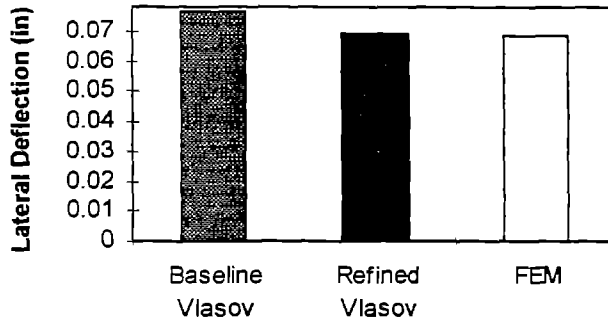
25% Thick Box Beam

15° Extension-Torsion Coupled Graphite/Epoxy Box Beam (L/D = 20)

Validation

Refined theory also validated for other cases
- Other ply lay-ups (0,30,45,90 degrees)
- Isotropic materials
- E-T coupled beams
- Through the thickness change in laminate

Validation Results
- Baseline Vlasov theory does not accurately capture the thick-walled effects
- Results generated by refined theory closely match the finite element results.

Parametric Studies

Goal is to determine the limitations of Vlasov in modeling thick-walled cross-sections

- First study investigates the role of the wall thickness

ε_{zs} vs
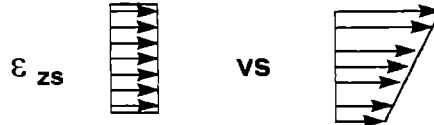
- Second study determines the role of transverse shear

ε_{nz}

ε_{zs}
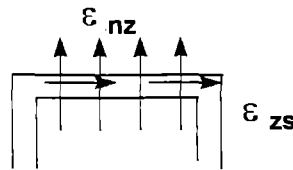
Parametric Study: Bending-Torsion Coupling as a Function of Thickness Ratio

Bending-Torsion Coupling Coefficient, K25 (lb-in) vs Thickness to Depth Ratio (%)

- Vlasov
- Refined Vlasov

Percent Difference in K25 (%) vs Thickness to Depth Ratio (%)
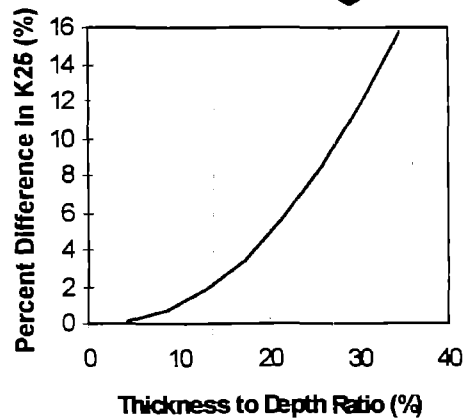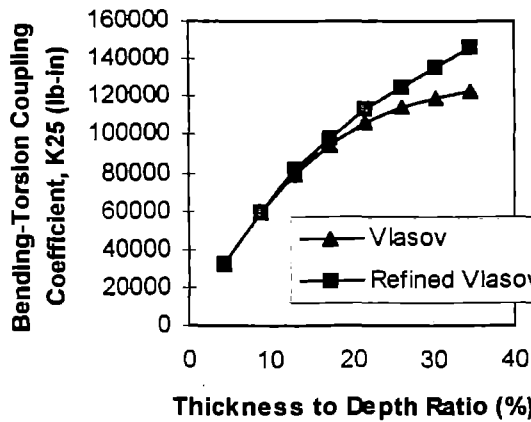
15° Bending-Torsion Coupled Graphite/Epoxy Box Beam
(L/D = 20)

Parametric Study: Tip Twist Due To Tip Torque as Function of Thickness Ratio

PENNSTATE
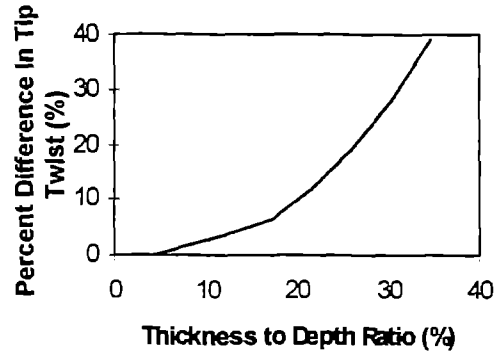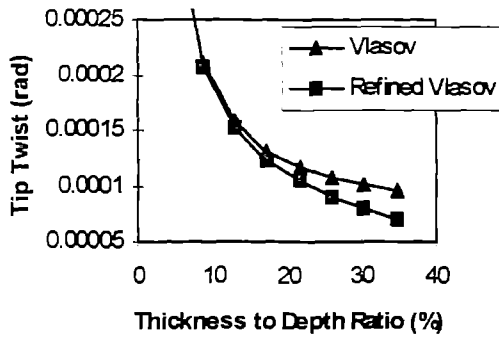
15° Bending-Torsion Coupled Graphite/Epoxy Box Beam
(L/D = 20)

Parametric Study: Lateral Deflection Due to Tip Bending Load
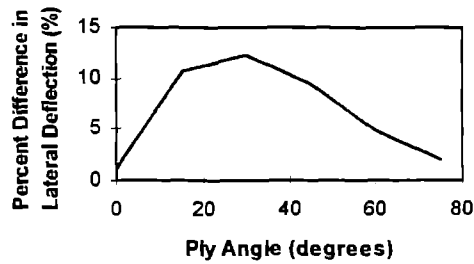
PENNSTATE

25% Thick E-T Graphite/Epoxy Box Beams of
Varied Ply Angles (L/D = 20)

16

Parametric Study: Lateral Deflection Due to Tip Bending Load
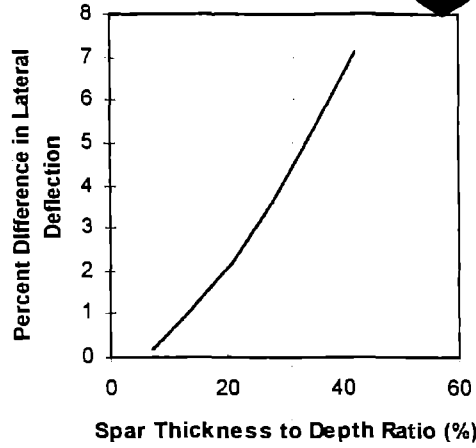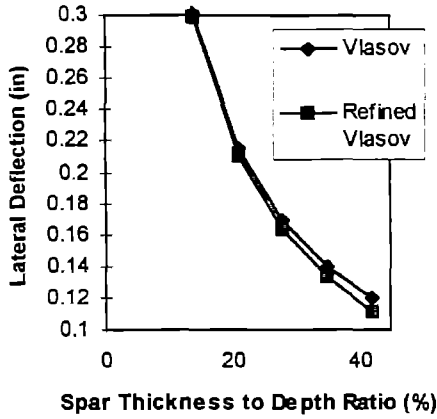
PENN**S**TATE

E-T NACA 0012 Graphite/Epoxy Blades of Varied Spar Thickness (spar $[15]_n$ skin $[+/-45]$)

Parametric Studies: Transverse Shear Stiffness

PENN**S**TATE
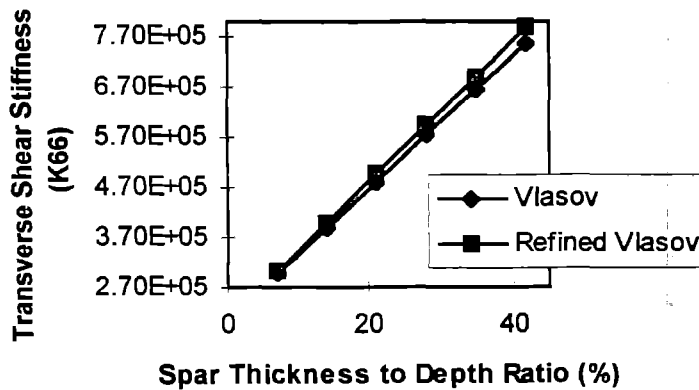
E-T NACA 0012 Graphite/Epoxy Blades of Varied Spar Thickness (spar $[15]_n$ skin $[+/-45]$)

17

Presentation Outline

PENNSTATE

- Introduction

- Derivation of Refined Theory

- Finite Element Models for Validation

- Validation and Parametric Studies

⟶ • Conclusions

Conclusions

PENNSTATE

- A refined theory was developed that accurately predicts the cross-sectional properties of thick walled composite beams

- The refined theory was validated against 3-D solid element

- Advantage of refined theory is that it gives results of comparable accuracy to that of FEM in a fraction of the time

Conclusions

- Baseline Vlasov tends to breakdown for thickness ratios of approximately 15% due to shear strain effects

- Transverse shear effects on bending stiffness can be noticed for ply angles in the 15° to 45° range and for thickness ratios greater than 20%

- Shear strain correction has a larger effect than higher order transverse shear theory

Asymptotically Correct Numerical Evaluation of Shear Effects in Composite Beams

Bogdan Popescu   Dewey H. Hodges

7th International Workshop on Dynamics and Stability Modeling of Rotorcraft Systems, Saint Louis, October 14-16, 1997

Abstract

The inclusion of the along-the-axis variation of the strain measures is considered in an asymptotically correct analysis. Consequently, the shear effect is captured as a refinement of the classical theory of beams. This leads to a Timoshenko-like formulation of the stiffness properties of the beam cross section which is important for short beams and high frequency vibrations. The way is also open for the study of other effects related to axial variation of the strain, as the Vlasov effect which is responsible for the restrained torsion of thin walled beams. The method applies for arbitrary geometries of the cross section and general anisotropic material and is based on a finite element formulation which confers the desired generality to treat complex structural configurations.

Asymptotically Correct Numerical Evaluation of Shear Effects in Composite Beams

Bogdan Popescu   Dewey H. Hodges

Saint Louis, October 14–16, 1997

1 Motivation

- Developing a tool to rigorously (*i.e.*, asymptotically correct) treat beam-like structures, especially helicopter rotor blades configurations where certain effects cannot be neglected. It is meant to cover:

1. general anisotropic material.

2. arbitrary cross-sectional geometry.

3. quick and compact results which allow for efficient structural analysis.

- This is further used in:

1. basic blade design.

2. dynamic analysis (vibrations).

3. aeroelastic studies of rotor blades.

4. global system dynamics of the rotor as a component of the whole structure.

2 Background

- Timoshenko's work in 1921

- Giavotto, Borri, Maffioli and Mussi (1983) – general cross-section.

- Berdichevschii and Starosel'skii (1983) – asymptotic theory was developed for the isotropic case.

- variational–asymptotic method is capable of taking advantage of the presence of small parameters in the model (Berdichevsky, 1982).

$$U = \mu\,\varepsilon^2 \left(\underbrace{1}_{\text{classic}} + \underbrace{\varepsilon}_{\text{trapeze}} + \underbrace{\left(\frac{h}{R}\right)^2}_{\text{initial } \kappa} + \underbrace{\left(\frac{h}{l}\right)^2}_{\text{shear}} + ... \right)$$

3   Method of Solution

3.1   Beam Kinematics

The position vector of an arbitrary point on the cross section

$$\bar{\mathbf{r}}(x_1, x_2, x_3) = \mathbf{r}(x_1) + x_\alpha \, \hat{\mathbf{t}}_\alpha \, (x_1) \tag{1}$$

$$\overline{\mathbf{R}}(x_1, x_2, x_3) = \mathbf{R}(x_1) + x_\alpha \, \hat{\mathbf{T}}_\alpha \, (x_1) + w_i(x_1, x_2, x_3) \, \hat{\mathbf{T}}_i \, (x_1) \tag{2}$$

$\hat{\mathbf{T}}_1$ is tangent to the beam axis, $\hat{\mathbf{B}}_\alpha$ are in the plane of the deformed beam cross-sectional plane.

$$\epsilon = \max(\gamma_{11}, 2\,\gamma_{12}, 2\,\gamma_{13}, h\,\kappa_1, h\,\kappa_2, h\,\kappa_3)) \tag{3}$$
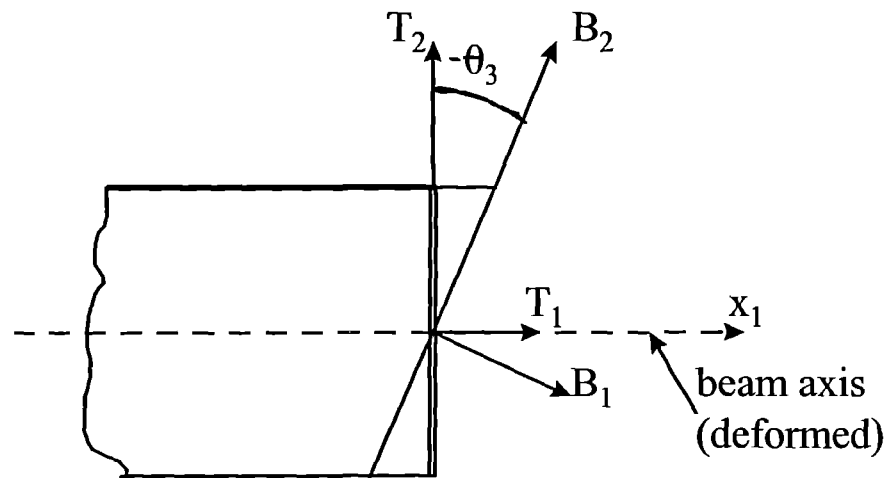
Figure 1: Reference systems for the shear effect in the deformed configuration

The definition of curvature due to deformation for prismatic beams

$$\hat{T}_i' = \beta \times \hat{T}_i \tag{4}$$

$$\hat{B}_i' = \kappa \times \hat{B}_i \tag{5}$$

$$\left\{ \begin{array}{c} \hat{B}_1 \\ \hat{B}_2 \\ \hat{B}_3 \end{array} \right\} = \left[\begin{array}{ccc} 1 & \theta_2 & -\theta_3 \\ -\theta_2 & 1 & 0 \\ \theta_3 & 0 & 1 \end{array} \right] \left\{ \begin{array}{c} \hat{T}_1 \\ \hat{T}_2 \\ \hat{T}_3 \end{array} \right\} \tag{6}$$

This leads to (by neglecting higher order terms)

$$\begin{array}{rcl} \beta_1 & = & \kappa_1 + \theta_2 \kappa_2 - \theta_3 \kappa_3 \\ \beta_2 & = & \kappa_2 - \theta_3' - \theta_2 \kappa_1 \\ \beta_3 & = & \kappa_3 - \theta_2' + \theta_3 \kappa_1 \end{array} \tag{7}$$

The following orders are assumed now (and will be confirmed later)

$$\theta_\alpha \sim \epsilon \frac{h}{l}; \qquad h\,\kappa_i \sim \epsilon \tag{8}$$

Since one can assume $\varepsilon \sim \left(\frac{h}{l}\right)^2$ as the case of interest for shear effects, $(\theta_\alpha\,\kappa_i)$ terms drop out as being of higher order.

3.2   The Strain Field

The 3–D strain components are

$$\Gamma = \{\Gamma_{11}^* \quad 2\Gamma_{12}^* \quad 2\Gamma_{13}^* \quad \Gamma_{22}^* \quad 2\Gamma_{23}^* \quad \Gamma_{33}^*\}^T \tag{9}$$

$$\Gamma = \underbrace{\Gamma_\varepsilon \, \varepsilon}_{\epsilon} + \underbrace{\Gamma_h \, w}_{\epsilon} + \underbrace{\Gamma_\ell \, w'}_{\epsilon \frac{h}{l}} \qquad (10)$$

where the warping field and the 1-D strain are

$$w = \{w_1 \quad w_2 \quad w_3\}^T \qquad (11)$$

$$\varepsilon = \{\gamma_{11} \quad \kappa_1 \quad \kappa_2 \quad \kappa_3\}^T \qquad (12)$$

$$\Gamma_h = \begin{bmatrix} 0 & 0 & 0 \\ \dfrac{\partial}{\partial x_2} & 0 & 0 \\ \dfrac{\partial}{\partial x_3} & 0 & 0 \\ 0 & \dfrac{\partial}{\partial x_2} & 0 \\ 0 & \dfrac{\partial}{\partial x_3} & \dfrac{\partial}{\partial x_2} \\ 0 & 0 & \dfrac{\partial}{\partial x_3} \end{bmatrix} \qquad (13)$$

$$\Gamma_\varepsilon = \begin{bmatrix} 1 & 0 & x_3 & -x_2 \\ 0 & -x_3 & 0 & 0 \\ 0 & x_2 & 0 & 0 \\ 0 & 0 & 0 & 0 \\ 0 & 0 & 0 & 0 \\ 0 & 0 & 0 & 0 \end{bmatrix} \tag{14}$$

$$\Gamma_l = \begin{bmatrix} I_3 \\ O_3 \end{bmatrix} \tag{15}$$

The quantities of the deformed geometry are still referred to the tangential system $\hat{T}$. The warping field must satisfy the four constraint equations which 'block' the rigid body modes

$$\langle w_i \rangle = 0 \tag{16}$$

$$\langle x_2 \, w_3 - x_3 \, w_2 \rangle = 0 \tag{17}$$

3.3 Next Approximation for the Shear Effect

Terms of up to order $\mu\epsilon^2\dfrac{h^2}{l^2}$ in the strain energy which are supposed to render a correct shear theory.

$$2U = \left\langle \Gamma^T D\, \Gamma \right\rangle \tag{18}$$

Consider the perturbation in the warping field

$$w = \underbrace{w_0}_{\epsilon} + \underbrace{w_1}_{\epsilon\frac{h}{l}} \tag{19}$$

The finite element discretization of the warping $w = [S]\, V$.

$$w_0 = [S]\, V_0; \qquad w_1 = [S]\, V_1 \tag{20}$$

$V_0 = \hat{V}_0 \, \varepsilon$ is the classical solution of the warping (strain energy asymptotically correct up to order $\mu \, \epsilon^2$). Replacing in the energy

$$
\begin{aligned}
2U_1 = {}& V_1'^T D_{l\varepsilon} \varepsilon + V_1'^T D_{lh_0} \varepsilon + V_1^T D_{h\varepsilon} \varepsilon + V_1^T D_{hh_0} \varepsilon + V_1^T D_{hl_0} \varepsilon' + \\
& V_1^T D_{hh} V_1 + \varepsilon'^T D_{l_0\varepsilon} \varepsilon + \varepsilon'^T D_{l_0 h_0} \varepsilon + \varepsilon'^T D_{l_0 l_0} \varepsilon' + \varepsilon'^T D_{hl_0}^T V_1 + \\
& \varepsilon^T D_{\varepsilon\varepsilon} \varepsilon + \varepsilon^T D_{\varepsilon h_0} \varepsilon + \varepsilon^T D_{l_0\varepsilon}^T \varepsilon' + \varepsilon^T D_{\varepsilon h} V_1 + \varepsilon^T D_{\varepsilon l} V_1' + \\
& \varepsilon^T D_{h_0\varepsilon} \varepsilon + \varepsilon^T D_{h_0 h_0} \varepsilon + \varepsilon^T D_{l_0 h_0}^T \varepsilon' + \varepsilon^T D_{hh_0}^T V_1 + \varepsilon^T D_{lh_0}^T V_1'
\end{aligned}
\tag{21}
$$

The variational equation with respect to $V_1(x_1)$

$$
E \, V_1 - \left[D_{l\varepsilon} + (D_{lh_0} - D_{hl_0}) \right] \varepsilon' + H \, \psi_{cl} \psi_{cl}^T D_{h\varepsilon} \varepsilon = H \, \psi_{cl} \, \mu
\tag{22}
$$

where μ are the Lagrange multipliers which enforce the constraints on V_1. The result from the first approximation was

$$
E \, V_0 + D_{h\varepsilon} \varepsilon = H \, \psi_{cl} \psi_{cl}^T D_{h\varepsilon} \varepsilon
\tag{23}
$$

the Lagrange multipliers are obtained

$$\mu = -\psi_{cl}^T \left[D_{l\varepsilon} + (D_{lh_0} - D_{hl_0}) \right] \varepsilon' + \psi_{cl}^T D_{h\varepsilon} \, \varepsilon \qquad (24)$$

Hence

$$E V_1 = (I - H \psi_{cl} \psi_{cl}^T) \left[D_{l\varepsilon} + (D_{lh_0} - D_{hl_0}) \right] \varepsilon' \qquad (25)$$

This system must be solved for $\hat{V}_1$ where $V_1 = \hat{V}_1 \, \varepsilon'$ was considered. Because E is singular a new matrix E_{cl}^+ is defined such that

$$E_{cl}^+ E = I - \psi_{cl}^T \psi_{cl} H \qquad (26)$$

and the solution is

$$V_1 = E_{cl}^+ D_s \varepsilon' \stackrel{\triangle}{=} \hat{V}_1 \, \varepsilon' \qquad (27)$$

where a new matrix was defined $D_s = D_{l\varepsilon} + (D_{lh_0} - D_{hl_0})$

Notice that $V_1 \sim \epsilon \frac{h}{l}$.

Next, the result is plugged in the expression for the strain energy which takes the form

$$2\,U_1 = \varepsilon^T\,A\,\varepsilon + 2\,\varepsilon^T\,B\,\varepsilon' + \varepsilon'^T\,C\,\varepsilon' + 2\,\varepsilon^T\,D\,\varepsilon'' \qquad (28)$$

where

$$A = D_{\varepsilon\varepsilon} + D_{h_0 h_0} - (D_{\varepsilon h_0} + D_{h_0 \varepsilon}) \qquad (29)$$

$$B = -(D_{\varepsilon l} - D_{h_0 l})\,\hat{V}_0 \qquad (30)$$

$$C = \hat{V}_1\,E\,\hat{V}_1 + D_{l_0 l_0} - (D_{l_0 h}\,\hat{V}_1 + \hat{V}_1\,D_{h l_0}) \qquad (31)$$

$$D = (D_{\varepsilon l} - D_{h_0 l})\,\hat{V}_1 \qquad (32)$$

The 1-D strain measures and their derivatives refer to quantities in the tangential system $\overset{\wedge}{\mathbf{T}}$. For Timoshenko-like beams express the bending curvature in the rotated system $\overset{\wedge}{\mathbf{B}}$.

$$\kappa_2 = \beta_2 + \gamma_{13}' \tag{33}$$

$$\kappa_3 = \beta_3 - \gamma_{12}' \tag{34}$$

where the definitions of the shear strain measures are

$$\gamma_{12} = -\theta_2; \qquad \gamma_{13} = \theta_3$$
$$\gamma_{1\alpha} = \frac{\partial u_1}{\partial x_\alpha} + \frac{\partial u_\alpha}{\partial x_1} \tag{35}$$

3.4 Equilibrium Equations

The equilibrium equations along the beam are

$$M'_\alpha = e_{\alpha\beta} Q_\beta - m_\alpha \tag{36}$$

$$N' = -p_1 \tag{37}$$

$$M'_1 = -m_1 \tag{38}$$

$$Q'_\alpha = -p_\alpha \tag{39}$$

For the case with no distributed applied moments

$$M'_\alpha = e_{\alpha\beta} Q_\beta \tag{40}$$

4   Solution for the Isotropic Case

Our goal is to write the strain energy in the more useful form (Timoshenko-like)

$$2\,U_1 = \bar{\varepsilon}^T\,S\,\bar{\varepsilon} \tag{41}$$

where $\bar{\varepsilon}$ is the extended strain vector of 1–D strain measures

$$\bar{\varepsilon} = \{\gamma_{11}\ \kappa_1\ \kappa_2\ \kappa_3\ \gamma_{12}\ \gamma_{13}\}^T \tag{42}$$

For a prismatic isotropic beam matrix S will be diagonal. For now, we look at the case when $\gamma'_{1i} = 0$, $\kappa'_1 = 0$, $\kappa''_\alpha = 0$, corresponding to the Timoshenko theory of bending. This allows for the determination of the shear rigidities

$$
\begin{aligned}
S_5 &= \frac{A_4^2}{C_4}\\
S_6 &= \frac{A_3^2}{C_3}
\end{aligned}
\tag{43}
$$

5   Solution for the Anisotropic Case

Internal forces are obtained

$$
\mathcal{M} = \left\{ \begin{array}{c} M_2 \\ M_3 \end{array} \right\} = \left[\frac{\partial^2 U_1}{\partial \kappa_\alpha \partial \bar{\varepsilon}_i} \right] \bar{\varepsilon}
\qquad
\mathcal{Q} = \left\{ \begin{array}{c} Q_2 \\ Q_3 \end{array} \right\} = \left[\frac{\partial^2 U_1}{\partial \gamma_{1\alpha} \partial \bar{\varepsilon}_i} \right] \bar{\varepsilon}
$$

using the equilibrium equations (40) one can obtain an equation

$$
M \bar{\kappa}' = Q \bar{\varepsilon} \implies \bar{\kappa}' = M^{-1} Q \bar{\varepsilon}
$$

where: $M = \left[\dfrac{\partial^2 U_1}{\partial \kappa_\alpha \partial \kappa_\beta} \right]$
$\qquad \bar{\kappa}' = \left\{ \begin{array}{c} \kappa_2' \\ \kappa_3' \end{array} \right\}$
$\qquad \varepsilon' = \left\{ \begin{array}{c} 0_{2 \times 1} \\ \bar{\kappa}' \end{array} \right\} = M^* Q \bar{\varepsilon}$

Hence, the energy can be written

$$2U_1 = \varepsilon^T A \varepsilon + 2\varepsilon^T B M^* Q \bar{\varepsilon} + \bar{\varepsilon}^T Q^T M^{*T} C M^* Q \bar{\varepsilon} = \bar{\varepsilon}^T S \bar{\varepsilon} \quad (44)$$

since M and Q contain elements of S, (44) we have a 21st order nonlinear system having as unknowns the elements of S.

6 Numerical Results

For the case of a isotropic beam with a square cross section, the shear rigidity has been obtained as

$$S_5 = S_6 = \frac{5}{6} G A \quad (45)$$

This result is an accordance with the exact theoretical results in the literature.

7 Conclusions

- numerical results validate the theory for the isotropic case.

- for composite beams a method of solving the nonlinear system has to be devised and tested. It can be seen that, in general, it is possible for all the stiffness coefficients to be affected.

- other cases not considered here are to be treated separately as for (i.e., $\gamma'_{11} \neq 0$, $\kappa'_1 \neq 0$, $\kappa''_\alpha \neq 0$).

- the case for which $\kappa'_1 \neq 0$ represents the so-called Vlasov effect - not Timoshenko-like.

- the 'D' term in the strain energy expression will be treated more rigorously at a later time.

- cases involving anisotropic materials are to be analyzed and compared with available results in the literature.

- the physical meaning of the newly introduced shear variable should be addressed.

Dynamic Response of Two-Celled Composite Beams with Optimum Extension-Twist Coupling

D. S. Dancila, C. Coates, W. K. Lentz
and E. A. Armanios

Overview

- **Motivation**

- **Objectives**

- **Optimum Extension-Twist Two-Cell Composite Beam Configurations**

- **Finite Element Predictions of Modal Characteristics**

- **Experimental Determinations**

- **Comparison of Results**

- **Conclusions**

Motivation

- **Two-Cell Beams - structural configurations of practical interest**

- **Extension-Twist Coupling - potential for rotating lifting surface performance enhancements**

- **Modal Characterization - essential step towards practical implementation**

Objectives

- **Generate reference FEM and experimental results for optimum extension-twist coupled beams for:**
  - analytical model validation
  - assessment of response for manufactured beams

- **Investigate the modal characteristics' sensitivity to lay-up perturbations around the extension-twist global optimum configuration**

Optimal Extension-Twist Two-Cell Composite Beam Configurations

- **Analytical model for static response of two-cell, thin-wall composite beams - Badir(1995)**
- **Optimal extension-twist coupled two-cell composite beams - Lentz(1997)**
  - **Numerical optimization, gradient-based method with penalty function to impose constraints**
  - **Constraints**
    - extension-twist coupling only
  - **Configuration - subclass of two-cell beams**
    - rectangular cross-section, equal cell size
    - 8-ply wall thickness
    - each cell - 4-ply circumferentially uniform stiffness wall
    - 4-ply circumferentially uniform stiffness outer wrapping

Optimal Extension-Twist Two-Cell Composite Beam Configurations (cont'd)

4 plies

4 plies   4 plies

25.2 mm

=   =

32 mm
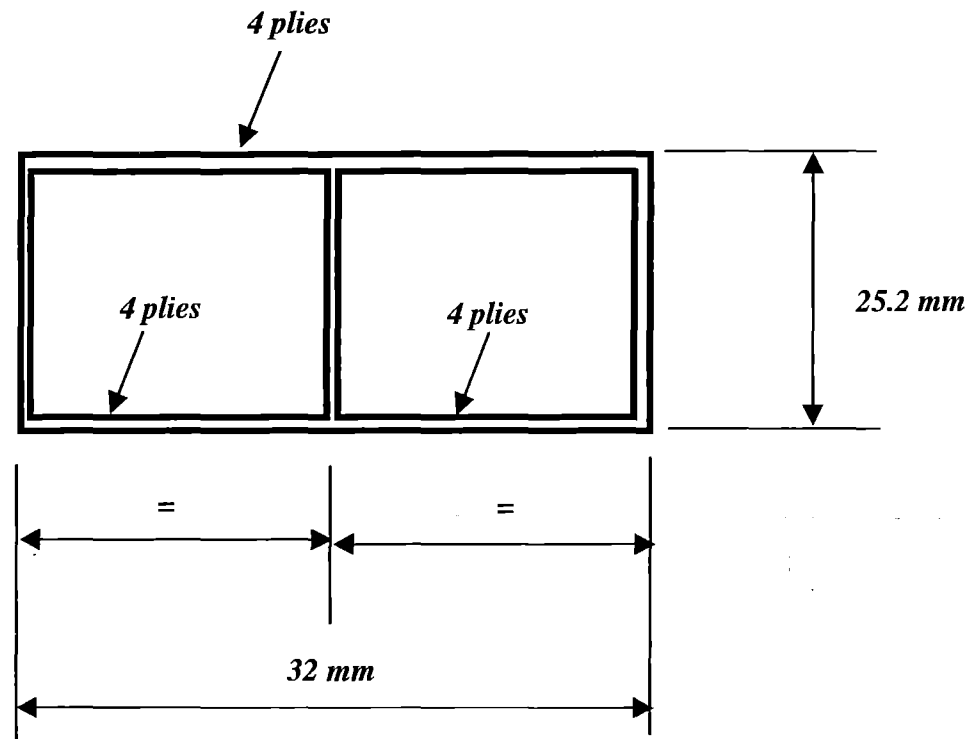
Optimal Extension-Twist Two-Cell Composite Beam Configurations (cont'd)

- **Material system - Fiberite T 300/954-3 graphite/cyanate**

E_{11}	135.6 GPa
E_{22}	9.96 GPa
G_{12}	4.2 GPa
ν_{12}	0.3
α_1	$4.34 \; 10^{-6} \; C^{-1}$
α_2	$37.0 \; 10^{-6} \; C^{-1}$
β_1	0
β_2	$5.56 \; 10^{-3} \; \varepsilon/\%$ weight
ρ	$1415 \; kg/m^3$

Optimal Extension-Twist Two-Cell Composite Beam Configurations (cont'd)

- **Optimum coupling configurations:**
  - global optimum
  - local optima

Left Cell	Right Cell	Overwrap	Coupling (rad/MNm)
83.7_4	**83.7_4**	**-29.2_4**	**61.5**
$85.9/86.1_2/84.8$	$86.5/86.0/85.3/85.2$	$-31.3/-32.0/-31.5_2$	61.1
83.4_4	83.4_4	$83.4/-29.3_3$	58.9
82.9_4	82.9_4	$82.9_2/-29.5_2$	54.2
$69.9/-80.5/-81.9/-83.6$	$88.6/88.2/86.0/85.3$	$36.2/35.8/34.4/37.3$	53.0

Finite Element Predictions of Modal Characteristics

- **Model configurations**
  - cantilevered boundary conditions
  - beam length: 422 mm
  - lay-ups :
    - global optimum
    - lay-up perturbations by ±3°
- **ABAQUS Finite Element Code**
- **Reduced integration quadrilateral shell elements (S4R)**
- **Model size: 2400 elements**
- **Solution maximum D.O.F. wavefront: 258**

Finite Element Predictions of Modal Characteristics (cont'd)

Modal Characteristics of Global Optimum Lay-up Beam

Mode No.	Frequency (Hz)	Mode shape description
1	112.0	First vertical bending
2	143.7	First horizontal bending
3	677.0	Second vertical bending
4	815.3	Second horizontal bending
5	1037.3	First extension-twist coupled mode
6	1733.6	First shell mode
7	1763.9	Third vertical bending
8	1830.9	Second shell mode
9	1939.4	Third horizontal bending
10	2300.4	Third shell mode

Finite Element Predictions of Modal Characteristics (cont'd)
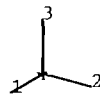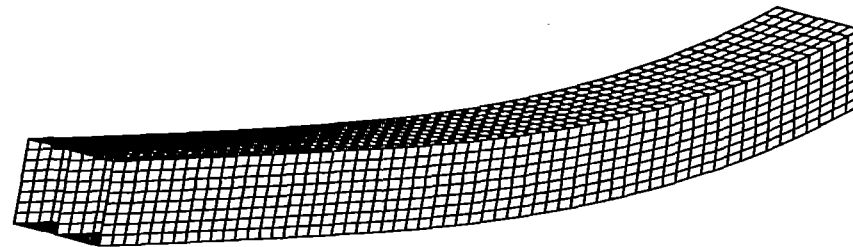
First Vertical Bending Mode Shape
112.0 Hz

No significant in-plane warping of the cross-section

Finite Element Predictions of Modal Characteristics
(cont'd)
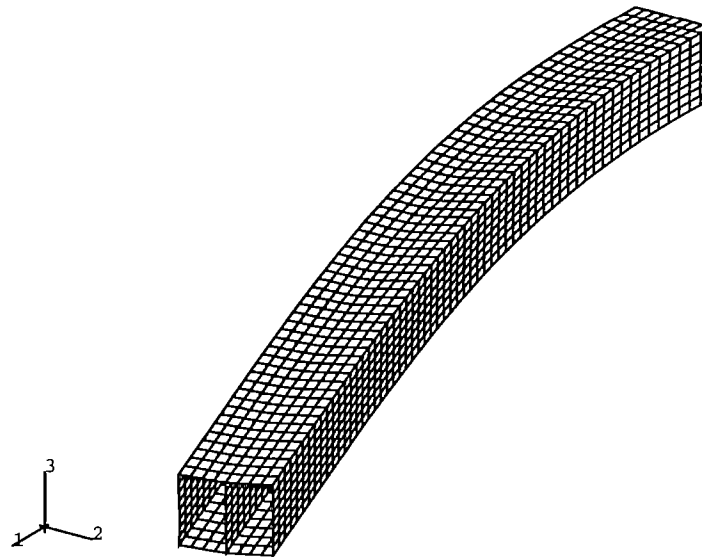
First Horizontal Bending Mode Shape
143.7 Hz

No significant in-plane warping of the cross-section

Finite Element Predictions of Modal Characteristics
(cont'd)
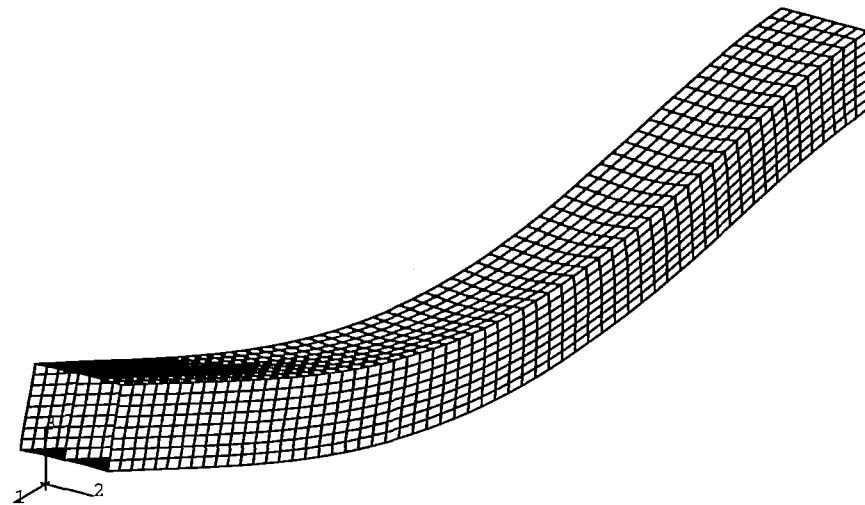
Second Vertical Bending Mode Shape
677.0 Hz

Noticeable in-plane warping of the cross-section

Finite Element Predictions of Modal Characteristics (cont'd)
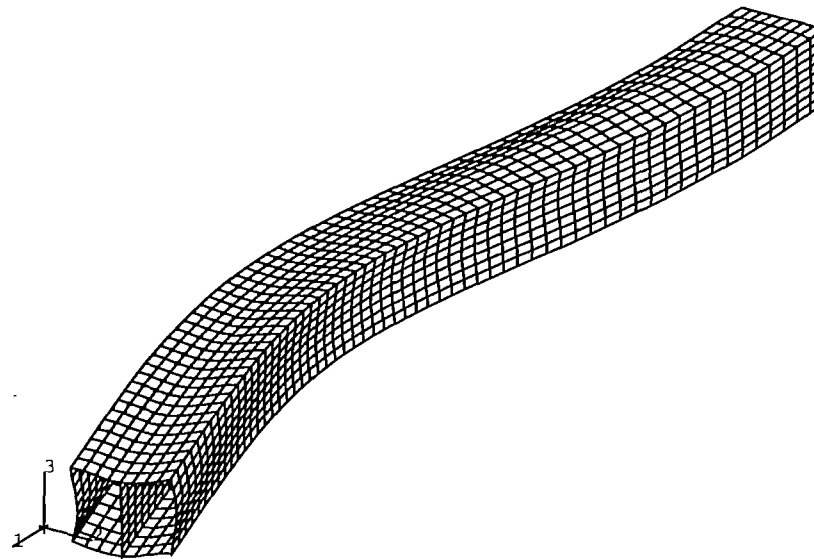
Second Horizontal Bending Mode Shape
815.3 Hz

Significant in-plane warping of the cross-section

Finite Element Predictions of Modal Characteristics (cont'd)
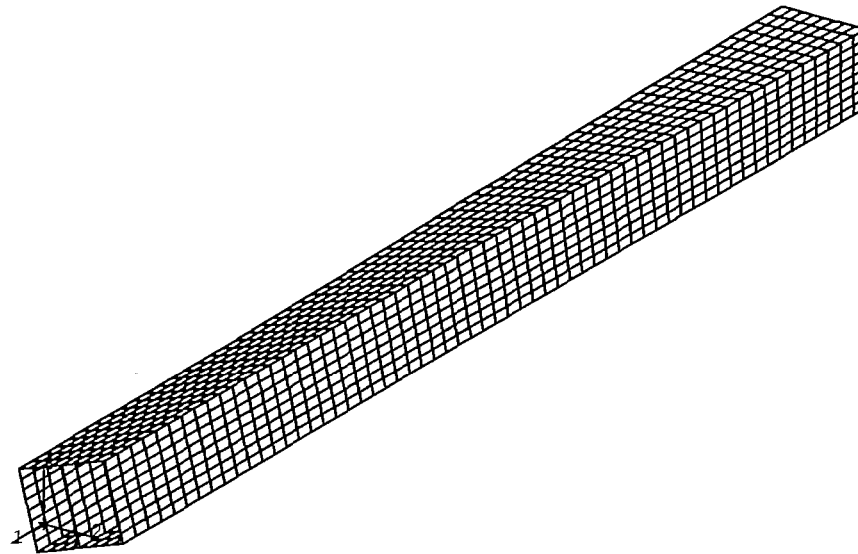
First Extension-Twist Coupled Mode Shape
1037.3 Hz

No significant in-plane warping of the cross-section

Finite Element Predictions of Modal Characteristics (cont'd)
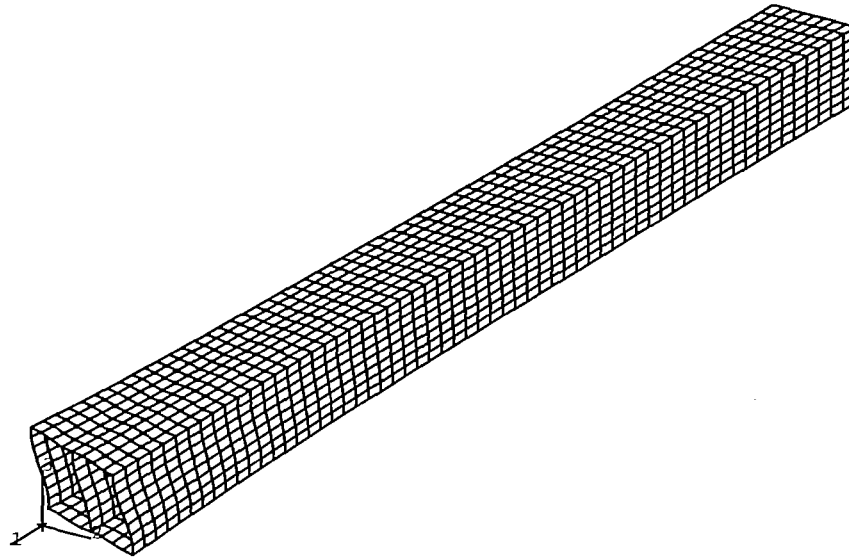
First Shell Mode Shape
1733.6 Hz

Significant in-plane warping of the cross-section

Finite Element Predictions of Modal Characteristics (cont'd)
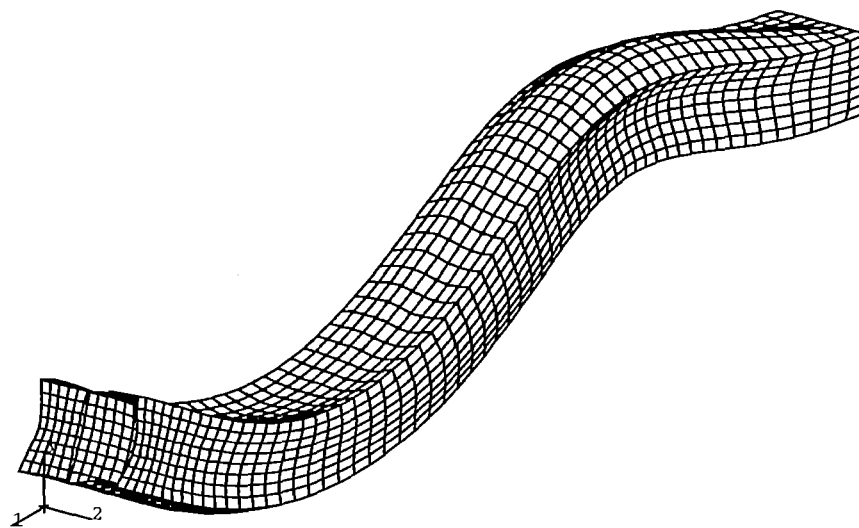
Third Vertical Bending Mode Shape
1763.9 Hz

Significant in-plane warping of the cross-section

Finite Element Predictions of Modal Characteristics
(cont'd)
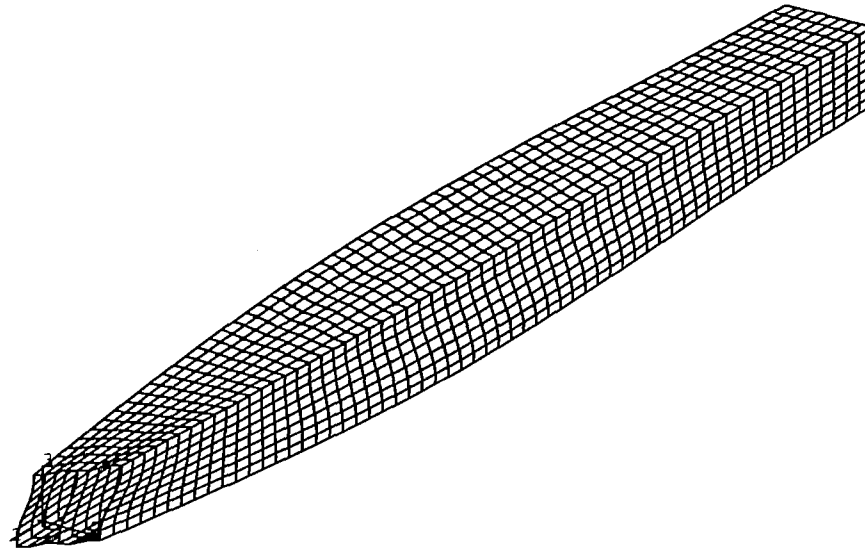
Second Shell Mode Shape
1830.9 Hz

Significant in-plane warping of the cross-section

Finite Element Predictions of Modal Characteristics (cont'd)
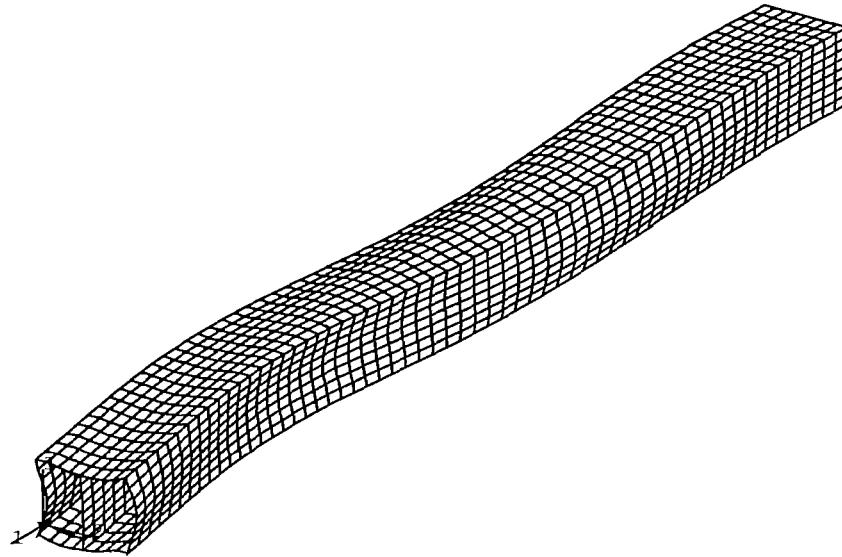
Third Horizontal Bending Mode Shape
1939.4 Hz

Significant in-plane warping of the cross-section

Finite Element Predictions of Modal Characteristics (cont'd)
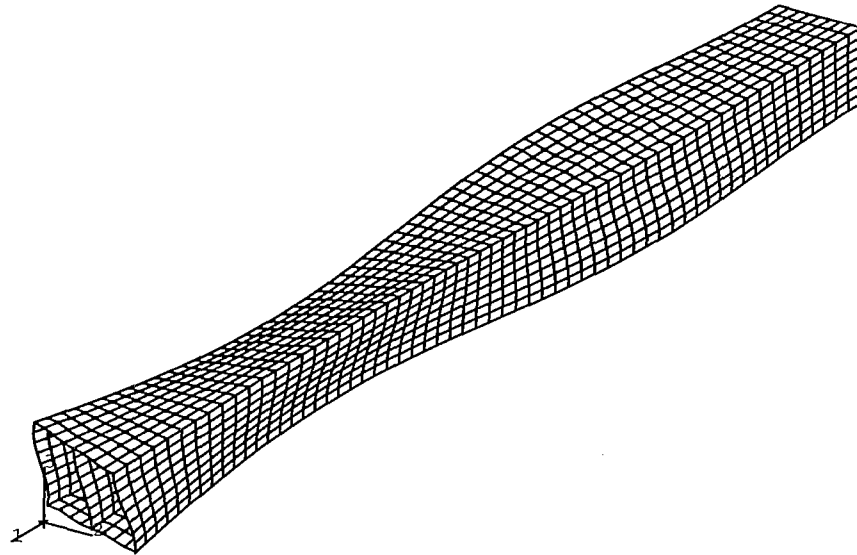
Third Shell Mode Shape
2300.4 Hz

Significant in-plane warping of the cross-section

Finite Element Predictions of Modal Characteristics (cont'd)

Variation of Natural Frequencies with Global Lay-up Perturbation Angle Near the Global Optimum

Mode	-3°		Global Optimum	+3°	
	Hz.	% Diff.	Hz	Hz	% Diff.
VB1	105.8	-5.54	112.0	119.4	6.61
HB1	135.4	-5.78	143.7	153.2	6.61
VB2	643.5	-4.95	677.0	716.3	5.81
HB2	772.5	-5.25	815.3	862.4	5.78
TE1	1083.2	4.42	1037.3	999.0	-3.69
S1	1678.3	-3.19	1733.6	1775.3	2.41
VB3	1696.9	-3.80	1763.9	1840.7	4.35
S2	1766.7	-3.51	1830.9	1883.1	2.85
HB3	1871.2	-3.52	1939.4	2010.0	3.64
S3	2194.4	-4.61	2300.4	2402.8	4.45

Finite Element Predictions of Modal Characteristics (cont'd)

Natural Frequencies for Global Optimum and Near-Global-Optimum Configurations

Seventh International Workshop on Dynamics and Aeroelastic Stability Modeling of Rotorcraft Systems

October 14-16, 1997
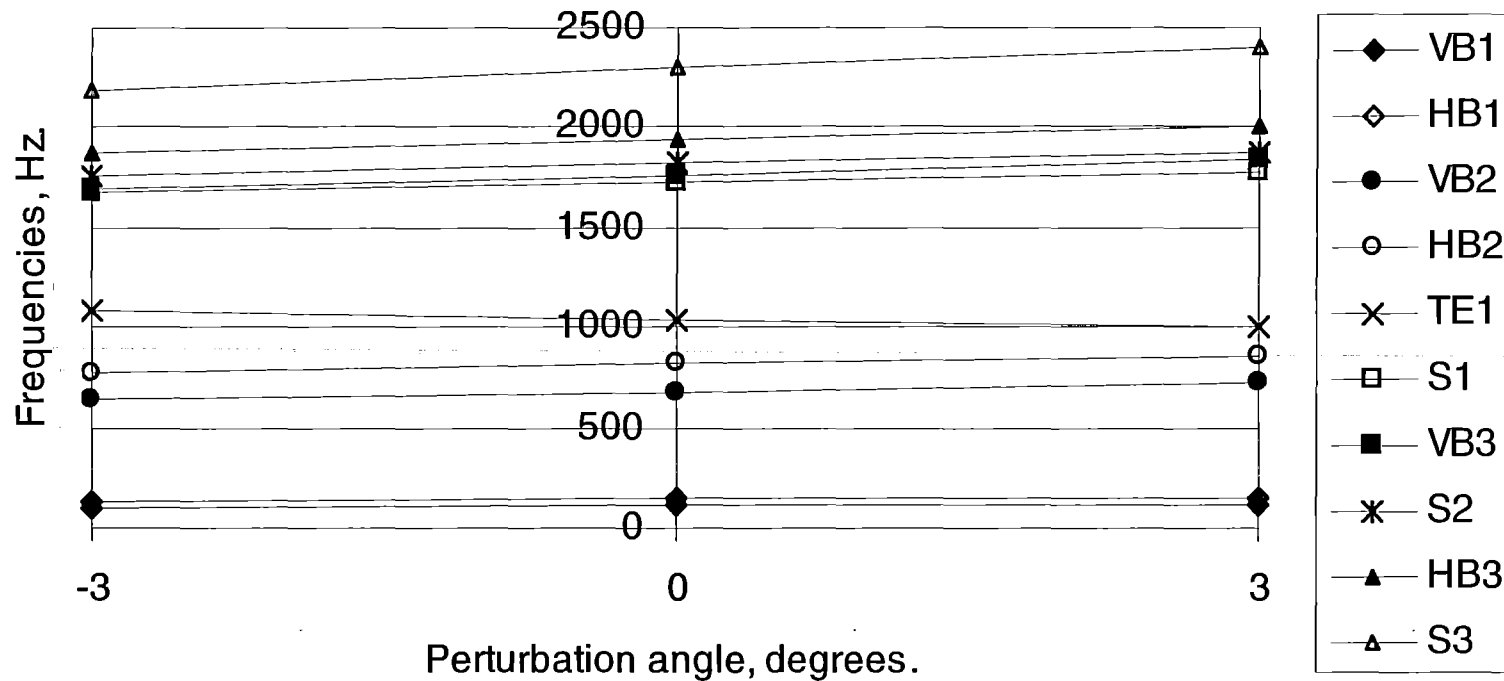
Experimental Determinations

- **Two-cell beam with global optimum lay-up manufactured and tested**

- **GenRad 2515 Test System used for data acquisition/primary processing**

  - **Impact excitation provided at selected locations with instrumented hammer (piezoelectric force transducer)**

  - **Response measured with piezoelectric accelerometer at selected location**

  - **Response time series converted to Transfer Function by FFT processing for each excitation/response location pair**

- **Star System PC software used for data processing**

  - **Ensemble of Transfer Functions processed by global curve-fitting algorithm to extract modal characteristics of structure**

Experimental Determinations
(cont'd)

Instrumented Two-Cell Composite Beam
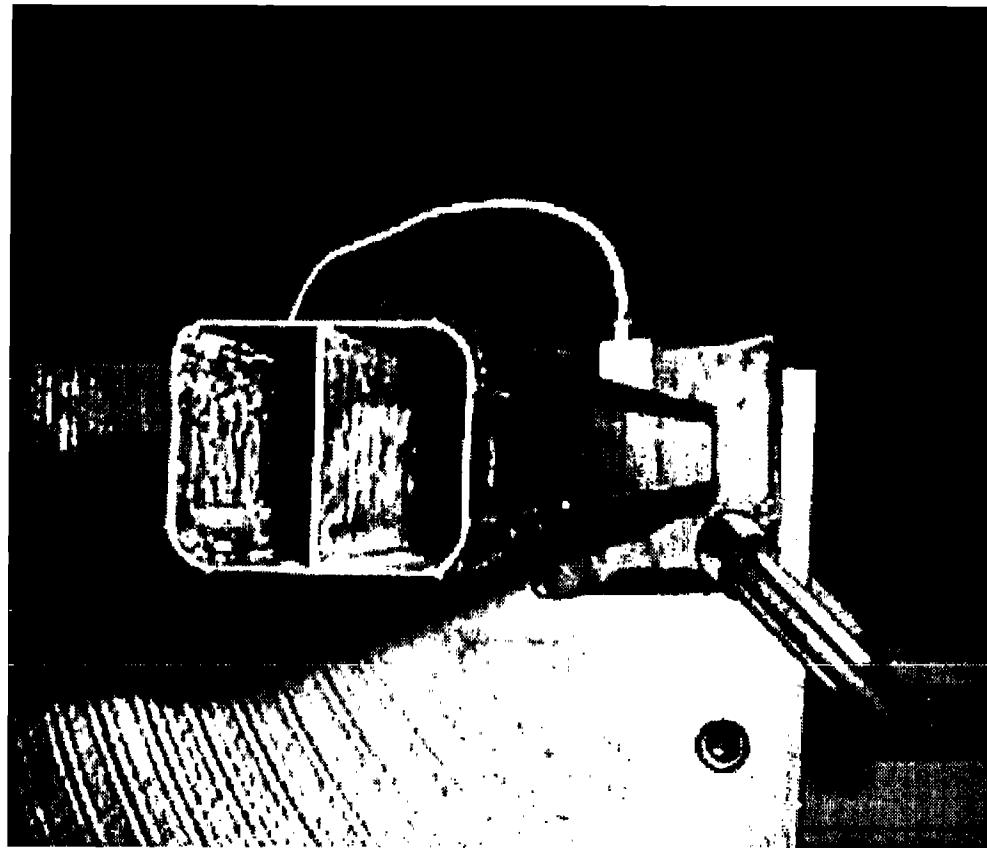
Experimental Determinations
(cont'd)

Instrumented Two-Cell Composite Beam - Side View
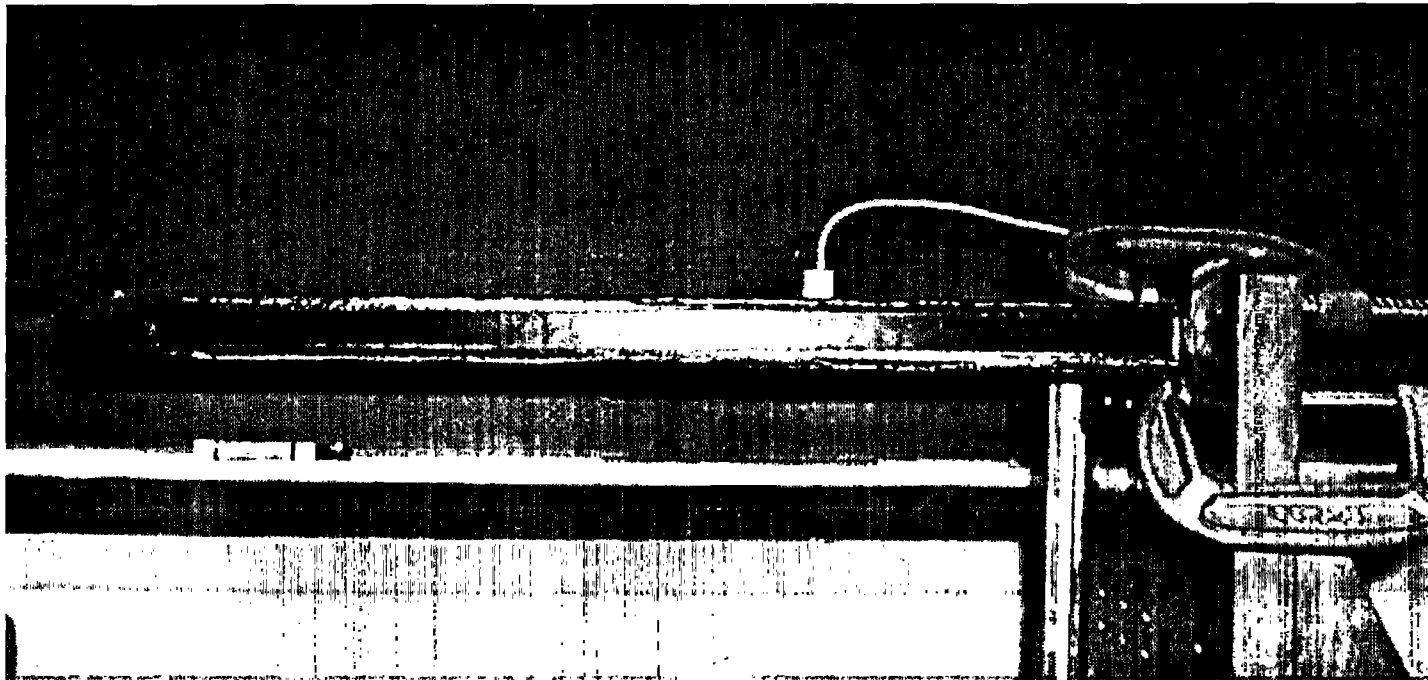
Experimental Determinations
(cont'd)

Transfer Function - Bode plot
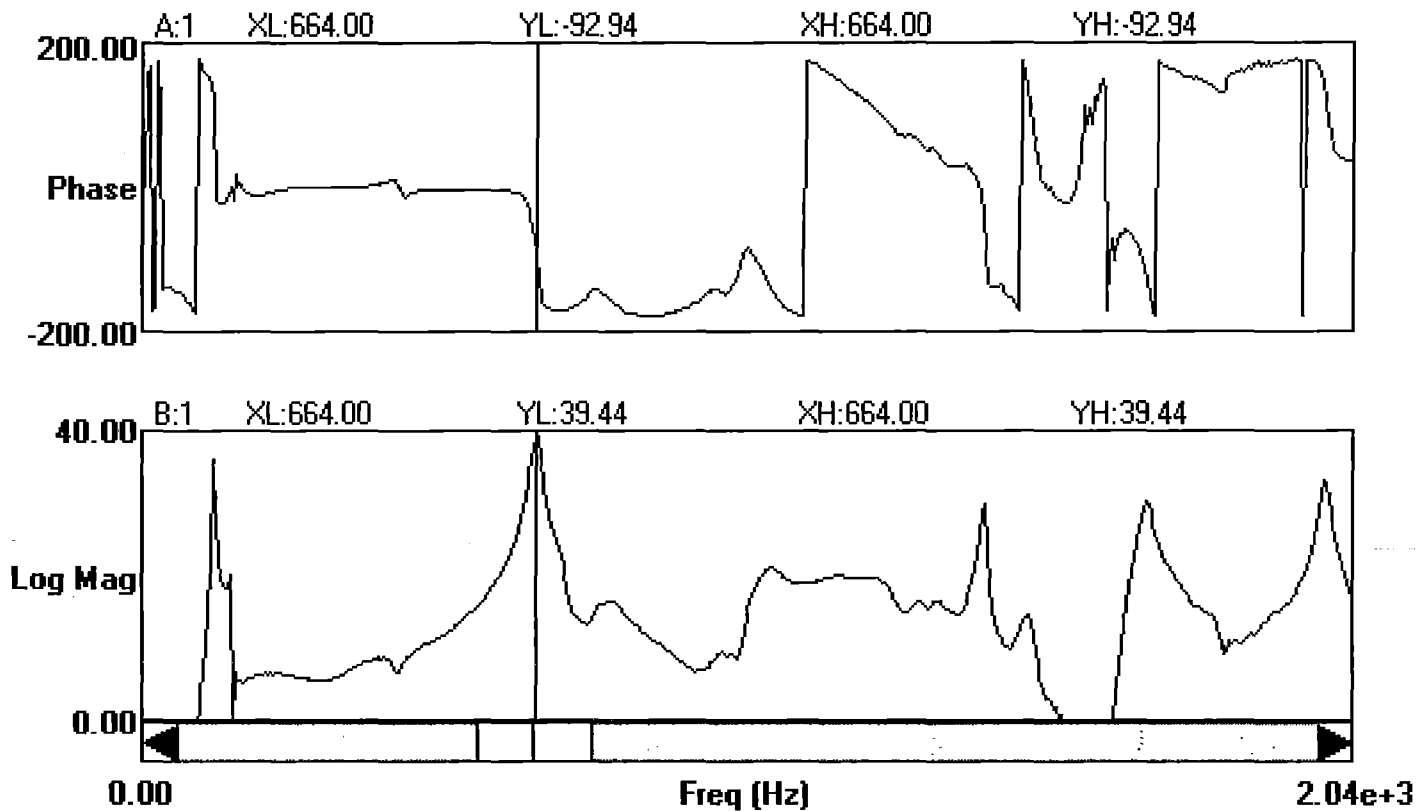
Experimental Determinations
(cont'd)

Transfer Function - Modal Identification by Curve Fitting

A:1   XL:90.00   YL:4.18   XH:185.00   YH:6.58

50.00

Log Mag

-30.00

B:2   XL:90.00   YL:6.58   XH:185.00   YH:7.88

50.00

Log Mag

-30.00

0.00   Freq (Hz)   250.00
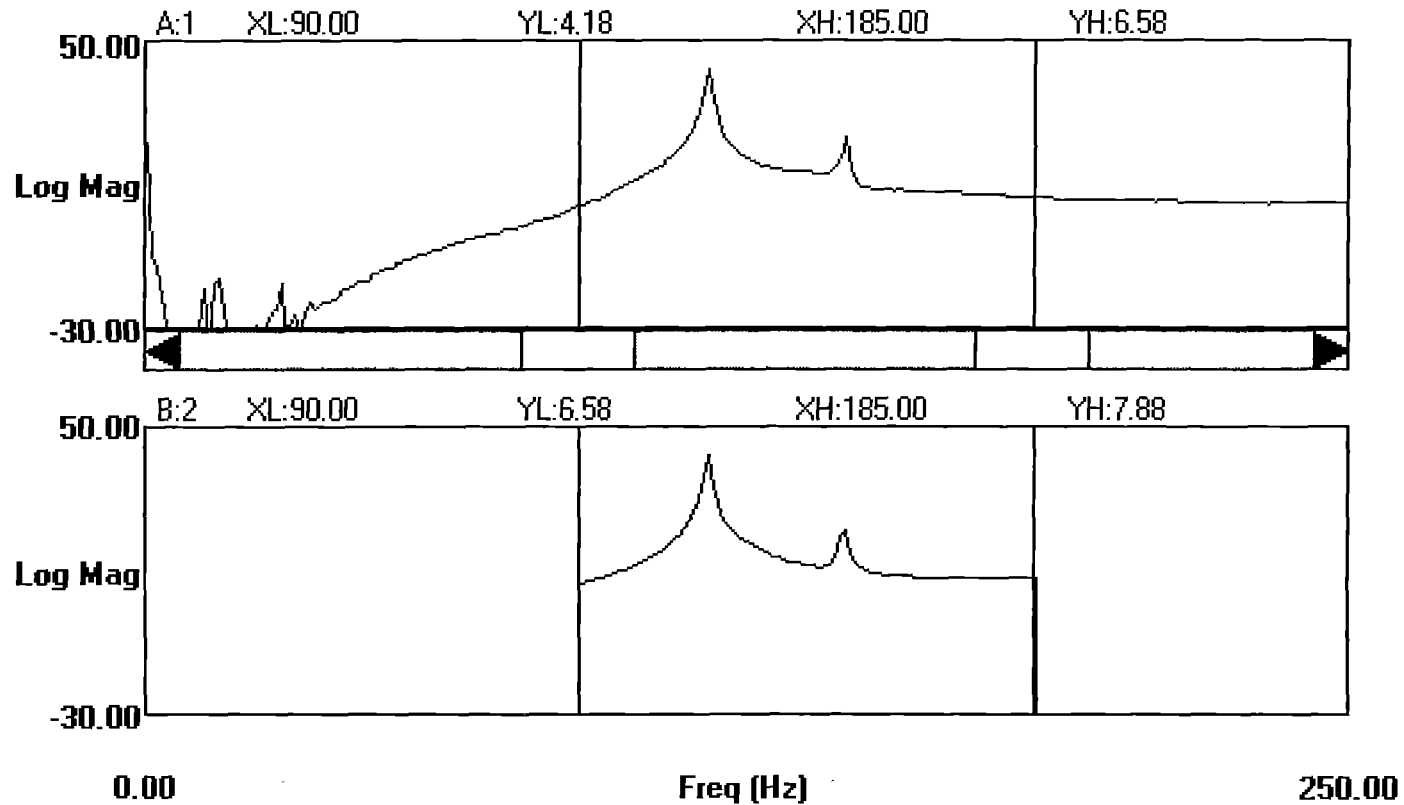
Comparison of Results

Finite Element and Experimental Values for Natural Frequencies

Mode	FEM	Experiment	
	Hz	Hz	% Diff.
VB1	112.0	117	4.46
HB1	143.7	146	1.60
VB2	677.0	662	-2.22
HB2	815.3	778	-4.58
TE1	1037.3	1050	1.22
S1	1733.6	1420	-18.09
VB3	1763.9	1500	-14.96
S2	1830.9	1690	-7.70
HB3	1939.4	2000	3.12

Conclusions

- **FEM and experimental investigation of two-cell beams with optimum coupling undertaken**

- **Good agreement between the two sets of results obtained for most modes**

- **Sensitivity of modal characteristics to lay-up perturbations around global optimum investigated**

- **FEM results appear to substantiate a hypothesis of in-plane nondeformability of the cross-section for low order mode shapes**

Acknowledgments

- **Present work supported by:**

    - **The National Rotorcraft Technology Center - Grant NCC2-945**

    - **The Georgia Space Grant Consortium**

On Dynamics of Elastic Anisotropic Beams

Vitali V. Volovoi,[*] **Dewey H. Hodges,**[†]
Georgia Institute of Technology, Atlanta, Georgia

Victor L. Berdichevsky,[‡]
Wayne State University, Detroit, Michigan

and **Vladislav G. Sutyrin**[§]
Detroit, Michigan

1   Introduction

The intent of this paper is to provide some insights into general scheme for construction of refined beam theories with inclusion of end effects and high frequency vibrations.[1] Such a refined theory is constructed by the introduction of new 1-D variables in addition to the four classical ones associated with extension, torsion and bending in two orthogonal directions. These additional 1-D variables represent high-frequency modes of vibration with a corresponding cross-sectional displacement field calculated by solving the appropriate 2-D problems over the cross section. Next, the asymptotic analysis is performed to ensure correct description of long-wavelength vibrations. As shown in this paper, this can be conveniently achieved by using frequency spectrum information available from the code described in Ref. [2]. So-called short wavelength extrapolation (*i.e.* change of variables that does not alter long-wavelength approximation) is further conducted to insure hyperbolicity of the resulting equations as well as proper description of the interaction between the various modes of vibrations.

Although the proposed model is not fully analytical in the sense that it does require numerical computations over the cross section, the amount of calculations is very small compared to 3-D finite element models, and parametric studies are easily conducted. Furthermore, once obtained, the 1-D stiffness coefficients for a given cross-sectional geometry

---

[*]Post Doctoral Fellow, School of Aerospace Engineering. Member, AIAA, AHS.
[†]Professor, School of Aerospace Engineering. Fellow, AIAA. Member, AHS.
[‡]Professor, Department of Mechanical Engineering. Member, AIAA, ASME.
[§]Consultant

and material properties can be applied repeatedly for various end conditions. Thus, this model is particularly suitable for tailoring and design of both wings and rotorblades.

2 Background and Present Approach

Due to the fact that properties of prismatic beams do not depend on the axial coordinate x_1, fundamental beam solutions have the form

$$u_i(x_2, x_3)e^{ikx_1 - \omega t} \tag{1}$$

where u_i are displacements, x_2, x_3 cross-sectional coordinates; k and ω are wavenumber and frequency, respectively. The k and ω and are solutions of an eigenvalue problem over the cross section, and as such they are connected by a transcendental equation (dispersion relationship). For a given real ω there is an infinite number of complex values k. However, for a relatively low frequency of vibrations there are only four real k corresponding to propagating waves along the beam. All other values of k are complex, and $\Im(k)$ has the sense of a decay rate as the waves travel away from the ends of the beam. The classical theory of beams with free lateral surfaces can be viewed as a truncated representation of the displacement field by the use of the first four of the basis eigenfunctions. The dispersion equation can be solved numerically for arbitrary geometrical and material cross-sectional properties by discretizing 2-D domain[3].

The need for an approximate beam or plate theory to give a good correlation of the resulting dispersion relations with those given by 3-D elasticity was well recognized at least as early as the beginning of this century. It was the discrepancy between the 3-D dispersion relationships and those given by classical beam theory that prompted Rayleigh[4] to take into account the inertia of cross-sectional rotation. Similarly, the introduction of shear deformation by Timoshenko[5] further improved correlation between dispersion equations of approximate and exact theories for a circular cross section. However, it was Mindlin who most likely should be credited for the first direct application of the 3-D dispersion relationships to constructing approximate theories. First it was done for plates[6] in which the so-called first "cut-off" frequency (i.e., the non-zero frequency for very long waves, in this case corresponding to the thickness-shear motions) was matched with the values given by the Rayleigh-Lamb solutions. Let us recall that Reissner's approach to the same problem[7] involved the assumed stress distribution and application of a complimentary variational principle. Both approaches provided remarkably close values for the so-called shear correction factor ($\pi^2/12$ and $5/6$, respectively). Then, similar concepts were employed for deriving a so-called tree-mode system of 1-D equations[8] for axially symmetric motions of an elastic rod with a circular cross section. The variational-asymptotic method[9, 10] provided a significant step toward understanding which 1-D variables have to be introduced in order to match the 3-D dispersion curves. The present approach follows the procedure that was applied originally to plates[11] subsequently to shells[12, 13], and finally to the extensional modes of vibration in isotropic beams[14].

2.1 Discretized formulation

The following procedure is similar to the one described in Ref. [3] and [15] with the differences emphasized herein. Variational formulation of the dynamic 3-D elasticity problem requires minimization of the following functional per unit length:

$$\mathcal{I} = \left\langle \Gamma^T D \Gamma \right\rangle - \left\langle \rho \dot{v}^T \dot{v} \right\rangle \tag{2}$$

where v is 3-dimensional vector of displacements, dots refer to time derivatives, $\langle\ \rangle$ is integration over the cross section, D is the 6×6 matrix of material coefficients, ρ is density and Γ is the 6×1 strain matrix that can be split into two parts:

$$\Gamma = \Gamma_h v + \Gamma_l v' \tag{3}$$

where prime refers to partial derivative with respect to axial coordinate and

$$\Gamma_h = \begin{bmatrix} 0 & 0 & 0 \\ \frac{\partial}{\partial x_2} & 0 & 0 \\ \frac{\partial}{\partial x_3} & 0 & 0 \\ 0 & \frac{\partial}{\partial x_2} & 0 \\ 0 & \frac{\partial}{\partial x_3} & \frac{\partial}{\partial x_2} \\ 0 & 0 & \frac{\partial}{\partial x_3} \end{bmatrix} \qquad \Gamma_l = \begin{bmatrix} 1 & 0 & 0 \\ 0 & 1 & 0 \\ 0 & 0 & 1 \\ 0 & 0 & 0 \\ 0 & 0 & 0 \\ 0 & 0 & 0 \end{bmatrix} \tag{4}$$

Discretization over the cross section allows for the following representation of the displacement field

$$v(x_1, x_2, x_3, t) = S(x_2, x_3) V(x_1, t) \tag{5}$$

Here S is a $3 \times N$ matrix of shape functions, and V is N-dimensional vector of nodal displacements. Substitution of Eqs. (3)–(5) into Eq. (2) yields

$$\mathcal{I} = \frac{1}{2} E_0 \left(V^T E V + V^T E_l V' + V'^T D_{ll} V' - \dot{V}^T M \dot{V} \right) \tag{6}$$

where symmetric matrices E, D_{ll}, M, and skew-symmetric matrix E_l are given by the following formulae:

$$\begin{aligned} E &= \left\langle [\Gamma_h S]^T D \Gamma_h S \right\rangle \\ E_l &= \left\langle [\Gamma_h S]^T D^* \Gamma_l S \right\rangle - \left\langle [\Gamma_l S]^T D \Gamma_h S \right\rangle \\ D_{ll} &= \left\langle [\Gamma_l S]^T D \Gamma_l S \right\rangle \\ M &= \left\langle \rho S^T S \right\rangle \end{aligned} \tag{7}$$

3
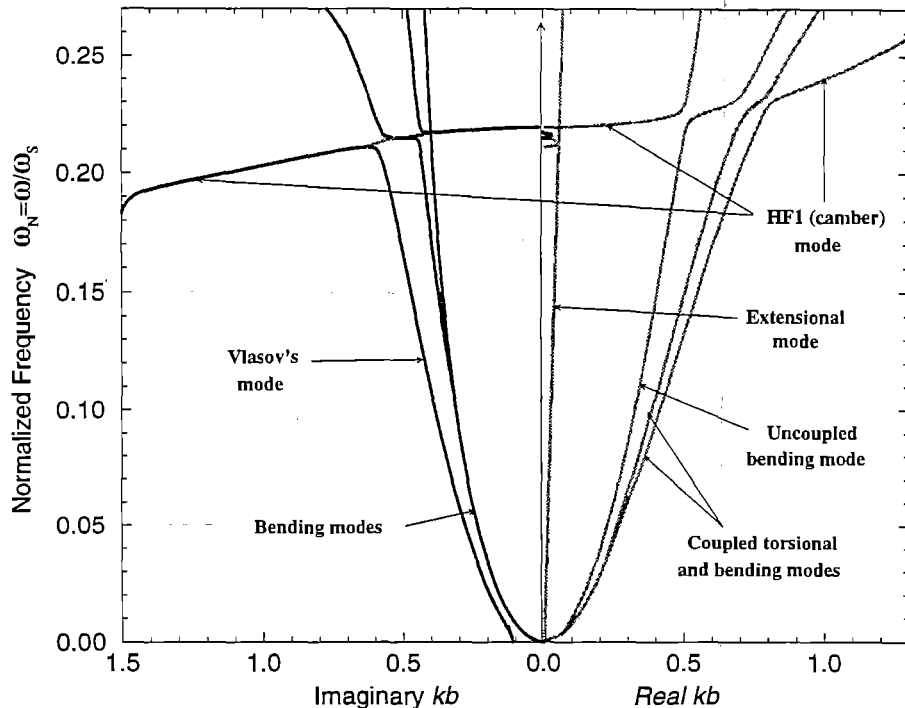
Figure 1: Dispersion curves (frequency spectrum) for anisotropic I-beam

Extraction of the fundamental solution in the form Eq. (1) is equivalent to the following eigenvalue problem:

$$\left(E - ikE_l + k^2 D_{ll} - \omega^2 M\right) u = 0. \tag{8}$$

Solutions of this eigenproblem represent the set of *dispersion curves* or *frequency spectrum*. Since for most of the interesting cases, k is either purely imaginary or real, it is convenient to use 2-D plots with the left part reserved for $\Im(k)$ and the right part for $\Re(k)$ (due to the intrinsic symmetry of the eigenproblem both these quantities can be considered positive without a loss of generality). A typical set of dispersion curves for anisotropic I-beam with a symmetric layup is depicted on Fig. 1. Frequency is normalized with respect to the equivoluminal (shear) wave which propagates the distance of a characteristic dimension of the cross section a in 1 second. Also, note that $\omega_s = \sqrt{\frac{G}{a^2 \rho}}$ where G is characteristic elastic modulus.

On the other hand, following the variational asymptotic procedure[3] in obtaining main terms with respect to small parameter $\frac{a}{l}$ where is $\equiv$ the diameter of beam, $\ell \equiv$ the charac-

teristic wavelength, requires two steps:

1. "Zeroth" approximation:

$$\left(E - \omega^2 M\right) V_0 = 0. \tag{9}$$

Solutions of this problem provide choice of 1-D variables Φ_p, $p = 1 \ldots K$: there are four solutions ψ_a , $a = 1 \ldots 4$ for $\omega = 0$ - which are low frequency or classical 1-D variables, the rest of the solutions for $\omega \neq 0$ corresponds to the high-frequency vibrations. Choice of the high frequency vibrations to be included ψ_p: $p = 5 \ldots K$ in the problem depends on the cross-sectional properties and the range of frequencies for application of the resulting beam theory[1].

2. Finding main terms in the Lagrangian with respect to the small parameter $\frac{a}{l}$. This requires perturbation of "Zeroth" approximation displacement field by "warping" W, retaining main terms in the Lagrangian with respect to the small parameter, and minimizing the resulting expression with respect to W. Generally speaking, different high-frequency modes have different ω_p, so that displacement field considered in the form

$$\Phi_p(x_1, t)\psi_p(x_2, x_3) + W_p \tag{10}$$

where W_p is "warping" which is orthogonal to the Ψ_p, so that $W_p^T M \Psi_p = 0$ can be expressed in the following form:

$$\left(E - \omega_p{}^2 M\right) W_p = \\ \left(\Psi_p' E_l + \Phi_p'' D_{ll} - \Phi_p \lambda_p M\right) \psi_p \tag{11}$$

here we have taken into consideration that vibration of this mode has frequency close to ω_p and introduced Lagrange multiplier λ_p to enforce orthogonality with ψ_p. For low frequency vibrations it is also possible to choose ψ_a in such a way that W_p will depend only on corresponding Φ_a and represent warping in exactly the same form, taking into consideration that $\omega_a = 0$. Let us note that the latter representation is somewhat unusual: The resulting "classical" beam equations are orthogonalized in a sense that corresponding displacement fields ψ_a are generally speaking a combination of a torsional mode, two bending modes, and extensional mode, so that stiffness matrix is diagonalized and the 1-D equations are decoupled. For example for the anisotropic I-beam with symmetric lay-up (see Fig. 1) which exhibits bending-torsional coupling, two of the corresponding diagonalized 1-D variables correspond to coupled motions. Of course, for isotropic beams this reduces to traditional torsional, bending, and extensional variables, and in general 1-D equations can be easily written in terms of those quantities.

Solutions of the eigenproblem posed by Eq. (8) satisfies Eq. (11) if terms with k are neglected compared to unity. This can be directly checked by substitution of the displacement field

5

Eq. (10) into Eq. (8) and recognizing that terms with ψ_p vanish on the left hand side of the equation, whereas terms with W_p can be neglected on the right hand side compared to the terms with ψ_p. Therefore, the eigenvectors of Eq. (8) taken for small k provide solutions for Eq. (11). The resulting displacement field is then given by:

$$V = \sum_{p=1}^{K} \Phi_p \psi_p + \Phi'_p \xi_p + \Phi''_p \eta_p \tag{12}$$

This displacement field is then substituted into Eq. (7) to obtain 1-D functional per unit length. Note that the last term should be considered only for "bending" variables, *i.e.* when low frequency variable corresponding to Ψ_a contains a bending mode and the corresponding contribution into Lagrangian due to Φ'_p that stems from the bending variable vanishes.

The next step is to perform a change of variables which does not alter long wavelengh approximation, but leads to the resulting 1-D system of equations being in hyperbolic form and accounts for interaction between the modes of vibration. Connecting shear high frequency branches with corresponding "bending" branches by factoring out a square term in the strain energy and making corresponding change of variables results in Timoshenko-like terms in the strain energy, while a similar procedure with kinetic energy couples the extensional mode with two other high frequency branches, resulting in equations similar to Mindlin's for circular cross section (see Ref. [8, 14]).

3   Intended Applications

The I-beam first studied has a symmetric cross section and is made from graphite-epoxy material with a $[0°/90°]_4$ layup in the web and a $[(0°/90°)_3/(\theta°)_2]$ in the flanges (see Fig. ??). Geometry is defined by the following ratios $a/b = 0.5$ and $h/b = 0.04$, where constants a, b and h are the height of the web, the width of the flanges, and the thickness, respectively. Dispersion curves depicted in Fig. 1 are for the angle $\theta = 15°$. For comparison, an isotropic beam of the same geometry has been studied, and the Fig. 2 depicts dispersion curves for Poisson's ratio $\nu = 0.42$.

For rectangular cross section high frequency (HF) branches are enumerated in order of ascending cut-off frequencies.

Comparing Fig. 1 and Fig. 2 with Fig. 3 vividly illustrates the differences between solid cross sections and thin-walled, open ones. In the latter case HF1 correspond to shear deformation and is effectively a bending mode which "strayed" from the hyperbolic path predicted by Euler theory. This explains the importance of Timoshenko theory. In the latter case this high frequency branch is relatively unimportant since there are other more significant effects: There is a evanescent branch stemming from point A on Fig. 2 with very slow decay rate that certainly has to be taken into consideration. Hence, the importance of Vlasov theory[16] Detailed study of this theory [17] revealed expected but still remarkable coincidence of the first non-classical branch with the torsional displacement of a cross section which is in full
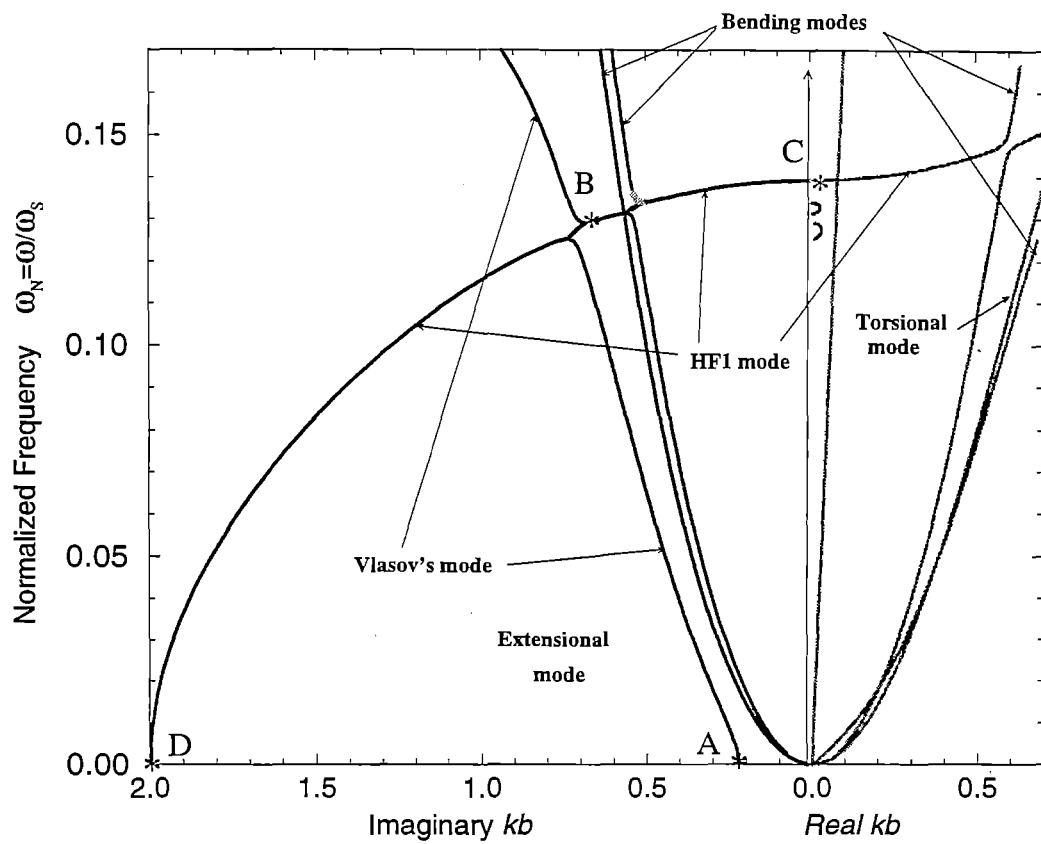
Figure 2: Dispersion curves (frequency spectrum) for an isotropic I-beam
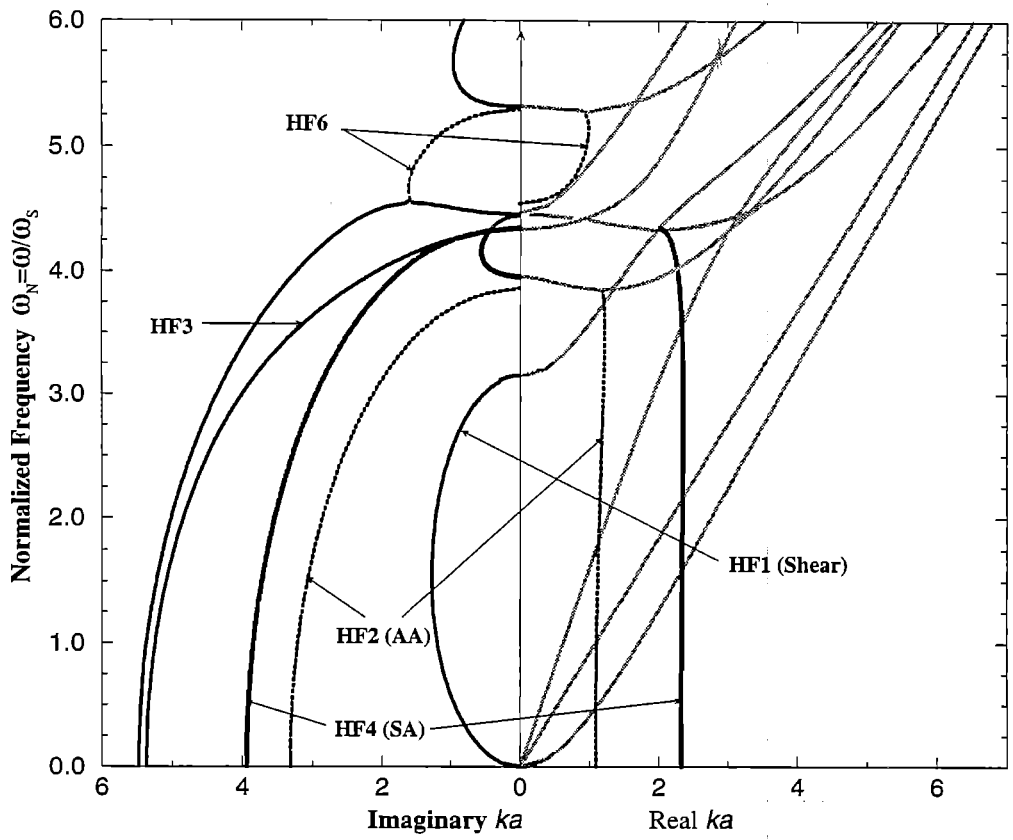
Figure 3: Dispersion curves (frequency spectrum) for an isotropic square cross section
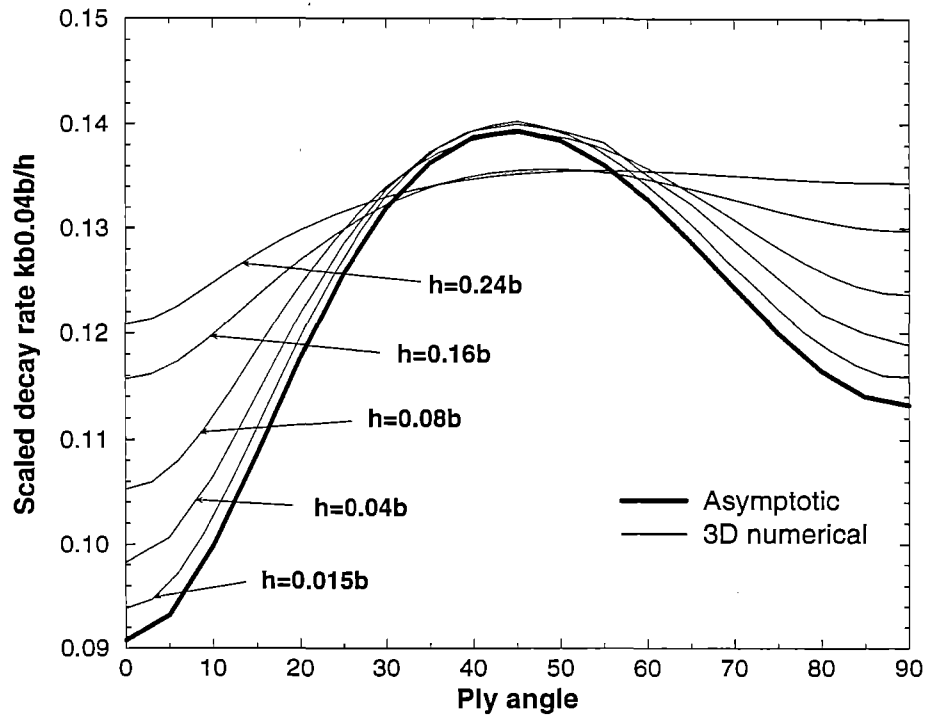
Figure 4: Decay rate for anisotropic I-beams

agreement with Vlasov's theory (see Fig. 5). Moreover, excellent quantitative correlation for the decay rate as provided by Vlasov's theory was observed. Fig. 4 demonstrates the results of parametric study for anisotropic I-beam. The angle θ of the two top plies for both top and bottom flanges is the varying parameter; h/b was also varied, while $a/b = 0.5$ is kept constant, and predictions for the decay rate were compared to numerical 3-D results. Note that in accordance with the asymptotic theory the rate of the decay varies linearly with the thickness, so it is convenient to normalize the decay rate with respect to the decay rate of some reference thickness (we have chosen $h = 0.04b$ as such reference point, because that was the thickness of the beam studied by the cited references). After this normalization all asymptotic curves will collapse into one. As expected correlation is the best for low h/b ratios, and the difference between asymptotic and 3-D results is indeed of order h/b. It is interesting to notice the decreasing sensitivity of the decay rate with respect to the varying ply angle as the thickness increases. In addition to "Vlasov" mode a different motion corresponding to HF1 mode can be important for higher frequencies. This relates to the fact that this different mode of vibrations starts to penetrate deeper into the interior of the
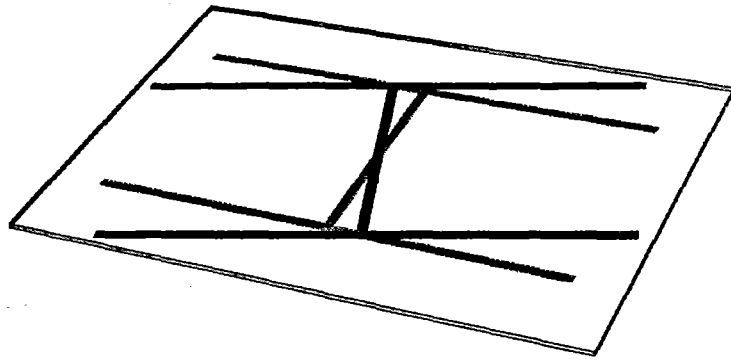
Figure 5: First "non-classical" (Vlasov) mode for isotropic I-beam: $\Im(bk) = 0.1103$
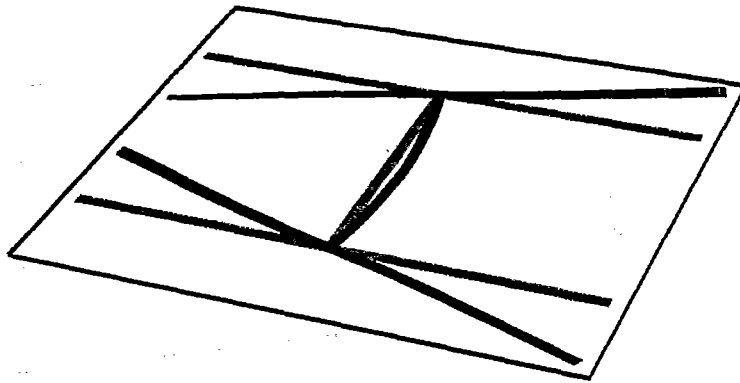
Figure 6: Second "non-classical" (camber) mode for isotropic I-beam: $\Im(bk) = 1.8988$

Session IV
Structure-Wake Interaction

An Accelerated, High Resolution Free-Vortex Wake Method for Comprehensive Rotor Analyses

Ashish Bagai[*]   J. Gordon Leishman[†]

Department of Aerospace Engineering,
Glenn L. Martin Institute of Technology,
University of Maryland,
College Park, Maryland 20742.

Abstract

The formulation and mathematical basis of the Maryland Free-Wake (MFW) Analysis is reviewed. The MFW can be used to predict the vortical rotor wake structure and inflow velocities for rotors operating in hover, forward flight, and during steady-state maneuvers. Another feature of the MFW is that it can solve for the interacting wake structures generated by multi-rotor configurations such as tandems and coaxials. For high resolution wake predictions, such as for aeroacoustic analyses, special acceleration algorithms have been developed to reduce the computational times but without loss of predictive accuracy. Several examples are presented showing rotor wake predictions and numerical convergence trends.

Nomenclature

a_1	Turbulent viscosity factor
C_T	Rotor thrust coefficient
h	Perpendicular distance between a point and a straight line segment, m
$\hat{i}, \hat{j}, \hat{k}$	Unit vectors, Cartesian coordinate system
k_{max}	Maximum number of collocation points on a vortex filament
l_{max}	Maximum number of blade azimuthal locations
$\vec{dl}$	Elemental unit vector, m
N_b	Number of blades
N_E	Number of Biot-Savart induced velocity evaluations

* Research Associate. Currently with Boeing Helicopters, Philadelphia, PA.
† Associate Professor.

N_{V_b}	Number of bound vortex segments
N_{V_f}	Number of free/far vortex segments
N_ψ	Number of discrete azimuthal locations
N_ζ	Number of free collocation points per vortex filament
n	Number of free-wake revolutions; vortex velocity profile
$\bar{q}$	Nondimensional steady pitch rate, q/Ω
R	Radius, m
r	Radial distance, m
$\vec{r}$	Position vector of a point, m
$\bar{r}$	Normalized radial distance, r/r_c
r_c	Vortex core radius, m
$\vec{r}_f$	Free vortex segment position vector, m
$\vec{r}_b$	Bound vortex segment position vector, m
$\vec{r}_{j,k}$	Collocation point position vector, m
$\vec{r}_{l,k}$	Position vector of the lth collocation point on the vortex filament trailed from the kth azimuth location, m
$\vec{r}_{l,k}^{n}$	n^{th} iteration corrected position vector, m
$\vec{r}_v$	Trailed vortex radial release point, m
$\tilde{\vec{r}}_{l,k}^{n}$	n^{th} iteration predicted position vector, m
t	Time, s
$\vec{V}$	Velocity vector, m/s
$\vec{V}_{ind}$	Induced velocity vector, m/s
$\vec{V}_\infty$	Free stream velocity vector, m/s
v_θ	Vortex tangential velocity, m/s
x, y, z	Global, fixed Cartesian coordinate system
$\Delta \vec{x}$	Rotor control input correction vector
$\tilde{x}, \tilde{y}, \tilde{z}$	Rotating, blade fixed coordinate system
$\tilde{x}_c$	Centroid of vorticity, blade fixed coordinates, m
α_s	Rotor shaft angle, $rad.$
β_0	Blade coning angle, $rad.$
Γ	Vortex circulation strength, m^2/s
Γ_f	Far/free vortex strength, m^2/s
Γ_b	Bound vortex strength, m^2/s
Γ_{avg}	Azimuthally averaged tip vortex strength
δ	Turbulent viscosity coefficient
Ω	Rotor rotational frequency, $rad./s$

ω	Relaxation parameter
$\Delta\zeta$	Vortex filament angular discretization step size, $rad.$
ζ	Wake age, $rad.$
ζ_k	kth collocation point along vortex filament
θ	Angle subtended between point of influence and influencing vortex line, $rad.$
λ_i	Uniform induced inflow
μ	Rotor advance ratio
ν	Kinematic viscosity of air, m^2/s
$\chi_x, \chi_y,$	Hub position vectors in fixed frame
χ_z	coordinates, m
$\Delta\psi$	Rotor azimuthal discretization step, $rad.$
ψ	Blade/rotor azimuth angle, $rad.$
ψ_b	Blade azimuthal location, $deg.$
ψ_j	jth rotor discretized azimuth location

Introduction

The ability to predict accurately the rotor aerodynamic environment is essential for the design of new rotorcraft with improved performance, increased maneuverability, minimized vibration levels, and reduced noise. Therefore, a great deal of emphasis is being placed on greatly improving the capabilities of predictive tools for use in the design of advanced rotary-wing aircraft. Because of the multidisciplinary nature of rotary-wing aircraft design, there are many constraints on the allowable levels of predictive methodologies. This is particularly the case for the aerodynamics modeling, where the need for computational efficiency or the need to have the model in a specific mathematical form can seriously limit the allowable level of sophistication.

The blade tip vortices are the most dominant structures in the rotor wake, and these are the primary flow features that must be modeled accurately. The tip vortices induce high local flow velocities and contribute significantly to the unsteady airloads produced on the blades. Accurate predictions of the rotor induced velocity field are important from the standpoint of predicting rotor performance, rotor aeroelasticity, and also the aircraft flight dynamics. Distortions to the wake structure during steady-state maneuvers, such as pitching and rolling, can produce significant changes in the wake structure and can be important for understanding counter-intuitive rotor behavior, such as the rotor off-axis response (Refs. 1-4). Furthermore, close interactions between blades and tip vortices can produce unsteady airloads of high magnitude and short duration that result in the generation of impulsive noise (e.g., Refs. 5,6). Key to all these issues is a robust and physically accurate mathematical model for the rotor wake.

While there are a multitude of numerical methods for predicting the effects of a rotor wake, ranging from simple momentum theory to modern computational fluid dynamics, free-vortex methods offer the greatest short-term potential for the accurate and computationally efficient prediction of the wake. In free-vortex methods, the vortical filaments trailed from the blades are allowed to convect under the action of the local velocity field to force-free locations. This behavior is governed by the vorticity transport equation, see for example Ref. 7. While, in general, 'free-wake' methods provide a high degree of versatility and accuracy with minimal dependency on empiricism, the large number of 'free' vortex elements required to model a rotor wake means that they are inherently costly for routine use. Furthermore, the inherent nonlinearity of the problem means that the formulation of efficient, numerically robust, and physically accurate algorithms is a very challenging objective. To this end, numerous free-wake solution methodologies have been developed, but have met with varied success, e.g. Refs. 8-16 and Refs. 17-22.

In a typical free-vortex scheme, the vortex filaments in the rotor wake are discretized along their lengths into segments connected by collocation points. The total induced velocity field at each collocation point is determined by the sum of the external velocity field and the velocity contributions induced by all the other vortex filaments in the rotor wake. The later is performed using the Biot-Savart law integrated along the lengths of the vortex filaments. This in itself, is not a computationally intensive task on a per element basis. However, because the vortex filaments must be discretized into short segments in areas of high curvature, the total number of evaluations required to determine the effects of each vortex segment on every collocation point in the wake can incur very large computational costs. For aeroacoustic predictions, the minimum azimuthal discretization resolution may be of the order of one degree or smaller. In such cases, the overhead required to compute a free-wake solution can easily become prohibitive for routine rotor design, even on a modern high end work station.

Several attempts have been made to improve computational efficiencies of free-wake methods. Schemes have been developed to optimize the algorithmic structures and exploit parallel computing capabilities (e.g., Ref. 23). Some methods have used simplified wake models based on ring vortices, limited wake distortion degrees of freedom (e.g., Refs. 24-26), or analytical approximations for curved vortex segments (Ref. 27). The most common approach, however, has simply been to reduce the number of induced velocity field calculations. This can be done by updating the induced velocities less frequently, by using fewer vortex elements in the discretized wake, or by subdividing the wake into near-field and far-field regions of weak and strong influence – see for example, Refs. 28-34. However, although successful in decreasing execution times, the resulting velocity field errors usually undermine the accuracy of the wake predictions.

Overview of MFW Analysis

The MFW algorithm, which was first reported in Refs. 35-40, is based on a non-Lagrangian relaxation approach. Specifically, the equations governing the rotor vortex wake structure are solved iteratively by means of a unique pseudo-implicit, predictor-corrector, relaxation method. This scheme has been shown to give the wake predictions excellent numerical stability and convergence characteristics, and can be applied over the entire flight regime, ranging from hover through to high speed forward flight, including vertical ascents and descents. Moreover, the scheme can be applied to predict the wake under steady-state maneuvering flight conditions, such as pitching or rolling motions. The MFW is also multi-rotor capable and can be used to model twin rotor systems such as tilt-rotors, tandems and coaxials – the aerodynamic interactions and mutually induced wake distortions between both rotor wakes being fully accounted for in the analysis.

In the MFW, the rotor wake may be modeled with varying (user selectable) degrees of sophistication. This may include concentrated tip vortices, additional secondary vortices, free or prescribed inboard trailers, as well as shed vortex elements to account for time-varying or azimuthal variations in blade loading. Under some flight conditions where secondary trailed vortices may be trailed only over a portion of the rotor azimuth, such as from a large spanwise gradient induced by a vortex, these are allowed to merge back into the main tip vortices over the remainder of the rotor revolution. The strength of each vortex element in the wake is mapped to the time (azimuth) when it was first created and trailed into the wake. Vortex circulation strengths may be assumed to remain constant over the discretized elements, or for some improved realism and a minor increase in cost, the strengths may be allowed to vary linearly over the segment lengths.

The vortex model itself has a direct bearing on the wake solution. In the MFW, vortex tangential (swirl) velocity profiles are represented using a variety of (user selectable) desingularized algebraic or exponential models. By default, a desingularized algebraic model that closely resembles the measured velocity profiles of actual rotor tip vortices is used. The viscous decay (core diffusion) of aging vortices is modeled in a manner consistent with experimental observations of rotor tip vortices. As an option, the vortex filaments can be modeled assuming multiple concentric cores of specified radii and strengths to emulate more complex vortex profiles.

One of the most significant features of the MFW is the ability to compute very high fidelity wake solutions than has been previously possible. Two special algorithms have been developed to reduce the number of Biot-Savart (induced velocity) calls and reduce execution times, but without sacrificing the predictive accuracy or numerical robustness of the MFW algorithm. The first method uses unequal discretization step sizes in the azimuthal direction and along the length of the vortex filaments. This method results in reduced per iteration run times. The second method is based on an adaptive grid sequencing approach where the wake solution is initiated using a low resolution wake geometry. As the wake relaxes with iterations, the resolution is increased sequentially until only the final few iterations are performed at the highest fidelity. Using these schemes, it is possible to compute accurate wake solutions of the order of one degree of azimuth or smaller, but at practical execution times. Such high resolution wake predictions are very important from the stand point of computing high fidelity blade airloads for acoustics analyses.

Mathematical Basis of the MFW

The free-wake problem is governed by the vorticity transport equation. This states that elements on a vortex filament convect with the fluid, and the resulting relationship can be written simply as

$$\frac{d\vec{r}(\psi,\zeta)}{dt} = \vec{V}(\vec{r}(\psi,\zeta)) \tag{1}$$

where $\vec{r}(\psi,\zeta)$ defines the position vector of an elemental segment lying on a vortex filament that is trailed from a rotor blade located at an azimuth ψ at time t, and where ζ defines the age of the element relative to when it was trailed into the wake. For the rotor problem, Eq. 1 can be rewritten in terms of ψ and ζ as

$$\frac{\partial \vec{r}(\psi,\zeta)}{\partial \psi} + \frac{\partial \vec{r}(\psi,\zeta)}{\partial \zeta} = \frac{1}{\Omega}\vec{V}(\vec{r}(\psi,\zeta)) \tag{2}$$

The right-hand-side velocity field (source term), accounts for the net, instantaneous, velocity encountered by an element on a vortex filament in the rotor wake. In addition to the free-stream and maneuver velocity contributions, the source term is comprised of the self- and mutually-induced velocities resulting from all the vortex filaments in the wake, as well as the induced contributions from the rotor blades.

The formulation used in the MFW model to integrate Eq. 2 involves three steps. 1. Discretization of the physical problem. 2. Transformation of the governing partial differential equations into finite difference equations. 3. Development of a numerical integration scheme. The present approach to solving Eq. 2 is based on a non-Lagrangian or relaxation method where the rotor time is discretized into a finite number of azimuthal increments of size $\Delta\psi$, with vortices of finite length trailed behind each rotor blade. Each vortex filament, in turn, is subdivided into segments of equal angular resolution, $\Delta\zeta$.

A collocation point at the inter-segment junction of each vortex segment on a particular filament defines a family of points that are interconnected with straight line vortex segments to represent that filament. Each vortex filament is attached to its respective blade at its point of origin, which defines the boundary condition in the ζ direction. Additional inboard trailed vortices, if required, are modeled in an identical manner. As the blades rotate, the wake collocation points are allowed to convect under the influence of the local velocity field and integrated over a finite time step or azimuthal increment. The PDE given in Eq. 2 governs the behavior of each and every wake collocation point. The actual number of collocation points depends on the number of trailed vortex filaments, the length of the vortices, the number of segments per filament, and the angular resolution in the azimuthal direction.

The induced velocity at an element in the wake can be determined as a sum of the induced contributions from the free vortex elements and also from any 'bound' elements such as the rotating blades. This velocity is written in terms of the Biot-Savart law as

$$\vec{V}_{ind}\left(\vec{r}(\psi,\zeta)\right) = \qquad\qquad (3)$$

$$\frac{1}{4\pi}\sum_{j=1}^{N_{V_f}}\int \frac{\Gamma_f(\psi_j,\zeta)\,d\vec{\zeta}_j\times(\vec{r}(\psi,\zeta)-\vec{r_f}(\psi_j,\zeta))}{|\vec{r}(\psi,\zeta)-\vec{r_f}(\psi_j,\zeta)|^3}$$

$$+\frac{1}{4\pi}\sum_{j=1}^{N_{V_b}}\sum_{i=1}^{i_{max}}\int \frac{\Gamma_b(\psi_j,i)\,d\vec{l}_{j,i}\times(\vec{r}(\psi,\zeta)-\vec{r_b}(\psi_j,i))}{|\vec{r}(\psi,\zeta)-\vec{r_b}(\psi_j,i)|^3}$$

where $\vec{r}(\psi,\zeta)$ is the position of the elemental vortex segment in the flow field, influenced by the total contributions of the jth free vortex located at $\vec{r}_f(\psi_j,\zeta)$ and of strength $\Gamma_f(\psi_j,\zeta)$, plus the influence of the ith bound vortex segment of the jth blade. The summation for the free vortices is carried over all N_{V_f} free vortices in the rotor wake (trailed and shed). The second term on the right-hand-side, accounts for the i_{max} vortex segments that make-up the N_{V_b} bound vortices that represent the blades. Because the strength of each bound vortex segment is dependent on its radial position along the blade span as well as the blade azimuth angle, its strength is represented by $\Gamma_b(\psi_j,i)$.

Note that the limits of integration over each free vortex filament in Eq. 3 extends from $\zeta = 0$ corresponding to the vortex-blade attachment (release) point, to the end of the filament at $\zeta \rightarrow \infty$. The integral for the bound (and shed) vortex elements are evaluated over their finite individual lengths. Fig. 1 shows the individual contributions of all the vortex elements in the rotor wake that contribute to the induced velocity at some free collocation point p on a vortex filament. Note that the blade 'bound' circulation and any specified prescribed trailed vortex filaments are not free vortices per se, but will contribute to the induced velocity field at free points in the wake.

Eq. 3 is a general expression for the induced velocity, and must be reduced into a more convenient form.
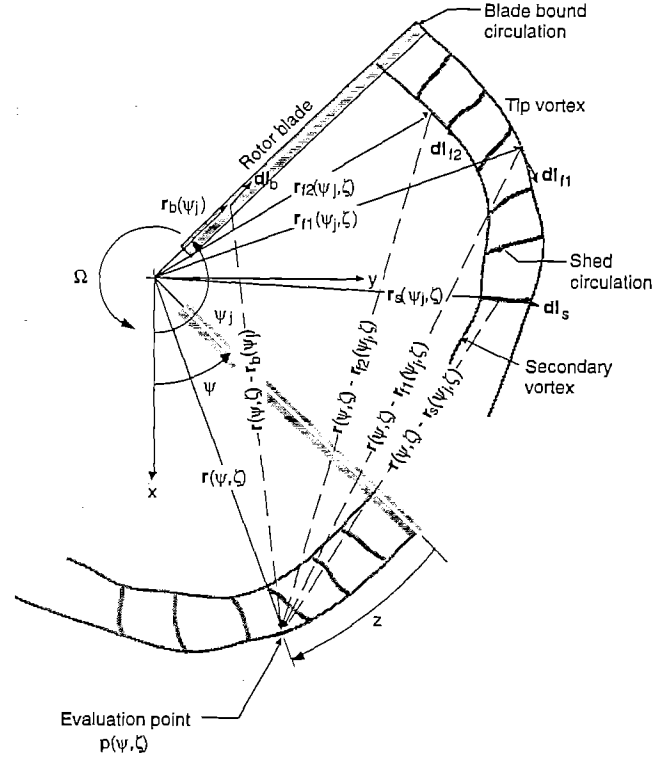
Figure 1: Induced velocities on a vortex element: free and bound vortex contributions

While the bound vortices are straight line elements, for which the Biot-Savart integral can be solved analytically, this is not possible for arbitrary curved vortex filaments. However, any curved filament can be modeled using a sufficiently large number interconnected straight line segments. Vortex collocation points at the inter-segment boundaries (see Fig. 2) are then convected through the flow-field at their respective local velocities. Eq. 3 is applied to each free collocation point and the induced velocities can be readily determined from geometrical considerations for the straight vortex filaments. The free collocation points convect through the flow field and change their positions under the influence of the induced velocity field as the wake evolves. The Biot-Savart law must, therefore, be re-evaluated repeatedly for each collocation point as the tip vortex geometries are allowed to evolve during the free-wake iterations. This is the primary cost in all free-wake models.

In the MFW, the discretization of the problem described above results in transforming the continuous physical domain into a discretized domain comprised of a finite number of elements. However, the governing equation in Eq. 2 still cannot be solved ana-
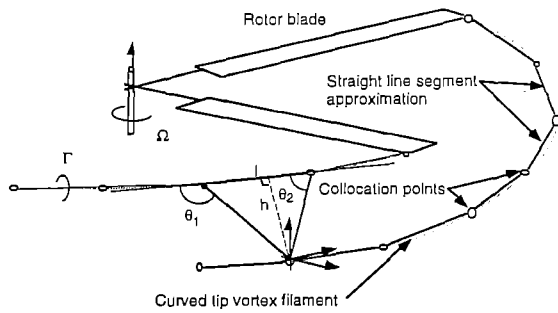
Figure 2: Straight line segment approximation of the tip vortices
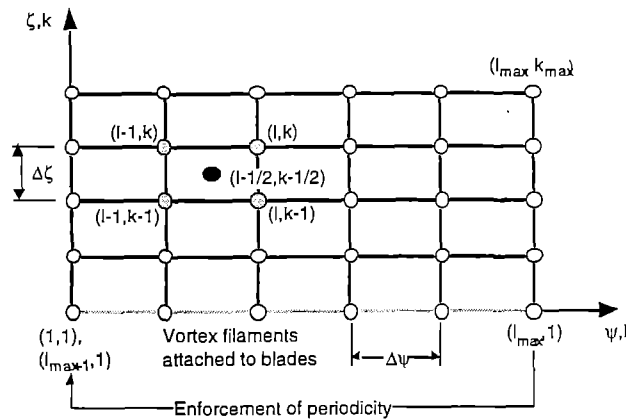
Figure 3: Discretized computational domain

lytically. A numerical integration scheme, therefore, must be developed. This requires the transformation of the PDE's into finite difference equations (FDE's). This is best described by first transforming the discretized physical domain into a computational domain. If the abscissa represents the ψ direction and the ordinate the ζ coordinates, the computational domain can be represented as shown in Fig. 3.

In the MFW, the partial derivatives of Eq. 2 are approximated in terms of finite differences using a five point central differencing and velocity averaging scheme, (Refs. 35-37). Using the notation defined in Fig. 3, the resulting FDE form of Eq. 2 can be written as

$$\vec{r}_{l,k} = \vec{r}_{l-1,k-1}$$
$$+ \frac{\Delta\psi}{\Omega}\left(\vec{V}_\infty + \frac{1}{4}\left(\vec{V}_{ind}(\vec{r}_{l-1,k-1}) + \vec{V}_{ind}(\vec{r}_{l-1,k})\right.\right.$$

$$\left.\left. + \vec{V}_{ind}(\vec{r}_{l,k-1}) + \vec{V}_{ind}(\vec{r}_{l,k})\right)\right) \quad (4)$$

Note that in the discretization process described above, both the ψ and ζ coordinates now represent the spatial locations of the collocation points in the rotor wake, and the time-domain has been by-passed. The evolution of the wake, therefore, cannot be determined by integrating Eq. 4 in a Lagrangian sense, but must involve an iterative procedure. The solution of the FDE in Eq. 4 is essentially governed by the unsteady, non-linear velocity or source terms on the right-hand-side of the equation. There is one such equation for each collocation point in the flow and this relates the position vectors of the collocation points to the local velocity field.

Numerical schemes used to integrate the FDE's using the procedure described above must be both numerically stable and accurate. From the stand point of most applications in rotorcraft problems, it is also essential to develop an highly efficient methodology. The numerical integration scheme used in the MFW analysis is essentially explicit. However, by including information that has already been calculated at 'upstream' points in the current iteration, a degree of implicitness can be introduced into the scheme. This results in a so-called *pseudo-implicit* method, which results in faster information propagation through the wake solution. To further enhance the numerical stability characteristics, the integration scheme is implemented as a two-step predictor-corrector sequence.

Let n represent the iteration index such that $r_{l,k}^n$ represents the position vector of the kth collocation point on the vortex filament trailed from a rotor blade located at ψ_l at the current, n^{th} iteration. Analogously, $r_{l,k}^{n-1}$ represents the position of the same point at the previous iteration, and $r_{l,k}^{n+1}$ will be its location at the next iteration. Using this notation, the pseudo-implicit, predictor and corrector steps derived from Eq. 4 can be presented in the following point-operator notation,

Predictor:

$$\vec{r}_{l,k}^{\,n} = \vec{r}_{l-1,k-1}^{\,n}$$
$$+ \left(\vec{r}_{l,k-1}^{\,n} - \vec{r}_{l-1,k}^{\,n}\right)\left(\frac{\Delta\psi - \Delta\zeta}{\Delta\psi + \Delta\zeta}\right)$$
$$+ \frac{2}{\Omega}\left(\frac{\Delta\psi\Delta\zeta}{\Delta\psi + \Delta\zeta}\right)\left(\vec{V}_\infty + \frac{1}{4}\left(\vec{V}_{ind}(\vec{r}_{l-1,k-1}^{\,n-1})\right.\right.$$
$$\left.\left. + \vec{V}_{ind}(\vec{r}_{l-1,k}^{\,n-1}) + \vec{V}_{ind}(\vec{r}_{l,k-1}^{\,n-1}) + \vec{V}_{ind}(\vec{r}_{l,k}^{\,n-1})\right)\right) \quad (5)$$

Corrector:

$$\vec{r}_{l,k}^{\,n} = \vec{r}_{l-1,k-1}^{\,n}$$
$$+ \left(\vec{r}_{l,k-1}^{\,n} - \vec{r}_{l-1,k}^{\,n}\right)\left(\frac{\Delta\psi - \Delta\zeta}{\Delta\psi + \Delta\zeta}\right)$$
$$+ \frac{2}{\Omega}\left(\frac{\Delta\psi\Delta\zeta}{\Delta\psi + \Delta\zeta}\right)\left(\vec{V}_\infty + \frac{1}{4}\left(\bar{\vec{V}}_{ind}(\vec{r}_{l-1,k-1})\right.\right.$$
$$\left.\left. + \bar{\vec{V}}_{ind}(\vec{r}_{l-1,k}) + \bar{\vec{V}}_{ind}(\vec{r}_{l,k-1}) + \bar{\vec{V}}_{ind}(\vec{r}_{l,k})\right)\right) \quad (6)$$

The velocities used by the corrector step are given by

$$
\begin{aligned}
\bar{\vec{V}}_{ind}(\vec{r}_{l-1,k-1}) &= +\omega \vec{V}_{ind}(\tilde{\vec{r}}^{n}_{l-1,k-1}) \\
&+ (1-\omega)\vec{V}_{ind}(\vec{r}^{n-1}_{l-1,k-1}) \\
\bar{\vec{V}}_{ind}(\vec{r}_{l-1,k}) &= \omega \vec{V}_{ind}(\tilde{\vec{r}}^{n}_{l-1,k}) \\
&+ (1-\omega)\vec{V}_{ind}(\vec{r}^{n-1}_{l-1,k}) \\
\bar{\vec{V}}_{ind}(\vec{r}_{l,k-1}) &= \omega \vec{V}_{ind}(\tilde{\vec{r}}^{n}_{l,k-1}) \\
&+ (1-\omega)\vec{V}_{ind}(\vec{r}^{n-1}_{l,k-1}) \\
\bar{\vec{V}}_{ind}(\vec{r}_{l,k}) &= \omega \vec{V}_{ind}(\tilde{\vec{r}}^{n}_{l,k}) \\
&+ (1-\omega)\vec{V}_{ind}(\vec{r}^{n-1}_{l,k})
\end{aligned} \tag{7}
$$

Note that both, predictor and corrector steps have the same degree of implicitness embedded within them. The predictor step is used to determine the approximate geometry at the current (n^{th}) iteration based on the velocity field computed from the previous iteration. This geometry is then used to approximate the source terms (induced velocity field) that corresponds to the predicted wake geometry. The corrector step then uses an average or weighted average of the velocities from the predictor step, as well as the velocities from the previous iteration that were originally used by the predictor step. The parameter, ω is a 'relaxation parameter' that can be adjusted to compute the weighted velocity average used by the corrector step. Typically, $\omega = 0.75$.

Because the original PDE (Eq. 2) is first-order in time and space, it requires the specification of an initial condition in the ψ direction and a boundary condition in the ζ direction. However, because the non-Lagrangian nature of the above formulation, the initial condition degenerates into a second boundary condition in the ψ direction. The boundary condition in the ζ direction, i.e., along the length of the vortex filaments, requires that the vortices be attached to the blades from which they are trailed. The boundary condition in the azimuthal or ψ direction implies wake periodicity, i.e., the wake structure is self-preserving and repeats itself every rotor revolution under steady-state conditions.

In addition to the implicitness of the iterative scheme, a further degree of implicitness can be introduced into the solution process by choosing a preferred direction of information propagation (Refs. 39 and 40). This is done by using the known or specified boundary conditions in the ζ direction, but by computing the free-wake solutions around the rotor azimuth as opposed to along the lengths of the vortex filaments. Such an approach is referred to as an *implicit boundary conditions* scheme, where wake collocation points are continuously updated in azimuthal sweeps thereby reducing the dependency on approximate, mid-iteration collocation point information. This is described in greater detail in Refs. 39 and 40.

Convergence Criterion

It is necessary to impose a convergence criterion on any relaxation scheme. In the present analysis, this is based on a measure of the L_2 norm of the change in the wake geometry between successive iterations. In practice, this RMS change can be written in the following form

$$
RMS = \frac{1}{l_{max}k_{max}}\sqrt{\sum_{\psi:l=1}^{l_{max}}\sum_{\zeta:k=1}^{k_{max}}\left(\vec{r}^{n}_{l,k} - \vec{r}^{n-1}_{l,k}\right)^2} \tag{8}
$$

Note that the RMS is normalized with respect to the number of free collocation points in the wake. Convergence is reached after the RMS value, normalized with respect to the first iteration RMS, drops below a certain prescribed threshold between two successive iterations. The normalized convergence threshold has been defined to be of the order of 10^{-4}, and the RMS change must fall below this value to ensure that the wake structure has properly converged. For an RMS value of this order of magnitude, the wake geometry exhibits no appreciable change between successive wake iterations. This then also ensures that the wake geometry has truly converged to a steady solution, and not just exhibited an initial convergence trend and reached a local minima.

Vortex Model

From the above discussion, it is clear that the free-wake is highly dependent upon the vortex induced velocity field as determined from the Biot-Savart law. In its original form as introduced in Eq. 3, the Biot-Savart law assumes an ideal or potential vortex. This, however, produces a singularity at an evaluation point that lies on the influencing vortex. Likewise, the induced velocities at points very close to the vortex will experience unrealistically large induced velocities. These can cause the evolving wake to become unstable, or at the very least, will result in a grossly over-distorted and non-physical wake solution. This is a problem common to most, if not all, free-wake methodologies.

In the MFW, a physical viscous core vortex model based on experimental measurements of rotor tip vortices has been used (Refs. 41 and 42). Vortex models used in free-wake analysis are typically defined in terms of their tangential or swirl velocity profiles. One series of general desingularized velocity profiles for rectilinear vortices may be written as (Ref. 43)

$$
v_\theta(r) = \frac{\Gamma\, r}{2\pi(r_c^{2n} + r^{2n})^{\frac{1}{n}}} \tag{9}
$$

Note that n is an integer variable and r is the distance along a radial emanating from the center of the vortex. The maximum tangential velocity occurs at

$r = r_c$, which is defined, by convention, as the viscous core radius. From Eq. 9, note that if $n \to \infty$, the Rankine vortex profile is obtained, and if $n = 1$, the Scully (Kauffman) velocity profile is recovered. While both these models have been popularly used in previous free-wake analysis, seemingly small differences in the assumed tangential velocity profile of the vortex model for the same core radius can have some effects on the computed wake induced velocities. Care must, therefore, be taken in selecting a vortex model. By default the MFW uses the $n = 2$ velocity profile, although the other models may be selected by the user.

In addition to the choice of vortex velocity profile model, the induced velocities are also sensitive to the dimensions of the vortex core radius. Physically, the initial size of the tip vortex core radius of helicopter rotors is known to be of the order of blade thickness, or typically 10-15% of mean blade chord (e.g., Ref. 42). However, for some numerical models used for rotor loads, performance, and acoustics, it is often necessary to select a larger than physically realistic core radius to avoid numerical problems. This is physically incorrect because the size of the vortex core radius has direct bearing on the predicted structure of the free tip vortex geometries in the far wake. Therefore, a physically correct vortex model and core size must be used, which must match as closely as possible the actual characteristics of rotor vortices.

In the present analysis, the vortex core model allows for viscous diffusion with age. One simple approach uses the Lamb-Oseen vortex diffusion model. Here, the variation of the vortex core radius, r_c with time or age, t, can be determined as (Ref. 44)

$$r_c \approx 1.12\sqrt{4\nu t} \tag{10}$$

In the MFW analysis, vortex diffusion has been accounted for using a modified form of Eq. 10 so as to include an 'eddy,' or turbulent viscosity coefficient δ, such that

$$r_c = 1.12\sqrt{4\nu\delta t} \tag{11}$$

Also, the ideal tip vortex starts with a zero core radius that grows with the square-root of time, and no assumptions need be made with regard to a starting core radius. In practice, however, the physical roll-up of a rotor tip vortex is very complicated, and usually produces a vortex that is already in some stage of decay. Eq. 11 can be modified to represent a variety of initial core radii and growth rates, which can override the default values and be specified by the user if required. For rotor applications, Eq. 11 can be rewritten in terms of rotor time or the age of a vortex element as $t = \zeta/\Omega$. Substituting $\nu = 1.46 \times 10^{-5}$ for air into Eq. 11 and simplifying gives

$$r_c = r_0 + 0.00855\sqrt{\delta\frac{\zeta}{\Omega}} \tag{12}$$

where r_0 is an initial (measured) vortex core radius at $t = 0$ and δ is an experimentally determined coefficient. The effect of δ is to increase the rate at which the vortex core grows with time. For a laminar vortex, δ would have a value of unity, however, in practice, it is found that the resulting diffusion of the vortex is non-physically slow. The eddy viscosity coefficient can be written as a function of the vortex Reynolds number, Γ/ν, as

$$\delta = 1 + a_1\frac{\Gamma_{avg}}{\nu} \tag{13}$$

Because the strength of the tip vortex varies with azimuth, an average vortex strength has been used to define δ, which is given by

$$\Gamma_{avg} = \frac{1}{j_{max}}\sum_{j=1}^{j_{max}}\Gamma_j \tag{14}$$

In general, δ will vary between fixed- and rotary-wing models, as well as between full and scaled rotor systems. In the MFW, the default value is $a_1 = 0.1 =$ constant. This value has been determined through numerical experimentation and comparison of predicted wake geometries with experimental measurements (Ref. 35). A more complete discussion on the effects of δ on the wake solution can be found in Refs. 35 and 37.

Acceleration Algorithms

The FDE's that define the free-wake problem must be evaluated for each and every collocation point in the rotor wake. The computational cost associated with free-wake iterations can be estimated directly as a function of the number of evaluations that must be performed to compute a wake solution. Let $N_\psi = 360°/\Delta\psi$ be the number of discrete azimuthal grid points. Likewise, for a vortex filament that is n rotor revolutions old, the number of free collocation points (= number of free vortex elements on that filament), is $N_\zeta = n\,360°/\Delta\zeta$. Therefore, a total of N_ζ^2 Biot-Savart evaluations must be performed for each free vortex filament at each of N_ψ locations to account for the total self-induced velocities at each collocation point from every other vortex element. Assuming that the wake is modeled using only a single (tip) free vortex filament, this results in $N_\psi\,N_\zeta^2$ evaluations to define the wake at all azimuth angles. For a rotor with N_b blades, a further $N_b\,(N_b - 1)\,N_\psi\,N_\zeta^2$ evaluations must be performed to account for mutually induced effects. The total number of Biot-Savart evaluations required per free-wake computation is given by

$$N_E = (1 + N_b\,(N_b - 1))\,N_\psi\,N_\zeta^2 \tag{15}$$

For equal step sizes, $\Delta\psi = \Delta\zeta \Rightarrow N_\zeta = nN_\psi$, and so the total number of evaluations becomes

$$N_E = (1 + N_b\,(N_b - 1))\,n\,N_\psi^3 \tag{16}$$

For a typical four bladed helicopter rotor, assuming three revolutions of free-tip vortices and equal discretization step sizes of 10 degrees, Eq. 16 shows that the Biot-Savart integral must be evaluated over 1.8×10^6 times to cover the entire computational domain just once. Doubling the resolution (i.e., using step sizes half the original size, such that $\Delta\psi = \Delta\zeta = 5°$) requires eight times that number, or over 14.5×10^6 evaluations. For acoustic analysis, where typically $\Delta\psi = \Delta\zeta = 0.5°$), over 10^8 induced velocity evaluations must be performed. For additional free vortex filaments, the mutual interactions between all the free vortices must also be computed, leading to further increases in computational effort. Clearly then, even a relatively modest reduction in the number of velocity field evaluations can potentially translate into significant reductions in CPU time.

A measure of the gain in computational efficiency can be made in terms of the CPU times required between coarse and refined wake grids. Assuming that the CPU time is directly proportional to the number of operations leads to the following hypothesis:

CPU time $\propto$ Number of operations $\propto$ Number of Biot-Savart evaluations $\propto$ Number of free collocation points $\propto$ Number of trailers, length of free vortex filaments, discretization resolution.

Based on the above proportionality assumptions, and by utilizing Eqs. 15 and 16, a computational cost index, CI, can be defined as a measure of the gain in computational efficiency. Three cost indices can be defined as the reciprocal of the ratios of relative CPU cost

$$CI^{-1} = \frac{CPU_0}{CPU_1} = \frac{N_{E_0}}{N_{E_1}} = N^3, \quad \Delta\psi = \Delta\zeta \qquad (17)$$

$$CI^{-1} = \frac{CPU_0}{CPU_1} = \frac{N_{E_0}}{N_{E_1}} = N, \quad \Delta\psi > \Delta\zeta$$

$$CI^{-1} = \frac{CPU_0}{CPU_1} = \frac{N_{E_0}}{N_{E_1}} = N^2, \quad \Delta\zeta > \Delta\psi$$

CPU_0 corresponds to the execution time required for a discretization resolution corresponding to step sizes $\Delta\psi_0$, $\Delta\zeta_0$. CPU_1 is the execution time required for a coarse resolution with step sizes $\Delta\psi_1 = N\Delta\psi_0$ and/or $\Delta\zeta_1 = N\Delta\zeta_0$. From Eq. 17, it will be seen that doubling the azimuthal step size relative to the baseline results in an algorithm that requires half the time (on a per iteration basis) of the baseline. Doubling the step sizes in the ζ direction reduces the CPU time by a factor of four, whereas doubling both the ψ and ζ step sizes increases the computational efficiency eight-fold.

The computational enhancement algorithms developed for the MFW accelerate the solutions by systematically decreasing the total number of Biot-Savart evaluations, and therefore, the CPU time required,
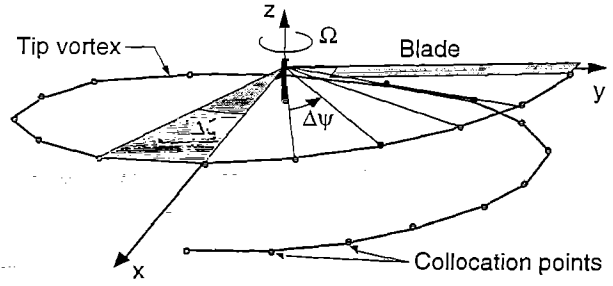
Figure 4: Rotor azimuth and vortex filament discretization
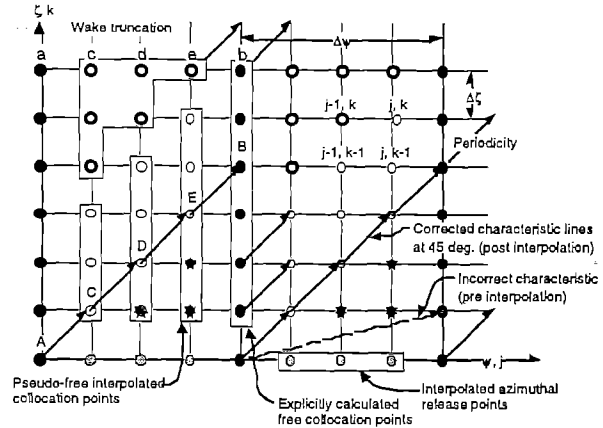
Figure 5: Discretized computational domain for linear velocity interpolation, $\Delta\psi > \Delta\zeta$.

while also maintaining the fidelity of the predictions.

Linear Velocity Interpolation

The underlying principle for using linear interpolation with unequal step sizes is to perform fewer explicit induced velocity evaluations, while retaining the accuracy and fidelity of the wake obtained with small equal discretization step sizes. This acceleration algorithm uses larger step sizes with linear interpolation to map the azimuthal and vortex filament discretizations. The induced velocity terms, denoted by $\vec{V}_{ind}$ in Eq. 4, are treated as before using velocity averaging and relaxation parameters (Refs. 36-38).

The computational economy of an interpolation algorithm is a consequence of not having to evaluate the Biot-Savart law for each and every collocation point in the computational domain. The position in space of every collocation point (whether calculated or interpolated) is still determined the same way. However, the self- and mutually-induced velocity fields are computed explicitly only between the free colloca-
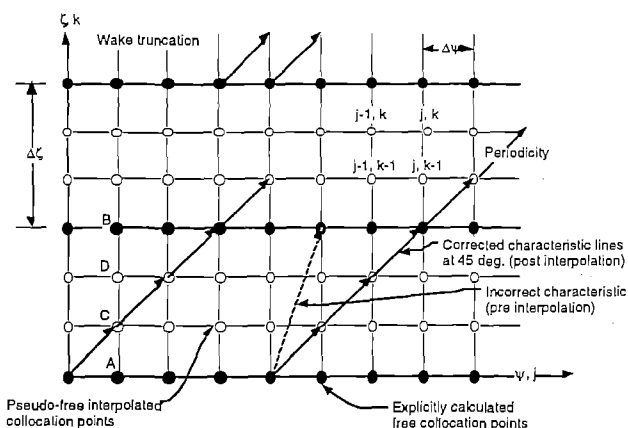
Figure 6: Discretized computational domain for linear velocity interpolation, $\Delta\psi < \Delta\zeta$.

tion points. Linear interpolation is used to determine the local induced velocity field at the interpolated or pseudo-free collocation points. This local, interpolated velocity field is then used at the pseudo-free collocation points to convect them to force-free locations in the rotor flow field, just as for the truly free points. Note again, however, that it is not the spatial positions of the collocation points that are being interpolated, but the local velocity field itself.

Note that two velocity interpolation algorithms are possible, depending upon the discretization ratios between the rotor azimuthal and vortex filament step sizes. If $\Delta\psi/\Delta\zeta > 1$, with $\Delta\psi$ being an integral multiple of $\Delta\zeta$, then interpolation is performed in the azimuthal direction. The discretized computational domain for this case is shown in Fig. 5. The solid symbols represent the explicitly computed collocation points, whereas the open points are those where the induced velocities are interpolated. The interpolation algorithm is applied to determine the local induced velocity field at each interpolated (open) point, and not to directly interpolate the spatial locations. All wake collocation points are allowed to convect through the flow field. While simple displacement interpolation could have been used, this would have resulted in a wake solution no different than that obtained using a coarse discretization with additional collocation points superimposed on the solution. In such a case, it would not be possible to obtain a solution approaching the predictive accuracy of a high resolution wake. Note that interpolation is performed between points that lie on different vortex filaments but on the same characteristic line (direction of information propagation) – i.e., points "C", "D" and "E" are interpolated using information at points "A" and "B."

Interpolation along the vortex filaments is applied

when the discretization step in the ζ direction is larger than the discretized azimuthal step size, i.e., $\Delta\zeta/\Delta\psi > 1$, and $\Delta\zeta$ is an integral multiple of $\Delta\psi$. For such cases, collocation points are interpolated between the originally specified, calculated collocation points along the length of the same vortex filaments. For example, in the discretized computational domain shown in Fig. 6, points "C" and "D" (open) are interpolated using information from calculated points "A" and "B" (solid) lying on the same vortex filament. The velocity field at each of the calculated, free collocation points is explicitly computed by invoking the Biot-Savart law, and these sparse, free collocation points are, again, assumed to be interconnected by straight line vortex segments. The local induced velocity field at each of the pseudo-free collocation points is linearly interpolated in the ζ direction. This approximate velocity field is then used to convect these points.

The gain in computational efficiency in using velocity interpolation, therefore, comes from the savings from performing fewer evaluations of the Biot-Savart law because it is not evaluated at the interpolated points. When applying interpolation algorithms, the characteristic lines of information propagation match the equal step size cases, these concepts also being illustrated in Figs. 5 and 6.

Adaptive Grid Sequencing

The adaptive grid sequencing algorithm starts the free-wake solution using a coarse grid. As the free-wake iterations proceed, the grid resolution is adaptively refined. As explained previously, wake convergence is measured as an L_2-Norm or root-mean-square (RMS) change in geometries between successive iterations, normalized with respect to the number of free collocation points in the wake, and relative to the first iteration RMS. The final few wake iterations are performed at the highest grid resolution. Using a low resolution grid during the initial iterations provides better initial condition to begin the subsequent higher resolution iterations. Gains in computational efficiency result as a consequence of faster convergence and by performing fewer overall induced velocity evaluations.

The initial iterations are performed assuming a coarse level wake. At each iteration level, only those rotor azimuthal locations and wake collocation points that correspond to the current level of discretization are treated freely. The 'interior' wake collocation points are not computed explicitly, but are treated as pseudo-free and are allowed to convect through the rotor flow at the interpolated velocity field. When the iteration block corresponding to a given resolution is complete, a new iteration block is then initiated using a higher resolution than before. The previous iteration solution is used as a starting value or initial wake geometry for this new iteration block. The process is

repeated until the final few iterations are performed at the highest resolution desired. This results in a wake geometry that is essentially identical to that obtained by performing all the iterations at the highest resolution, but with up to an order of magnitude reduction in computing effort.

Results and Discussion

Axial Flight

Axial flight conditions can often prove to be challenging for free wake models from the stand point of numerical stability. Many existing schemes exhibit non-physical numerical instabilities in the solution for the tip vortex locations, especially in hover. The MFW has demonstrated to be free of these numerical instabilities.

Sample results, obtained from a coupled, rotor trim/free-wake solution are presented in Fig. 7 using two revolutions of free wake and for a discretization resolution of $\Delta\psi = \Delta\zeta = 10°$. The figures show isometric views of the wake for a four bladed rotor of solidity, $\sigma = 0.095$, operating at a nominal thrust coefficient of $C_T = 0.008$. In pure axial ascent, Fig. 7(a), the wake extends far below the rotor and contracts smoothly in accordance with classical momentum theory. The smooth contraction of the wake is also apparent from Fig. 7(b), from which it is also clear that the solution is free of non-physical numerical perturbations or distortions. Axial descent, Fig. 7(c) exhibits a more interesting trend. The wake for this flight condition lies entirely above the rotor, and expands radially outward, a result that is again consistent with momentum theory. The predicted wake geometries are azimuthally symmetric, as expected under axial flight conditions.

Forward Flight

Steady, Level Flight

Tip vortex predictions in forward flight for advance ratios ranging from $\mu = 0.05$ to 0.3 are shown in Fig. 8. The progressive increase in wake skew angle with increasing advance ratio is clearly apparent. Moreover, the lateral roll-up of the trailed wake, downstream of the advancing and retreating blades can also be seen.

The corresponding fore and aft vertical displacements of the tip vortices in the longitudinal plane of the rotor are shown in Fig. 9(a) and (b) versus wake age. Of interest are the forward wake boundaries, which show the trajectories of the tip vortices passing above the rotor tip-path-plane. This has also been observed experimentally (e.g., Ref. 45). Moreover, the effects of blade passage events on the wake (axial) displacements can also be seen. Comparisons between
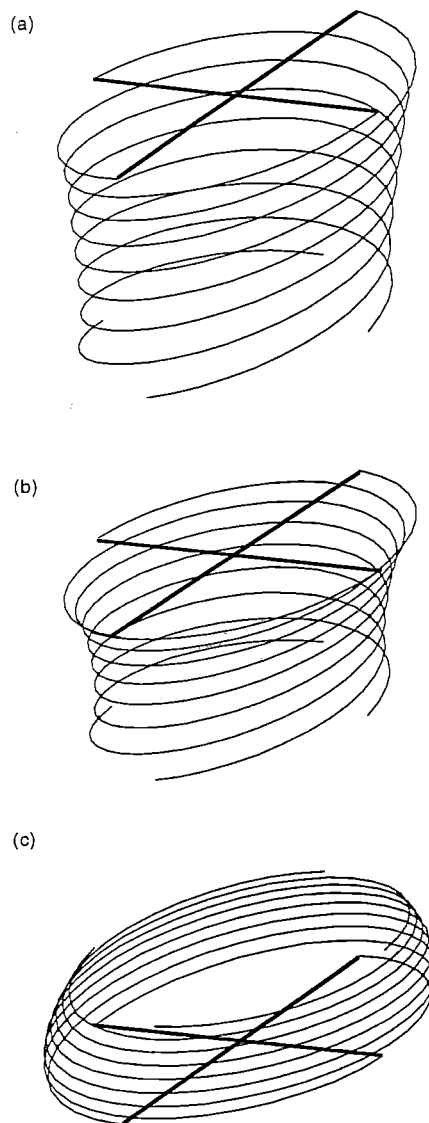
Figure 7: Isometric wake geometries in axial flight, (a) vertical ascent at $\lambda_c = 0.72$, (b) hover, (c) vertical descent at $\lambda_c = -0.72$

wake predictions from the MFW analysis with experimental measurements have demonstrated the physical accuracy of the wake solution for various flight conditions – see Refs. 35-36.

Descending Flight

Descending forward flight can be simulated by specifying an aft tilt of the rotor shaft, $\alpha_s = 2°$ for $C_T = 0.008$, and $\mu = 0.1$. The vertical displacements versus wake age at the front of the rotor disk are shown in Fig. 10. Compared with Fig. 9, it is clear that the tip vortices trailed from the blades at the

(a)

(b)

(c)

(d)
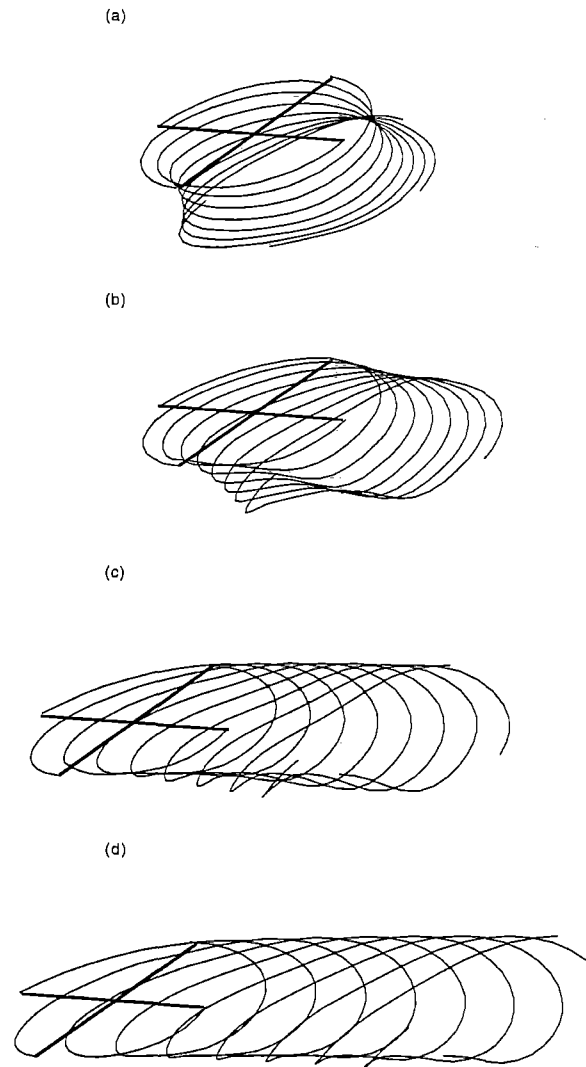
Figure 8: Predicted wake geometries in forward flight, $C_T = 0.008$, $\alpha_s = -2°$, (a) $\mu = 0.05$, (b) $\mu = 0.1$, (c) $\mu = 0.2$, (d) $\mu = 0.3$

Figure 9: Fore and aft vertical displacements of the tip vortices in forward flight
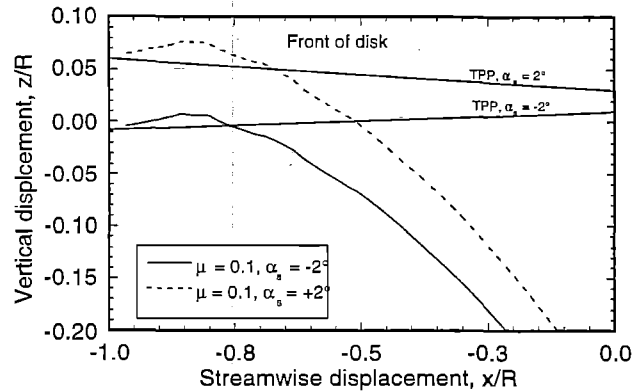
Figure 10: Vertical wake displacements in descending forward flight, front of rotor disk

front of the disk travel well above and further downstream before passing back down through the rotor disk. It is well known that under such descent conditions, blade-vortex interaction (BVI) events can be severely exasperated, leading to increased rotor noise and vibration. Contour maps of the instantaneous inflow velocities for forward and backward shaft tilts of the rotor at an advance ratio of 0.2 are shown in Fig. 11. In the regions of high velocity gradients, large temporal aerodynamic loads are produced on the blades. From Fig. 11, it can also be seen that the likelihood of BVI increases on the retreating side of the rotor.

Maneuvering Flight

The MFW analysis can be applied to determine wake structures under steady-state maneuvering conditions, such as constant rate pitching and rolling. Sample wake predictions have been performed for a rotor in forward flight ($\mu = 0.1$), executing a steady nose-up pitch maneuver at a rate of $\bar{q} = 0.008$. A

Figure 12: Pitching wake boundaries

Figure 13: Wake convergence trends in axial and forward flight

In general, it can be seen that the wake converges faster (in fewer iterations) with increasing advance ratio. It can be seen that the solutions relax smoothly in all cases, and convergence is monotonic and absolute.

Wake Acceleration

The results presented above were for a nominal discretization of 10° in the azimuthal direction and along the vortex filament lengths. Although considerably more refined than most previously available free-wake analyses, the application of free-wake schemes to determine high resolution blade loads for acoustics analyses require even finer resolutions. However, because the cost increases approximately with the cube power of the number of wake elements, very high resolution wake predictions suffer from very high run times. Some wake models also impose a lower bound on the level of discretization to avoid numerical problems. The wake acceleration schemes described previously have been developed to allow for very high resolution wake geometries to be computed at reasonable exe-

Figure 11: Wake induced inflow in steady level flight (upper), and descending forward flight (lower)

comparison of the wake boundaries in the longitudinal plane of the rotor between the maneuvering and level flight cases serves to illustrate the modified wake structure produced by the pitching motion – see Fig. 12. The rotor induced velocity field is also modified as a consequence – the effects on the rotor response have been identified as a possible source of rotor cross-coupling (Refs. 1-4).

Wake Convergence

Numerical convergence trends of the wake for the flight conditions discussed above are shown in Fig. 13.

cution times and without sacrificing the accuracy of the predicted solution.

Using linear interpolation with $\Delta\psi = 1°$ and $\Delta\zeta = 10°$, tip vortex geometry predictions for a tandem rotor configuration have been obtained, providing an effective wake resolution of 1 degree. The specified rotor geometry and spacing is representative of a CH-47D configuration, with a significant overlap between the two rotors and their wakes. The operating advance ratio is 0.1 and both rotor shafts are tilted forward 1 deg. Top, side and rear views of the predicted wake geometries are shown in Fig. 14.

It is clear that the wakes from the two rotors undergo significant mutually induced distortions, particularly in the region where the two rotors overlap each other. The rear portion of the wake from the front rotor is convected closer to the rotor tip-path-plane (Fig. 14, side view) under the influence of the wake from the rear rotor. Such interactions can potentially lead to significant increases in BVI and the associated generation of impulsive noise and vibration. The fore portion of the wake from the rear rotor is also significantly distorted, with increased vertical tip vortex displacements. Recall that the full mutual interactions between both rotor wakes have been accounted for in these calculations.

For twin rotors, wake convergence is monitored separately for the vortices trailed by both rotors. The convergence characteristics of the tandem rotor wakes are shown in Fig. 15, and like the single rotor, demonstrate that convergence is absolute and monotonic for both wakes.

Predicted wake geometries for a tilt-rotor configuration in forward-flight with multiple trailed vortex filaments including the effects of the shed wake are shown in Fig. 16. The wake was discretized using vortex element step sizes of $\Delta\zeta = 15°$ and a rotor azimuthal discretization of $\Delta\psi = 5°$. The wake convergence threshold was specified to within a 0.09% relative change in wake structure between consecutive iterations. As for the tandem-configuration, wake convergence was monitored independently for all free vortices from both rotors – see Fig. 17.

Summary and Conclusions

The basis and mathematical formulation of the MFW free-vortex wake analysis has been reviewed. The MFW is based on a non-Lagrangian pseudo-implicit, predictor-corrector, relaxation algorithm. The MFW can be used to predict the vortical rotor wake structure and inflow velocities for rotors operating in axial and forward flight. Solutions can also be obtained during steady-state maneuvers, such as coordinated turns. Another feature of the MFW is that it can solve for the interacting wake structures generated by multi-rotor configurations such as tandems and coaxials. Acceleration schemes have been formulated
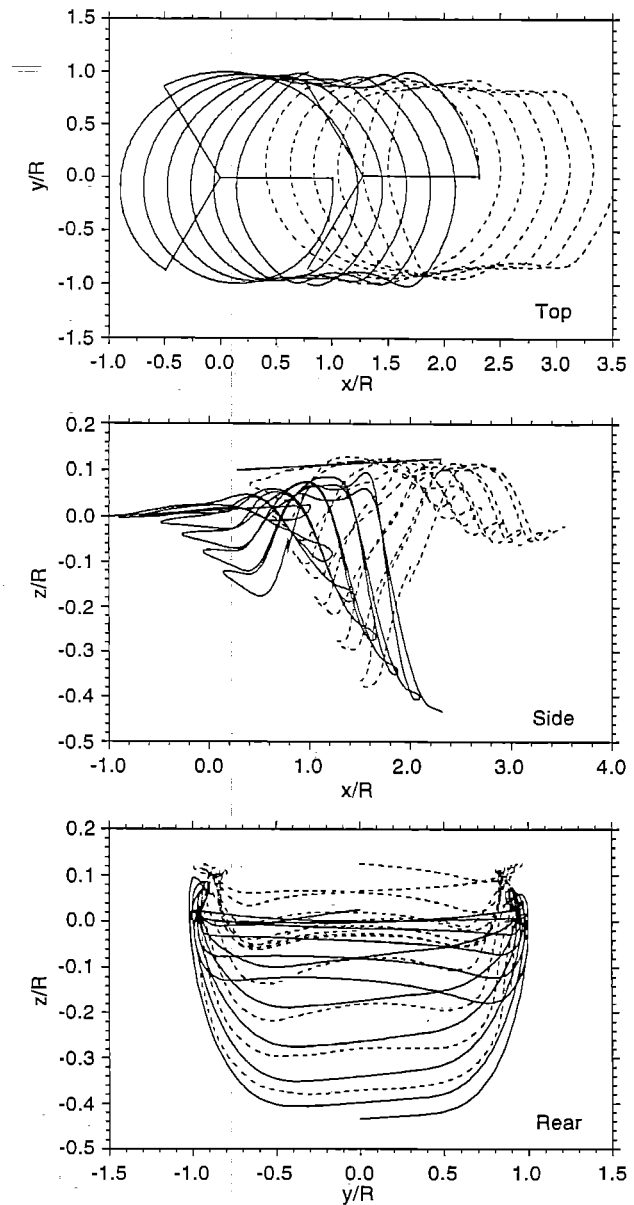
Figure 14: High resolution wake geometry for a tandem rotor configuration using linear interpolation; 1 deg. effective discretization ($\Delta\zeta/\Delta\psi = 10$)

to reduce the execution times for wake geometry predictions, but without loss in predictive accuracy or numerical robustness of the method. Some of these acceleration schemes are generic, and can be applied to other wake models.

The MFW allows for various user selectable options to allow the rotor wake to be modeled with varying degrees of sophistication – these ranging from single tip vortices to multiple trailed filaments and shed
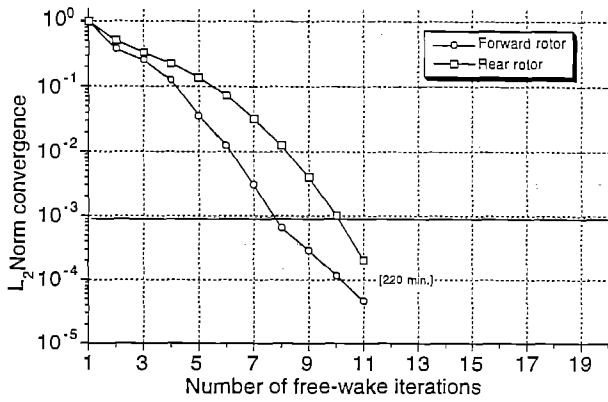
Figure 15: Convergence characteristics for the tandem rotor configuration, 1 deg. effective resolution.

circulation elements. Various desingularized vortex and viscous diffusion models can be used, some of which are user selectable. Examples of the predicted wake geometries for various flight conditions, ranging from axial flight to steady maneuvering forward-flight, have been presented to demonstrate the capabilities of the scheme. Very high resolution wakes for multi-rotor configurations can also be computed, which are useful for aeroacoustic analyses. Absolute convergence of the numerical solutions has been demonstrated for all flight conditions and levels of wake discretization, demonstrating the robustness and stability of the wake scheme. The numerical attributes and wide range of possible applications, along with realistic computational costs, make the MFW ideally suited for inclusion into comprehensive schemes for rotor performance, aeroacoustics, aeroelasticity and flight mechanics analyses.

Acknowledgments

References

[1] Rosen, A., Isser, A., "A New Model of Rotor Dynamics During Pitch and Roll of a Hovering Helicopter," *Journal of the American Helicopter Society,* Vol. 30, No. 3, July 1995, pp. 17-28.
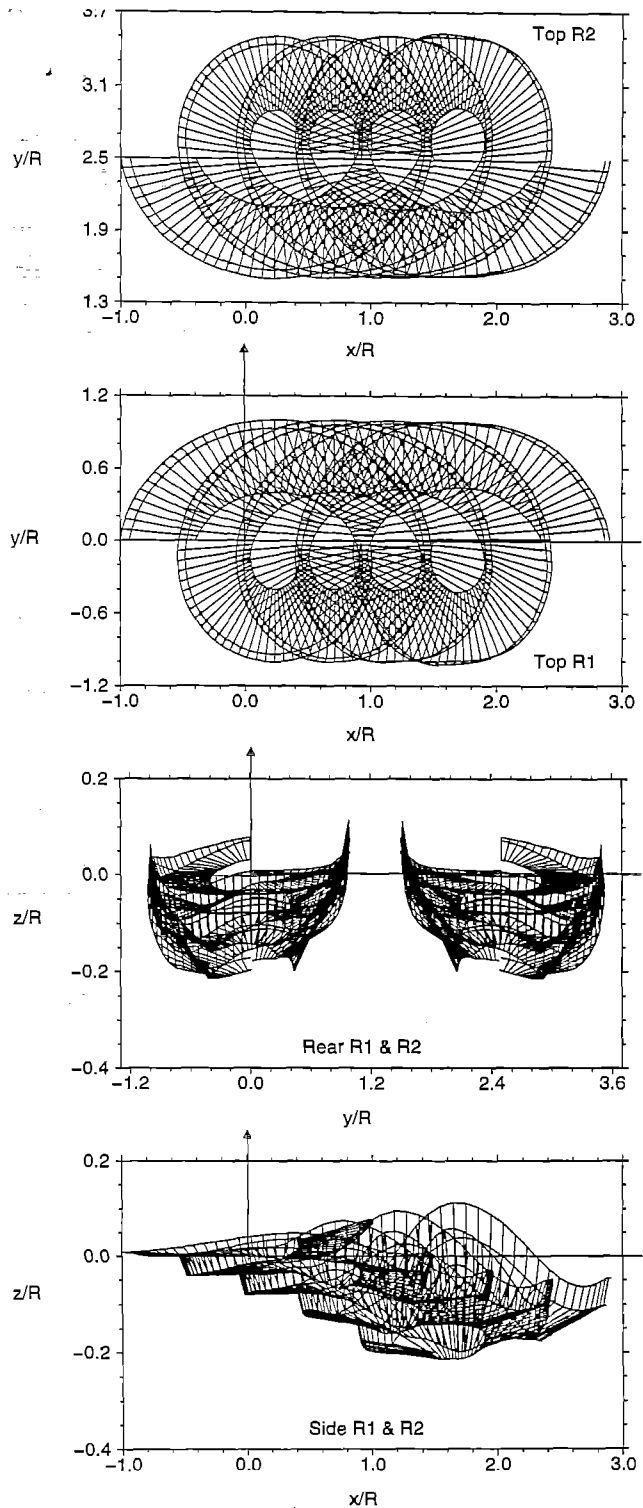
Figure 16: Predicted wake geometries, tilt rotor configuration – top, rear and side views using linear interpolation, $N_b = 2$, $\Delta\psi = 5°$, $\Delta\zeta = 15°$, $\mu = 0.15$, $\alpha_s = -2°$.
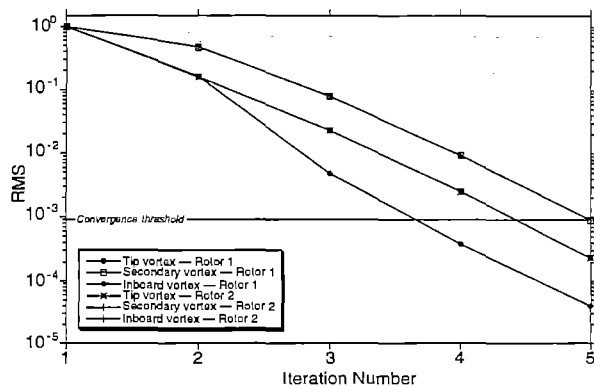
Figure 17: Example convergence histories

[2]von Grünhagen, W., "Dynamic Inflow Modeling for Helicopter Rotors and its influence on the Prediction of Crosscoupling," Presented at the *American Helicopter Society* Aeromechanics Specialist Conference, Fairfield County, Connecticut, Oct. 11-13, 1995.

[3]Keller, J. D., Curtiss, H. C., "Modeling the Induced Velocity of a Maneuvering Helicopter," Proceedings of the 52nd Annual Forum of the American Helicopter Society, Washington, D.C., June 4-6, 1996.

[4]Basset, P. M., "Modeling the Dynamic Inflow on the Main Rotor and the Tail Components in Helicopter Flight Mechanics," Presented at the 22nd European Rotorcraft Forum, Brighton, UK, Sept. 17-19, 1996.

[5]Sternfield, H., Schairer, J. O., "Study of Rotor Blade Tip Vortex Geometry for Noise and Airfoil Applications," Boeing Helicopters Report No. D8-2464-1A, Philadelphia, PA, Dec. 1969.

[6]Schmitz, F. H., "Aeroacoustics of Flight Vehicles, Theory and Practice, Vol. 1, Noise Sources," NASA Reference Publication 1258, Vol. 1, Aug. 1991, pp. 65-149.

[7]Batchelor, G. K., *An Introduction to Fluid Dynamics*, Cambridge University Press, Cambridge, England, 1967, p. 264.

[8]Scully, M. P., "A Method of Computing Helicopter Vortex Wake Distortion," Massachusetts Institute of Technology, Report No. ASRL TR 138-1, June 1967.

[9]Bliss, D. B., Quackenbush, T. R., Bilanin, A. J., "A New Methodology for Helicopter Free Wake Analysis," Proceedings of the 39th Annual National Forum of the American Helicopter Society, St. Louis, MO, May 9-11, 1983.

[10]Bliss, D. B., Wachspress, D. A., Quackenbush, T. R., "A New Approach to the Free wake Problem for Hovering Rotors," Proceedings of the 41st Annual National Forum of the American Helicopter Society, Ft. Worth, TX, May 1985.

[11]Bliss, D. B., Dadone, L., Wachspress, D. A., "Rotor Wake Modeling for High Speed Applications," Proceedings of the 43rd Annual National Forum of the American Helicopter Society, St. Louis, MO, May 1987.

[12]Johnson, W. R., "Wake Model for helicopter Rotors in High Speed Flight," NASA CR-177507, US-AVSCOM TR-88-A-008, Nov. 1988.

[13]Quackenbush, T. R., Bliss, D. B., Wachspress, D. A., Ong C. C., "Free Wake Analysis of Hover Performance Using a New Influence Coefficient Method," NASA CR-4309, July 1990.

[14]Miller, W. O., Bliss, D. B., "Direct Periodic Solutions of Rotor Free Wake Calculations," *Journal of the American Helicopter Society*, Vol. 38, No. 2, April 1993, pp. 53-60

[15]Crouse, G. L., Jr., Leishman, J. G., "A New Method for Improved Free-Wake Convergence in Hover and Low Speed Forward Flight," Proceedings of the 21st AIAA Aerospace Sciences Meeting and Exhibit, Reno, NV, Jan. 11-14, 1993.

[16]Quackenbush, T. R., Lam, C. M. G., Wachspress, D. A., Bliss, D. B., "Analysis of High Resolution Unsteady Airloads for Helicopter Rotor Blades," Proceedings of the 50th Annual National Forum of the American Helicopter Society, Washington, D. C., May 11-13, 1994.

[17]Clark, D. R., Leiper, A. C., "The Free Wake Analysis – A Method for the Prediction of Helicopter Rotor Hovering Performance," *Journal of the American Helicopter Society*, Vol. 15, No. 1, Jan. 1970, pp. 3-11.

[18]Sadler, S. G., "A Method for Predicting Helicopter Wake Geometry, Wake-Induced Flow and Wake effects on Blade Airloads," Proceedings of the 27th. Annual Forum of the American Helicopter Society, Washington, D.C., May 1971.

[19]Sadler, S. G., "Development and Application of a Method for Predicting Rotor Free Wake Positions and Resulting Rotor Blade Air Loads," Vol. 1 – Model and Results, NASA CR-1911, Dec. 1971.

[20]Sadler, S. G., " Main Rotor Free Wake Geometry Effects on Blade Air Loads and Response for Helicopters in Steady Maneuvers," Vol. 1 – Theoretical Formulation and Analysis of Results, NASA CR-2110, Sept. 1972.

[21]Berry, J. D., "Prediction of Time-Dependent Fuselage Pressures in the Wake of a Helicopter Rotor," Proceedings of the 2nd International Conference on Basic Rotorcraft Research, University of Maryland, College Park, MD, Feb. 16-18, 1988.

[22]Egolf, T. A., "Helicopter Free Wake Prediction of Complex Wake Structures Under Blade-Vortex Interaction Operating Conditions," Proceedings of the 44th Annual Forum of the American Helicopter Society, Washington, D.C., June 16-18, 1988.

[23]Egolf, T. A., Massar, J. P., "Helicopter Free Wake Implementation on Advanced Computer Architecture," Proceedings of the 2nd International Conference on Basic Rotorcraft Research, University of Maryland, College Park, MD, Feb. 16-18, 1988.

[24]Miller, R. H., "A Simplified Approach to the Free Wake Analysis of a Hovering Rotor," Vertica, Vol. 6, 1982, pp. 89-95.

[25]Miller, R. H., "Vortex Theory for Hovering Rotors," AIAA Journal, Vol. 20, No. 12, Dec. 1982, pp. 1754-1756.

[26]Miller, R. H., "Application of Fast Free Wake Analysis Techniques to Rotors," Vertica, Vol. 8, No. 3, 1984, pp. 255-261.

[27]Beddoes, T. S., "A Wake Model for High Resolution Airloads," Proceedings of the 2nd International Conference on Basic Rotorcraft Research, Triangle Park, NC, 1985.

[28]Landgrebe, A. J., "An Analytical Method for Predicting Rotor Wake Geometry," Journal of the American Helicopter Society, Vol. 14, No. 4, Oct. 1969, pp. 20-32.

[29]Scully, M. P., "Computation of Helicopter Rotor Wake Geometry and Its Influence on Rotor Harmonic Airloads," Massachusetts Institute of Technology, ASRL TR 178-1, March 1975.

[30]Johnson, W., "A Comprehensive Analytical Model of Rotorcraft Aerodynamics and Dynamics, Part I: Analysis Development," NASA TM 81182, 1980.

[31]Bliss, D. B., Teske, M. E., Quackenbush, T. R., "A New Methodology for Free Wake Analysis Using Curved Vortex Elements," NASA CR-3958, December 1987.

[32]Chua, K., Quackenbush, T. R., "A Fast Three-Dimensional Vortex Method for Unsteady Wake Calculations," Proceedings of the 10 AIAA Applied Aerodynamics Conference, Palo Alto, CA, June 22-24, 1992, Paper No. AIAA-92-2624-CP.

[33]Bliss, D. B., Miller, W. O., "Efficient Free Wake Calculations Using Analytical/Numerical Matching," Journal of the American Helicopter Society, Vol. 38, No. 2, April 1993, pp. 43-52.

[34]Miller, W. O., "A Fast Adaptive Resolution Method for Efficient Free Wake Calculations," Proceedings of the 49th. Annual National Forum of the American Helicopter Society, St. Louis, MO, May 19-21, 1993.

[35]Bagai, A., "Contributions to the Mathematical Modeling of Rotor Flow-Fields using a Pseudo-Implicit Free-Wake Analysis," Doctoral Dissertation, Department of Aerospace Engineering, University of Maryland at College Park, 1995. UM-AERO 95-20.

[36]Bagai, A., Leishman, J. G., "Rotor Free-Wake Modeling using a Pseudo-Implicit Technique – Including Comparisons with Experiment," Journal of the American Helicopter Society, Vol. 40, No. 3, July 1995, pp. 29-41.

[37]Bagai, A., Leishman, J. G., "Rotor Free-Wake Modeling Using a Pseudoimplicit Relaxation Algorithm," AIAA Journal of Aircraft, Vol. 32, No. 6, Nov.-Dec. 1995, pp. 1276-1285.

[38]Bagai, A., Leishman, J. G., "Free-Wake Analysis of Tandem, Tilt-Rotor and Coaxial Rotor Configurations," Journal of the American Helicopter Society, Vol. 41, No. 3, July 1996, pp. 196-207.

[39]Bagai, A., Leishman, J. G., "Adaptive Grid Sequencing and Interpolation Schemes for Accelerated Rotor Free-Wake Analyses," Proceedings of the 53rd Annual Forum of the American Helicopter Society, Virginia Beach, Virginia, April 29 - May 1, 1997.

[40]Bagai, A., Leishman, J. G., "Accelerated, High Resolution Free-Vortex Wakes for Rotor Aeroacoustic Analysis," Proceedings of the 15th AIAA Applied Aerodynamics Conference, Atlanta, Georgia, June 23 - 25, 1997.

[41]Leishman, J. G., Baker, A. M., Coyne, A. J., "Measurements of Rotor Tip Vortices Using Three-Component Laser Doppler Velocimetry," Journal of the American Helicopter Society, Vol. 41, No. 4, October 1996, pp. 342-353.

[42]Coyne, A. J., Bhagwat, M. J., Leishman, J. G., "Investigation into the Rollup and Diffusion of Rotor tip Vortices using Laser Doppler Velocimetry" Proceedings of the 53rd Annual Forum of the American Helicopter Society, Virginia Beach, Virginia, April 29 - May 1, 1997.

[43]Vatistas, G. H., Kozel, V., Mih, W. C., "A Simpler Model for Concentrated Vortices," Experiments in Fluids, 11, 1991, pp. 73-76.

[44]Lamb, Sir Horace, Hydrodynamics, 6th Edition, Cambridge University Press, 1932, pp. 592-593, 668-669.

[45]Leishman, J. G., Bagai, A., "Fundamental Studies of Rotor Wakes in Low Speed Forward Flight using Wide-Field Shadowgraphy," Proceedings of the 9th Applied Aerodynamics Conference, Baltimore, Sept. 1991.

AEROELASTIC OPTIMIZATION OF A COMPOSITE TILT ROTOR

Ömer Soykasap and Dewey H. Hodges

School of Aerospace Engineering,
Georgia Institute of Technology,
Atlanta, Georgia

ABSTRACT:

Composite tilt rotor aeroelastic optimization is performed by using the mixed variational formulation based on exact intrinsic equations of motion for dynamics of moving beams by Hodges along with the finite-state dynamic inflow theory by Peters and He.

A composite box beam model is used to represent the principal load carrying member of the rotor blade. The blade is discretized using finite elements. Each wall used to model the box beam is made of 24 laminated orthotropic composite plies.

For the optimization, design variables are blade twist, box width and height, horizontal and vertical wall thicknesses, the ply angles of the laminated walls and nonstructural masses. The rotor is optimized for the figure of merit in hover and the axial efficiency in forward flight while keeping the same thrust levels in both flight modes. Blade weight, autorotational inertia, and geometry are considered as constraints. Davidon-Fletcher-Powell technique is used for the unconsrained optimization. Results obtained are presented in the paper for effects such as extension-twist coupling, choice of layups, and cross-sectional geometry of the blade.

AEROELASTIC OPTIMIZATION OF A COMPOSITE TILT ROTOR

by
Ömer Soykasap and Dewey H. Hodges

School of Aerospace Engineering
Georgia Institute of Technology
Atlanta, Georgia

OUTLINE

- Introduction

- Aeroelastic Analysis

- Optimization Implementation

- Optimization Results

- Conclusions

INTRODUCTION

- Tilt rotor aircraft is one of the most important vehicles that are capable of vertical take off and landing (VTOL).

- The tilt rotor aircraft combines the high-speed efficiency of a turboprop aircraft with VTOL capabilities of a helicopter.

In this study, composite tilt-rotor aeroelastic optimization is performed by using

- the mixed variational formulation based on the exact intrinsic equations of motion for dynamics of moving beams by Hodges

- and the finite-state dynamic inflow theory by Peters and He.

AEROELASTIC ANALYSIS

- A composite box beam model is used to represent the principal load-carrying member of the rotor blade.

- The blade is discretized using finite elements. Each wall used to model the box beam is made of 24 laminated orthotropic composite plies.
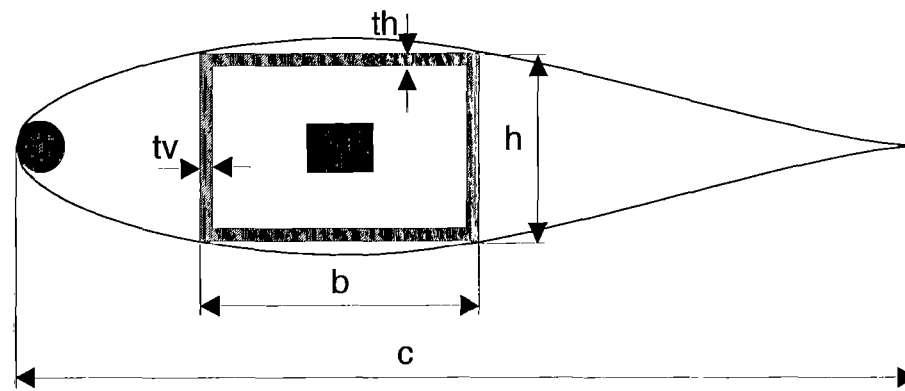
Figure 1. The blade cross section

- Aeroelastic analysis uses Shang's code AEROSCOR, extended to include axial flow.

- Structural Analysis:

Cross-Section Analysis

↓
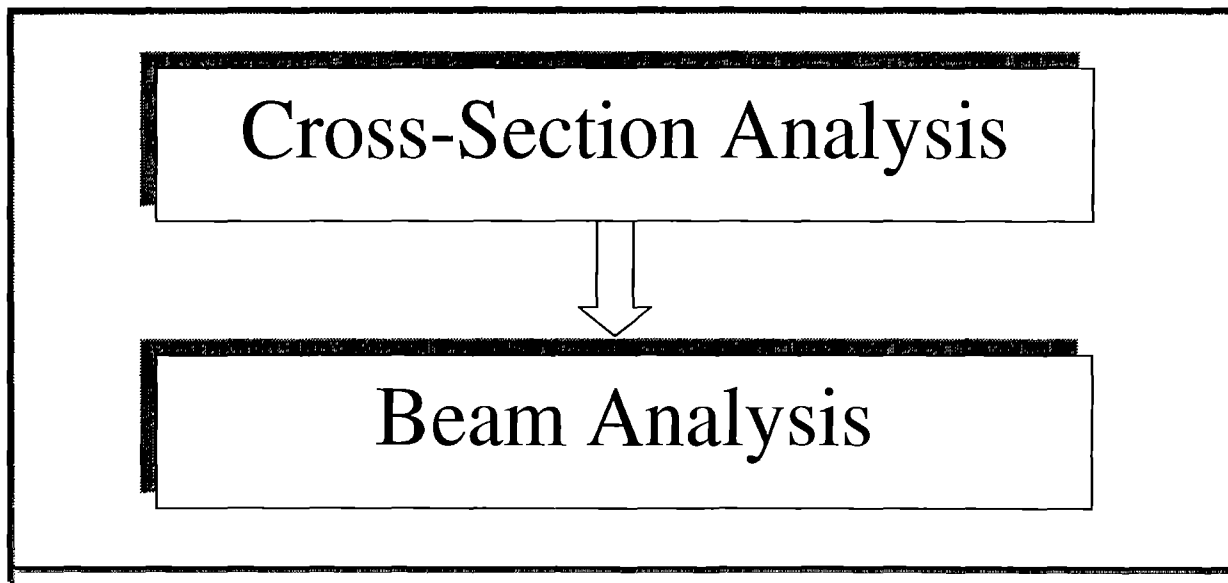
Beam Analysis

Cross-Section Analysis

- The beam stiffness coefficients are obtained from anisotropic thin-walled closed-section beam theory (Berdichevsky et al.), based on asymptotic reduction of shell theory.

- For a realistic cross-section, analysis can be done by VABS.

Beam Analysis

- A nonlinear beam theory based on exact intrinsic equations for dynamics of beams in a moving frame by Hodges is used.

- The theory presents a compact and complete variational formulation that is ideal for finite element analysis.

- The intrinsic equations are derived from Hamilton's principle, which is written as

$$\int_{t_1}^{t_2} \int_0^R \left[\delta(K-U) + \delta\bar{W} \right] drdt = \bar{\delta A}$$

where K and U are kinetic and strain energy densities per unit length, respectively, and δA is the virtual action at the extremities of the space-time domain.

- The internal force and moments vectors F_B and M_B, and linear and angular momentum vectors P_B and H_B are related by the beam constitutive laws to the strain and force measures, and velocity and momentum measures:

$$\left\{ \begin{array}{c} F_B \\ M_B \end{array} \right\} = [S] \left\{ \begin{array}{c} \gamma \\ \kappa \end{array} \right\} \quad , \quad \left\{ \begin{array}{c} P_B \\ H_B \end{array} \right\} = \left[\begin{array}{cc} m\Delta & m_e \\ m_e & I \end{array} \right] \left\{ \begin{array}{c} V_B \\ \Omega_B \end{array} \right\}$$

Aerodynamic Analysis

The finite-state dynamic inflow theory by Peters and He is used in the aerodynamic modeling.

- The blade sectional aerodynamic lift, drag and moment developed are based on an unsteady thin airfoil model.

- The unsteady induced flow is computed from a 3-D dynamic wake theory.

- The inflow is expanded as

$$\bar{\lambda}(\bar{r}, \bar{\psi}, \bar{t}) = \sum_{m=0}^{\infty} \sum_{n=m+1, m+3, \ldots}^{\infty} \phi_n^m(\bar{r}) \left[a_n^m(\bar{t}) \cos(m\hat{\psi}) + b_n^m(\bar{t}) \sin(m\hat{\psi}) \right]$$

where the $\phi_n^m(\bar{r})$'s are the radial inflow shape functions.

OPTIMIZATION IMPLEMENTATION

- The optimum rotor is posed as a constrained maximization problem with multiobjective.

- Design variables are blade twist, box width and height, horizontal and vertical wall thickness, the ply angle of the laminated walls and nonstructural masses.

- The optimization problem is stated as

$$\text{Maximize} \quad F(X) = K_1 F_M + K_2 \eta_{cr}$$

$$\text{Subject to} \quad g_i(X) \le 0 \qquad \text{for } i = 1, m$$

$$h_j(X) = 0 \qquad \text{for } j = 1, 2$$

$$X_i^l \le X_i \le X_i^u \qquad \text{for } i = 1, n$$

where $F_M = Tv/P$ and $\eta_{cr} = TV/P$

Equality Constraints

It is assumed that the optimum rotor must be capable of the same thrust levels in both flight regimes:

$$h_1 = T_{hover} - \left(T_{hover}\right)_{ref} = 0$$

$$h_2 = T_{cruise} - \left(T_{cruise}\right)_{ref} = 0$$

Inequality Constraints

Constraints imposed on the optimization are blade mass, autorotational inertia, strength, and geometry:

- The first constraint imposed is blade mass as

$$g_1 = m/m_{ref} - 1 \leq 0$$

- Next, the wall thickness is constrained so as not violate the modeling approach:

$$g_i = 10(t_h/h)_i - 1 \leq 0 \qquad \text{for } i = 2,3,...,13$$

$$g_i = 10(t_v/b)_i - 1 \leq 0 \qquad \text{for } i = 14,15,..., 25$$

- Then, the blade mass inertia for autorotation is considered as a constraint:

$$g_{26} = 1 - I_A/I_{A\,ref} \leq 0$$

- To prevent the blade stall, angle of attacks for both flight regimes are constrained:

$$g_{27} = \alpha_1 / \alpha_{\text{ref}} - 1 \leq 0$$
$$g_{28} = \alpha_2 / \alpha_{\text{ref}} - 1 \leq 0$$

- Finally, Tsai-Wu failure criterion is used to prevent the material failure:

$$g_{29} = F - 1 \leq 0$$

where

$$F = \sigma_1 \left(\frac{1}{\sigma_{1T}} - \frac{1}{\sigma_{1C}} \right) + \sigma_2 \left(\frac{1}{\sigma_{2T}} - \frac{1}{\sigma_{2C}} \right) + \frac{\sigma_1^2}{\sigma_{1T}\sigma_{1C}}$$
$$- \frac{\sigma_1\sigma_2}{\sqrt{\sigma_{1T}\sigma_{1C}\sigma_{2T}\sigma_{2C}}} + \frac{\sigma_2^2}{\sigma_{2T}\sigma_{2C}} + \frac{\tau_{12}^2}{\tau_{12s}^2}$$

- The ADS (Automated Design Synthesis) optimization code is used as a optimizer

OPTIMIZATION RESULTS

Baseline Tilt Rotor

- The reference rotor is an existing three-bladed gimballed rotor based on the XV-15.

- The typical operating points are

  Hover : $C_T/\sigma = 0.13$, $\Omega = 565$ rpm at sea level

  Forward flight: $C_T/\sigma = 0.05$, $\Omega = 458$ rpm, and V=300 knots at 16000 ft

- Rotor properties are

Number of blades	3
Radius of rotor disc	3.81 m
Blade cord	35.6 cm
Blade mass	47.48 kg
Precone angle	2.5 deg
Autorotation inertia	109.89 kg m^2

Figure 2. Blade chord distribution
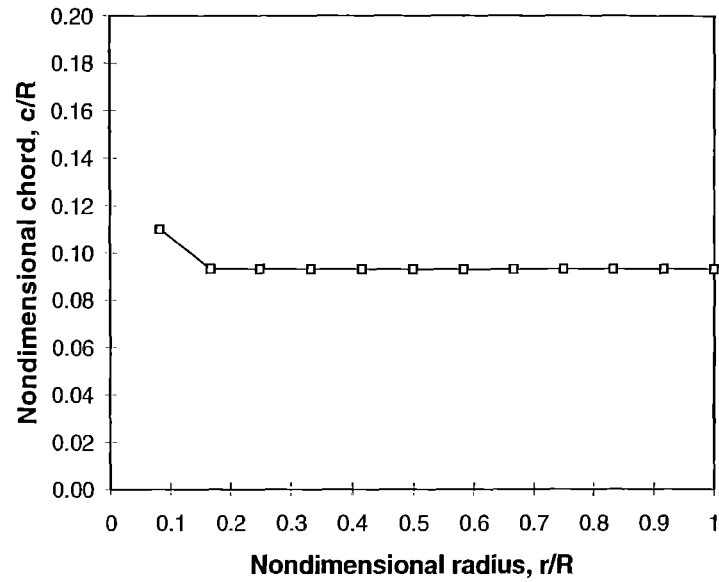
Figure 3. Blade twist distribution
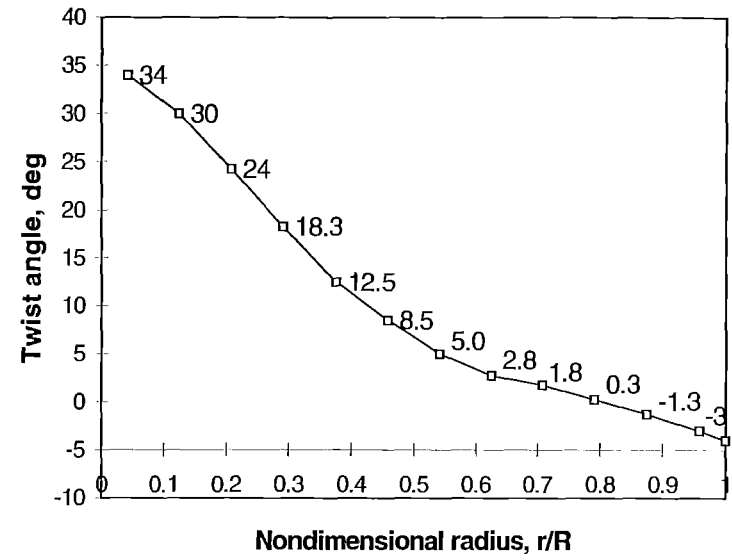
Figure 4. Blade mass distribution
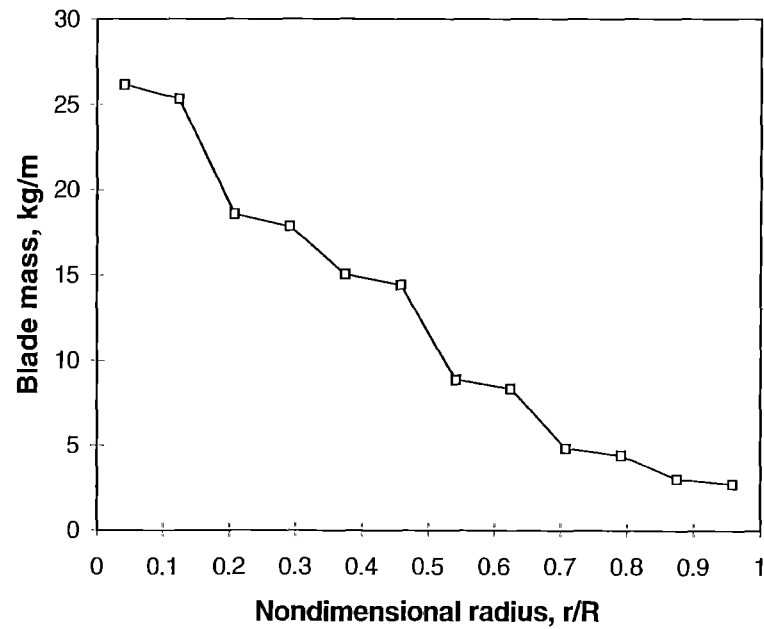
- The box beam is made of AS4/3501-6. The blade is divided into 12 finite elements. Each wall used to model the box beam is made of 24 laminated plies.

- Orientation angles of the laminates are assumed to be same for each wall to take advantage of extension-twist coupling and ease of manufacture.

Design Sensitivity

- The design sensitivity is the rate of change of F_M and η_{cr} (normalized by the trimmed values) with respect to a design variable.

- Sensitivities are obtained by using the finite-difference technique, and are given on the following figures.

Figure 5. Sensitivity for ply angle
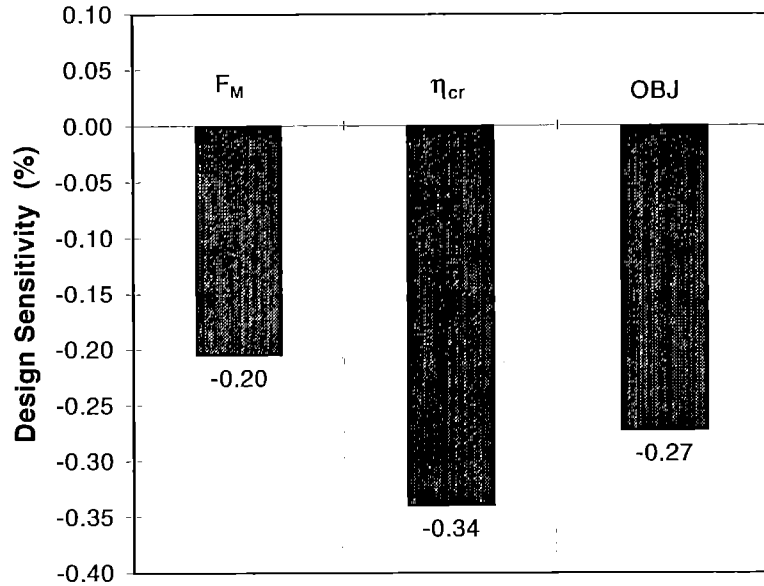
Figure 6. Sensitivity for twist
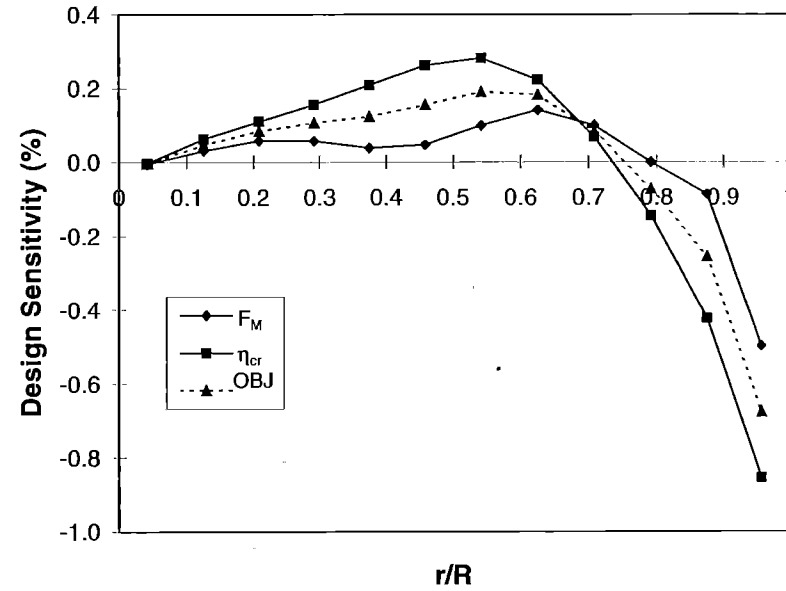
Figure 7. Sensitivity for box width
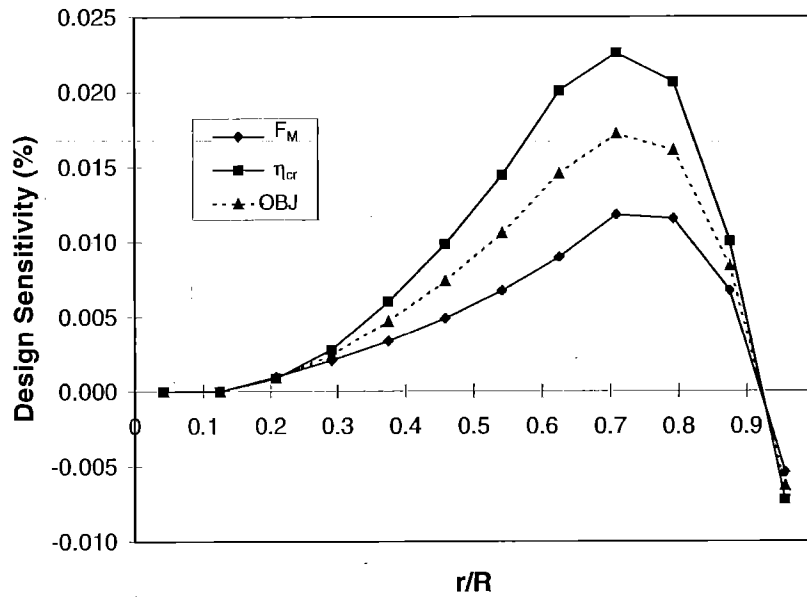
Figure 8. Sensitivity for box height
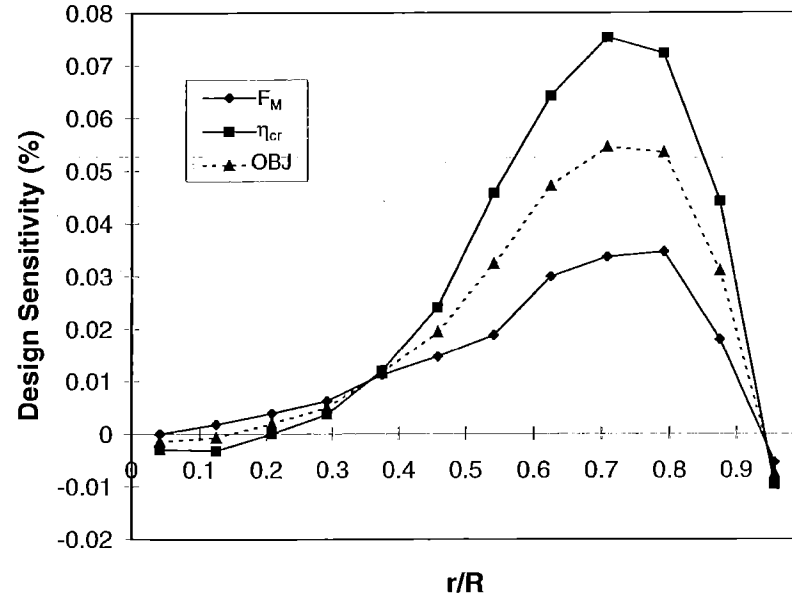
Figure 9. Sensitivity for horizontal wall thickness
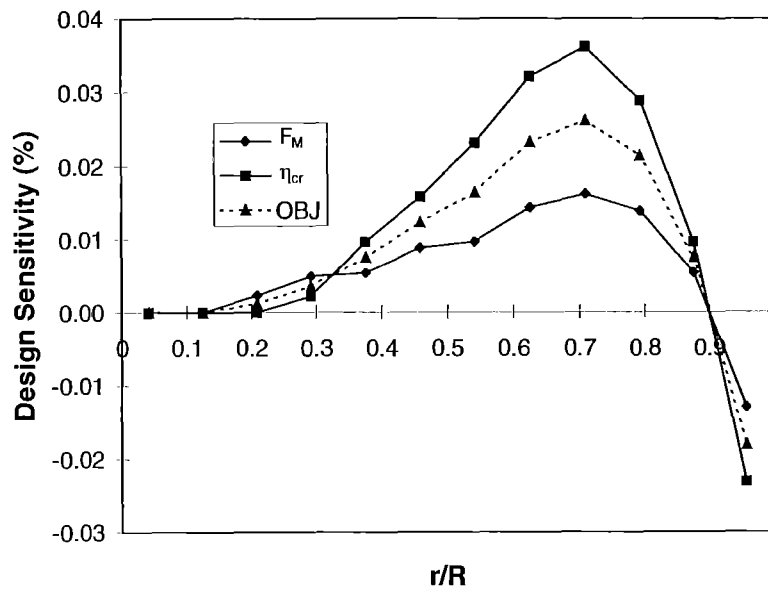
Figure 10. Sensitivity for vertical wall thickness
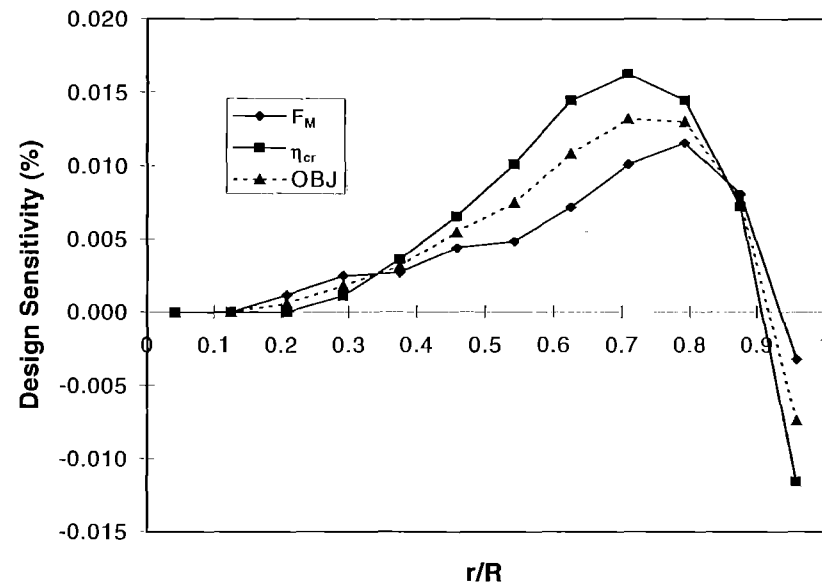
Figure 11. Sensitivity for lumped mass inside the box
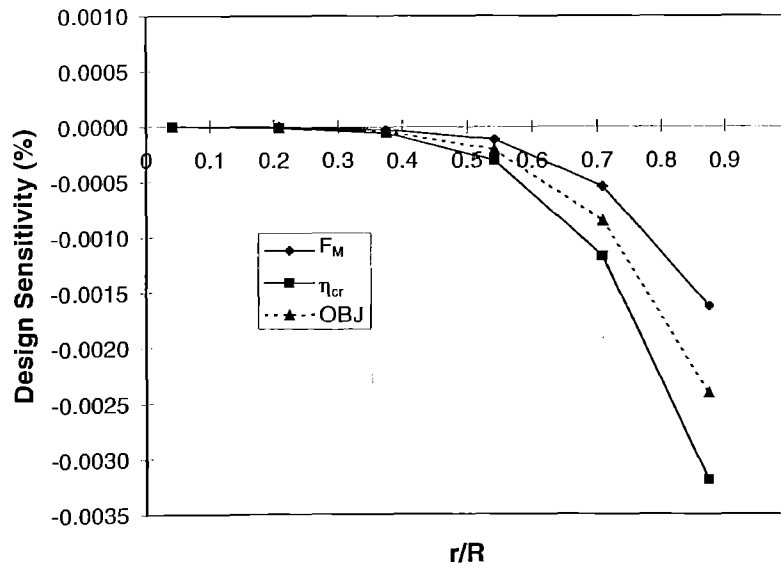
Figure 12. Sensitivity for leading edge weight
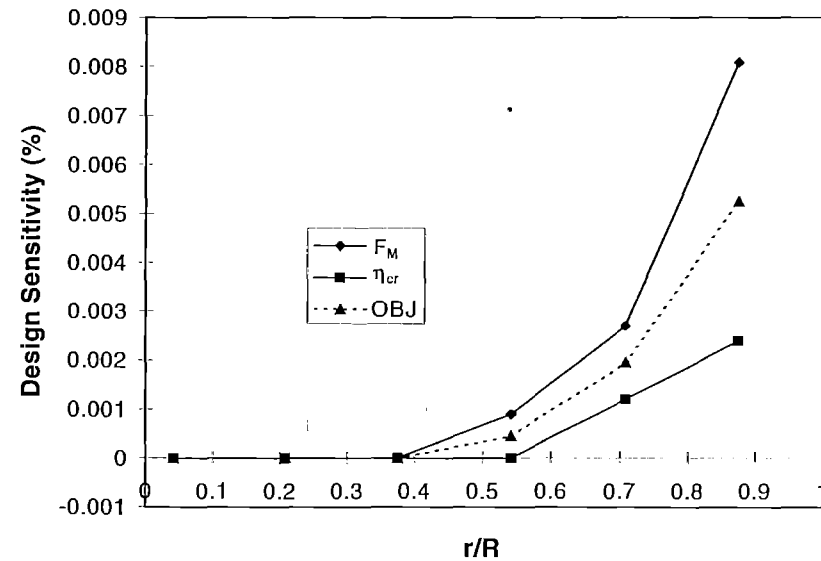
- The performance is more sensitive to ply angle and twist than to other design variables.

- The performance is more sensitive to box width, height, and thicknesses around the quarter chord whereas it is more sensitive to lumped mass inside the box and leading edge weight near the tip.

Results

- The baseline tilt rotor was designed to perform both hover and forward flight capability. The weighting factors are taken to be $K_1=K_2=0.5$.

- To accomplish the multiobjective design goal, a multistep approach is applied.

- To see the extension-twist coupling effect on the performance, the results are obtained for the unconstrained optimization problem taking into account the ply angle as a design variable.

- Davidon-Fletcher-Powell technique is used for the problem considered. Optimum solutions are given for hover, forward flight and for both flights.

	Ply angle (deg)	F_M	η_{cr}	Increase (%)
Baseline	5	.74191	.83025	-
Hover	-10.736	.75375	-	1.60
Forward flight	-33.501	-	.87659	5.58
Optimum for both	-22.561	.75064	.87478	3.39

The effect of ply angle on the rotor performance is shown on the Figure 13.

- Next, twist angle at each finite element of the blade is considered as a design variable as well as ply angle. Starting from the previous optimum ply angle, objective function is maximized.

	F_M	η_{cr}	Increase (%)
Baseline	.74191	.83025	-
Optimum	.74864	.87747	3.43

- Finally, the box beam design variables and non-structural masses are included in the optimization problem, which requires total 73 design variables. Starting from the optimum ply angle, objective function is maximized.

	F_M	η_{cr}	Increase (%)
Baseline	.74191	.83025	-
Optimum	.75130	.87523	3.46

Figure 13. The Effect of ply angle on the performance
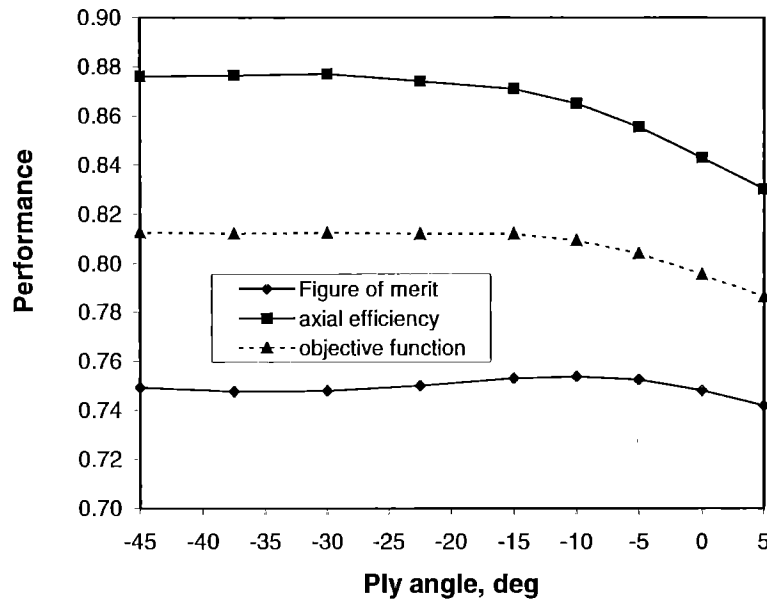
Figure 14. Optimum twist distribution
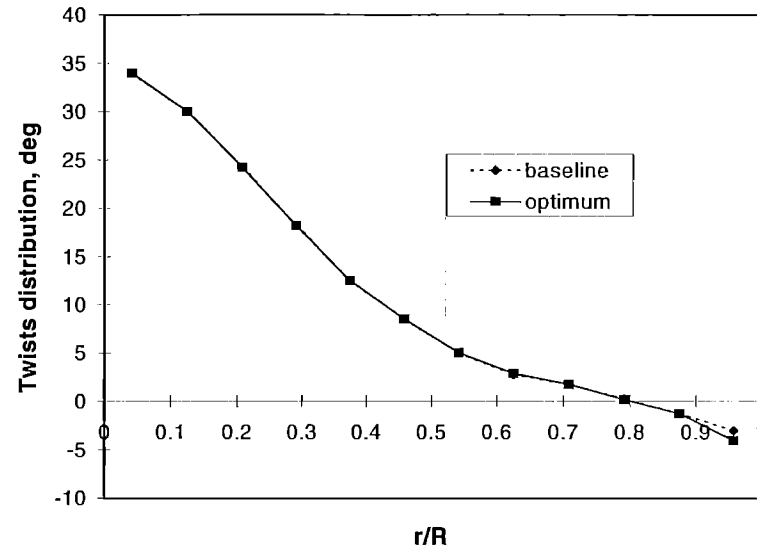
Figure 15. Optimum horizontal wall thickness
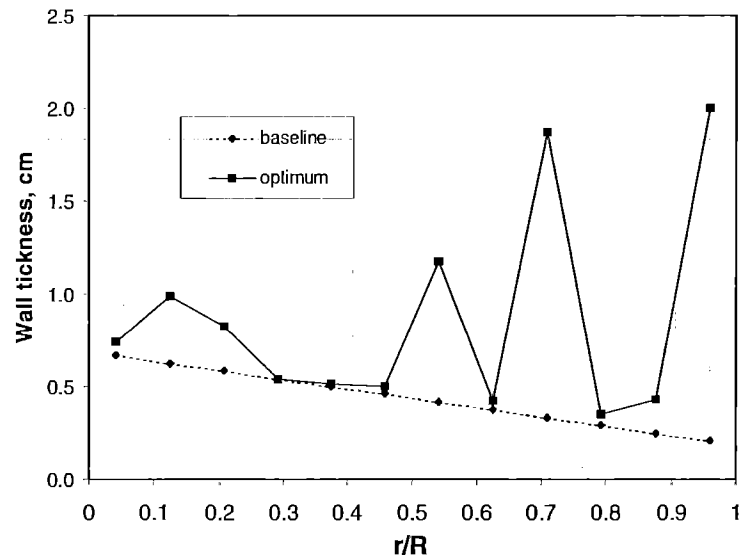
Figure 16. Optimum vertical wall thickness
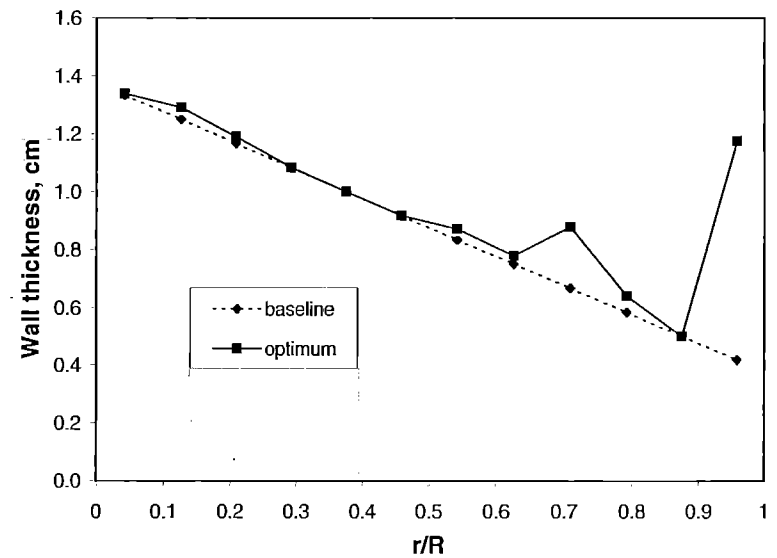
CONCLUSIONS

- This study has described the progress in the development of an aeroelastic optimum design of a composite tilt rotor. At this stage the problem is considered as an unconstrained optimization problem.

- Optimizing the extension-twist coupling for the rotor performance yields significant improvements. Optimum design is compared with the XV-15 tilt rotor performance.

- Design sensitivity show that the performance is more sensitive to twist angle and ply angle than to other design variables.

- Constraint problem will be a future study.

THEODORSEN LIFT DEFICIENCY FUNCTION
IN PERSPECTIVE OF FINITE STATE PARADIGM

MICHAEL J. SOBOL
Graduate Student

SWAMI KARUNAMOORTHY
Professor and Director of Mech. Eng.

Department of Aerospace & Mechanical Engineering
Parks College of Engineering & Aviation
Saint Louis University, Saint Louis, MO. 63156

and

DAVID A. PETERS
Professor and Chairman
Department of Mechanical Engineering
Washington University, St. Louis, MO. 63130

ABSTRACT

The finite state paradigm of dynamic wake has been recognized as the viable applied aerodynamic theory, and it is an exact solution to the three dimensional potential flow equations. This theory has been successfully applied to both rotary wing and fixed wing (stopped rotors) in aeroelastic analysis. However, its application is limited to a low range of reduced frequency ($0 < k < 0.15$). The limitation is due to the convergence of the harmonic expansion of flow field. This expansion converges effectively and efficiently for the average or uniform inflow while it does not converge for the gradient of induced flow. This limits the application of present finite state model to reduced frequencies for which the gradient is not important.

Theodorsen function is first expressed in terms of Bessel functions that are equivalent to uniform inflow and gradient of inflow. Then, it is compared with the results of finite state approximation. The results show that the effect of neglecting the inflow gradient becomes critical at $k=0.3$ for the real part of Theodorsen lift deficiency function and $k=0.15$ for imaginary part of the function. Also, an emphasis is given to determine the inflow gradient by 2-D finite state model assuming that the uniform inflow is known from Theodorsen model. This study gives a better understanding of the problem and serves as a building block for a hybrid model with uniform inflow from 3-D theory (outer expansion) and inflow gradient from 2-D theory (inner expansion). Such a model would remove the limitation on reduced frequency and expand its range of application.

THEODORSEN LIFT DEFICIENCY FUNCTION IN PERSPECTIVE OF FINITE STATE PARADIGM

MICHAEL J. SOBOL

SWAMI KARUNAMOORTHY

DAVID A. PETERS

SEVENTH INTERNATIONAL WORKSHOP ON DYNAMICS
AND AEROELASTIC STABILITY MODELING OF
ROTORCRAFT SYSTEMS, ST. LOUIS

SCOPE OF WORK

TO UNDERSTAND THE LIMITATION IN THE
  CONVERGENCE OF THE HARMONIC EXPANSION OF
  FLOW FIELD

ANALYTICAL EXPERIMENT ON THEODORSEN
  FUNCTION AND TO FIND THE EQUIVALENT OF
  INFLOW GRADIENT

TO SERVE AS A BUILDING BLOCK FOR A POSSIBLE
  HYBRID MODEL WITH 3-D UNIFORM INFLOW AND
  2-D INFLOW GRADIENT

FINITE STATE PARADIGM

IT IS A VIABLE APPLIED AERODYNAMIC THEORY TO
MODEL THE DYNAMIC WAKE FOR ROTORCRAFT
AEROELASTIC PROBLEMS.

IT IS BASED ON THE EXACT SOLUTION TO THE
THREE DIMENSIONAL POTENTIAL FLOW
EQUATIONS.

THE INDUCED FLOW IS EXPRESSED AS A SET OF
HIERARCHICAL LINIEAR DIFFERENTIAL
EQUATIONS.

INDUCED FLOW

$$\frac{\partial \lambda}{\partial t} + U\frac{\partial \lambda}{\partial x} = \frac{1}{2\pi}\frac{d\Gamma/dt}{(b-x)}$$

$$\lambda = \sum_{n=0}^{\infty} \lambda_n \cos(n\phi) \qquad x = b\cos(\phi)$$

$$-b < x < b$$

INDUCED FLOW EQUATIONS

$$\left(\overline{\lambda}\right)_0^* - \frac{1}{2}\left(\overline{\lambda}\right)_2^* + \left(\overline{\lambda}\right)_1 = \frac{\left(\overline{\Gamma}\right)^*}{\pi}$$

$$\frac{1}{2n}\left[\left(\overline{\lambda}\right)_{n-1}^* - \left(\overline{\lambda}\right)_{n+1}^*\right] + \overline{\lambda}_n = \frac{\left(\overline{\Gamma}\right)^*}{n\,\pi}$$

$$\overline{\lambda}_n = \frac{\lambda_n}{b\omega_\alpha}$$

THEODORSEN FUNCTION

$$C(k) = \frac{H_1^{(2)}(k)}{H_1^{(2)}(k) + iH_0^{(2)}(k)}$$

$$= \frac{I_2}{I_1 + I_2}$$

$$I_1 = \frac{\pi}{2i} H_0^{(2)}(k) \qquad I_2 = -\frac{\pi}{2} H_1^{(2)}(k)$$

FINITE STATE APPROXIMATION

$$C(k) = \frac{1 + \frac{1}{2}\lambda_1}{1 + \lambda_0 + \frac{1}{2}\lambda_1}$$

$$\widetilde{C}(k) = \frac{1}{1 + \lambda_0}$$

FINITE STATE PERSPECTIVE

FOR $\Gamma=1$

$$\lambda_0=\frac{I_1}{I_3} \qquad \frac{1}{2}\lambda_1=\frac{I_2}{I_3} - 1$$

$$\widetilde{C}(k) = \frac{I_3}{I_1+I_3} \qquad I_3=\frac{1}{ik}(e)^{-ik}$$

CHALLENGES

$$\begin{bmatrix} 2 & -ik \\ ik & 4 \end{bmatrix} \begin{Bmatrix} \lambda_1 \\ \lambda_2 \end{Bmatrix} = 4\ ik \begin{Bmatrix} 1 - \dfrac{\lambda_0}{2} \\ 1 \end{Bmatrix}$$

ALTERNATE APPROACH

FOR $\theta = 1$

$$\lambda_0 = \frac{I_1}{I_1 + I_2}$$

$$\lambda_1 = \frac{2(I_2 - I_3)}{I_1 + I_2}$$

ANALYTICAL EXPERIMENTS

1. STUDY THE VARIATION OF THEODORSEN FUNCTION WITHOUT THE TERM EQUIVALENT TO INFLOW GRADIENT.

2. STUDY THE SIMILAR BEHAVIOUR FOR THE FINITE STATE APPROXIMATION TO THEODORSEN FUNCTION.

3. STUDY THE HYBRID FORMULATION WHERE THE UNIFORM INFLOW IS FROM THEODORSEN THEORY AND GRADIENT OF INFLOW IS FROM FINITE STATE THEORY.

4. DETERMINE THE INFLOW GRADIENT BY FINITE STATE METHOD ASSUMING THAT THE UNIFORM INFLOW IS KNOWN FROM THEODORSEN THEORY.

Real Lamda 0

■ THEODORSEN
◆ FINITESTATE

k/1+k

Imag Lamda 0

■ THEODORSEN
◆ FINITESTATE

k/1+k
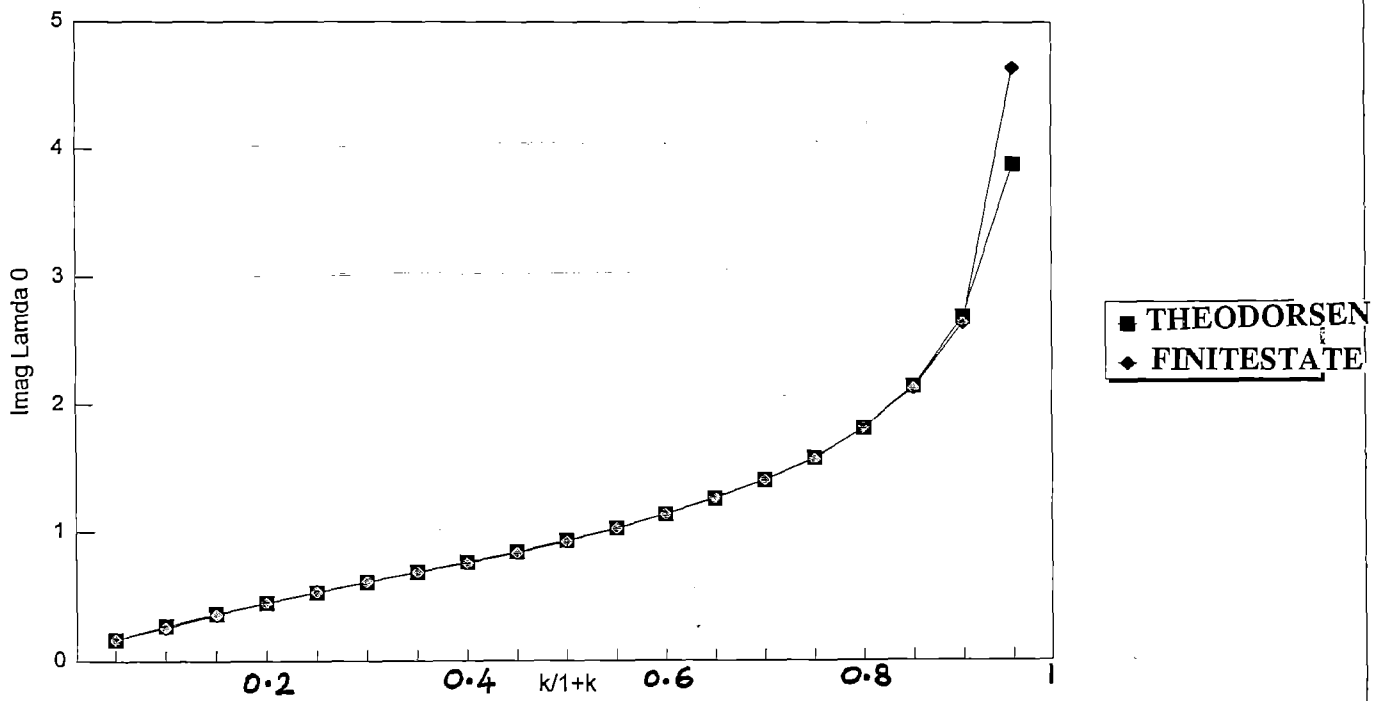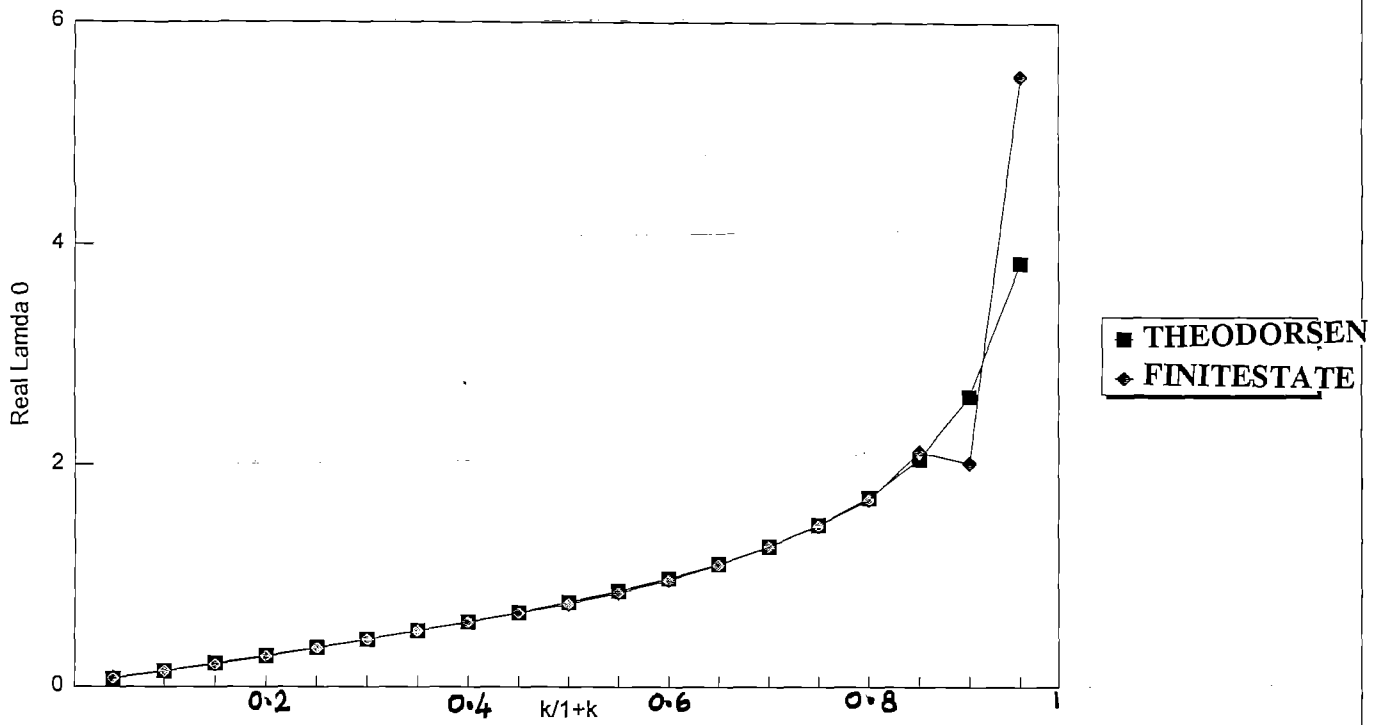
VARIATION OF UNIFORM INFLOW
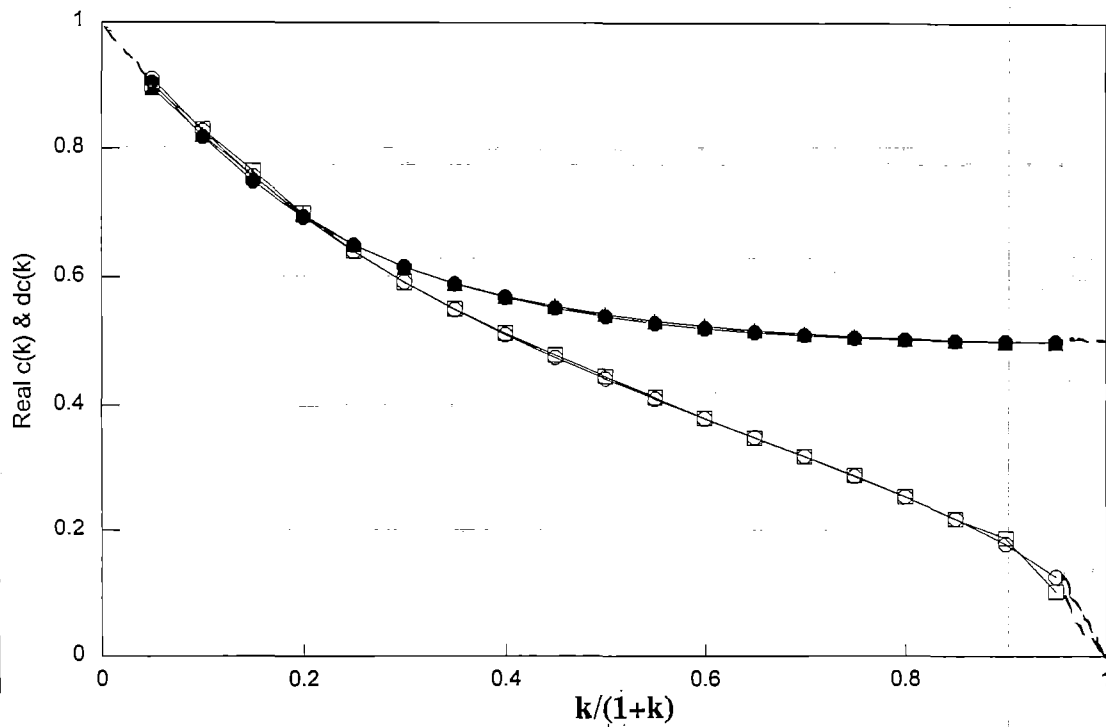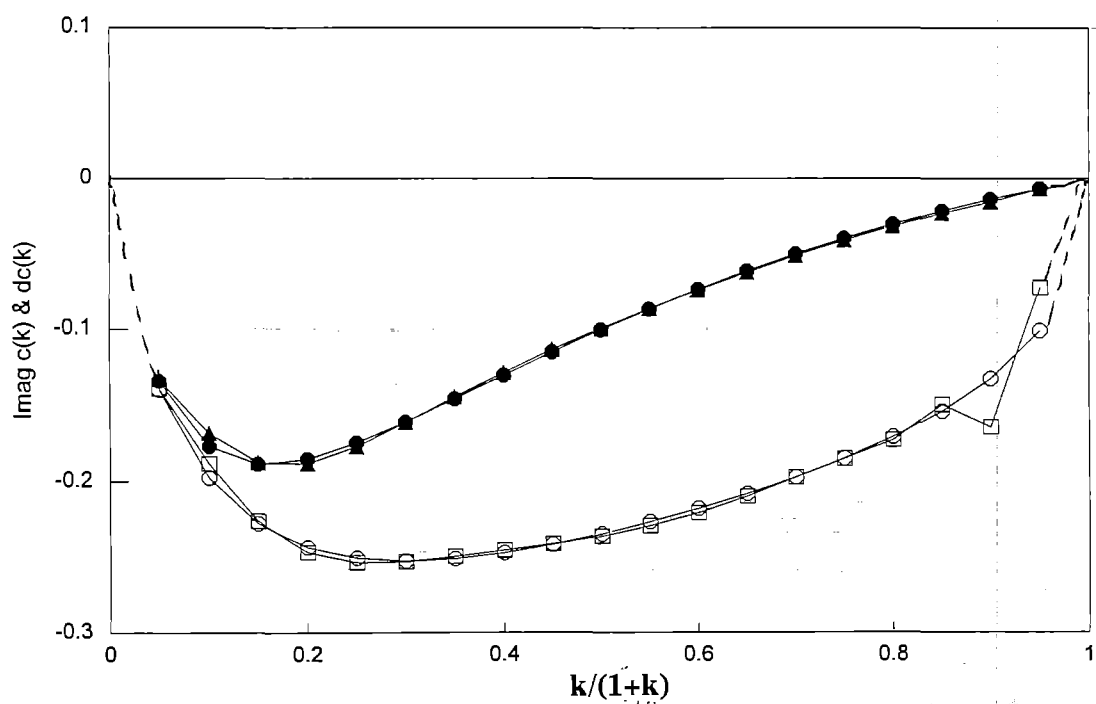
EFFECT OF INFLOW GRADIENT ON C(k)
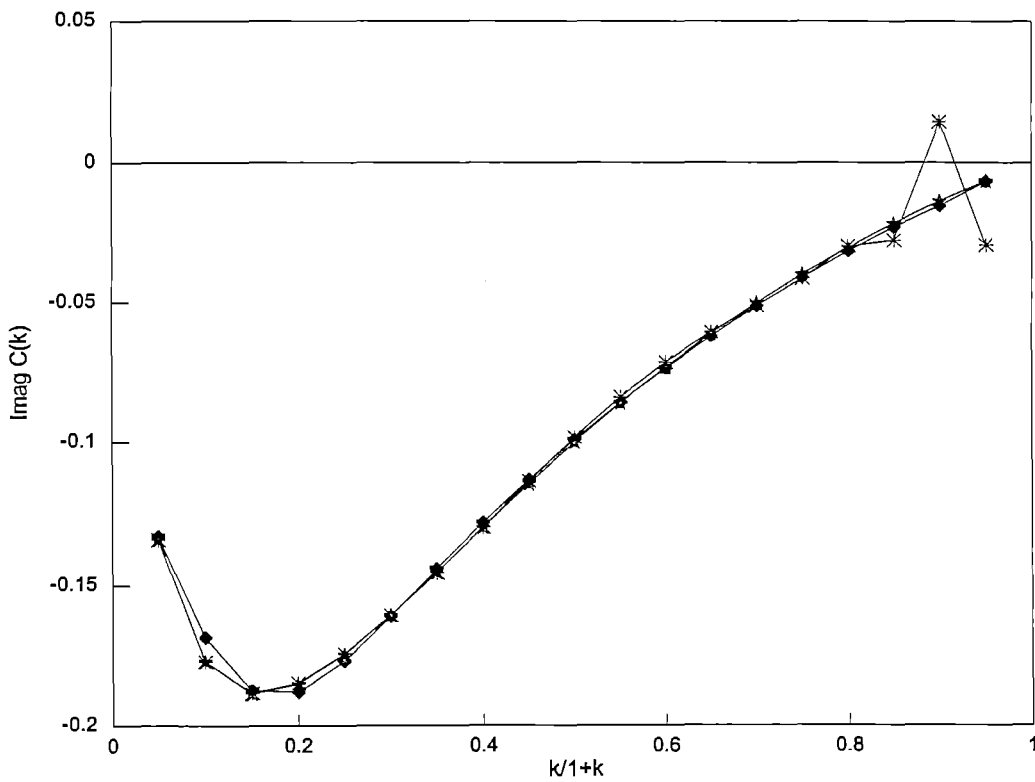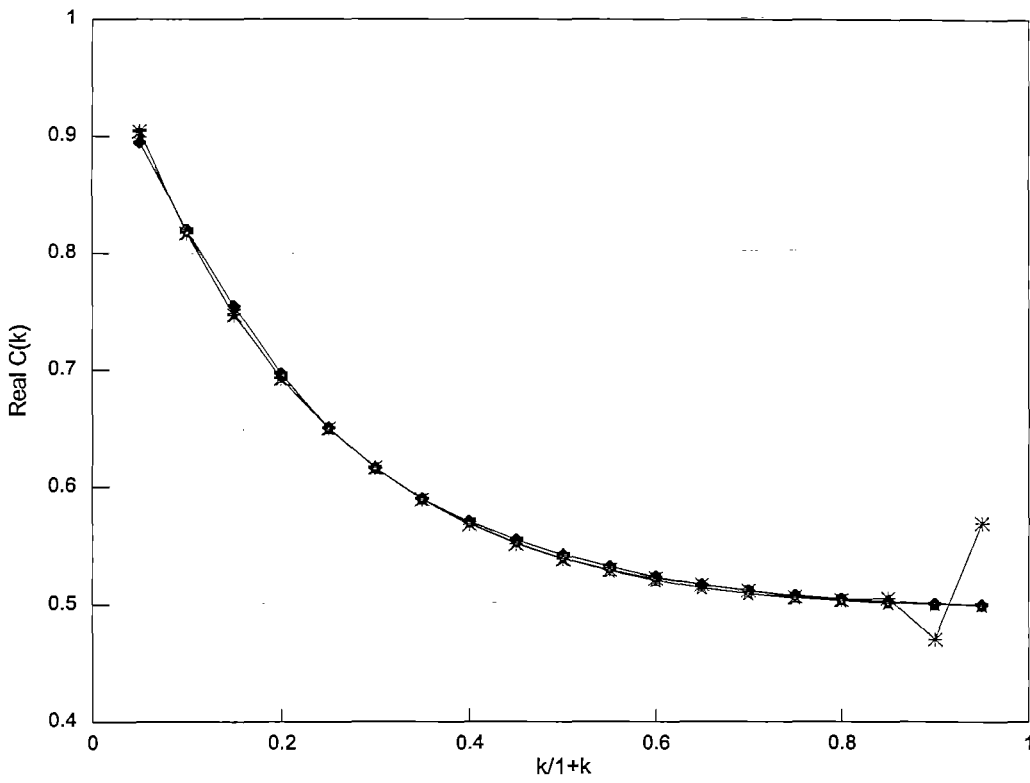
VARIATION OF C(k) WITH k/(1+k)
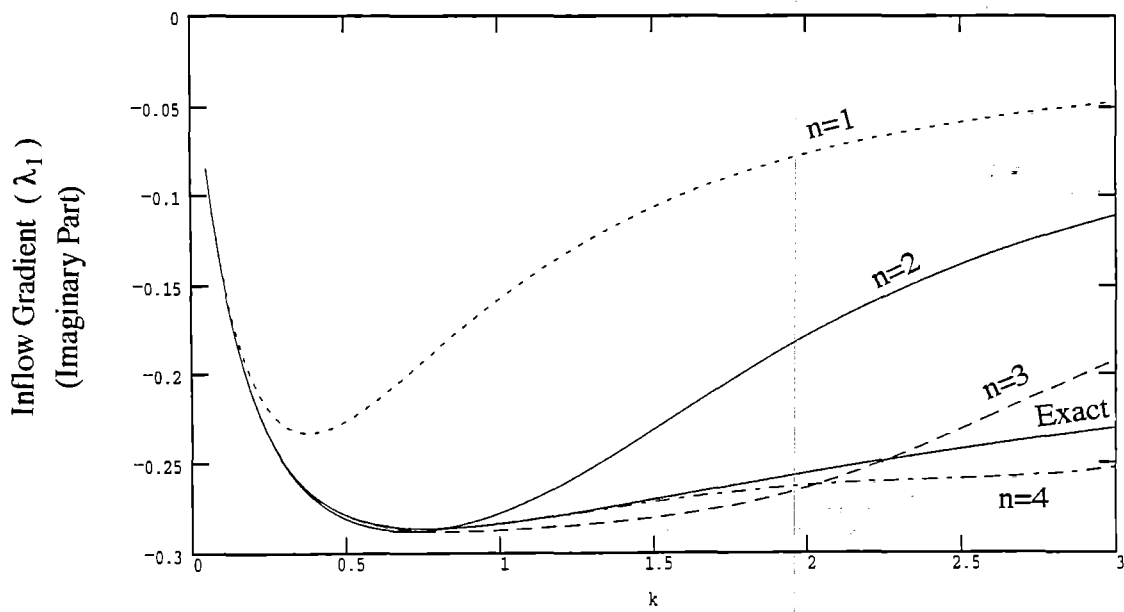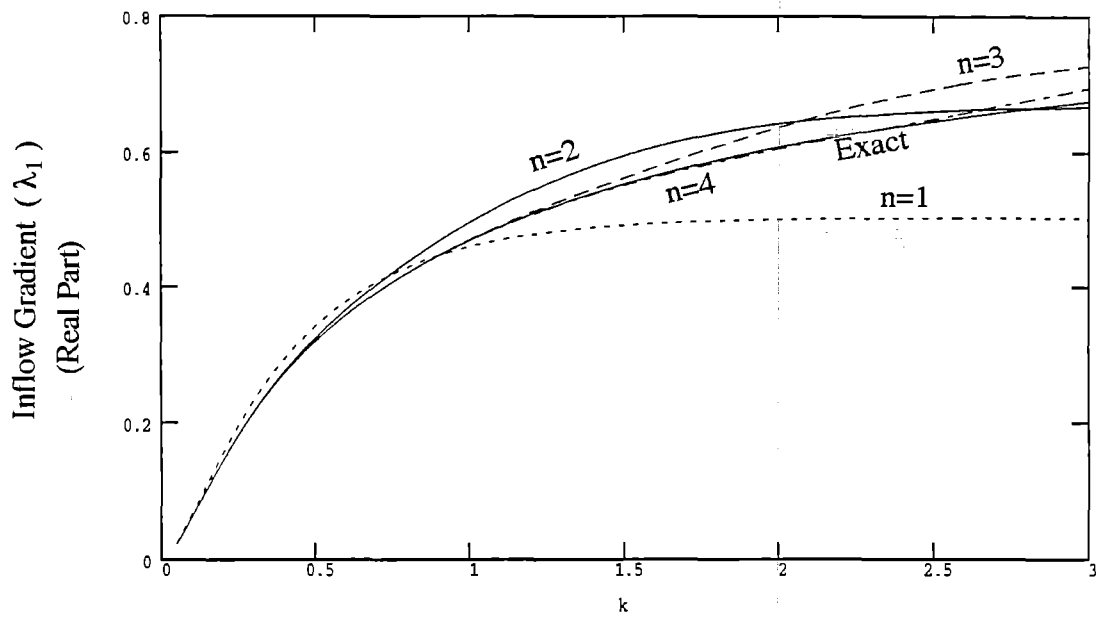
Variation of Inflow Gradient with respect to Reduced Frequency
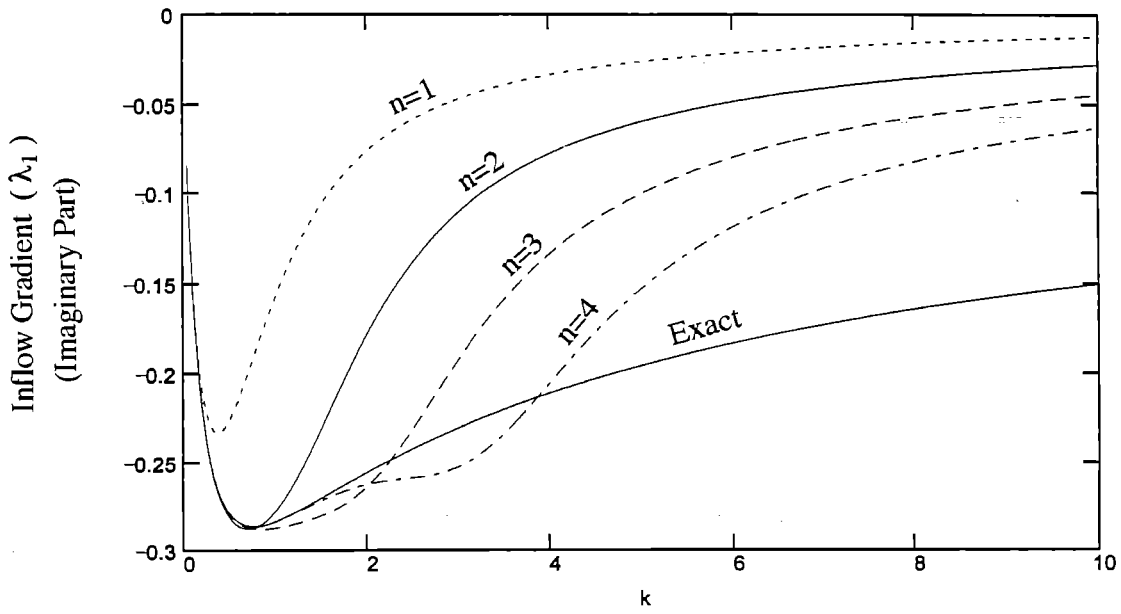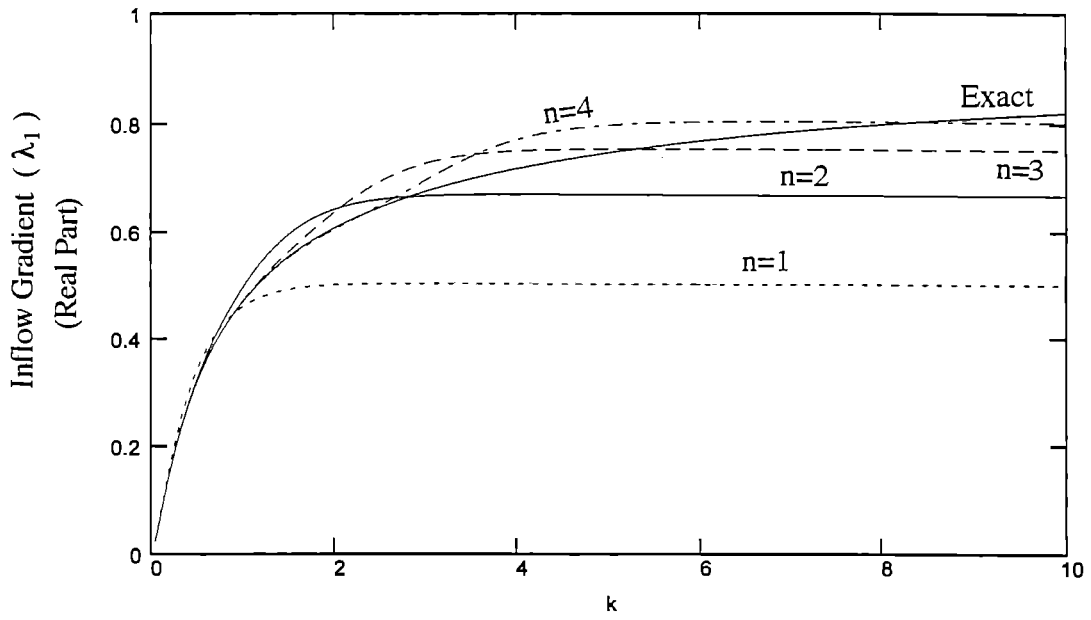
Variation of Inflow Gradient with respect to Reduced Frequency

CONCLUSIONS

THEDORSEN FUNCTION IS FOR THE FIRST TIME
  EXPRESSED IN TERMS OF BESSEL FUNCTIONS
  THAT ARE EQUIVALENT TO UNIFORM INFLOW
  AND INFLOW GRADIENT.

THE EFFECT OF INFLOW GRADIENT ON
  THEODORSEN FUNCTION IS IDENTICAL FOR
  BOTH EXACT MODEL AND APPROXIMATE FINITE
  STATE MODEL.

THE COMPUTED INFLOW GRADIENT FOR GIVEN
  UNIFORM INFLOW IS ALMOST AGREE WITH
  EXACT MODEL FOR n=2, IN THE RANGE 0<k<1.
  HOWEVER, FURTHER STUDY IS REQUIRED.

Hingeless-Rotor Aeromechanical Stability in Hover and Forward Flight With Wake Dynamics

J. Nagabhushanam
Professor
Department of
Aerospace Engineering
Indian Institute of Science
Bangalore, India

G.H. Gaonkar
Professor
Department of
Mechanical Engineering
Florida Atlantic University
Boca Raton, FL 33431

Presented at the Seventh International Workshop on Dynamics and Aeroelastic Stability Modeling of Rotorcraft Systems at Washington University, St. Louis, MO, October 14-16, 1997
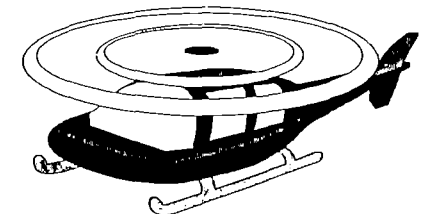
FAU
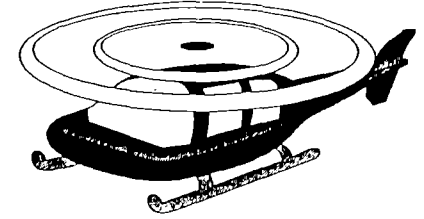
Investigation Covers

❶ **Ground Contact, Hover and Trimmed Forward Flight**

❷ **Sensitivity of the Damping Predictions to Modeling Wake Dynamics (from no-inflow to dynamic inflow to full wake dynamics)**

❸ **Parametric Study**

❹ **Correlations**
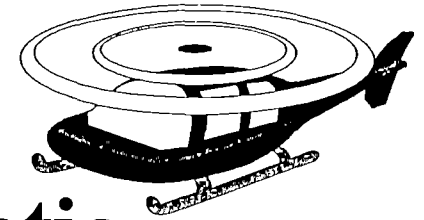
Coupled Rotor-Body Schematic
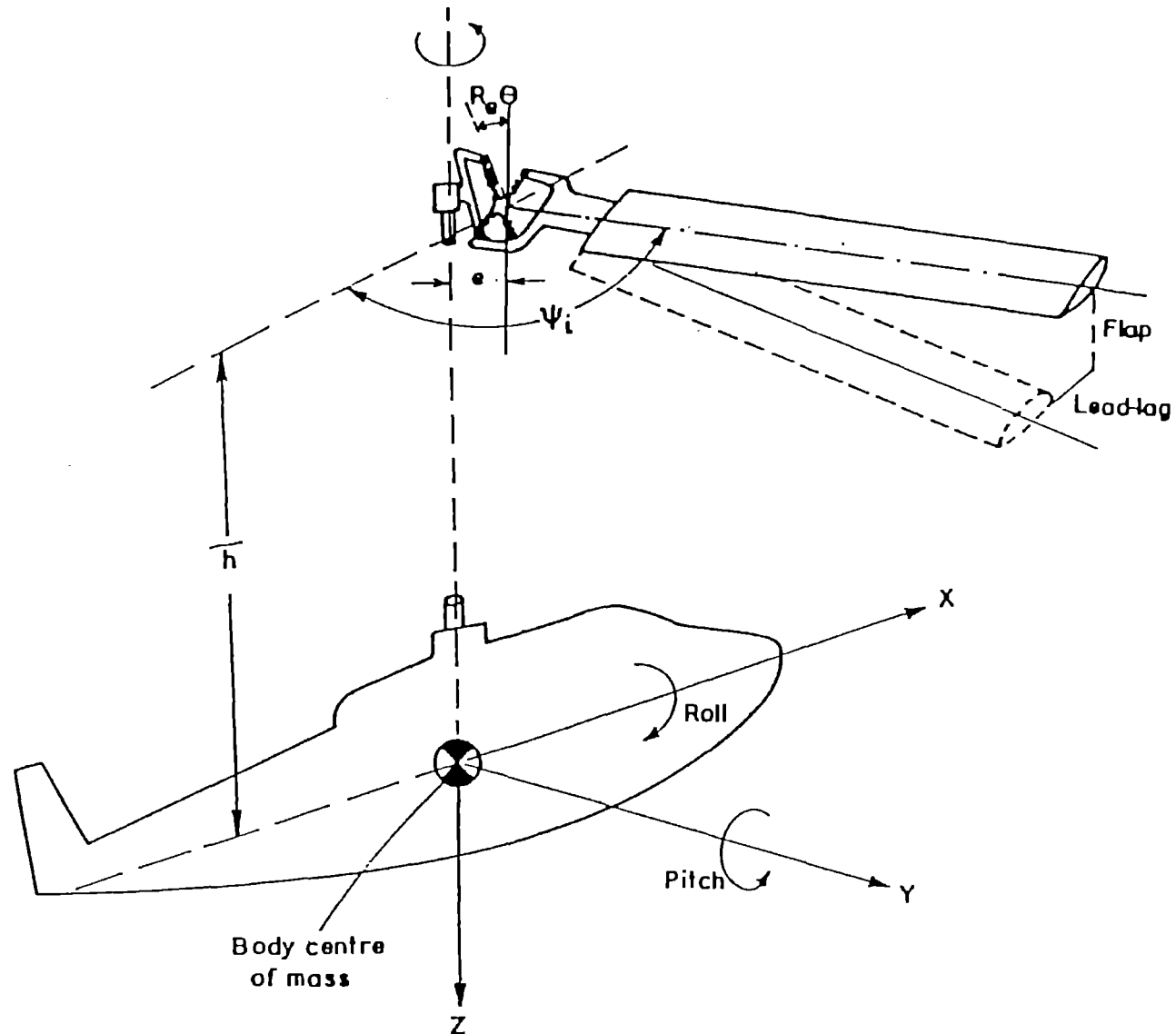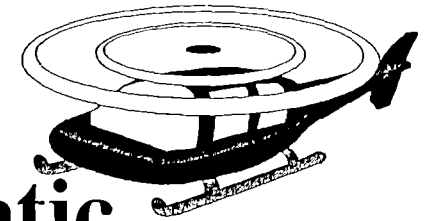
Unsteady Aerodynamics Schematic
(Feedback Loop)
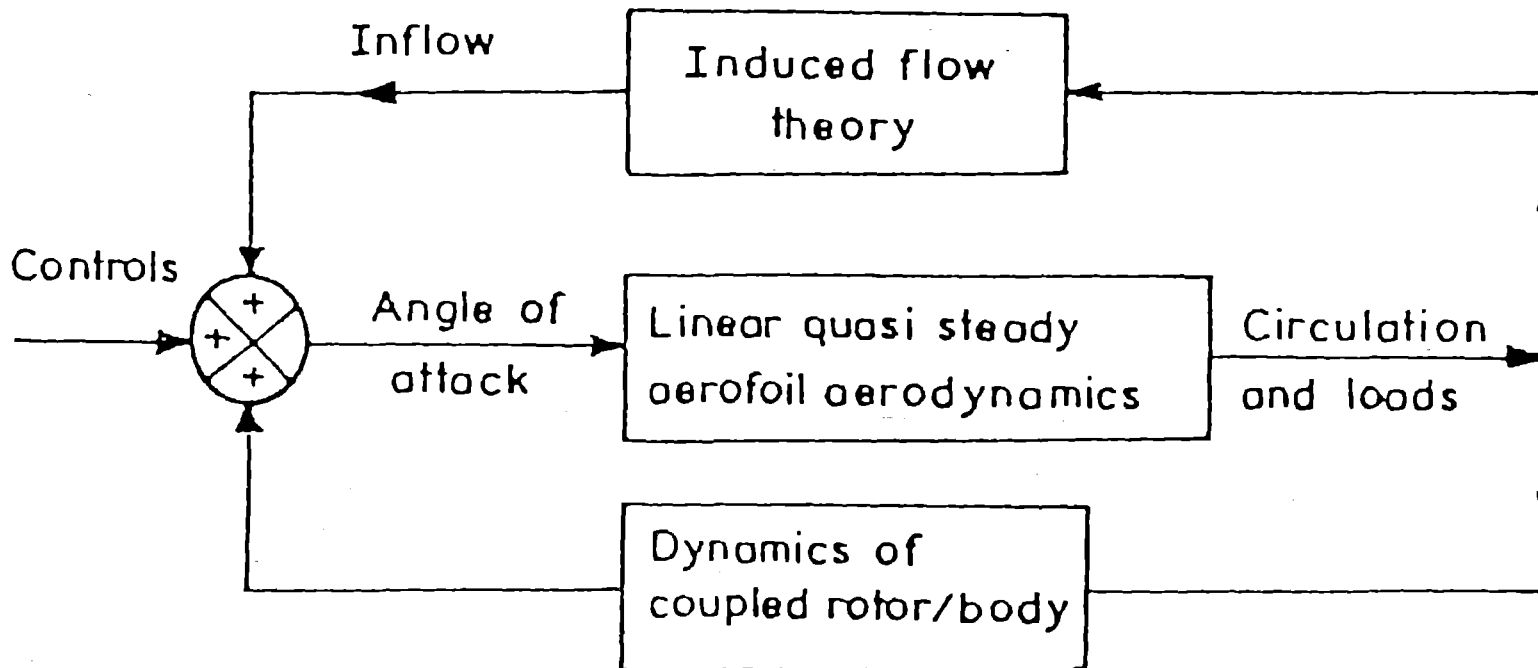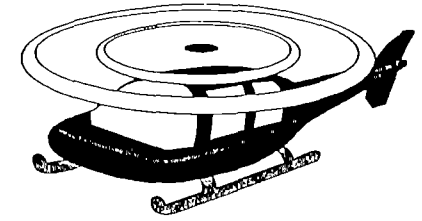
Wake Equations

Inflow on the i-th blade

$$\lambda\left(\overline{r}_i, \psi_i, t\right) = \sum_{r=0}^{\infty} \sum_{j=r+1, r+3}^{\infty} \phi_j^r\left(\overline{r}_i\right) \left[\alpha_j^r(t) \cos(r\psi_i) + \beta_j^r(t) \sin(r\psi_i)\right]$$

Inflow parameters

$$V = \frac{\left[\mu^2 + (\lambda_t + \lambda_m)\lambda_t\right]}{\sqrt{(\mu^2 + \lambda_t^2)}}, \qquad V_t = \sqrt{(\mu^2 + \lambda_t^2)}$$
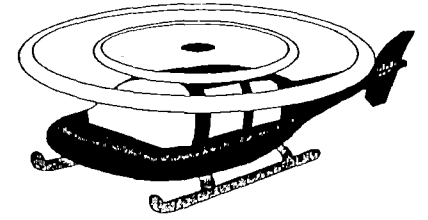
Wake Equations (Contd.)

Wake states are governed by

$$\mathbf{M}\left\{\dot{\alpha}_j^r\right\} + \mathbf{V}\mathbf{L}_c^{-1}\left\{\alpha_j^r\right\} = 0.5\left\{\tau_n^{mc}\right\}$$

$$\mathbf{M}\left\{\dot{\beta}_j^r\right\} + \mathbf{V}\mathbf{L}_s^{-1}\left\{\beta_j^r\right\} = 0.5\left\{\tau_n^{ms}\right\}$$

Coupled Rotor-Body-Wake Equations
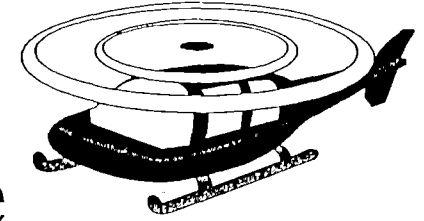
$$\dot{X} = f(X,C,t)$$

X = Rotor-Body-Wake States

  (lag, flap, pitch, roll and wake states)

C = Control-Input Vector

  (Collective pitch θ_0, Cyclic Pitch Components

  θ_c and θ_s, and shaft tilt angles α_{pitch} and α_{roll})
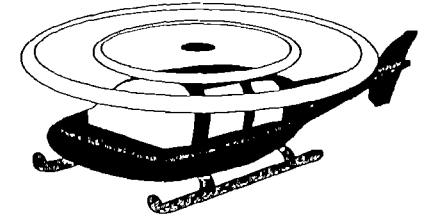
Illustration:

Number of Blades	$Q = 3$
Number of Harmonics	$M = 3$

X has 26 states:

    10 wake states

    4 body states

    12 blade states in multiblade coordinates of
    flap and lag
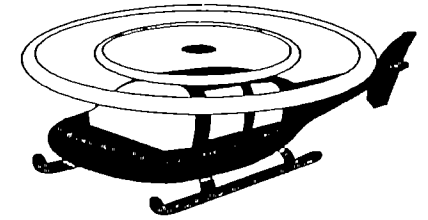
Analysis

❶ **Periodic Shooting With Damped Newton Iteration**

❷ **Floquet Analysis**

(The finite-state wake model introduces periodic coefficients even in axial flight)
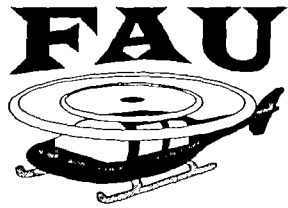
Outline

➥Convergence of the control inputs, periodic responses and damping levels with respect to the number of wake harmonics for increasing advance ratio μ and thrust level C_T / σ :

$$0 \leqslant \mu \leqslant 0.4 \text{ and } 0.05 \leqslant C_T/\sigma \leqslant .15$$

➥Parametric study

❶ Advance Ratio ($0 \leqslant \mu \leqslant 0.4$)

Thrust Level ($0.05 \leqslant C_T/\sigma \leqslant .15$)

Number of Blades ($Q = 3, 4$ and 5)

❷ Comparison of the predictions from the finite-state and dynamic inflow models
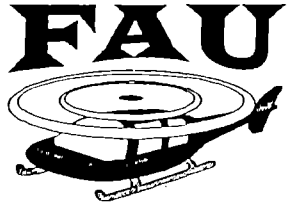
Outline

➥ **Correlation**

❶ **Bousman's database in the ground-contact conditions**

❷ **Comparison of the correlations from the finite-state wake,**

dynamic inflow and vortex models
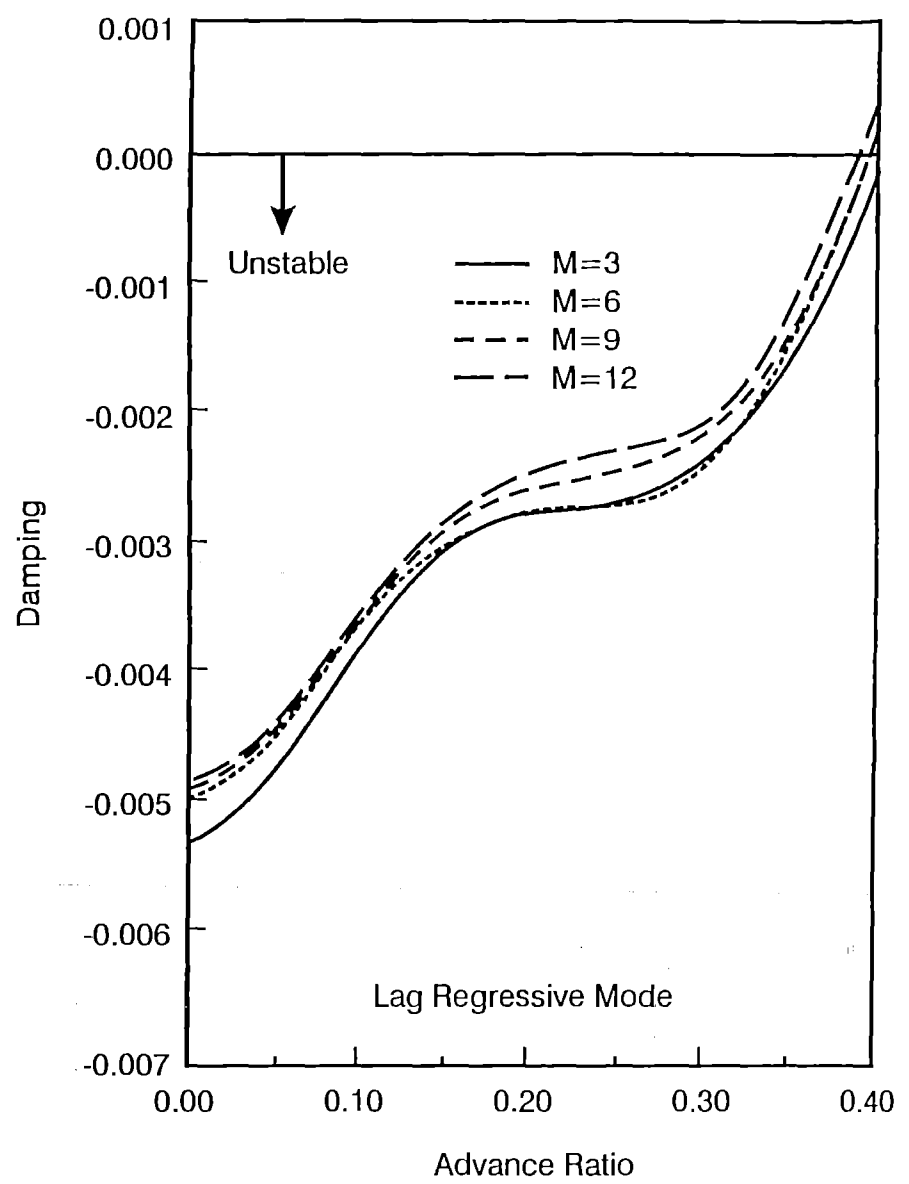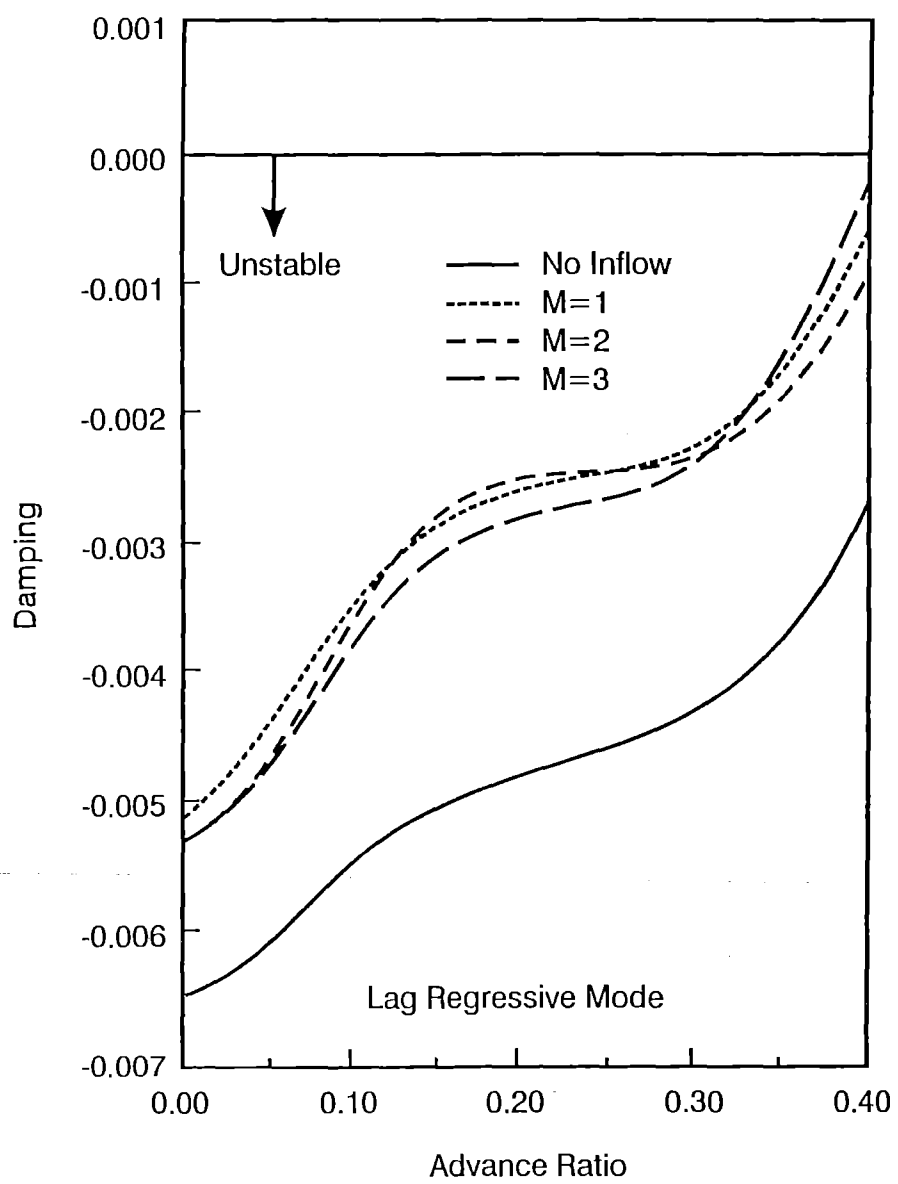
Fig. 1. Lag Regressive-Mode Damping With Increasing Number of Wake Harmonics
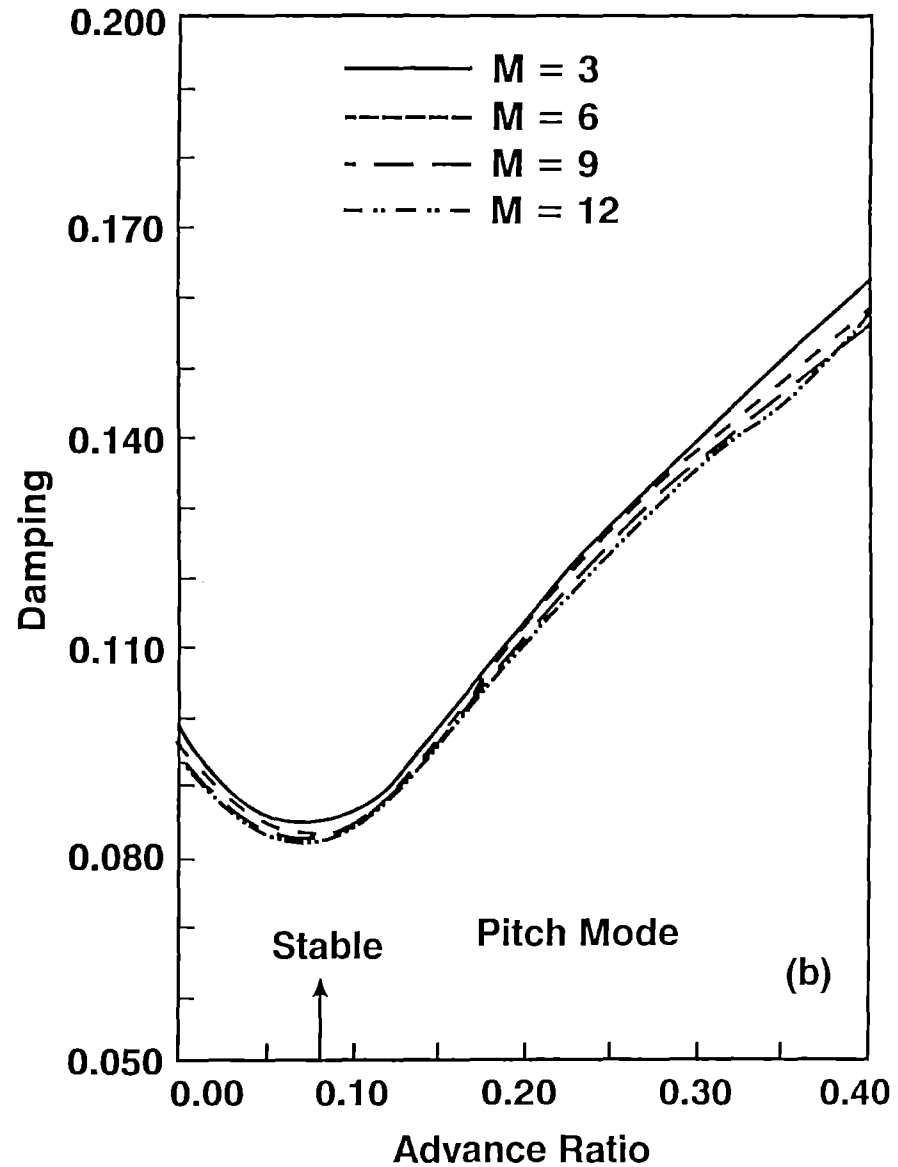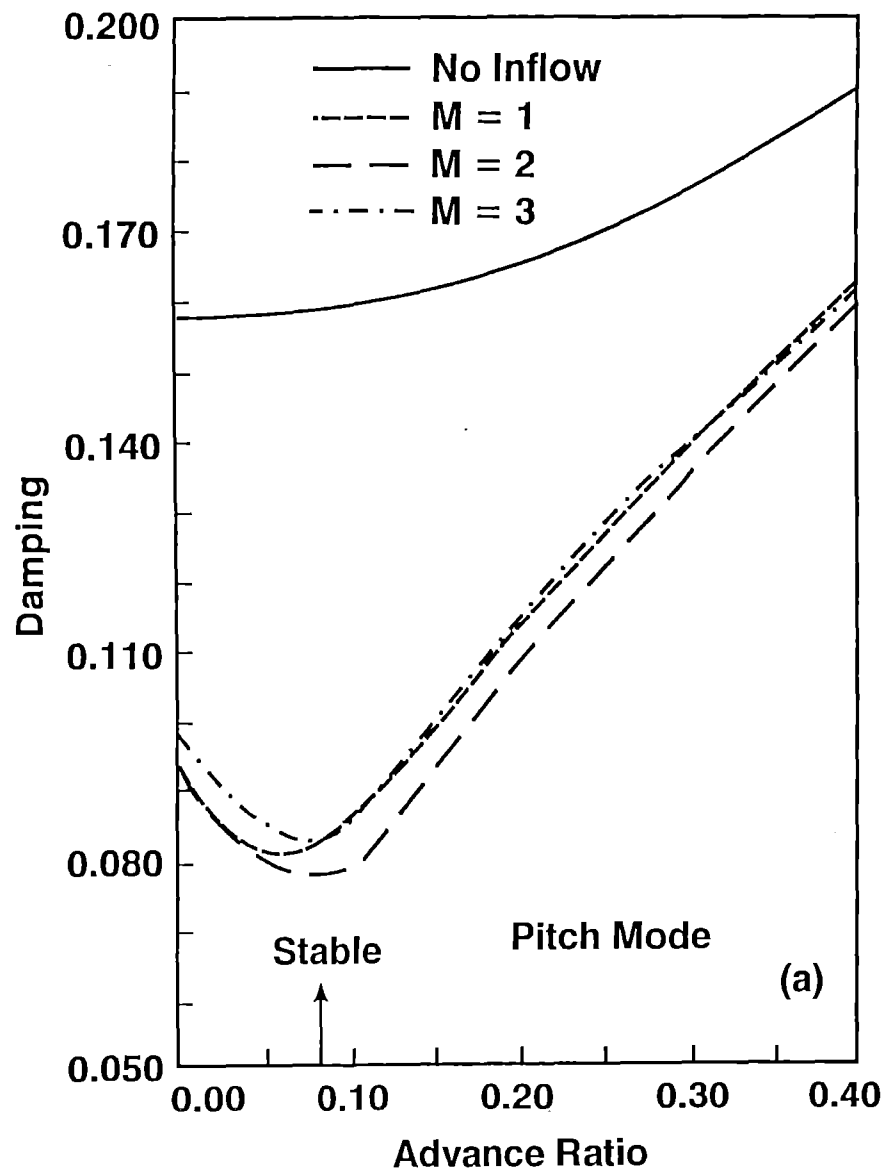
Fig. 2. Body Pitch-Mode Damping With Increasing Number of Wake Harmonics
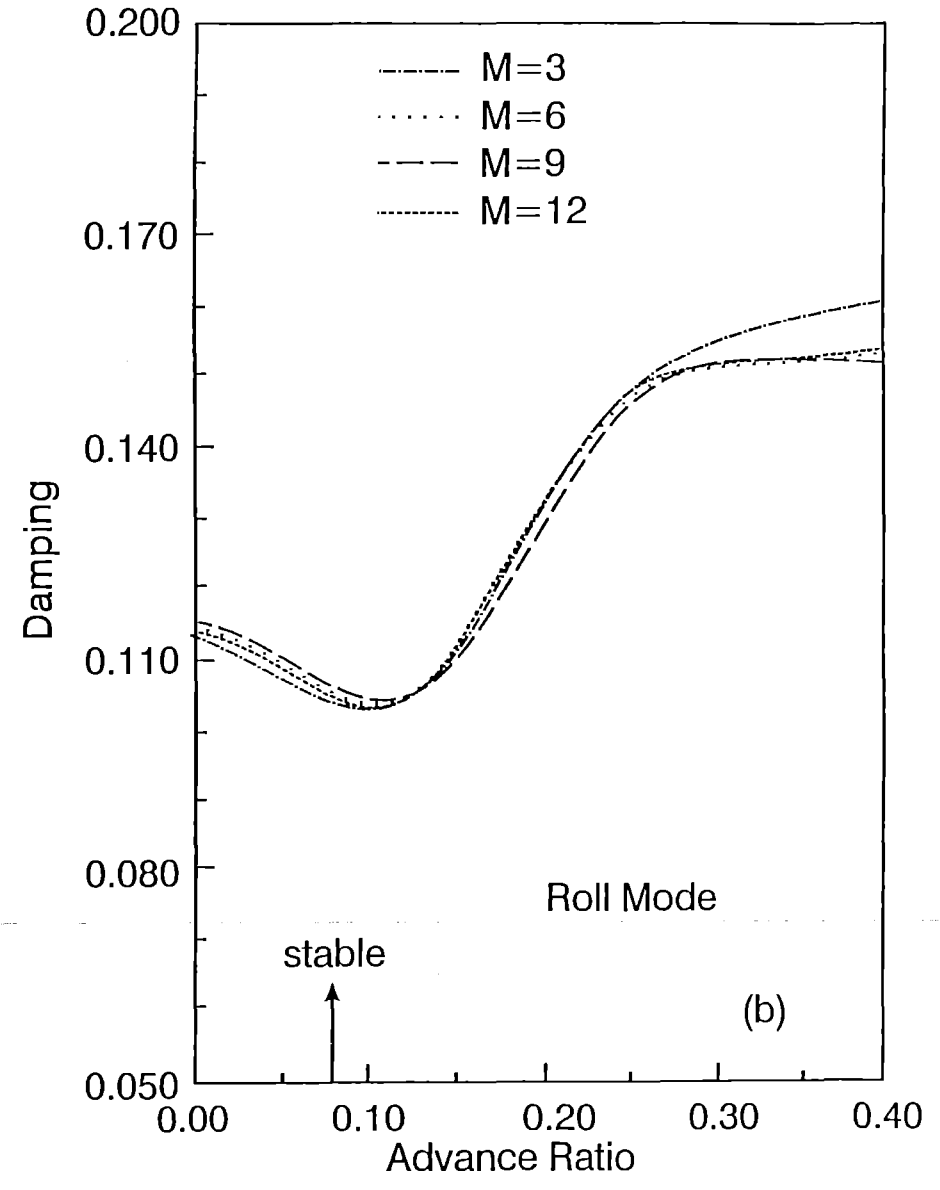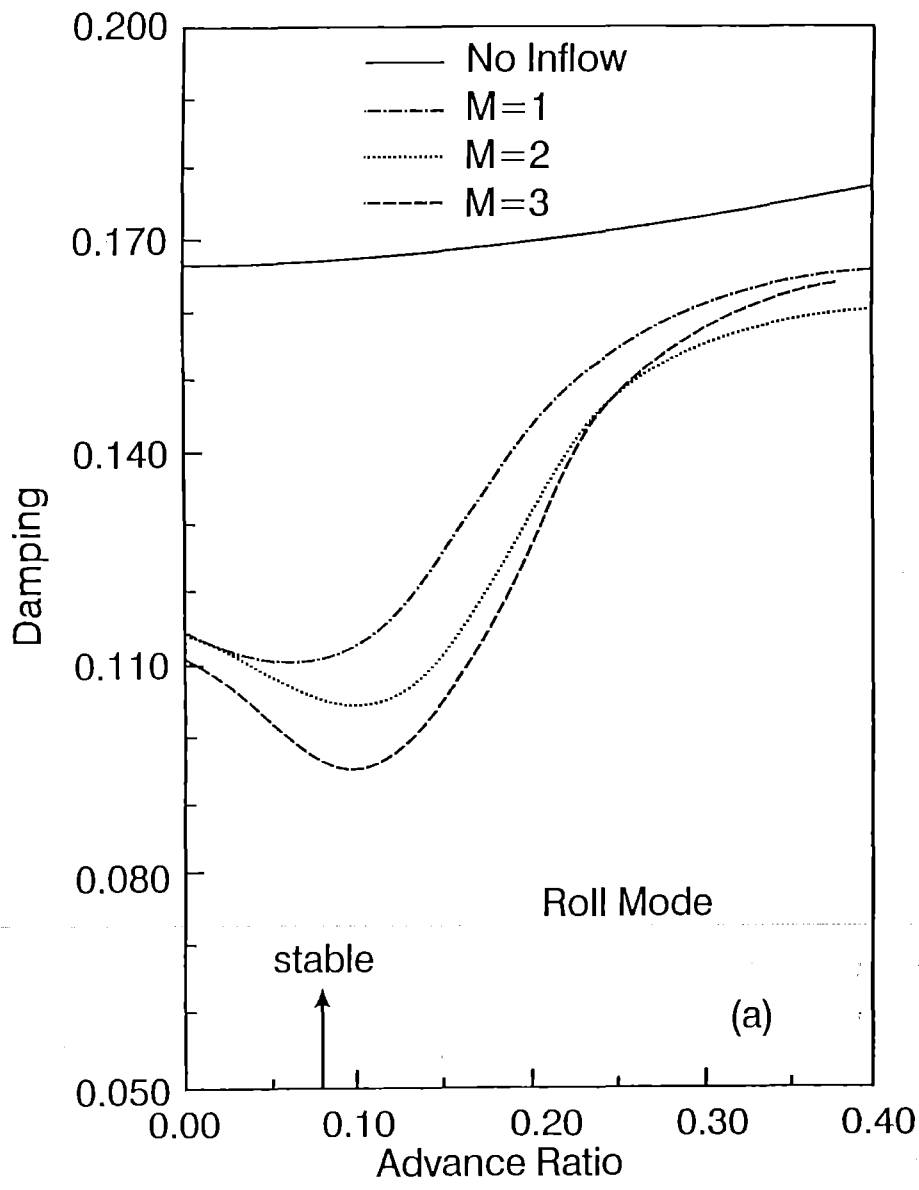
Fig. 3. Body Roll-Mode Damping With Increasing Number of Wake Harmonics
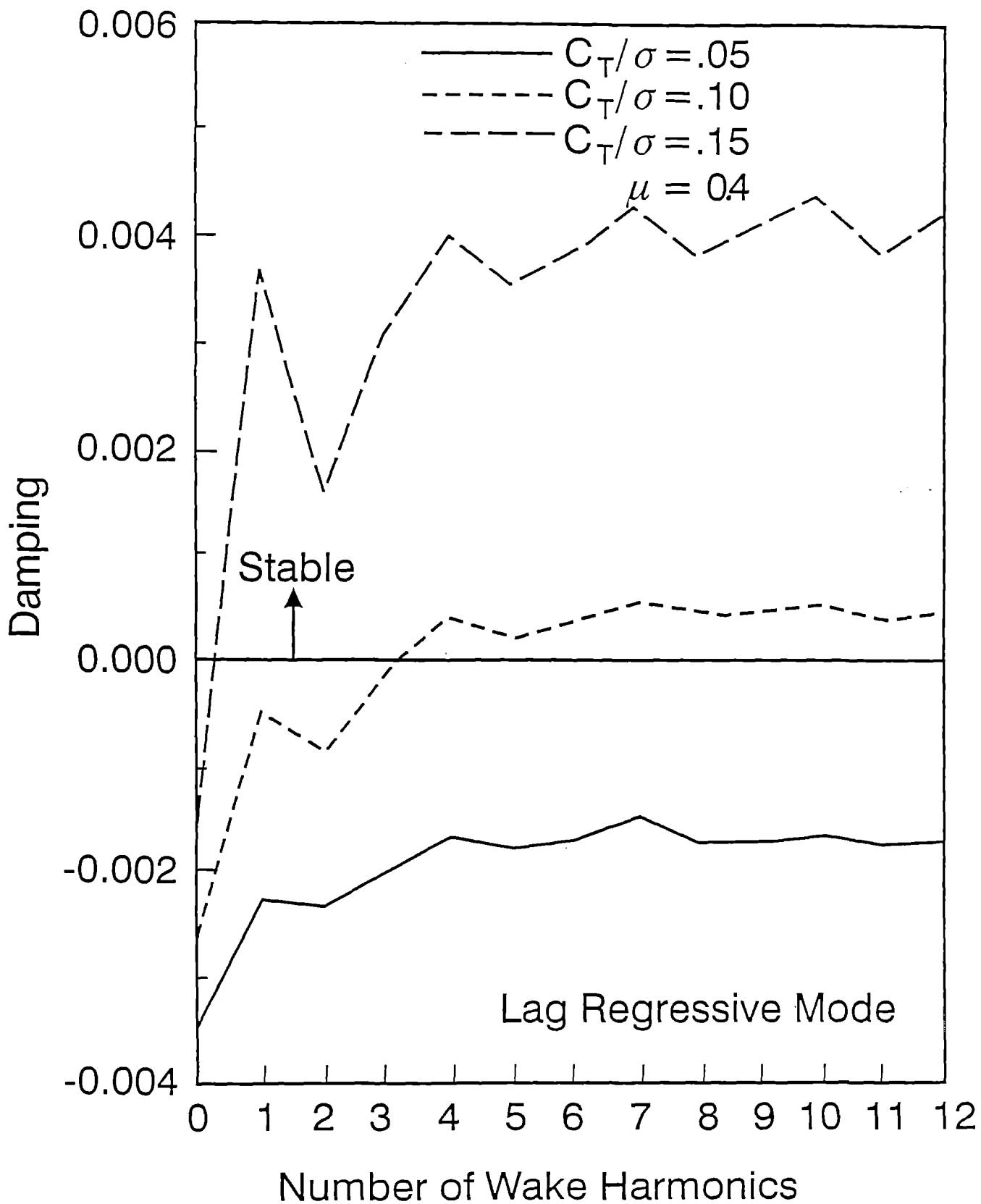
Fig. 4. Oscillatory Convergence of Lag Regressive-Mode Damping
With Increasing Number of Wake Harmonics
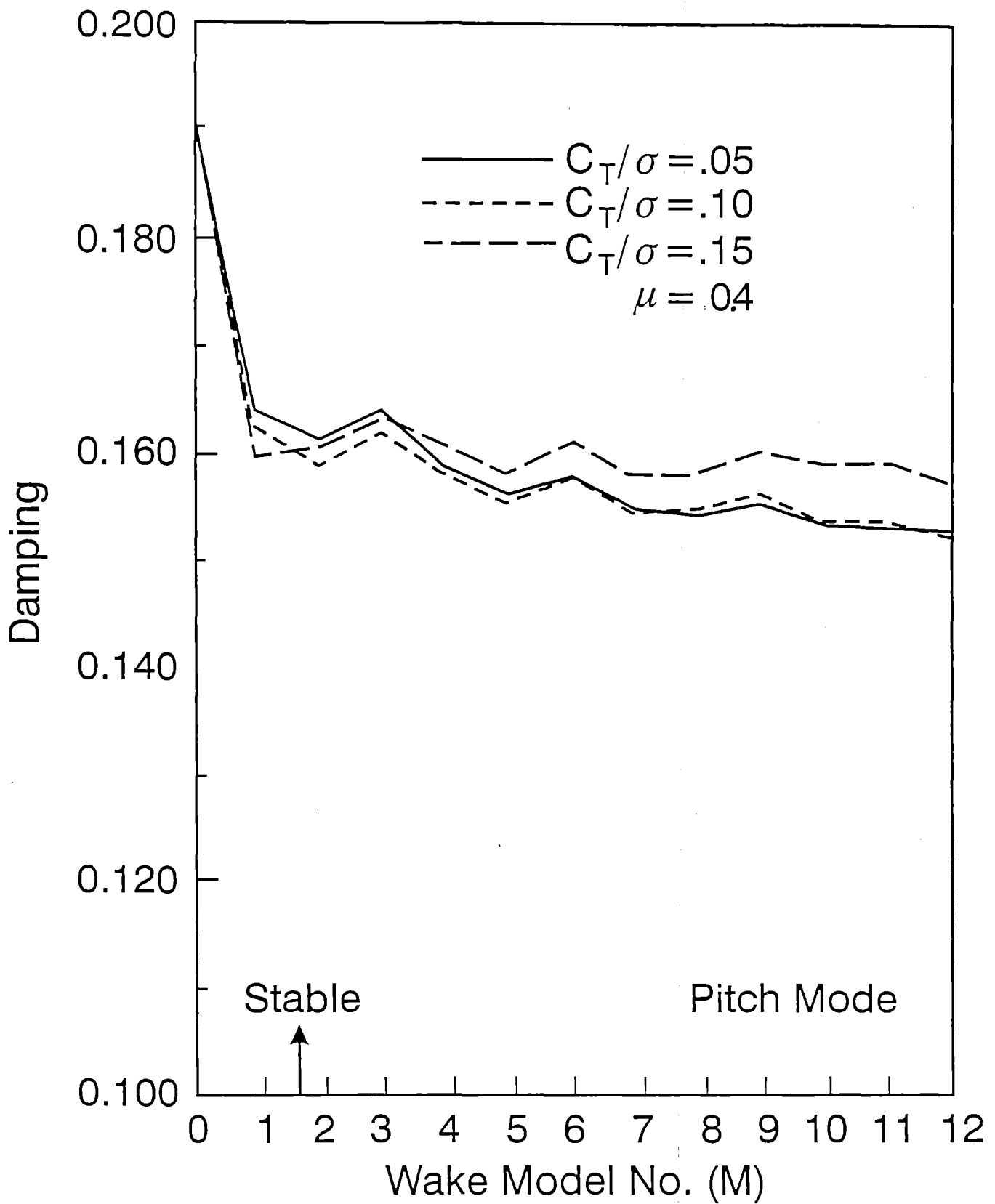
Fig. 5. Oscillatory Convergence of Pitch-Mode Damping
With Increasing Number of Wake Harmonics
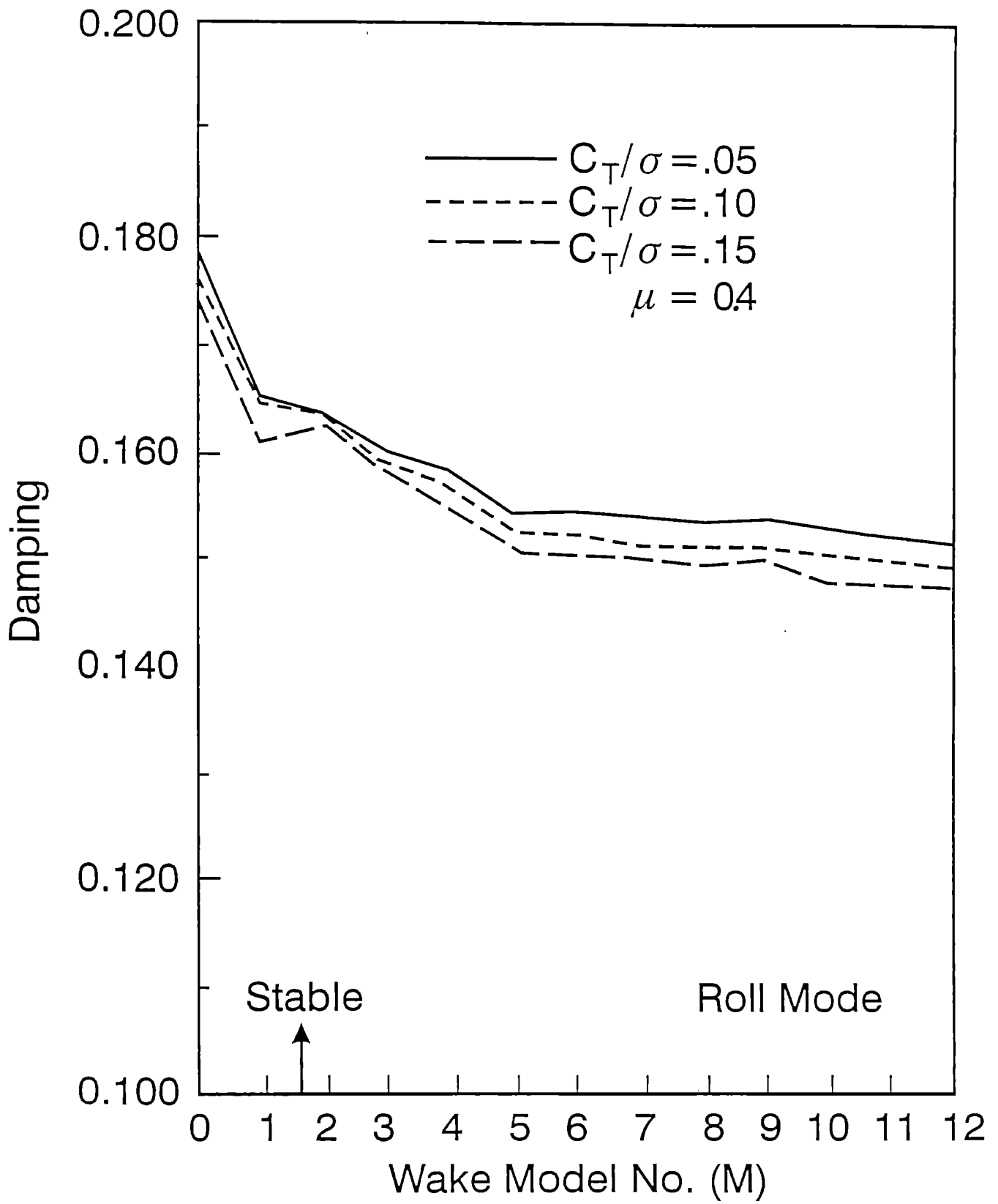
Fig. 6. Oscillatory Convergence of Roll-Mode Damping
With Increasing Number of Wake Harmonics
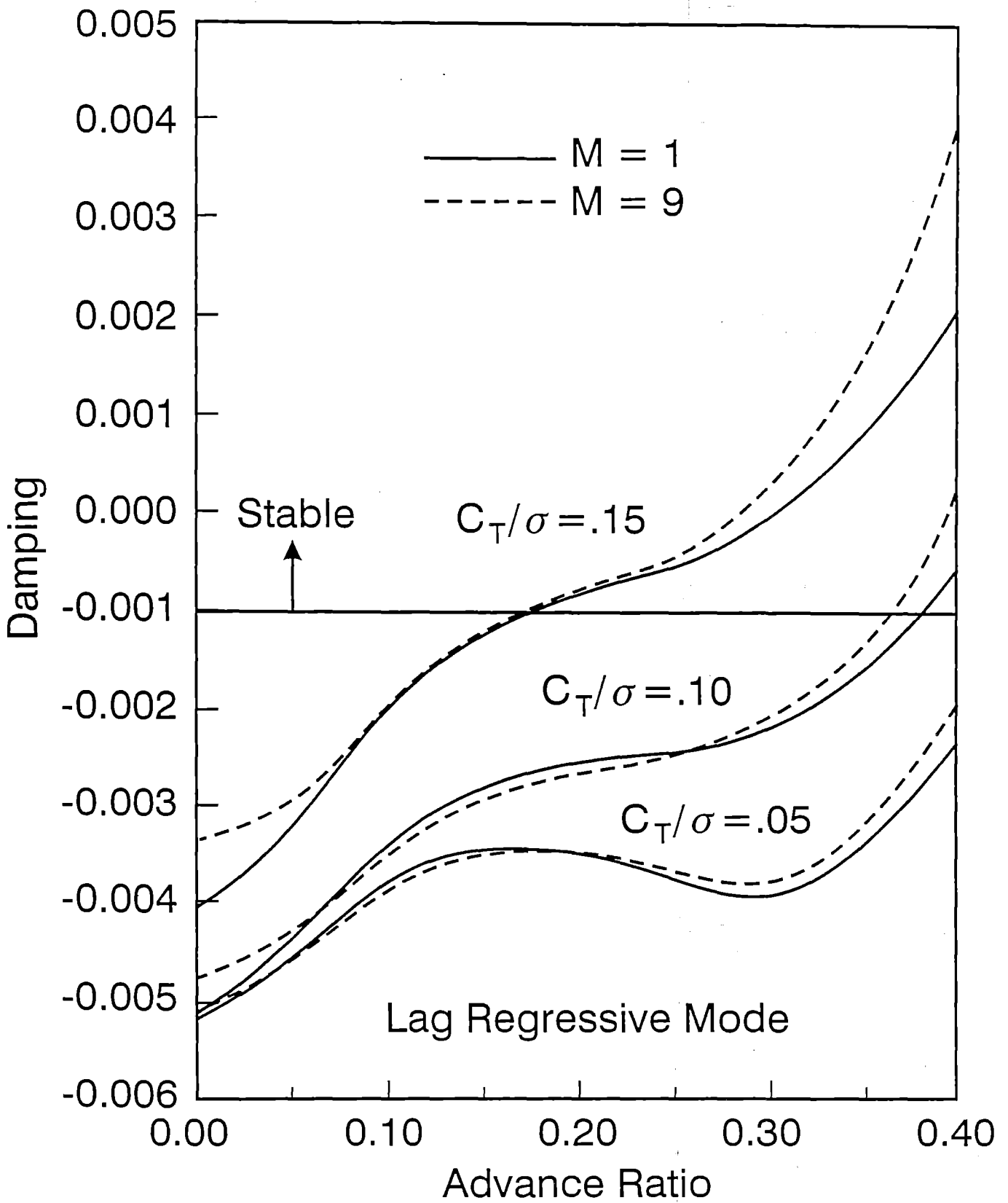
Fig. 7. Lag Regressive-Mode Damping With Increasing
Advance Ratio and Thrust Level
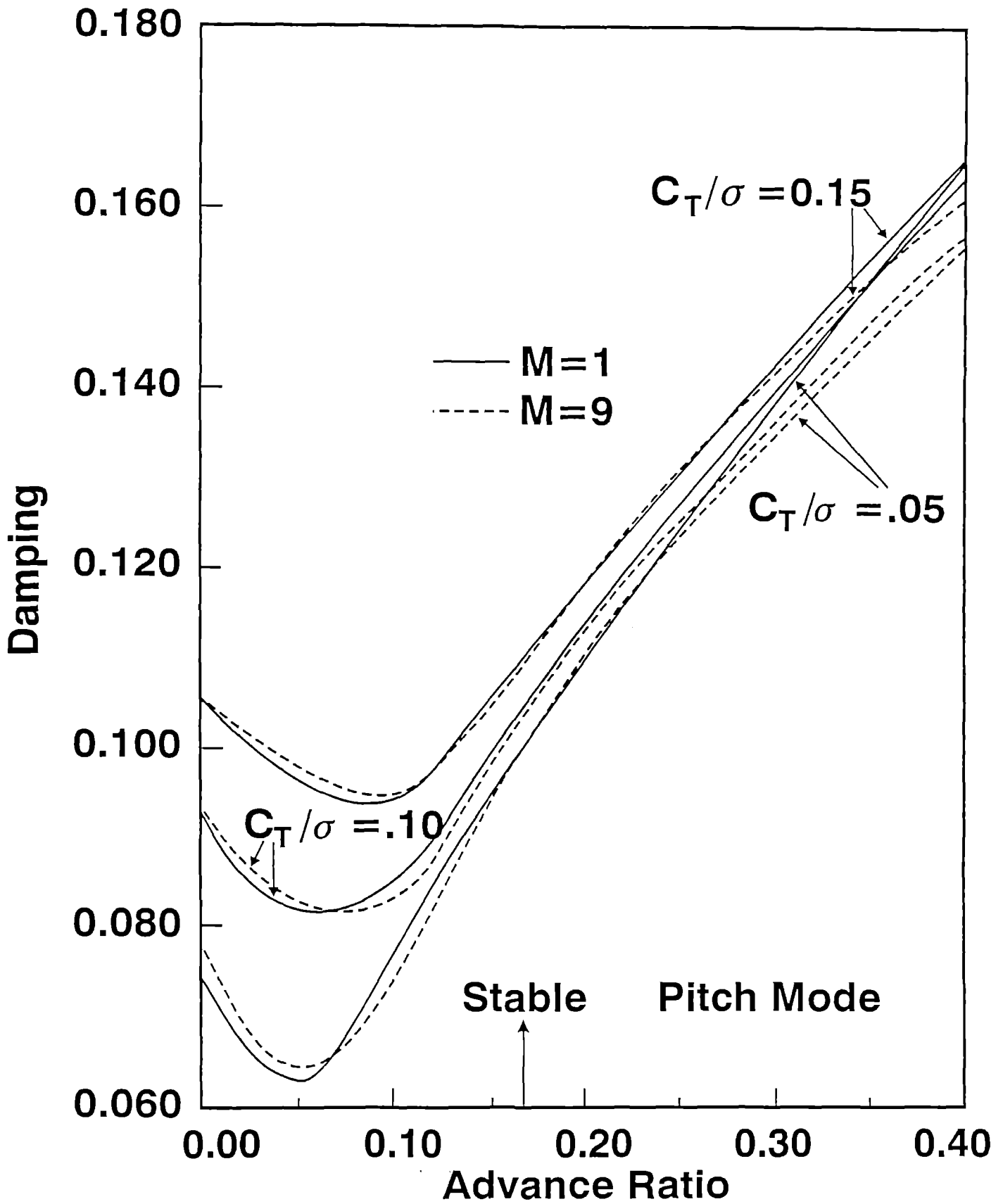
Fig. 8. Body Pitch-Mode Damping With Increasing
Advance Ratio and Thrust Level
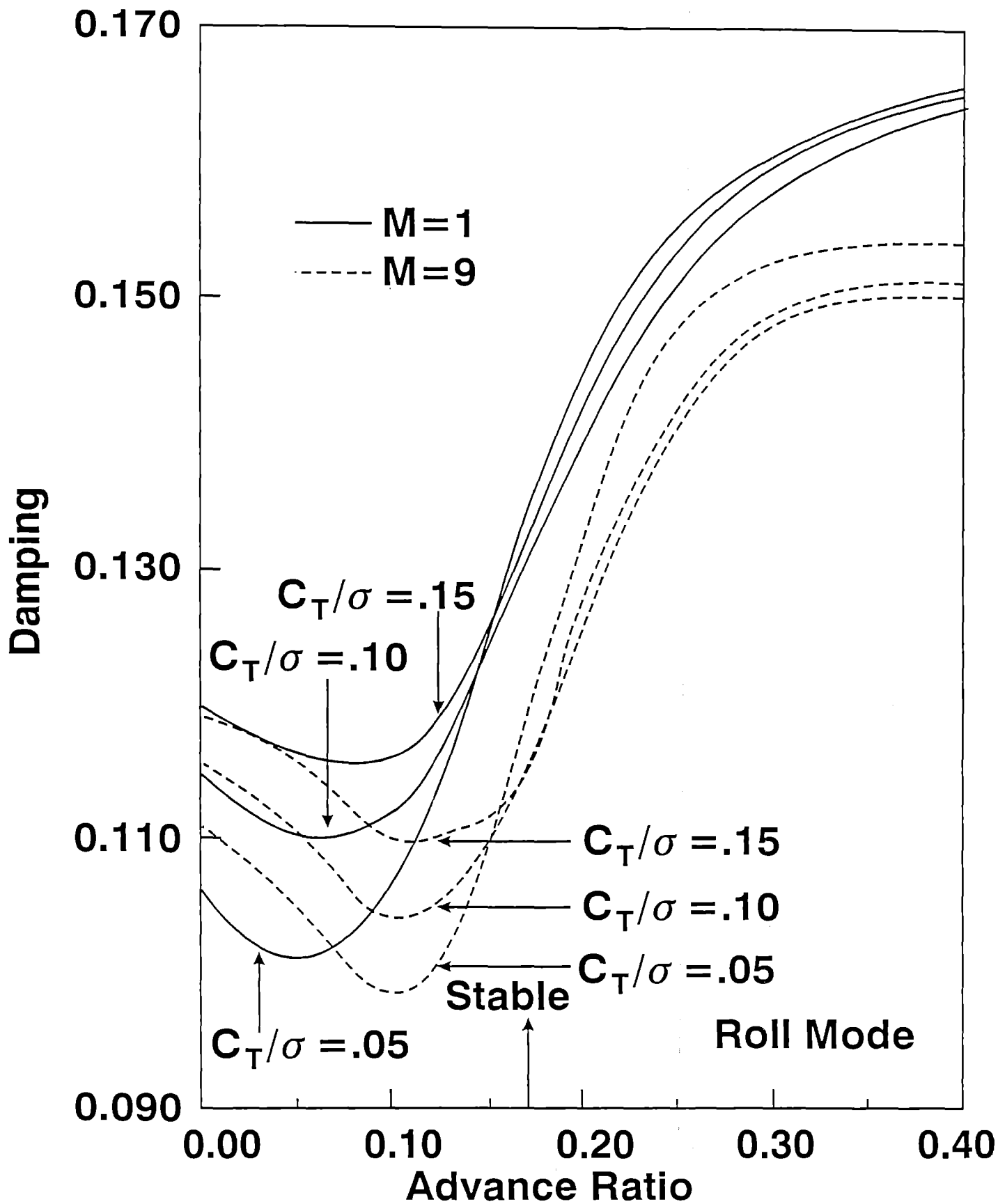
Fig. 9. Body Roll-Mode Damping With Increasing
Advance Ratio and Thrust Level
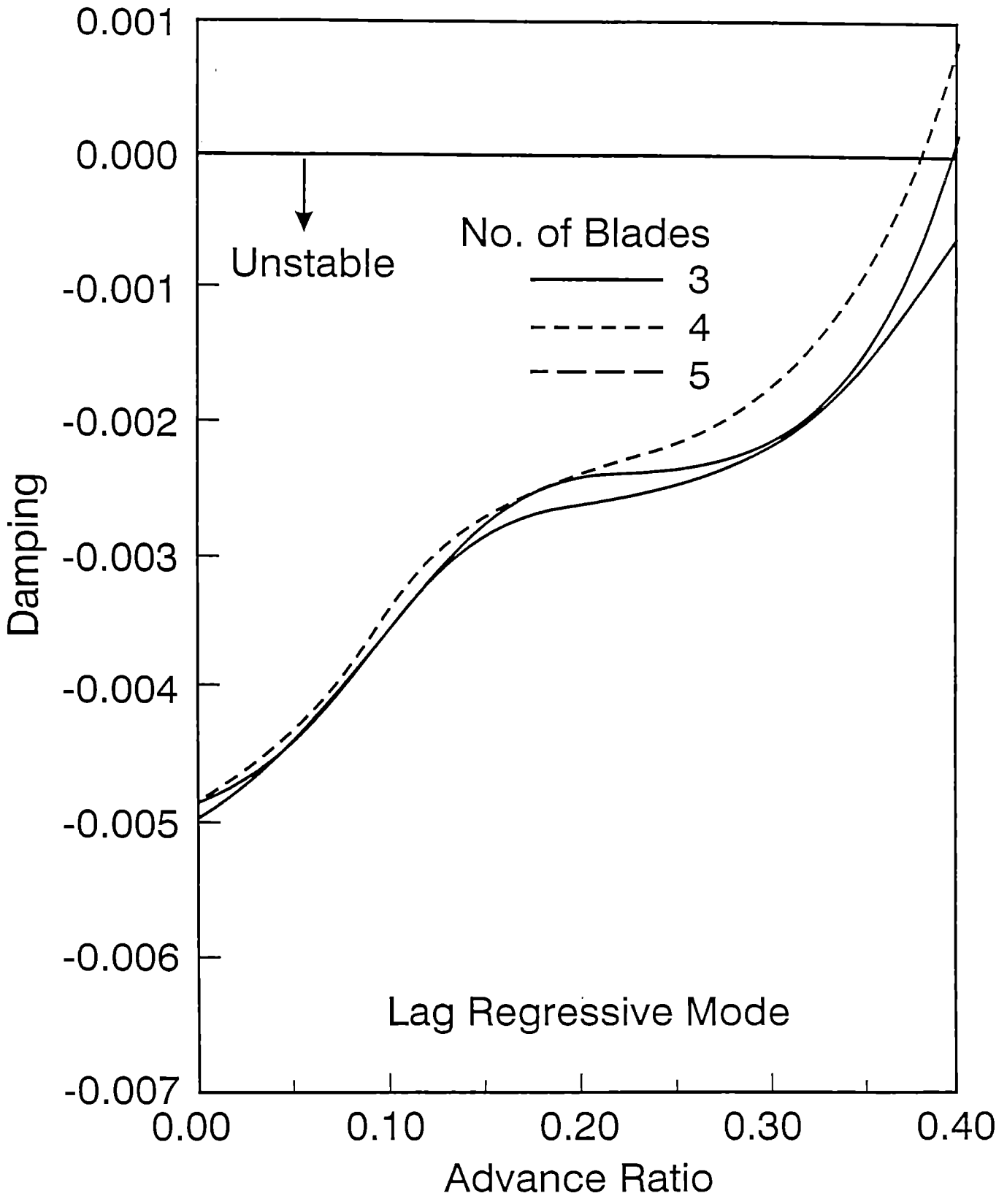
Fig. 10. Lag Regressive-Mode Damping With Increasing
Advance Ratio and Number of Blades
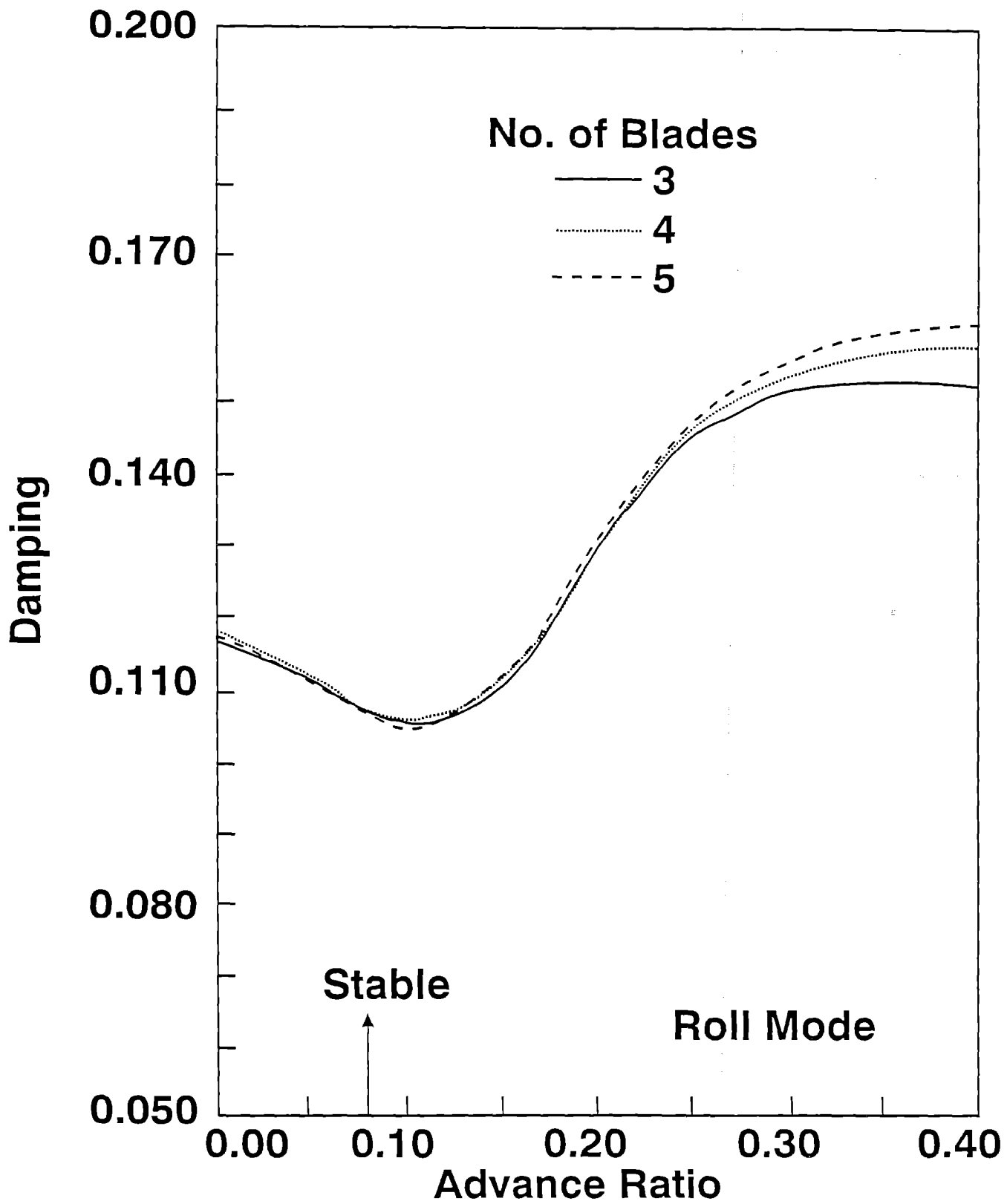
Fig. 11. Body Pitch-Mode Damping With Increasing
Advance Ratio and Number of Blades
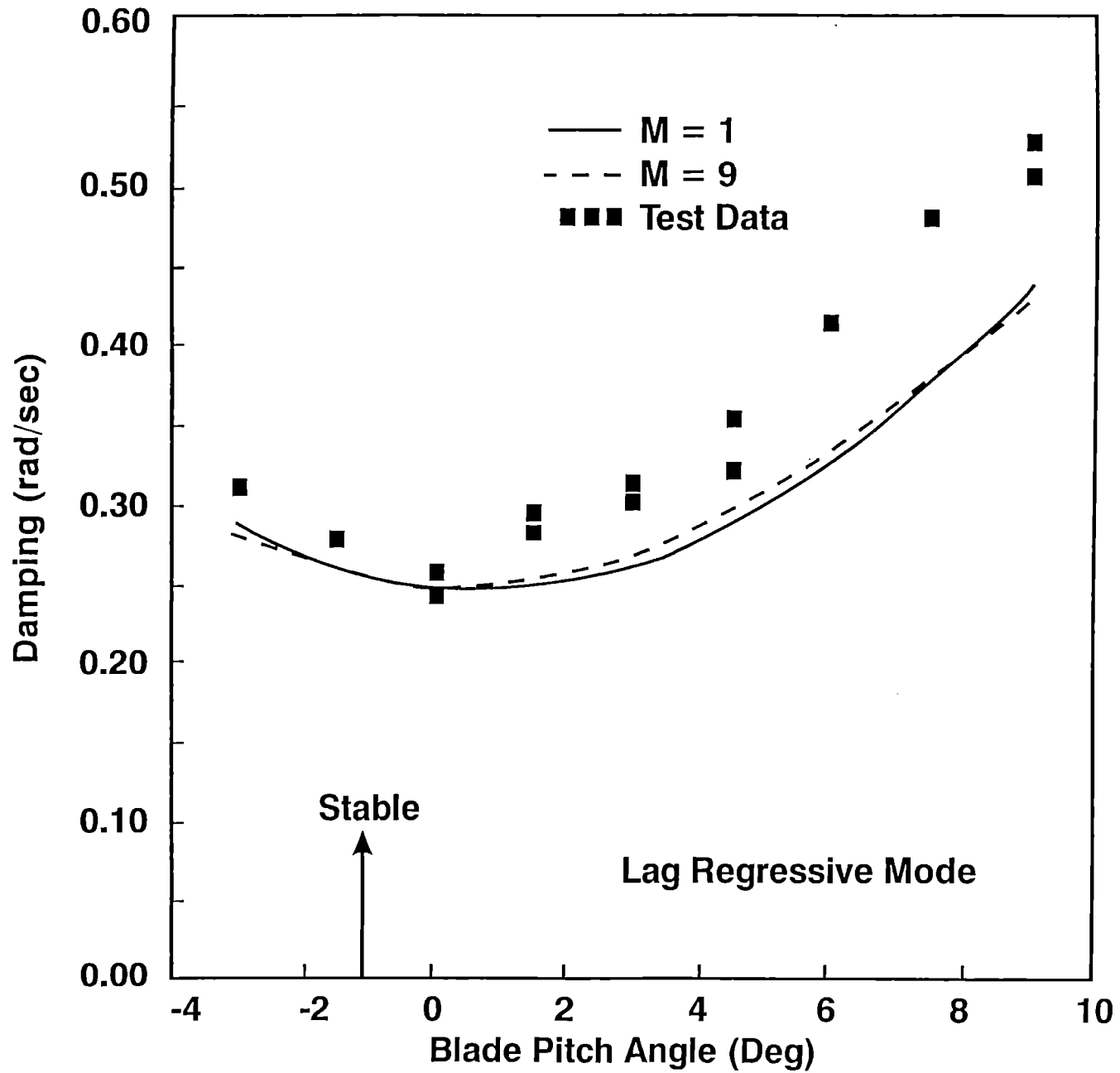
Fig. 12. Lag Regressive-Mode Damping With Increasing Blade Collective Pitch for Configuration 1 at 650-RPM Rotor Speed
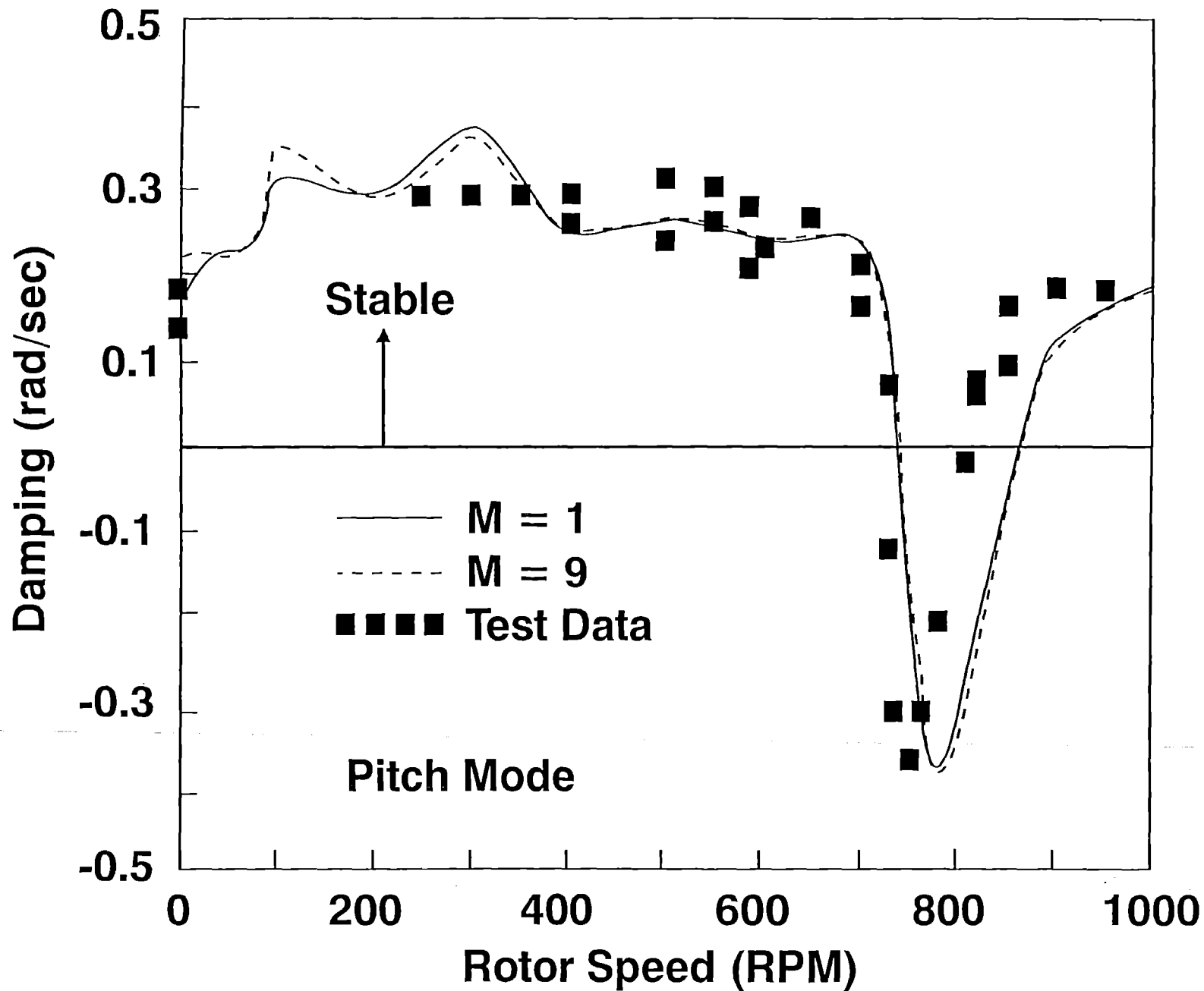
Fig. 13. Lag Regressing-Mode Damping With Increasing Rotor Speed
for Configuration 1 at Zero-Degree Blade Collective Pitch
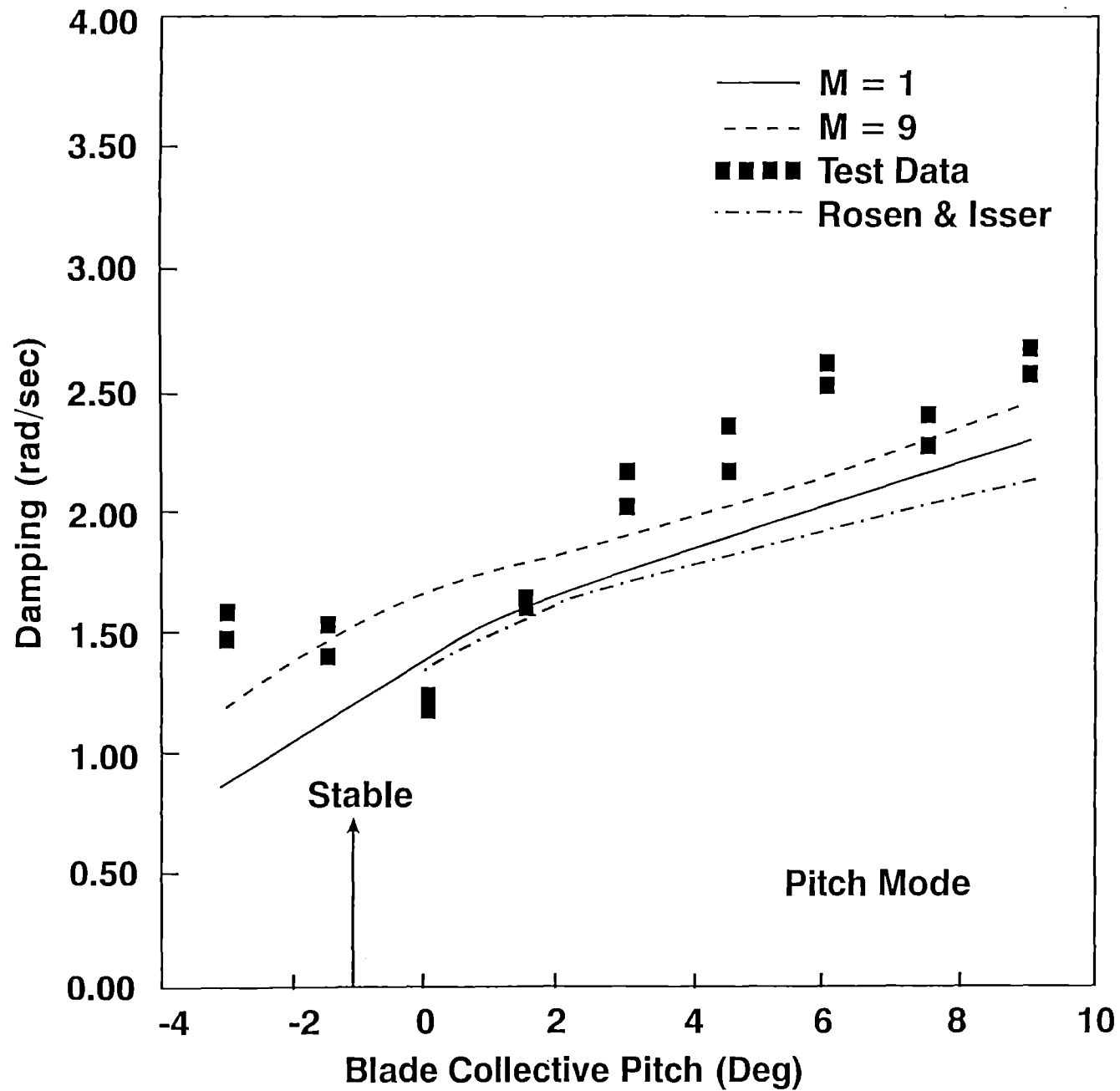
Fig. 14. Body Pitch-Mode Damping With Increasing Blade Collective Pitch
for Configuration 1 at 650-RPM Rotor Speed
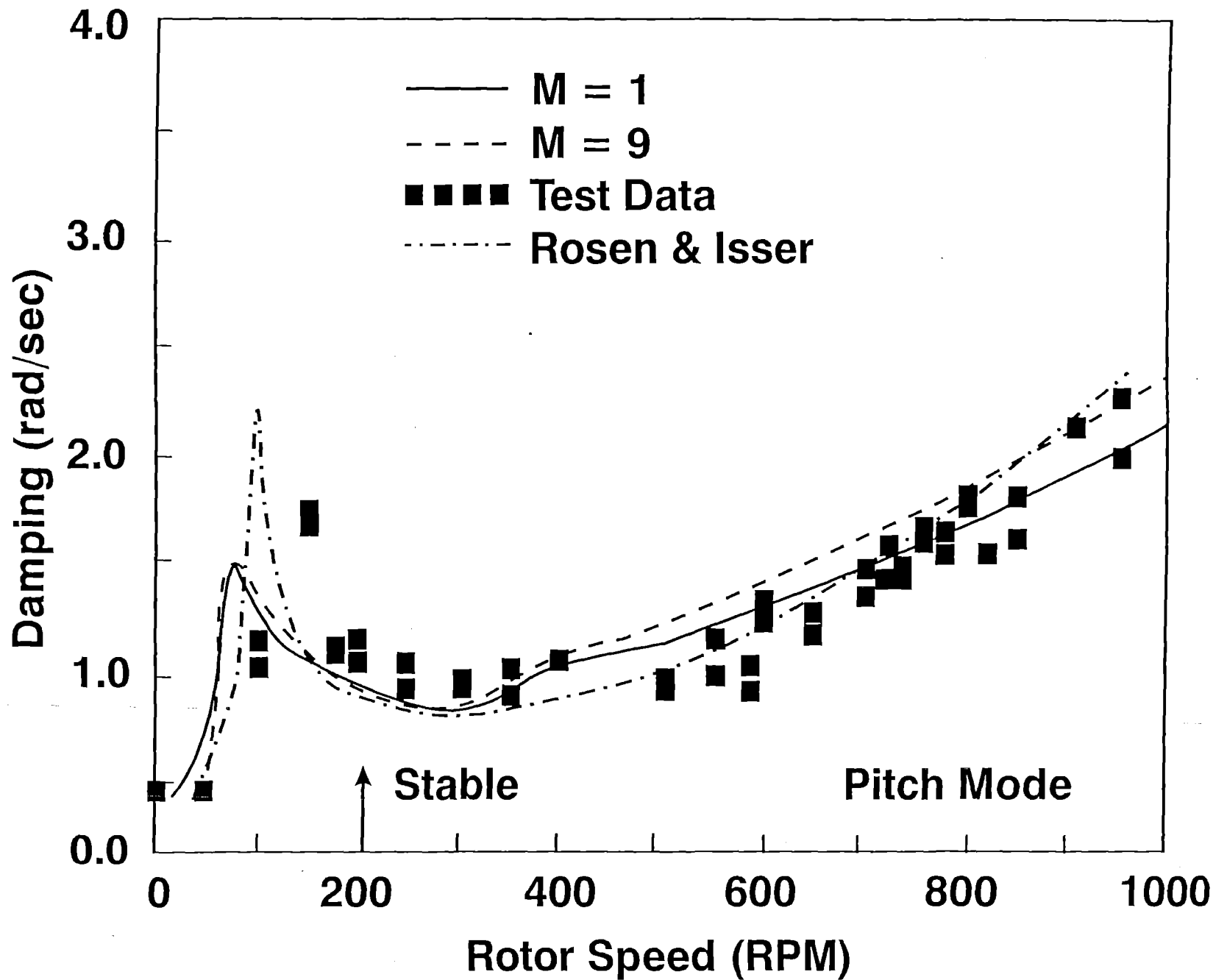
Fig. 15. Body Pitch-Mode Damping With Increasing Rotor Speed
for Configuration 1 at Zero-Degree Blade Collective Pitch
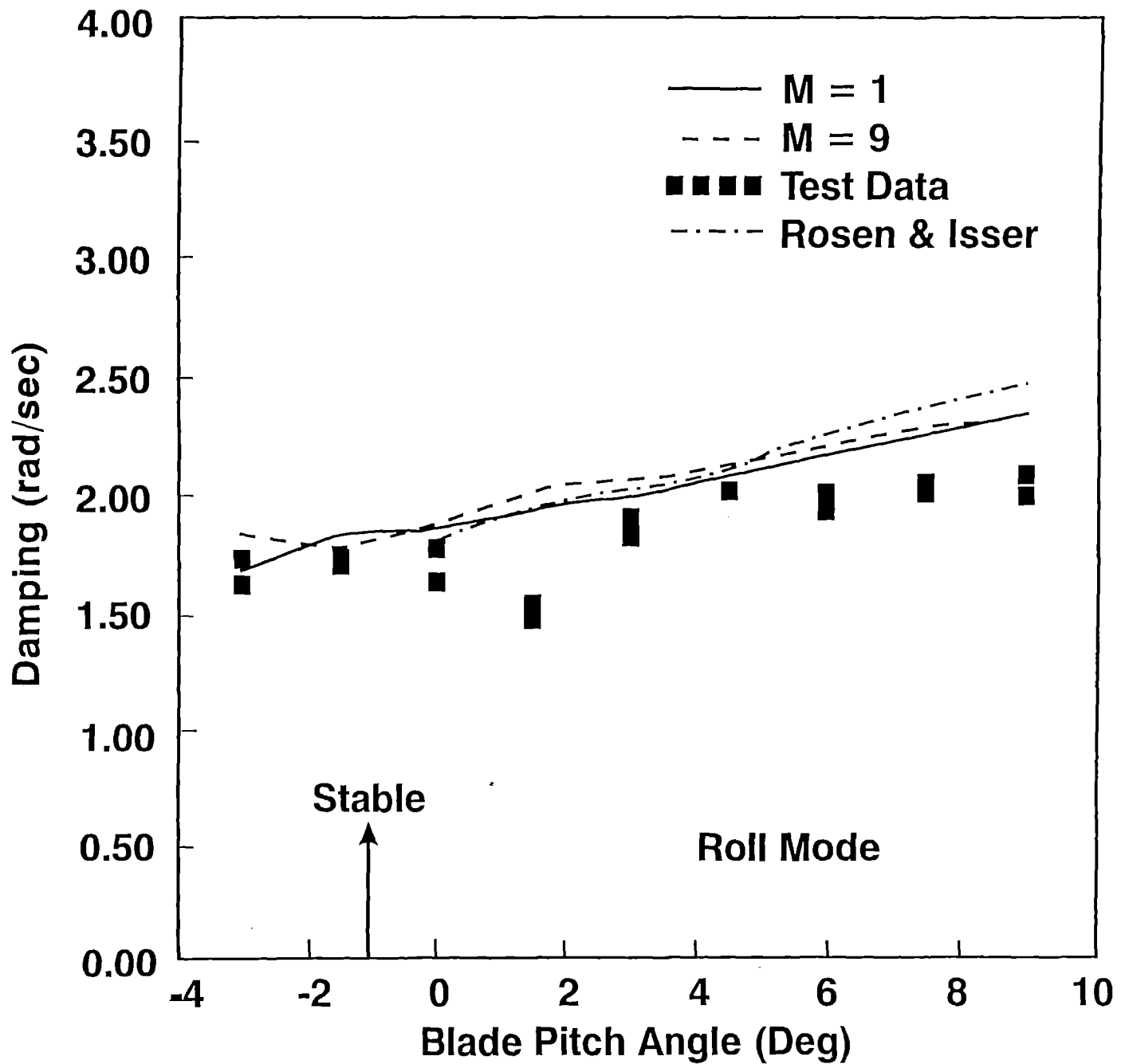
Fig. 16. Body Roll-Mode Damping With Increasing Blade Collective Pitch
for Configuration 1 at 650-RPM Rotor Speed
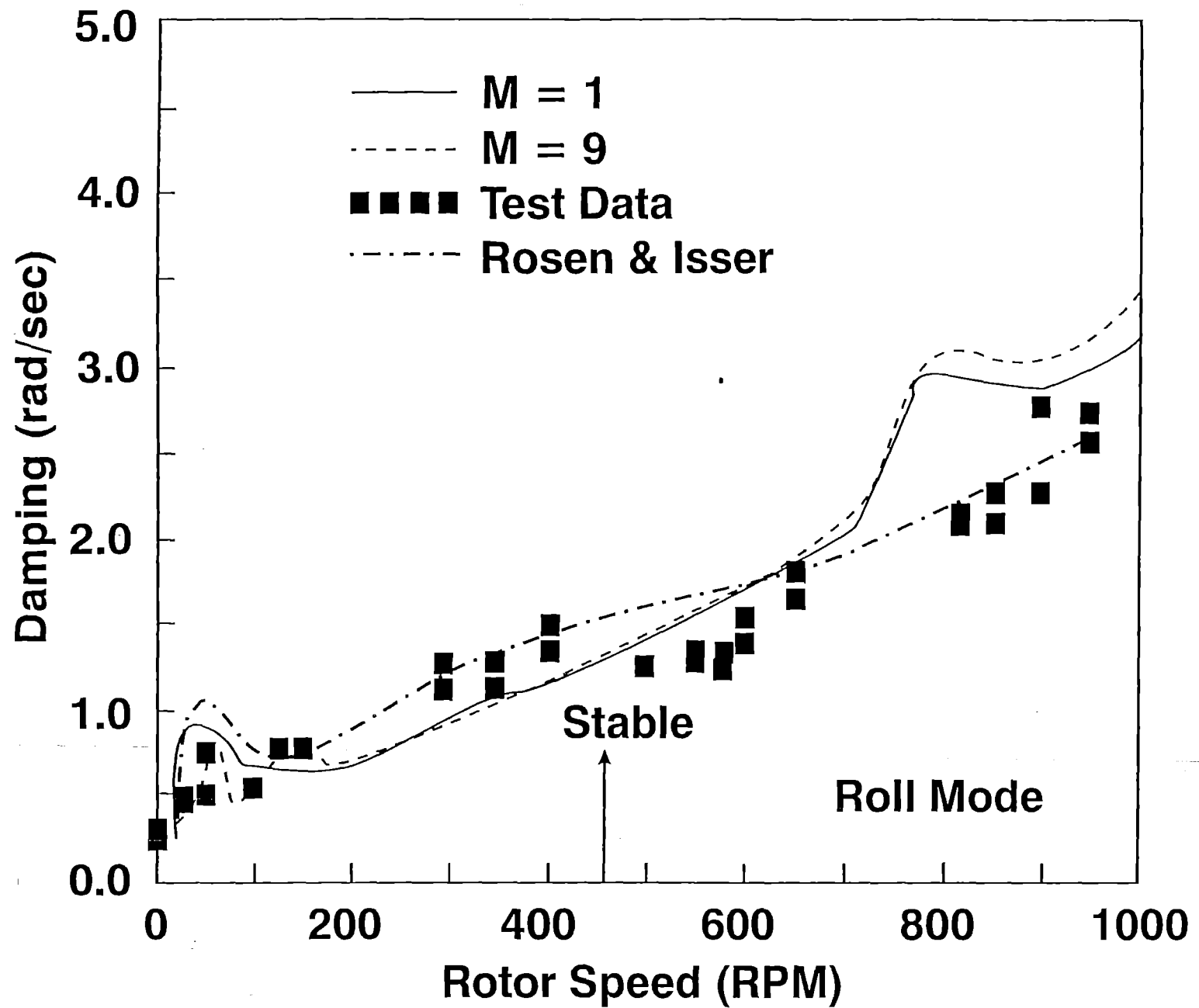
Fig. 17. Body Roll-Mode Damping With Increasing Rotor Speed for
Configuration 1 at Zero-Degree Blade Collective Pitch
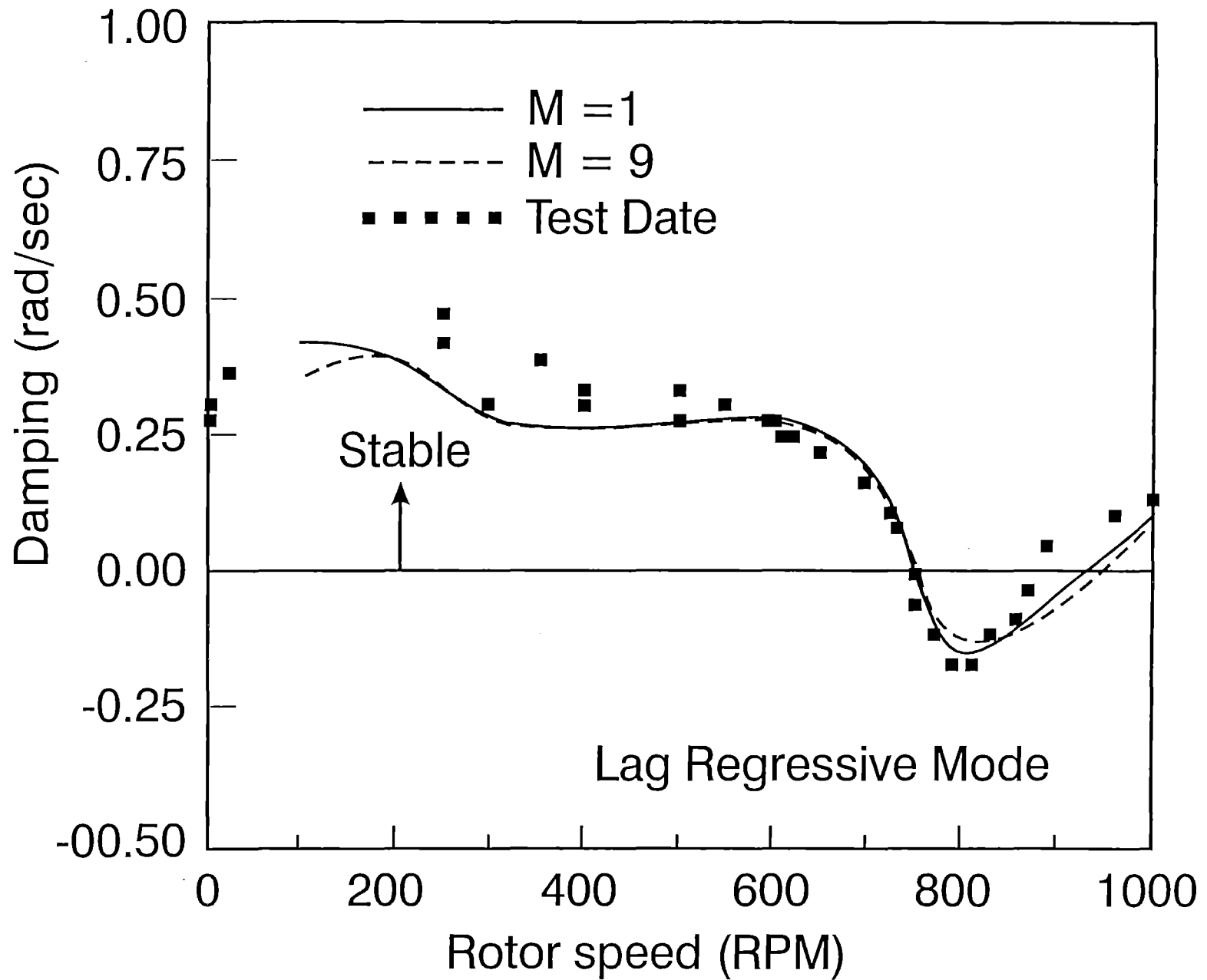
**Fig. 18. Lag Regressive-Mode Damping With Increasing Rotor Speed
for Configuration 4 at Zero-Degree Blade Collective Pitch**
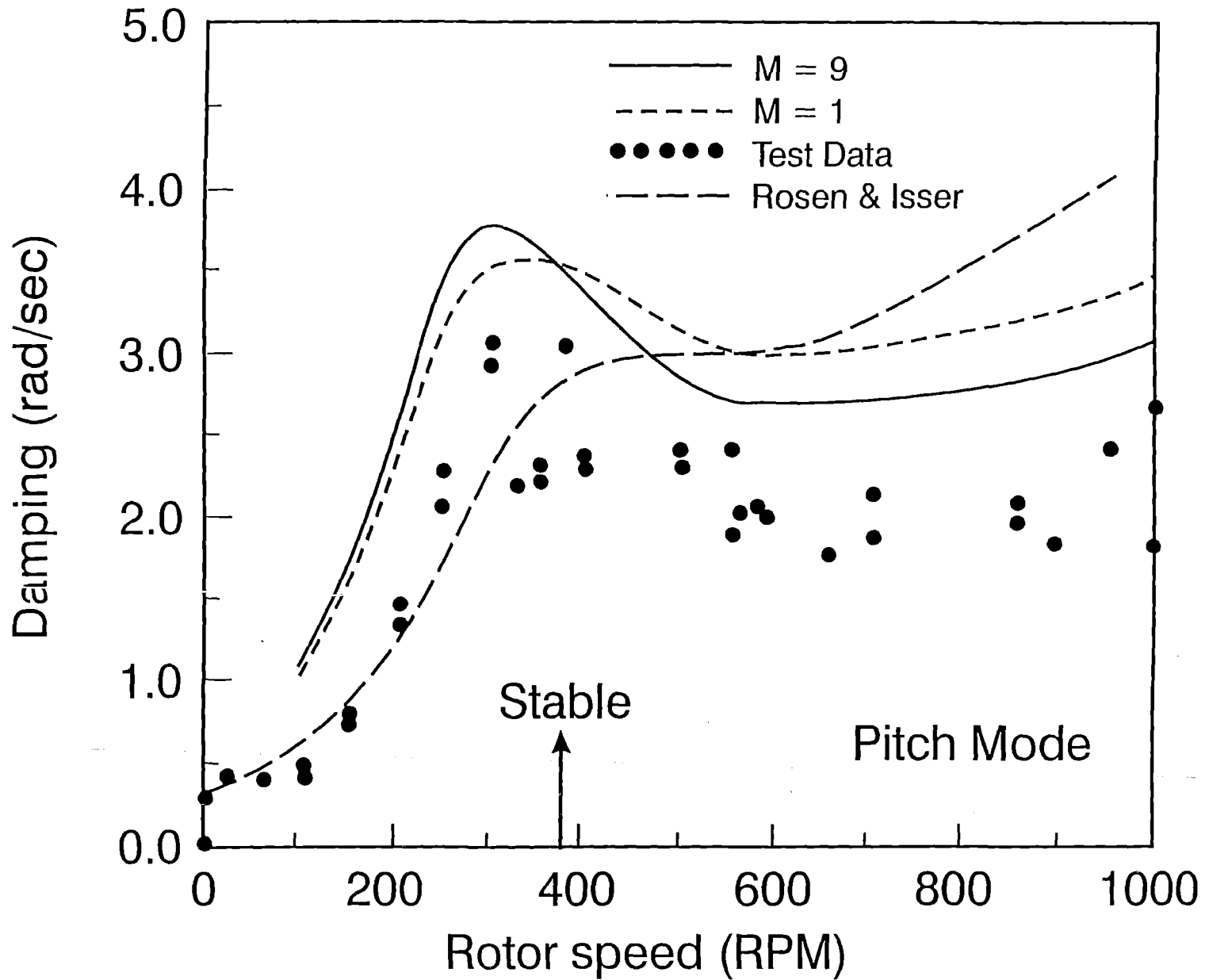
Fig. 19. Body Pitch-Mode Damping With Increasing Rotor Speed for Configuration 4 at Zero-Degree Blade Collective Pitch
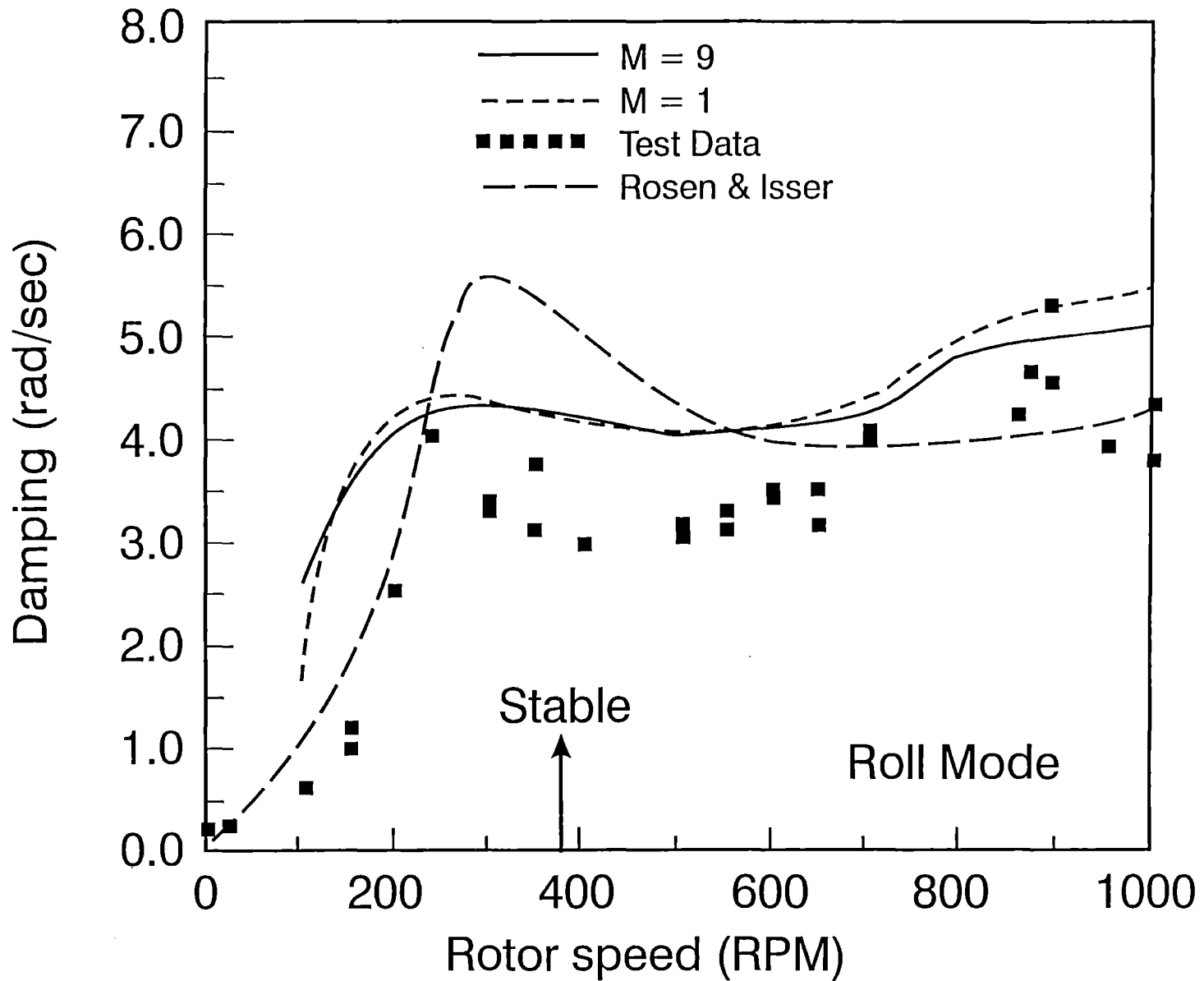
Fig. 20. Body Roll-Mode Damping With Increasing Rotor Speed for Configuration 4 at Zero-Degree Blade Collective Pitch
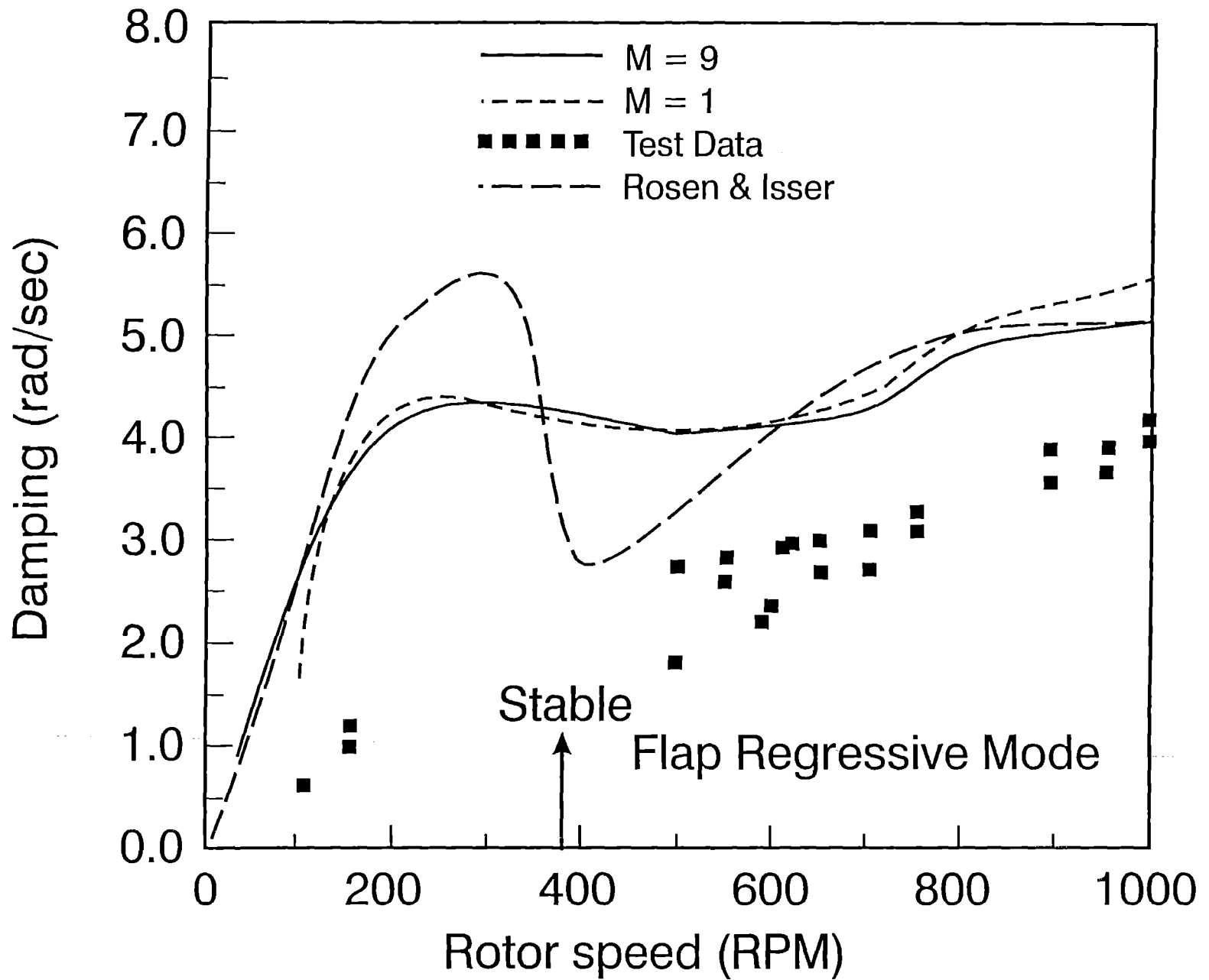
Fig. 21. Flap Regressive-Mode Damping With Increasing Rotor Speed for Configuration 4 at Zero-Degree Blade Collective Pitch
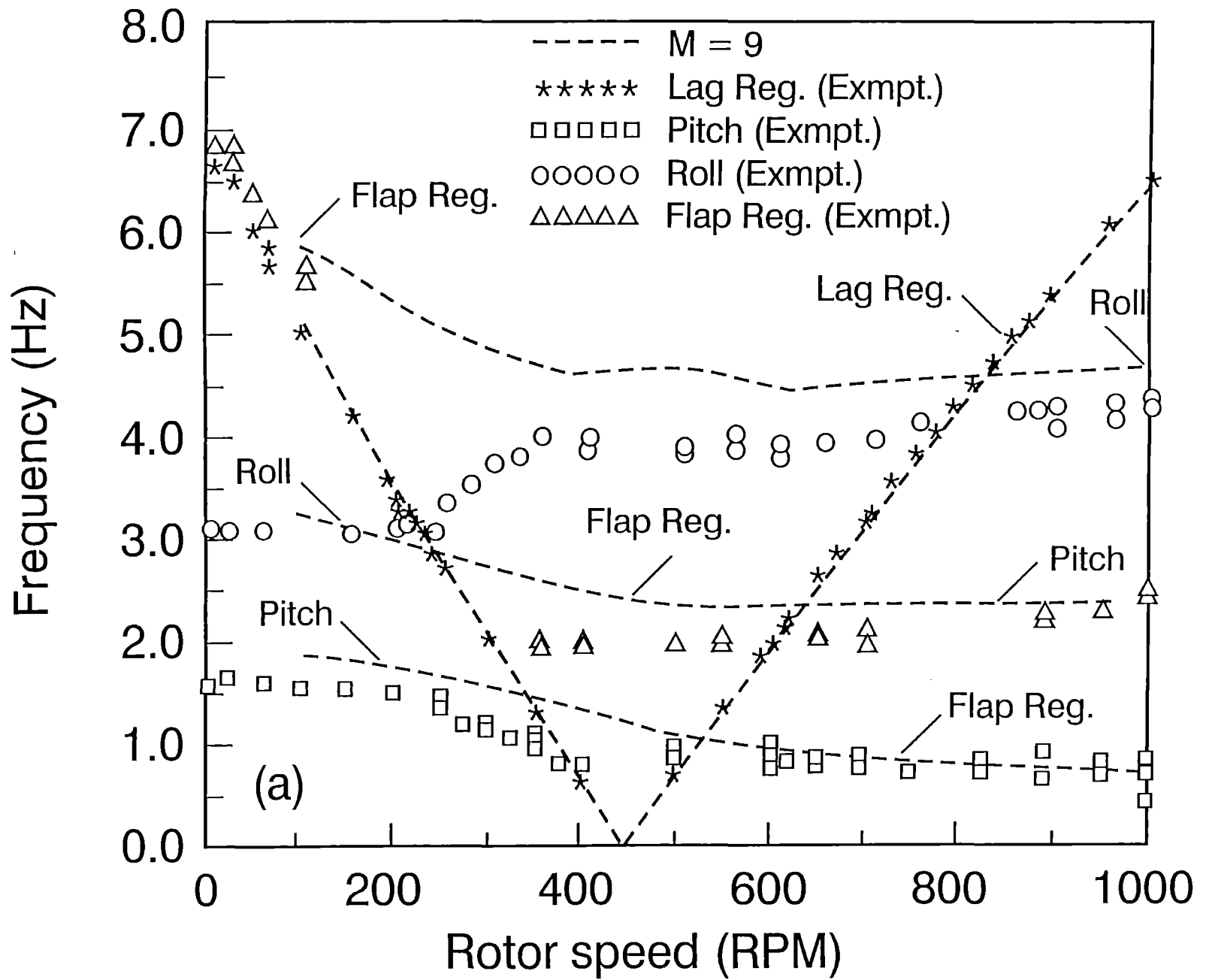
Fig. 22 a. Mode Frequencies With Increasing Rotor Speed for
Configuration 4 at Zero-Degree Blade Collective Pitch
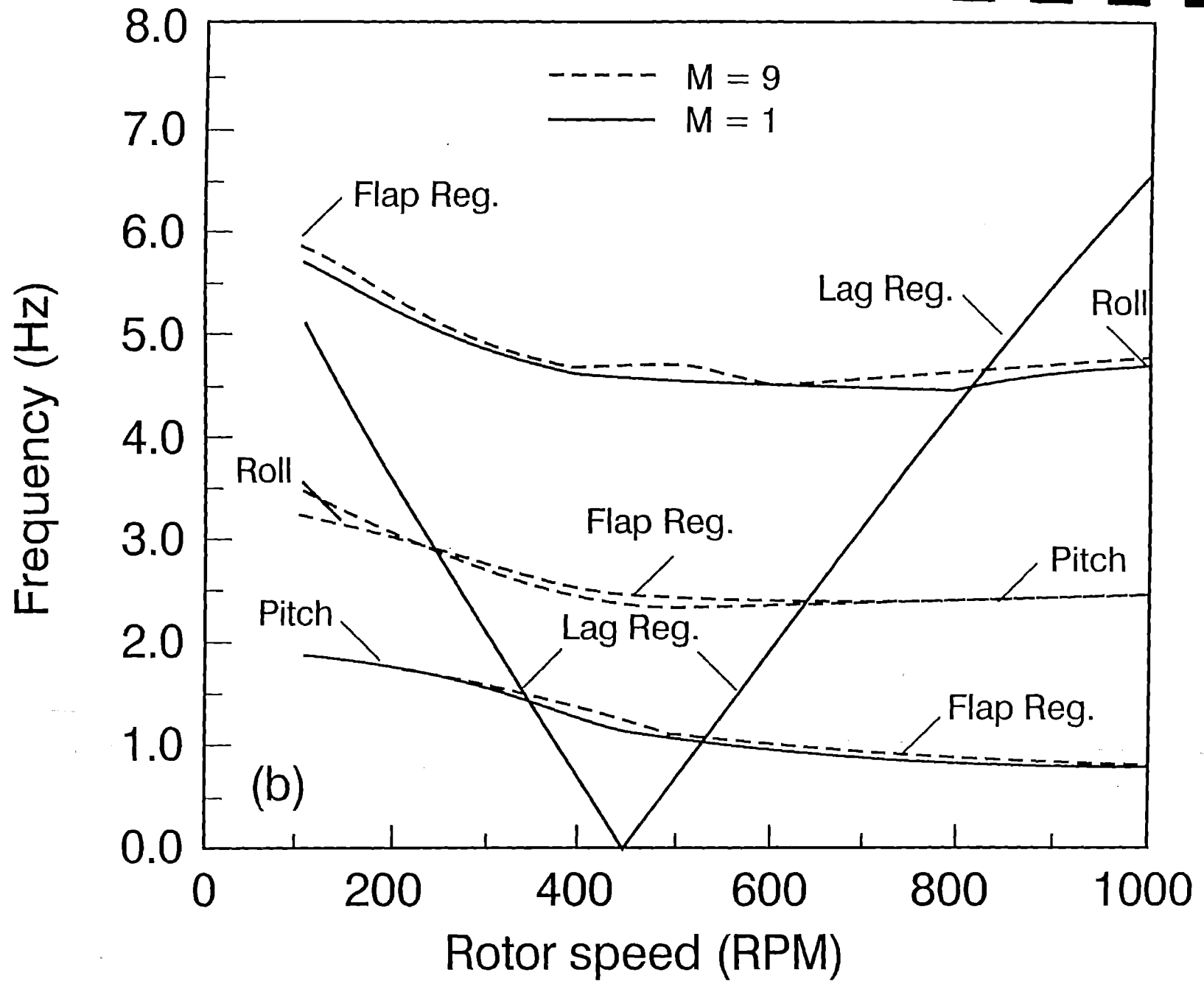
Fig. 22 b. Mode Frequencies With Increasing Rotor Speed for Configuration 4 at Zero-Degree Blade Collective Pitch
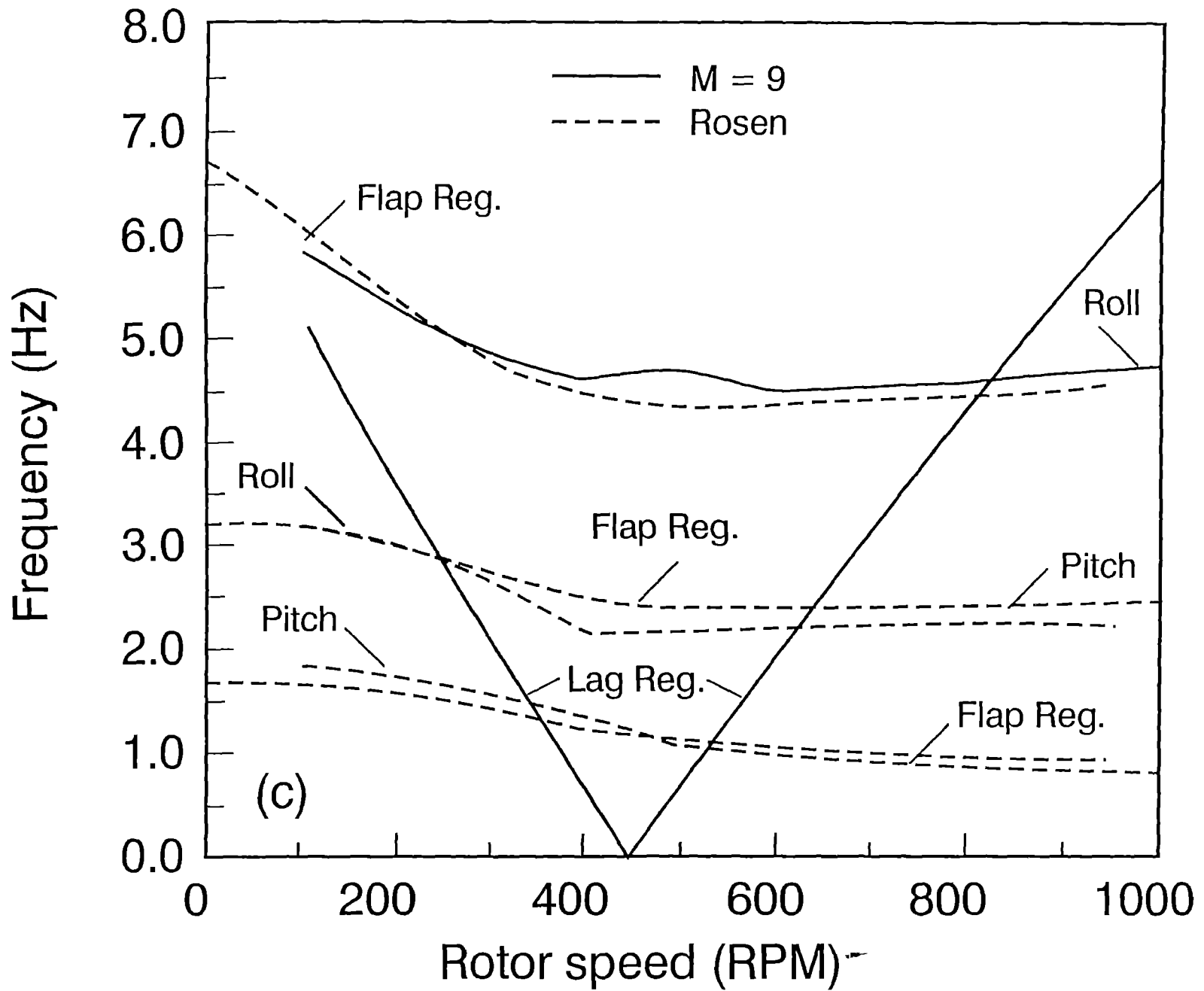
Fig. 22 c. Mode Frequencies With Increasing Rotor Speed for Configuration 4 at Zero-Degree Blade Collective Pitch
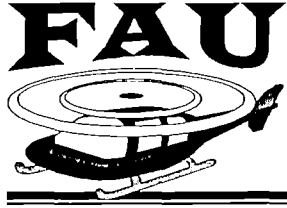
Conclusions

Convergence of Predictions: Control Inputs, Periodic
Responses and Damping Levels

$0 \leq$ Advance Ratio $\mu \leq 0.4$; $0.05 \leq$ Thrust Level $C_T / \sigma \leq 0.15$

☒ For $0 \leq \mu \leq 0.4$ and $0.05 \leq C_T / \sigma \leq 0.15$, the predictions
with nine harmonics converge in the sense that the
maximum error relative to the predictions with 10 or
more harmonics is less than 5%.

☒ The number of harmonics required for convergence
generally increases with increasing advance ratio μ and
thrust level C_T / σ
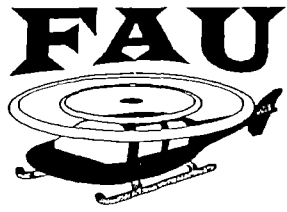
Conclusions

Parametric Study

(Dynamic Inflow and Full Wake Dynamics; Trimmed Flight; Parameters: $0 \leq$ Advance Ratio $\mu \leq 0.4$;

$0.05 \leq$ Thrust Level $C_T / \sigma \leq 0.15$; $3 \leq$ Number of Blades $Q \leq 5$)

⊠ The differences in the predictions with the dynamic inflow and finite-state wake models generally increase with increasing thrust level and advance ratio

⊠ The damping level of the lag-regressing mode increases with increasing advance ratio

⊠ The damping levels of the body modes show a bucket-like variation with increasing advance ratio

⊠ The basic characteristics of aeromechanical stability are not sensitive to the number of blades

Conclusions

FAU
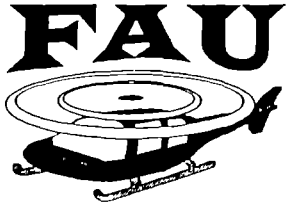
Correlation Study
(Configuration 1 and 4)

☒Overall, a good correlation is obtained from the finite-state wake model for the lag regressing, body roll and pitch, and flap regressing modes

☒For the lag regressing mode, the correlations from the finite-state wake and dynamic inflow models are nearly identical

☒For the body pitch and roll modes the correlations from the finite-state wake, dynamic inflow and vortex models generally agree
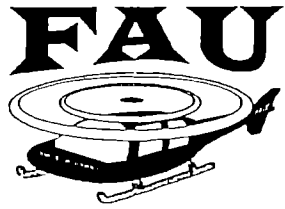
Conclusions

☒For Configuration 1 (no data), the predictions from the finite-state wake and dynamic inflow models are fairly close. Despite the similarity of the predictions from the finite-state wake and vortex models, there are appreciable quantitative differences; this merits further investigation

☒Within the data range (Configuration 4, $500 \leq \Omega \leq 1000$ RPM), the finite state wake, dynamic inflow and vortex models provide nearly identical correlation.

Coupled Rotor/Fuselage Vibration Analysis for a Teetering Rotor and Comparison with Flight Test Data

Hyeonsoo Yeo   Inderjit Chopra

Alfred Gessow Rotorcraft Center
Department of Aerospace Engineering
University of Maryland, College Park, MD 20742

A comprehensive vibration analysis of a coupled rotor/fuselage system for a two-bladed teetering rotor using finite element methods in space and time is developed that incorporate consistent rotor/fuselage structural, aerodynamic and inertial couplings and a modern free wake model. Coupled nonlinear periodic blade and fuselage equations are transformed to the modal space in the fixed frame and solved simultaneously. The elastic line airframe model of the AH-1G helicopter from the DAMVIBS program is integrated into the elastic rotor finite element model. Analytical predictions of rotor controls, blade loads and vibration are compared with flight test data. Predicted rotor control angles, blade torsional, and chord bending moments show relatively good agreement with test data. Blade beam bending moments overpredicts test measurements and needs further investigation. Calculated 2/rev and 4/rev vertical vibration levels at pilot seat show good correlation with the flight test, but predicted lateral vibration levels are much higher than measurements particularly at high advance ratios. In future, parametric studies will be carried out to investigate the sensitivity of different design parameters and modeling refinements on the prediction of blade loads and vibration.

1

Coupled Rotor/Fuselage Vibration Analysis for a Teetering Rotor and Comparison with Flight Test Data

HYEONSOO YEO
Graduate Research Assistant

INDERJIT CHOPRA
Professor & Director

Alfred Gessow Rotorcraft Center
University of Maryland at College Park

Motivation

University of Maryland

- **Helicopter vibration**
  - **Structural fatigue of components**
  - **Human discomfort**

- **Ride quality**
  System reliability
  Maintenance cost
  Equipment performance

- **Prediction of vibration at early design stage is essential**

N_b/rev
hub forces
& moments
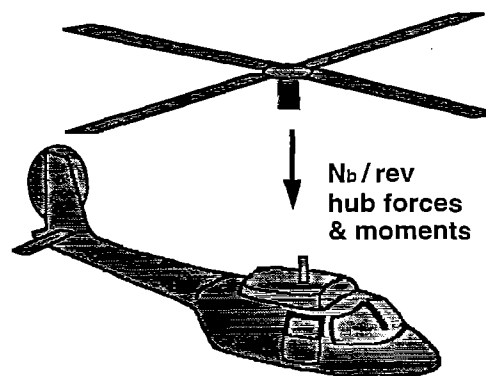
Objective

- **Develop a comprehensive vibration prediction methodology**

  - Coupled elastic rotor/fuselage system

  - Consistent rotor/fuselage structural, aerodynamic and inertial coupling modeling

  - Finite element methods in space and time

- **Teetering rotor modeling**
- **Comparison with flight test data**

State-of-the Art

- **Flapping blade - Rigid fuselage**

  Hohenemser & Yin (1979) : concentrated inertia & support spring

- **Flapping blade - Elastic fuselage**

  Hsu & Peters (1980) : unifrom beam (plunge, roll & pitch motions)

- **Elastic blade (flap, lag, & torsion) - Rigid fuselage**

  For aeromechanical stability analysis

- **Elastic blade (flap, lag, & torsion) - Elastic fuselage**

  Vellaichamy & Chopra (1992,1993), Chiu & Friedmann (1995,1996)

- **Elastic blade (flap, lag, & torsion) - Elastic fuselage - Refined aerodynamics (free wake+unsteady aerodynamics)**

  Yeo and Chopra (1997)

DAMVIBS

DAMVIBS :

- Design Analysis Methods for VIBrationS

- NASA Langley and Bell, Boeing, McDonnell Douglas, Sikorsky involved

Goals :
- Airframe finite element modeling

- Difficult components modeling refinement

- Coupled rotor-airframe vibration analysis

- Airframe structural optimization
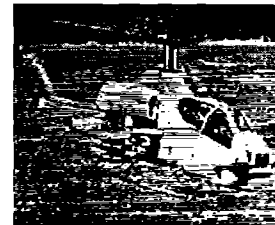
Challenges to Helicopter Vibration Analysis

- **Highly flexible rotating blades**
  - Nonlinearity and couplings

- **Complex and unsteady aerodynamic environment**
  - Compressibility effects at advancing blade
  - Dynamic stall and reverse flow at retreating blade
  - Blade tip vortices
  - Blade/vortex interaction

- **Rotor-fuselage couplings and interactions**

Problem Statement

Nb / rev
hub loads

Feedback of
fuselage motion
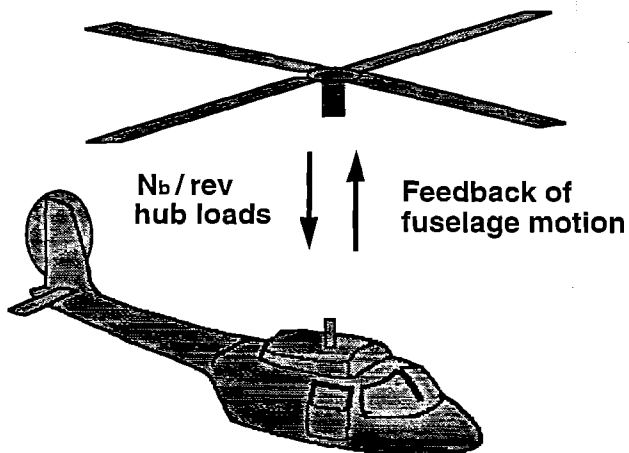
Modeling Assumptions

- **Fuselage vibration excited by main rotor**
  - Rotor/body interactional aerodynamics neglected

- **Tracked rotor**
  - All blades are identical and
    have the same periodic motion
  - pN_b/rev harmonics transmitted to the fuselage
    (p integer)

- **Steady vibration**
  - maneuver, transient flight, gust response
    not considered

- **Rotor shaft is assumed rigid**
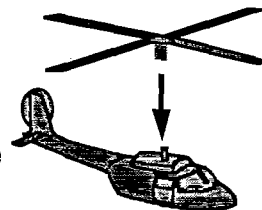
Modeling & Analysis

- **Elastic blade model**
  - Based on UMARC
  - Slender beam with flap and lag bending, elastic twist and axial deflection
  - 15 DOF finite element model
  - Incorporation of six hub degrees of freedom

- **Elastic fuselage model**
  - Finite element stick model
  - Lateral & vertical bending, twist, and axial deflection
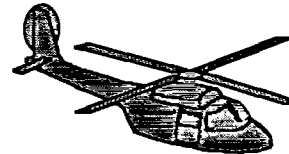
Teetering Rotor

β_T = Teetering angle

β_p = Precone angle

w = elastic flap bending
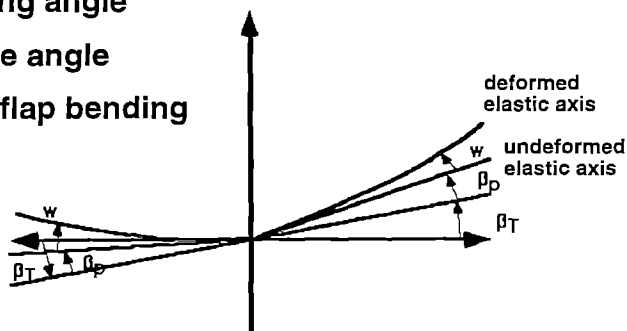
Teetering equation : Blade flap moment = 0

Equations of Motion

Hamilton's variational principle

$$\delta\Pi = \int_{t_1}^{t_2} (\delta U - \delta T - \delta W)\ \mathbf{dt} = 0$$

$$\delta U = \left[\ \sum_{b=1}^{N_b} \delta U_b\ \right] + \delta U_F \qquad \text{Strain Energy}$$

$$\delta T = \left[\ \sum_{b=1}^{N_b} \delta T_b\ \right] + \delta T_F \qquad \text{Kinetic Energy}$$

$$\delta W = \left[\ \sum_{b=1}^{N_b} \delta W_b\ \right] + \delta W_F \qquad \text{Work Done}$$

blades   fuselage

Nonlinear equations of motion are derived explicitly in fixed frame
Ordering scheme is applied to neglect higher order terms

Kinetic Energy

- **Blade velocity in the deformed frame**

$$\bar{V} = (V_{bx} + V_{fx})\,\hat{i} + (V_{by} + V_{fy})\hat{j} + (V_{bz} + V_{fz})\hat{k}$$

$$V_{bx} = \dot{x}_1 - y_1 \cos(\beta_p + \beta_T) - z_1\dot{\beta}_T$$

$$V_{by} = \dot{y}_1 - x_1 \cos(\beta_p + \beta_T) - z_1 \sin(\beta_p + \beta_T)$$

$$V_{bz} = \dot{z}_1 + x_1\dot{\beta}_T + y_1 \sin(\beta_p + \beta_T)$$

$$V_{fx} = (\dot{x}_f - h\dot{\alpha}_s - y_{CG}\dot{\psi}_s)\cos\psi + (\dot{y}_f + h\dot{\phi}_s + x_{CG}\dot{\psi}_s)\sin\psi$$

$$V_{fy} = -(\dot{x}_f - h\dot{\alpha}_s - y_{CG}\dot{\psi}_s)\sin\psi + (\dot{y}_f + h\dot{\phi}_s + x_{CG}\dot{\psi}_s)\cos\psi + x\dot{\psi}_s$$

$$V_{fz} = \dot{z}_f + x\dot{\alpha}_s \cos\psi - x\dot{\phi}_s \sin\psi + x_{CG}\dot{\alpha}_s - y_{CG}\dot{\phi}_s$$

$\dot{x}_f$, $\dot{y}_f$, $\dot{z}_f$ = **hub velocities** β_T = **teetering angle**
$\dot{\alpha}_s$, $\dot{\phi}_s$, $\dot{\psi}_s$ = **hub angular velocities**

Aerodynamic Model

University of Maryland

- **Local blade velocities consist of**
  - Free stream
  - Blade motion relative to the hub
  - Hub motion relative to the inertial frame

- **Velocities and blade loads are calculated in the deformed frame**
- **Compressibility and reversed flow effects included**
- **Time-domain unsteady aerodynamics (Leishman model)**
- **Pseudo-implicit free wake model (Bagai-Leishman model)**

Aerodynamics

University of Maryland

- **Blade velocity in the rotating deformed frame**
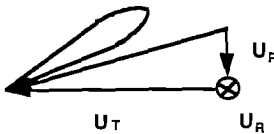
$$\frac{U_{Rf}}{\Omega R} = \left(\dot{x}_f - h\dot{\alpha}_s - y_{CG}\dot{\psi}_s\right)\cos\psi + \left(\dot{y}_f + h\dot{\phi}_s + x_{CG}\dot{\psi}_s\right)\sin\psi$$

$$\frac{U_{Tf}}{\Omega R} = \left(\dot{x}_f - h\dot{\alpha}_s - y_{CG}\dot{\psi}_s\right)\sin\psi\cos\theta_0 + \left(\dot{y}_f + h\dot{\phi}_s + x_{CG}\dot{\psi}_s\right)\cos\psi\sin\theta_0$$

$$+ \sin\theta_0\left(\dot{z}_f - \dot{\phi}_s x\sin\psi + \dot{\alpha}_s x\cos\psi + x_{CG}\dot{\alpha}_s - y_{CG}\dot{\phi}_s\right) + x\dot{\psi}_s\cos\theta_0$$

$$\frac{U_{Pf}}{\Omega R} = \sin\theta_0\left(\left(\dot{x}_f - h\dot{\alpha}_s - y_{CG}\dot{\psi}_s\right)\sin\psi - \left(\dot{y}_f + h\dot{\phi}_s + x_{CG}\dot{\psi}_s\right)\cos\psi\right)$$

$$+ \cos\theta_0\left(\dot{z}_f - \dot{\phi}_s x\sin\psi + \dot{\alpha}_s x\cos\psi + x_{CG}\dot{\alpha}_s - y_{CG}\dot{\phi}_s\right)$$

θ_0 = rigid pitch angle due to control pitch and pretwist
$= \theta_{75} + \theta_{tw}$ (x/R -0.75) $+ \theta_{1c}\cos\psi + \theta_{1s}\sin\psi$

Blade Loads

- **Force summation method**

Longitudinal $L_u = L_u^A + L_u^I + L_u^{If}$ Torsion $M_x = -L_v W + L_w V + M_u$

Lateral $L_v = L_v^A + L_v^I + L_v^{If}$ Beam $M_y = L_u W - L_w X + M_v$

Vertical $L_w = L_w^A + L_w^I + L_w^{If}$ Chord $M_z = -L_u V + L_v X + M_w$

$$L_u^{If} = -m\left[\ddot{x}_f \cos\psi + \ddot{y}_f \sin\psi - h\ddot{\alpha}_s \cos\psi + h\ddot{\phi}_s \sin\psi - 2x\dot{\psi}_s + (x_{CG}\sin\psi - y_{CG}\cos\psi)\ddot{\psi}_s\right]$$

$$L_v^{If} = -m\left[\ddot{y}_f \cos\psi - \ddot{x}_f \sin\psi + h\ddot{\alpha}_s \sin\psi + h\ddot{\phi}_s \cos\psi + (x + x_{CG}\cos\psi + y_{CG}\sin\psi)\ddot{\psi}_s\right]$$

$$L_w^{If} = -m\left[\ddot{z}_f + (x\cos\psi + x_{CG})\ddot{\alpha}_s - 2x\dot{\alpha}_s \sin\psi - (x\sin\psi + y_{CG})\dot{\phi}_s - 2x\dot{\phi}_s \cos\psi\right]$$

Analysis Procedure

- **Normal mode form**

- **Fixed frame coordinate transformation**

$$\begin{bmatrix} M_{rr} & M_{rt} & M_{rfe} \\ M_{tr} & M_{tt} & M_{tfe} \\ M_{fr} & M_{ft} & M_{ffe} \end{bmatrix} \begin{Bmatrix} \ddot{\xi} \\ \ddot{\beta}_T \\ \ddot{p}_{fe} \end{Bmatrix} + \begin{bmatrix} C_{rr} & C_{rt} & C_{rfe} \\ C_{tr} & C_{tt} & C_{tfe} \\ C_{fr} & C_{ft} & C_{ffe} \end{bmatrix} \begin{Bmatrix} \dot{\xi} \\ \dot{\beta}_T \\ \dot{p}_{fe} \end{Bmatrix}$$

$$+ \begin{bmatrix} K_{rr} & K_{rt} & K_{rfe} \\ K_{tr} & K_{tt} & K_{tfe} \\ K_{fr} & K_{ft} & K_{ffe} \end{bmatrix} \begin{Bmatrix} \xi \\ \beta_T \\ p_{fe} \end{Bmatrix} = \begin{Bmatrix} F_{rr} - M_{rfr}\ddot{p}_{fr} - C_{rfr}\dot{p}_{fr} \\ F_{tt} - M_{tfr}\ddot{p}_{fr} - C_{tfr}\dot{p}_{fr} \\ F_{ffe} - C_{ffr}\dot{p}_{fr} \end{Bmatrix}$$

Analysis Procedure

- Simultaneous solution of rotor and fuselage equations

- Finite element method in time used to calculate coupled rotor-fuselage response

- Periodic boundary condition for both rotor and fuselage

- Equilibrium of vibratory hub loads
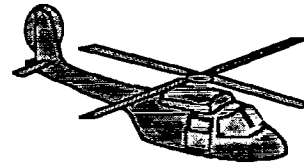
Rotor Properties

AH-1G helicopter

Number of blade	2
Rotor radius	22 (ft)
Chord	27 (in)
Rotor Speed	324 (RPM)
Lock number	5.078
Precone angle	2.75 (deg)
Twist angle at tip	-10 (deg)
Control system spring rate	396000 (in-lb/rad)
Pitch link moment arm	9.067 (in)
Lift curve slope	6.159
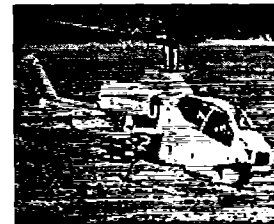
Blade Frequencies

• Collective mode (hingeless boundary condition)

Present Analysis		C81	
flap 1	1.04	1.04	
flap 2	2.79	2.9	
flap 3	4.81	4.74	(/ rev)
lag 1	1.43	1.3	
torsion 1	2.58	2.33	

Fuselage Model

· Elastic-line model of AH-1G helicopter
· 36 beam elements

Pilot Seat
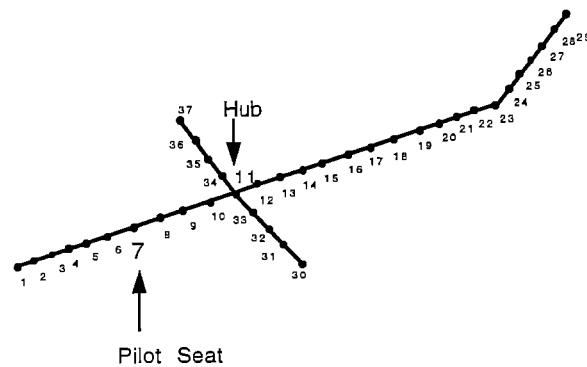
Fuselage Frequencies

Present Analysis		NASTRAN	
vertical	1.44	1.47	
bending	3.16	3.31	
	5.1	4.72	(/ rev)
lateral	1.36	1.26	
bending	3.07	3.09	

Results

- Effect of aerodynamic modeling

- Rotor control angles

- Blade torsional and chord and
  beam bending moments

- Hub forces

- Vibration at pilot seat
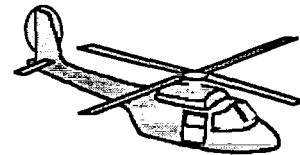
Effect of Aerodynamic Modeling
4/rev acceleration at pilot seat

University of Maryland

4 bladed hingeless blade + elastic line body

Vertical Acceleration

- linear inflow + quasisteady
- linear inflow + unsteady
- free wake + unsteady

g

Advance Ratio

Lateral Acceleration

g
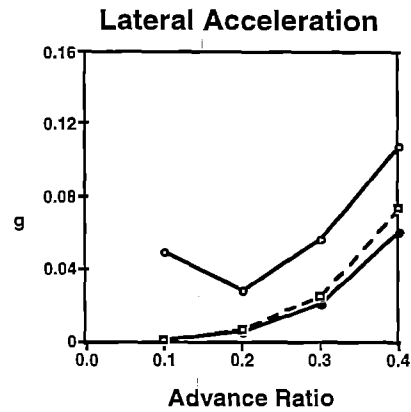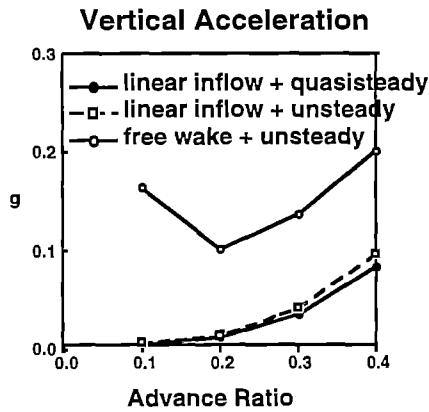
Advance Ratio

Rotor Controls

University of Maryland

○ □ ● Test Data

$\theta_{0.75}$ Collective

θ_{1c} Lateral cyclic

degree

θ_{1s} longitudianl cyclic

Advance Ratio

Blade Torsional Moments
at advance ratio 0.15

University of Maryland

1/rev · 2/rev · 3/rev

Legend:
- Hub Fixed
- Rigid Body Motion
- Elastic Line Body
- □ Flight test

Blade Radius

Chord Bending Moments
at advance ratio 0.15

University of Maryland

1/rev · 2/rev · 3/rev

Legend:
- Hub Fixed
- Rigid Body Motion
- Elastic Line Body
- □ Flight test

Blade Radius

Beam Bending Moments
at advance ratio 0.15

University of Maryland

1/rev

2/rev

Hub Fixed
Rigid Body Motion
Elastic Line Body
□ Flight test

3/rev

Blade Radius

Blade Radius

Blade Radius

Blade Torsional Moments
at advance ratio 0.32

University of Maryland

1/rev

2/rev

Hub Fixed
Rigid Body Motion
Elastic Line Body
□ Flight test

3/rev

Blade Radius

Blade Radius

Blade Radius

Chord Bending Moments
at advance ratio 0.32

University of Maryland

1/rev
2/rev
3/rev

Hub Fixed
Rigid Body Motion
Elastic Line Body
Flight test

Blade Radius

Beam Bending Moments
at advance ratio 0.32

University of Maryland

1/rev
2/rev
3/rev

Hub Fixed
Rigid Body Motion
Elastic Line Body
Flight test

Blade Radius

2/rev Hub Forces

longitudinal

lateral

vertical

Legend:
- ----- Hub Fixed
- – – – Rigid Body Motion
- ——— Elastic Line Body

Vertical Acceleration at pilot seat

2/rev

4/rev

□ Test Data

(g)

2/rev Hub Forces

longitudinal

lateral

vertical

Legend:
- - - - - Hub Fixed
- — - Rigid Body Motion
- ——— Elastic Line Body

Advance Ratio

Vertical Acceleration at pilot seat

2/rev

4/rev

(g)

□ Test Data

Advance Ratio

Lateral Acceleration at pilot seat

University of Maryland

Conclusions

University of Maryland

- **Unsteady aerodynamics is important at high advance ratios and free wake is essential for the prediction of vibration at all forward speeds**

- **In general, there is good agreement in rotor controls**

- **Comparison between calculated blade torsional and chord bending moments and measured data shows relatively fair agreement, but beam moment significantly overpredict measured data and need to be investigated further**

Conclusions

- Estimated 2/rev and 4/rev vertical acceleration at pilot seat shows satisfactory correlation with flight test data

- 2/rev lateral acceleration level at the pilot seat is overpredicted at all advance ratios and 4/rev lateral acceleraion level shows good agreement at low advance ratios and overpredicts at high advance ratios

Session V
Vibration and Dynamics

Convergence of Nonlinear Finite Elements for Rotorcraft Applications

Tim Jackson

Advisor: Dr. David A. Peters

Department of Mechanical Engineering

Washington University

St. Louis, Missouri

AGENDA

1) Motivation
2) Derivation of Equations
 - exact
 - approximate
3) Finite Element Approach
 - stiffness matrix & load vector
 - solution methods
4) Numerical Results
5) Conclusions

MOTIVATION

•Add extensibility to helicopter rotor blade equations
   –nonlinearity
   –1D → 2D problem

•2G-CHAS

   –FE code diverges

DERIVATION OF EQUATIONS

Basic Geometry and Order of Terms

$$\cdot \; \text{let}: \; \in = 0.1$$

$$\cdot \frac{w}{R} \approx O(\in)$$

$$\cdot \frac{u}{R} \approx O(\in^2)$$

$$\cdot \kappa \approx O(\in)$$

$$\cdot w' \approx O(\in)$$

$$\cdot u' \approx O(\in^2)$$
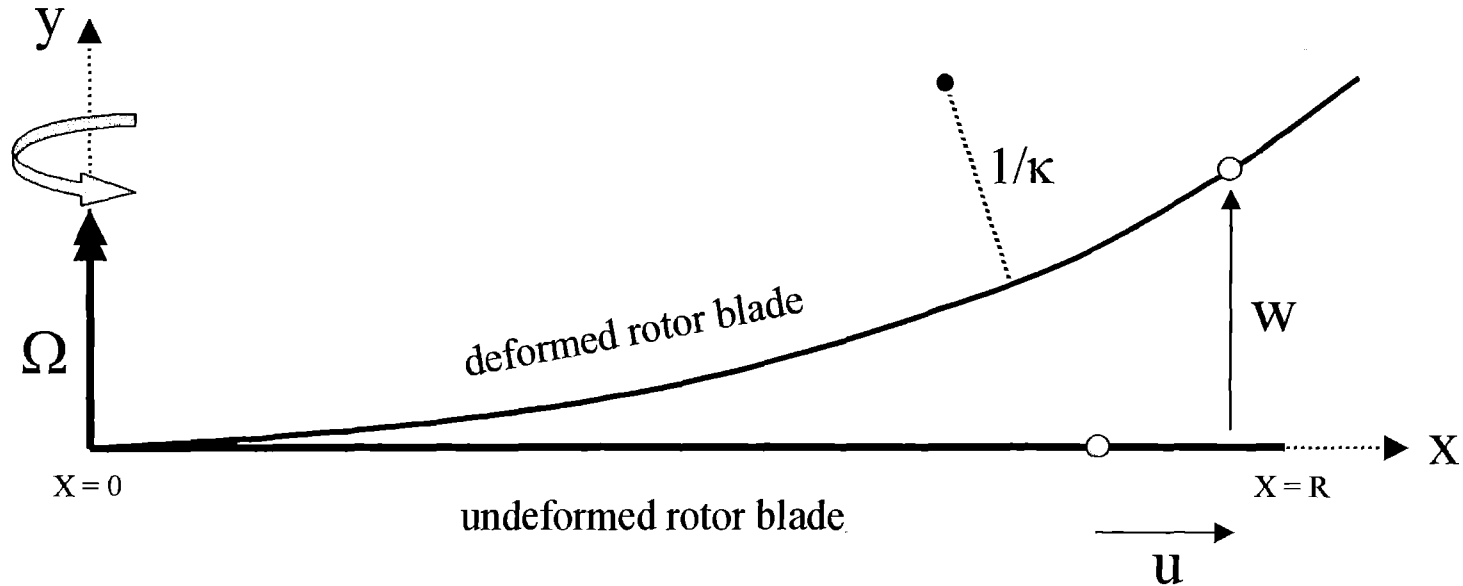
$$\cdot R w'' \approx 0.3 \approx O(\in)$$

$$\cdot R u'' \approx O(\in^2)$$

$$\cdot R^2 w''' \approx 1 \approx O(\in^0)$$

$$\cdot R^2 u''' \approx O(\in^2)$$

4

DERIVATION OF EQUATIONS

Basic Geometry and Order of Terms (continued)
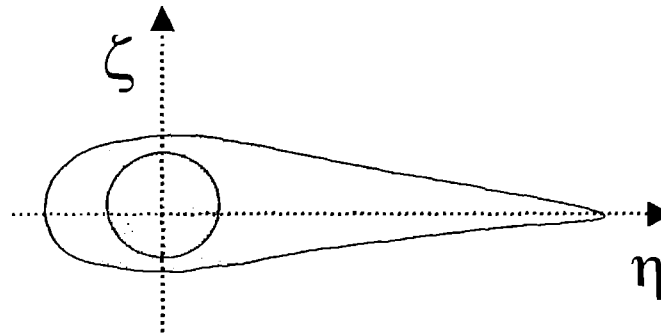
Rotor Blade Cross-Section

$$\cdot \frac{\zeta}{R} \approx 0.01 \approx \in^2 \qquad \cdot \frac{A}{R^2} \approx \frac{\zeta^2}{R^2} \approx 3x10^{-3} \qquad \cdot \frac{EI}{m\Omega^2 R^4} \approx 3x10^{-3}$$

$$\cdot \frac{\eta}{R} \approx 0.03 \approx \in^2 \qquad \cdot \frac{I}{R^4} \approx \frac{\eta\zeta^3}{12R} \approx 3x10^2 \qquad \cdot \frac{EA}{m\Omega^2 R^2} \approx 3x10^2$$

$$\cdot \kappa\zeta \approx O(\in^3)$$

$$\boxed{\therefore EI << EA}$$

DERIVATION OF EQUATIONS

Stress-Strain Relations

· undeformed length $= \Delta x$

· length of deformed centerline $= (1 + \varepsilon_o) \Delta x$

· $\Delta \beta = \kappa (1 + \varepsilon_o) \Delta x$

· length of any arc $= \Delta \beta (\dfrac{1}{\kappa} + \zeta)$

$$= (1 + \varepsilon_o + \kappa \zeta + \varepsilon_o \kappa \zeta) \Delta x$$

Deformed Element
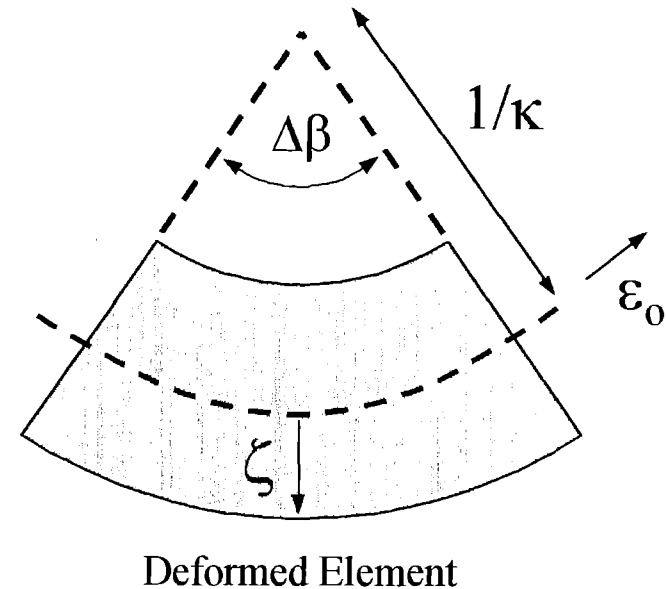
· engineering strain : $\varepsilon_E = \dfrac{(1 + \varepsilon_o + \kappa \zeta + \varepsilon_o \kappa \zeta) dx - dx}{dx}$

$$\boxed{\varepsilon_E = \varepsilon_o + \kappa \zeta + \varepsilon_o \kappa \zeta}$$

6

DERIVATION OF EQUATIONS

Stress-Strain Relations (continued)

· stress : $\sigma = E(\varepsilon_E + \alpha \varepsilon_E^{\,2})$ (where $\alpha = 0$ if the material is linear for engineering strain ε_E)

· combining stress and strain relations and using terms up to $O(\in^6)$:

$$\sigma = E(\varepsilon_o + \kappa \zeta + \varepsilon_o \kappa \zeta + \alpha \varepsilon_o^{\,2} + \alpha \kappa^2 \zeta^2 + 2\alpha \varepsilon_o \kappa \zeta)$$

7

DERIVATION OF EQUATIONS

Tension and Bending Moment

- assume E is constant across the cross-section and along the length of the blade
- assume A and I are constant along the length of the blade

tension : $T = \sigma A = \iint\limits_{A} E(\varepsilon_o + \kappa\zeta + \varepsilon_o\kappa\zeta + \alpha\varepsilon_o^2 + \alpha\kappa^2\zeta^2 + 2\alpha\varepsilon_o\kappa\zeta)d\eta d\zeta$

$$\boxed{T = EA(\varepsilon_o + \alpha\varepsilon_o^2) + EI_\eta\alpha\kappa^2}$$

if $\alpha = 0$

$\Rightarrow$

$$\boxed{T = EA\varepsilon_o}$$

bending moment : $M = \dfrac{I_\eta\sigma}{\zeta} = \dfrac{EI_\eta}{\zeta}(\varepsilon_o + \kappa\zeta + \varepsilon_o\kappa\zeta + \alpha\varepsilon_o^2 + \alpha\kappa^2\zeta^2 + 2\alpha\varepsilon_o\kappa\zeta)$

$$\boxed{M = EI_\eta\kappa[1 + (2\alpha + 1)\varepsilon_o]}$$

if $\alpha = 0$

$\Rightarrow$

$$\boxed{M = EI\overline{\kappa}}$$

Geometry Relations

$$\Delta\beta = \kappa(1+\varepsilon_o)\Delta x \quad \Rightarrow \quad \beta' = \kappa(1+\varepsilon_o)$$

$$\text{let } \overline{\kappa} = \kappa(1+\varepsilon_o) \qquad \therefore \quad \beta' = \overline{\kappa}$$

DERIVATION OF EQUATIONS

Geometry Relations (continued)

$$w = \int_0^x (1 + \varepsilon_o) \sin \beta \, d\xi \qquad\qquad u = \int_0^x (1 + \varepsilon_o) \cos \beta \, d\xi - x$$

$$w' = (1 + \varepsilon_o) \sin \beta \qquad\qquad u' = (1 + \varepsilon_o) \cos \beta$$

$$w'' = \beta'(1 + \varepsilon_o) \cos \beta + \varepsilon_o' \sin \beta \qquad u'' = -\beta'(1 + \varepsilon_o) \sin \beta + \varepsilon_o' \cos \beta$$

$\cdot$ solving for ε_o' : $\boxed{\varepsilon_o' = u'' \cos \beta + w'' \sin \beta}$

$\cdot$ solving for β' : $\beta' = \boxed{\overline{\kappa} = \dfrac{(w'' \cos \beta - u'' \sin \beta)}{(1 + \varepsilon_o)}}$

10

Approximations

•substituting approximations for cos β and sin β and using terms up to $O(\epsilon^3)$:

$$\varepsilon_o \approx u' + \frac{1}{2}w'^2$$

$$\beta \approx w' - \frac{1}{3}w'^3 - w'u'$$

$$\overline{\kappa} \approx w''(1-u'-w'^2) - u''w'$$

$\sin \beta \approx w'$

$\cos \beta \approx \sqrt{1-w'^2} \approx 1 - \frac{1}{2}w'^2$
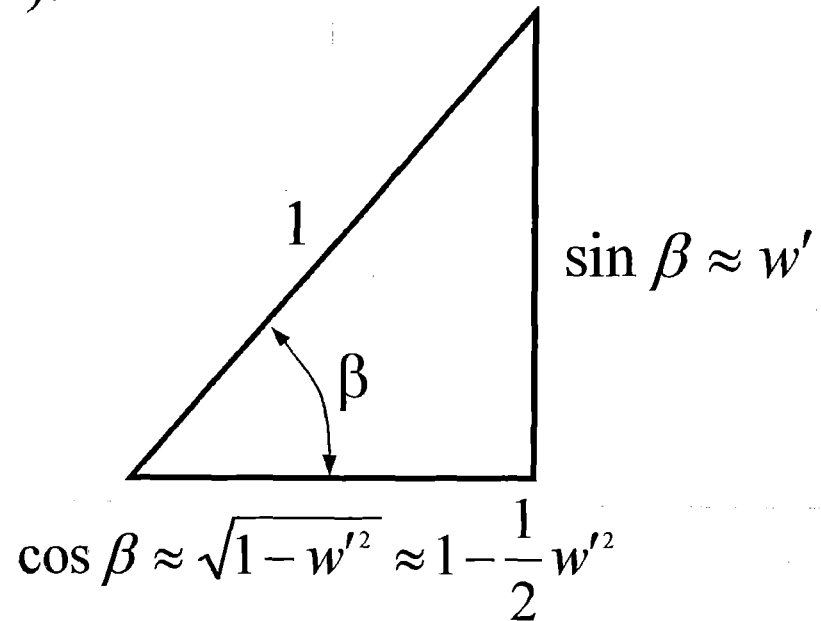
DERIVATION OF EQUATIONS

Equilibrium

Equations

•balancing forces yields the **exact equations**:

$$m\ddot{u} - \left[\frac{M'\sin\beta}{1+\varepsilon_o} + T\cos\beta \right]' = (x+u)m\Omega^2 - L(1+\varepsilon_o)\sin\beta$$

$$m\ddot{w} + \left[\frac{M'\cos\beta}{1+\varepsilon_o} - T\sin\beta \right]' = L(1+\varepsilon_o)\cos\beta$$

•using equations for T and M ($\alpha = 0$), approximations for β, ε_o, and $\bar{\kappa}$, and terms up to $O(\in^3)$, the **approximate equations** are:

$$m\ddot{u} - EA(u'' + w'w'') = (x+u)m\Omega^2 - L(w')$$

$$m\ddot{w} + EIw'''' - EA(u''w' + u'w'' + \frac{3}{2}w'^2w'') = L(1+u')$$

13

FINITE ELEMENT APPROACH

Energy and Virtual Work

$$T = \int_0^R \frac{1}{2} m \left[\dot{u}^2 + \dot{w}^2 + \Omega^2 (x+u)^2 \right] dx$$

$$V = \int_0^R \frac{1}{2} \left[EA\varepsilon_o^2 + EI\bar{\kappa}^2 \right] dx$$

$$\delta W = \int_0^R L \left[\cos\beta \, \delta w - \sin\beta \, \delta u \right] (1 + \varepsilon_o) dx$$

where: $\bar{\kappa} \approx w''(1 - u' - w'^2) - u''w'$

$\varepsilon_o \approx u' + \dfrac{1}{2} w'^2$

14

Static Equilibrium Equation

· let $u = \bar{u} + \tilde{u}$ where $\bar{u} \equiv$ static displacement

and $\tilde{u} \equiv$ small perturbation $= \displaystyle\sum_{i=1}^{n} r_i(t)\Psi_i(x)$

· let $w = \bar{w} + \tilde{w}$ where $\bar{w} \equiv$ static displacement

and $\tilde{w} \equiv$ small perturbation $= \displaystyle\sum_{i=1}^{n} q_i(t)\Phi_i(x)$

· Lagrange applied to energies and virtual work:

$$T = \frac{1}{2}\langle \dot{r}_i \quad \dot{q}_i \rangle [M] \begin{Bmatrix} r_j \\ q_j \end{Bmatrix} + \frac{1}{2}\langle r_i \quad q_j \rangle [K_{rot}] \begin{Bmatrix} r_j \\ q_j \end{Bmatrix} + \langle r_i \quad q_i \rangle \{F_{rot}\}$$

$$V = \frac{1}{2}\langle r_i \quad q_j \rangle [K_{mat}] \begin{Bmatrix} r_j \\ q_j \end{Bmatrix} + \langle r_i \quad q_i \rangle \{F_{con}\}$$

$$\delta W = \langle \delta r_i \quad \delta q_i \rangle \{F_{lift}\} + \langle \delta r_i \quad \delta q_j \rangle [K_{aero}] \begin{Bmatrix} r_j \\ q_j \end{Bmatrix}$$

15

FINITE ELEMENT APPROACH

Static Equilibrium Equation

•forming the static equilibrium equation:

$$[K_{mat} - K_{rot} - K_{aero}]\begin{Bmatrix} r_i \\ q_i \end{Bmatrix} = \{F_{lift} - F_{con} - F_{rot}\}$$

where:

K_{mat} = material stiffening

K_{rot} = rotational stiffening

K_{aero} = aerodynamic stiffening

F_{lift} = lift forces

F_{con} = conservative forces

F_{rot} = rotational forces

•using terms up to $O(\in^3)$, the static equilibrium equation is written as:

$$[K]\{\tilde{X}\} = \{F\}$$

where :

$[K]$ = stiffness matrix, $[K(\bar{u}, \bar{u}', \bar{u}'', \bar{w}, \bar{w}', \bar{w}'', \Phi, \Phi', \Phi'', \Psi, \Psi', \Psi'')]$

$\{F\}$ = load vector, $\{F(\bar{u}, \bar{u}', \bar{u}'', \bar{w}, \bar{w}', \bar{w}'', \Phi, \Phi', \Phi'', \Psi, \Psi', \Psi'')\}$

$\{\tilde{X}\}$ = nodal vector

16

Nondimensionalization

helicopter rotor blade

root ——o[   ] tip

|——→ x   x = R

|——→ ξ   ξ = 1
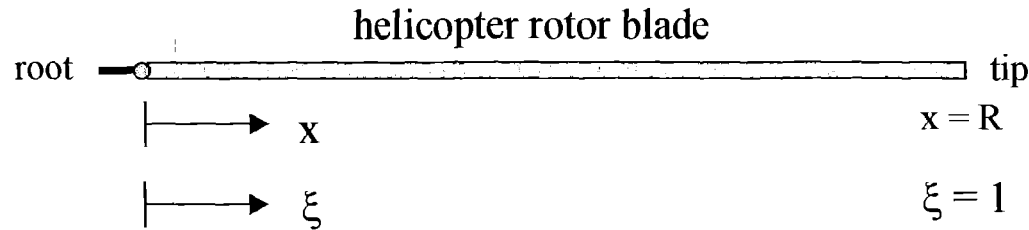
•nondimensionalize w.r.t.
blade length (underbar _):

$$\xi = \frac{x}{R} \quad \Rightarrow \quad \frac{d}{dx} = \frac{1}{R}\frac{d}{d\xi}$$

•nondimensionalize u and w
terms (and their derivatives):

$$\overline{u} = R\underline{\overline{u}} \qquad \overline{w} = R\underline{\overline{w}}$$

$$\widetilde{u} = R\underline{\widetilde{u}} \qquad \widetilde{w} = R\underline{\widetilde{w}}$$

•multiply both sides of static equilibrium equation by: $\dfrac{1}{m\Omega^2 R^2}$

$$\frac{1}{m\Omega^2 R^2}[K]\{X\} = \frac{1}{m\Omega^2 R^2}\{F\}$$

17

FINITE ELEMENT APPROACH
Discretization
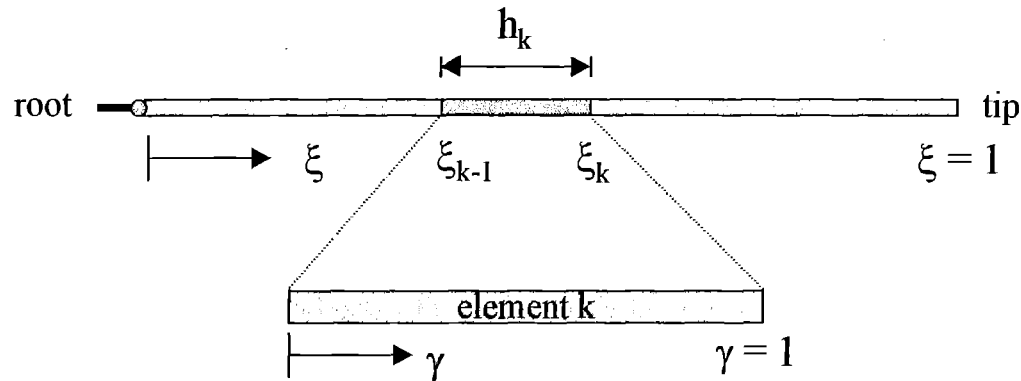
•mapping for finite element:

•derivatives:

$$\gamma = \frac{\xi - \xi_{k-1}}{\xi_k - \xi_{k-1}} = \frac{\xi - \xi_{k-1}}{h_k}$$

$$\therefore \ d\gamma = \frac{1}{h_k} d\xi$$

$$(\ )' = \frac{1}{Rh}(\ )^+$$

where:

$$(\ )'' = \frac{1}{(Rh)^2}(\ )^{++}$$

$$(\ )' = \frac{d}{dx}$$

$$(\ )^+ = \frac{d}{d\gamma}$$

18

FINITE ELEMENT APPROACH

Shape Functions

•choose Hermite cubic shape functions for both Φ and Ψ
- physical meaning for nodes (displacements and slopes at element ends)
- 2nd order differentiable (required by stiffness matrix and load
vector in both u and w directions)

$$\widetilde{u} = \sum_{i=1}^{4} r_i(t)\Psi_i(x)$$

$$\widetilde{w} = \sum_{i=1}^{4} q_i(t)\Phi_i(x)$$

19
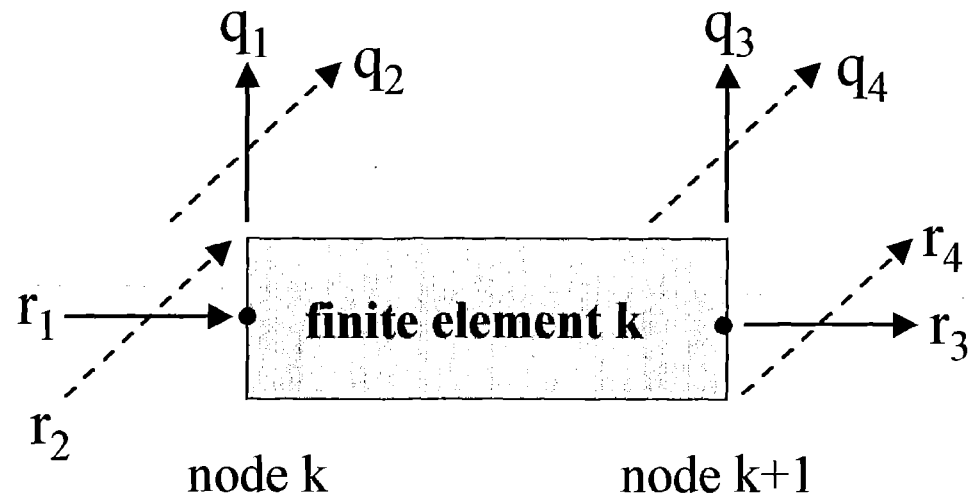
FINITE ELEMENT APPROACH

Shape Functions (continued)

$$\widetilde{u} = \sum_{i=1}^{4} r_i(t)\Psi_i(x)$$

$$\widetilde{w} = \sum_{i=1}^{4} q_i(t)\Phi_i(x)$$

finite element k

node k   node k+1

$\Phi_1 \,\&\, \Psi_1$ $\Phi_2 \,\&\, \Psi_2$ $\Phi_3 \,\&\, \Psi_3$ $\Phi_4 \,\&\, \Psi_4$

20
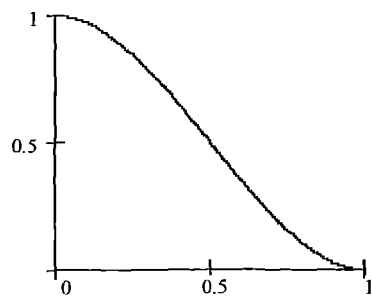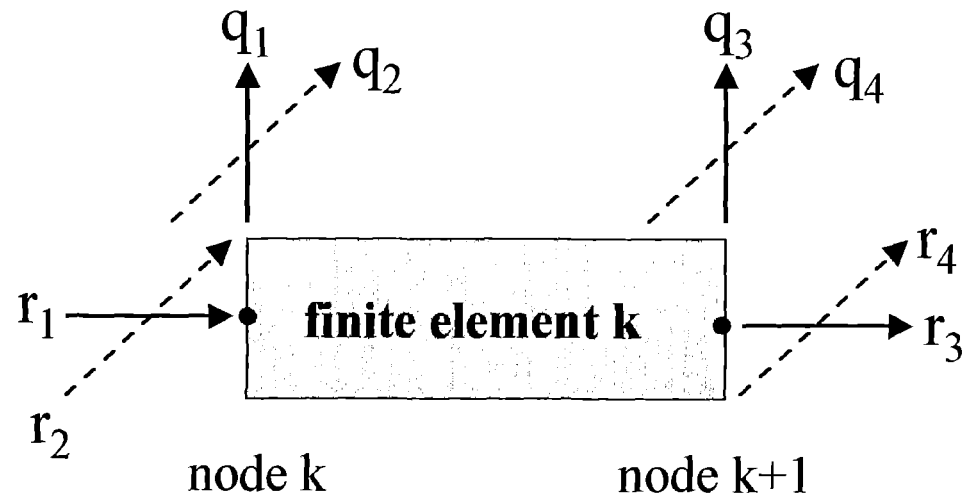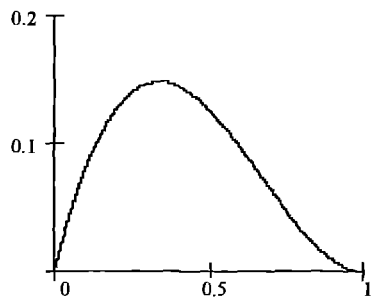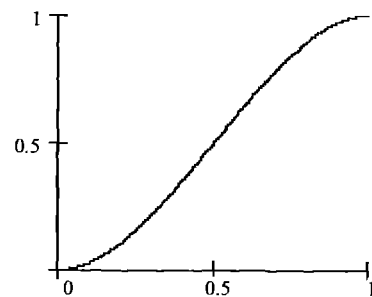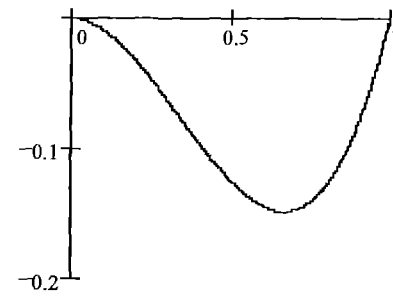
FINITE ELEMENT APPROACH

Element Stiffness Matrix $[K^{<k>}]$

$$\int_0^1 \frac{EA}{m\Omega^2 R^2}\frac{1}{h}\Psi_i^{+}\Psi_j^{+}\,d\gamma$$

$$+\int_0^1 \frac{EI}{m\Omega^2 R^4}\frac{1}{h^5}[\Psi_i^{+}\Psi_j^{+}\underline{\overline{w}}^{oo^2}+\Psi_i^{+}\Psi_j^{++}\underline{\overline{w}}^{++}\underline{\overline{w}}^{+}$$

$$+\Psi_i^{++}\Psi_j^{+}\underline{\overline{w}}^{++}\underline{\overline{w}}^{+}+\Psi_i^{++}\Psi_j^{++}\underline{\overline{w}}^{+2}]\,d\gamma$$

$$-\int_0^1 h\Psi_i\Psi_j\,d\gamma$$

$$+\int_0^1 \frac{L}{m\Omega^2 R}\frac{1}{h}\Psi_i\Psi_j^{+}\underline{\overline{w}}^{+}\,d\gamma$$

$$\int_0^1 \frac{EA}{m\Omega^2 R^2}\frac{1}{h^2}\Psi_i^{+}\Phi_j^{+}\underline{\overline{w}}^{+}\,d\gamma$$

$$-\int_0^1 \frac{EI}{m\Omega^2 R^4}\frac{1}{h^4}[\Psi_i^{+}\Phi_j^{++}(2\underline{\overline{w}}^{++})+\Psi_i^{++}\Phi_j^{+}(\underline{\overline{w}}^{++})+\Psi_i^{++}\Phi_j^{++}(\underline{\overline{w}}^{+})]\,d\gamma$$

$$+\int_0^1 \frac{L}{m\Omega^2 R}\Psi_i\Phi_j^{+}\left(1+\frac{\overline{u}^{+}}{h}+\frac{3}{2h^2}\underline{\overline{w}}^{+}\right)^2\,d\gamma$$

$$\int_0^1 \frac{EA}{m\Omega^2 R^2}\frac{1}{h^2}\Phi_i^{+}\Psi_j^{+}\underline{\overline{w}}^{+}\,d\gamma$$

$$-\int_0^1 \frac{EI}{m\Omega^2 R^4}\frac{1}{h^4}[\Phi_i^{++}\Psi_j^{+}(2\underline{\overline{w}}^{++})+\Phi_i^{+}\Psi_j^{++}(\underline{\overline{w}}^{++})+\Phi_i^{++}\Psi_j^{++}(\underline{\overline{w}}^{+})]\,d\gamma$$

$$-\int_0^1 \frac{L}{m\Omega^2 R}\Phi_i\Psi_j^{+}\left(1-\frac{1}{2h^2}\underline{\overline{w}}^{+2}\right)\,d\gamma$$

$$\int_0^1 \frac{EA}{m\Omega^2 R^2}\Phi_i^{+}\Phi_j^{+}\left(\frac{\overline{u}^{+}}{h^2}+\frac{3}{2h^3}\underline{\overline{w}}^{+2}\right)\,d\gamma$$

$$-\int_0^1 \frac{EI}{m\Omega^2 R^4}[\Phi_i^{+}\Phi_j^{+}\left(\frac{2\underline{\overline{w}}^{++2}}{h^5}\right)+\Phi_i^{+}\Phi_j^{++}\left(\frac{4\underline{\overline{w}}^{++}\underline{\overline{w}}^{+}}{h^5}+\frac{\overline{u}^{++}}{h^4}\right)$$

$$+\Phi_i^{++}\Phi_j^{+}\left(\frac{4\underline{\overline{w}}^{++}\underline{\overline{w}}^{+}}{h^5}+\frac{\overline{u}^{++}}{h^4}\right)+\Phi_i^{++}\Phi_j^{++}\left(\frac{2\overline{u}^{+}}{h^4}+\frac{2\underline{\overline{w}}^{+2}}{h^5}-\frac{1}{h^3}\right)]\,d\gamma$$

$$+\int_0^1 \frac{L}{m\Omega^2 R}\Phi_i\Phi_j^{+}\left(\frac{\underline{\overline{w}}^{+3}}{h^3}+\frac{\underline{\overline{w}}^{+}\overline{u}^{+}}{h^2}\right)\,d\gamma$$

FINITE ELEMENT APPROACH

Element Load Vector $\{F^{<k>}\}$

$$-\int_0^1 \frac{L}{m\Omega^2 R} \Psi_i [\overline{\underline{w}}^+ \left(1 + \frac{\overline{\underline{u}}^+}{h} + \frac{\overline{\underline{w}}^{+^2}}{2h^2}\right)] d\gamma$$

$$+\int_0^1 \Psi_i h(\xi + \overline{\underline{u}}) d\gamma$$

$$-\int_0^1 \frac{1}{2} \frac{EA}{m\Omega^2 R^2} \Psi_i^+ \left(\frac{\overline{\underline{w}}^{+^2}}{h^2} + \frac{2\overline{\underline{u}}^+}{h}\right) d\gamma$$

$$-\int_0^1 \frac{1}{2} \frac{EI}{m\Omega^2 R^4} [\Psi_i^+ \left(\frac{2\overline{\underline{w}}^{++^2}}{h^4}\right) + \Psi_i^{++} \left(\frac{2\overline{\underline{w}}^{++} \overline{\underline{w}}^+}{h^4}\right)] d\gamma$$

$$+\int_0^1 \frac{L}{m\Omega^2 R} \Phi_i (h + \overline{\underline{u}}^+) d\gamma$$

$$-\int_0^1 \frac{1}{2} \frac{EA}{m\Omega^2 R^2} \left(\frac{2\overline{\underline{u}}^+ \overline{\underline{w}}^+}{h^2} + \frac{\overline{\underline{w}}^{+^3}}{h^3}\right) d\gamma$$

$$-\int_0^1 \frac{1}{2} \frac{EI}{m\Omega^2 R^4} \Phi_i^+ \left(\frac{2\overline{\underline{w}}^{++}}{h^3}\right) d\gamma$$

22

Finite Element Meshes

1) fixed length
2) tip variable
3) tip and root variable
4) quadratic
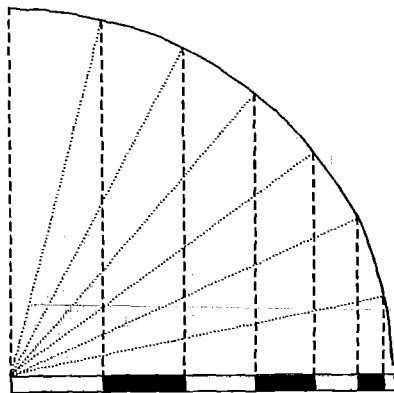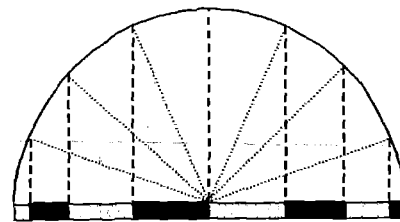
tip variable   tip and root variable   quadratic

rotor blade

root   tip

23
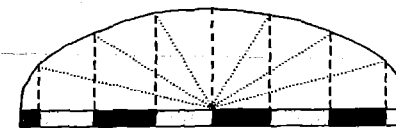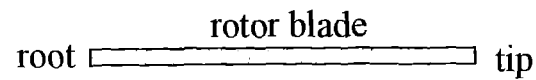
FINITE ELEMENT APPROACH
Solution Methods

1) [K]⁻¹{F} Method

iterate :

$$[K]^{-1}\{F\} = \{\tilde{X}\} \quad \Rightarrow \quad \tilde{u} \text{ and } \tilde{w}$$

$$\overline{u}_{new} = \overline{u}_{old} + \tilde{u}$$

$$\overline{w}_{new} = \overline{w}_{old} + \tilde{w}$$

until convergence of $\overline{u}$ and $\overline{w}$

2) Secant Method

use method on a system of equations

for a single function (1 DOF) :

$$x_{n+1} = x_n - f(x_n)\frac{x_n - x_{n-1}}{f(x_n) - f(x_{n-1})}$$

where $f(x) = Kx - F$

24
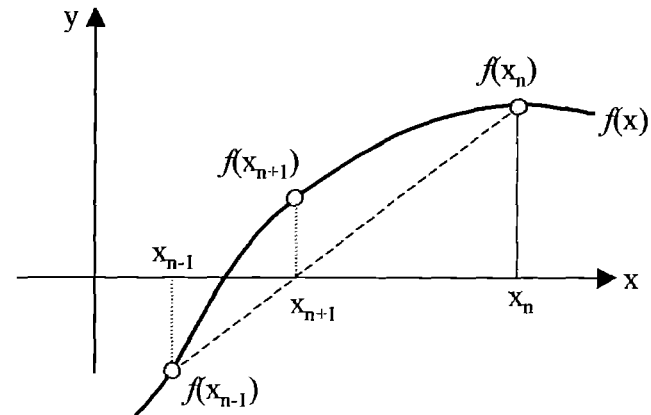
Solution Methods (continued)

1) [K]⁻¹{F} METHOD

$$\{\overline{X}\}_n = \{0\}$$

$$\therefore \quad \underline{\overline{u}}_n = \underline{\overline{u}}_n^+ = \underline{\overline{u}}_n^{++} = \underline{\overline{w}}_n = \underline{\overline{w}}_n^+ = \underline{\overline{w}}_n^{++} = 0$$

where **n = 1** (iteration #1)

initial guess

$$\{\overline{X}\}_n \;\Rightarrow\; \underline{\overline{u}}_n \; \underline{\overline{u}}_n^+ \; \underline{\overline{u}}_n^{++} \; \underline{\overline{w}}_n \; \underline{\overline{w}}_n^+ \; \underline{\overline{w}}_n^{++} \;\Rightarrow\; \text{compute}: \; [K]_n \text{ and } \{F\}_n$$

advance iteration index: $\quad n = n+1$

$$\therefore \quad \{\overline{X}\}_{n+1} \Rightarrow \{\overline{X}\}_n$$

$$\{\tilde{X}\}_n = [K]_n^{-1}\{F\}_n$$

$$\{\tilde{X}\}_n \;\Rightarrow\; \text{compute}: \; \underline{\tilde{u}}_n \quad \underline{\tilde{w}}_n$$

do the same for $()^+$ and $()^{++}$

$$\{\overline{X}\}_{n+1} = \{\tilde{X}\}_n + \{\overline{X}\}_n$$

no

compute:

$$\underline{\overline{u}}_{n+1} = \underline{\overline{u}}_n + \underline{\tilde{u}}_n$$

$$\underline{\overline{w}}_{n+1} = \underline{\overline{w}}_n + \underline{\tilde{w}}_n$$

do the same for $()^+$ and $()^{++}$

end iteration process

yes

$$\left| \underline{\overline{u}}_{n+1} - \underline{\overline{u}}_n \right| \leq tol\,?$$

$$\left| \underline{\overline{w}}_{n+1} - \underline{\overline{w}}_n \right| \leq tol\,?$$

$$tol = \epsilon^4$$

25

FINITE ELEMENT APPROACH

Solution Methods (continued)

$$2)\ \text{SECANT METHOD}$$

$$\{\overline{X}\}_n = \{0\}$$

$$\therefore\ \underline{\overline{u}}_n = \underline{\overline{u}}_n^+ = \underline{\overline{u}}_n^{++} = \overline{w}_n = \overline{w}_n^+ = \overline{w}_n^{++} = 0$$

where **n = 1** (iteration #1)

initial guess

$$\{\overline{X}\}_n\ \Rightarrow\ \overline{u}_n\ \overline{u}_n^+\ \overline{u}_n^{++}\ \overline{w}_n\ \overline{w}_n^+\ \overline{w}_n^{++}\ \Rightarrow\ \text{compute}:\ [K]_n\ \text{and}\ \{F\}_n$$

advance iteration index: $\quad n = n+1$

$$\therefore\ \{\overline{X}\}_{n+1}\ \Rightarrow\ \{\overline{X}\}_n$$

$$\{\overline{X}\}_{n+1} = \{\overline{X}\}_n - \eta \left[\frac{\partial f_j}{\partial \overline{X}_i}\right]_n^{-1} \{f_j\}_n$$

where: $\quad f_j = \sum_k K_{j,k}\overline{X}_k - F_j$

$$\frac{\partial f_j}{\partial \overline{X}_i} = \sum_k \frac{\partial K_{j,k}}{\partial \overline{X}_i}\overline{X}_k + K_{j,i} - \frac{\partial F_j}{\partial \overline{X}_i}$$

no

end
iteration
process

yes

$$\left|\underline{\overline{u}}_{n+1} - \underline{\overline{u}}_n\right| \leq tol\,?$$

$$\left|\overline{w}_{n+1} - \overline{w}_n\right| \leq tol\,?$$

$$tol = \epsilon^4$$

$$\{\overline{X}\}_{n+1}\ \Rightarrow\ \text{compute}:\ \underline{\overline{u}}_{n+1}\quad \overline{w}_{n+1}$$

do the same for ( )$^+$ and ( )$^{++}$

26
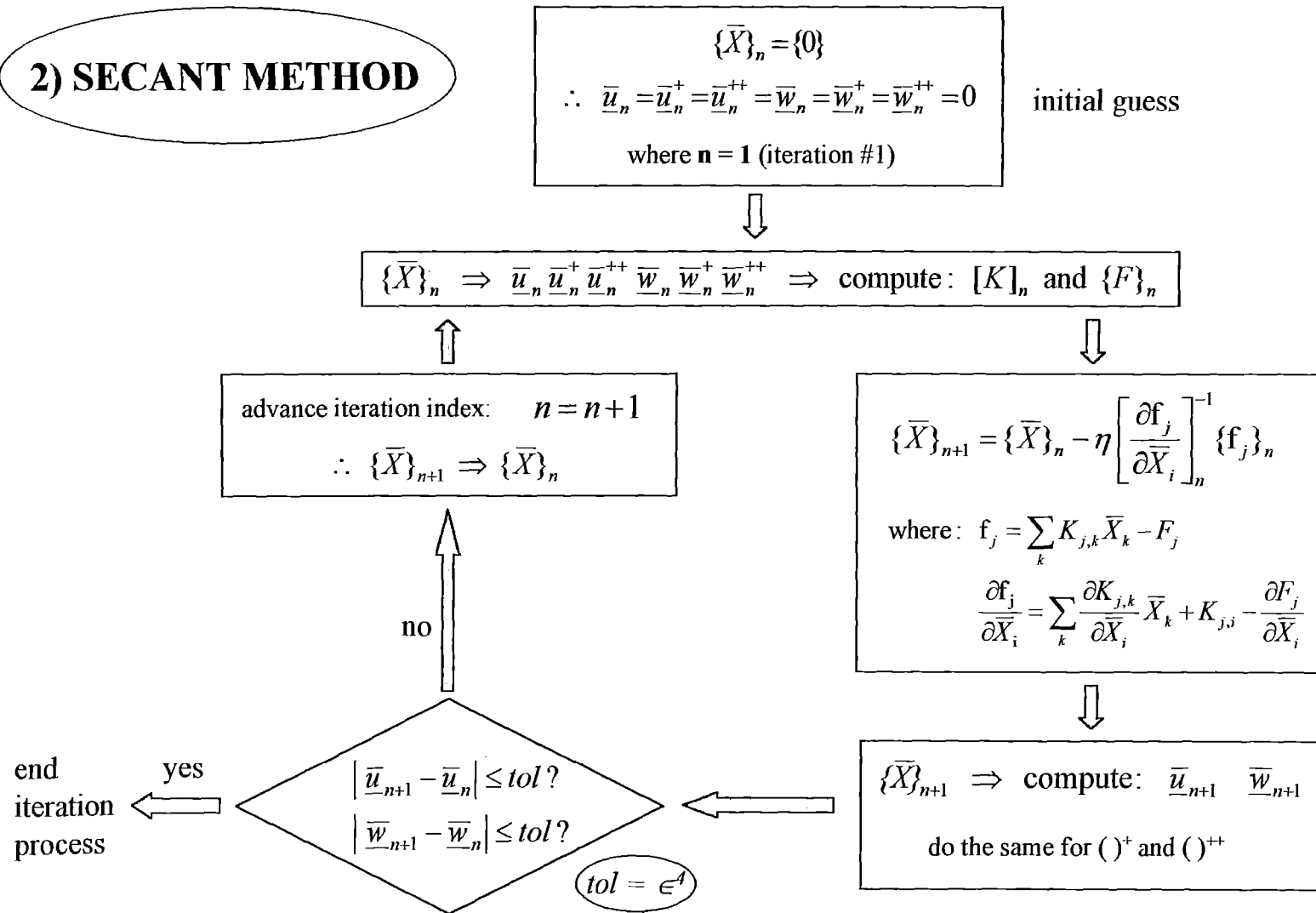
NUMERICAL RESULTS

Model Parameters

MBB helicopter rotor blade

$\Omega = 45$ rad/sec

R = 200 in

A = 2 in^2

m = 0.3 lb/in

EA = 1 x 10^7 lb

EI = 5 x 10^6 lb-in^2

c = 11 in

nondimensional parameters

$$\frac{EA}{m\Omega^2 R^2} = 1.5 \times 10^2$$

$$\frac{EI}{m\Omega^2 R^4} = 1.8 \times 10^{-3}$$

$$\frac{L}{m\Omega^2 R} = \left(\frac{x}{R}\right)\beta_o$$

where $\beta_o = 0.052356$

27

NUMERICAL RESULTS
First Iteration - W vs. Blade Length

FE Data Plotted With Approx. D.E. Solution - **ZERO INITIAL CONDITIONS**
MBB Helicopter / Hingeless Blade / 5 Fixed FE / [K]⁻¹{F} Method
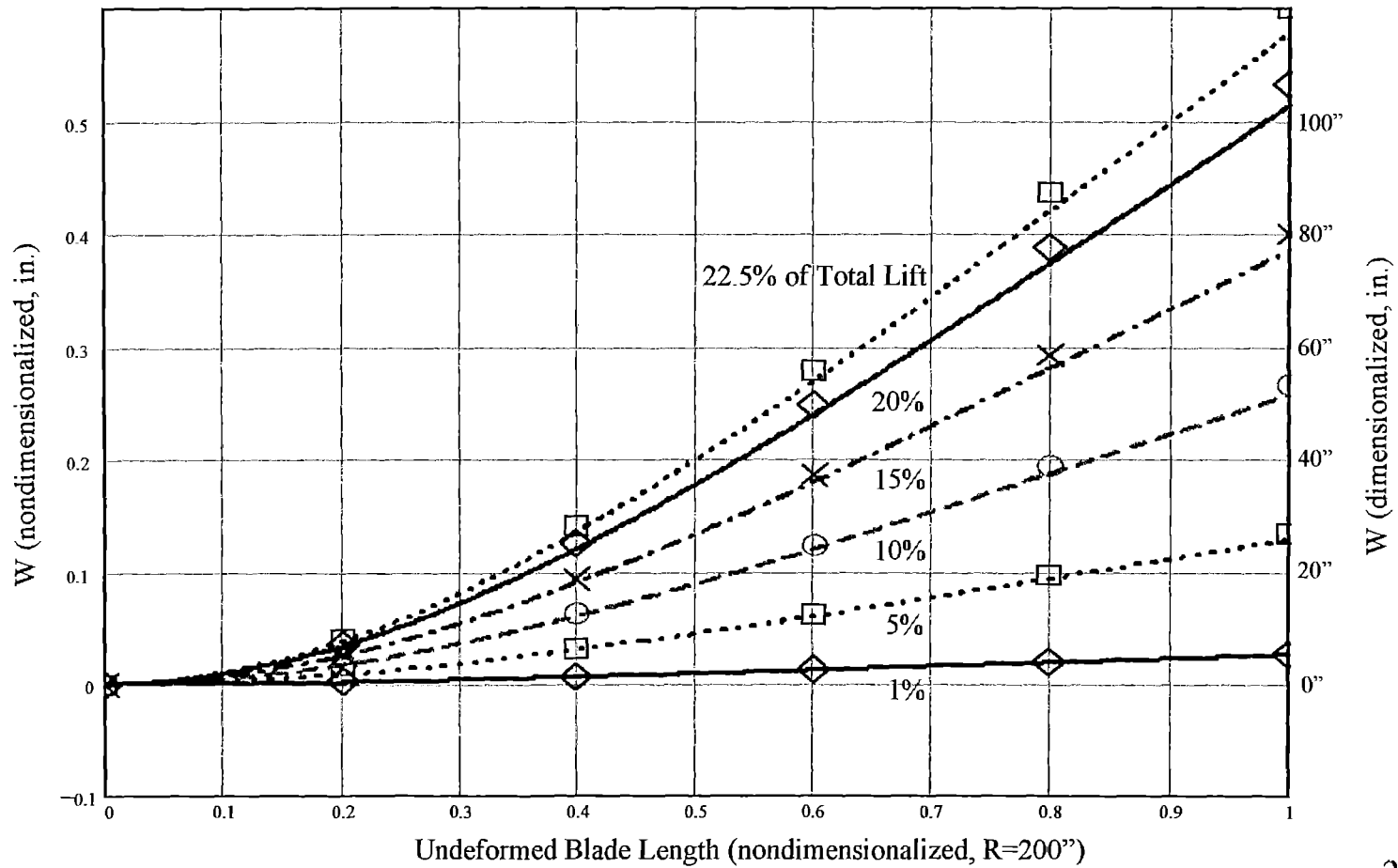
NUMERICAL RESULTS
Convergence Wall & Refined Method

•convergence obtained for lift values up to 22.5% of total using $[K]^{-1}\{F\}$ method (number of elements and/or mesh size has no effect on convergence)

   –zero value initial guesses for u and w (and their derivatives) cause the w-direction result of the first iteration to be up to 50 times larger than the last iteration (converged solution)

   –poor results from the first iteration cause divergence when seeking greater than 22.5% lift

•**good initial guesses for u, u´, and u´´ are key!**

•refined $[K]^{-1}\{F\}$ method: 1) get 0% lift solution 2) use 0% lift solution as initial guess for seeking 100% lift solution; results for the MBB/hingeless case are:

| START | $\rightarrow$ | 0% lift (2 iterations) | $\rightarrow$ | 100% lift (3 iterations) | $\rightarrow$ | CONVERGENCE |

29
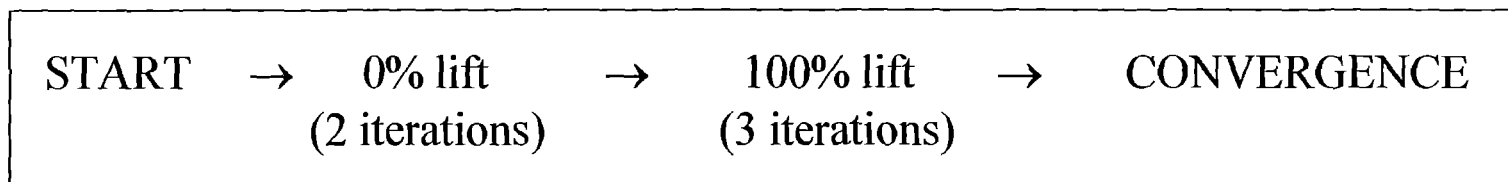
NUMERICAL RESULTS
U vs. Blade Length

MBB Helicopter / Hingeless Blade / 5 Fixed FE / Refined inv[K]{F} Method
Final Iteration (convergence)
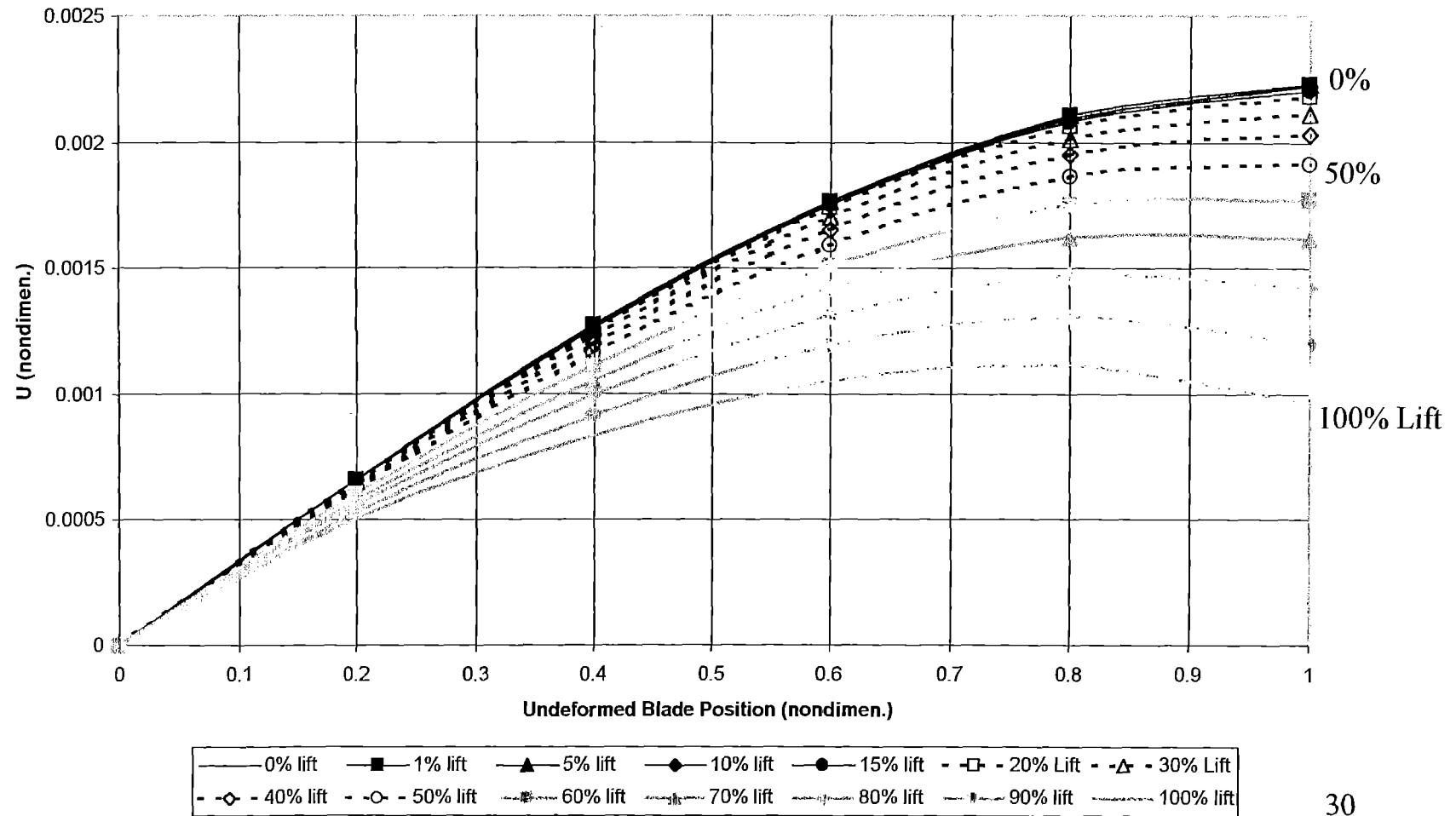
NUMERICAL RESULTS

W vs. Blade Length

MBB Helicopter / Hingeless Blade / 5 Fixed FE / Refined inv[K]{F} Method
Final Iteration (convergence)

31
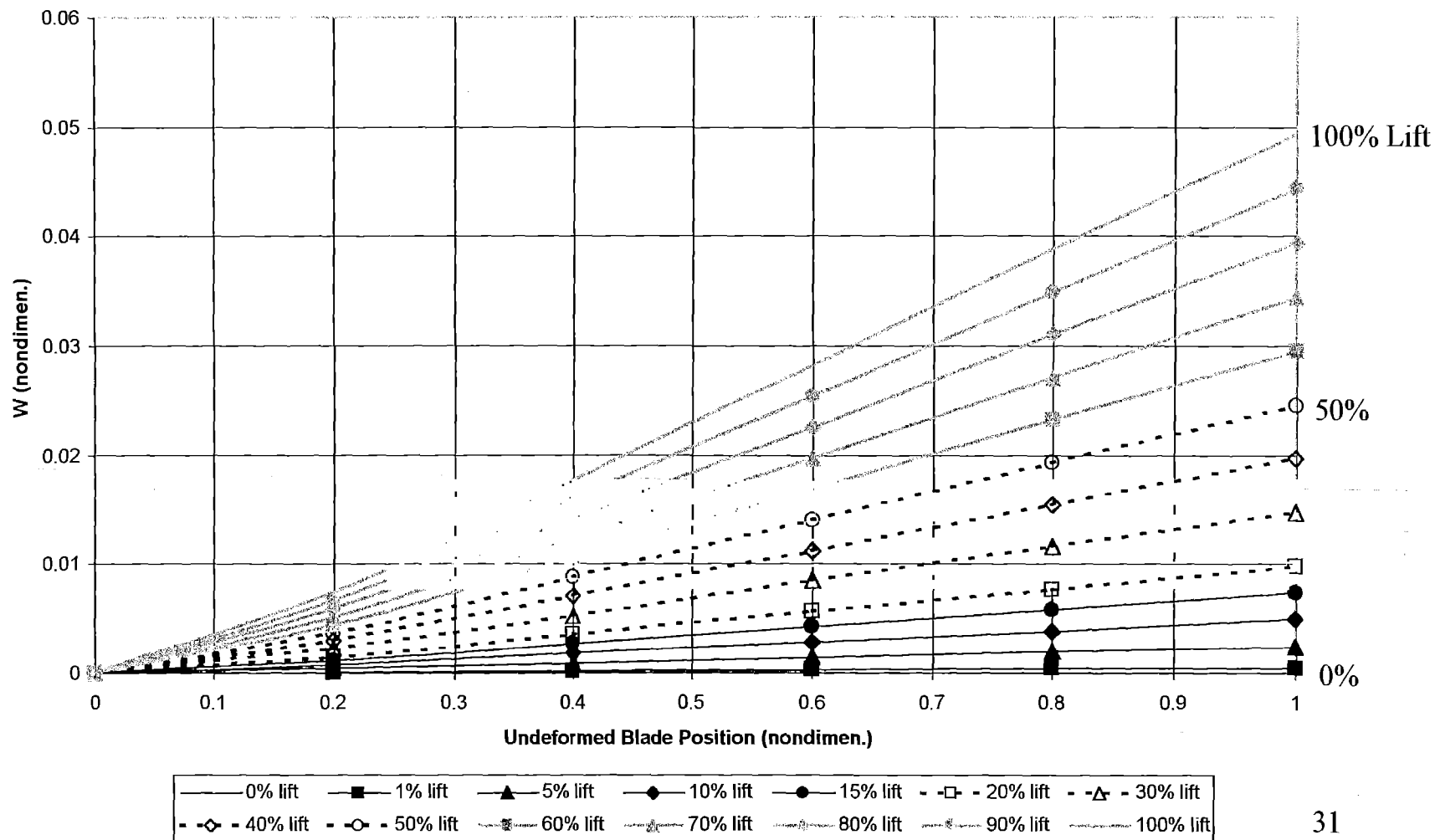
CONCLUSIONS

1) $[K]^{-1}\{F\}$ METHOD:

- convergence obtained using lift up to 22.5% of total (with zero initial guess for all w's and u's)

- modify method: use results from 0% lift program run as the initial guess for program runs with lift >20% (convergence in 5 iterations for 100% lift)

- mesh-size refinement does not reduce the number of iterations needed for convergence

- increasing the number of elements does not reduce the number of iterations needed for convergence; it does, however, increase the computation time (minimum # of elements needed is one)

2) SECANT METHOD: does not converge for any percentage of lift

32

ENERGY PRESERVING/DECAYING SCHEMES FOR NON-LINEAR ELASTIC MULTIBODY SYSTEMS

M. BORRI, C.L. BOTTASSO, AND L. TRAINELLI

Dipartimento di Ingegneria Aerospaziale, Politecnico di Milano, Milano, Italy.

1. INTEGRATING ON MANIFOLDS WHILE PRESERVING INVARIANTS

In this work, we are concerned with the time integration of non-linear flexible multibody systems. In general, the term multibody assumes slightly different meanings in the context of different applications and in the use of different scientific communities. For our purposes, we define a multibody as a *Finite Element Model*, where the elements idealize rigid bodies, mechanical constraints, beams, shells etc. We are interested in systems with *complex topologies*, where each body undergoes *large displacements* and *rotations* (but only small strains). Clearly, the definition of a multibody given, for example, by a control engineer interested in real-time robotic simulations could be significantly different. The typical applications that we have in mind deal with the modeling of *helicopters* (complete vehicle, rotors, transmissions), but are clearly not limited to these.

The dynamical systems that are the object of our study are governed by equations of motion that are *stiff* in nature. There is a very rich literature on the integration of stiff ODE's and of DAE's, so rich that we will not even attempt to review it, but simply refer the reader to comprehensive works on this subject, as for example [4, 6].

Papers on multibody formulations are produced at a phenomenal rate, as a quick look at some of the major computational mechanics journals will prove. The usual approach for developing a new code is typically based on *(i)* deriving the equations of motion, *(ii)* applying some known integrator with suitable (usually only linear) properties to the numerical discretization of the equations in the temporal domain. In general, the integrator knows little about the actual structure of the equations being solved. In particular, it seldom knows at all that it is dealing with the proper rotation group SO(3) (the real heart and soul of anything that has to do with rigid bodies, beams and shells).

As the literature clearly shows, this approach works quite well in the majority of the situations. However, there are a few cases when conventional integrators will badly fail. If our original goal was the development of a *robust general purpose* piece of software, then we are in trouble, since we know that sooner or later our code will crash (to the dismay of the poor user that knows nothing about non-linear stability).

A simple but nasty example (not even a multibody) was given by Simo et al. in Ref. [8]. Simo and his collaborators showed that an apparently harmless simulation

---

of a beam in free flight can crash the midpoint rule, the trapezoidal rule and a fourth-order Runge-Kutta scheme (and probably any scheme not associated with non-linear conservation laws).
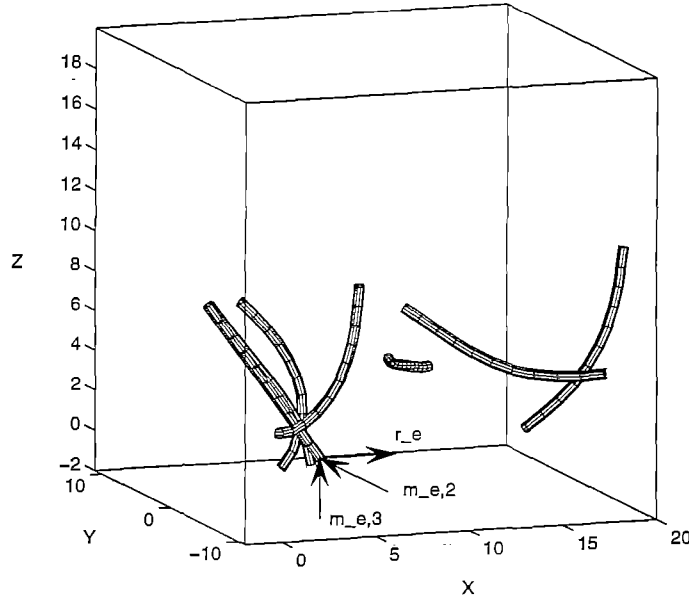
FIGURE 1. The dynamic simulation of a beam in free flight.

In our search for robustness, we could at this point turn to other integrators, until we find one that does not crash for the particular problem in question. But will this approach solve the problem once for all? Clearly not.

A possible solution, and a nice solution indeed, is to reverse the development process. Once we have realized that the equations of motion that we are dealing with have a special structure, we can design specific algorithms (rather than using generic schemes) that "understand" the equations they are integrating. This "understanding" is then exploited for designing schemes that ensure the exact algorithmic conservation of important invariants of the solution (typically the energy, which is associated with the concept of non-linear unconditional stability).

This idea was applied with success to rigid bodies [9], shells [7], beams [8], and finally multibodies [1]. But the success was probably due to the fact that only relatively simple, nice and smooth examples were tried in those papers. In fact, it is very well known that one usually needs some form of numerical dissipation for preventing energy transfers from the lower modes of a discretized elastic system to the higher (usually meaningless) modes. It is clear that an energy preserving scheme can not have any such dissipation mechanism.

Depending on the problem, the performance of an energy preserving scheme will therefore range from excellent to unacceptable. If higher modes of the system are excited during the simulation, the numerical response will be affected by high frequency oscillations. This numerical "noise" could in principle be filtered in a post-processing phase. But, when the state of the system contributes to the

determination of the forces acting on it (read always, in practice, for realistic problems, eg. the aerodynamic loads), this noise will bring the system on the wrong trajectory.

But not only can we get the wrong solution, we can even get no solution at all! We do not need complex examples to show this. Consider in fact the swing depicted in Figure 2, first discussed in [2].
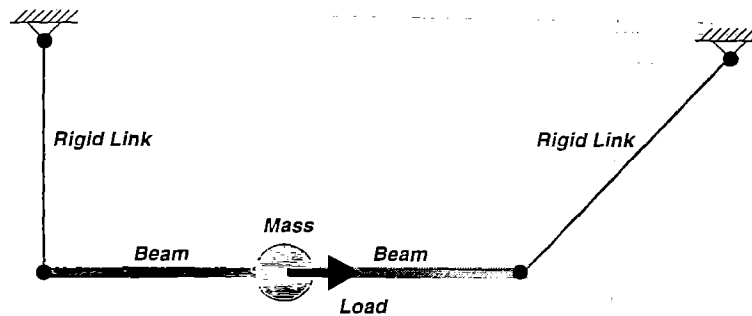
FIGURE 2. The swing problem, that easily crashes energy preserving schemes.

The trajectories of five points on the swing are plotted in Figures 3,4. The first plot shows the results obtained using four spatial elements. After the lining up of the left link and the beam, the motion becomes highly oscillatory until the program crashes (failure to converge during the Newton process). Things become even worse refining the mesh. Figure 4 shows the trajectories of the same points computed using a spatial discretization of eight elements. The program crashes earlier in the simulation in this case. The reason is clear: a finer discretization means a greater number of degrees of freedom, which results in higher frequency components being excited.

To understand the reason of this failure, we can simply take a qualitative look at the time histories of some quantities, for example the axial stress in Figure 5 and the horizontal velocity in Figure 6. The oscillatory behavior of the response hinders the convergence process and causes the computation to blow up, even if the average (filtered) values of the responses have a nice and smooth behavior.

So, how can we control the high frequency content of the system being integrated, and at the same time have a non-linearly unconditionally stable process? A possible solution is to design schemes (again, building on the "understanding" by the algorithms of the equations being integrated) that are associated with an energy decay inequality. We essentially require the energy of the system at the end of an integration step to be equal to the energy at the beginning of the step plus a small dissipated (negative) energy. This idea was first pursued in [2] and [3].

Apart from this "reversed" design process, our approach differs from the usual practice in another important aspect. The classical approach for dealing with mechanical problems with rotations derives first the equations of motion, and then, referring the equations at the center of mass, decouples them into purely rotational and purely translational parts. In reality, while this is always possible when dealing with one single rigid body, the same practice is usually not possible or not convenient in the analysis of beams and shells. Moreover, by decoupling the problem, one misses completely the *intimate structure* of the complete equations.

Trajectories of the beam nodes A,B,C,D,E – EP (4 elements)
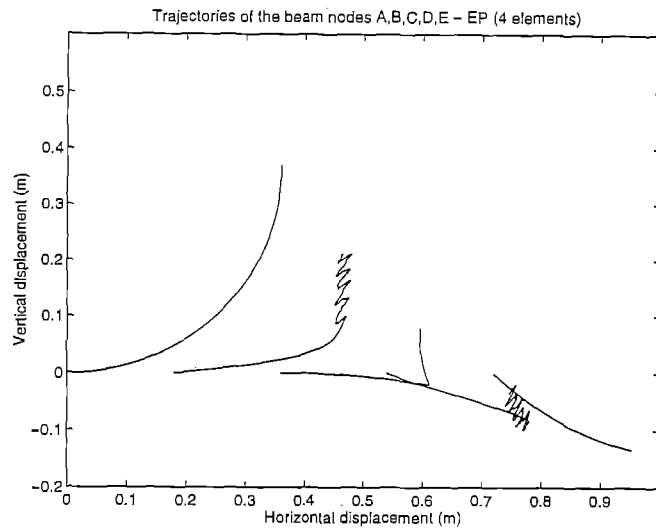
FIGURE 3. Energy preserving integration, four spatial elements.

Trajectories of the beam nodes A,B,C,D,E – EP (8 elements)
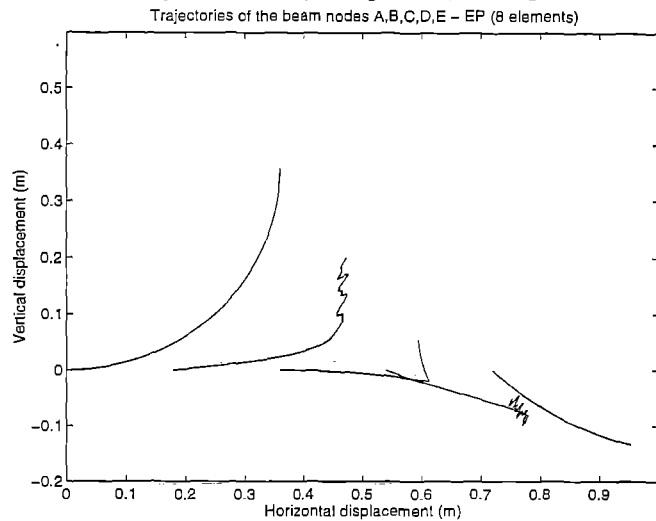
FIGURE 4. Energy preserving integration, eight spatial elements.

In this work we attack the problem in a slightly different way. We write the equations of motion at a *fixed pole* (rather than a moving pole, as usually done in mechanics). We argue that these, rather than the equations of pure rotational dynamics in SO(3), are the true prototype equations for mechanical systems involving rotations. This way, we are able to generalize the concepts of vector, orientation tensor and cross product to a six-dimensional space. The resulting configuration space is here termed SR(6). As for the reduced problem of pure rotation, two "points" in this extended space are related by an *exponential map*, that can be
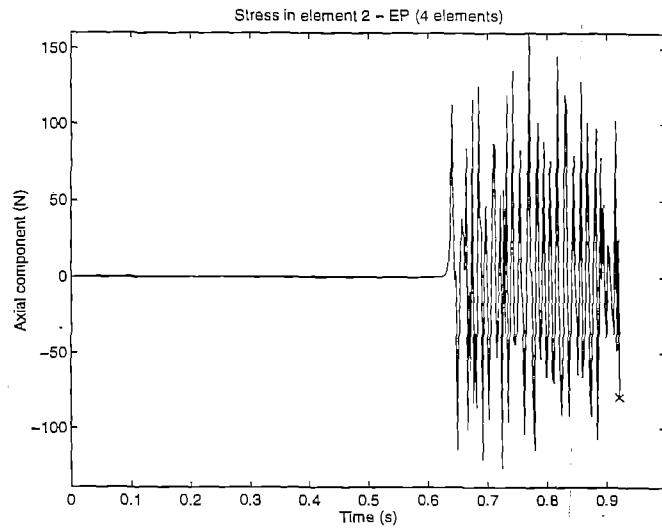
FIGURE 5. Energy preserving integration, time history of the axial stress.
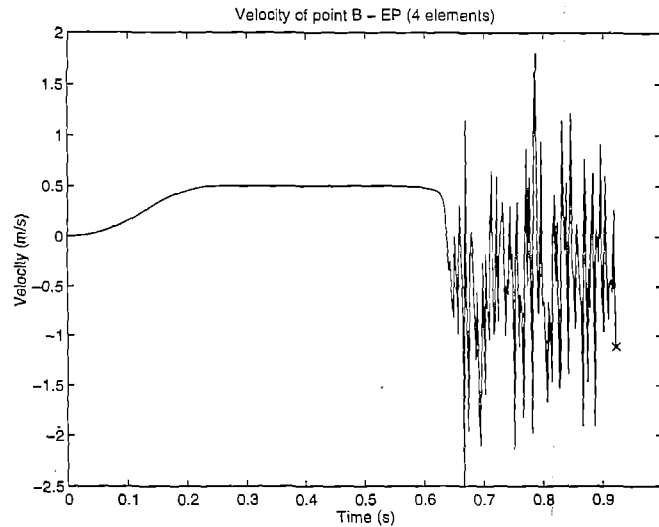
FIGURE 6. Energy preserving integration, time history of the horizontal velocity.

expressed in finite form thanks to some recursive properties of the generalized cross product. This is the starting point for our algorithmic developments.

For obtaining numerical approximations of the equations of evolution, we consider the vast class of Runge-Kutta (RK) methods. There is great wealth of theoretical as well as practical (implementational) knowledge concerning these methods. In fact, RK schemes provide a powerful framework for deriving effective algorithms for stiff and non-stiff problems. Classical references on the subject are [4, 5, 6].

Our first goal is that of deriving integrators that, by design, *remain on the manifold.* We accomplish this result by modifying the basic RK scheme so as to accommodate configuration updates performed via the exponential map. This way, we obtain modified RK methods that, for any choice of the tableau, can be shown to guarantee the conservation of *total momentum* in the absence of external loading. This methodology defines a procedure for integrating the equations of motion using standard RK tableaux, and at the same time *(i)* preserving the structure of the differential manifold, *(ii)* and preserving an important invariant of motion.

Generalizing our previous work [3], we show that our modified RK format accommodates as special cases both the energy preserving and the energy decaying schemes. This gives us a unified framework for dealing with the integration of structural equations defined on non-linear differential manifolds. Under the same umbrella, we can use standard RK tableaux of any order for the integration of "well behaved" problems. However, we also have the option to switch to energy preserving or energy decaying versions of the integration procedure in case of more difficult situations, or whenever non-linear conservation laws become necessary.

This algorithmic framework opens the way to automated adaptive procedures, where suitable error indicators drive the selection process of the time step size h, of the order of accuracy p, *and of the method* (tableau in this case), in order to ensure efficiency and reliability of the computation. We leave the design of such an error indicator an open question, for now.

2. NUMERICAL RESULTS

2.1. Three-dimensional Beams. The first example that we propose deals with the free flight of a three-dimensional beam. Figure 7 shows the overall motion of the beam in the first seconds of simulation, with deformed shapes sketched at intervals of one second.
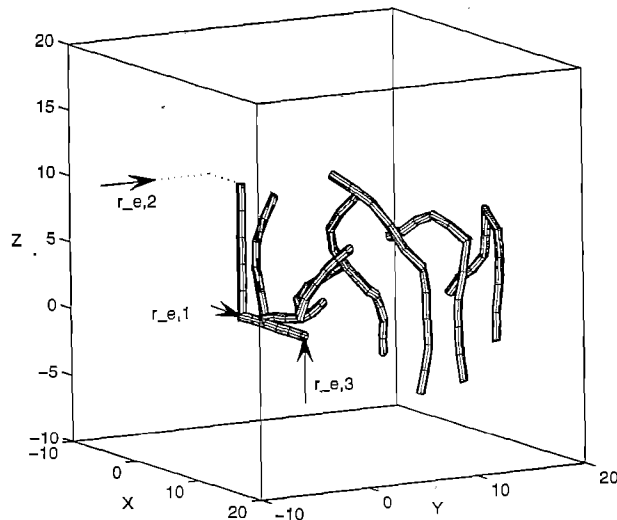
FIGURE 7. The right angle beam in free flight.

Figure 8 shows the time histories of the total and normalized mechanical energies of the systems obtained with the energy decaying scheme. The first plot shows that the energy is essentially constant during the free flight of the beam. However, the second plot proves what predicted by the analysis: at each step a small amount of energy is dissipated, making the energy strictly decaying.
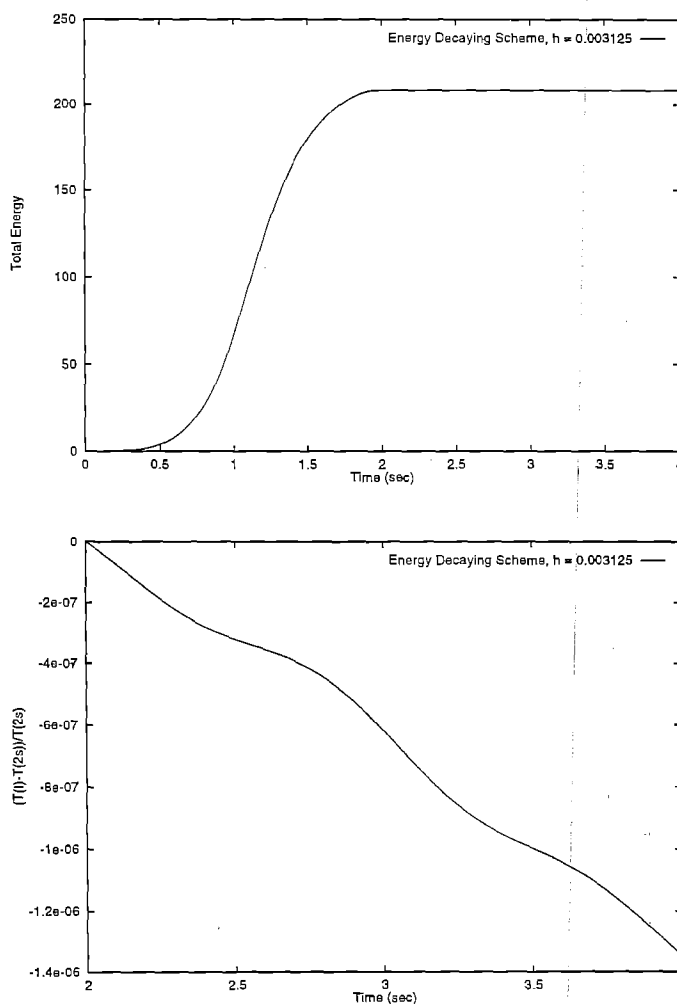
FIGURE 8. Mechanical energy for the right angle beam in free flight. Top: total energy; bottom: normalized energy.

A second example sheds some light on the energy dissipation mechanism. We consider a beam hinged at the root, shown in Figure 9. The beam is initially at rest and is loaded at the tip with a short triangular pulse in time. The conservative integration give rise to high frequency oscillations which are "filtered" in the dissipative case. This is clearly shown in Figure 10, where we show the result of a Fourier analysis conducted on the computed axial force at the beam root.

M. BORRI, C.L. BOTTASSO, AND L. TRAINELLI
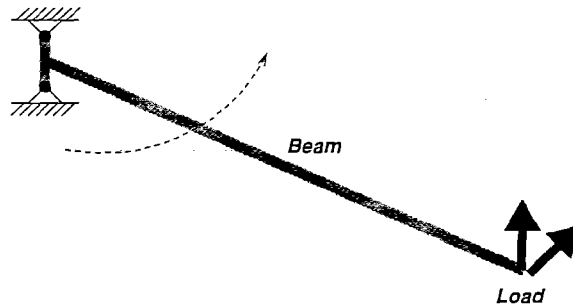
FIGURE 9. The hinged beam.
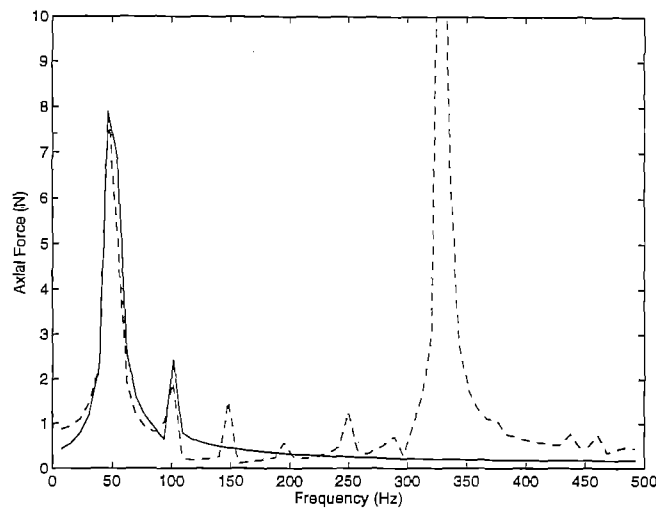
FIGURE 10. Frequency content of the axial stress resultant for the hinged beam.

2.2. **Flexible Multibody Systems.** We conclude this brief description of our work, by going back to the swing problem of the Introduction. In Figures 11,12 we present the time histories of the horizontal velocity and axial stress at two points on the beam, computed with both the energy preserving and decaying schemes. The ability of the latter scheme to get rid of the oscillatory components of the solution, even in this dramatic case, is particularly striking.

3. CONCLUSIONS AND FUTURE DEVELOPMENTS

We have developed a family of RK integrators that, *by design*, remain on the manifold and are momentum preserving. This was obtained with a sort of "reversed" development process, that ensures that the algorithms "understand" the problem being solved and its structure. This family of methods include, as special cases, *Energy Preserving* and *Energy Decaying* schemes. These methods has been extended to deal with *constraints*, both of the holonomic and non-holonomic types.

Stress in element 2 – EP vs ED (4 elements)
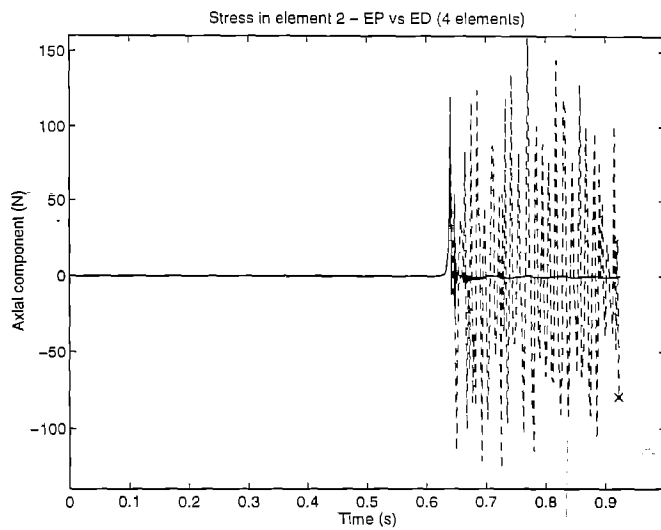
FIGURE 11. Energy preserving and decaying integrations, time history of the axial stress.

Velocity of point B – EP vs ED (4 elements)
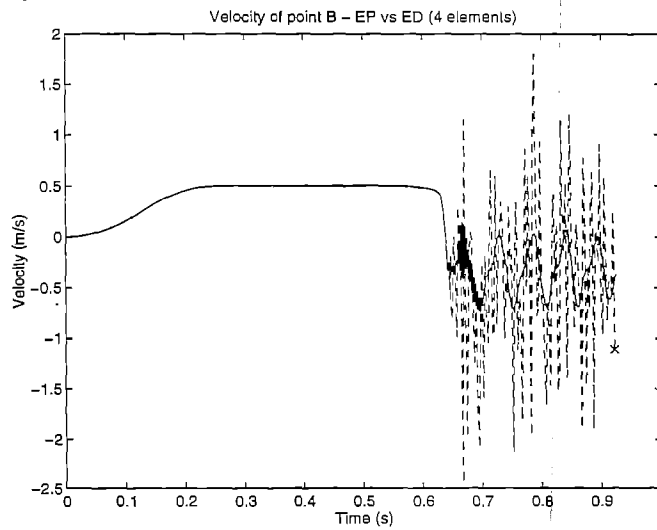
FIGURE 12. Energy preserving and decaying integrations, time history of the horizontal velocity.

We therefore have a *general framework* for modeling mechanical systems composed of rigid bodies, beams and shells.

Our next developments will try to address realistic applications of engineering interest (eg. helicopter rotors and transmissions), and we will start working on error indication techniques as a first step towards including automated adaptive capabilities in our code.

REFERENCES

[1] O.A. Bauchau, G. Damilano and N.J. Theron, Numerical integration of nonlinear elastic multibody systems, *Int. J. Numer. Methods Engrg.* **38** (1995) 2727–2751.

[2] O.A. Bauchau and N.J. Theron, Energy decaying scheme for nonlinear elastic multibody systems, *Comput. & Struct.* **59** (1996) 317–331.

[3] C.L. Bottasso and M. Borri, Energy preserving/decaying schemes for non-linear beam dynamics using the helicoidal approximation, *Comput. Methods Appl. Mech. Engrg.* **143** (1997) 393–415.

[4] J.C. Butcher, *The Numerical Analysis of Ordinary Differential Equations. Runge-Kutta and General Linear Methods* (John Wiley & Sons Ltd., 1987).

[5] E. Hairer, S.P. Nørsett and G. Wanner, *Solving Ordinary Differential Equations I. Nonstiff Problems* (Springer-Verlag, 1987).

[6] E. Hairer and G. Wanner, *Solving Ordinary Differential Equations II. Stiff and Differential-Algebraic Problems* (Springer-Verlag, 1991).

[7] J.C. Simo and N. Tarnow, A new energy and momentum conserving algorithm for the nonlinear dynamics of shells, *Int. J. Numer. Methods Engrg.* **37** (1994) 2527–2549.

[8] J.C. Simo, N. Tarnow and M. Doblare, Non-linear dynamics of three-dimensional rods: exact energy and momentum conserving algorithms, *Int. J. Numer. Methods Engrg.* **38** (1995) 1431–1473.

[9] J.C. Simo and K.K. Wong, Unconditionally stable algorithms for rigid body dynamics that exactly preserve energy and momentum, *Int. J. Numer. Methods Engrg.* **31** (1991) 19–52.

RECENT DEVELOPMENTS IN THE ANALYSIS AND EXPERIMENTAL TESTING FOR TRANSIENT ROTOR ENGAGE AND DISENGAGE OPERATIONS

Jonathan A. Keller
Graduate Research Asst.

Edward C. Smith
Assistant Professor

Hao Kang
Visiting Scholar

Department of Aerospace Engineering
The Pennsylvania State University, University Park, PA 16802

This paper presents the recent developments in the analysis and experimental testing for transient rotor engage and disengage operations, which includes:

1. Experimental and Theoretical Analysis of Helicopter Rotor Blade-Droop Stop Impacts
A theoretical an experimental study of the transient response of an articulated rotor blade experiencing a droop stop impact was conducted. During a rotor blade and droop stop impact, the boundary conditions of the blade change from a hinged to a cantilevered condition. Refinements in the transient response algorithm at the moment of impact are presented and are shown to improve the correlation with experimentally measured transient response results. Material damping in the model beam was measured by hammer impact tests. The measured material damping is used in the analysis and also shown to result in improved correlation with the experimentally measured transient response results.

2. Transient Analysis for Engage and Disengage Operations of Gimballed Tiltrotors
A transient response analysis for gimballed tiltrotors undergoing engage and disengage operations is developed. Initially, a two degree of freedom rigid blade analysis was formulated. Using this simple analysis, simulations of the gimballed rotor response showed that excessive flapping motions and high hub spring loads could occur during engage and disengage operations. Simulation results for a two bladed teetering rotor were validated against model wind tunnel results. For improved accuracy, an elastic blade flap-torsion finite element model for the rotor blades was formulated. Using the finite element model, transient response analysis results for a three bladed gimballed rotor are presented and ongoing work is introduced.

PENNSTATE

Recent Developments in the Analysis and Experimental Testing for Transient Rotor Engage and Disengage Operations

Jonathan A. Keller
Graduate Research Asst.

Edward C. Smith
Assistant Professor

Hao Kang
Visiting Scholar

Department of Aerospace Engineering
The Pennsylvania State University

Background and Motivation   PENNSTATE

- Potential for blade-fuselage contact due to excessive aeroelastic flapping at low rotor speeds (< 20% full RPM)

- Particularly bad problem for shipboard operations and adverse weather conditions

- Motivated by H-46 Sea Knight "tunnel strikes"

Background and Motivation
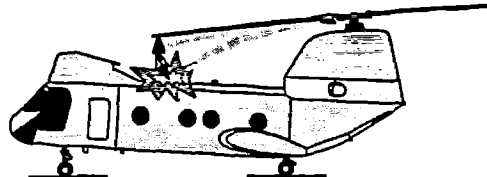
H-46 Tunnel Strike History

100 +

?

Tunnel Strikes

Tunnel Strikes

1964   1974   1984   1997   2025

Timeline

H-46
Deployed

Projected H-46
Phase Out

Background and Motivation
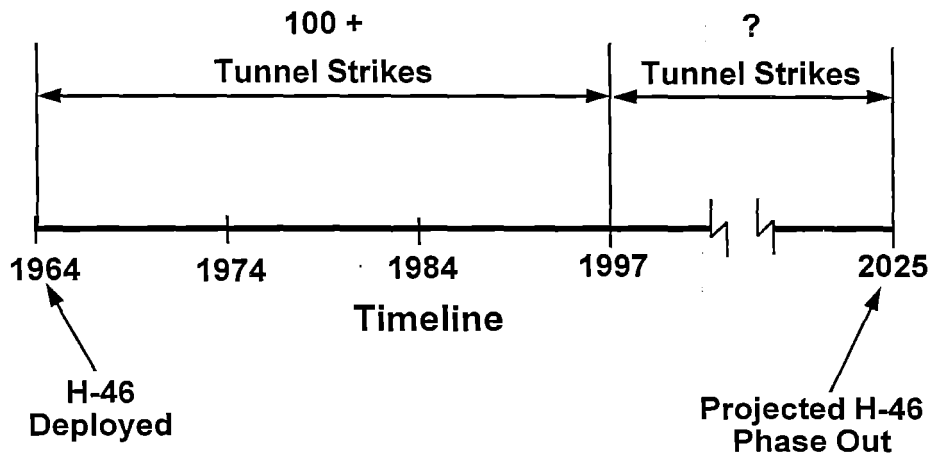
- Many unique factors to simulate
    - Ship airwake environment
    - Rotor RPM vs. Time
    - Blade elasticity
    - Ship motion
    - Inputs to rotor system
    - Droop/gimbal stop impacts
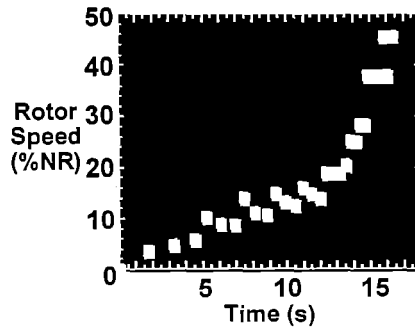
PENNSTATE

Refinements in the Analysis for Droop or Gimbal Stop Impacts

Formulation of a Transient
Analysis of Teetering and
Gimballed Rotors

Experimental and Theoretical Analysis for
Helicopter Rotor Blade-Droop Stop Impacts
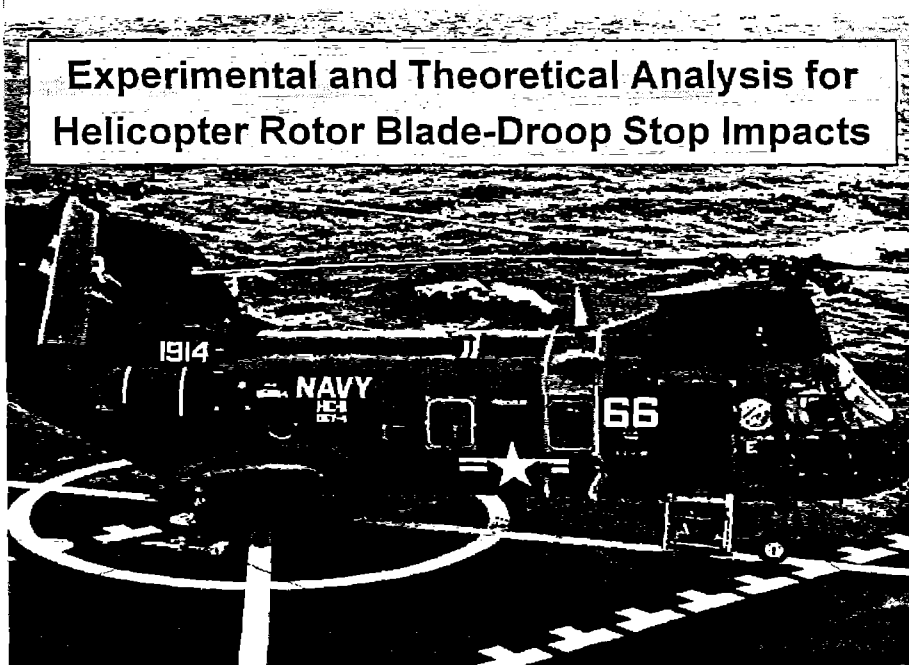
Refinements in the Analysis for Droop or Gimbal Stop Impacts

⟶ • **Background and Objectives**

• **Approach and Results**

   - **Algorithm Refinement**

   - **Material Damping**

• **Conclusions**

Background and Motivation

• **Droop stop impact contributes to excessive elastic bending of rotor blade**
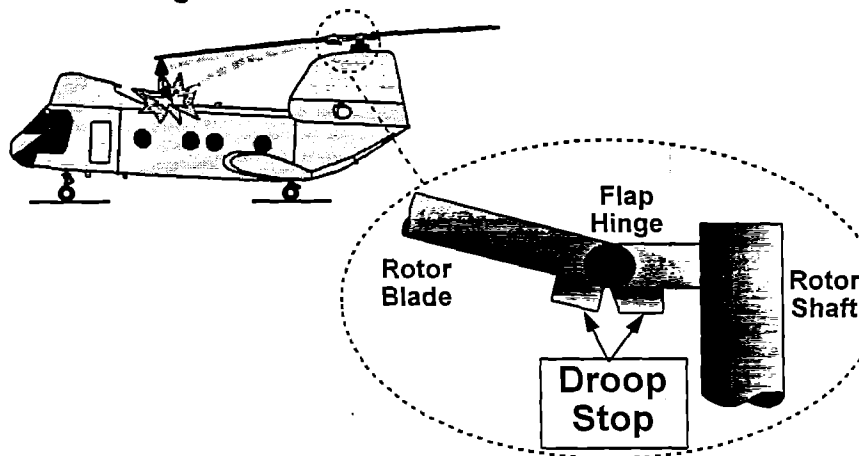
Background and Motivation
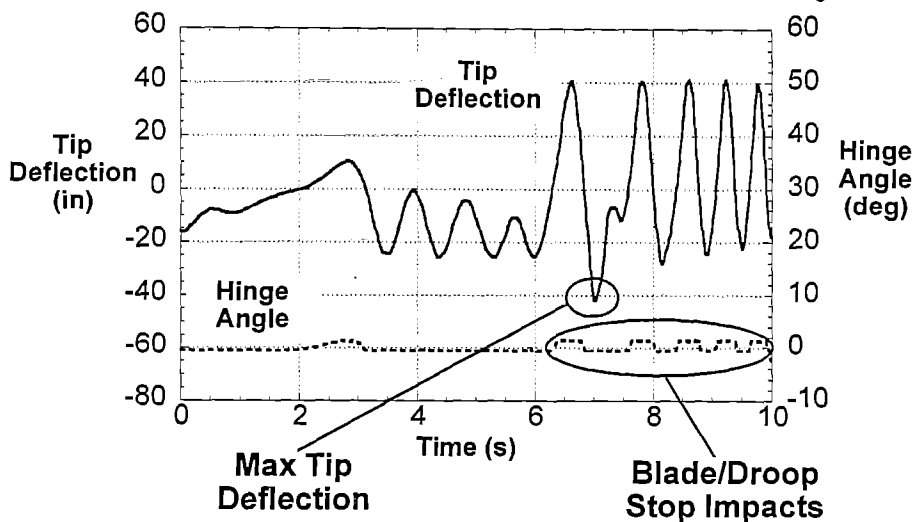
Related Research

- Leone, 1964 (*AHS Journal*)
  - Blade-droop stop impacts at full RPM
  - Measured and predicted root bending moments
- Fathi and Popplewell, 1994 and Lo, 1980 (*J. of Sound&Vib.*)
  - Cantilever beam impacting rigid stop
  - Used unconstrained modes only
- Molnar, et al. 1976 (*J. of Pressure Vessel Technology*)
  - Gap restrained piping systems
  - Used unconstrained modes only
  - Compared direct vs. modal solution efficiencies

Related Research

- Rogers and Pick, 1976-77 (*Nuclear Engr. & Design*)
  - FEM solution of pipe vibrating between rigid stops
  - Used both unconstrained and constrained modes
- Davies and Rogers, 1979 (*Nuclear Engr. & Design*)
  - Use of either unconstrained or constrained modes
  - Undamped motion described using either set of modes
- Keller and Smith, 1997 (*SDM Conf. Proceedings*)
  - Model rotor blade impacting droop stop
  - Used both constrained and unconstrained modes
  - "Discontinuities" found in solution

Objectives

- Refine algorithm for blade-droop stop impact

- Measure material damping of model blade

- Include material damping in analytic solution

- Assess effect of algorithm refinement and damping

Refinements in the Analysis for Droop or Gimbal Stop Impacts

- • Background and Objectives

- • Approach and Results

→   - Algorithm Refinement

      - Material Damping

- • Conclusions

Model Beam Schematic

Linear Motion Potentiometer

Accelerometer

Strain Gages

β_{hinge} (t=0)

w_{tip} (t=0)
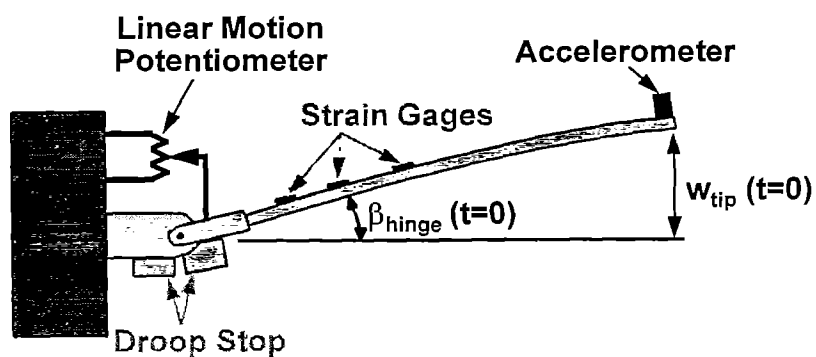
Droop Stop

Modeling Approach

Hinged modes
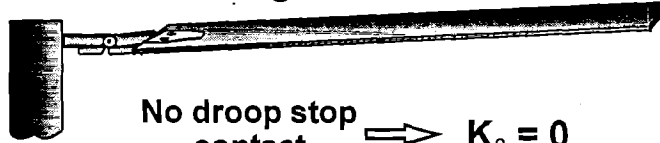
No droop stop contact $\implies$ $K_\beta = 0$

Cantilevered modes

Droop stop contact $\implies$ $K_\beta = 10^6 \int m\, g\, x\, dx$

Analysis Approach

• Two sets of natural frequencies and mode shapes

- No Droop Stop Contact

$$[K_{beam} - \omega^2 M_{beam}]\, \Phi = 0$$

$$\implies \omega_h\ \Phi_h$$

- Droop Stop Contact

$$[K_{beam} + K_\beta - \omega^2 M_{beam}]\, \Phi = 0$$

$$\implies \omega_c\ \Phi_c$$

"Modal Swapping" - Old Method

$$M\ddot{q} + C\dot{q} + Kq = F$$

Let $q = \Phi\alpha$

No   Droop Stop Contact ?   **Yes**

$\Phi = \Phi_h$ $\Phi = \Phi_c$

$$\overline{M}\ddot{\alpha} + \overline{C}\dot{\alpha} + \overline{K}\alpha = \overline{F}$$
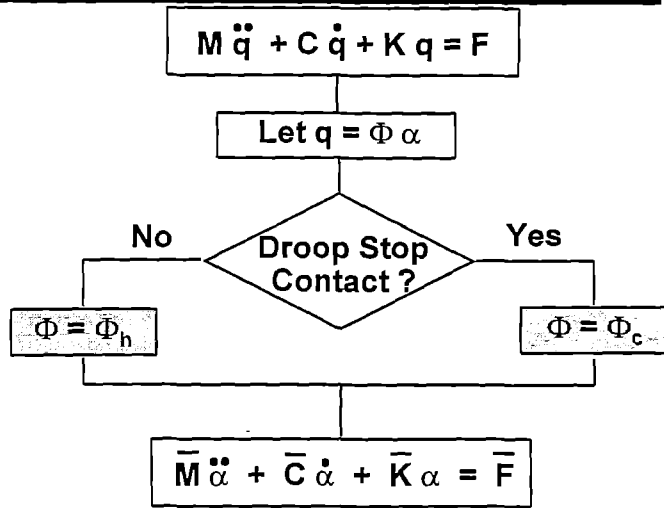
"Modal Swapping" - NEW Method
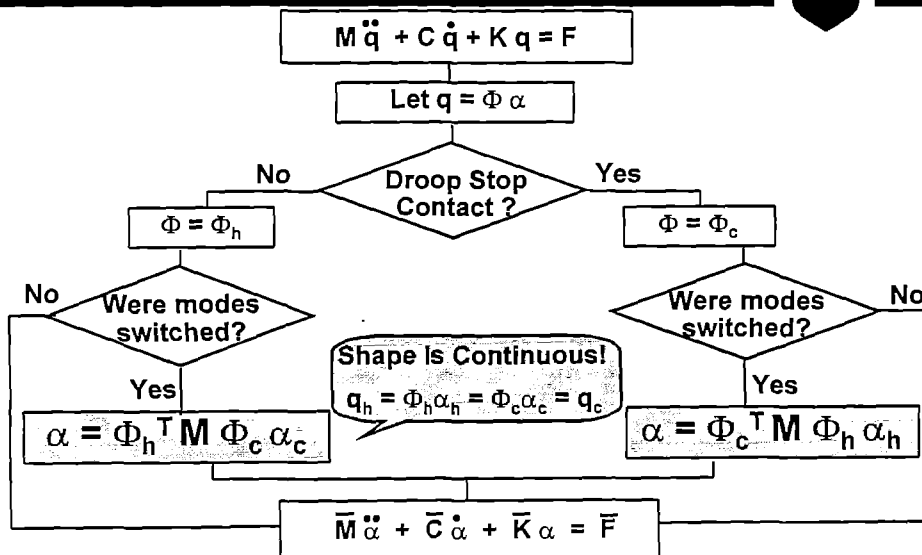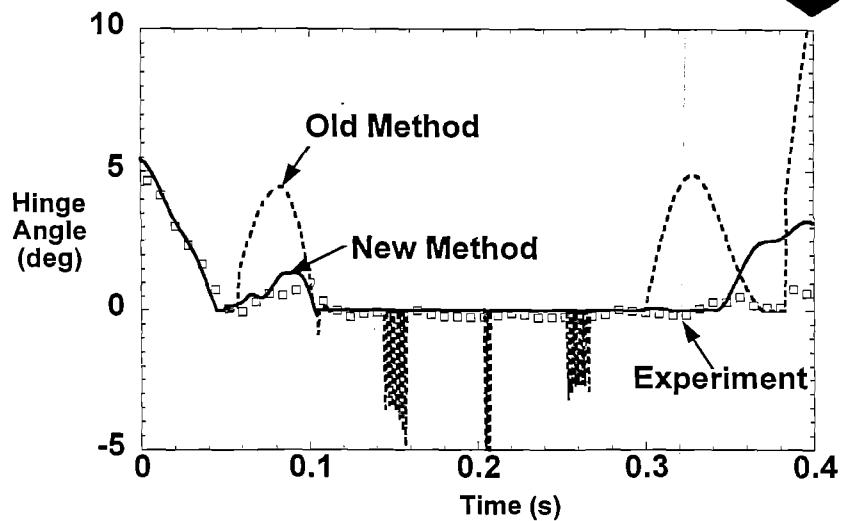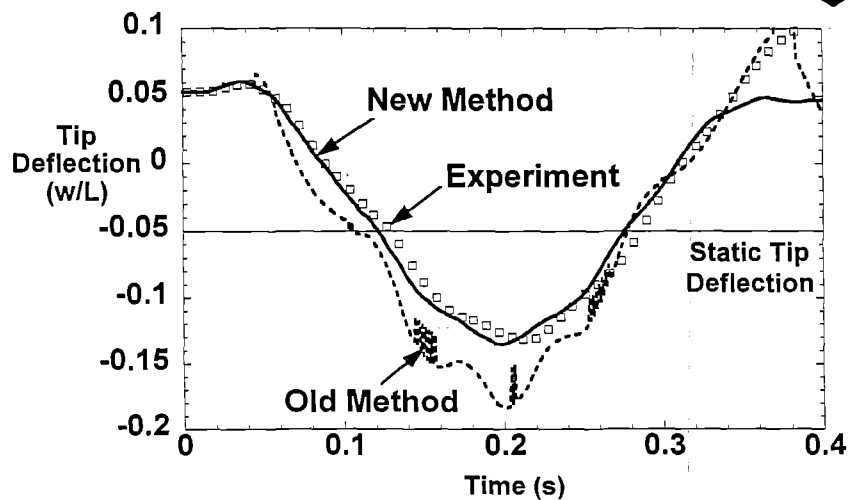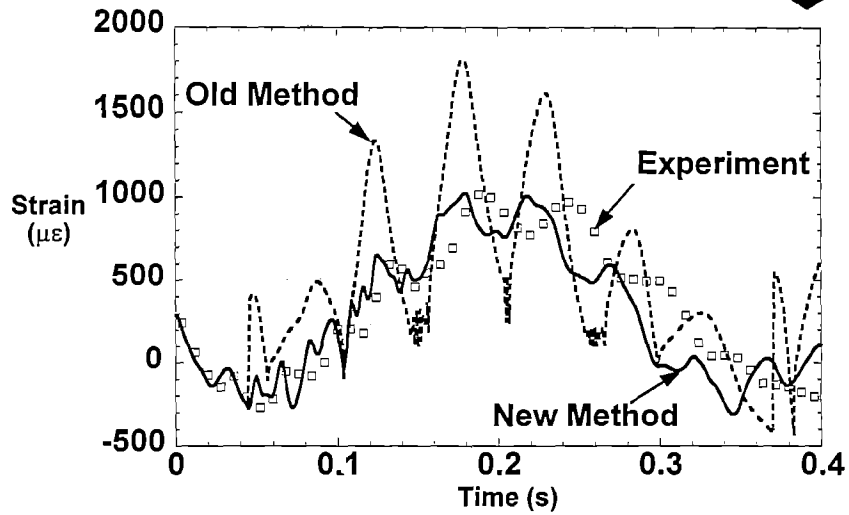
$$M\ddot{q} + C\dot{q} + Kq = F$$

Let $q = \Phi\alpha$

No   Droop Stop Contact ?   **Yes**

$\Phi = \Phi_h$ $\Phi = \Phi_c$

No   Were modes switched?   Were modes switched?   **No**

Shape Is Continuous!
$q_h = \Phi_h\alpha_h = \Phi_c\alpha_c = q_c$

Yes   **Yes**

$\alpha = \Phi_h{}^T M \Phi_c \alpha_c$ $\alpha = \Phi_c{}^T M \Phi_h \alpha_h$

$$\overline{M}\ddot{\alpha} + \overline{C}\dot{\alpha} + \overline{K}\alpha = \overline{F}$$

5.5° Drop Angle

PENN STATE

Old Method

New Method

Hinge Angle (deg)

Experiment

Time (s)

5.5° Drop Angle

PENN STATE

New Method

Experiment

Tip Deflection (w/L)

Static Tip Deflection

Old Method

Time (s)

5.5° Drop Angle

PENNSTATE

Refinements in the Analysis for Droop or Gimbal Stop Impacts

PENNSTATE

- Background and Objectives

- Approach and Results

    - Algorithm Refinement

→   - Material Damping

- Conclusions

- **Fixed Response / Roving Input test**
  - Excitation by roving hammer impact (11 points)
  - Measured by fixed accelerometer
  - Tests performed with hinged and cantilevered BCs

Mode	Hinged ζ (%$\zeta_{critical}$)	Cantilevered ζ (%$\zeta_{critical}$)
Rigid Body	$\cong 0.0$	N/A
1st Bending	4.5	$\cong 0.0$
2nd Bending	0.9	0.4
3rd Bending	0.2	0.9

5.5° Drop Angle   PENNSTATE
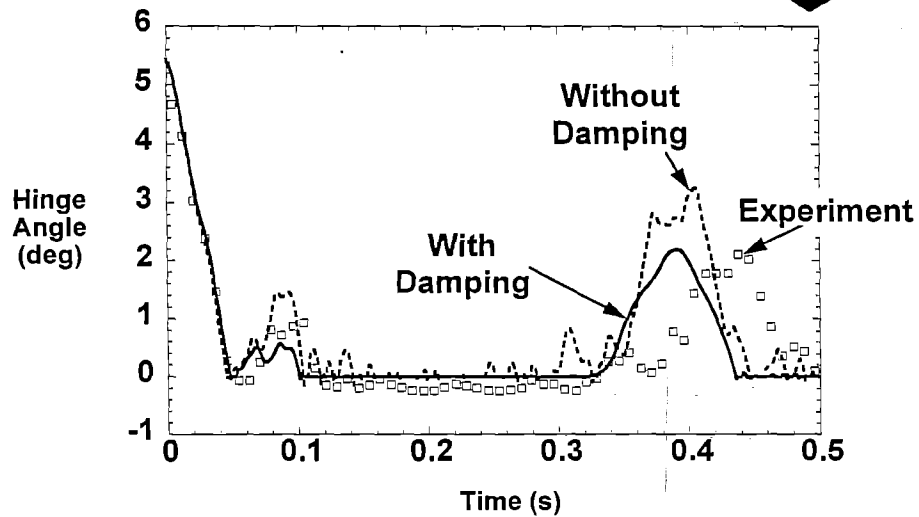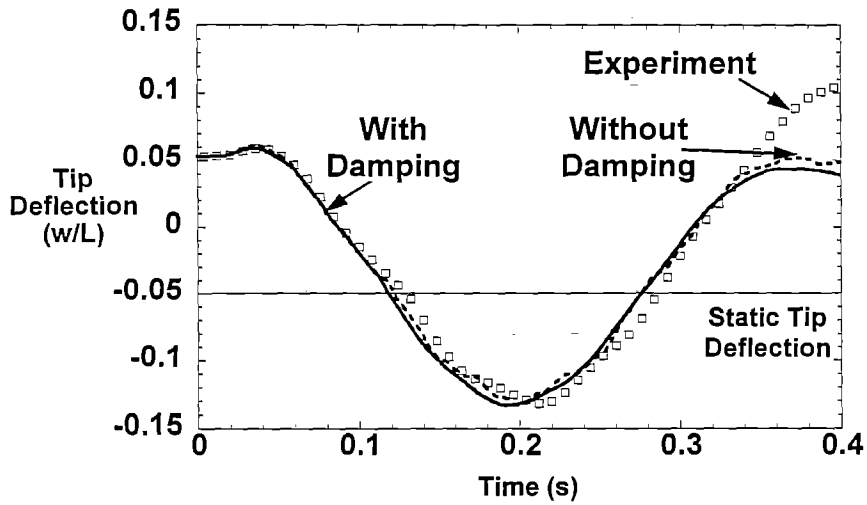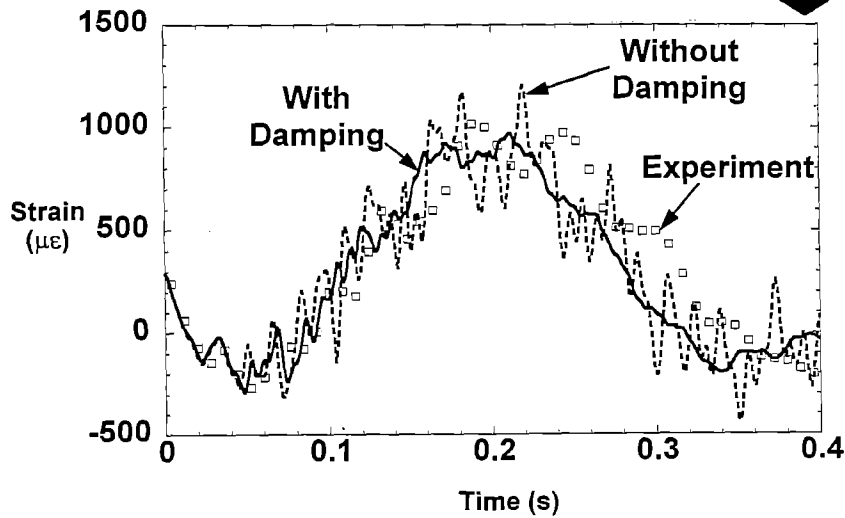
Refinements in the Analysis for Droop or Gimbal Stop Impacts

PENNSTATE

- Background and Objectives

- Approach and Results

    - Algorithm Refinement

    - Material Damping

→ • Conclusions

Conclusions

PENNSTATE

- Rotor blade-droop stop impacts key factor in tunnel strikes

- Utilized FEM approach to simulate impacts

- Modal amplitude "correction" essential when modes are swapped

- Performed hammer impact tests to measure material damping

- Material damping improves correlation in hinge angle and strain simulations but does not effect tip deflection

PENNSTATE

Refinements in the Analysis for
Droop or Gimbal Stop Impacts

Formulation of a Transient Analysis of Teetering and Gimballed Rotors

Transient Analysis for Engage
and Disengage Operations of
Gimballed Tiltrotors
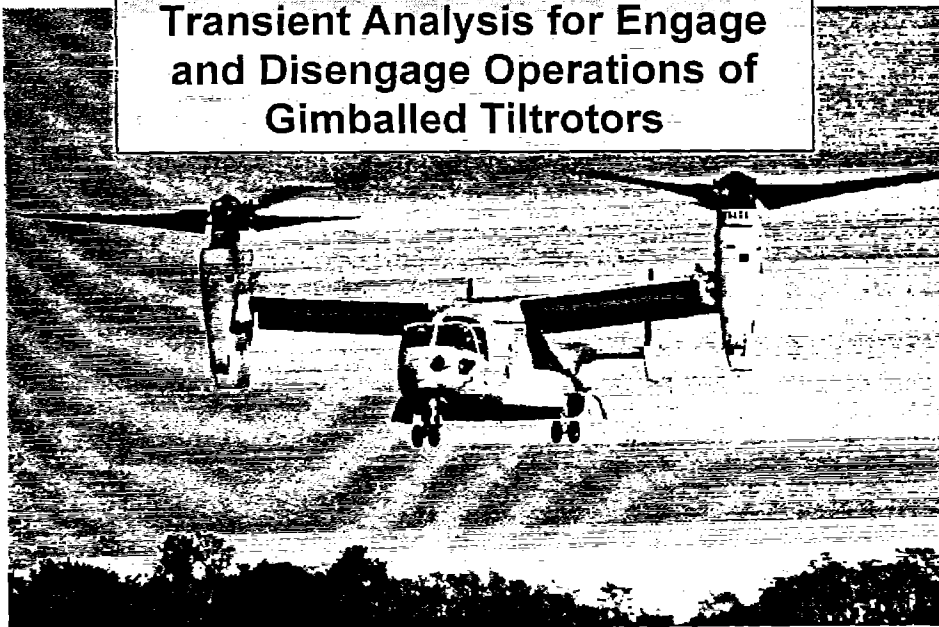
Transient Analysis for Engage and Disengage Operations of Gimballed Tiltrotors

PENN**STATE**

⟶ • **Background and Motivation**

• **Approach and Analysis**

   Rigid Blade Gimballed Rotor Modeling

   Elastic Blade Gimballed Rotor Modeling

• **Further Work**

Background and Motivation

PENN**STATE**
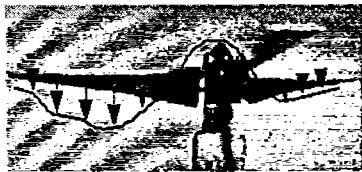
• No studies of engage/disengage
• USMC purchasing 100's of V-22s
• 3-bladed gimballed rotor
• Shorter blades - highly twisted
• Excessive gimbal tilt angles can occur during engage/disengage
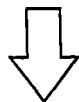
Air on all 3 blades contributes to high gimbal flapping at low Ω
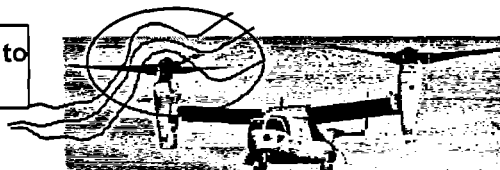
Gimballed Rotor Schematic

PROPROTOR HUB

MAST

RUBBER HUB SPRING

GIMBAL RESTRAINT

HUB UNDEFLECTED   HUB DEFLECTED
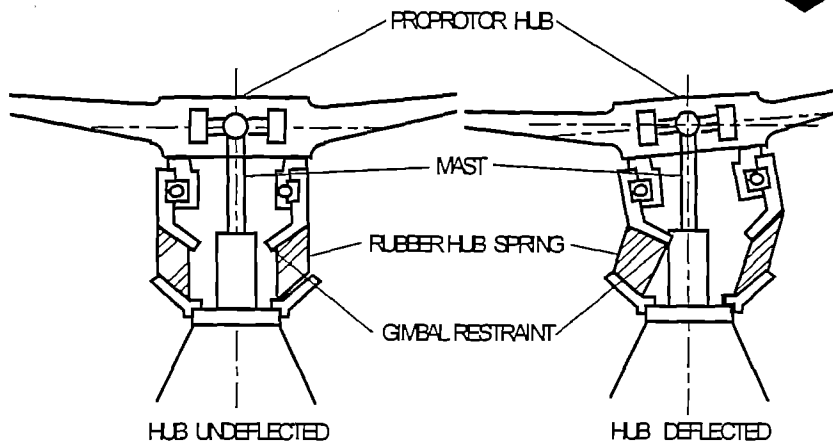
The Gimballed/Teetering Rotor Aeroelastic Research

Teetering Rotor:

•**Shamie and Friedmann, 1976, AHS Forum**

____ Aeroelastic Stability of Complete Rotors with Application to a Teetering Rotor in Forward Flight

•**Kawakami, 1977, J. of Sound and Vibration**

—— Dynamics of an Elastic Seesaw Rotor

Gimballed Rotor:

•**Johnson, May 1974, NASA TN D-7677**

—— Dynamics of Tilting Proprotor Aircraft in Cruise Flight

•**Nixon, 1993, Ph.D. Dissertation**

____ Aeroelastic Response and Stability of Tiltrotor with Elastically Coupled Composite Blades

Objectives

- Formulate Transient Response Analysis

  for Gimballed Rotor

  —— Rigid gimballed rotor blades

  —— Elastic gimballed rotor blades

- Validate With Newman's Experimental Data

- Preliminary Parametric Study

Transient Analysis for Engage and Disengage Operations of Gimballed Tiltrotors

- Background and Motivation

→ • Approach and Analysis

  Rigid Blade Gimballed Rotor Modeling

  Elastic Blade Gimballed Rotor Modeling

- Further Work

Precone

modeling

β_p

Hub Spring

β_G

Gimbal Restraint

Flapping Angle

Structural Modeling

- Variable Rotor RPM
- Hub Spring
- Rigid Rotor
- Gimbal Restraint

Aerodynamic Modeling

- Quasi-Steady
- Unsteady/Dynamic Stall
- Modifications of Very High Angle of Attack

$$\begin{bmatrix} 1 & 0 \\ 0 & 1 \end{bmatrix} \begin{Bmatrix} \ddot{\beta}_{GC} \\ \ddot{\beta}_{GS} \end{Bmatrix} + \begin{bmatrix} 0 & -2 \\ 2 & 0 \end{bmatrix} \begin{Bmatrix} \dot{\beta}_{GC} \\ \dot{\beta}_{GS} \end{Bmatrix} + \begin{bmatrix} -\dfrac{2}{N}\dfrac{K_{\beta_{GC}}}{I_b\,\Omega^2} & 0 \\ 0 & -\dfrac{2}{N}\dfrac{K_{\beta_{GS}}}{I_b\,\Omega^2} \end{bmatrix} \begin{Bmatrix} \beta_{GS} \\ \beta_{GS} \end{Bmatrix} = $$

$$\begin{Bmatrix} \dfrac{2}{N}\sum_{m=1}^{N} (\int_0^1 F_z^m r\,dr)\cos\psi^m + \dfrac{2}{N}\dfrac{k_{restraint}(\beta_{max} - \beta_{restraint})}{I_b\,\Omega^2}\cos\psi_{max} \\ \dfrac{2}{N}\sum_{m=1}^{N} (\int_0^1 F_z^m r\,dr)\sin\psi^m + \dfrac{2}{N}\dfrac{k_{restraint}(\beta_{max} - \beta_{restraint})}{I_b\,\Omega^2}\sin\psi_{max} \end{Bmatrix}$$

Analysis of Gimbal Restraint Contact PENNSTATE

Calculate the maximum tilt angle and corresponding azimuth of rotor

$$\psi_{max}=\tan^{-1}(\frac{\beta_{GC}}{\beta_{GS}}) \; , \; \beta_{max}=\beta_{GC}\cos(\psi_{max})+\beta_{GS}\sin(\psi_{max})$$

$\beta_{max}<\beta_{droop}$ ← β_{max} → $\beta_{max}>\beta_{droop}$

β_{GC} β_{max} β_{GS}

Without the effect of gimbal restraint

Include the stiffness due to gimbal restraint contact
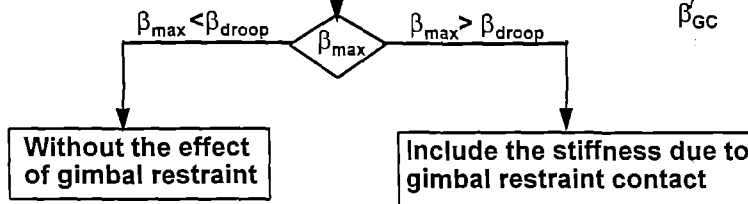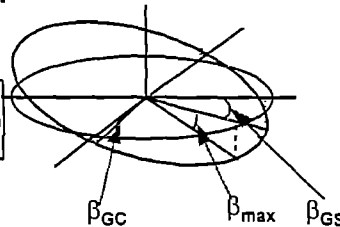
Analysis Method   PENNSTATE

- model
- time integration
- 4th Order Runge-Kutta

$$\dot{y} = Ay + f$$

where

$$A = \begin{bmatrix} 0 & I \\ (1)M^{-1}K & (-1)M^{-1}C \end{bmatrix}, \; f = \begin{Bmatrix} 0 \\ Q \end{Bmatrix}, \; y = \begin{Bmatrix} q \\ \dot{q} \end{Bmatrix}$$

Validation
———— UK 2 Blades, Teetering Model Test

Teeter Angle (deg)	Rotor Speed (RPM)	Teeter Angle (deg)	Rotor Speed (RPM)
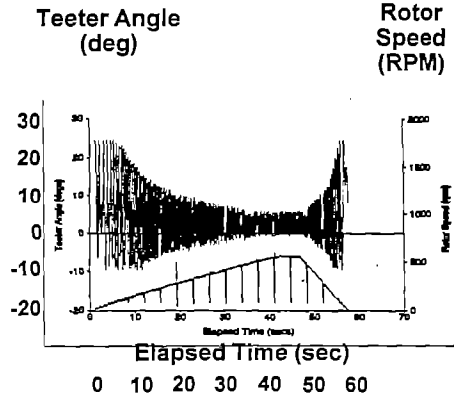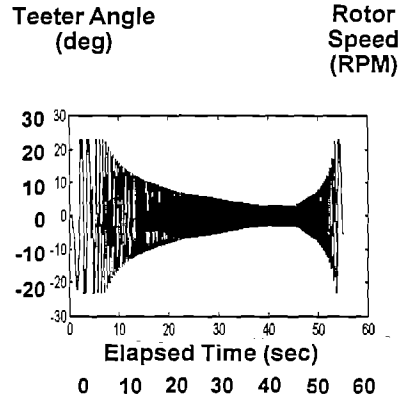
Elapsed Time (sec)	Elapsed Time (sec)
0 10 20 30 40 50 60	0 10 20 30 40 50 60
Wind Tunnel Tests	**Theoretical Prediction**

Source: Newman, University of Southampton Doctoral Thesis, March 1995

Transient Response Prediction

Gimballed Rotor Properties

Number of Blades	3
Radius, ft	19
chord, in	25.07
rotating speed, RPM	397
Flapping Spring rate, ft-lb/deg	250
Lock Number	4.9
ν_β	1.02

Transient Flapping Prediction of V-22 Rotor

PENNSTATE

Flapping Angle (deg)

Gimbal Restraint Contacts

Hub & blades load?

Need Elastic Blade Model

——— V=35knots

·········· V=50knots

$V_{vertical} = 20\%V$
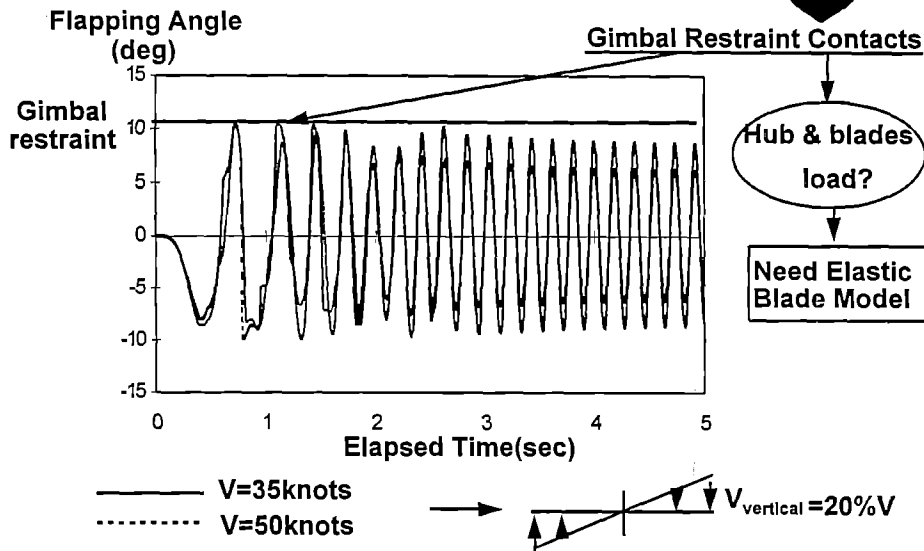
Elastic Blade Gimballed Rotor Finite Element Modeling

PENNSTATE
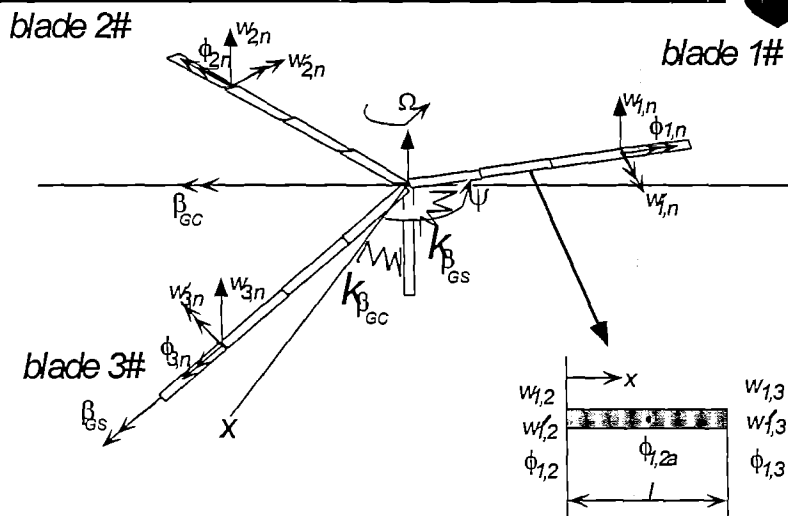
Elastic Blade Gimballed Rotor
Finite Element Equations

Hamilton's Principle for Gimballed Rotor

$$\delta \Pi = \int_{t_1}^{t_2} (\delta T - \delta U + \delta W)\, dt = 0$$

where

Variation of Strain Energy

$$\delta U = (\sum_{m=1}^{N} \delta U_b) + \underbrace{\delta U_h}_{\substack{hub \\ spring}} + \underbrace{\delta U_r}_{\substack{gimbal \\ restraint}}$$

$$\underbrace{\phantom{(\sum_{m=1}^{N}\delta U_b)}}_{blade}$$

Variation of Kinetic Energy

$$\delta T = (\sum_{m=1}^{N} \delta T_b)$$

Variation of Virtual Work

$$\delta W = (\sum_{m=1}^{N} \delta W_b)$$

Elastic Blade Gimballed Rotor
Finite Element Equations

$$\delta \Pi = \underbrace{\int_{\psi_I}^{\psi_F} (\sum_{m=1}^{N} \delta q_m^{T} (M_{b_m} \ddot{q}_m + C_{b_m} \dot{q}_m + K_{b_m} q_m - F_{b_m})\, d\psi}_{multi\text{-}blade}$$

$$+ \underbrace{\int_{\psi_I}^{\psi_F} \left[\delta w'_{l,l}, \delta\phi_{l,l}\right]\left[k_\beta\right]\begin{Bmatrix} w'_{l,l} \\ \phi_{l,l} \end{Bmatrix}}_{gimbal\ spring} + \underbrace{K_{restraint}(\beta_{max} - \beta_{restraint})\delta\beta_{max})\, d\psi}_{gimbal\ restraint}$$

where

$$\left[k_\beta\right] = \begin{bmatrix} k_{\beta_{cc}}\cos^2\psi + k_{\beta_{cs}}\sin^2\psi, & -k_{\beta_{cc}}\cos\psi\sin\psi + k_{\beta_{cs}}\cos\psi\sin\psi \\ -k_{\beta_{cc}}\cos\psi\sin\psi + k_{\beta_{cs}}\cos\psi\sin\psi, & k_{\beta_{cc}}\sin^2\psi + k_{\beta_{cc}}\cos^2\psi \end{bmatrix}$$

$$\beta_{max} = (w'_{l,l}\cos\psi - \phi_{l,l}\sin\psi)\cos\psi_{max} + (w'_{l,l}\sin\psi + \phi_{l,l}\cos\psi)\sin\psi_{max}$$

$$\delta\beta_{max} = (\delta w'_{l,l}\cos\psi - \delta\phi_{l,l}\sin\psi)\cos\psi_{max} + (\delta w'_{l,l}\sin\psi + \delta\phi_{l,l}\cos\psi)\sin\psi_{max}$$

$$+\delta\psi_{max}(-(w'_{l,l}\cos\psi - \phi_{l,l}\sin\psi)\sin\psi_{max} + (w'_{l,l}\sin\psi + \phi_{l,l}\cos\psi)\cos\psi_{max})$$

$$\psi_{max} = \tan^{-1}\left(\frac{w'_{l,l}\sin\psi + \phi_{l,l}\cos\psi}{w'_{l,l}\cos\psi - \phi_{l,l}\sin\psi}\right) \qquad \delta\psi_{max} = \frac{\phi_{l,l}}{w'^2_{l,l} + \phi^2_{l,l}}\delta w'_{l,l} + \frac{w'_{l,l}}{w'^2_{l,l} + \phi^2_{l,l}}\delta\phi_{l,l}$$

Global Assembled System Equation

$$\mathbf{M}\ddot{q} + \mathbf{C}\dot{q} + \mathbf{K}q - \mathbf{F} = 0$$

$$q = \{w'_{1,1}, \phi_{1,1}, \phi_{1,1a}, w_{1,2}, w'_{1,2}, \phi_{1,2}, \phi_{1,2a}, w_{1,3}, w'_{1,3}, \phi_{1,3}, \cdots, \}_{\text{blade 1}}$$

$$\phi_{2,1a}, w_{2,2}, w'_{2,2}, \phi_{2,2}, \phi_{2,2a}, w_{2,3}, w'_{2,3}, \phi_{2,3}, \cdots, {}_{\text{blade 2}}$$

......

$$\phi_{N_b,1a}, w_{N_b,2}, w'_{N_b,2}, \phi_{N_b,2}, \phi_{N_b,2a}, w_{N_b,3}, w'_{N_b,3}, \phi_{N_b,3}, \cdots$$

blade N_b

$$w'_{m,I} = w'_I \cos\psi + \phi_I \sin\psi$$
$$\phi_{m,I} = -w'_I \sin\psi + \phi_I \cos\psi$$

Teeter Angle (deg) — 14°

Rotor Speed (RPM) Blade Tip Deflection w/R Rotor Speed (RPM)

Elapsed Time (sec)   Elapsed Time (sec)

.... rigid blade
——— elastic blade

Further Work

- Refinement of Aerodynamic Model

  Improve modeling of high angles of attack

- Structural Modeling

  Add lag Degree to finite element model of gimballed rotor blades

- V-22 Transient Analysis and Validation

- Examine Blade and Hub Loads During Engage and Disengage Operations

An Active Nonlinear Vibration Absorber

Shafic S. Oueini and Ali H. Nayfeh

Department of Engineering Science and Mechanics

Virginia Polytechnic Institute and State University

Blacksburg, VA 24061-0219

Shafic Oueini
Virginia Tech

- Introduction
  - Background
  - Development of the control law
- Theoretical Analysis
  - Steady-state and transient performance
  - Numerical simulation
- Experiments on a Cantilever Beam
  - Piezoceramic **linear** actuator
  - Terfenol-D **nonlinear** actuator
- Conclusions

- Development of the Control Law

- Theoretical Analysis

  – Amplitude- and frequency-response curves

  – Numerical simulation

- Experiments on Cantilever Beams

  – Piezoceramic **linear** actuator

  – Terfenol-D **nonlinear** actuator

- Performance Evaluation

Shafic Oueini
Virginia Tech

- Nonlinear vibration absorbers

  – Passive pendulum absorber - Haxton and Barr (1972)

  – Semi-active pendulum absorber - Cartmell and Lawson (1994)

- Control using internal resonance

  – Active quadratic coupling - Golnaraghi (1991, 1994)

  – Experimental application with a circuit - Oueini and Golnaraghi (1996)

  – Digital implementation – Khajepour and Golnaraghi (1997)

- Equation of plant

$$\ddot{u} + 2\mu\dot{u} + \omega^2 u = F\cos(\Omega t) + T$$

where

$$\Omega \approx \omega$$

- Equation of controller and control signal

$$\ddot{v} + 2\zeta\dot{v} + \lambda^2 v = \alpha u v$$

where

$$\lambda \approx \frac{1}{2}\Omega \quad \text{and} \quad T(t) = \gamma v^2$$

- Approximate solution

$$u \approx a\cos(\Omega t - \Psi) \quad \text{and} \quad v \approx b\cos\left[\frac{1}{2}(\Omega t - \Phi - \Psi)\right]$$

- Modulation equations

$$\dot{a} = -\mu a + \gamma b^2 \sin\Phi + f\sin\Psi$$
$$\dot{b} = -\zeta b - \alpha a b \sin\Phi$$
$$a\dot{\beta} = \gamma b^2 \cos\Phi - f\cos\Psi$$
$$b\dot{\varphi} = \alpha a b \cos\Phi$$

where

$$\Phi = \tau t - 2\varphi + \beta \quad \text{and} \quad \Psi = \sigma t - \beta$$

- Linear solution

$$a = \frac{f}{\sqrt{\sigma^2 + \mu^2}}$$

$$b = 0$$

$$\sigma = \Omega - \omega$$

Shafic Oueini
Virginia Tech

- Nonlinear solution

$$a^* = \frac{\zeta}{|\alpha|}$$

$$b^* = \sqrt{\frac{-\zeta\mu + [(\alpha f)^2 - (\sigma\zeta)^2]^{\frac{1}{2}}}{\alpha\gamma}}$$

$$f > \sqrt{\frac{\zeta^2(\mu^2 + \sigma^2)}{\alpha^2}}$$

$$G = \sqrt{\frac{\zeta^2(\mu^2 + \sigma^2)}{\alpha^2}}$$

Shafic Oueini
Virginia Tech

$$RS = 2\sqrt{\left(\frac{\alpha f}{\zeta}\right)^2 - \mu^2}$$

Shafic Oueini
Virginia Tech

- Plant and controller

$$\ddot{u} + 2\mu\,\dot{u} + u = F\cos\left(\Omega t\right) + \gamma\,v^2$$

$$\ddot{v} + 2\zeta\,\dot{v} + \frac{1}{4}\Omega^2\,v = \alpha\,u\,v$$

- Simulation parameters

$$\Omega = 1 \quad F = 0.02$$

$$\mu = 0.01 \quad \zeta = 0.00001$$

$$\alpha = \gamma = 0.0026$$

Plant response when $\Omega = \omega = 1$ and $F = 0.02$

Numerical Simulation – Effect of Varying γ
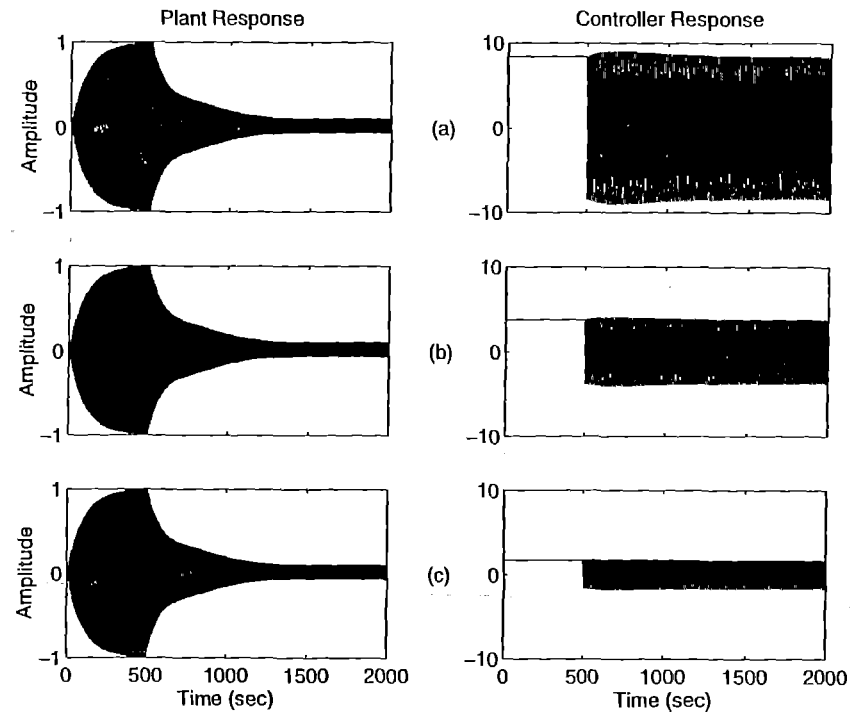
Plant and controller response when $\Omega = \omega = 1$ and $F = 0.02$

Piezoceramic Actuator – Actuator and Sensor Location

Shafic Oueini
Virginia Tech
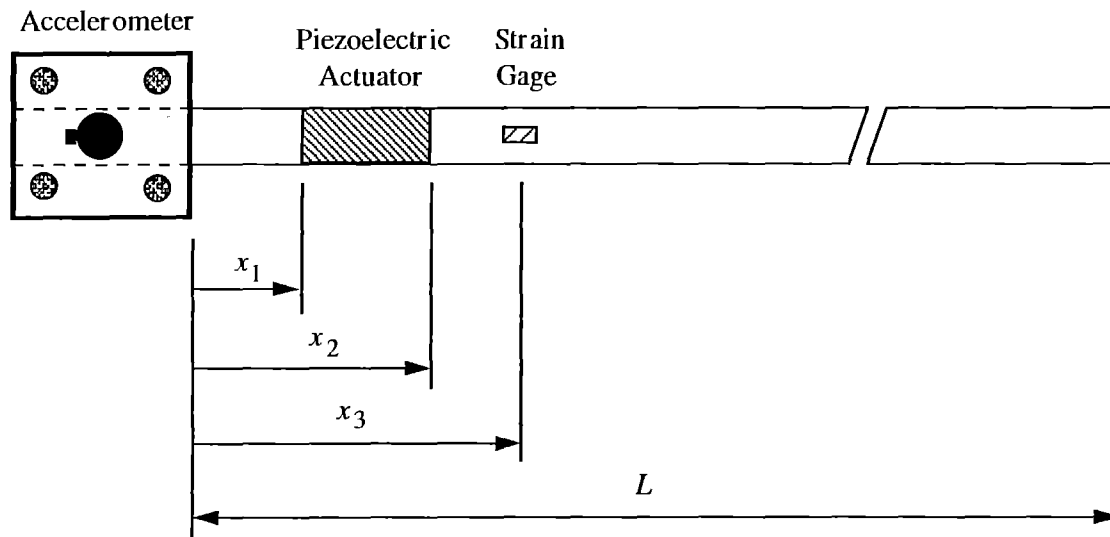
The Experimental Setup
Piezoelectric Actuator
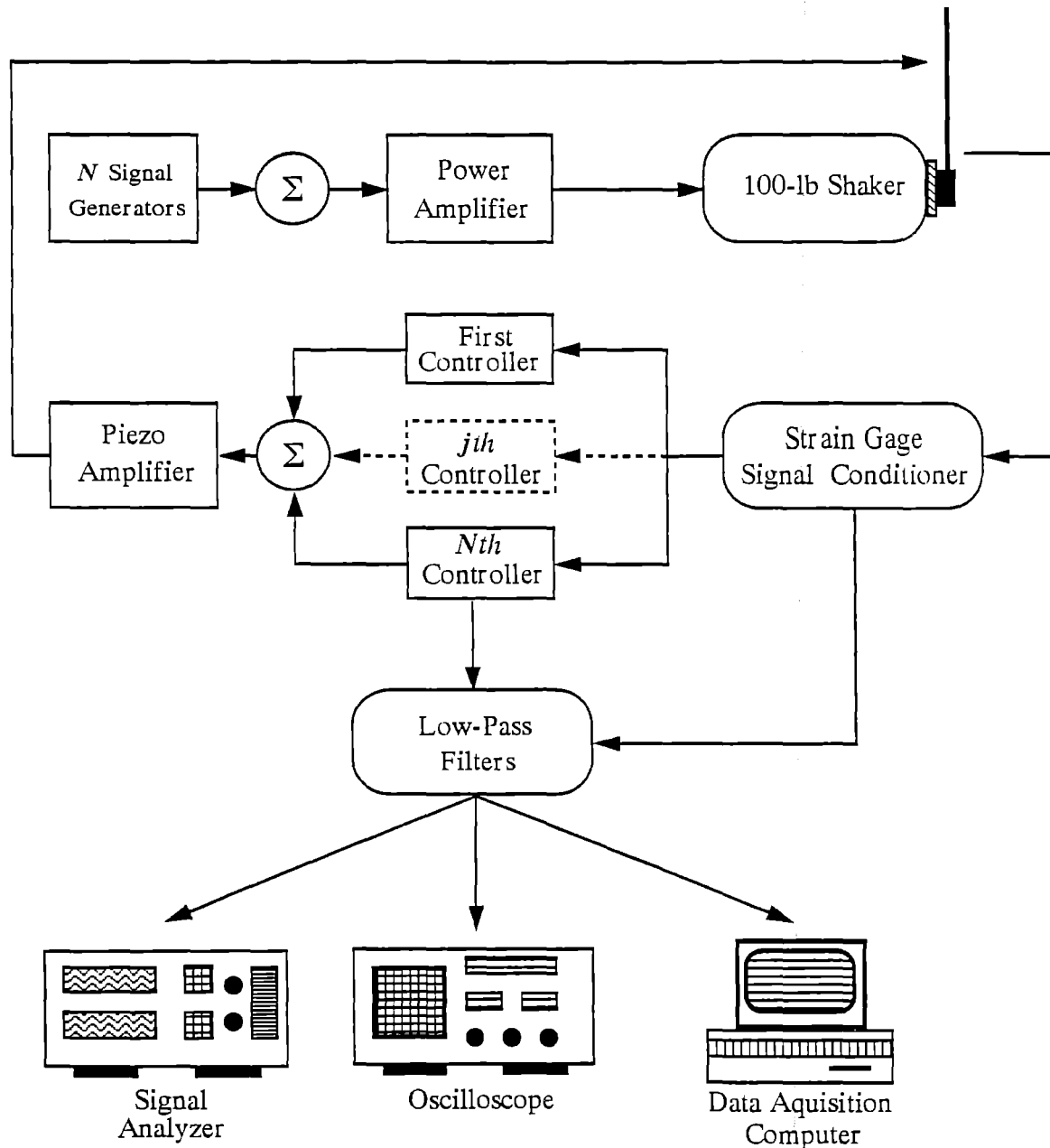
Piezoceramic Actuator – Single Mode Control

Response of Beam
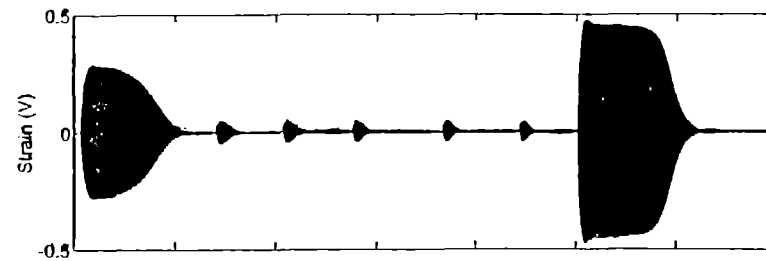
Response of Controller
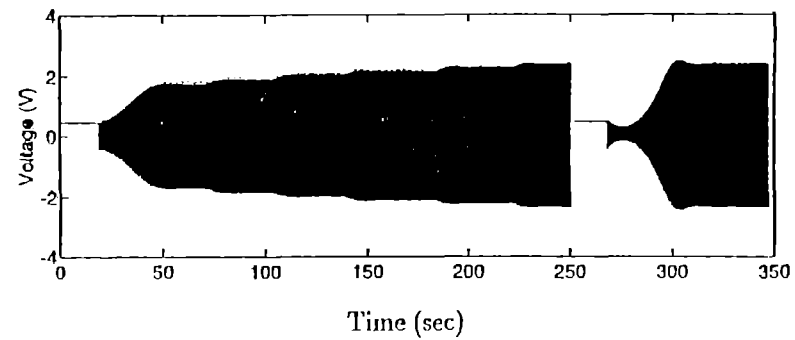
Closed-loop response for increasing forcing.
$\Omega \approx 11.5$ Hz

Piezoceramic Actuator – Two-Mode Control
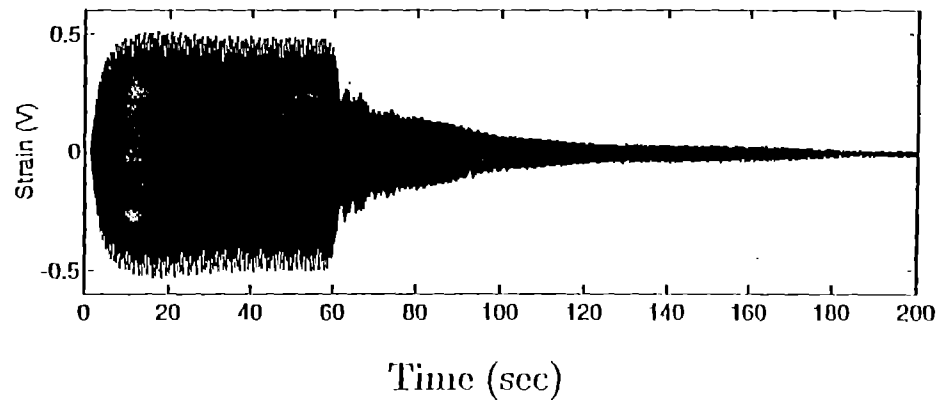
Closed-loop response for constant forcing.
$\Omega_1 \approx 4.3$ Hz and $\Omega_2 \approx 26.5$ Hz

Terfenol-D Actuator – Construction and Constitutive Law

Shafic Oueini
Virginia Tech

Prestress Housing

Solenoid
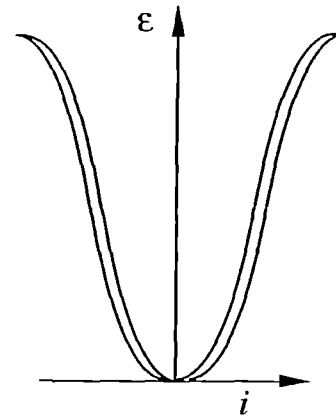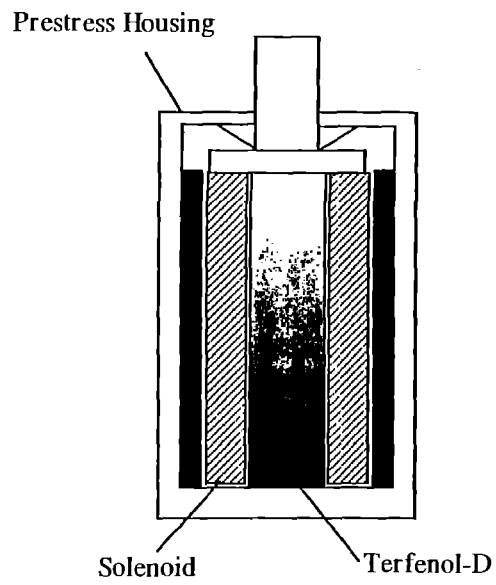
Terfenol-D

$$\varepsilon \approx K i^2$$

Terfenol-D – Actuator and Sensor Configuration

Shafic Oueini
Virginia Tech
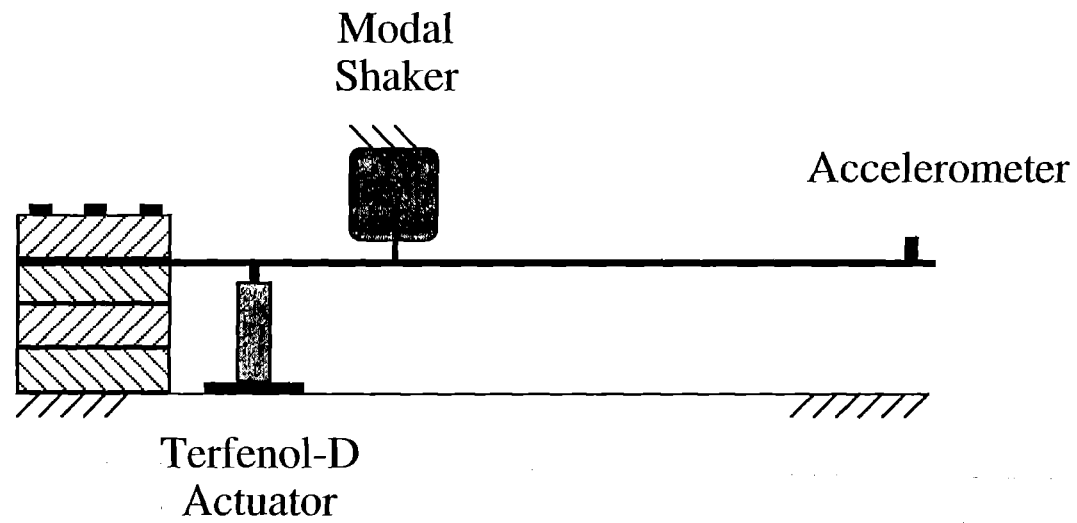
Modal
Shaker

Accelerometer

Terfenol-D
Actuator
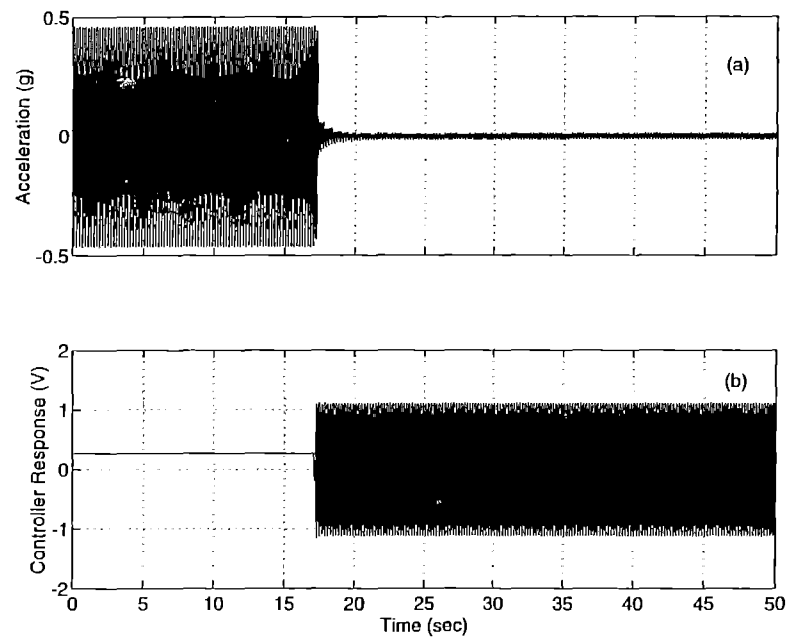
Beam and controller response when $\Omega_2 \approx 47.5$ Hz

Piezoceramic Actuator – Two-Mode Control

Shafic Oueini
Virginia Tech

Beam and controller response when $\Omega_1 \approx 11.5$ Hz
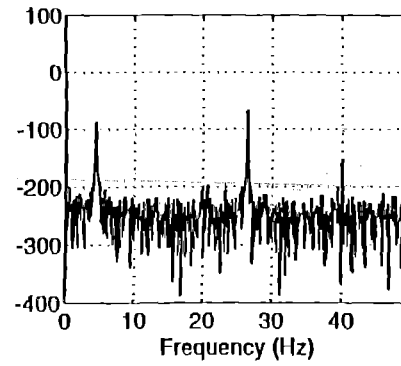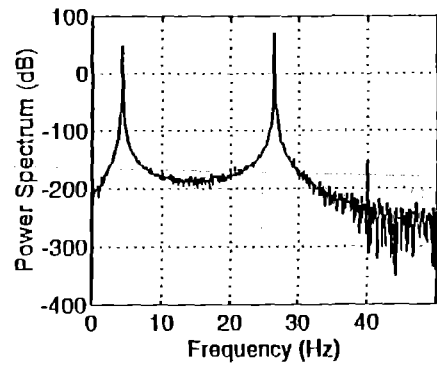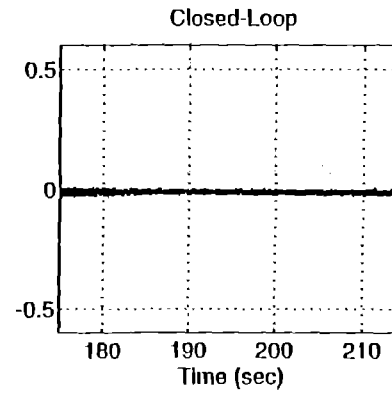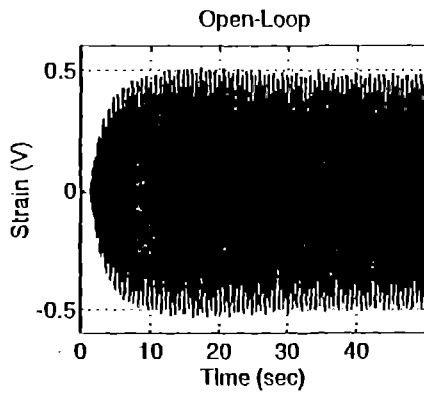
Piezoceramic Actuator – Effect of Varying α

Shafic Oueini
Virginia Tech
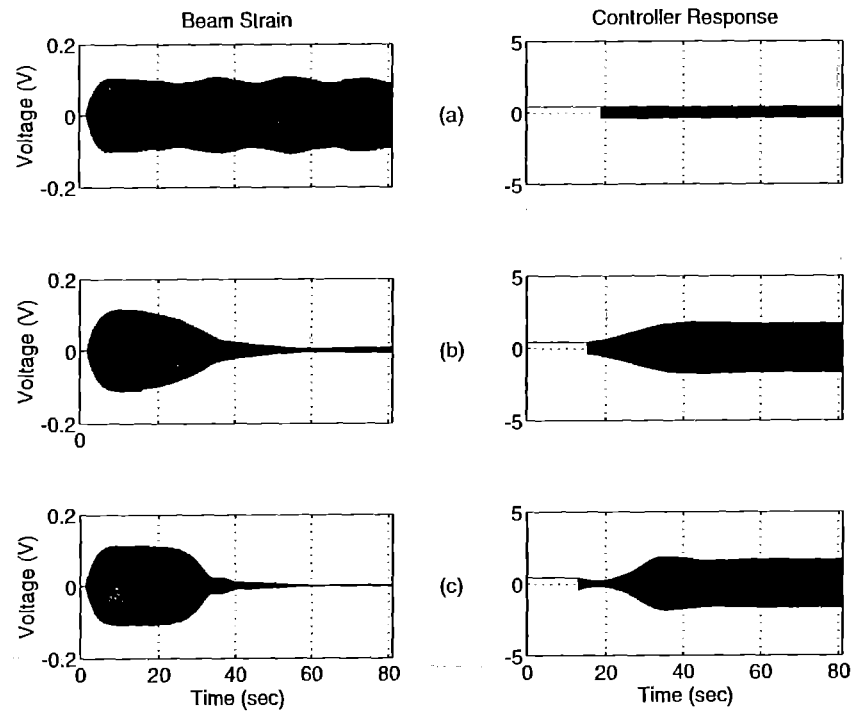
Beam and controller response when $\Omega_1 \approx 11.5$ Hz

- Devised a novel active nonlinear vibration absorber based on the saturation phenomenon

- Investigated the steady-state and transient performance of the strategy

- Successfully tested the technique through linear and nonlinear actuators

- Demonstrated the performance of the strategy with strain and acceleration feedback

The Influence of Low Strain Amplitude, Temperature, and Precompression on the Dynamic Behavior of Elastomeric Damper Materials

Christian R. Brackbill
Doctoral Candidate

L. Eric Ruhl
Graduate Research Assistant

George A. Lesieutre
Associate Professor

Edward C. Smith
Assistant Professor

The Pennsylvania State University
Department of Aerospace Engineering
233 Hammond Building
University Park, PA 16802

Abstract

The dynamic behavior of elastomeric damper materials is investigated experimentally and analytically. Experimental stress-strain time histories are generated for a range of strain amplitudes (0.1 - 30%), frequencies (0.05 - 40Hz), and temperatures (-40 - 200°F), with and without static precompression (22%). The experimental results show that the material dynamic properties change rapidly as strain amplitude increases, and are relatively independent of temperature, frequency, and precompression at higher amplitudes.

An initial linear viscoelastic model is developed to capture the material behavior over a range of frequencies and temperatures. This model is shown to fit the experimental data at a given strain amplitude. The amplitude-dependence is addressed by incorporating nonlinear functions of the material stress into the linear relaxation equations. This nonlinear model shows trends similar to those observed in the experimental data; however, the amplitude dependence is currently not fully captured over a broad frequency or temperature range.

Department of Aerospace Engineering
Rotorcraft Center of Excellence
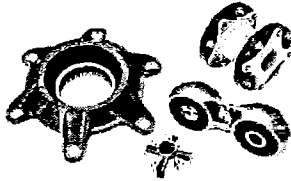
PENNSTATE

The Influence of Low-Strain Amplitude,
Temperature, and Precompression on the
Dynamic Behavior of Elastomeric Damper
Materials

Christian R. Brackbill, PhD candidate
Eric Ruhl, MS candidate
Dr. George A. Lesieutre, Associate Professor
Dr. Edward C. Smith, Assistant Professor

Seventh International Workshop on Dynamics and Aeroelastic Modeling of Rotorcraft Systems
Session V. Vibration and Dynamics   Thursday, October 16, 1997

Presentation Outline

PENNSTATE

⇨• **Background & Motivation** ⇦

• **Experimental Approach and Results**

• **Analytical Approach and Results**

• **Conclusions & Future Work**

Slide 1

Background and Motivation:
Helicopter Applications

PENNSTATE

Elastomeric components have demonstrated
the potential to perform effectively and reliably:

Centering Bearing   Spherical Bearing

Hub /
Mast

Main Blade Spar
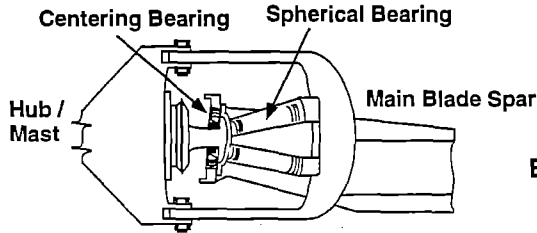
CH-53D Hub Schematic

**Examples of Rotorcraft with
Elastomeric Components**

- Bell (Model 412, V-22)
- Boeing (Model 360, V-22)
- MDHS (AH-64, Explorer)
- Sikorsky (CH-53, UH-60)
- MBB (BO-108, BK-117)

Slide 2

Background and Motivation:
Helicopter Applications

PENNSTATE

Schematic of a Typical Bearingless Rotor

Torque
Tube

Elastomeric
Shear Damper

Rotor
Hub

Flexbeam

Spherical
Elastomeric Bearing
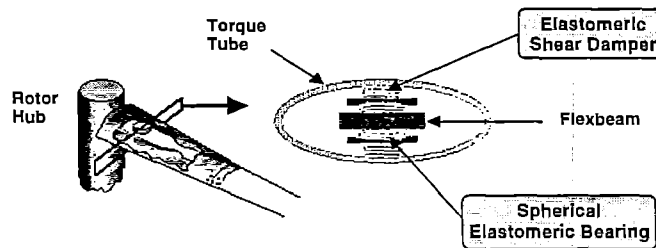
**Elastomer Dynamic
Properties Depend On**

- Strain Amplitude
- Temperature
- Frequency

Focus of Current Research

- Combined Temperature &
  Frequency Dependence
- Low Strain Amplitude
  Nonlinearity (0.1 - 30 %)
- Static Precompression

Background and Motivation:
Rotorcraft Elastomeric Damper Research

PENN STATE

Elastomeric Damper Models:

- **Complex Modulus Based Models:**
  - McGuire (Lord, 1976)
  - Felker *et al* (NASA/Bell 1987)
  - Hausmann and Gergley (MBB, 1992)

- **Time Domain Models:**
  - Gandhi and Chopra (UMD, 1994)
  - Ingle, Tarzanin, Panda (Boeing, 1994+)
  - Smith, Lesieutre, *et al*, (PSU, 1994+)
  - Kunz (MDHS, 1996)

Background and Motivation:
Penn State Elastomeric Damper Research Activities

PENN STATE

Experimental Characterization

- quasi-static behavior
- harmonic shear testing
- transient testing

— low strain amplitude
— temperature dependence
— material self-heating
— static precompression

Analytical Modeling

- helicopter elastomeric dampers
- Anelastic Displacement Fields (ADF) material model
- strain dependence (large strains)

Multiple-ADF model for:
1) temperature
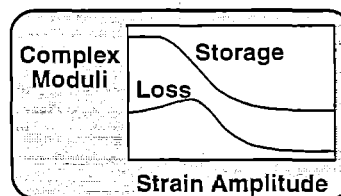2) frequency
3) low-strain nonlinearity

PENN**STATE**

- **Background & Motivation**

➡ • **Experimental Approach and Results** ⬅

- **Analytical Approach and Results**

- **Conclusions & Future Work**

Experimental Approach:
Key Related Research

PENN**STATE**

- **Beale, 1995, PSU, Harmonic shear testing**
  - medium to high dynamic amplitudes (>= 10%)
  - single & dual frequency
  - static strain offset

- **Byers, 1996-97, PSU, Temperature Effects**
  - medium to high dynamic amplitudes (>= 10%)
  - single frequency, - 40° F to +200° F
  - material self-heating (thermography system)
  - Validation of Hausmann's approach using PSU data

- **Payne, *et al*, 1962, UK**
  - Carbon black-filled natural rubber
  - Strain range: 0.1% to ~50%

- **Sternstein, *et al*, 1997, RPI**
  - Extended Payne's work to Silicone
  - Strain range: 0.1% to 10%

Complex Moduli — Storage, Loss vs. Strain Amplitude

Experimental Approach: PENNSTATE
Penn State Elastomeric Damper Research Activities

Experimental Characterization

- quasi-static behavior
- harmonic shear testing
- transient testing

  — low strain amplitude
  — temperature dependence
  — material self-heating
  — static precompression

Analytical Modeling

- helicopter elastomeric dampers
- Anelastic Displacement Fields (ADF) material model
- strain dependence (large strains)

Multiple-ADF model for:
  1) temperature
  2) frequency
  3) low-strain nonlinearity

Experimental Approach: PENNSTATE
Motivation

- **Low Strain Amplitude**
  1) Comanche low-amplitude limit cycle instabilities
     (Panda & Mychalowycz, Boeing)
  2) Little existing research (Payne, Sternstein)

- **Ambient Temperature Dependence**
  Army certification: -60° F to +120° F

- **Material Self Heating**
  Problems with V-22 Hub Springs

- **Static Pre-compression**
  Pitch bearings: high centrifugal loading

Experimental Approach:
Research Objectives

PENNSTATE

- Generate experimental data to support model characterization:
  low dynamic strain harmonic data at various temperatures and frequencies

- Generate additional experimental data to support model validation:
  time-domain data at various temperatures, including dual-frequency, quasi-static, and transient loadings

- Experimental study of precompression effects

Experimental Approach:
Schematic of Characterization Facility

PENNSTATE
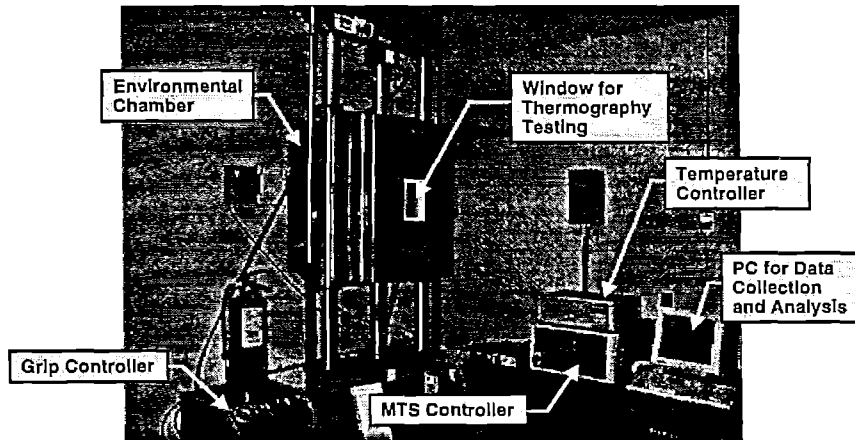
Experimental Approach: Test Specimens

Force @ 0.1% strain amplitude:
- Ⓐ ~ 3.6 lbs
- Ⓑ ~ 21.4 lbs

Ⓐ

Ⓑ

Elastomer

Medium to High Amplitude Specimen

Shear Direction

Precompression

Precompression

Low Amplitude Specimen
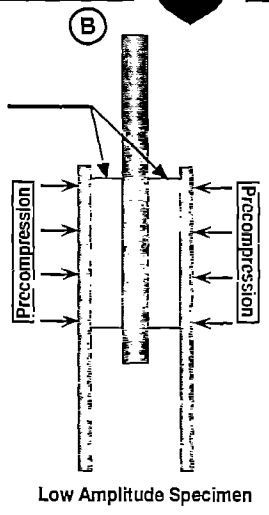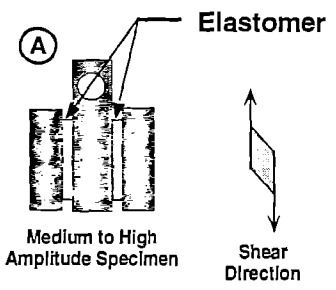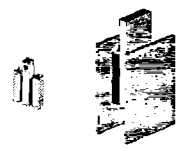
Specimen Types:
3 High Damping / Moderate Stiffness
1 Low Damping / High Stiffness
1 Low Damping / Low Stiffness

Experimental Approach: Current Test Matrix

Shear Strain Amplitude (%)

Frequency (Hz)	0.10	0.15	0.25	0.35	0.50	0.70	1.00	1.50	2.00	3.50	5.00	7.00	10.00	20.00	50.00
0.05															
0.10															
0.35															
1.00															
3.50															
10.00															
30.00															

Temperature (°F)

| -40	0	32	75	100	150	212

Precompression (% Strain)

0	10	22

Experimental Approach:
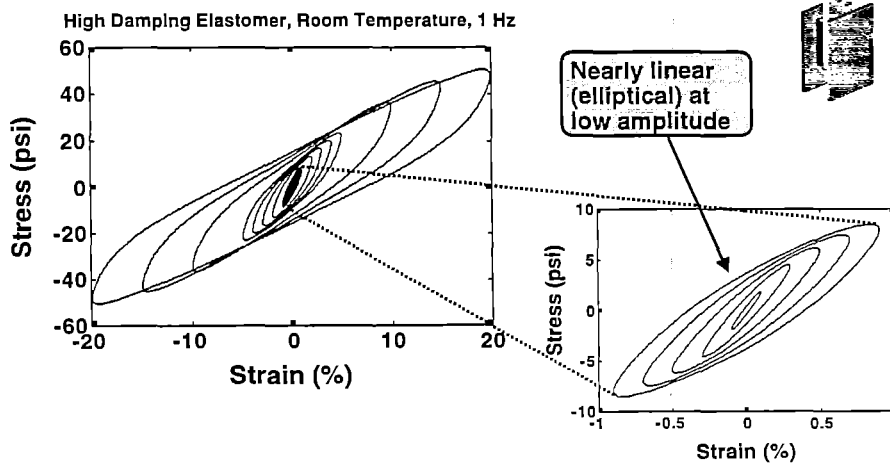*Typical Results*

- • **Material Hysteresis at Low Strain Amplitude**

- • **Material Hysteresis - Temperature Effects**

- • **Variation of moduli with amplitude and temperature**

- • **Variation of moduli with amplitude and frequency**

- • **Variation of moduli with amplitude and precompression**

Typical Experimental Results:
Material Hysteresis at Low Strain Amplitude

Variation of material hysteresis with strain amplitude:

High Damping Elastomer, Room Temperature, 1 Hz
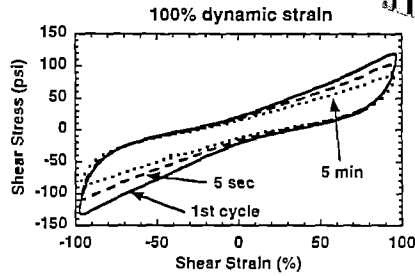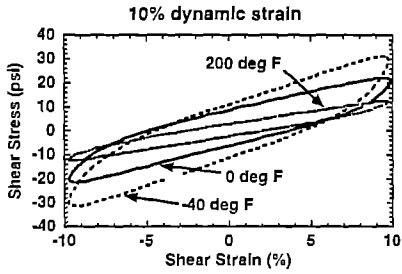

Nearly linear (elliptical) at low amplitude

Typical Experimental Results: Material Hysteresis - Temperature Effects

PENNSTATE

High Damping Elastomer, 4 Hz forcing:

Ambient Effects:
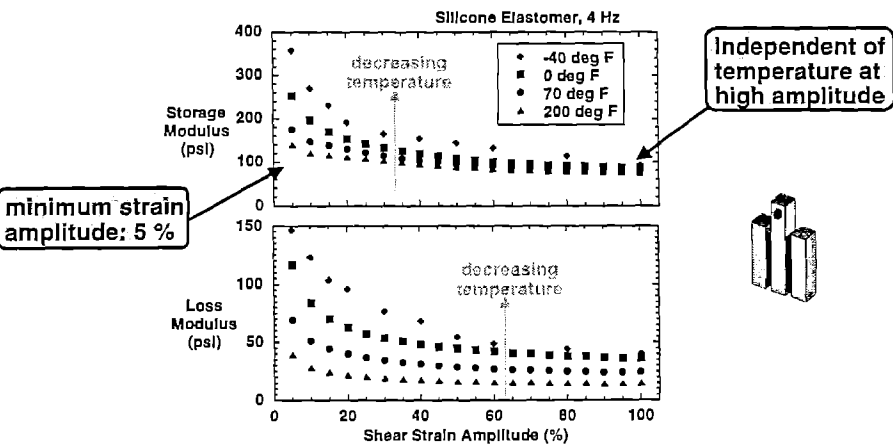
slope and area decrease with increasing temperature

Self Heating Effects:

slope and area decrease with time (material hysteresis)

Typical Experimental Results: Variation of Material Complex Moduli

PENNSTATE

Variation of moduli with amplitude and temperature:

Independent of temperature at high amplitude

minimum strain amplitude: 5 %

Typical Experimental Results:
Variation of Material Complex Moduli

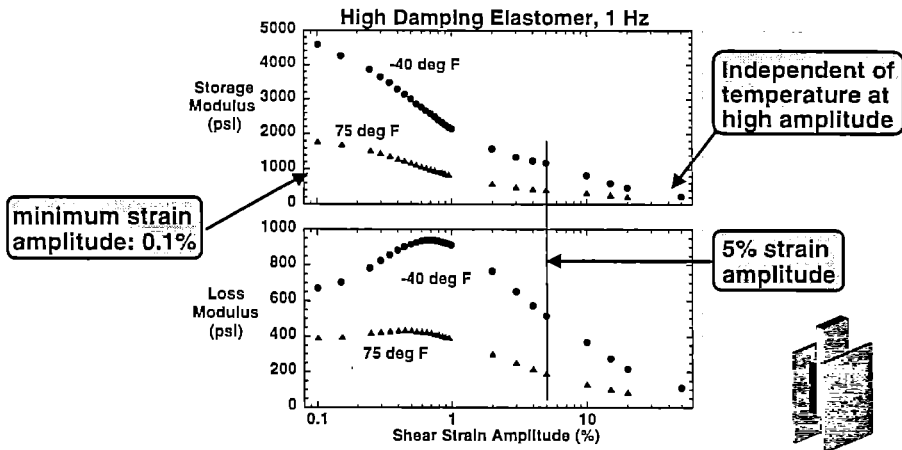PENNSTATE
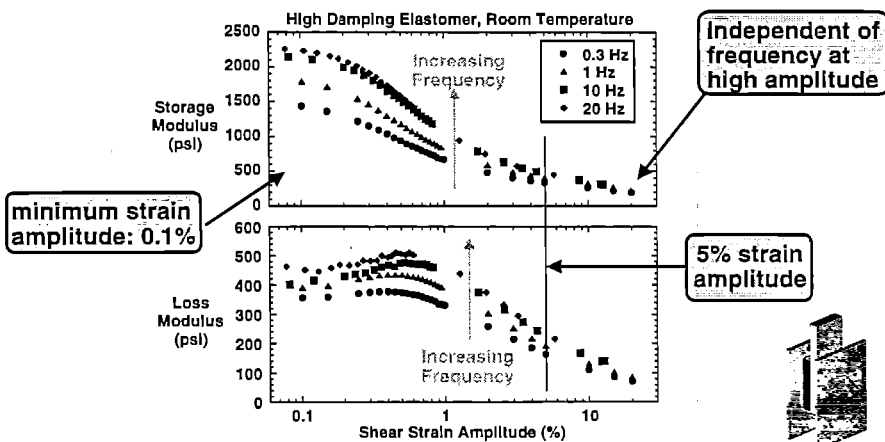
Variation of moduli with amplitude and temperature:

High Damping Elastomer, 1 Hz

Storage Modulus (psi)

-40 deg F

75 deg F

Independent of temperature at high amplitude

minimum strain amplitude: 0.1%

Loss Modulus (psi)

-40 deg F

75 deg F

5% strain amplitude

Shear Strain Amplitude (%)

Typical Experimental Results:
Variation of Material Complex Moduli

PENNSTATE

Variation of moduli with amplitude and frequency:

High Damping Elastomer, Room Temperature

Storage Modulus (psi)

Increasing Frequency

- 0.3 Hz
- 1 Hz
- 10 Hz
- 20 Hz

Independent of frequency at high amplitude

minimum strain amplitude: 0.1%

Loss Modulus (psi)

5% strain amplitude
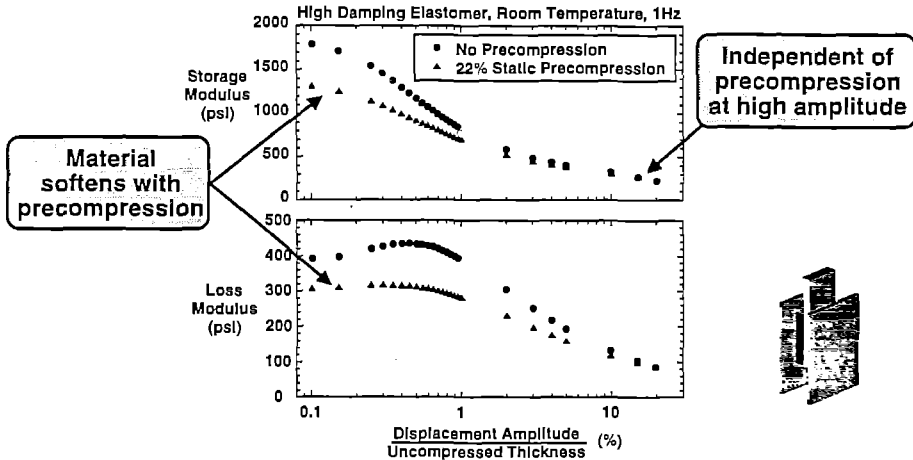
Increasing Frequency

Shear Strain Amplitude (%)

Typical Experimental Results:
Variation of Complex Moduli with Precompression

PENNSTATE

Variation of moduli with amplitude and precompression:

High Damping Elastomer, Room Temperature, 1Hz

- No Precompression
- 22% Static Precompression

Independent of precompression at high amplitude

Material softens with precompression

Storage Modulus (psi)

Loss Modulus (psi)

$\dfrac{\text{Displacement Amplitude}}{\text{Uncompressed Thickness}}$ (%)

Experimental Results:
Discussion

PENNSTATE

- **Hysteresis trends**
  - Hysteresis loops become elliptical at very low strains
  - Slope and area decrease with increasing temperature
  - Characteristic nonlinear shape at high amplitude

- **Moduli trends**
  - Peak in loss moduli coincides with the largest rate of change of the storage moduli
  - Storage modulus independent of temperature, frequency, and precompression at high amplitude
  - Moduli appear to level off at very low & very high strains

Presentation Outline

- Background & Motivation

- Experimental Approach and Results

⇒ - Analytical Approach and Results ⇐

- Conclusions & Future Work

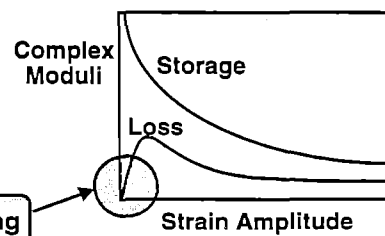**Analytical Approach:**
Key Related Research

Low Strain Amplitude Nonlinearity:

- Hausmann & Gergely, 1992, MBB

- Gandhi and Chopra, 1994-96, U.Maryland

Complex Moduli — Storage — Loss — Strain Amplitude

Enforced "zero" damping at "zero" amplitude

- Panda, *et al*, 1995-97, Boeing
  - "Variable Friction Damping" / Nonlinear Spring model
  - Addressed dual frequency and low-amplitude limit cycle behavior

Analytical Approach:
Key Related Research

PENNSTATE

Penn State Modeling Approaches:

- **Govindswamy, *et al,* 1994-95, PSU**
  - Characterization and Validation of a nonlinear Anelastic Displacement Fields (ADF) Model
  - Limited to larger dynamic amplitudes (>= 10% strain amplitude)
  - rigid blade aeroelastic stability analysis
  - single frequency

- **Brackbill, *et al,* 1995-96, PSU, temperature effects**
  - medium to high dynamic amplitudes (>= 1% strain amplitude)
  - broad temperature range: - 70° F to +300° F
  - material self-heating
  - introduction to multi-ADF model (improved temperature & frequency performance)

> **Nonlinearities:** short-time (elastic) response, material relaxation behavior, and the static response

---

Analytical Approach:
Key Related Research

PENNSTATE

Nonlinear Viscoelasticity:

- **Strganac, Texas A&M, 1997**
  - focus on "nonlinear time-dependent response"
  - concept of "time-stress superposition"
  - related to research by Schapery

- **Johnson, *et al,* Army Research Lab, 1993-1997**
  - large-strain nonlinear viscoelasticity
  - "stretch ratios" as internal variables
  - time-domain finite element modeling

> **Concentrate on nonlinearity in the material relaxation behavior**

Background and Motivation:
Penn State Elastomeric Damper Research Activities

PENN STATE

Experimental Characterization

* quasi-static behavior
* harmonic shear testing
* transient testing

— low strain amplitude
— temperature dependence
— material self-heating
— static precompression

Analytical Modeling

* helicopter elastomeric dampers
* Anelastic Displacement Fields (ADF) material model
* strain dependence (large strains)

Multiple-ADF model for:
1) temperature
2) frequency
3) low-strain nonlinearity

Analytical Approach:
Objectives

PENN STATE

* **Develop an initial linear model for combined temperature and frequency dependence**
  Method of Anelastic Displacement Fields

* **Develop a refined nonlinear modeling approach**
  Improved performance over low strain amplitude range

* **Validate the material model**
  Compare to time-domain experimental data
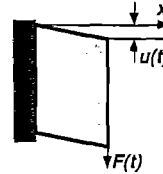
Initial linear multi-ADF model for temperature and frequency dependence:

Constitutive Equations

$$\sigma = G_u \left(u' - \sum_{i=1}^{N} u_i'^A \right)$$

Anelastic strain

Unrelaxed dynamic shear modulus

Material in Simple Shear

$$\sigma_i^A = G_u \left(u' - c_i u_i'^A \right) = \alpha_T \frac{c_i G_u}{\Omega_i} \dot{u}_i'^A \quad \textbf{(N equations)}$$

Total strain

Coupling parameter

Inverse of relaxation time

Temperature Shift Function

In general, a multi-ADF model is used for materials with "weaker" frequency dependence (i.e. elastomers):

Storage
Modulus

1-ADF Model

multi-ADF Model
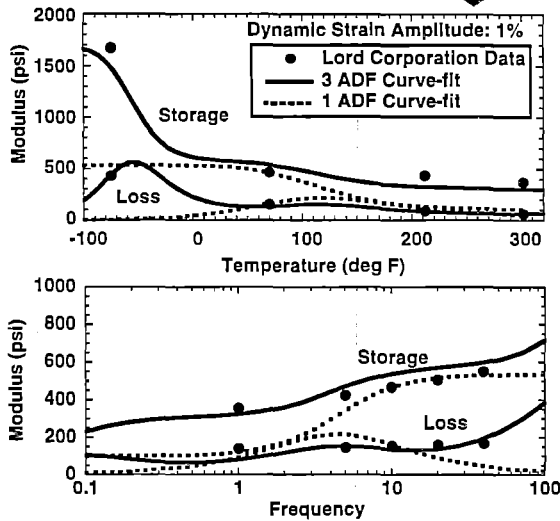
Increasing Frequency ⟹
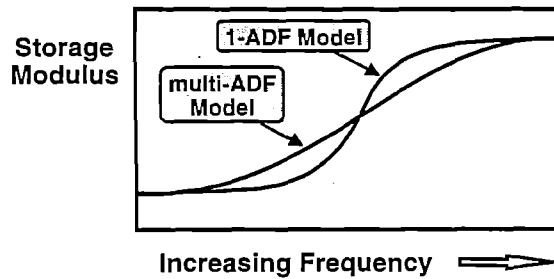
⟹ Multi-ADF model is more effective over a broad temperature and frequency range

Analytical Approach:
Linear Curve-fit Example

PENN**STATE**

- Fit linear Multi-ADF model to *low-amplitude* data

- Data should be nearly *linear* and include several temperatures and frequencies

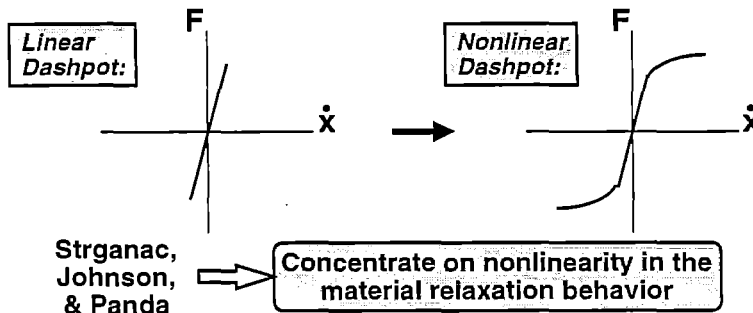- Note: Example uses 1% strain amplitude - too large

Dynamic Strain Amplitude: 1%
● Lord Corporation Data
— 3 ADF Curve-fit
----- 1 ADF Curve-fit

Storage
Loss

Modulus (psi)
2000
1500
1000
500
0
-100   0   100   200   300
Temperature (deg F)

Modulus (psi)
1000
800
600
400
200
0
0.1   1   10   100
Frequency

Storage
Loss

Analytical Approach:
Nonlinear Model for Amplitude Dependence

PENN**STATE**

- **Current approach:** modify the internal relaxation behavior of the material using nonlinear functions of the anelastic stress

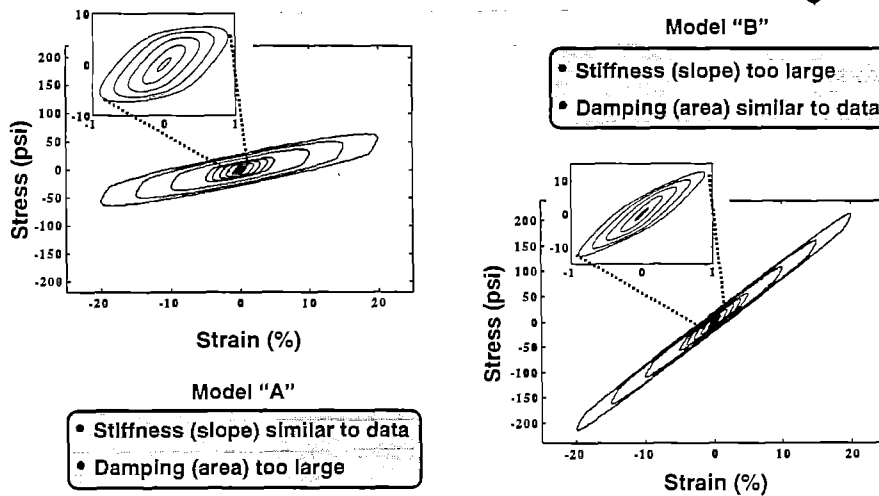- Curve-fit nonlinear equations to experimental stress time-histories

Linear Dashpot:
F
x̊

Nonlinear Dashpot:
F
x̊

Strganac, Johnson, & Panda

Concentrate on nonlinearity in the material relaxation behavior

Analytical Approach:
Nonlinear Model Synthesis

PENNSTATE
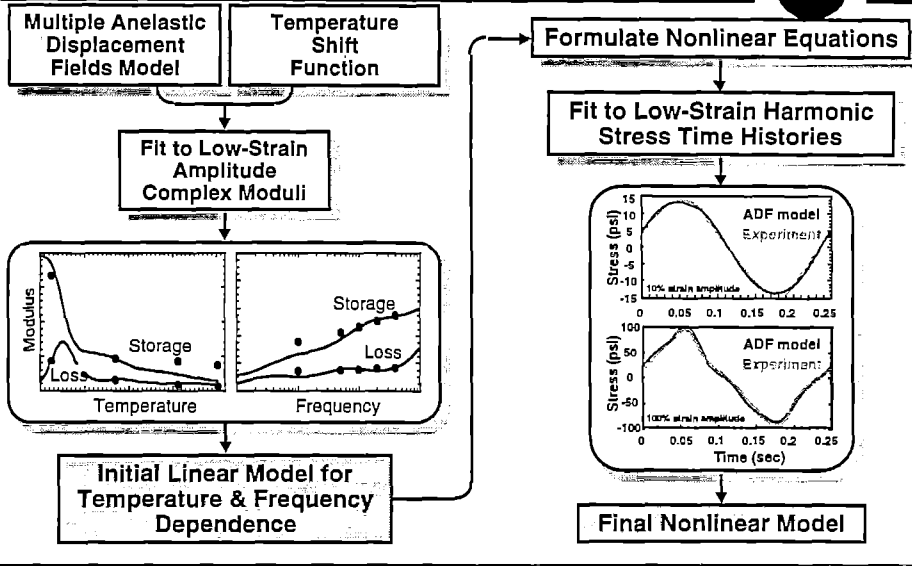
Analytical Study:
Variation of Material Hysteresis Behavior

PENNSTATE

Analytical Study:
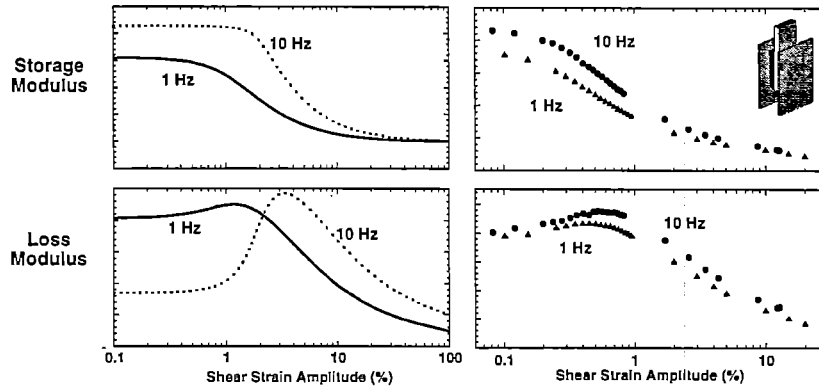**Variation of Material Complex Moduli**

PENNSTATE

Variation of Moduli with Amplitude and Frequency
for a High Damping Elastomer at Room Temperature

Analytical Results:
Discussion

PENNSTATE

- **Initial linear model**
  - Linear Multi-ADF model fits material complex modulus data over a range of frequencies and temperatures
  - Initial characterization used data at 1% strain amplitude: NOT linear data

- **Nonlinear model**
  - Peak in loss moduli coincides with the largest rate of change of the storage moduli - trend matches experimental data
  - Nonlinear predictions are not accurate over a broad frequency and temperature range: most likely due to incorrect linear characterization

Presentation Outline

PENNSTATE

- Background & Motivation

- Experimental Approach and Results

- Analytical Approach and Results

⇨• Conclusions & Future Work ⇦

Conclusions

PENNSTATE

<u>Experimental:</u>
- Low strain amplitude harmonic data was generated over the following ranges:
  - Amplitudes: 0.1 to 50%
  - Frequencies: 0.05 to 40Hz
  - Temperatures: -40 to 200°F
  - With and without precompression

- Dynamic material property trends:
  - Linear behavior at very low strains
  - Dynamic properties change rapidly as strain amplitude increases
  - Properties are relatively independent of temperature, frequency, and precompression at high amplitude

Conclusions

<u>Analytical Model</u>:

- A nonlinear model was developed in the following manner:
  - An initial linear model was developed to capture the material temperature and frequency dependence
  - Nonlinear relaxation behavior was introduced to model the material amplitude dependence

- Analytical modeling trends
  - Dynamic material properties are captured over a range of frequencies and temperatures at a specific strain amplitude (linear model)
  - Dynamic material properties are captured over a range of strain amplitudes for a specific frequency and temperature (full nonlinear model)

Future Work

- Low strain amplitude harmonic data is currently being generated using the 5 new test specimens

- Time domain data for model validation will be generated in the following forms:
  - dual frequency
  - quasi-static
  - transient loadings
  - material self-heating

- The linear model will be characterized using very low strain amplitude data

- Nonlinear model characterization and validation will then proceed

Rotorcraft Lag Damping Using Highly Distributed Tuned Vibration Absorbers

Chad A. Hébert
Graduate Research Assistant

George A. Lesieutre
Associate Professor

Rotorcraft Center of Excellence
Department of Aerospace Engineering
The Pennsylvania State University

Abstract

Damping of the rotor blade lag mode is especially critical in soft in-plane rotors. Lag damping is typically provided by hydraulic or elastomeric dampers. An alternative approach to providing damping over a broad frequency range is presented. This is accomplished with multiple individual vibration absorbers which are highly distributed in both space and frequency. The mass for the absorbers comes from a portion of the mass of the leading edge weight structure already incorporated into the blade. These absorbers are modeled as frequency dependent mass which is distributed along an elastic blade. By varying the number of discrete tuning frequencies, mass per unit length of the absorber system, loss factor of spring material and frequency range of the absorbers, the amount of damping produced can be varied. Through careful selection of these design parameters, substantial damping over a broad frequency range is obtained. In an initial conceptual, these absorbers are embedded inside the blade leading edge weight structure, which reduces total rotor weight, complexity and drag. In addition, future research issues critical to the effective implementation of this concept are addressed.

Rotorcraft Lag Damping Using Highly Distributed Tuned Vibration Absorbers

Chad A. Hébert

George A. Lesieutre

Penn State University
Aerospace Engineering

7th Intl. Workshop on Dynamics & Aeroelastic
Stability Modeling of Rotorcraft Systems
October, 1997
St. Louis, MO

Overview

- Background : Lag Damping

- Concept : Highly Distributed Vibration Absorbers

- Model : Blade with Absorber System

- Results

- Summary & Future Research

Rotorcraft Lag Damping

- Soft in-plane rotors, air & ground resonance

  - Hydraulic
  - Elastomers
  - Active Constrained Layers
  - Electrorheological Fluids
  - Magnetorheological Fluids

Lag Dampers

- Current approaches
  - Increase total rotor weight
  - Increase complexity of rotor system
  - Increased rotor hub drag

- Proposed approach
  - Use mass of existing leading edge weights
 - Provide adequate damping
  - Reduce rotor weight, complexity, drag

Damping Using Highly Distributed Tuned Vibration Absorbers
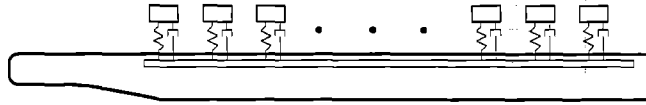
- Zapfe, 1997

- Multiple individual vibration absorbers highly distributed

  in both **SPACE** and **FREQUENCY**

- Frequency dependent elastic foundation,

  distributed damping or *distributed mass*

Vibration Absorber System In Blade

- Leading edge weights approx. 15 - 20 %
  of blade weight

- Portion of L. E. weights used in
  vibration absorber system
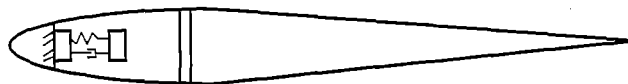

- Previously inert mass now productive in damping

Frequency Dependent Mass

- Absorber system modeled as a frequency dependent complex mass per unit length

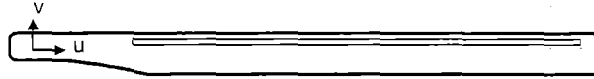$$\rho A_d(\omega) = \sum_{i=1}^{N} \frac{\rho A_i \, \omega_i^2 \left(1 + j\eta_i\right)}{\omega_i^2 \left(1 + j\eta_i\right) - \omega^2}$$

N - number of discrete tuning frequencies
ρA_i - mass per unit length
ω_i - natural freq. of ith portion of absorber
η_i - loss factor of spring material

Frequency Dependent Mass

- Combination of Individual Vibration Absorbers
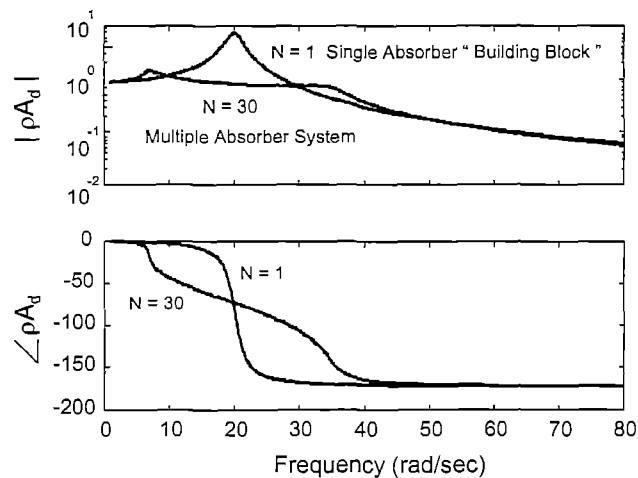
Blade Model

- Hingeless blade modeled as an elastic beam

- Lag motion

$$\rho A \ddot{v} + EI_{zz}(v'')'' - Pv'' - \rho A \Omega^2 v = P_y(x,t)$$

$$\text{where} \quad P = \int_x^L \rho A \Omega^2 x_1 dx_1 \longrightarrow \text{CF Load}$$
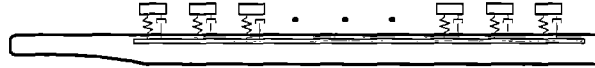
- Finite element discretization

$$[M]\left\{\ddot{q}\right\} + \left[[K] + \Omega^2([K_G] - [M])\right]\left\{q\right\} = \{F(q,t)\}$$

Nominal Blade / Rotor Parameters

- Operating speed : $\Omega_{Nominal}$ = 28 rad/sec

- Non-dimensional rotating lag frequency : ν_ζ = .62 / rev

- Blade length = 8 m, blade chord = 0.5 m

- Blade mass = 139 kg

Blade with Absorber System Model

- Outboard of blade flexure
- Initial collocation of section mass centers
- Distributed continuous system
- Complex mass and stiffness

$$[M(\omega)]\{\ddot{q}\} + [[K] + \Omega^2([K_G] - [M(\omega)])]\{q\} = \{F(q,t)\}$$

→ Model used to study dynamic behavior of blade with absorber system

- Iterative eigensolution

Design Parameters

- N - number of discrete tuning frequencies (ω_i)

- ρA_i - mass per unit length of absorber system

- η_i - loss factor of spring material

- Frequency range of absorbers

Absorber Tuning Frequency Range

- Range of absorber tuning frequencies should include:
  - Blade natural vibration frequencies
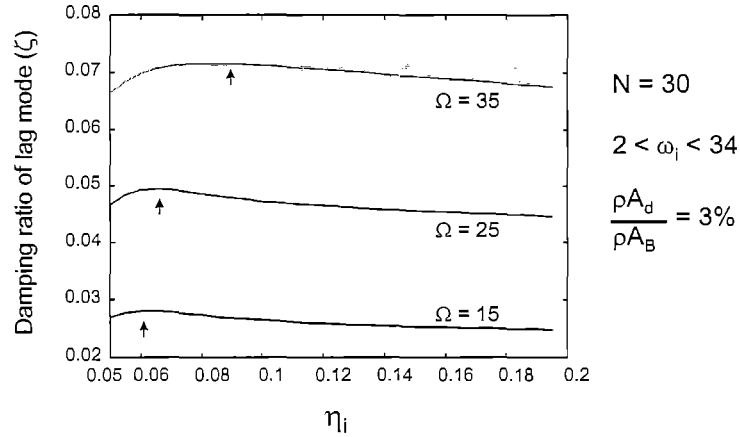 - Progressive low frequency lag mode
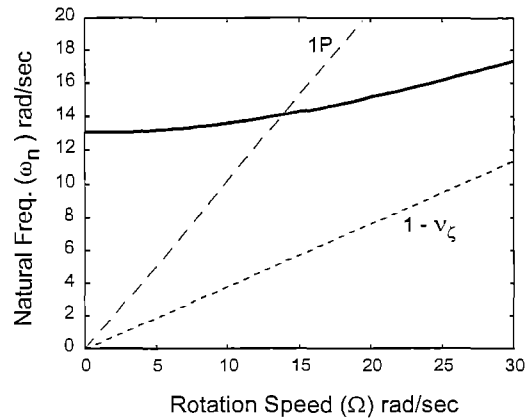
Relationship Between N and η_i
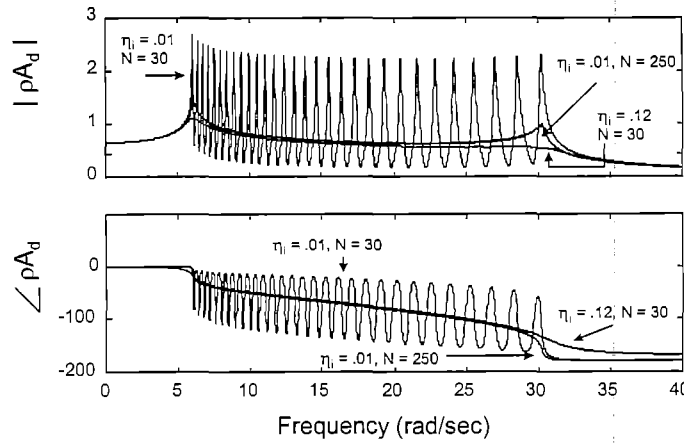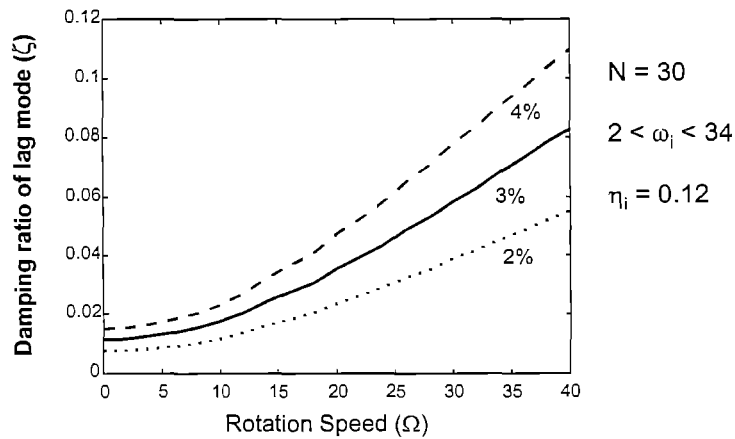

→ Desire Smooth Response with Frequency
  - N small for producibility
  - Reasonably high η_i

Selecting Loss Factor of Absorbers

N = 30

$2 < \omega_i < 34$

$\dfrac{\rho A_d}{\rho A_B} = 3\%$

➡ $\eta_i \geq .07$ for optimal damping at various rotation speeds

Selecting Absorber / Blade Mass Ratio

N = 30

$2 < \omega_i < 34$

$\eta_i = 0.12$

➡ Damping ratio increases with mass ratio and rotation speed

Selecting Tuning Frequency Range

- Constant absorber / blade mass ratio = 3 %

Plot axes: Damping ratio of lag mode (ζ) vs Rotation Speed (Ω). Curves labeled 6-30 (rad/s), 2-34 (rad/s), 18 (rad/s).
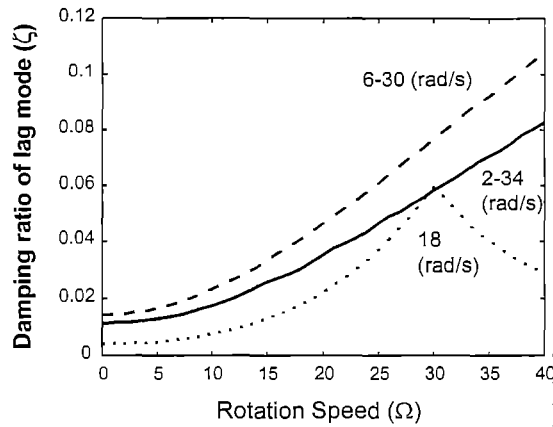
➡ Smaller tuning range yields higher damping

Conceptual Design
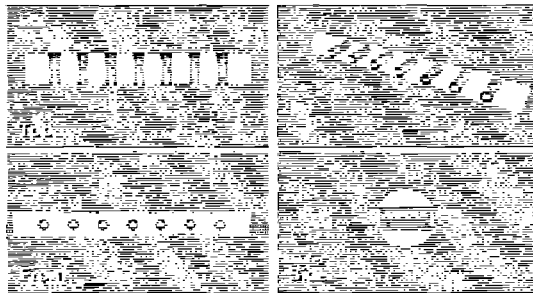
- Mass surrounded by rubber embedded in leading edge weight structure

Summary & Conclusions

- Multiple vibration absorbers highly distributed
  both in **SPACE** and **FREQUENCY**

- Inert mass now productive

- Promising damping results without
  added weight, complexity and drag

- Optimization of design (N, η_i, ω_i, ρA_i)
  provides substantial damping of the lag mode

Future Research

- Physical realizations
  - Fit within leading edge weight envelope
  - Stroke must not impact inner cavity of blade

- Effect on c.g. of blade cross-section
  - Blade flap - lag - torsion coupling; aerodynamics
  - Helicopter and blade stability

- Experimental Demonstration
  - Effective implementation
  - Performance